Readings and materials for Ray Krone's course on Cohesive Sediment Transport, 1991, thanks to preservation by Jamie Anderson until 2025. Some lessons are eternal.

DEPARTMENT OF CIVIL ENGINEERING University of California, Davis

ECI 261, CCOHESIVE SEDIMENT TRANSPORT

I CLAY MINERALS

Particle shapes, dimensions
Crystal structure of clay minerals
Surface charges and cation exchange capacities

II COHESION OF SUSPENDED PARTICLES

Double layer theory
Factors that determine the distribution of sorbed ions
Sodium Adsorption Ratio
London-Van der Waals' forces
Cohesion/Dispersion boundaries

III AGGREGATION PROCESSES

Brownian motion
Differential settling velocities
Velocity gradients
Relative rates of aggregation

IV MECHANICAL PROPERTIES OF AGGREGATES FORMED IN VELOCITY GRADIENTS

Aggregate structures
Aggregate densities
Aggregate shear strengths

V DEPOSITION OF SUSPENDED PARTICLES

Settling velocities

Deposition when aggregation rates are slow

Deposition during rapid aggregation

Interchange with bed and sorting

Relation of aggregate properties to bed surface properties

Deposition from high concentration suspensions

VI BED PROPERTIES

Consolidation
Gelling
Role of organisms
Density and shear strength profiles

VII EROSION PROCESSES

Surface and bulk erosion Erosion by currents Erosion by waves

Cohesive Sediment Transport 3-7-87

VIII ESTUARIAL HYDRODYNAMICS

Tides
Resonances
Mixing zone stratification and circulations
Seasonal changes
Wind effects

IX SEDIMENT SOURCES

River sources
Shelf sources
Bank erosion and aeolian sources

X SEDIMENT CIRCULATION IN ESTUARIES

Temporal aspect of transport processes
Sediment losses
Sediment budgets
Effects of changing sediment input

XI EFFECTS OF SUSPENDED SEDIMENT ON WATER QUALITY Algae control

Sorption and scavenging of toxic materials

XII DESIGN OF NAVIGATION FACILITIES FOR MINIMUM SHOALING RATES

Harbor enclosures and walls
Minimizing deposition rates
Maximizing erosion of material deposited during slack water

XIII MODELING COHESIVE SEDIMENT TRANSPORT

Problems suitable for modeling
Obtaining current, tide, and wave data
Boundary conditions
Advection -- diffusion equation
Source and sink functions
Problems with settling velocities
Representing the sediment bed
Modeling systems over long times

There is no text for this course. Copies of reports and papers will be provided. Course ECI 260, NON-COHESIVE SEDIMENT TRANSPORT is recommended preparation. A field trip to selected sites on the San Francisco Bay system is included in the course.

One problem set is assigned each week. A term paper on a relevant subject of your choice is required. A take-home final examination will be distributed on the last class period. Grades will be based on 40% homework, 40% final examination, and 20% on the term paper.

Cohesive Sediment Transport 3-7-87

Look up:

pyrophyllite:

colloidal:

amorphous:

CHAPTER 3

Soil Mineralogy

3.1 INTRODUCTION

Although it is not possible at the present time to express the engineering properties of a soil quantitatively in terms of composition, a knowledge of soil mineralogy is essential to a fundamental understanding of soil behavior. Mineralogy is the primary factor controlling the size, shape, and physical and chemical properties of soil particles.

The solid phase of a given soil may contain various amounts of crystalline clay and nonclay minerals, noncrystalline clay material, organic matter, and precipitated salts. The inorganic, crystalline minerals comprise by far the greatest proportion of the solid phase in most soils encountered in engineering problems, and the amount of nonclay mineral is usually considerably greater than the proportion of clay minerals present. However, the clay may influence behavior to an extent much greater than in simple proportion to the amount present.

The term "clay" is sometimes ambiguous. When used as a particle size term, it refers to all constituents of a soil smaller than some given size, usually 2 μm. As a mineral term it refers to specific minerals termed the "clay minerals". Clays are small crystalline particles of one or more members of a small group of minerals. They are primarily hydrous aluminum silicates, with magnesium or iron occupying all or part of the aluminum positions in some minerals, and with alkalis (e.g., sodium, potassium) or alkaline earth (e.g., calcium, magnesium) also present as essential constituents in some of them (Grim, 1962, 1968). Not all clay mineral particles are finer than 2 µm (or whatever boundary may be chosen to define a clay size) nor are all nonclay minerals coarser than 2 μ m. Thus, the amounts of clay size and clay mineral in

any soil may not be the same. To avoid confusion, it is best to use clay size when referring to compositions in terms of particle size and clay mineral content or simply clay content when speaking of mineral compositions.

The physical characteristics of cohesionless, nonclay soils are determined mainly by particle size, shape, surface texture, and size distribution. The mineral composition is of importance primarily as it influences hardness, cleavage, and resistance to chemical attack that determine these characteristics. By and large, however, the nonclay particles may be treated as relatively inert materials whose interactions are predominantly physical in nature. Convincing evidence in support of this has been obtained recently through study of the properties of lunar soils. Soils on the Moon have a silty, fine sand gradation, but their composition is totally different than that of terrestrial soils. The engineering properties of lunar soils and terrestrial fine sands are remarkably similar, however.

The clay minerals occur in particles of such small size that physico-chemical interactions with each other and with the water-electrolyte phase of a soil may be great. The clay phase may exert an influence on physical properties far exceeding its relative abundance in the soil.

The small size of clay particles precluded study of details of their structure prior to development of X-ray diffraction methods. Since then the study of clay minerals has been very extensive, aided in addition by the development of such techniques as electron microscopy, differential thermal analysis, and the electron probe. A large number of different clay minerals have been identified on the basis of composition. On the basis of structure, however, these minerals fall into a relatively small number of groups, and, fur-

thermore, only a limited number of the different minerals are found with a significant abundance in the soils commonly encountered in engineering practice.

3.2 NONCLAY MINERALS IN SOILS

The gravel and sand fractions as well as the bulk of the silt fraction of a soil are composed of nonclay minerals. As soils are the products of the breakdown of pre-existing rocks and soils, they represent products of weathering. It would be expected, therefore, that the predominent mineral constituents of any soil would be those that are one or more of the following:

- 1. Very abundant in the source material.
- 2. Highly resistant to weathering, abrasion, and impact.
- Weathering products.

The clay minerals are generally derived from weathering of pre-existing materials. The predominant nonclays, however, are usually rock fragments or mineral grains of the common rock-forming minerals. In igneous rocks, which represent the original source material for many soils, the most prevalent minerals are the feldspars (about 60 percent) and the pyroxenes and amphiboles (about 17 percent). Quartz accounts for about 12 percent of these rocks, micas for 4 percent, and other minerals for about 8 percent.

In most soils, however, the most abundant nonclay mineral by far is quartz, with small amounts of feldspar and mica sometimes present. The pyroxenes and amphiboles are seldom found to any significant extent. Carbonate minerals, mainly calcite and dolomite, are also found in some soils and occur as bulky particles, shells, precipitates, or in solution. Carbonates may dominate the composition of some deep sea sediments. Iron and aluminum oxides are abundant in residual soils of tropical regions.

Quartz is composed of silica tetrahedra grouped in such a way as to form spirals, with all tetrahedral oxygens bonded to silicon. As discussed in Chapter 2, the tetrahedral structure has a high stability. In addition, the spiral grouping of tetrahedra produces a structure without cleavage planes, quartz is already an oxide, there are no weakly bonded ions in the structure, and the mineral has a high hardness. These factors account for the persistence of quartz in the nonclay fraction of soils.

In the case of the feldspars, Marshall (1964) states: "The predominance of the feldspars among minerals of the lithosphere" makes their disappearance by

The solid part of the earth.

weathering quantitatively the most important chemical reaction since solidification of the earth's crust." The feldspars are silicate minerals with a three-dimensional framework structure wherein part of the silicon is replaced by aluminum. The excess negative charge resulting from this replacement is balanced by cations such as potassium, calcium, sodium, strontium, and barium. As these cations are relatively large, their coordination number is also large. This results in the formation of an open structure and low bond strengths between units. As a consequence, there are cleavage planes, the hardness is only moderate, and feldspars are relatively easily broken down, which accounts for their lack of abundance in soils as compared to their abundance in igneous rocks.

Mica has a sheet structure composed of tetrahedral and octahedral units. Sheets are stacked one on the other and bonded primarily by potassium ions in 12-fold coordination that provide an electrostatic bond of moderate strength. In comparison with the bonds within layers, however, this bond is weak, thus accounting for the perfect basal cleavage of the micas. As a result of the platy morphology of mica plates, sand and silts containing only a few percent mica

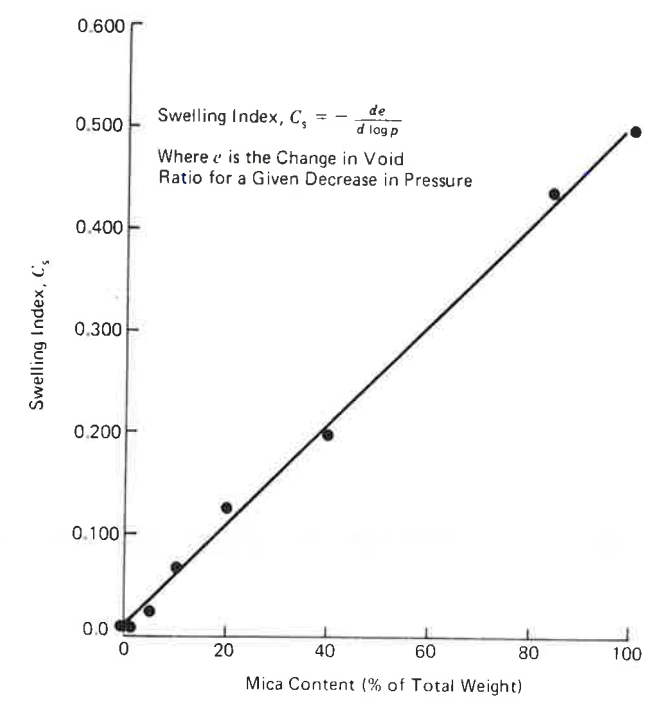


Fig. 3.1 Swelling index as a function of mica content for coarse-grained mixtures (Data from Terzaghi, 1931).

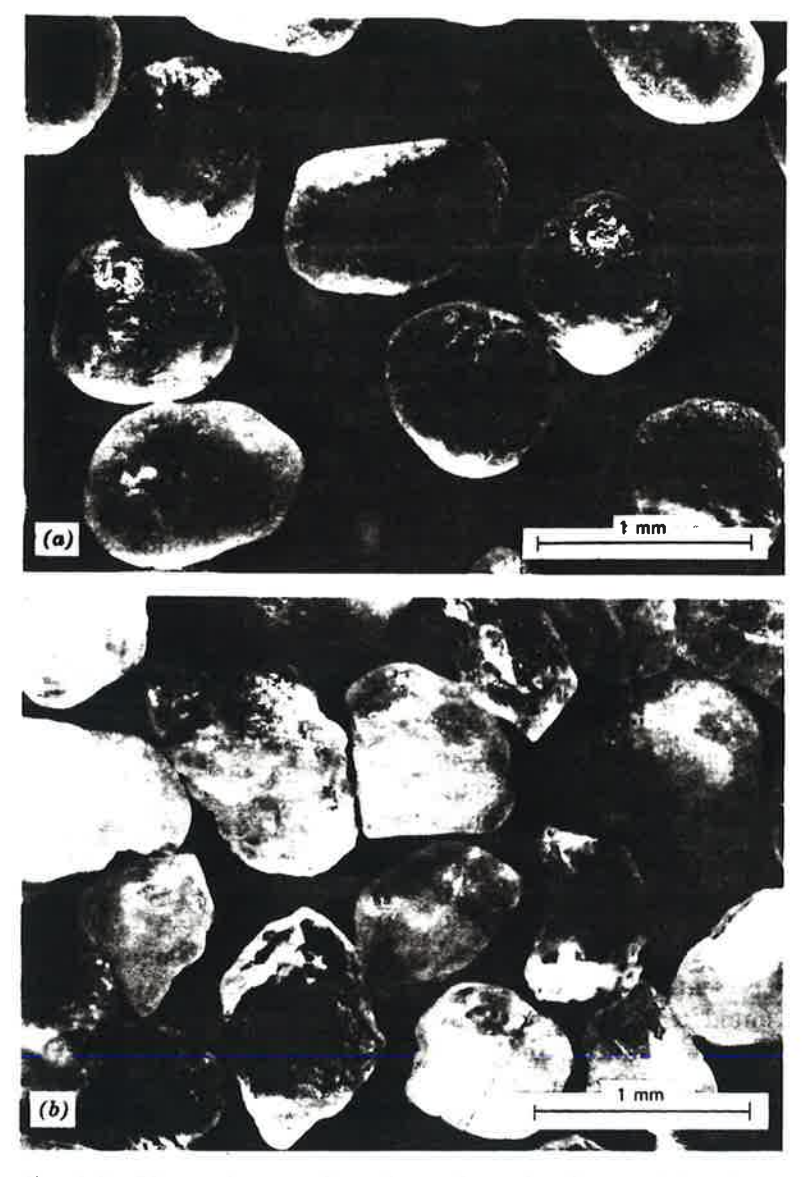


Fig. 3.2 Photomicrographs of sand and silt particles from several soils (a) Ottawa standard sand (Courtesy K. L. Lee). (b) Monterey sand (Courtesy K. L. Lee). (c) Sacramento River sand. (d) Eliot sand (Courtesy K. L. Lee). (e) Lunar soil mineral grains (Photo Courtesy Johnson Space Center). Squares in background area are 1 × 1 mm. (f) Recrystallized breccia particles from lunar soil (Photo Courtesy Johnson Space Center). Squares in background grid are 1 × 1 mm.

may exhibit both high compressibility and large swelling during unloading, as may be seen in Fig. 3.1 for coarse-grained mixtures of sand and mica.

The crystal structures and compositions of the amphiboles, pyroxene, and olivine are such that they are rapidly broken down by weathering; hence, they are absent from most soils.

Examples of silt and sand particles from different natural soils are shown in Fig. 3.2. Such particles can be classified in terms of angularity or roundness. Figure 3.3 shows one system that has been used for this purpose. Elongated and platy particles in soils can give rise to preferred orientations, which, in turn, can result in anisotropic mechanical properties.

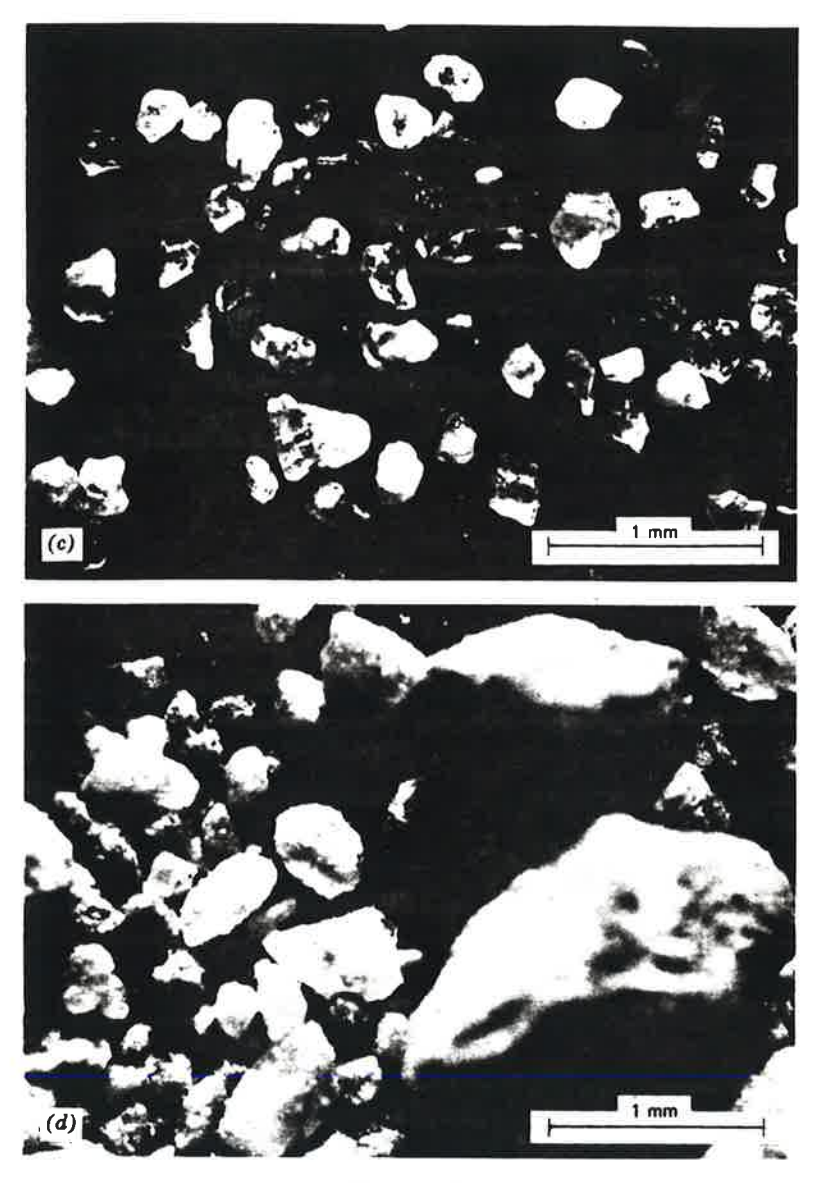


Figure 3.2 (continued).

Another characteristic that influences mechanical behavior is the surface texture.

3.3 STRUCTURAL UNITS OF THE LAYER SILICATES

The clay minerals that are commonly found in soils belong to the larger mineral family termed phyllosilicates, which also contains other layer silicates such as serpentine, pyrophyllite, talc, mica, and chlorite that are themselves considered clay minerals by some when they occur in the clay-size fraction of a soil. The clay minerals usually occur in small particle sizes, and they ordinarily have unit cells with a resid-

ual negative charge. Most clay minerals exhibit plasticity when mixed with limited amounts of water, and they have relatively high resistance to weathering.

The structures of the common layer silicates can be considered in terms of two simple structural units. The different clay mineral groups are characterized by the stacking arrangements of sheets* (sometimes chains) of these units and the manner in which two successive two- or three-sheet layers are held together.

• In conformity with the recommendations of the Nomenclature Committee of the Clay Minerals Society (Bailey et al., 1971), the following terms are used: a plane of atoms, a sheet of basic structural units; and a layer of unit cells composed of two, three, or four sheets.

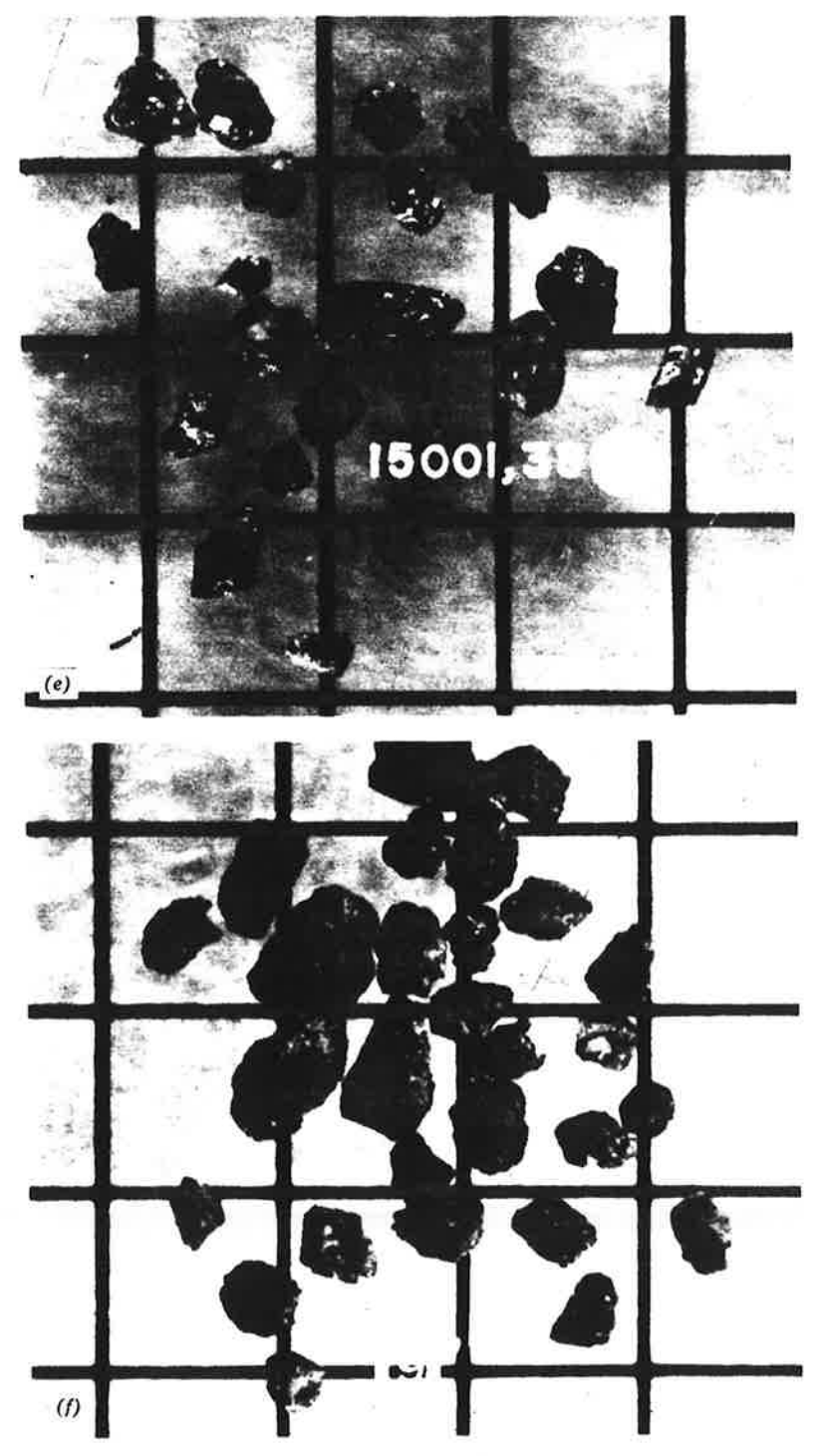


Figure 3.2 (continued).

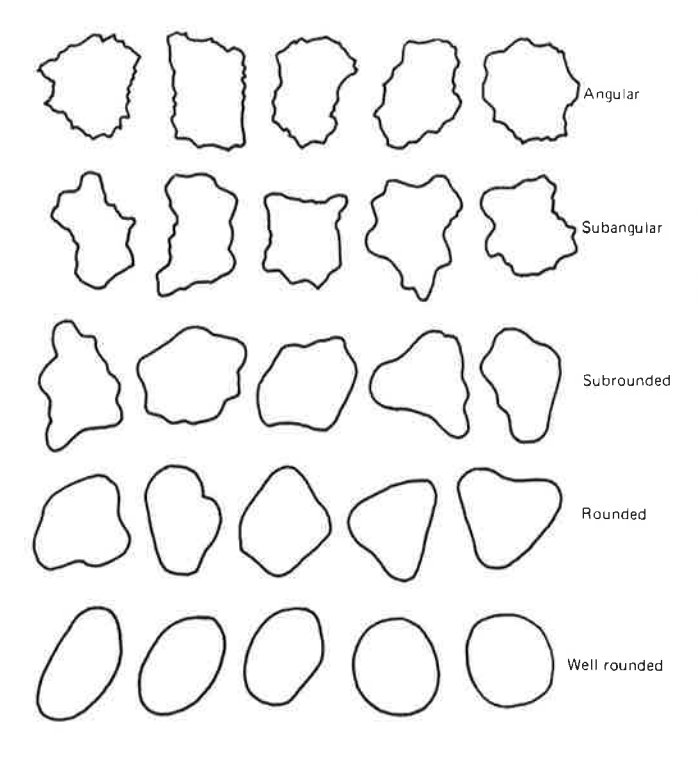


Fig. 3.3 Classification of shapes for sand and silt size particles. (Roundness of mineral particles as seen in silhouette; Müller, 1967).

Differences among minerals within clay mineral groups arise chiefly from differences in the type and amount of isomorphous substitution within the crystal structure. Because the possible substitutions are nearly endless in number, and because the development of crystal structure may range from very poor to nearly perfect, it is not surprising that the study of clay minerals appears imposing to the beginner, and the classification and naming of clay minerals provides an endless challenge to the expert. However, a

knowledge of the structural and compositional characteristics of each group without detailed study of the subtleties of each specific mineral is adequate for many engineering purposes.

The two basic units in clay mineral structures are the silica tetrahedron, with a silicon ion tetrahedrally coordinated with four oxygens, and the aluminum or magnesium octahedron, wherein an aluminum or magnesium ion is octahedrally coordinated with six oxygens or hydroxyls. The make-up of these basic units is shown in Figs. 3.4 and 3.5.

Silica sheet

In most clay mineral structures the silica tetrahedra associate in a sheet structure. Three of the four oxygens of each tetrahedron are shared to form a hexagonal net, as shown in Fig. 3.6. The bases of the tetrahedra are all in the same plane and the tips all point in the same direction. The structure can repeat indefinitely and has the composition $(Si_4O_{10})^4$. Electrical neutrality can be obtained by replacement of four oxygens by hydroxyls or by union with a sheet of different composition that is positively charged. The oxygen-to-oxygen distance is 2.55 Å, the space available for the silicon ion is 0.55 Å, and the thickness of the sheet in clay mineral structures is 4.63 Å (Grim, 1968).

Silica chains

In some of the less common clay minerals, silica tetrahedra are arranged in bands (double chains) of composition (Si₄O₁₁)⁶-. Electrical neutrality is achieved and the bands are bound together by means of aluminum and/or magnesium ions. A diagrammatic sketch of this structure is shown in Fig. 2.11. Minerals in this group resemble the amphiboles in structure.

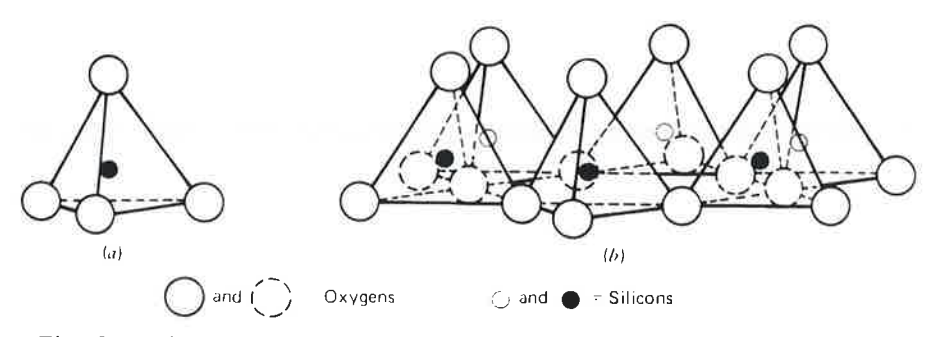


Fig. 3.4 Silica tetrahedron and silica tetrahedra arranged in a hexagonal network.

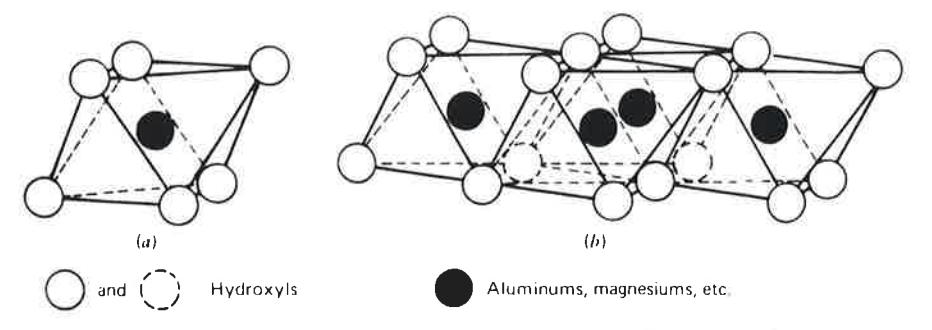


Fig. 3.5 Octahedral unit and sheet structure of octahedral units.

Octahedral sheet

This sheet structure is composed of magnesium or aluminum coordinated octahedrally with oxygens or hydroxyls. In some cases, other cations are present in place of Al³⁺ and Mg²⁺, such as Fe²⁺, Fe³⁺, Mn²⁺, Ti⁴⁺, Ni²⁺, Cr³⁺, and Li⁺. Figure 3.5b is a schematic diagram of such a sheet structure. The oxygen-to-oxygen distance is 2.60 Å, the (OH)–(OH) distance is 2.94 Å, and the space available for the octahedrally coordinated cation is 0.61 Å. The thickness of the sheet is 5.05 Å in clays (Grim, 1968).

If the cation is trivalent, then only two-thirds the possible cationic spaces are normally filled, and the structure is termed *dioctahedral*. In the case of aluminum, the composition is $Al_2(OH)_6$ and, by itself, gives the mineral gibbsite. When found in clay mineral structures, an aluminum octahedral sheet is often referred to as a gibbsite sheet.

If the octahedrally coordinated cation is divalent, then all possible cation sites normally are filled, and the structure is *trioctahedral*. In the case of magnesium, the composition is Mg₃(OH)₆ giving the min-

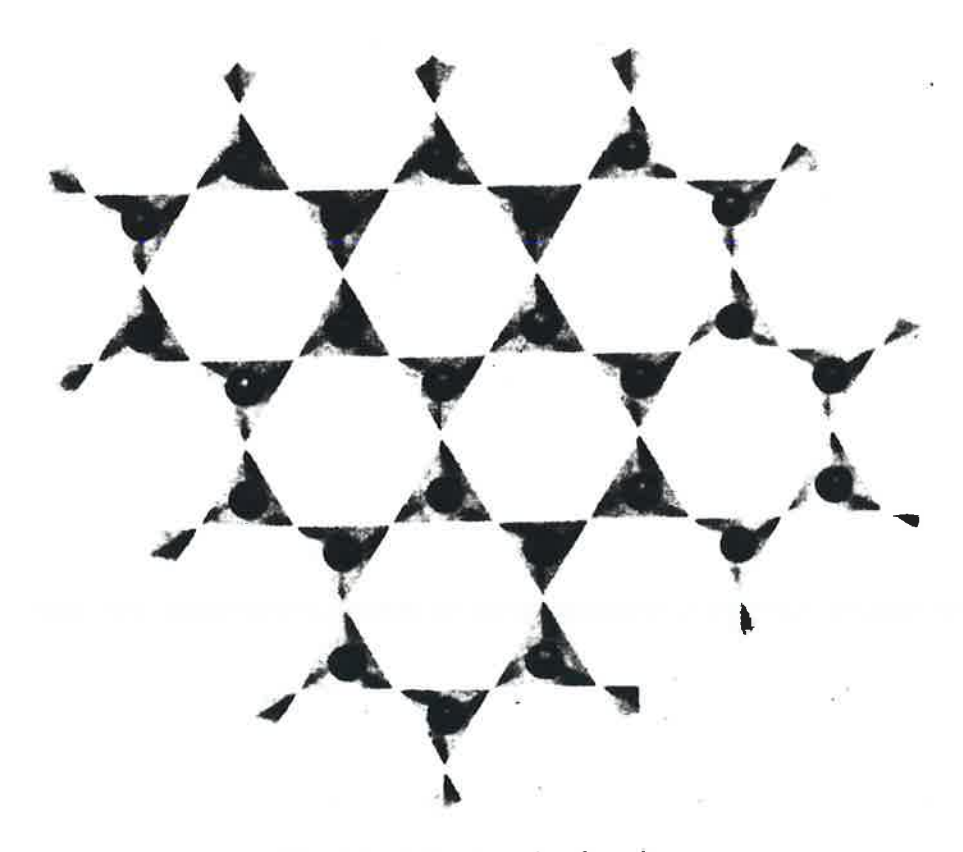


Fig. 3.6 Silica sheet in plan view.

eral brucite. In clay mineral structures, a sheet of magnesium octahedra is termed a brucite sheet.

In the following description of clay mineral structures schematic representations are used for the different structural units:

Silica sheet (tips up) or	(tips down)
Octahedral sheet	(Various cations in octa- hedral coordination)
Gibbsite sheet G	(Octahedral sheet cations are mainly aluminum)
Brucite sheet B	(Octahedral sheet cations are mainly magnesium)

Water layers are found in some structures and may be represented by 00000000 for a single layer, 00000000 for a double layer, and so on. Atoms of a specific type, for example, potassium are represented thus: K.

The diagrams are indicative of the clay mineral layer structure only. They do not indicate the correct width-to-length ratios for the minerals. The structures shown are idealized; in actual minerals, irregular substitutions and interlayering are common. Furthermore, the naturally occurring minerals are not necessarily formed by direct assembly of the basic units described above. The "building block" approach is useful, however, for the development of conceptual models.

3.4 CLASSIFICATION OF CLAY MINERALS

A complete classification system for the layer silicates that make up the various clay minerals should probably take into account three criteria (Warshaw and Roy, 1961). These are:

- 1. The height of the unit cell or "thickness of layer".
- Composition, whether dioctahedral or trioctahedral, and ionic content of layer.
- 3. Stacking sequence of layers and degree of orderliness of stacking.

Grouping clay minerals according to crystal structure and stacking sequence of layers is convenient, since the members of the same group have somewhat similar engineering properties. The classification scheme for layer silicates recommended by the Nomenclature Committee of the Clay Minerals Society (Bailey et al. 1971) was developed on this basis, and is shown in Table 3.1.

The basic structure for each mineral group has been included schematically in Table 3.1. All the minerals have unit cells consisting of two, three, or four sheets. The two-sheet minerals are made up of a silica sheet and an octahedral sheet. The unit cell of the three-sheet minerals is composed of either a dioctahedral or trioctahedral sheet sandwiched between two silica sheets. Unit cells may be stacked closely together or water layers may intervene. The four-sheet structure of chlorite is composed of a 2:1 layer plus an interlayer hydroxide sheet.

Micalike clay minerals (illite, hydrous mica) are very common in soils encountered in practice, and hence their importance is much greater than implied by the table. In some soils inorganic clay-like material is found which has no detectable specific crystal structure and, thus, cannot be classified into one of the groups listed in Table 3.1. Such material is termed allophane.

The 2:1 mineral groups differ from each other mainly in terms of the type and amount of interlayer "glue". For example, the smectites are characterized by loosely held cations between layers, the micas by firmly fixed potassium ions between layers, and vermiculite by one or two layers of water and cations. The chlorite group may be viewed as an end member of a sequence leading to 2:1 layers bonded by an organized hydroxide sheet. The charge per formula unit is variable both within and between groups (Table 3.1), and this reflects the fact that the range of compositions is great as a result of varying amounts of isomorphous substitution. Because of this the boundaries between groups are somewhat arbitrary.

Isomorphous substitution

The concept of isomorphous substitution was introduced in Section 2.8 in connection with description of some of the silicate crystals. Isomorphous substitution is an important factor in the structure and behavior of the clay minerals. In an ideal gibbsite sheet, only two-thirds of the octahedral spaces are filled, and all of the cations are aluminum. In an ideal brucite sheet, all the octahedral spaces are filled by magnesium. In an ideal silica sheet, all the tetrahedral spaces are filled by silicons. In the naturally occurring clay minerals, however, some of the tetrahedral and octahedral positions are occupied by cations other than those in the ideal structure. Common examples are aluminum in place of some silicon, magnesium instead of aluminum, and ferrous iron (Fe2+) for magnesium. This occupation of an octahedral or tetrahedral position by a cation other than the one

Table 3.1 Proposed Classification Scheme for Phyllosilicates Related to Clay Minerals

Туре	Group $(x = \text{charge per } formula \text{ unit})$	Subgroup	Species®	Basic Structure
1:1	Kaolinite-serpentine $x \sim 0$	Kaolinites Serpentines	Kaolinite, halloysite Chrysotile, lizardite, anti- gorite	
2:1	Pyrophyllite-talc $x \sim 0$ Smectite- or Montmorillonite- Saponite $x \sim 0.25-0.6$	Pyrophyllites Talcs Dioctahedral Smectites or Montmorillonites Trioctahedral Smectites or Saponites	Pyrophyllite Talc Montmorillonite, beidellite, nontronite Saponite, hectorite, sauconite	
2:1	Vermiculite $x \sim 0.6-0.9$ Mica ^b $x \sim 1$ Brittle mica $x \sim 2$	Dioctahedral vermiculites Trioctahedral vermiculites Dioctahedral micas Trioctahedral micas Dioctahedral brittle micas Trioctahedral brittle micas	Dioctahedral vermiculite Trioctahedral vermiculite Muscovite, paragonite Biotite, phlogopite Margarite Clintonite	
2:1:1	Chlorite x variable	Dioctahedral chlorites Di,trioctahedral chlorites Trioctahedral chlorites	Donbassite Cookeite, sudoite Pennite, clinochlore, prochlorite	

Only a few examples are given.

^b The status of *illite* (or *hydromica*), *sericite*, and so on, are left open because it is not clear whether or at what level they would enter the table; many materials so indicated may be interstratified.

Bailey et al. (1971).

normally found, without change in crystal structure, is isomorphous substitution. The tetrahedral and octahedral cation distributions develop during initial formation of the mineral, not by later replacement.

3.5 INTERSHEET AND INTERLAYER BOND-ING IN THE CLAY MINERALS

The stacking of silica, gibbsite, and brucite sheets to form the basic clay mineral layer is such that a single plane of atoms is common to both the tetrahedral and octahedral sheets. Thus, bonding between these sheets is of the primary valence type and very strong. On the other hand, the bonds holding the unit cell layers together may be of several types, and they may be sufficiently weak that the physical and chemical behavior of the clay may be influenced by the response of these bonds to changes in environmental conditions.

Isomorphous substitution in all the clay minerals, with the possible exception of the kaolinites, gives clay particles a net negative charge. To preserve electrical neutrality cations are attracted and held on the surfaces and the edges, and in some clays, between the unit cells. These cations are termed "exchangeable cations" because in most instances cations of one type may be replaced by cations of another type. The quantity of exchangeable cations required to balance the charge deficiency of a clay is termed the "cation exchange capacity" (cec) and is usually expressed as milliequivalents* per 100 grams of dry clay.

• Equivalent weight = combining weight of an element = (atomic weight/valence).

Number of milliequivalents = 1000× (weight of element/atomic weight) × valence.

The number of ions in an equivalent = (Avogadro's number/

Avogadro's number = 6.02×10^{23} . An equivalent contains 6.02×10^{23} electron charges or 96,500 coulombs, which is 1 Faraday.

Five types of interlayer bonding in the layer silicates are possible (Marshall, 1964).

- 1. Neutral parallel layers are held by van der Waals bonds. Bonding is relatively weak; however, relatively stable crystals of appreciable thickness may form as evidenced by the nonclay minerals pyrophyllite and talc, although cleavage parallel to the layers in these minerals is easy.
- 2. In minerals such as kaolinite, brucite, and gibbsite there are opposing layers of oxygen and hydroxyl or hydroxyl and hydroxyl. This gives rise to hydrogen bonding as well as van der Waals bonding between layers, which provides a fairly strong bond that will not separate in the presence of water but can still provide good cleavage.
- 3. Neutral silicate layers may be separated by layers of highly polar water molecules giving rise to hydrogen bonding.
- 4. Cations required to provide electrical neutrality may take up positions that control interlayer bonding characteristics. In the micas, some of the silicon is replaced by aluminum in the silica sheets. The resulting charge deficiency is balanced in part by potassium ions between mineral layers. Since the size of the potassium ion is such that it fits into the holes formed by the bases of the silica tetrahedra in the silica sheet (Fig. 3.4), it provides a strong bond between mica layers. In the chlorites, the charge deficiencies resulting from substitutions in the octahedral sheet in the 2:1 sandwich are balanced by a charge excess on the one-sheet layer interleaved between the three-sheet layers. This provides a strongly bonded structure that, while exhibiting cleavage, will not lead to separation in the presence of water or other polar liquids.
- 5. When the surface charge density is moderate, as in the case of the smectites and vermiculites, the silicate layers may readily take up polar molecules, and balancing cations may hydrate, resulting in a separation of layers and expansion. The strength of the interlayer bond is low and a sensitive function of charge distribution, hydration energy of the cation, geometry of cation in relation to the silicate surface, surface ion configuration, and structure of the polar molecule.

The smectite and vermiculite particles swell; whereas, particles of the nonclay minerals pyrophyl-

lite and talc, which have comparable structures, do not. There are two possible explanations for this and direct evidence in support of either is difficult to obtain (van Olphen, 1963).

- 1. The interlayer cations in the smectites hydrate, and the hydration energy overcomes the attractive forces between unit layers. There are no interlayer cations in pyrophyllite, hence, no swelling.
- 2. Water does not hydrate the cations but is adsorbed on oxygen surfaces by hydrogen bonds. There is no swelling in pyrophyllites and talc because the surface hydration energy is too small to overcome the van der Waals forces between layers, which are greater in these minerals because of a smaller interlayer distance.

3.6 THE 1:1 MINERALS

Structure

The kaolinite-serpentine minerals are composed of alternating silica and octahedral sheets as shown schematically in Fig. 3.7. The tips of the silica tetrahedra and one of the planes of atoms in the octahedral sheet are common. The tips of the tetrahedra all point in the same direction, toward the center of the unit cell. In the plane of atoms common to both sheets, twothirds of the atoms are oxygens and are shared by both silicon and the octahedral cations. The remaining atoms in this plane are (OH) and are located so that each is directly below the hole in the hexagonal net formed by the bases of the silica tetrahedra. If the octahedral layer is brucite, then a mineral of the serpentine subgroup results; whereas, dioctahedral gibbsite layers lead to clay minerals in the kaolinite subgroup. Trioctahedral 1:1 minerals are relatively rare, usually occur mixed with kaolinite or illite, and are hard to identify. A diagrammatic sketch of the kaolinite structure is shown in Fig. 3.8. The structural formula is (OH)₈Si₄Al₄O₁₀, and the charge distribution is indicated in Fig. 3.9.

Mineral particles of the kaolinite subgroup consist of the basic layers stacked in the c direction. The bonding between successive layers is both by van der Waals forces and hydrogen bonds. This bonding is of sufficient strength that there is no interlayer swelling.

Because of slight differences in the oxygen-to-oxygen distances in the tetrahedral and octahedral layers there is some distortion of the ideal hexagonal tetrahedral network. The upward directed Si-O bond is

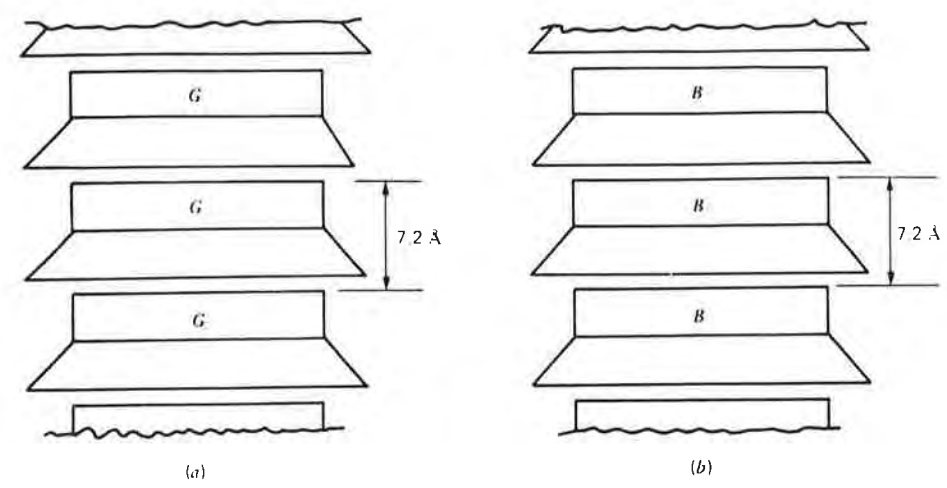


Fig. 3.7 Schematic diagrams of the structures of kaolinite and serpentine (a) Kaolinite. (b) Serpentine.

slightly tilted to fit the overlying octahedron. Apparently, because of this, the mineral kaolinite, which is the most important member of the subgroup and a common soil mineral, is triclinic instead of monoclinic. The unit cell dimensions are a=5.16 Å, b=8.94 Å, c=7.37 Å, $\alpha=91.8^{\circ}$, $\beta=104.5^{\circ}$, and $\gamma=90^{\circ}$.

Variations between members of the kaolinite subgroup consist of the way layers are stacked above each other and possibly in the position of aluminum ions within the available sites in the octahedral sheet. Dickite and nacrite are rarely found. The dickite unit cell is made up of two unit layers, and the nacrite unit cell contains six. Both appear to form as a result of hydrothermal processes. Dickite is fairly common as a secondary clay in the pores of sandstone and in coal beds.

Halloysite

The mineral halloysite is a particularly interesting member of the kaolinite subgroup. Two distinct forms of this mineral exist as shown in Fig. 3.10; one a nonhydrated form having the same structural composition as kaolinite ($(OH)_8Si_4Al_4O_{10}$) and the other a hydrated form consisting of unit kaolinite layers separated from each other by a single layer of water molecules having the composition $(OH)_8Si_4Al_4O_{10} \cdot 4H_2O$. The basal spacing in the c direction, $d_{(001)}$ for nonhydrated halloysite is about 7.2 Å, as for kaolinite. Because of the interleaved water layer, $d_{(001)}$ for hydrated halloysite is about 10.1 Å. The difference between these values, 2.9 Å, is the approximate thickness of a single layer of water molecules. A partially

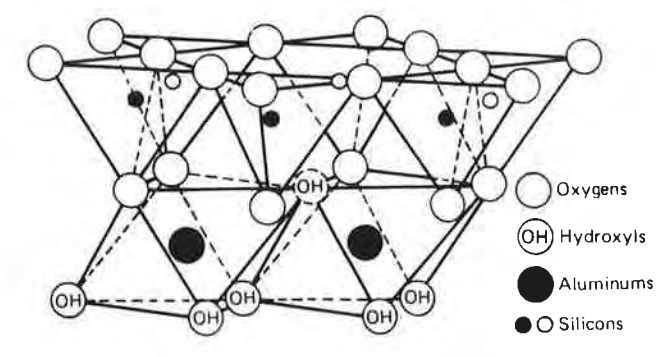


Fig. 3.8 Diagrammatic sketch of the kaolinite structure.

hydrated form with basal spacing in the range of 7.4 to 7.9 Å may also occur.

Hydrated halloysite, which has also been termed halloysite (4H₂O), can dehydrate irreversibly to halloysite (2H₂O) sometimes known as metahalloysite.

Isomorphous substitution and exchange capacity

Controversy exists as to whether or not any isomorphous substitution exists within the structure of the kaolinites. Nonetheless, values of cation exchange capacity for kaolinite in the range of 3 to 15 meq/100 g and from 5 to 40 meq/100 g for halloysite have been measured. Thus, clear evidence exists that the particles possess a net negative charge. Possible sources of this charge deficiency are:

1. Substitution of Al³⁺ for Si⁴⁺ in the silica sheet or a divalent ion for Al³⁺ in the octahedral sheet. Replacement of only one Si in every 400

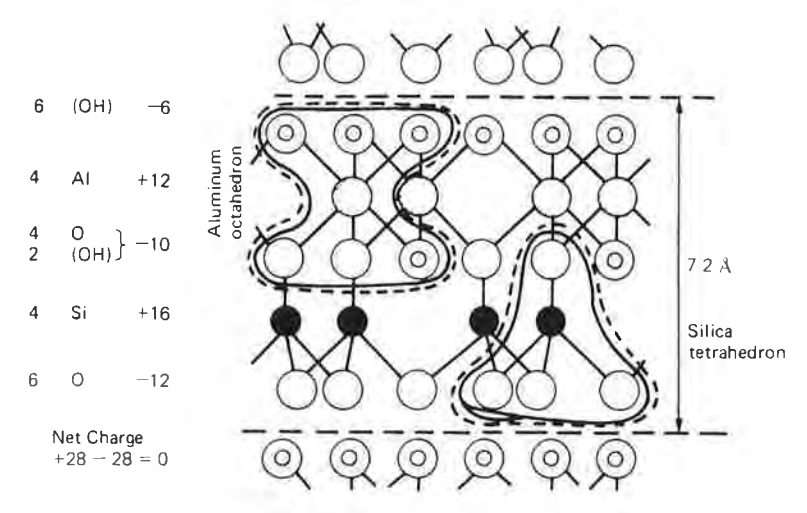


Fig. 3.9 Charge distribution in kaolinite.

would be adequate to account for the exchange capacity of many kaolinites, so proof of substitution using analytical methods is not easily obtained.

- The hydrogen of exposed hydroxyls may be replaced by an exchangeable cation. This mechanism may be doubtful, however, since the hydrogen would probably not be replaceable under the conditions of most exchange reactions (Grim, 1968).
- Broken bonds around particle edges give rise to unsatisfied charges that are balanced by adsorbed cations.

Considerable evidence exists that kaolinite particles are actually charged positively on their edges when in a low (acid) pH environment, but negatively charged in a high (basic) pH environment. Low exchange capacities are measured under low pH conditions and high exchange capacities are obtained for determinations at high pH. This supports broken bonds as a

partial source of exchange capacity. That a positive cation exchange capacity is measured under low pH conditions when edges are positively charged indicates that some isomorphous substitution must exist as well.

Because interlayer separation does not occur in kaolinite, balancing cations must adsorb on the exterior surfaces of the particles.

Morphology and surface area

Well-crystallized particles of kaolinite (Fig. 3.11), nacrite, and dickite occur as well-formed six-sided plates. The lateral dimensions of these plates may range from about 0.1 to 4 μ m, and their thickness may be about 0.05 to 2 μ m. Stacks of kaolinite layers up to 4000 μ m in thickness have been observed, although they are not common. Poorly crystallized kaolinite generally occurs as less distinct hexagonal plates, and the particle size is usually smaller than for the well-crystallized varieties.

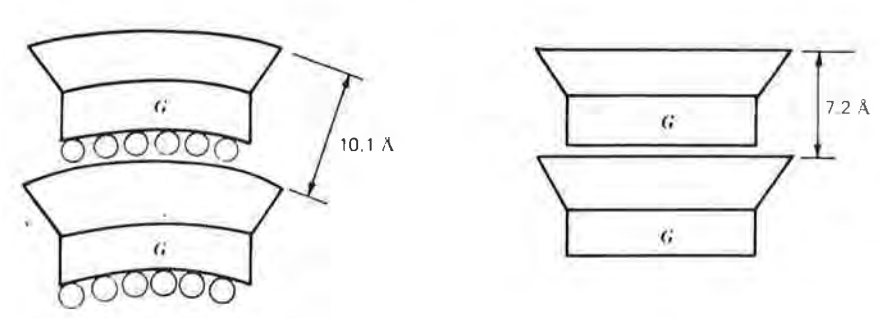


Fig. 3.10 Schematic diagrams of the structure of halloysite. (a) Hydrated halloysite. (b) Non-hydrated halloysite.



Fig. 3.11 Electron photomicrograph of well-crystallized kaolinite from St. Austell, Cornwall, England, Picture width is 17 μ m (Tovey, 1971).

The morphology of halloysite is among the most interesting of any of the clay minerals. The hydrated form of this mineral occurs as cylindrical tubes of overlapping sheets of the kaolinite type (Fig. 3.12). The c-axis at any point nearly coincides with the tube radius. The formation of tubes has been explained (Bates, Hildebrand, and Swineford, 1950) on the basis of a misfit in the b direction of the silica and gibbsite sheets. The b dimension of kaolinite is 8.93 Å. In gibbsite, however, it is only 8.62 Å. This implies that the (OH) spacings in kaolinite are somewhat stretched in order to obtain the proper fit with the silica sheet. Evidently in hydrated halloysite, the reduced interlayer bond, caused by the intervening layer of water molecules, enables the (OH) layer to revert to 8.62 Å resulting in a curvature of the unit with the hydroxyls on the inside and the bases of the silica tetrahedra on the outside. The outside diameters of the tubular particles range from about 0.05 to 0.20 μ m with a median value of 0.07 μ m. The wall thickness is about 0.02 μ m (Bates, Hildebrand, and Swineford, 1950). The tubes may range in length from a fraction to several micrometers. Electron microscope studies have shown that drying of hydrated halloysite may result in a splitting or unrolling of the tubes.



Fig. 3.12 Electron photomicrograph of halloysite from Bedford, Indiana. Picture width is 2 μ m (Tovey, 1971).

The specific surface area of kaolinite is of the order of 10 to 20 $\rm m^2/g$ of dry clay; whereas, that of hydrated halloysite is in the range of 35 to 70 $\rm m^2/g$.

3.7 THE SMECTITE MINERALS

Structure

The minerals of the smectite group have a prototype structure similar to that of pyrophyllite, consisting of an octahedral sheet sandwiched between two silica sheets, as shown schematically in Fig. 3.13 and diagrammatically in three dimensions in Fig. 3.14. All the tips of the tetrahedra point toward the center of the unit cell. The oxygens forming the tips of the tetrahedra are common to the octahedral sheet as well. The remaining anions in the octahedral sheet that fall directly above and below the hexagonal holes formed by the bases of the silica tetrahedra are hydroxyls.

The layers formed in this way are continuous in the a and b directions and stacked one above the other in the c direction. Bonding between successive layers is by van der Waals forces and by cations that may be present to balance charge deficiencies in the structure. These bonds are weak and easily separated

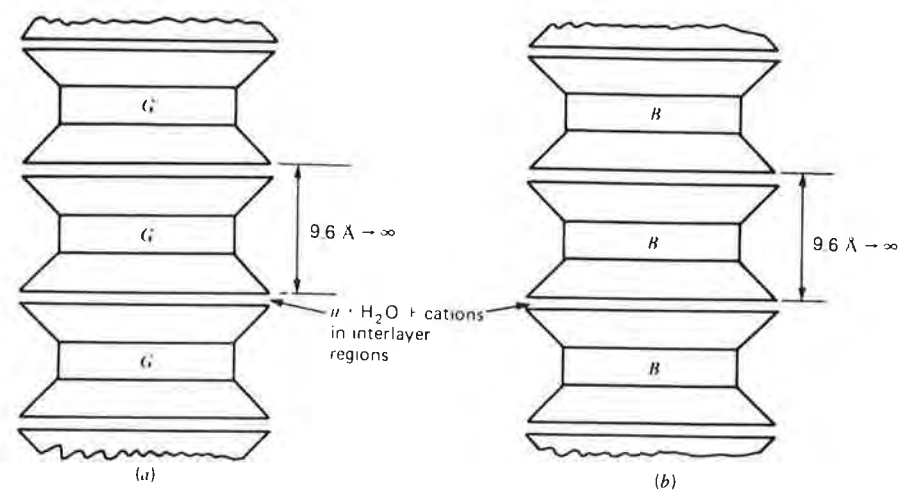


Fig. 3.13 Schematic diagrams of the structures of the smectite minerals (a) Montmorillonites. (b) Saponites.

by cleavage or adsorption of water or other polar liquids. The basal spacing in the c direction, $d_{(001)}$, is variable, ranging from about 9.6 Å to complete separation.

The theoretical composition in the absence of lattice substitutions is $(OH)_4Si_8Al_4O_{20} \cdot n$ (interlayer) H_2O . The structural configuration and the corre-

Exchangeable Cations

nH₂O

Oxygens OH Hydroxyls Aluminum, Iron, Magnesium
O and Silicon, Occasionally Aluminum

Fig. 3.14 Diagrammatic sketch of the montmorillonite structure.

sponding charge distribution are shown in Fig. 3.15. The structure shown is electrically neutral overall, and it is the same as that of the nonclay mineral pyrophyllite.

Isomorphous substitution in the smectite minerals

The factor that sets the minerals of the smectite group apart from the pyrophyllite-talc as a clay mineral class is extensive substitution for aluminum and silicon within the lattice by other cations. Aluminum in the octahedral sheet may be replaced by magnesium, iron, zinc, nickel, lithium, or other cations.

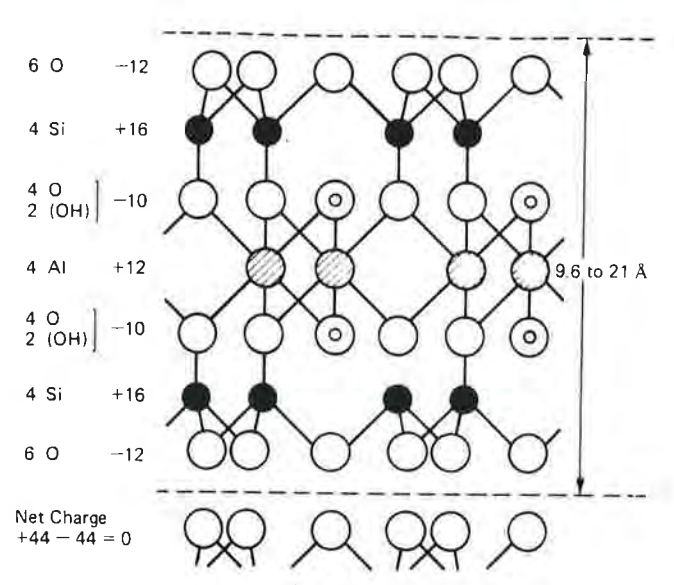


Fig. 3.15 Charge distribution in Pyrophyllite (type structure for montmorillonite).

Aluminum may replace up to 15 per cent of the silicon ions in the tetrahedral sheet. Possibly some of the silicon positions can be occupied by phosphorous (Grim, 1968).

Substitutions for aluminum in the octahedral sheet may be one-for-one or three-for-two (since aluminum occupies only two-thirds the possible octahedral sites) in any combination from a few to complete replacement. The only restriction appears to be that the resulting structure is either almost exactly dioctahedral (montmorillonite subgroup) or exactly trioctahedral (saponite subgroup). The charge deficiency resulting from these substitutions is in the range of 0.5 to 1.2, and it is usually close to 0.66 per unit cell. A charge deficiency of this amount is readily obtained by replacement of every sixth aluminum by a magnesium. Montmorillonite, the most common mineral of the group, has this composition. The charge deficiency resulting from these substitutions is balanced by exchangeable cations that take up positions between the unit cell layers and on the surfaces of particles.

Some minerals of the smectite group and their structural formulas are listed in Table 3.2. An arrow indicates the source of the charge deficiency, assumed to be 0.66 in each case, and the amount of exchangeable sodium required to balance the structure. More than one formula may be found in the literature for several of the minerals, differing in the relative amounts of substitution in different parts of the structure. This reflects both the great variety of compositions that may exist within the same basic crystal structure and the difficulties of identification and classification. Thus, the formulas given in Table 3.2 cannot be taken as absolute, but as indicative of the general character of the mineral.

Because of the large amount of unbalanced substitution in the smectite minerals, they exhibit high cation exchange capacities, generally in the range of 80 to 150 meq/100 g.

Table 3.2 Some Minerals of the Smectite Group

Mineral	Tetrahedral Sheet Substitutions	Octahedral Sheet Substitutions	Formula/Unit Cella
Dioctahedral, Smectites or			ä
Montmorillonites Montmorillonite	None	1 Mg ²⁺ for every sixth Al ³⁺	$(OH)_4Si_8(Al_{3.34}Mg_{0.66}) O_{20}$
			Na _{0.88}
Beidellite	Al for Si	None	(OH) ₄ (Si _{6.34} Al _{1.66}) Al _{4.34} O ₂₀
Nontronite	Al for Si	Fe3+ for Al	$Na_{0.66}$ $(OH)_4(Si_{7.34}Al_{0.66}) Fe_4^{3+}O_{20}$ \downarrow $Na_{0.66}$
			1440,00
Trioctahedral, Smectites or			
Saponites Hectorite	None	Li for Mg	$(OH)_4Si_8(Mg_{5.34}Li_{0.66}) O_{20}$
			Na _{0.66}
Saponite	Al for Si	Fe ³⁺ for Mg	(OH) ₄ Si _{7,34} Al _{0,66}) Mg ₆ O ₂₀
Sauconite	Al for Si	Zn for Mg	$\begin{array}{c} \operatorname{Na}_{0.66} \\ (\operatorname{OH})_4 (\operatorname{Si}_{8-y} \operatorname{Al}_y) (\operatorname{Zn}_{8-x} \operatorname{Mg}_x) \operatorname{O}_{20} \\ \downarrow \end{array}$
*			Na _{0.66}

^a Two formula units are needed to give one unit cell. After Ross and Hendricks (1945); Marshall (1964); and Warshaw and Roy (1961).

Morphology and surface area

Because of the very small sizes in which particles of the smectite minerals are usually found and their tendency to break down into sheets of unit cell thickness when dispersed in water, clear electron micrographs are not easily obtained. Montmorillonite usually occurs as equidimensional flakes so thin as to appear more like films as shown in Fig. 3.16. Particles may range in thickness from 10 Å (unit cell) upwards to about 1/100 of the width. The long axis of the plates may be up to several micrometers in length; however, it is usually less than 1 or 2 μ m.

In cases where there is a large amount of substitution of iron and/or magnesium for aluminum, for example, nontronite, particles have a lath or needle-like shape. It has been postulated (Grim, 1962) that these shapes result from the fact that the Mg²⁺ ion and the Fe³⁺ ion are somewhat large for the octahedral lattice, and, hence, the structure is subjected to a directional strain.

The specific surface of the smectites is extremely large. The primary surface, that is, surface due to particle surfaces exclusive of interlayer zones, is generally in the range of 50 to 120 m²/g. The secondary specific surface that may be exposed by expanding the

Fig. 3.16 Electron photomicrograph of montmorillonite (bentonite) from Clay Spur, Wyoming. Picture width is 7.5 μ m (Tovey, 1971).

lattice so that polar fluids can penetrate between layers may range from 700 to 840 m²/g.

Bentonite

A very highly plastic, swelling clay material known as bentonite is widely used for a variety of purposes ranging from drilling muds for soil borings to clarification of beer and wine. The bentonite familiar to most geotechnical engineers is a highly colloidal, expansive clay that is an alteration product of volcanic ash and has a liquid limit of 500 percent or more. It is widely used as a backfill during the construction of slurry trench walls, as a grout material, as a sealant for piezometer installations, and for other special applications (Boyes, 1972).

When encountered naturally, or as a seam in rock formations or as a major constituent of soft shales, bentonite may be a continuing source of slope stability problems. Slide problems at Portugese Bend along the Pacific Ocean in southern California and in the Bearpaw shale in Saskatchewan can both be attributed in part to the presence of bentonite. Stability problems in underground construction may be caused by the presence of montmorillonite in joints and faults (Brekke and Selmer-Olsen, 1965).

3.8 THE MICALIKE CLAY MINERALS

Perhaps the most commonly occurring clay mineral found in the soils encountered in engineering practice has a structure similar to that of muscovite mica, and is termed "illite" or "hydrous mica." Although illite was not listed specifically in Table 3.1, it can be conveniently considered on the same level as kaolinite and montmorillonite. Vermiculite also is often found as a clay phase constituent of soils. Although it is classed as a separate group in Table 3.1, its structure is related to that of biotite mica.

Structure

The basic structural unit for the muscovite micas (white micas), shown schematically in Fig. 3.17a, is the three-layer silica-gibbsite-silica sandwich that forms pyrophyllite. The tips of all the tetrahedra in each silica sheet point toward the center and are common with octahedral sheet ions.

Muscovite differs from pyrophyllite in that about one-quarter of the silicon positions are filled by aluminum, and the resultant charge deficiency is balanced by potassium ions between the layers. The layers are continuous in the a and b directions and stacked in

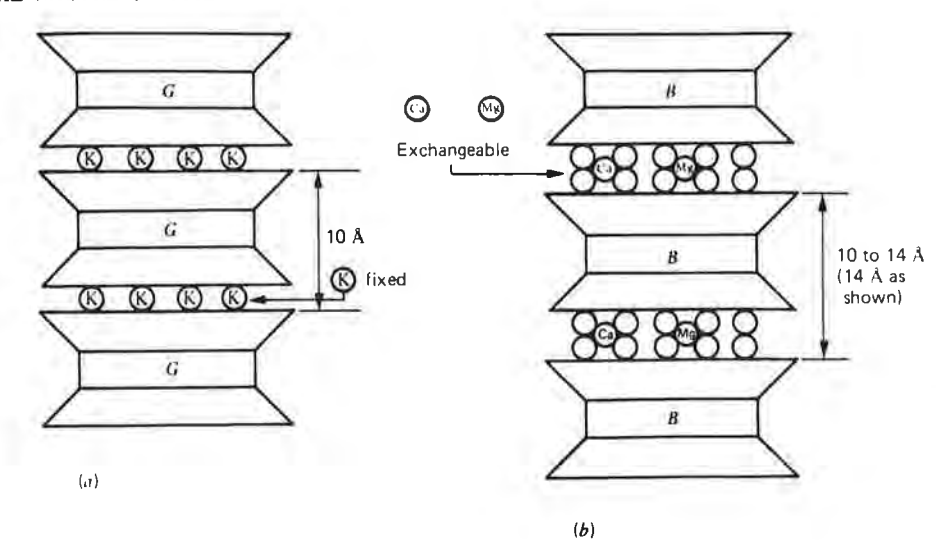


Fig. 3.17 Schematic diagram of the structures of muscovite, illite, and vermiculite. (a) Muscovite and illite. (b) Vermiculite.

the c direction. The diameter of the potassium ion, 1.33 Å, is such that it fits snugly in the 1.21 Å diameter hexagonal hole formed by the bases of the silica tetrahedra, where it is in 12-fold coordination with the six oxygens of each layer.

A diagrammatic three-dimensional sketch of the muscovite structure is shown in Fig. 3.18. The struc-

tural configuration and charge distribution are shown in Fig. 3.19, where it may be noted that the unit cell is electrically neutral and has the formula $(OH)_4K_2$ - $(Si_6Al_2)Al_4O_{20}$. Muscovite is the dioctahedral end member of the micas and contains only Al^3 + in the octahedral layer. Phlogopite (brown mica) is the trioctahedral end member, having the octahedral positions filled entirely by magnesium. Its formula is $(OH)_4K_2(Si_6Al_2)Mg_6O_{20}$. The biotites (black micas) are trioctahedral, with the octahedral positions filled

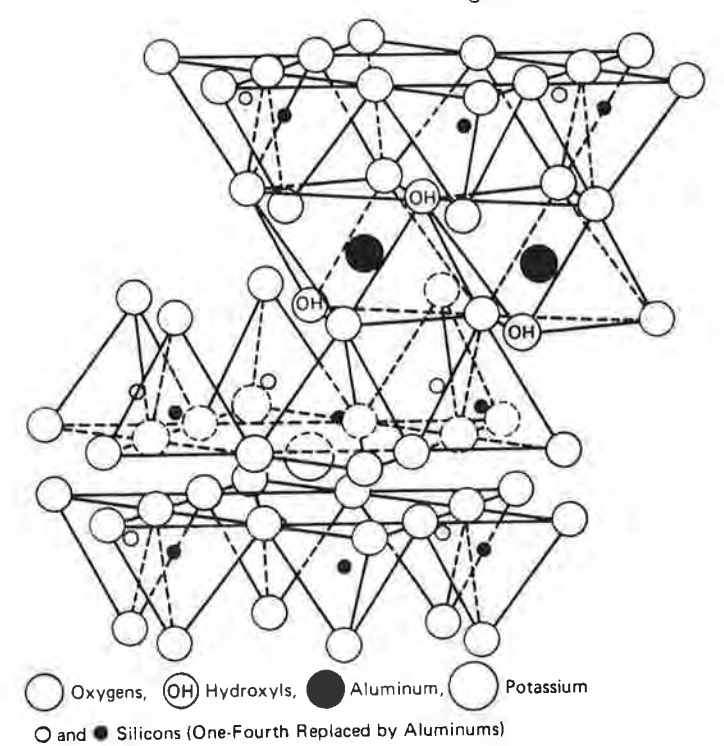


Fig. 3.18 Diagrammatic sketch of the structure of muscovite.

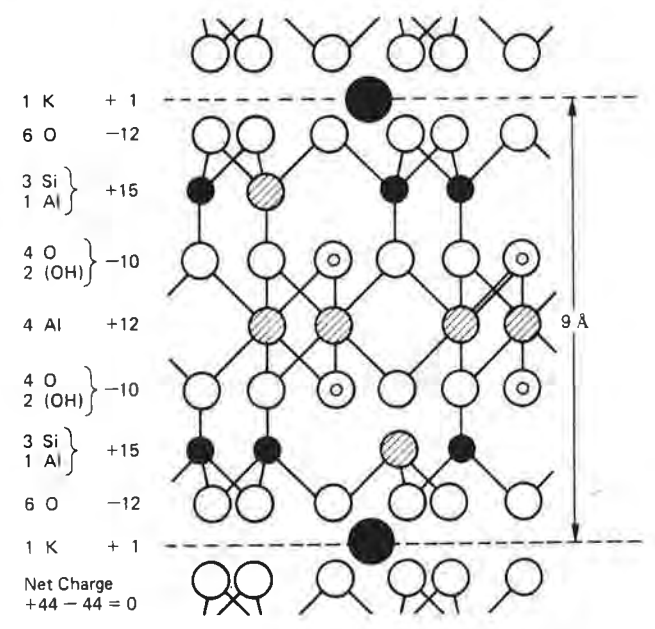


Fig. 3.19 Charge distribution in muscovite.

mostly by magnesium and iron. It has the general prmula $(OH)_4K_2(Si_6Al_2)(MgFe)_6O_{20}$. The relative proportions of magnesium and iron may vary widely.

Illites differ from mica in the following ways (Grim, 1968):

- 1. Fewer of the Si⁴⁺ positions are occupied by Al³⁺ in illite.
- 2. There is some randomness in stacking of layers in illite.
- 3. There is relatively less potassium in illite. Well organized illite contains 9 to 10 percent K₂O (Weaver and Pollard, 1973).
- 4. The size of illite particles occurring naturally is very small.

Some illite may contain magnesium and iron in the octahedral sheet as well as aluminum (Marshall, 1964). Iron-rich illite, usually occurring as earthy green pellets, is termed glauconite.

The vermiculite structure consists of a regular interstratification of biotite mica layers and double molecular layers of water, as shown schematically in Fig. 3.17b. Actually, the thickness of the water layer between biotite units depends largely on the cation present in this region that balances charge deficiencies in the biotitelike layers. With magnesium or calcium present (the usual case in nature), there are two water layers, giving a basal spacing of 14 Å. A general formula for vermiculite is

$$(OH)_4(MgCa)_x(Si_{8-x}Al_x)$$
 $(Mg \cdot Fe)_6O_{20}yH_2O$
 $x \sim 1 \text{ to } 1.4, y \sim 8$

Isomorphous substitution and exchange capacity

Isomorphous substitution in both the illite and vermiculite structure is extensive. The charge deficiency in illite is 1.3 to 1.5 per unit cell. In illite the charge deficiency is located primarily in the silica sheets and is balanced partly by the nonexchangeable potassium ions between layers. Thus, the cation exchange capacity of illite is less than that of montmorillonite, amounting to 10 to 40 meq/100 g. Values of exchange capacity greater than 10 to 15 meq/ 100 g may be indicative to some expanding layers (Weaver and Pollard, 1973). In the absence of the fixed potassiums, the exchange capacity would be about 150 meq/100 g. The interlayer bonding by potassium is sufficiently strong that the basal spacing of illite remains fixed at 10 Å in the presence of polar jiquids.

In vermiculite, the charge deficiency is of the order of 1 to 1.4 per unit cell. Since the interlayer cations are exchangeable, the exchange capacity for this mineral is high, amounting to 100 to 150 meq/100 g. The basal spacing $d_{(001)}$ of the vermiculites is influenced by both the type of cation and dehydration. With magnesium and calcium in the exchange positions, the basal spacing is only 10.5 to 11 Å. Lithium gives 12.2 Å. The interlayer water can be driven off by heating to temperatures higher than 100°C . This dehydration is accompanied by a reduction in basal spacing to about 10 Å. The mineral quickly rehydrates and expands again to 14 Å when exposed to moist air at room temperature.

Morphology and surface area

Illites usually occur as very small, flaky particles mixed with other clay and nonclay materials. Illite deposits of high purity have not been located, as has been the case for kaolinite and montmorillonite. The flaky illite particles may have a hexagonal outline if well crystallized. The long axis dimension ranges from 0.1 μ m or less to several micrometers, and the plate thickness may be as small as 30 Å. An electron photomicrograph of illite is shown in Fig. 3.20.

Vermiculite may occur in nature as large crystalline masses having a sheet structure somewhat similar in appearance to mica. In soils, vermiculite occurs as



Fig. 3.20 Electron photomicrograph of illite from Morris, Illinois. Picture width is 7.5 μ m (Tovey, 1971).

small particles mixed with other clay minerals. Specific data concerning shape and size of these particles are not available.

Values of specific surface in the range of about 65 to $100 \text{ m}^2/\text{g}$ have been reported for illite. The primary surface area of the vermiculites is about 40 to $80 \text{ m}^2/\text{g}$ and the secondary (interlayer) surface may be as high as $870 \text{ m}^2/\text{g}$.

3.9 THE CHLORITE MINERALS

Structure

The chlorite structure consists of alternating micalike and brucitelike layers as shown schematically in Fig. 3.21. The structure is similar to that of vermiculite, except that an organized octahedral sheet replaces the double water layer between mica layers. As with the kaolinites, smectites, and illites, the layers are continuous in the a and b directions and stacked in the c direction with basal cleavage. The basal spacing is fixed at 14 Å.

Isomorphous substitution

The central sheet of the mica layer is trioctahedral with magnesium as the predominate cation. There is often partial replacement of Mg²⁺ by Al³⁺, Fe²⁺, and Fe³⁺. The silica sheets are unbalanced by substitution of Al³⁺ for Mg²⁺ in the brucite layer. The various members of the chlorite group differ in the kind and amounts of substitution and in the stacking of successive layers. The cation exchange capacity of the chlorites is in the range of 10 to 40 meq/100 g.

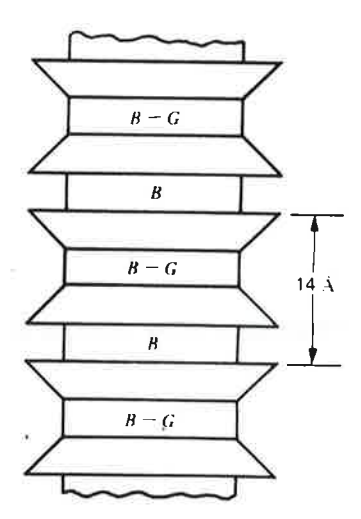


Fig. 3.21 Schematic diagram of the structure of chlorite.



Fig. 3.22 Electron Photomicrograph of Attapulgite from Attapulgis, Georgia. Picture width is 4.7 μ m (Tovey, 1971).

Morphology

Chlorite minerals are found as microscopic grains of platy morphology and poorly defined crystal edges in altered igneous and metamorphic rocks and soils derived therefrom. In soils, chlorites always appear to occur in mixtures with other clay minerals. Little specific information is available concerning particle size.

3.10 CHAIN STRUCTURE CLAY MINERALS

As indicated previously, some clay minerals are formed from bands (double chains) of silica tetrahedra. The minerals attapulgite, sepiolite, and palygorskite differ primarily in the replacements within the structure. These minerals have lathlike shapes with particle diameters of 50 to 100 Å and lengths of 4 to 5 μ m. These minerals are not commonly encountered in soils of engineering interest. Figure 3.22 shows an electron photomicrograph of bundles of attapulgite particles.

3.11 SUMMARY OF CLAY MINERAL CHARACTERISTICS

Table 3.3 presents a summary of the important structural, compositional, and morphological charac-

teristics of the important clay minerals. Data concerning the structural characteristics of tetrahedral and octahedral sheet structures are included, as well as values of ionic radii for the elements common in clays.

3.12 MIXED LAYER CLAYS

More than one type of clay mineral is usually found in most soils. Because of the great similarity in crystal structure among the different minerals, it is common, and not at all surprising, that interstratification of two or more different layer types often occurs within a single particle.

Interstratification may be regular, with a definite repetition of the different layers in sequence, or it may be random. According to Weaver and Pollard (1973), randomly interstratified minerals are second only to illite in abundance. The most abundant mixed-layer material is composed of expanded, water bearing layers and contracted nonwater bearing layers. Montmorillonite—illite is most common, although chlorite—vermiculite and chlorite—montmorillonite are often encountered. Rectorite is a regular interstratified clay with high charge, micalike layers with fixed interlayer cations alternating in a regular manner with low charge, montmorillonitelike layers with exchangeable cations capable of hydration.

3.13 NONCRYSTALLINE CLAY MATERIALS

Allophane

Noncrystalline silicate clay materials are generally termed allophane. These materials are noncrystalline, in the sense that they are amorphous to X rays, because there is insufficient long range order of the octahedral and tetrahedral units to produce sharp diffraction effects, although in some cases crude order may exist leading to diffraction bands. The allophanes have no definite composition or shape and may exhibit a wide range of physical properties. Some noncrystalline clay material is probably found in nearly all fine-grained soils. It may be particularly common in some soils formed from volcanic ash.

Oxides

There are probably no soils on earth that do not contain some amount of colloidal oxides and hydrous oxides (Marshall, 1964). The details of their occurrence and influence on the physical properties of a

soil have not been studied much. The oxides and hydroxides of aluminum, iron, and silicon are of the greatest interest since they are the ones most frequently encountered. These materials may occur as gels or precipitates and coat mineral particles, or they may cement particles together. They may occur also as distinct crystalline units, for example, gibbsite, boehmite, hematite, and magnetite. Limonite and bauxite are sometimes found and represent amorphous mixtures of iron and aluminum hydroxides, respectively.

3.14 ORIGIN OF CLAY MINERALS

Clay minerals may be formed by one or more of the processes listed below (Keller, 1964):

- [1.] Crystallization from solutions.
- 2. Weathering of silicate minerals and rocks.
- 3. Diagenesis, reconstitution, and ion exchange.
- 4. Hydrothermal alterations of minerals and rocks.
- 5. Laboratory synthesis.

Clay minerals are commonly found in the filling material (gouge) in joints, shears, and faults in rock, and often as an alteration product in the rock immediately adjacent to these discontinuities. Hydrothermal alterations may also lead to the formation of clay veins in rocks and zones of clay around hot springs and geysers. Clays formed in this way are not important constituents of soils; however, their presence in joints, shears, and faults is of great importance in the stability of underground openings and other rock structures.

The bulk of the clay minerals found in soils are formed by processes (1), (2), and (3). Further consideration of the nature of these processes is given in Chapter 4. In some cases, a silicate mineral, especially feldspar, may be replaced by a clay mineral within a granular rock structure as a result of various alteration processes. This may be of particular importance in the formation of decomposed granite, a brokendown rock material that is a frequent source of problems in foundation and earth work construction. The replacement mainly of feldspar by kaolinite is common.

3.15 PRACTICAL IMPLICATIONS

Mineralogy controls the sizes, shapes, and surface characteristics of the particles in a soil. These features, along with interactions with the fluid phase, determine plasticity, swelling, compression, strength,

J. K. Mitchell Fundamentals of Soil Belowing

Table 3.3 Summary of Clay

Structural

1. Silica Tetrahedron: Si atom at center. Tetrahedron units form hexagonal network = Si4O₆(OH)₄

2. Gibbsite Sheet: Aluminum in octahedral coordination. Two-thirds of possible positions filled. Al₂(OH)₆—O-O = 2.60 Å.

3. Brucite Sheet: Magnesium in octahedral coordination. All possible positions filled. Mg₃(OH)₆—O-O = 2.60 Å

Type S	Sub-Group and chematic Structure	Mineral	Complete Formula/Unit Cella	Octahedral Layer Cations	Tetrahedral L Cations		
All	ophane	Allophanes	Amorphous	+	_		
Ка	olinite	≯ Kaolinite	(OH) ₈ Si ₄ Al ₄ O ₁₀	Ala	Si ₄	Little	O-OH Hydrogen Strong
	6	Dickite	$(OH)_8Si_4Al_4O_{10}$	Al ₄	Si ₄	Little	O-OH Hydrogen Strong
1:1	25	Nacrite	$(OH)_{0}Si_{4}Al_{4}O_{10}$	Ala	Si ₄	Little	O-OH Hydrogen Strong
iost	$\frac{G}{S}$	Halloysite (dehydrated)	$(OH)_8Si_4Al_4O_{10}$	Ale	Si ₄	Little	O-OH Hydrogen Strong
CONTROL		Halloysite (hydrated)	(OH) ₈ Si ₄ Al ₄ O ₁₀ .4H ₂ O	Ala	Si ₄	Little	O-OH Hydrogen Strong
(OI	ntmorillonite H) ₄ Si ₈ Al ₄ O ₂₀ ,NH ₂ O teoretical Unsub- tituted)	Montmorillonite	(OH) ₄ Si ₈ (Al ₃ 34.Mg. ₆₆)O ₂₀ ,nH ₂ O ↓ • Na. ₆₆	Al _{3,34} Mg,66	Sis	Mg for Al, Net charge always = 0.66-/unit cell	O-O Very weak expand ing lattice
٠,	\sqrt{S}	Beidellite	(OH)4(Si7.34.Al 66)(Al4)O20.nH2O	Ala	Si7.24Al.66	Al for Si, Net charge always = 0.66-/for	O-O Very weak expand
1 (m)		Nontronite	$\begin{array}{c} Na_{.06} \\ (OH)_4(Si_{7.34},Al_{.06})Fe_4z+O_{2,1}nH_2O \\ \downarrow \\ Na_{.06} \end{array}$	Fe ₄	Si7 34AI.66	unit cell Fe for Al, Al for Sl, Net charge always = 0.66-/for unit cell	ing lattice O-O Very weak expanding lattice
Q	$\frac{S}{S}$						
2:1 Sap	onite	Hectorite	(OH) ₄ Si ₈ (Mg _{5.34} .Li _{.66})O ₂₀ .nH ₂ O	Mg6,34Li.66	Sia	Mg, Li for Al, Net	O-O Very weak expans
	B	Saponite	(OH) ₄ (Si _{7.34} Al _{.66})Mg ₆ O ₂₀ .nH ₂ O	Mg, Fe ²⁺	Si7.34Al.66	0.66-/unit cell Mg for Al, Al for Si, Net charge always = V 0.66-/for unit cell Zn for Al	ing lattice O-O Very weak expand
7	B	Sauconite	Na.56 (Si6.54Ali.06)Al.44Fe.34Mg.36Zn4.86O20(OH)4 ↓ ↓ ↓	At 44Fe,34Mg,34Zn4.80	Si6.94Ål1.06		ing lattice O-O Very weak expan ing lattice
doen't	drous Mica Illite) S G S S S G	Illites	$(K, H_2O)_2(Si)_8(Al, Mg, Fe)_{4.6}O_{20}(OH)_4$	$(Al,Mg,Fe) {\leftarrow}_6$	(Al,Si)e	Some Si always replaced by Al. Balanced by K between layers.	K ions: strong
Ver	miculite	Vermiculite	$\begin{array}{l} (OH)_{4}(Mg,Ca)_{x}(Si_{\theta-x}.Al_{x})(Mg,Fe)_{6}O_{20}.yH_{2}O\\ x = 1 \ to \ 1.4, \ y = 8 \end{array}$	(Mg,Fe) ₆	(Si,Al) ₈	Al for Si net charge of 1 to 1.4/unit cell	Weak
2:1:1 Chl	orite S B S S	Chlorite (Several varieties known)	(OH)4(SiAl)8(Mg.Fe)6O20 (2:1 layer) (MgAl)6(OH)12 Interlayer	(Mg,Fe)s (2:1 layer) (Mg,Al)s Interlayer	(Si,Al) ₈	Al for Si in 2:1 layer Al for Mg in Interlayer	
Chain Structure		Sepiolite	Si ₄ O ₁₁ (Mg,H ₂) ₃ H ₂ O ₂ (H ₂ O)			Fe or Al for Mg	
~ VI WO FULL		Attapulgite	$(OH_2)_{4-}(OH)_2Mg_4Si_8O_{20}, 4H_2O$			Some for Al for Si	Weak = chains linked by 0

a Arrows indicate source of charge deficiency. Equivalent Na listed as balancing cation. Two formula units (Table 3.2) are required per unit cell. Electron Microscope Data.

Mineral Characteristics

Units

All bases in same plane. O-O = 2.55 Å—Space for Si = 0.55 Å—Thickness 4.93 Å. C-C height = 2.1 Å. H-OH = 2.94 Å. Space for ion = 0.61 Å. Thickness of unit = 5.05 Å. Dioctahedral. OH = 2.94 Å. Space for ion = 0.61 Å. Thickness of unit = 5.05 Å. Trioctahedral.

	cture—Continued				Cation Exchange	Specific	Specific Surface	Occurrence in So of Engineering
Crystal Structure	Basal Spacing		Shape		Cap.(meq/100 gm)	Gravity	m²/gm.	Interest
			Irregular, some- what rounded	:05-1 μ				Common
riclinic a = 5.14, $b = 8.93$, $c = 7.37\alpha = 91.6^{\circ}, \beta = 104.8^{\circ}, \gamma = 89$	7.2 Å		6-sided flakes	$0.1-4 \mu \times)$ single to 3000 × 4000(sta	3-15	2.60-2.68	10-20	Very Common
foncelinic a = 5.15, $b = 8.95$, $c = 14.42\beta = 96^{\circ}48'$	14.4 A	Unit cell con- tains 2 unit layers	6-sided flakes	0.07-300 × 2.5- 1000 μ	1-30			Rare
Imost Orthorhombic a = 5.15, b = 8.96, c = 43 $\beta = 90^{\circ}20'$	43 Å	Unit cell con- tains 6 unit layers	Rounded flakes	1 μ × .025–.15 μ				Rare
a = 5.14 in O-Plane a = 5.06 in OH-Plane b = 8.93 in O-Plane	7.2 Å	Random stack- ing of unit cells	Tubes	.07 μ O.D. .04 μ I.D. 1 μ long.	5-10	2.55-2.56		Occasional
b = 8.62 in OH-Plane ∴layers curve	10.1 Å	Water layer between unit cells	Tubes	1 μ long.	5-40	2.0 -2.2	35–7 6	Occasional
dr	9.6Å—Complete separation	Dioctahedral	Flakes (Equi- dimensional)	>10 Å × up to 1	0 μ 80-150	2.35-2.7	50-120 Primary 700-840 Secondar	Very Common
	9.6 Å—Complete separation	Dioctahedral						Rare
2	9.6 Å—Complete separation	Dioctahedral	Lathe J	Breadth = 1/5 length to severa μ × unit cell	110–150 l	2.2 -2.7		Rare
	9.6 Å—Complete separation	Trioctahedral		To 1 μ × unit cell breadth = 0.02	l 17.5			Rare
	/	Trioctahedral	Similar to Mont.	-0.1μ Similar to Mont.	70-90	2.24-2.30		Rare
	*	Trioctahedral	Broad Laths	50 Å Thick				Rare
	10 Å	Both Dioctra- hedral and Trioctahedral	Flakes	.0031 μ × up to 10 μ	10-40	2.6 -3.0	65-100	Very Common
a = 5.34, b = 9.20 $c = 28.91, \beta = 93^{\circ}15'$	() { 10.5-14	Alternating Mios and double H ₂ O layers	Similar ro Illite		100–150		40-80 Primary 870 Secondary	Fairly Common
onoclinic (Mainly) a = 5.3, b = 9.3 c = 28.52, β = 97°8'	14 Å		Similar to Illite	1 μ	10–40	2.6 -2.96		Сошшоп
onoclinic $a = 2 \times 11.6$, $b = 2 \times 7.86$		Chain	Flakes or Fibers		20–30	2.08		Rare
$c = 5.33$ $a_0 \sin \beta = 12.9 b_0 = 18$ $c_0 = 5.2$		Double Silica Chains	Laths	Max, $4-5 \mu \times 50-100 \text{ Å}$ Width = 2t	20–30			Occasional

References
Grim, R. E. (1968) Clay Mineralogy, 2d edition, McGraw-Hill, New York.
Brown, G. (editor) (1961) The X-ray identification and Crystal Structure of Clay Materials, Mineralogical Society (Clay Minerals Group), London.

Table 3.3 Continued

IONIC RADII							
ION	Nonhydrated Radius Angstroms	Hydrated Radius Angstroms	ION	Nonhydrated Radius Angstroms	Hydrated Radius Angstroms	ION	Nonhydrated Radius Angstroms
Li+1	0.68-0.78	7.3-10.3	Ca+2	1.06-1.17	9.6	O-3	1.32
Na+L	_0.98	5.6- 7.90	Sr+2	1.27-1.34	9.6	OH-1	1.33
K+	1.33	3.8- 5.32	Ba+a	1.43-1.49	8.8	Mn	0.93
NH ₄ +1	1.43	5.37	Al+a	0.45-0.79		Fe+++	0.67
Rb ⁺¹	1.49	3.6- 5.09	La	1.22-1.30		Fe++	0.82
Ca+1	1.65	3.6- 5.05	Cl-1	1.81			
Mg ⁺³	0.78-0.89	10.8	Si+4	0.31-0.39			

Some deviation from listed radii may be expected in specific crystal structures.

and hydraulic conductivity behavior. Thus, mineralogy can be considered fundamental to the understanding of geotechnical properties, even though mineralogical determinations are not made for many geotechnical investigations. Instead, other characteristics that reflect both composition and engineering properties, such as Atterberg limits and grain size distribution, are determined.

Mineralogy is related to soil properties in much the same way as the composition and structure of cement and aggregates are to concrete, or as the composition and crystal structure of a steel are to its strength and deformability. In the case of all three of these engineering materials—soil, concrete, and steel—the mechanical properties can be measured directly, but the properties cannot be explained without consideration of mineralogy.

SUGGESTIONS FOR FURTHER STUDY

Bohor, B. F., and Hughes, R. E. (1971), "Scanning Electron Microscopy of Clays and Clay Minerals", Clays and Clay Minerals, Vol. 19, no. 1. pp. 49-54.

Brown, G., Ed. (1961), X-Ray Identification and Crystal Structure of the Clay Minerals, 2nd ed., Mineralogical Society of London.

Clays and Clay Minerals (Journal of the Clay Minerals Society), published six times annually by the Pergamon Press, New York.

Grim, R. E. (1962), Applied Clay Mineralogy, McGraw-Hill, New York.

Grim, R. E. (1968), Clay Mineralogy, 2nd ed., McGraw-Hill, New York.

Hurlbut, C. S. (1957), Dana's Manual of Mineralogy, 16th ed., Wiley, New York.

Marshall, C. E. (1964), The Physical Chemistry and Mineralogy of Soils, Vol. 1-Soil Materials, Wiley, New York.

Millot, G. (1970), Geology of Clays, Chapman and Hall, London.

Rich, C. I., and Kunze, G. W. (Ed.) (1964), Soil Clay Mineralogy, A Symposium, University of North Carolina Press, Chapel Hill.

Weaver, C. E., and Pollard, L. D. (1973), The Chemistry of Clay Minerals, Developments in Sedimentology 15, Elsevier, Amsterdam, 213 pp.

colloids gelotinous substance of small, insoluble, non diffusible-08-91

tannale:

CHAPTER 7

Clay-Water-Electrolyte System

7.1 INTRODUCTION

In Chapter 3 the composition, structure, and some of the characteristics of soil minerals were described. In Chapter 6 consideration was given to water and its interaction with soil particles. Interactions between soil particles, adsorbed cations, and water arise because there are unbalanced force fields at the interfaces between the constituents. When two particles are brought into close proximity, their respective force fields begin to overlap and may influence the behavior of the system if the magnitudes of these forces are large relative to the weights of the particles themselves. Clay particles, because of their small size and large surface area, are well known to be susceptible to such effects.

The effects of surface force interactions and small particle size are manifested by a variety of interparticle attractive and repulsive forces, which, in turn, influence or control the flocculation—deflocculation behavior of clays in suspension and the volume change and strength properties of clays at void ratios common to clay deposits encountered in engineering practice. Since the fabric acquired by a clay deposit at the time of formation may have a profound influence on its subsequent engineering properties, an understanding of factors influencing flocculation—deflocculation behavior is of considerable usefulness. Furthermore, postdepositional or postconstruction changes in engineering properties may be brought about by changes in physico-chemical forces of interaction.

Colloid chemistry provides a means for description of interactions in the clay-water-electrolyte system. In this chapter, the distributions of cations and anions adjacent to clay surfaces are considered, and the consequences in terms of particle interactions in suspen-

sions are examined. No attempt is made to give a rigorous treatment of colloid chemistry, emphasis is on the development of an understanding and appreciation for interactions in the systems of interest to geotechnical engineers.

One point that is sometimes confusing is that clays are usually treated as lyophobic (liquid-hating) or hydrophobic (water-hating) colloids rather than as lyophilic or hydrophilic colloids, even though water wets clays and is adsorbed on particle surfaces. This has resulted (van Olphen, 1963) from the need, historically, to distinguish colloids, such as clay, from colloids already termed hydrophilic, such as gums, which exhibit such an affinity for water that they spontaneously form a colloidal solution. Hydrophobic colloids are now considered to be those which are liquid dispersions of small solid particles; are twophase systems with a large interfacial area; have a behavior dominated by surface forces; and can flocculate in the presence of small amounts of salt. Claywater-electrolyte systems satisfy all these criteria.

7.2 ION DISTRIBUTIONS IN CLAY-WATER SYSTEMS

In a dry clay, adsorbed cations are tightly held by the negatively charged clay surfaces. Cations in excess of those needed to neutralize the electro-negativity of the clay particles and their associated anions are present as salt precipitates. When the clay is placed in water the precipitated salts go into solution. Because the adsorbed cations are responsible for a much higher concentration near the surfaces of particles, there is a tendency for them to diffuse away in order to equalize concentrations throughout. Their freedom to do so, however, is restricted by the negative electric field originating in the particle surfaces. The escaping

$$\sum_{i=0}^{k} B_{i,k}(t) = \sum_{i=0}^{k-1} B_{i,k-1}(t)$$

This calculation is straightforward, using the <u>recursive definition</u> and cleverly rearranging the sums:

$$\sum_{i=0}^{k} B_{i,k}(t) = \sum_{i=0}^{k} [(1-t)B_{i,k-1}(t) + tB_{i-1,k-1}(t)]$$

$$= (1-t) \left[\sum_{i=0}^{k-1} B_{i,k-1}(t) + B_{k,k-1}(t) \right] + t \left[\sum_{i=1}^{k} B_{i-1,k-1}(t) + B_{-1,k-1}(t) \right]$$

$$= (1-t) \sum_{i=0}^{k-1} B_{i,k-1}(t) + t \sum_{i=1}^{k} B_{i-1,k-1}(t)$$

$$= (1-t) \sum_{i=0}^{k-1} B_{i,k-1}(t) + t \sum_{i=0}^{k-1} B_{i,k-1}(t)$$

$$= \sum_{i=0}^{k-1} B_{i,k-1}(t)$$

(where we have utilized $B_{k,k-1}(t) = B_{-1,k-1}(t) = 0$).

Once we have established this equality, it is simple to write

$$\sum_{i=0}^{n} B_{i,n}(t) = \sum_{i=0}^{n-1} B_{i,n-1}(t) = \sum_{i=0}^{n-2} B_{i,n-2}(t) = \cdots = \sum_{i=0}^{1} B_{i,1}(t) = (1-t) + t = 1$$

The partition of unity is a very important property when utilizing Bernstein polynomials in geometric modeling and computer graphics. In particular, for any set of points $\mathbf{P_0}$, $\mathbf{P_1}$, ..., $\mathbf{P_n}$, in three-dimensional space, and for any \mathbf{t} , the expression

$$\mathbf{P}(t) = \mathbf{P}_0 B_{0,n}(t) + \mathbf{P}_1 B_{1,n}(t) + \dots + \mathbf{P}_n B_{n,n}(t)$$

is an <u>affine combination</u> of the set of points P_0 , P_1 , ..., P_n and if $0 \le t \le 1$, it is a convex combination of the points.

Degree Raising

Any of the lower-degree Bernstein polynomials (degree < n) can be expressed as a linear combination of Bernstein polynomials of degree n. In particular, any Bernstein polynomial of degree n-1 can be written as a linear combination of Bernstein polynomials of degree n. We first note that

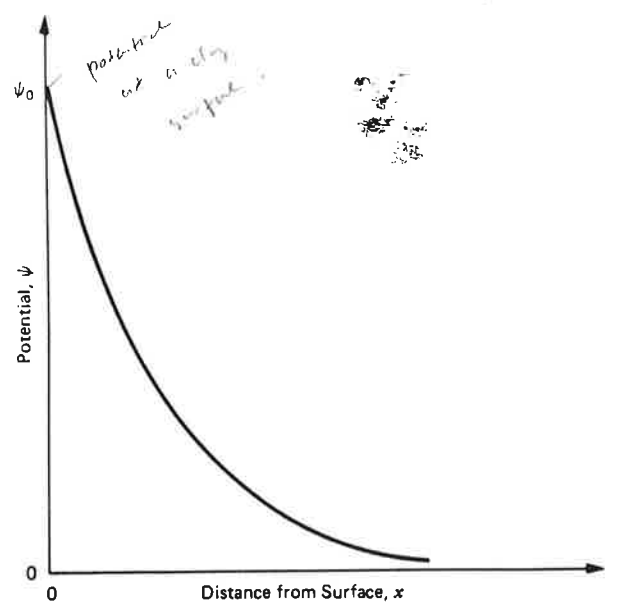


Fig. 7.2 Variation of electrical potential with distance from a charged surface. Except in very unusual cases ψ in soils is negative.

The concentration of ions of type i, n_i , in a force field at equilibrium is given by the Boltzmann equation

$$n_{io} \exp\left(\frac{E_{io} - E_i}{kT}\right) \tag{7.1}$$

where the subscript o represents the reference state, conveniently taken to be the conditions at a large distance from the surface, E is the potential energy, T is temperature (°K), and k is the Boltzmann constant $(1.38 \times 10^{-16} \text{ erg/°K})$. Concentrations n_4 and n_{60} are expressed as ions/cm³.

For ions in an electric field, the potential energy is given by

$$E_i = v_i e \psi \tag{7.2}$$

where v_i is the ionic valence, e is the unit electronic charge $(16.0 \times 10^{-20} \text{ coulomb or } 4.8 \times 10^{-10} \text{ esu})$, and ψ is the electrical potential at the point.* Potential varies with distance from a charged surface in the manner shown by Fig. 7.2. In clays, ψ is negative because of the negative surface charge. The potential at the surface is designated as ψ . As $E_{io} = 0$, because $\psi = 0$ at a large distance from the surface,

$$E_{io} - E_i = -v_i e \psi$$

• The electrical potential ψ is defined as the work to bring a positive unit charge from the reference state to the specified point in the electric field.

and the Boltzmann equation becomes

$$n_i = n_{io} \exp\left(\frac{-v_i e \psi}{kT}\right) \tag{7.3}$$

Equation (7.3) relates concentration to potential, as illustrated by Fig. 7.3. For negatively charged clay particles $n_{i}^{+} > n_{io}$ and $n_{i}^{-} < n_{io}$.

The Poisson equation relates potential, charge, and distance

$$\frac{d^2\psi}{dx^2} = -\frac{4\pi\rho}{D} \tag{7.4}$$

where x is distance from the surface, ρ is charge density, and D is dielectric constant. The charge density in the double layer is contributed by the ions so that

$$\rho = e \sum v_i n_i \tag{7.5}$$

Substitution for n_i from equation (7.3) gives

$$\rho = e \sum v_i n_{io} e^{(-v_i e \psi/kT)}$$
 (7.6)

which when substituted into equation (7.4) yields

$$\frac{d^2\psi}{dx^2} = -\frac{4\pi e}{D} \sum v_i n_{io} e^{(-v_i e\psi/kT)}$$
 (7.7)

Equation (7.7) is the general differential equation for the electric double layer adjacent to a planar surface. Its solution provides a basis for computation of electrical potential and ion concentrations as a function of distance from the surface.

For the case of a single cation and anion species of equal valence, that is, i = 2,

$$|v_{+}| = |v_{-}| \equiv v, n_{o}^{+} = n_{o}^{-} \equiv n_{o}$$

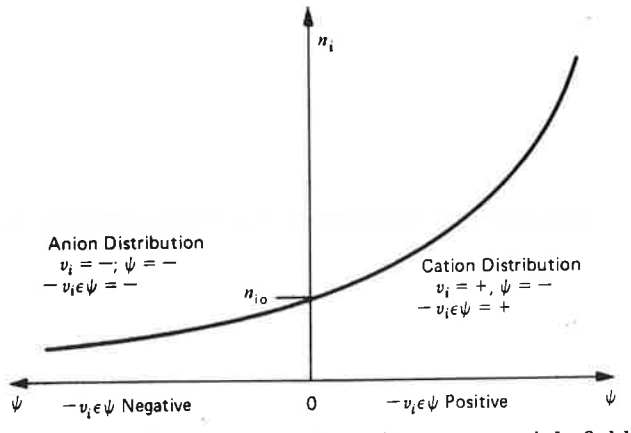


Fig. 7.3 Ionic concentrations in a potential field according to the Boltzmann equation.

genal

1

equation (7.7) simplifies to the Poisson-Boltzmann equation

$$\frac{d^2\psi}{dx^2} = \frac{8\pi n_0 ve}{D} \sinh \frac{ve\psi}{kT}$$
 (7.8)

for which solutions are available (Verwey and Overbeek, 1948; Bolt and Peech, 1953; Bolt, 1955a, 1956; Babcock, 1963; van Olphen, 1963).

As the influence of ions of the same sign as the surface charge (termed co-ions) is not very important (van Olphen, 1963, p. 252), the solutions can be applied to a good approximation when i = 2, but $|v_+| \neq |v_-|$. In the case where there is more than one counterion species (ions of the opposite sign as the surface charge, cations in the case of clays) the analysis is more complex, but some solutions are available. A few of the solutions are given here (Bolt, 1955a, 1956; van Olphen, 1963, and Collis-George and Bozeman, 1970).

There is a difference between the boundary conditions assumed for many classical colloid chemical treatments of the double layer and those appropriate for clays. In many systems, behavior is dictated in terms of a constant surface potential, which is controlled by the concentration of "potential-determining ions" in solution. A similar condition may hold for double layers that form on the edges of clay particles, as the solution characteristics control the association and dissociation of alumina in the edges of the octahedral sheets. However, the clay surfaces, which provide by far the major part of the surface area, exhibit a constant surface charge, determined by the isomorphous substitution in the clay structure. Solutions appropriate to the case of constant surface charge are given here; van Olphen (1963) compares the two solutions for some simple cases.

Single diffuse double layer

Solutions are commonly given in terms of the dimensionless quantities

$$y = \frac{ve\psi}{kT} \qquad \text{if a positional }$$

$$z = \frac{ve\psi_0}{kT} \qquad \text{(7.9)}$$

and

$$\xi = Kx$$

where

$$K^2 = \frac{8\pi n_0 e^2 v^2}{DkT} \text{ (cm}^{-2})$$
 (7.10)

In terms of these variables equation (7.8) becomes

$$\frac{d^2y}{d\xi^2} = \sinh y \tag{7.11}$$

Boundary conditions for the first integration are that for $\xi = \infty$, y = 0, and $dy/d \xi = 0$. Thus,

$$\frac{dy}{d\xi} = -2 \sinh\left(\frac{y}{2}\right) \tag{7.12}$$

The boundary condition for the second integration is that for $\xi = 0$, y = z ($\psi = \psi_0$), which leads to

$$e^{x/2} = \frac{e^{x/2} + 1 + (e^{x/2} - 1) e^{-\xi}}{e^{x/2} + 1 - (e^{x/2} - 1) e^{-\xi}}$$
(7.13)

Equation (7.13) describes a roughly exponential decay of potential with distance from a surface at given potential $(y_0 \sim \psi_0)$.

In the case where the surface potential is small (less than about 25 mV), $ve\psi/kT \ll 1$, and equation (7.8) may be approximated by

$$\frac{d^2\psi}{dx^2} = K^2\psi \tag{7.14}$$

where

$$\psi = \psi_0 e^{-Kz} \tag{7.15}$$

and the potential decreases purely exponentially with distance. In this case, the center of gravity of the diffuse charge is located at a distance x = 1/K from the surface. Consequently, the quantity (1/K) is often referred to as the "thickness" of the double layer.

The double layer charge is given by

$$\sigma = -\int_0^\infty \rho \ dx \tag{7.16}$$

and, using the Poisson equation, we obtain (74)

$$\sigma = \frac{D}{4\pi} \int_0^\infty \frac{d^2\psi}{dx^2} \, dx = -\frac{D}{4\pi} \left(\frac{d\psi}{dx} \right)_{x=0}$$
 (7.17)

 $y = \frac{ve\psi}{kT}$ y of the slope of the potential function at the surface $(d\psi/dx)_{x=0}$ can be found from equation (7.12), lead-

$$\sigma = \left(\frac{2n_0 DkT}{\pi}\right)^{1/2} \sinh \frac{z}{2} \tag{7.18}$$

for the general case, and to

ase, and to
$$\sigma = \left(\frac{DK}{4\pi}\right)\psi_0 \tag{7.19}$$

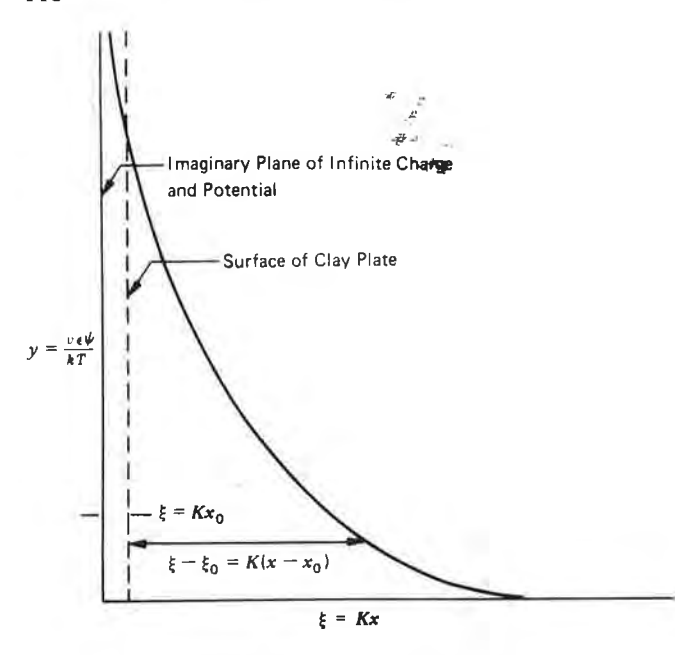


Fig. 7.4 Potential vs. distance relationship used to develop equation (7.20).

for the case of small ψ_0 . With the relationship between concentration and potential defined by equation (7.3), that between potential and distance by equation (7.13) or (7.15), and charge and surface potential related by equation (7.18) or (7.19), the double layer is completely described, provided the solution con-

centration n_0 , cation valence v, and either the surface charge σ or surface potential ψ_0 are known.

A somewhat simpler relationship between potential and distance than equation (7.13) can be obtained (Bolt, 1955a) by choosing the zero point for the ξ axis at an imaginary plane, a distance x_0 behind the true surface, where the potential reaches infinity (Fig. 7.4). This gives

$$\exp(-y) = \frac{\cosh \xi + 1}{\cosh \xi - 1} = \coth^2\left(\frac{\xi}{2}\right) \quad (7.20)$$

$$\xi_0 = Kx_s = \frac{4vc_0}{K\Gamma} \tag{7.21}$$

where c_0 is the concentration at a large distance from the surface in mmole/cm³ (= $1000n_0/N$ where N is Avogadro's number) and Γ is the surface charge density in meq/cm² (cation exchange capacity per specific surface). The relationship between the dimensionless potential function y and the dimensionless distance function ξ , as given by equation (7.20), is plotted in Fig. 7.5. Equation (7.21) is an approximation that is valid except for very high c_0 or very low Γ . Another form of equation (7.21) is

$$x = \frac{4}{v\beta\Gamma} \tag{7.22}$$

where $\beta = 8\pi F^2/1000DRT \approx 1 \times 10^{15}$ cm/mmole at 20°C, F is the Faraday constant, and R is the gas con-

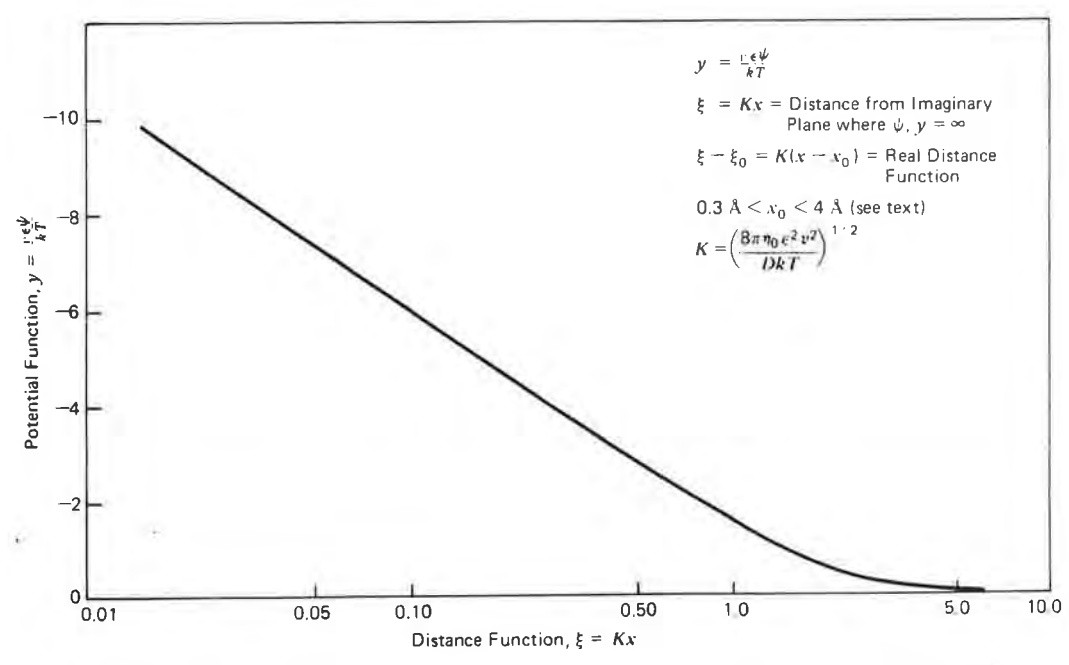


Fig. 7.5 Potential function vs. distance function for a single double layer.

stant-kN. According to Bolt (1956), x_0 can be approximated by 1/v Å for illite, 2/v Å for kaolinite, and 4/v Å for montmorillonite. It is evident from these values that the correction required to the distance functions to account for the distance to the imaginary plane where $\psi = \infty$ is small.

Although the case of a single diffuse double layer is not representative of the physical conditions in most actual clay systems because double layers of adjacent particles will usually overlap, the solutions are

useful in practice to provide estimates of thickness of diffuse layer, surface potentials, and effects of changes in solution composition.

Interacting double layers

The potential and charge distributions for the case of interacting double layers from parallel flat plates, separated at distance 2d are shown in Fig. 7.6. The potential function at the midplane, $y = ve\psi_d/kT$, is denoted by u, and the integration boundary condi-

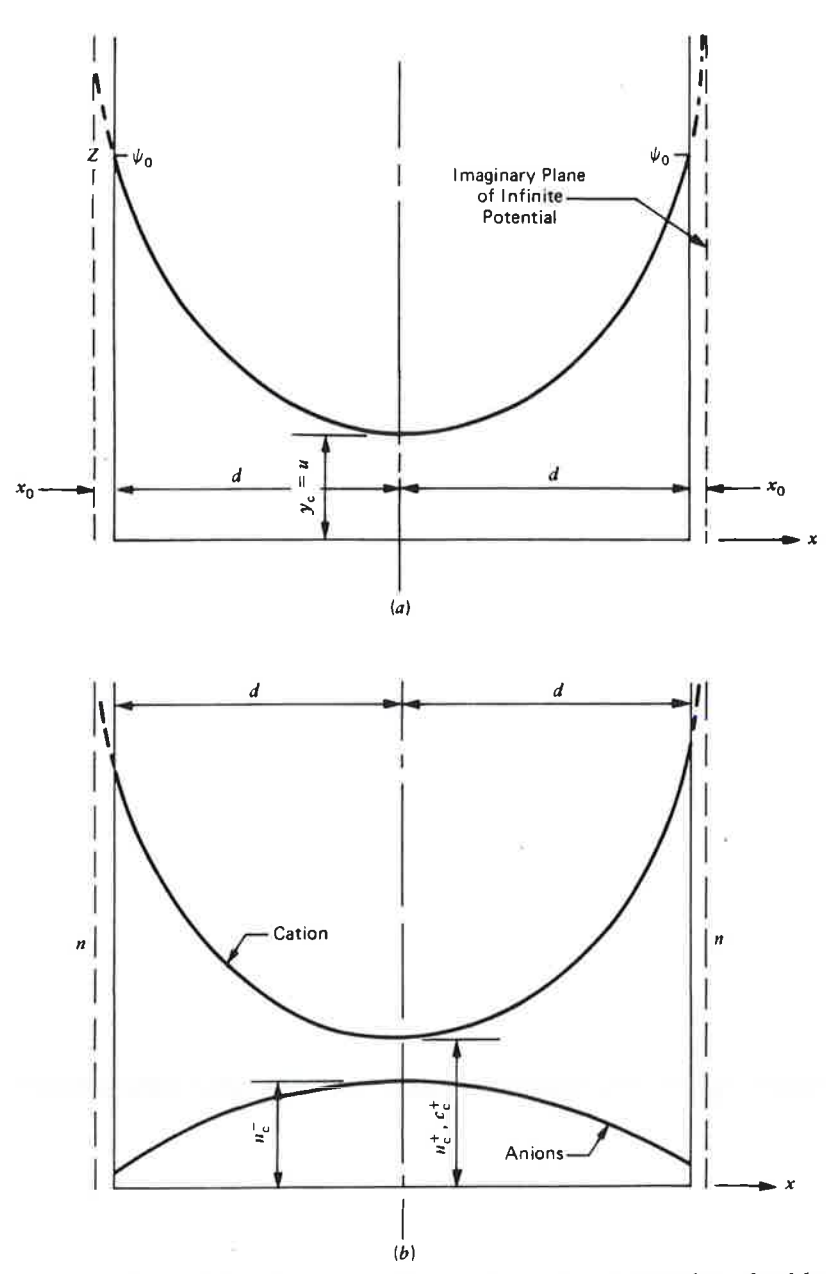


Fig. 7.6 Potential and charge distributions for interacting double layers from parallel flat plates. (a) Potential. (b) Charge.

tions for equation (7.11) are that for $\xi = Kd$, y = u, and $dy/d\xi = O$. The second integration using the boundary condition imposed on equation (7.12) leads to

$$\int_{z}^{u} (2 \cosh y - 2 \cosh u)^{-1/2} dy = -\int_{0}^{d} d\xi = -Kd$$
(7.23)

The integral in equation (7.23) can be evaluated using tables to give the midplane potential (from u) for given values of surface potential 2d and K. Corresponding values of Kd, z, and u are given by Verwey and Overbeek (1948), which are useful for computation of midplane potentials as a function of variations in plate distance and electrolyte concentration for the case of constant surface potential. Convenient tabulations for conditions of constant surface charge are given by van Olphen (1963).

For small interactions, that is, for large values of Kd, as would be the case for large plate separation, high n, high v, or small ψ_0 , the midplane potential can be taken as the sum of the double layer potentials at distance d based on the solutions for a single plate, that is,

$$u = 2y_d \tag{7.24}$$

Concentrations at the midplane can be obtained from Boltzmann's equation:

$$n_{-} = n_0 e^u$$
 and $n_{+} = n_0 e^{-u}$ (7.25)

Alternatively, midplane concentrations c_c may be computed using the following equation (Bolt, 1956):

$$v(\beta c_0)^{1/2}(x_0 + d) = 2\left(\frac{c_0}{c_c}\right)^{1/2} \int_{\phi - 0}^{\pi/2} \frac{d\phi}{(1 - (c_0/c_c)^2 \sin^2\phi)^{1/2}}$$
(7.26)

where all terms are previously defined. Values for the complete elliptic integral are given in standard tables.

The preceeding solutions all have been developed for systems containing a single cation species; however, as in the case of the single double layer, they are applicable to systems where $v_+ \neq v_-$, because the coions have little influence on the results. For systems containing mixed valent cations (e.g., Na+ and Ca²⁺), the equations are not applicable.

Collis-George and Bozeman (1970) have developed a double layer equation for heterovalent systems applicable to the case of constant surface charge. It shows that in a clay containing both monovalent and divalent cations there is a much greater concentration of divalent cations than monovalent cations near the particle surface even if the concentration of monovalent ions is much greater in the bulk solution.

Since the overlap of double layers of the same sign is potentially the source of an interparticle repulsion, it is reasonable to inquire if double layers in typical soils are sufficiently thick that interactions between those of adjacent particles can occur. If the quantity 1/K is taken as the "thickness" of the double layer, then values of 10 Å in a 0.1 M solution of monovalent cation, increasing to 100 Å in a 0.001 M solution are obtained. For water distributed uniformly on surfaces of clay particles, the water layer thickness is equal to half the particle spacing or d in Fig. 7.5. This thickness is given by the water content (cm3/g) divided by the surface area (cm²/g). For a water content of 50 percent and a specific surface in the range of 50 to 300 m^2/g , values of d from 17 to 100 Å are obtained, indicating that spacings are likely to be well within the range where interactions are important. In fact, in many cases, spacings may be small due to nonparallelism of particles, and the effects of other types of interparticle forces, including physical interactions between particles, may override the influences of double layer interactions.

Nonetheless, relationships of the type developed in this section are useful for understanding long range forces that control flocculation—deflocculation behavior, for study of swelling properties, and for analysis of some aspects of ion exchange.

7.4 INFLUENCES OF SYSTEM VARIABLES ON THE DOUBLE LAYER ACCORDING TO THE GOUY THEORY

Computations of ionic and potential distributions adjacent to charged surfaces show that the thickness of the double layer is sensitive to variations in surface charge density σ or surface potential ψ_0 , electrolyte concentration n_0 , cation valence v, dielectric constant of the medium D, and temperature T. An approximate quantitative indication of the influences of these factors can be seen in terms of the "thickness" of the double layer as given by

$$\frac{1}{K} = \left(\frac{DkT}{8\pi n_0 e^2 v^2}\right)^{1/2} \tag{7.27}$$

From this relationship it may be noted that the thickness decreases inversely as the valence and the square root of the concentration and that it increases with the square root of dielectric constant and temperature, other factors remaining constant.

Since the long range interparticle repulsive force depends on the amount of overlap or interaction between adjacent double layers, one can estimate the probable influences on behavior that result from changes in the system variables. In general, the thicker the double layer the less the tendency for particles in suspension to flocculate and the higher the swelling pressure in cohesive soils.

A numerical example is helpful for the quantitative illustration of the influence of system variables. Concentrations and potential distributions in single double layers will be developed using the relationships given in the previous section, and midplane concentrations and potentials are computed using Table III-2 of van Olphen (1963). The following conditions are assumed for the example: a montmorillonite clay with a specific surface of 800 m²/g and a cation exchange capacity of 83 meq/100 g, constant surface charge, and solutions of $0.83 \times 10^{-4} M$ NaCl, $0.83 \times 10^{-4} M$ CaCl₂ in water and $0.83 \times 10^{-4} CaCl_2$ in water and $0.83 \times 10^{-4} M$ NaCl in ethyl alcohol.

The following constants are needed: N= Avogadro's number = 6.02×10^{23} ions/mole; $k=1.38\times 10^{-16}$ ergs/°K; $e=4.80\times 10^{-10}$ esu; $D_{\rm water}=80$; and $D_{\rm ethyl\ alcohol}=24.3$.

The surface charge density is

$$\Gamma = \frac{0.83 \text{ meq/g}}{800 \text{ m}^2/\text{g}}$$

$$= \frac{0.83}{800} \text{ (meq/m}^2\text{)} \times \text{ (m}^2/10^4 \text{ cm}^2\text{)}$$

$$= 0.1035 \times 10^{-6} \text{ (meq/cm}^2\text{)}$$

$$\sigma = \Gamma \times \frac{F}{1000} = 0.1035 \times 10^{-6} \text{ (meq/cm}^2\text{)}$$

$$\times (96.5 \text{ coulomb/meq}\text{)}$$

$$= 10.0 \times 10^{-6} \text{ coulomb/cm}^2$$

$$\sigma = 10.0 \times 10^{-6} \text{ coulomb/cm}^2 \div 3.33$$

$$\times 10^{-10} \text{ coulomb/esu}$$

$$= 3.0 \times 10^4 \text{ esu/cm}^2$$

Effect of electrolyte concentration

A concentration change from $0.83 \times 10^{-4} M$ NaCl to $0.83 \times 10^{-2} M$ NaCl in water solution is considered. n_0 is the molarity \times N \times 10⁻³ ions/cm³ and is equal to $6.02 \times 10^{20} M$ ions/cm³; kT is equal to

 0.4×10^{-13} ergs at 290°K (17°C). For 0.83×10^{-4} M NaCl,

$$n_0 = 5.0 \times 10^{16} \text{ ions/cm}^3$$

$$K^2 = \frac{8\pi n_0 e^2 v^2}{DkT} = \frac{8\pi \times 5.0 \times 10^{16} \times (4.8 \times 10^{-10})^2 \times 1^2}{80 \times 0.4 \times 10^{-13}}$$

$$= 9.0 \times 10^{10}$$

$$K = 3.0 \times 10^3 \text{ cm}^{-1}$$

$$\frac{1}{K} = \text{"thickness'' of double layer} = 3.33 \times 10^{-6} \text{ cm}$$

$$= 333 \text{ Å}$$

and for $0.83 \times 10^{-2} M$ NaCl,

$$n_0 = 5.0 \times 10^{18} \text{ ions/cm}^3$$
 $K = 3.0 \times 10^6 \text{ cm}^{-1}$
 $\frac{1}{K} = \text{"thickness"} = 3.33 \times 10^{-7} \text{ cm} = 33.3 \text{ Å}$

The surface potential is given by equation (7.18).

$$\sigma = \left(\frac{2n_0 DkT}{\pi}\right)^{1/2} \sinh\left(\frac{z}{2}\right)$$

$$\sinh\left(\frac{z}{2}\right) = 3.0 \times 10^4 \left(\frac{\pi}{2n_0 \times 80 \times 0.4 \times 10^{-13}}\right)^{1/2}$$

$$= \frac{3.0 \times 10^4}{(n_0)^{1/2}} (49.1 \times 10^{10})^{1/2}$$

$$\sinh\left(\frac{z}{2}\right) = \frac{2.10 \times 10^{10}}{(n_0)^{1/2}}$$

For $0.83 \times 10^{-4} M$ NaCl

$$\sinh\left(\frac{z}{2}\right) = \frac{2.10 \times 10^{10}}{(5.0 \times 10^{18})^{1/2}} = \frac{2.10 \times 10^{10}}{2.23 \times 10^{8}}$$

$$= 0.94 \times 10^{2} = 94$$

$$\frac{z}{2} = \frac{ve\psi_{0}}{2kT} = 5.235$$

$$z = 10.47$$

$$\psi_{0} = \frac{kTz}{ve} = \frac{0.4 \times 10^{-13}}{1 \times 4.80 \times 10^{-10}}$$

$$\times 300^{*} \times 10^{3} \times 10.47 = 262 \text{ mV}$$

The corresponding values for $0.83 \times 10^{-2} M$ NaCl are

$$\sinh\left(\frac{z}{2}\right) = 9.4$$

* 1.0 esu of electrical potential is 299.79 V.

charge density. Furthermore, because we are dealing with a constant surface charge, the number of excess cations plus deficient anions in region ACD must equal that in region A'C'D'.

When the same systems are analyzed in terms of interacting parallel plates using van Olphen's (1963) tabulations, the results for surface and midplane potentials and concentrations as a function of plate spacing (2d) are as shown in Figs. 7.9 and 7.10. Values of water content are shown corresponding to half the plate spacings. The average value of half the plate spacing is given by the thickness of the water layer on each surface, or the water content divided by the specific surface, as noted earlier.

Figure 7.9 shows that interparticle spacing has essentially no influence on the surface potential except for half distances less than about 20 Å. The mid-

plane potential, however, is very sensitive to both spacing and concentration. Figure 7.10 indicates that interactions extend to much greater particle spacings for the low electrolyte concentration system. One mechanism of clay swelling is related to double layer interactions (Chapter 13), and higher swell pressures are associated with greater interactions. Thus, swelling behavior depends in part on the electrolyte concentration.

Effect of cation valence

For solutions of the same molarity and a constant surface charge, a change in cation valence affects both the surface potential and the thickness of the double layer. The surface potential function z computed from equation (7.18) is independent of valence. Thus, for the example considered (0.83 \times 10⁻⁴ M NaCl and

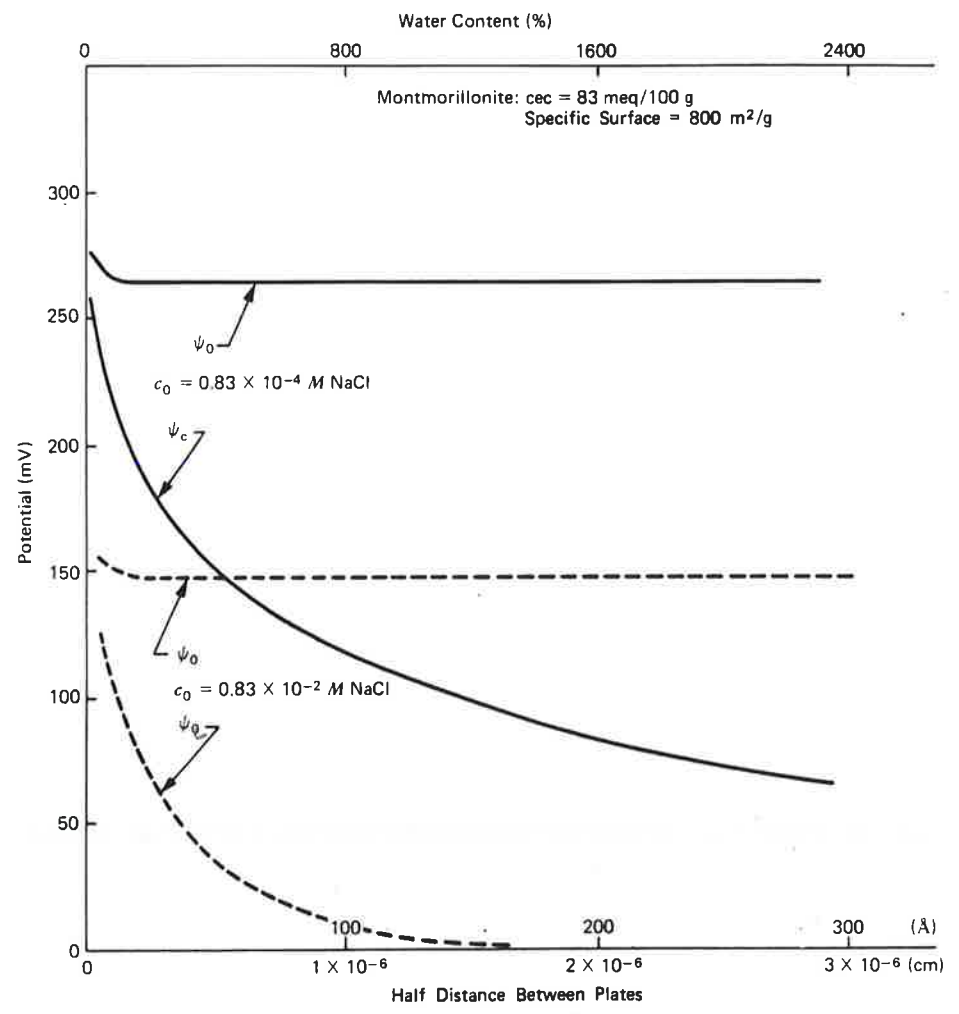


Fig. 7.9 Effect of electrolyte concentration on surface and midplane potentials for interacting parallel plates.

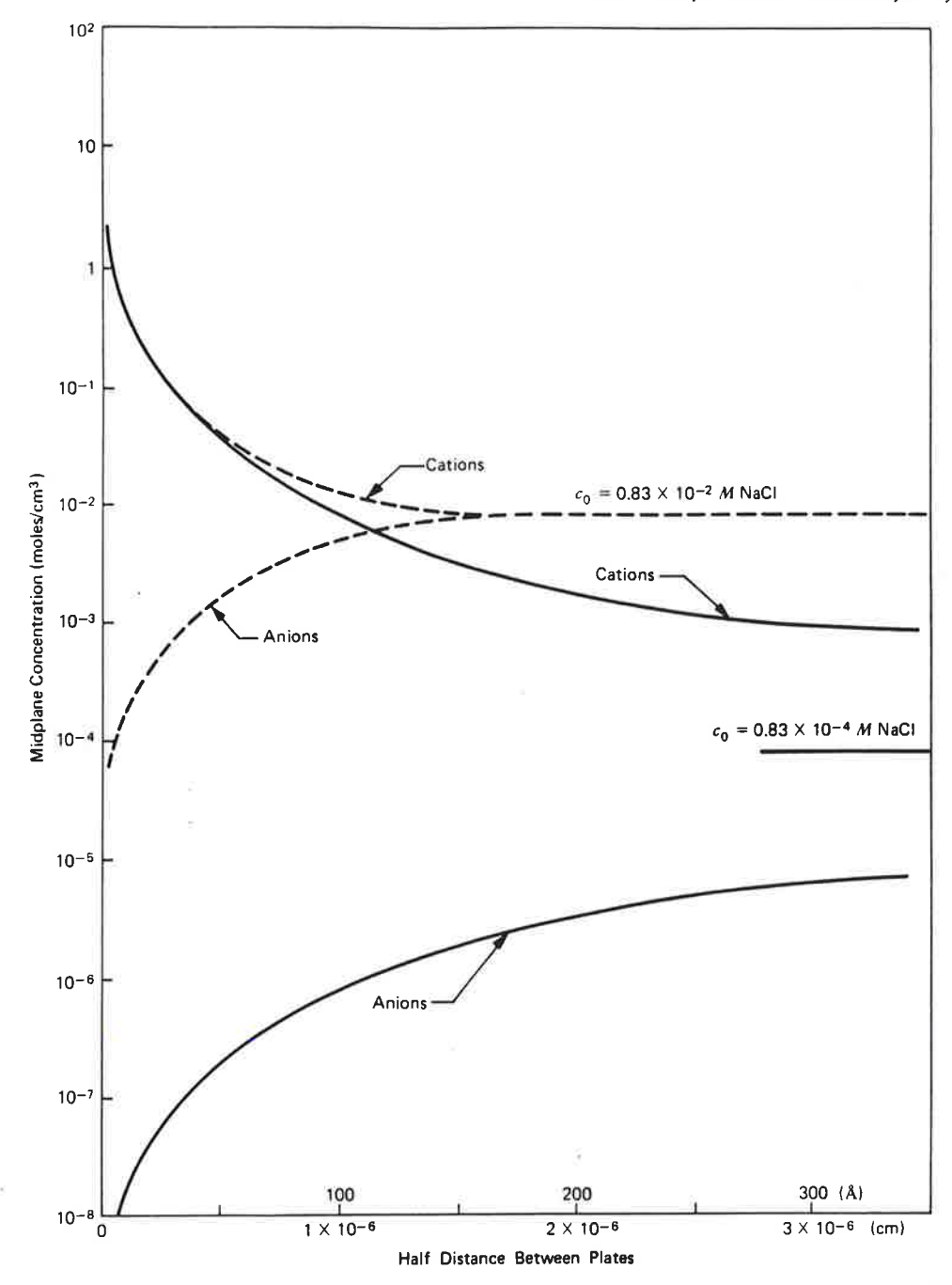


Fig. 7.10 Effect of electrolyte concentration on midplane concentration—parallel plates.

CaCl₂, $n=5\times 10^{16}$ ions/cm³), z is equal to 10.47, as computed previously. As ψ_0 varies inversely as v, the surface potential in the CaCl₂ system will be half that of the NaCl system, that is, $(\psi_0)_{\rm Na}=262$ mV, $(\psi_0)_{\rm Ca}=131$ mV. The effect of valence on double layer thickness can be seen through its effect on 1/K from equation (7.10)

$$\frac{1}{K} \propto \frac{1}{v}$$

The distributions of Na+ and Ca²⁺ are shown in Fig. 7.11. It also follows that an increase in valence will suppress the midplane concentrations and potential between interacting plates, thus leading to a decrease in interplate repulsion.

The preferential adsorption of multivalent ions, which is a well-established experimental fact, also predicted by the theory of Collis-George and Bozeman cited previously, means that even relatively small amounts of di- or trivalent cations added to claywater-monovalent electrolyte systems can have a significant influence on physical properties.

Effect of dielectric constant

The dielectric constant of the electrolyte-pore fluid system should influence both the surface potential and the double layer thickness. In dealing with a constant surface charge, the surface potential function will increase as D decreases, according to

$$\sinh\left(\frac{z}{2}\right) = \left(\frac{\pi}{2n_0 DkT}\right)^{1/2} \sigma \tag{7.28}$$

For a 0.83×10^{-4} M solution of NaCl in ethyl alcohol (D = 24.3) as opposed to water (D = 80),

$$\sinh\left(\frac{z}{2}\right) = 94 \times \left(\frac{80}{24.3}\right)^{1/2} = 170$$

$$\frac{z}{2} = \frac{ve\psi_0}{kT} = 5.83$$

$$z = 11.66$$

and

$$\psi_0 = 292 \text{ mV}$$

are obtained as compared with 262mV with water.

The effect of dielectric constant on thickness of the double layer is given by

$$\frac{1}{K} \propto D^{1/2}$$

so that with alcohol as the dielectric the layer will be reduced in thickness by a factor of (24.3/80)^{1/2} or 0.55.

Detailed consideration of the influences of dielectric constant may seem academic because the pore fluid in soils usually is water, but there may be special instances where liquids such as oil and waste chemicals are the pore fluid. The dielectric constant of these materials is different from that of normal water.

Effect of temperature

According to equations (7.18) and (7.27), an increase in temperature causes an increase in double layer thickness and a decrease in surface potential for a constant surface charge all other factors constant.

However, an increase in temperature results also in a decrease in the dielectric constant. The following tabulation shows the nature of the variation for water.

` '	DT
88	2.40×10^{4}
80	2.34×10^{4}
78.5	$2.34 imes 10^4$
66	$2.20 imes 10^4$
	80 78.5

The small variation of the product DT with change in temperature means, theoretically, that the double layer should not be influenced greatly. This assumes, of course, that the values of the dielectric constant are unaffected by particle surface forces and ionic concentration. It also accounts, in part, for apparent contradictory findings reported in the literature on the effects of temperature change on such soil properties as strength, compressibility, and swelling.

7.5 SHORTCOMINGS OF DOUBLE LAYER THEORY AND ADDITIONAL FACTORS INFLUENCING BEHAVIOR

The validity of the Gouy-Chapman theory may be examined in at least two ways: in terms of its completeness in taking into account factors likely to influence behavior, and in terms of its ability to describe observed behavior. The first of these is considered here, and the second is examined in several places in later chapters.

Effects of secondary energy terms

Several energy terms should be important in real systems (Bolt, 1955a). These are the effect of the electrical field strength on the dielectric constant, coulombic interaction between the ions, and short range repulsion between the surface and ions. The results from a corrected theory are almost the same as those from the simple theory for double layer interaction, although a corrected theory is more suitable for description of ion exchange.

Adsorbed water effects

The effects of the electric field and water structure on the water pressure in the double layer may be important (Low, 1961; Ravina and Zaslavsky, 1972), and this may influence behavior. Some revision of the theory has been proposed to take these effects into account.

effect of ion size-The Stern layer

The application of the relationships presented in the last section to some systems may lead to impossibly high ion concentrations next to the surface. This is because the theory deals with point charges; whereas, ions are of finite size. Thus, the actual concentration adjacent to the surface will be less than predicted. The hydrated radii of some cations in soils

Ion	Hydrated Radius (Å)
Li+	7.3-10.0
Na+	5.6- 7.9
Na' K+	3.8- 5.3
	5.4
NH+	3.6- 5.1
Rb+	3.6- 5.0
Ca+	10.8
Mg ²⁺	9.6
Ca ²⁺	9.6
Sr ²⁺ Ba ²⁺	8.8

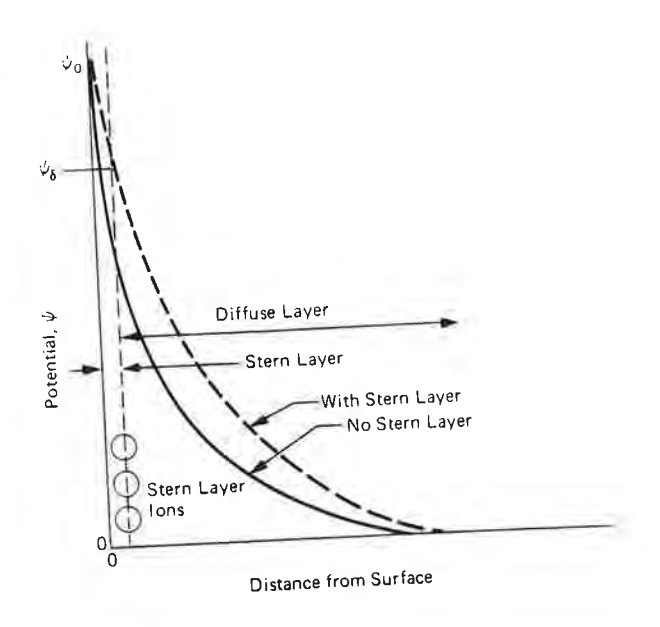
The Gouy-Chapman theory has been corrected for his effect (Stern, 1924), and the theory is summarized by van Olphen (1963) for both single and interacting flat double layers. The so-called "Stern layer" is assumed to consist of counterions in a closely packed layer close to the surface with an adjacent diffuse layer extending into the solution. The equations enable computation of the charge in each layer and the potential at their interface.

The physical consequences of the development of a Stern layer in terms of potential and cation distributions are shown in Fig. 7.12. From a particle interaction standpoint, the larger the ion size the thicker the layer required to accommodate the necessary number of cations, and hence the greater the repulsion.

The effect of pH

Clay particles may have hydroxyl (OH) exposed on their surfaces and edges. The tendency for the hydroxyl to dissociate,

is strongly influenced by the pH*; the higher the pH, the greater the tendency for the H+ to go into solu-



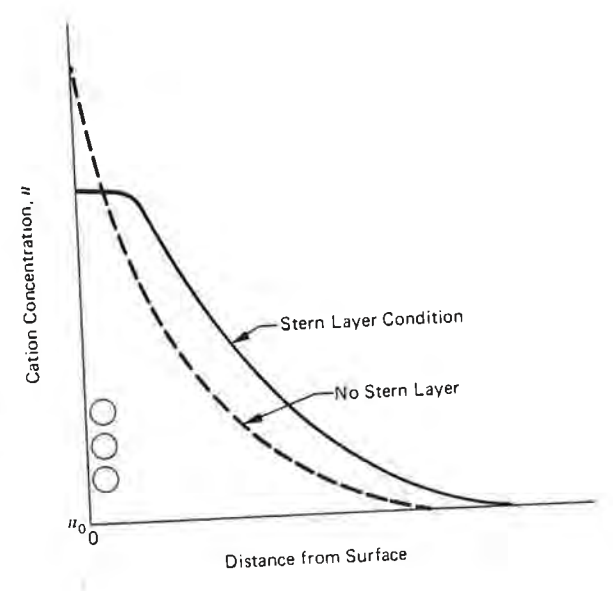


Fig. 7.12 Effect of Stern layer on cation concentration and double layer potential.

tion, and the greater the effective negative charge of the particle.

In addition to this, alumina, which is exposed at the edges of clay particles, is amphoteric and ionizes positively at low pH and negatively at high pH. As a consequence, positive double layers may develop at the edges of some clay particles in an acid environment. Such double layers are of the constant surface potential type, as opposed to constant surface charge, with H+ serving as the potential determining ion.

[•] $pH = \frac{1}{\log_{10}H^* \text{ concentration}}$; $pH < 7 - \text{acid-high } H^* \text{ concentration}$ tion, and pH > 7-basic-low H+ concentration.

Because of both of these considerations, pH plays a very important role in the behavior of clay suspensions. A low pH promotes a positive edge to negative surface interaction, often leading to flocculation from suspension. Stable suspensions or dispersions of clay particles often require high pH conditions. While a proper understanding of the behavior of many claywater systems cannot be obtained without consideration of the influences of pH, quantitative relationships for doing so do not appear to be available at present.

Effects of anion adsorption

The theory as developed assumes attraction of cations to the negatively charged clay surfaces and repulsion of all anions, leading to concentration distributions of the type shown in Fig. 7.8. There may be situations, however, where specific anions are attracted to and essentially become part of particle surfaces or edges, thereby increasing the electronegativity.

Attraction of anions, particularly those such as phosphate, arsenate, and borate, which have about the same size and geometry as the silica tetrahedron, appears well established. Phosphates, in particular, seem strongly attracted, as certain of the phosphate compounds are among the most effective deflocculating agents for soil suspensions. Little is known about whether or not clays can have anion exchange spots on basal surfaces, although replacement of (OH)— is a plausible mechanism.

7.6 ENERGY AND FORCE OF REPULSION

Knowledge of the potential and charge distributions between interacting double layers can be used to compute the energy and force of electrostatic repulsion per unit area of plate. The repulsive energy V_R is given by

$$V_{\rm R} = 2(F_{\rm d} - F_{\rm \infty}) \tag{7.29}$$

where $F_{\rm d}$ is the free energy of the double layer per unit area at a plate spacing of 2d, and F_{∞} is the free energy of a single noninteracting double layer. Tabulations of $F_{\rm d}$ and F_{∞} for the constant surface potential case are available (Verwey and Overbeek, 1948).

The repulsive force per unit area (repulsive pressure) can be computed as the difference in osmotic pressure (see Chapter 13) midway between plates relative to that in the equilibrium solution. The osmotic pressure difference depends directly on the difference in numbers of ions in the two regions, that is,

$$p \propto n_c^+ + n_c^- - (n_0^+ + n_0^-)$$

 $\therefore p \propto n_0 e^u - n_0 + n_0 e^{-u} - n_0 = 2n_0 (\cosh u - 1)$

The resulting equation is (van Olphen, 1963)

$$p = 2n_0kT (\cosh u - 1) (7.30)$$

127

which is valid for both constant charge and constant potential surfaces, with u computed for the appropriate condition. A corresponding equation may be written using Bolt's formulation or equation (7.26). These relationships have been used, with varying degrees of success, as a basis for the physico-chemical description of clay swelling, and are considered further in Chapter 13.

7.7 LONG RANGE ATTRACTION

Fluctuating dipole bonds (van der Waals forces) act between all units of matter and are the source of attraction between colloidal particles (Section 2.4). The attractive energy between pairs of molecules $V_{\rm A}$ (London, 1937) was extended by Casimir and Polder (1948) to obtain the attraction between parallel plates by assuming interaction to be additive. The following equation was obtained:

$$V_{\mathbf{A}} = -\left[\frac{\mathbf{A}}{48\pi} \frac{1}{d^2} + \frac{1}{(d+\delta)^2} - \frac{2}{(d+\delta/2)^2}\right] \quad (7.30)$$

where d is the half distance between plates measured from the plane of surface layer atoms, σ is the thickness of the plate measured between the same planes, and A is the van der Waals constant, which is in the range 10^{-11} to 10^{-14} ergs. van Olphen (1963) suggests A to be of the order of 10^{-12} ; whereas, Derjaguin (1960) considers 5×10^{-14} a more reasonable value. Equation (7.30) has been widely used in conjunction with relationships for repulsion as a function of distance for the development of net curves of interaction between parallel plates (Verwey and Overbeek, 1948).

Later work, e.g., Lifshitz (1955), Derjaguin (1960), has shown that the van der Waals forces are electromagnetic, and that the instantaneous electric moment is frequency dependent. As a result the Casimir-Polder theory is invalid but is a good approximation for particle separations less than about 1000 Å. The Lifshitz theory (Lifshitz, 1955; Dyzaloshinskii et al., 1961) applies for all particle separations. The general results of these theories (Ingles, 1962) are that the at-

tractive forces are dependent on distance according to

Casimir-Polder Theory
$$F_1 \alpha \frac{Ak}{d^3}$$

Lifshitz Theory
$$F_2 \alpha \frac{Bk'}{d^4}$$

where A, B, k and k' are constants. A is of the order of 10^{-13} erg and B, an analytically deducible constant, is of the order of 10^{-19} erg-cm. Black et al (1960) determined a force per cm² between parallel quartz plates given by

$$F_2 = \frac{C}{d_u^4} \, \text{dyne/cm}^2 \tag{7.31}$$

where d_{μ} is separation distance in μm and

$$C = 1.0 \times 10^{-3}$$
 to 2.0×10^{-3} (experimental)

$$C = 0.6 \times 10^{-3}$$
 to 1.6×10^{-3} (theoretical—
Lifshitz theory)

The close agreement between theory and experiment is encouraging, as past results were often in conflict.

For the general case of two bodies separated by a medium, the complex dielectric constant must be known for the full range of frequencies. Although the resulting equations are complicated, some simplification is possible in certain cases (Dzyaloshinskii et al, 1961). For two clay particles having static dielectric constants D_{10} , separated at distance d by a pore fluid having a static dielectric constant D_{30} , the following relationship is obtained

$$F_2 = \frac{\pi}{480} \frac{hc}{d^4} \frac{1}{\sqrt{D_{30}}} \frac{D_{10} - D_{30}}{D_{10} + D_{30}} \Phi \left(\frac{D_{10}}{D_{30}} \right)$$
(7.32)

where h is Planck's constant and c is the velocity of light. The function Φ (D₁₀/D₃₀) is shown in Fig. 7.13. The static dielectric constant of clay particles D₁₀, is approximately 4.0.

Evaluation of the coefficient of $1/d^4$ in equation (7.32) (which is the same as C in equation (7.31)), as a function of the dielectric constant of the medium separating particles D_{30} , for d in μ m, gives the result shown in Fig. 7.14. Thus, according to the Lifshitz theory the dielectric constant of the pore fluid in a clay should influence the attractive forces in the manner shown.

As interparticle repulsions due to double layer interactions increase monotonically $(1/K \alpha D^{1/2})$ with increasing dielectric constant, the net force of interaction should vary in the manner shown in Fig. 7.15 (Moore and Mitchell, 1974). Figure 7.16 shows the

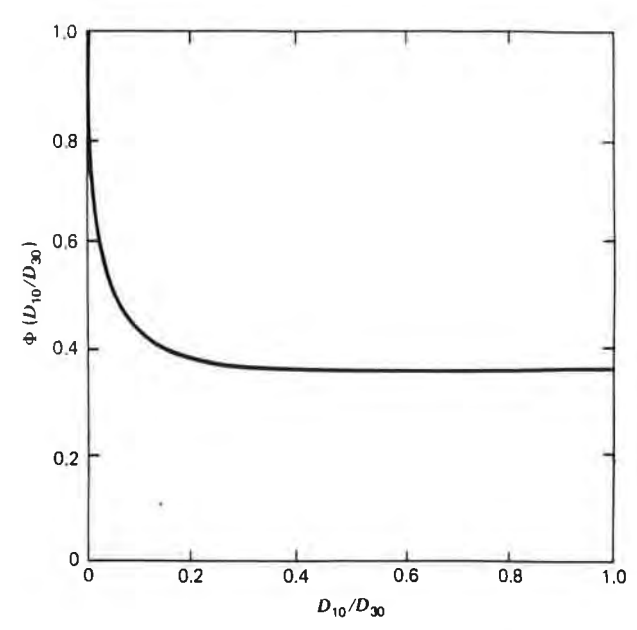


Fig. 7.13 Dielectric constant function for attractive force calculation by Lifshitz theory (After Dzaloshinskii, Lifshitz, and Pitaevskii, 1961).

variation of undrained strength (normalized to that with water as the pore fluid) with dielectric constant of the pore fluid for three series of tests on kaolinite. In each case, samples were consolidated initially in water, followed by leaching with water-miscible pore fluids. Since it seems reasonable that strength should depend on the net attractive force between particles, and the variation in strength with D_{30} is similar to

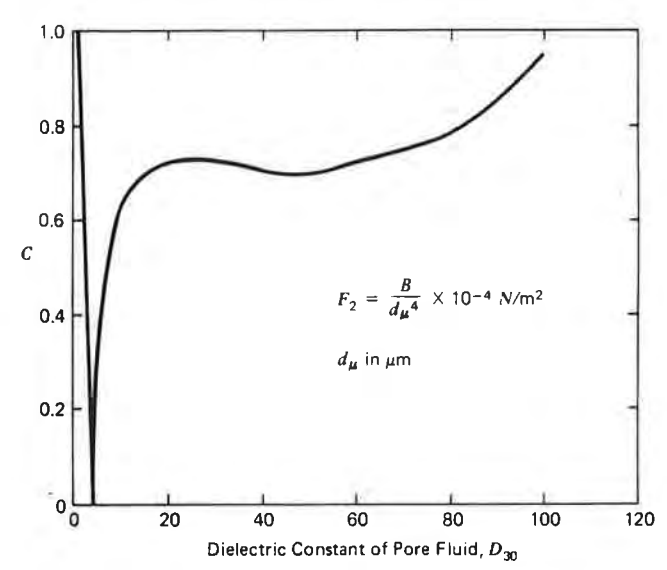


Fig. 7.14 Effect of dielectric constant of the pore fluid on van der Waals attraction.

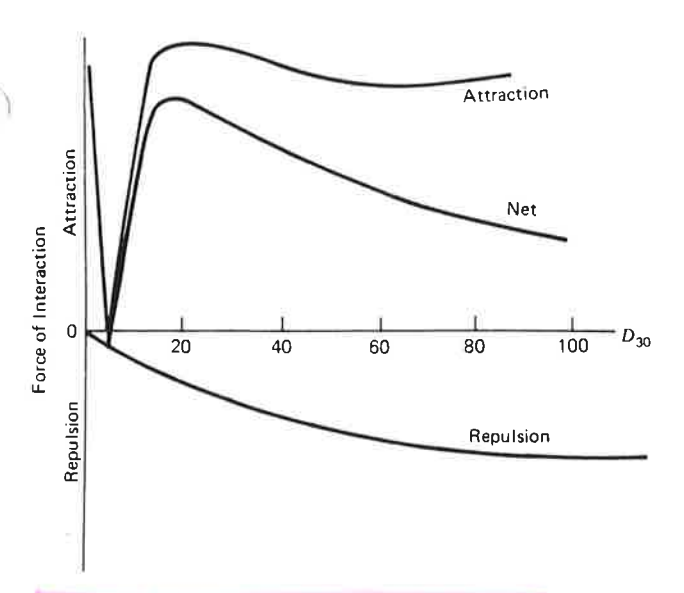


Fig. 7.15 Combined forces of interaction.

that of the van der Waals attraction (Figs. 7.14 to 7.16), there appears some support for the use of the Lifshitz theory for van der Waals forces in clay systems.

Although a condition of perfectly parallel plates is not a probable particle arrangement in a clay soil, and particle corners, edges, and asperities are likely to be in contact with adjacent particles, the average particle surface to particle surface distance should be great enough (a few tenths of a micrometer or more) to justify application of the Lifshitz theory. It should be noted also that for the case of interaction of a flat plate and one or two spheres the attractive force decays as $1/d^3$ instead of $1/d^4$ (Ingles, 1962).

7.8 NET ENERGY AND FORCE OF INTERACTION

Double layer repulsions and van der Waals electromagnetic attractions combine in the manner shown schematically in Fig. 7.17. The energy of repulsion is sensitive to changes in electrolyte concentration, cation valence, dielectric constant, and pH; whereas, the attractive energy is sensitive only to changes in the dielectric constant and temperature. In cases where the net curve of interaction exhibits a high repulsive energy barrier, particles in suspension are prevented from close approach, and the suspension will be stable. In cases where the repulsive energy barrier does not exist, particles are drawn into close proximity and flocculation results, represented by

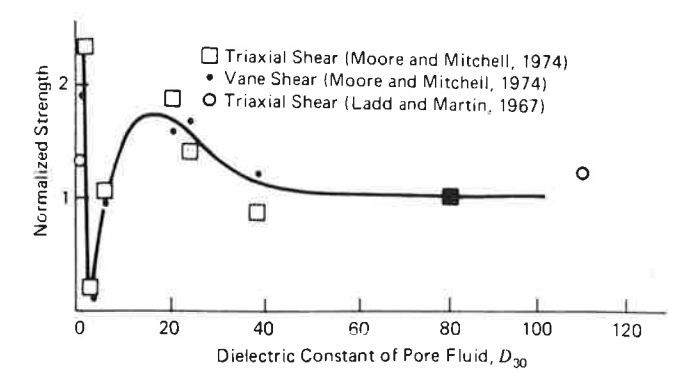


Fig. 7.16 Effect of the dielectric constant of the pore fluid on the strength of Peerless #2 kaolinite.

the minima in the energy curves. In this case, flocs of several particles settle together from suspension.

The character of the net curve of interaction may have a major influence on the particle arrangements in sedimented deposits of clay. Changes in system chemistry, which in turn can cause changes in the net curve of interaction, may have important consequences in terms of the behavior of the soil when disturbed or subjected to the action of flowing water.

7.9 CATION EXCHANGE—GENERAL CONSIDERATIONS

From the considerations in Section 7.5, it is apparent that the type and amount of different cations in a clay-water-electrolyte system have a major influence on double layer interactions. Changes in these interactions may lead to changes in physical and physicochemical properties. Under a given set of environmental conditions (temperature, pressure, pH, total electrolyte concentration), a clay adsorbs cations with a fixed total charge. Exchange reactions involve replacement of these ions with a group of different ions having the same total charge. The exchange of ions of one type by ions of another type does not affect the structure of clay particles themselves.

Common ions in soils

The most commonly found cations in soils are calcium (Ca²⁺), magnesium (Mg²⁺), sodium (Na⁺), and potassium (K+), usually in that decreasing order of abundance for residual and nonmarine sedimentary soils. The commonest anions in soils are sulfate (SO_4^{2-}), chloride (Cl⁻), phosphate (PO_4^{3-}) and nitrate (NO_3^{-}).

equal, trivalent cations are held more tightly than divalent, and divalent more tightly than monovalent. Ordinarily small cations tend to displace large cations. A typical replaceability series is

$$\begin{array}{l} Na^+ < Li^+ < K^+ < Rb^+ < Cs^+ < Mg^{2+} < Ca^{2+} \\ < Ba^{2+} < Cu^{2+} < Al^{3+} < Fe^{3+} < Th^{4+}_{M^{\prime}} \end{array}$$

It is possible, however, to displace a cation of high replacing power, such as Al³⁺, by one of low replacing power, such as Na⁺, by mass action, wherein the concentration of sodium in solution is made very high relative to that of aluminum.

Rate of exchange

The rate of exchange varies with clay type, solution concentrations, temperature, and so on. In general, however, exchange reactions in the kaolin minerals are almost instantaneous. In illites, a few hours may be needed for completion, because a small part of the exchange capacity may be between unit layers. A longer time is required in the smectites, because the major part of the exchange capacity is located in the interlayer region.

Organic ions

Organic anions and cations may be adsorbed by clays as well as inorganic ions, and both exchange adsorption and adsorption onto particle surfaces in place of previously adsorbed water molecules may occur (van Olphen, 1963). Although clay-organic reactions have not been studied extensively by engineers, they are of importance in the technology of drilling fluids, in stability control of clay suspensions, in the manufacture of lubricants as flocculation aids, in soil stabilization, and in soil conditioners for agricultural purposes.

7.10 STABILITY OF ADSORBED ION COMPLEXES ON CLAYS

Ion exchange reactions usually occur in aqueous environment; however, clays can also take ions from trace concentrations in solution of rather insoluble substances by exchange and adsorption reactions, even when little water is present. The deterioration of clay samples after prolonged storage in Shelby tubes is a good example of this. The process, sometimes termed galvanic action, involves adsorption by the clay minerals of iron ions as soon as they pass into solution from the tube. Because the clay takes up the iron ions quickly there remains a tendency for further solution

of the metal tube, so the process continues. The result is that after some weeks or months the clay in contact with the sample tube is altered, and no longer representative of the *in situ* material. Hence, some organizations now use stainless steel, brass, or tube williners to minimize this corrosive process.

Other examples may be cited of how a clay of one ionic form may alter to another over relatively short time periods, depending on the disequilibrium with the environment. The results of a number of studies have been published in which a clay was reported as a "hydrogen clay," in that special treatments had been used in an attempt to make the clay homoionic in hydrogen. The behavior of such clays was generally observed to be characteristic not of a clay containing monovalent adsorbed cations, but more nearly like that of a material with di- or trivalent cations. Subsequent work has shown that after preparation of "hydrogen clays," aluminum ions move from octahedral lattice positions and displace the hydrogen ions from the exchange sites, producing an aluminum clay.

Findings of this type underscore difficulties in attempting to study homoionic clay systems. They also raise questions relative to proper interpretation of clay behavior under changed environmental conditions. The selectivity of clay surfaces for different ions in mixed ion systems is temperature-dependent. Bischoff, Greer, and Luistro (1970) found that the composition of the interstitial waters of a clayey marine sediment was altered as a result of a change in tem perature from 5°C at the ocean bottom to 22.5°C in the laboratory, as shown in Fig. 7.18. As the free pore water concentrations of potassium and chlorine were increased by 13 and 1.4 percent, respectively, whereas magnesium and calcium were depleted by 2.5 and 4.9 percent, it can be inferred that the proportions of these constituents in the exchange complex were changed in the opposite direction.

Fanning and Pilson (1971) tound that the interstitial silica concentration in water squeezed from a marine sediment was 51 percent higher after warming to a temperature 20°C greater than the *in situ* value, and the pH was also slightly higher. It would appear, therefore, that until the effects of temperature change on the chemistry of fine-grained soils are better understood, testing at *in situ* temperature would be desirable.

7.11 THEORIES OF ION EXCHANGE

A number of theories have been proposed for the quantitative description of the equilibrium concen-

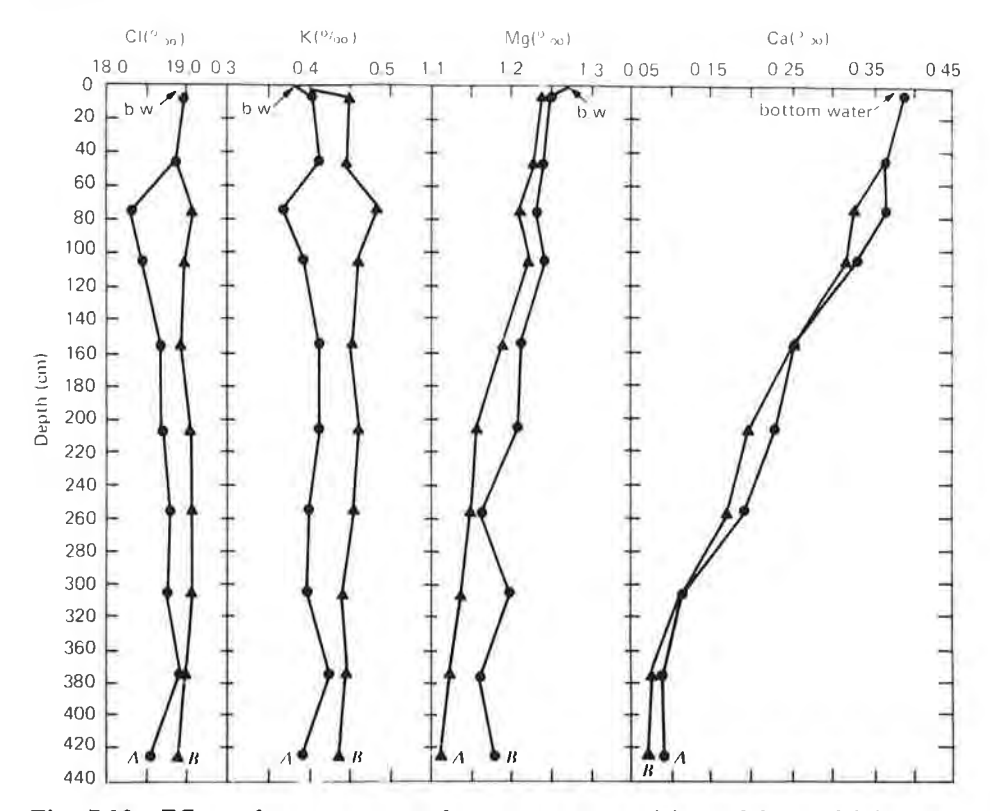


Fig. 7.18 Effect of temperature change on composition of interstitial water of a marine sediment (Bischoff, Greer, and Luistro, 1970). Relationship of depth to concentrations (in parts per thousand) of chloride, potassium, magnesium, and calcium in interstitial water from the San Pedro basin; A refers to samples squeezed at in situ temperature 5.0°C), and B refers to those equilibrated to laboratory temperature (22.5°C) for 1 hr prior to squeezing. Core location, 33°28'12"N, 118°20'09"W; water depth, 950 m.

trations of different cations in the adsorbed layer in terms of concentrations in the bulk solution. Approaches to the problem have included application of the mass law, kinetic theory, Donnan theory, and double layer theory. None has been completely satisfactory because of the great complexity of the system and the large number of variables involved.

Approaches based on double layer theory (Bolt, 1955b; van Olphen, 1963; Bolt and Page, 1965) and on the mass law appear to have given the best results. In the case of mixed cations of the same valence, double layer theory predicts the ratio of counterion concentrations in the double layer to be the same as in the equilibrium solution. Because of differences in ion size and specific interaction energies, however, substantial deviations may exist.

From double layer theory, it may be derived (Collis-George and Bozeman, 1970) that in monovalentdivalent systems the ratio of divalent to monovalent cations is much higher in the double layer than in the equilibrium solution. This accords well with experimental observations. For practical purposes the Gapon equation is useful for assessing the proportions of monovalent and divalent ions, except in highly acid soils.

If the subscript s refers to the exchange complex of the soil, the subscript e refers to the equilibrium solution, M and N are monovalent ion concentrations, and P refers to the concentration of divalent ions, then

$$\left(\frac{M^+}{N^+}\right)_s = k_1 \left(\frac{M^+}{N^+}\right)_e \tag{7.33}$$

$$\left(\frac{M^+}{P^{2+}}\right)_s = k_2 \left[\frac{M^+}{(P^{2+})^{1/2}}\right]_s$$
 (7.34)

where k_1 and k_2 are selectivity constants. The relationships given by equations (7.33) and (7.34) are in-

corporated in the statement of Schofield's ratio law, which is: A change in bulk solution concentration will not change the adsorbed ion equilibrium if the concentration of monovalent ions is changed in one ratio, the concentration of divalent ions in the square of that ratio, and the concentration of trivalent ions in the cube of that ratio.

As an example, if the proportions of Na+ and Ca²⁺ in the adsorbed complex are equal, and the concentration of Na+ in the free solution is doubled, then the concentration of Ca²⁺ in the free solution must be quadrupled if the proportions of adsorbed ions are to remain the same.

A useful practical form of the Gapon equation is

$$\left(\frac{Na^{+}}{Ca^{2+} + Mg^{2+}}\right)_{s} = k \left[\frac{Na^{+}}{[(Ca^{2+} + Mg^{2+})/2]^{1/2}}\right]_{e} (7.35)$$

where concentrations are in milliequivalents per liter. The quantity

$$\left[\frac{\text{Na}^{+}}{[(\text{Ca}^{2+} + \text{Mg}^{2+})/2]^{1/2}}\right]_{e} = \text{SAR (meq/liter)}^{1/2} \quad (7.36)$$

is termed the sodium adsorption ratio (SAR). It can be determined by chemical analysis of the pore water (saturation extract). The selectivity constant k has been found to have a value of 0.017 for a wide range of soils. Thus, for these soils, if the composition of the pore fluid is known, the relative amounts of monovalent and divalent ions in the adsorbed cation complex can be estimated.

The proportion of sodium in the adsorbed layer has an important bearing on the structural status of a soil, and is often described in terms of the exchangeable sodium percentage (ESP), defined by

$$ESP = \frac{(Na^{+})_{s}}{\text{total exchange capacity}} \times 100 \quad (7.37)$$

The results of a number of studies (e.g., Richards, 1954; Aitchison and Wood, 1965; Ingles, 1968; Ingles and Aitchison, 1969; Sherard, Decker, and Ryker, 1972a; and Arulanandan et al., 1973) have indicated that the ESP and the SAR provide a good indication of the stability of clay soil structure to breakdown and particle dispersion, at least in the case of nonmarine clays. Soils with ESP greater than about 2 percent are susceptible to spontaneous dispersion in water. Both acid and alkaline soils may be dispersive, as well as many soils with very high porewater salt contents, up to and exceeding 100 meq./liter.

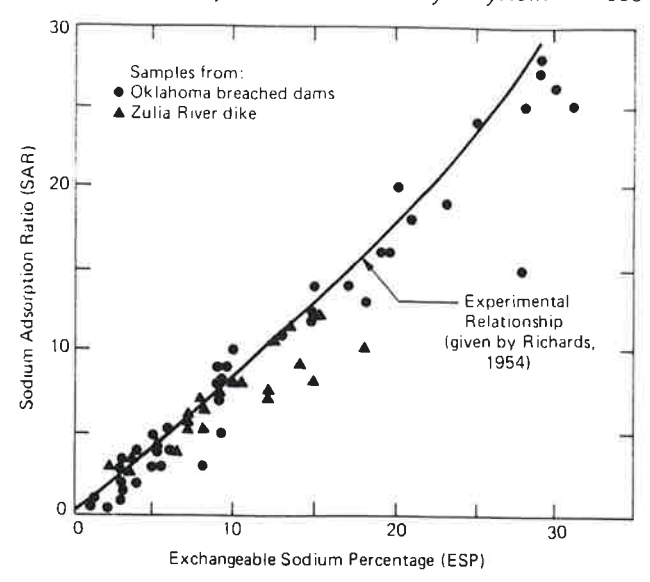


Fig. 7.19 Correlation between exchangeable sodium percentage and sodium adsorption ratio (Sherard, Decker, and Ryker, 1972).

For most soils the SAR and ESP are uniquely related, as may be seen by manipulation of equations (7.36) and (7.37), and from the test data (Sherard, Decker, and Ryker, 1972a, and Richards, 1954) shown in Fig. 7.19. Since the SAR is more easily determined than is the ESP, it is more widely used in practice.

7.12 ANION EXCHANGE

Clays may contain anion exchange sites, although little is known about them. Certainly, in low pH systems where particle edges are charged positively, anion adsorption would be expected. Tannates are widely used to improve the stability of drilling fluids (van Olphen, 1963). The tannate anions are adsorbed at particle edges by complexing with the exposed octahedral aluminum ions. This leads to a reversal in edge charge from positive to negative and prevents edge-to-face flocculation.

Sodium polyphosphates are effective soil dispersants, which have had application in soil engineering (Lambe, 1954b) for the construction of high density, low permeability clay blankets for use as storage reservoir liners. A major factor controlling the effectiveness of these materials is the adsorption of the negative phosphate radical on particle edges.

Anions, particularly bicarbonate, appear to have played a role in erosion (by dispersion) in Australia (Ingles, 1972) in soils of low to moderate sodium content.

7.13 PRACTICAL IMPLICATIONS

The analysis of clay an colloids provides insight into long-range repulsivatind attractive forces and the influences of system values, such as pore solution chemistry, type of adsorbed cations, and type of clay on them. The theory accounts for flocculation and deflocculation phenomena, both of which play an important part in the development of soil fabric and structure, which in turn exert a major influence on mechanical properties (Chapters 11 and 12). Long range repulsive forces caused by overlapping double layers have been used to describe the compression and swelling behavior of some clays (Chapter 13), and dispersion phenomena due to changes in the relative proportions of monovalent and divalent cations in the double layer can be used to account for erosion of clays and tunneling failures in dams (Chapter 11).

Some methods of soil stabilization depend, at least in part, on changes in double layer interactions and ion exchange to alter interparticle forces and particle arrangements in order to achieve a soil structure with properties suited for a particular application. One example is the use of dispersing chemicals to produce a high density and deflocculated particle arrangements to insure a very low permeability. Another is the use of a flocculating chemical to give a higher strength or more open particle arrangement to facilitate drainage.

Ion exchange reactions are important in the properties and stability control of drilling muds and slurries. Groundwater quality, underground waste disposal, and pollutant transport through soils are all influenced by the ion exchange properties of the soils. As the composition of the exchange complex relative to that of the pore water is influenced by both temperature and composition of the free water and as mechanical properties are influenced by the adsorbed ion types, suitable controls on laboratory testing conditions are needed if properties are to be correctly measured.

SUGGESTIONS FOR FURTHER STUDY

Ingles, O. G. (1968), "Soil Chemistry Relevant to Engineering Behavior of Soils," Chapter 1 in Soil Mechanics
—Selected Topics (I. K. Lee, Ed.,) American Elsevier,
New York.

van Olphen, H. (1963), An Introduction to Clay Col Chemistry, Wiley Interscience, New York.

Verwey, E. J. W., and Overbeek, J. Th. G. (1948), Theory of the Stability of Lyphobic Colloids, Elsevier, Amsterdam, New York, London.

1/KON/F

Prediction of Oceanic Particle Size Distributions from Coagulation and Sedimentation Mechanisms

JAMES R. HUNT

Environmental Engineering Science, California Institute of Technology, Pasadena, CA 91125

An explanation is offered for observed oceanic particle size distributions considering only particle removal by coagulation and sedimentation. The analysis includes three coagulation and sedimentation. The analysis includes three coagulation mechanisms: Brownian, shear, and differential-sedimentation, for a continuous distribution of particle size. The size distribution is assumed to be in steady state with a constant flux of particle volume through the distribution. Predicted size distributions are power-law functions of the particle diameter with exponents —2.5 for Brownian coagulation, —4.0 for shear coagulation, —4.5 for differential-sedimentation coagulation, and —4.75 for gravitational settling. Observed size distributions for oceanic waters and digested sewage sludges are compared with the predictions. One consequence of the theory is the prediction of increased particle concentration at oceanic thermoclines in response to a decrease in fluid turbulence.

R many environmental pollutants and govern the efficiency of water and wastewater treatment processes. Unfortunately, one of these removal mechanisms, coagulation, is not as yet quantified for the continuous particle size distributions encountered in oceanic waters and treatment plants.

In oceanic waters there is considerable interest in the residence time of particles and associated trace elements and in similarities of oceanic size distributions (Lal (1); Lerman et al. (2)). Various particle-removal





Cottan (5)), and sedimentation of zooplankton fecal pellets (Smayda nechanisms have been considered, including dissolution (Lal and Lerman (3)), sedimentation of individual particles (McCave (4); Brun-(6)). Acceleration of particle sedimentation by coagulation was discussed by Arrhenius (7), but more recently investigators have dismissed the importance of coagulation in the ocean (3, 5, 6).

In estuaries and water and wastewater treatment processes, Sholkovitz (8), Edzwald et al. (9), and O'Melia (10) have discussed the importance of coagulation in aiding the removal of colloidal and suspended matter. Coagulation in these systems has been examined experimentally either for a particle suspension uniform in size where Smoluchowski's lation and sedimentation are inferred through changes in turbidity or sidered the dynamics of the particle size distribution during coagulation suspended particle volume. These approaches have not adequately contheories can be tested, or for a continuous size distribution, where coaguand sedimentation.

oceanic waters and digested sewage sludge. Sensitivity of the predictions lation and sedimentation. Predictions of size distributions are obtained that are in reasonable agreement with measured size distributions from to fluid turbulence and fluid density presents a plausible explanation for zones of higher particle concentration observed in the oceanic water column. The analysis does not include zooplankton fecal pellet production, particle breakup, or dissolution, nor does it directly incorporate In this chapter, mechanisms of particle removal are limited to coagubiological productivity.

Mechanisms

of particle sizes. The most appropriate function for describing the dy-In natural and polluted waters there exists a continuous distribution namics of a continuous size distribution is the particle size distribution $n(d_{\mu})$ defined in the expression

$dN = n(d_{\rm p})d(d_{\rm p})$

where dN is the number of particles per fluid volume with diameters in the range d_{ν} to $d_{\nu} + d(d_{\nu})$. The particle size distribution has units of represents a fluid length unit and [1] a particle length unit. Dimensional number per milliliter per micrometer, expressed as [L-31-1], where [L] units are important in the analysis that follows.

Removal or loss of a particle of a given size from a volume of fluid is assumed to occur through only two physical processes: sedimentation and coagulation. Sedimentation removes particles from the volume of fluid, while coagulation transfers many smaller particles into fewer larger particles within the fluid volume.

Oceanic Particle Size Distributions HUNT 11.

The sedimentation flux of particles in the size range $d_{\scriptscriptstyle p}$ to $d_{\scriptscriptstyle p}+d(d_{\scriptscriptstyle p})$

$$\frac{g}{18\nu} \left(\frac{\rho_{\rm p} - \rho_{\rm f}}{\rho_{\rm f}} \right) d_{\rm p}^2 n(d_{\rm p}) d(d_{\rm p}) \qquad [\text{L}^2\text{t}^{-1}] \tag{1}$$

The flux is the Stokes' settling velocity of a spherical particle times the number of particles in that size interval. In the expression, g is the gravitational acceleration, ν the kinetic viscosity, and $\rho_{\rm p}$ and $\rho_{\rm r}$ the particle and fluid densities. The time unit is indicated by [t].

The loss of particles of sizes d, and d, by coagulation is

$$\beta(d_i, d_j) \ n(d_i) \ d(d_i) \ n(d_j) \ d(d_j)$$
 [L-3t-1] (2

spherical particles. Collisions of the smallest particles are attributable geometry and has dimensions of fluid volume per time [L3t-1]. There are three coagulation mechanisms, each with its own collision function for where $\beta(d_i, d_j)$ is the collision function determined by the collision primarily to thermal or Brownian motion with a collision function

$$\beta_b(d_i, d_j) = \frac{2}{3} \frac{kT}{\mu} \frac{(d_i + d_j)^2}{d_i d_j} \tag{3}$$

where k is the Boltzmann constant, T the absolute temperature, and μ the fluid viscosity. Fluid shear in laminar or turbulent flow will cause particles moving with the fluid to collide. The collision function for shear coagulation is

$$\beta_{\rm sh}(d_i, d_j) = \frac{G}{6} (d_i + d_j)^3$$
 (4)

where G is the mean shear rate of the fluid. In laminar flow the shear rate is given by the velocity gradient, while in turbulent flow the shear rate is approximately (11)

$$G = \left(\frac{\epsilon}{\nu}\right)^{1/2} \tag{5}$$

where e is the rate of turbulent energy dissipation.

The third coagulation mechanism, differential sedimentation, occurs when a particle falling at its terminal settling velocity collides with a lower settling particle. This is represented as a cross-sectional area of collision multiplied by the difference in Stokes' settling velocities of the colliding particles

$$\beta_{da} (d_i, d_j) = \frac{\pi g}{72\nu} \left(\frac{\rho_p - \rho_t}{\rho_t} \right) (d_i + d_j)^2 |d_i^2 - d_j^2|$$
 (6)

forces. Corrections for these surface and fluid forces are available for cal collisions and do not include electrostatic, van der Waals, or viscous belt et al. (12) in the absense of electrostatic forces for particles uniform These expressions for the collision function assume purely geometri-Brownian coagulation and have been verified experimentally by Lichtenin size. For shear coagulation, corrections have been computed for collisions between spheres of equal size, and experimental agreement with theory has been obtained only when electrostatic forces are absent (van de Ven and Mason (13); Zeichner and Schowalter (14)). Disferentialsedimentation coagulation of hydrosols has not been examined theoretically or experimentally.

nisms, but solution of such an equation, analytically or numerically, is not possible at this time. The main hindrances to a direct solution are A general equation for the dynamics of the particle size distribution could be written incorporating sedimentation and coagulation mechathe complexity of the general dynamic equation (11) and the unknown A partial solution of the general dynamic equation has been obtained by using a similarity or self-preserving transformation. The concept was hydrosol coagulation. The self-preserving transformation will not be used in this analysis because a general self-preserving transformation has corrections to the collision functions to account for the neglected forces. introduced by Friedlander (11), and has been applied to aerosol and not been shown to exist for simultaneous Brownian, shear, and differenial-sedimentation coagulation and gravitational settling. Also, quantitative application of the self-preserving transformation requires knowledge of the unknown corrections to the collision functions for shear and differential-sedimentation coagulation. Because these circumstances prevent direct solutions of the particle size distribution, it is necessary to make some major simplifications while still retaining the characteristics of the coagulation and sedimentation mechanisms.

Simplification

The first simplification is to assume only one coagulation or sedimentation mechanism is dominant in a subrange of particle size. Figure 1 turbulence and low density particles. Because the collision functions fluid forces, this plot only approximates the dominance of a coagulation Brownian motion is the dominant collision mechanism, while particles from 1 to about 100 µm collide because of fluid shearing. Collisions is a comparison of the collision functions for collision of an arbitrary particle with a particle of 1 µm in diameter. Values of the collision functions were obtained directly from Equations 3, 4, and 6 for low fluid plotted do not include the previously mentioned particle surface and mechanism over a particle size interval. For particles less than $1 \mu m$,

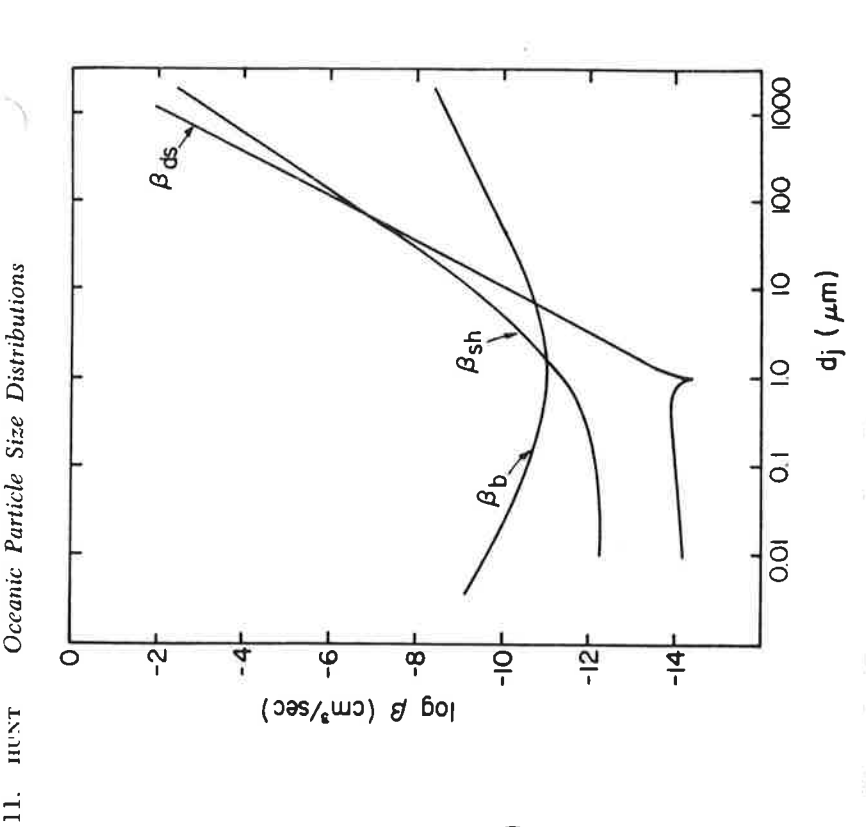


Figure 1. Comparison of the collision functions for Brownian, shear, and differential-sedimentation coagulation $(\mathbf{d_i} = 1.0~\mu\text{m}; \ T = 14^\circ\text{C}; \ G = 3~sec^{-1}; (\rho_p - \rho_f)/\rho_f = 0.02)$

sedimentation coagulation. Replotting Figure 1 for collisions other than those with 1-µm particles would shift the curves but still would retain the ordering of the dominant mechanisms: Brownian, shear, and differential sedimentation with increasing size of colliding particle. Particle of a 1-µm particle with particles greater than 100 µm are by differentialremoval by gravitational settling cannot be compared with the collision functions in Figure 1, but it is reasonable to assume that the largest particles would be removed from the fluid volume by settling.

Three further assumptions are necessary in the analysis. First, particles are assumed to have a low stability, independent of particle size. Destabilization can be achieved by compressing the electrical double layer in a high ionic strength solution or by neutralizing the surface charge through specific chemical interactions with hydrated metal ions or organic polymers. Second, the particle size distribution is in a dynamic steady state. For each small interval of particle size, the rate of particle

either the volume coagulated from the interval or the particle volume lost from the fluid volume by sedimentation. This steady-state assumption implies the existence of a constant flux of particle volume through the distribution that is equal to the rate of formation of small particles volume transferred into the size interval by coagulation is balanced by and to the rate of large particle removal by sedimentation. The flux of particle volume is denoted by E with units of particle volume per fluid volume per time [13L-3t-1].

The third assumption requires the particle size distribution to be a function of six variables: (1) particle diameter; (2) the flux of particle volume through the distribution; parameters representing: (3) Brownian sedimentation mechanisms are obtained from fluid and particle constants coagulation; (4) shear coagulation; (5) differential-sedimentation coagulation; and (6) gravitational settling. Parameters for the coagulation and appearing in Equations 1, 3, 4, and 6. The resulting parameters and the units obtained from the mechanism equations are:

Brownian

$$K_{\rm b} = \frac{kT}{\mu}$$
 [L³t·

Shear

 $[\Gamma_{3}I_{-3}I_{-1}]$

Differential sedimentation

$$K_{\mathrm{ds}} = \frac{g}{\nu} \left(\frac{\rho_{\mathrm{p}} - \rho_{\mathrm{f}}}{\rho_{\mathrm{f}}} \right) \quad [\mathrm{L}^{3}]^{-4} \mathrm{t}^{-1}]$$

Settling

$$S = \frac{g}{\nu} \left(\frac{\rho_p - \rho_t}{\rho_t} \right) \quad [L]^{-2} t^{-1}]$$

ential sedimentation is second order in the particle size distribution from The parameters for differential-sedimentation coagulation and settling Equation 2, while gravitational settling is first order in the size distribution as seen in Equation 1. All parameters were chosen to be independent have the same grouping of constants but different units because differof particle size, assuming further that particle density is also independent of particle size.

Prediction

Based on these assumptions, the particle size distribution has the following functional form

Oceanic Particle Size Distributions

11. HUNT

$$n = n(d_{\mathbf{p}}, E, K_{\mathbf{b}}, G, K_{\mathbf{ds}}, S)$$

3

The assumption of steady state removed the time dependence.

Predictions of the particle size distribution are obtained by considering subranges of particle size where only one coagulation mechanism or gravitational settling is dominant. For the smallest particle sizes Brownian coagulation is dominant and the functional relationship is

$$n = n(d_{\mathbf{p}}, E, K_{\mathbf{b}}) \tag{8}$$

which contains four variables (n, d_p, E, K_b) and three dimensions (L, I, K_b) t). Dimensional analysis is used to group the variables into a unique nondimensional expression (15)

$$A_{\rm b} = n(d_{\rm p}) \ d_{\rm p}^{5/2} \left(\frac{K_{\rm h}}{E}\right)^{1/2}$$
 (9)

where A_b is a dimensionless constant. Solving for the particle size distribution gives

Brownian

$$n(d_{\rm p}) = A_{\rm b} \left(\frac{E}{K_{\rm b}}\right)^{1/2} d_{\rm p}^{-2.5}$$
 (10)

Using the same technique for regions dominated by shear, differential sedimentation, and settling, the predicted size distributions are

$$n(d_{\rm p}) = A_{\rm sh} \left(\frac{E}{G}\right)^{1/2} d_{\rm p}^{-4}$$
 (11)

Differential sedimentation

$$n(d_{\rm p}) = A_{\rm ds} \left(\frac{E}{K_{\rm ds}}\right)^{1/2} d_{\rm p}^{-4.5}$$
 (12)

Settling

$$n(d_{\mathbf{p}}) = A_{\mathbf{s}} \left(\frac{E}{S}\right)^{3/4} d_{\mathbf{p}}^{-4.75}$$
 (13)

Equations 10 and 13 were derived earlier by Friedlander (16, 17) for aerosols. The method of dimensional analysis arrives at predictions that contain dimensionless coefficients Ab, Ash, Ads, and As which must be determined experimentally. 251

Comparison of Predictions with Observations

with observations from oceanic waters and sewage sludge digesters. The Table I compares the predicted shape of the particle size distribution comparison is limited to the dependence of the particle size distribution on the particle diameter because fluid and particle parameters appearing in the predicted equations were not available. In plots of the logarithm of the size distribution vs. the logarithm of the particle diameter, Equaions 10, 11, 12, and 13 become straight lines with slopes -2.5, -4, -4.5, and -4.75, respectively. Oceanic and digested sewage sludge size distributions are also observed to have one or more linear regions in such a plot, as summarized in Table I.

was measured by Harris (18) with an electron microscope over the size ange 0.08 to $8.0 \,\mu m$. For particles less than $2 \,\mu m$ in diameter the ob-Particles in the size range 2 to 8 μ m had a greater slope than expected or shear coagulation. Slopes close to the value predicted for shear coaguation were found in the two sets of North Atlantic data, both of which were obtained by electronic particle counters. Sheldon's data as reported by McCave (4) also contained some size distributions with a second inear region for the largest diameters which could be caused by either differential-sedimentation coagulation or gravitational settling. The size distributions reported by Lerman et al. (2) were limited to the size range ornia coastal waters with an electronic particle counter over the size range 1 to $20~\mu m$. The observed slopes were close to the slope, predicted or shear coagulation. Anaerobically digested sewage sludges were sized by Faisst (20) over the range of 1 to 70 µm. Both sludges had a region corresponding to shear coagulation and a second region with slopes ex-The particle size distribution of deep water from the Gulf of Mexico served slope was -2.65, close to the Brownian prediction of -2.5. from 1 to $6 \mu m$ and only one linear region was observed. Peterson (19) measured particle size distributions in natural and sewage-polluted Caliceeding differential-sedimentation and gravitational-settling predictions.

The observed distributions have particle diameter dependencies in reasonable agreement with the predictions, but these comparisons should ters appearing in the predicted equations are measured. A number of the assumptions required in the analysis appear reasonable. Both oceanic residence times of the fluid and particles in suspension. The assumption of particle destabilization is reasonable in seawater because experiments by Sholkovitz (8) and Edzwald et al. (9) have shown that maximum destabilization for colloids and particles occurred at salinities less than not be taken as verification of the predictions. Verification requires coagulation experiments under controlled conditions where all the paramewaters and digesters would likely be in a steady state because of the long that of seawater. Stability studies are not available for digested sewage

	2.č- 3.č-	I.∳— I.∳—		Los Angeles City Los Angeles County
,	29.⊁ <i>—</i>	8.0 ± 0.4		Lerman et al. (2) California coastal waters (19) Digested sewage sludge (20)
`	59 V —	₽.4-A •2.0 ± 7.8-	39.2 <i>—</i>	Observed Gulf of Mexico (18) Worth Atlantic Sheldon in McCave (4)
ō7.₽—	č.₽—	0.4	3.2—	Predicted
lnnortnhrrnri) gurlltək 04<	ปรับราชานิก หอบโลปกาลเก่าจริ 04<	07-z wəys	$z>$ u v_i u.no. q	Dominant Mechanism Approximate Particle Size (m4)
	Vs. Log dp	Des of Log n (d1)	and Observed Slo	lable 1. Predicted

"Standard deviation.

Application

In this section the sensitivity of the predicted size distributions to fluid turbulence and fluid density is examined above, in, and below an bution at steady state has increased suspended particle volume in response oceanic thermocline. This analysis shows that a coagulating size distrito a decrease in fluid turbulence or an increase in fluid density. This may provide an explanation for the observed maximums in particle concentration and turbidity at oceanic thermoclines (Carder et al. (21)). Jerlov (22) has argued that higher thermocline concentrations result either from the minimum in eddy diffusivity at the thermocline which decreases turbulent transport through the thermocline, or from the increase in fluid density which traps low density particles.

and resulting fluid density gradient. These gradients will have two effects The important feaures of a thermocline are the temperature gradient on the predicted coagulating particle size distributions. First, turbulence the values of the parameters for differential-sedimentation coagulation is suppressed by the fluid stability corresponding to minimums in eddy depth, the settling velocity of particles decreases, which in turn decreases diffusivity and shear rate G. Second, as the fluid density increases with Kan and gravitational settling S.

The effects of changes in shear rate and fluid density on the predicted particle size distribution are more easily illustrated graphically by transforming size distributions into volume distributions (II)

$$\frac{dV}{d(\log d_p)} = \frac{2.3\pi}{6} d_p^4 n(d_p) \tag{14}$$

The predicted volume distributions are

Brownian

$$\frac{dV}{d(\log d_{\rm p})} = \frac{2.3\pi}{6} A_{\rm b} \left(\frac{E}{K_{\rm b}}\right)^{1/2} d_{\rm p}^{1.5} \tag{15}$$

Shear

$$\frac{dV}{d(\log d_{\rm p})} = \frac{2.3\pi}{6} A_{\rm sh} \left(\frac{E}{G}\right)^{1/2} \tag{16}$$
 [imentation]

Differential sedimentation

qV

$$\frac{d(\log d_{\rm p})}{d} = \frac{1}{6} A_{\rm ds} \left(\frac{1}{K_{\rm ds}} \right) d_{\rm p}^{-0.5} \tag{1}$$

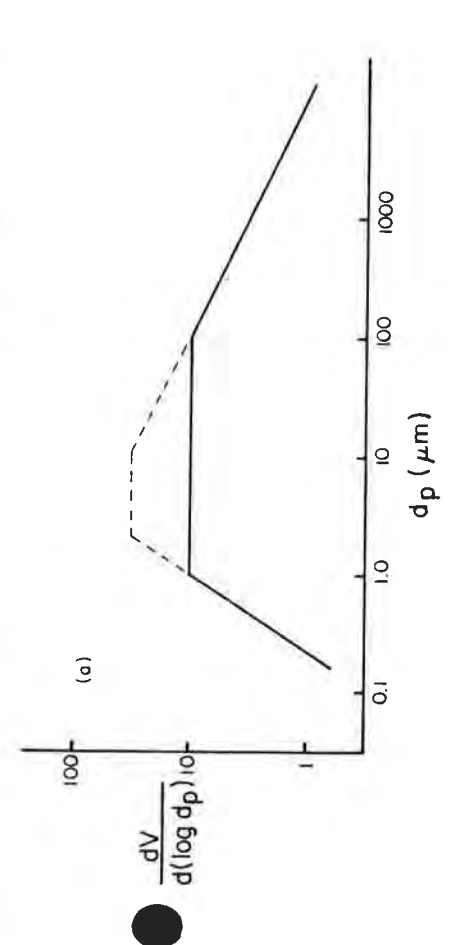
Settling

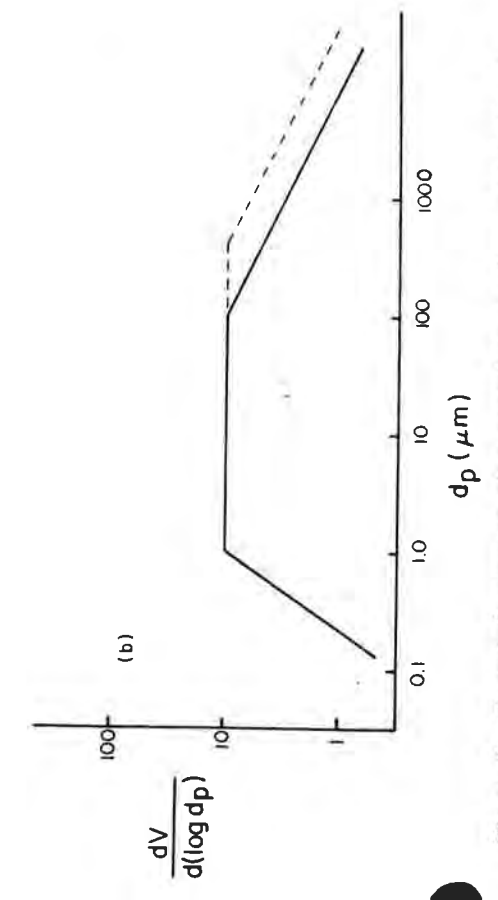
$$\frac{dV}{d(\log d_{\rm p})} = \frac{2.3\pi}{6} A_{\rm s} \left(\frac{E}{S}\right)^{3/4} d_{\rm p}^{-0.75} \tag{18}$$

Oceanic Particle Size Distributions 11. HUNT

Because the dimensionless coefficients and parameters appearing in Equations 15-18 are not available, a surface water size distribution is assumed, and the sensitivity of the size distribution to changes in shear rate and fluid density is examined graphically.

Volume distributions for the surface water and for waters with a lower shear rate and a greater fluid density typical of a thermocline are plotted in Figure 2. For the surface water distribution, Brownian coagulation is assumed to be dominant for particles less than 1 μ m in diameter,





tude decrease in shear rate ((——) surface layer; (---) decreased turbulence); (b) factor of 4 decrease in $(\rho_p - \rho_l)|\rho_l$ ((——) surface layer; (---) Expected response of a coagulating volume distribution to changes in fluid properties at an oceanic thermocline: (a) order of magnilence); (b) factor of 4 decrease in $(\rho_p - \rho_l)/\rho_l$ ((——) surface lay increased fluid density). Ordinate units are arbitrary. Figure 2.

Oceanic Particle Size Distributions

II. HUNT

mentation controls the particle size distribution for particles greater than 100 µm. For the size distributions representing conditions in the thermocline, only the shear rate G or the differential-sedimentation parameter Kus is modified; all other parameters, including E, are held constant. Conclusions are similar if gravitational settling is assumed dominant for shear coagulation dominates the range 1 to 100 μm , and differential sediparticles greater than 100 µm instead of differential-sedimentation coagu-

The volume distributions are plotted in Figure 2 on log-log scales to display the power-law relationships of the predictions, Equations 15, 16, and 17. This representation distorts the volume distribution, which should otherwise be plotted on semilog scales so that the total volume can be obtained by visually integrating the distribution.

Figure 2a illustrates the change in volume distribution in response measured the change in the average turbulent energy dissipation rate an order-of-magnitude decrease in the shear rate. Grant et al. (23) with depth from the surface through the thermocline and found a decrease of two orders of magnitude, corresponding to a one order-of-magnitude decrease in the shear rate (Equation 5). With the lowered shear tude according to Equation 16, but the range of shear coagulation dominance decreases. Brownian coagulation is important for larger particle sizes, and differential sedimentation dominates at diameters smaller than rate, the volume distribution in the shear subrange increases in magnithose in the surface distribution.

Figure 2b demonstrates the effect of increasing the fluid density for very light particles such that the factor $(\rho_p - \rho_I)/\rho_I$ decreases arbitrarily tion to larger particles. This is represented by a decrease in parameter by a factor of four. The increase in fluid density lowers the settling velocity of particles and limits the importance of differential sedimenta-K_{as}, which increases the volume distribution in the differential-sedimentation subrange according to Equation 17. Shear coagulation has a larger subrange of dominance. The coagulating size distributions predict an increase in suspended suggests that the effect of diminished turbulence is more important than the density increase. An alternate explanation is that particles become Both of these conditions are present at the thermocline, while at greater The zones of higher particle concentration occur in the thermocline which neutrally buoyant in the thermocline and are trapped. Detailed size disparticle volume in response to lower turbulence or higher fluid density. depths turbulence is not suppressed and the fluid density remains high. tribution measurements at varying depths in oceanic waters are necessary to determine the role of coagulation in increasing the particle concentration at the thermocline.

Conclusion

This chapter has presented a theoretical derivation of continuous assumptions required in the analysis are not overly severe and appear tion of increased particle concentration at oceanic thermoclines, as has particle size distributions for a coagulating and settling hydrosol. The to hold true in oceanic waters with low biological productivity and in been observed. This analysis has possible applications to particle dynamdigested sewage sludge. Further support of this approach is the predicwater treatment processes. Experimental verification of the predicted size distribution is required, and the dimensionless coefficients must be ics in more complex systems; namely, estuaries and water and wasteevaluated before the theory can be applied quantitatively.

Acknowledgment

The author thanks James J. Morgan for his support during the development of this theory.

Glossary of Symbols

 $A_{\rm b}$, $A_{\rm sh}$, $A_{\rm ds}$, $A_{\rm g}=$ dimensionless coefficients for Brownian, shear, and differential-sedimentation coagulation, and gravitational settling

 $d_p = \text{particle diameter}[1]$

dN = number of particles per fluid volume in a small interval

of particle diameter [L-3]

E = particle volume flux through the size distribution

 $[1_3\Gamma_{-3}^{-1}]$

g = gravitational acceleration

 $G = \text{shear rate } [L^3]^{-3}t^{-1}]$

k = Boltzmann constant

 $K_{\rm b}, K_{\rm ds} = {
m Brownian}$ and differential-sedimentation coagulation parameters [L 3 t $^{-1}$], [L 3 l 4 t $^{-1}$]

[1] = particle length unit

[L] = fluid length unit

 $n(d_p) = \text{particle size distribution } [L^{-3|-1}]$

 $S = \text{gravitational-settling parameter}[Ll^{-2}t^{-1}]$

[t] = time unit

T = absolute temperature

 β_b , β_{ab} , β_{ds} = collision functions for Brownian, shear, and differentialsedimentation coagulation [L3t-1]

€ = rate of turbulent energy dissipation

 $\rho_{\rm l}$, $\rho_{\rm r} = {\rm particle}$ and fluid density $\nu = \text{kinematic viscosity}$ $\mu = dynamic viscosity$

Addendum

Theoretical predictions for Brownian and shear coagulation have been verified experimentally for clay particles in artificial seawater (24).

Literature Cited

- 1. Lal, D. "The Oceanic Microcosm of Particles," Science 1977, 198(4321), 977 - 1009
- 2. Lerman, A.; Carder, K. L.; Betzer, P. R. "Elimination of Fine Suspensoids in the Oceanic Water Column," Earth Planet. Sci. Lett. 1977, 37(1),
 - Lal, D.; Lerman, A. "Dissolution and Behavior of Particulate Biogenic Matter in the Ocean: Some Theoretical Considerations," J. Geophys. Res. 1973, 78(30), 7100-7111.

 4. McCave, I. N. "Vertical Flux of Particles in the Ocean," Deep-Sea Res. 1975, 22, 491-502.
- Brun-Cottan, J. C. "Stokes Settling and Dissolution Rate Model for Marine Particles as a Function of Size Distribution," J. Geophys. Res. 1976, 81 (9), 1601–1606.
 Smayda, T. J. "The Suspension and Sinking of Phytoplankton in the Sea," Oceanogr. Mar. Biol. Annu. Rev. 1970, 8, 353–414.
 Arrhenius, G. In "The Sea," Hill, M. N., Ed.; Wiley-Interscience: New York, 1963; Vol. 3, pp. 655–727.
 Sholkovitz, E. R. "Flocculation of Dissolved Organic and Inorganic Matter During the Mixing of River Water and Seawater," Geochim. Cosmochim.

- Edzwald, J. K.; Upchurch, J. B.; O'Melia, C. R. "Coagulation in Estuaries," Environ. Sci. Technol. 1974, 8(1), 58-63.
 O'Melia, C. R. In "Physicochemical Processes for Water Quality Control"; Weber, W. J., Ed.; Wiley-Interscience: New York, 1972; pp. 61-109.
 Friedlander, S. K. "Smoke, Dust and Haze: Fundamentals of Aerosol Behavior"; Wiley-Interscience: New York, 1977.
 Lichtenbelt, J. W. Th.; Pathmamanoharan, C.; Wiersema, P. H. "Rapid
- Coagulation of Polystyrene Latex in a Stopped-Flow Spectrophotometer,
- J. Colloid Interface Sci. 1974, 49, 281-285.
 van de Ven, T. G. M.; Mason, S. G. "The Microrheology of Colloidal Dispersions VII. Orthokinetic Doublet Formation of Spheres," Colloid Folym. Sci. 1977, 255(5), 468-479.
 14. Zeichner, G. R.; Schowalter, W. R. "Use of Trajectory Analysis to Study Stability of Colloidal Dispersions in Flow Fields," AIChE J. 1977, 23(3), 13.
- Lin, C. C.; Segel, L. A. "Mathematics Applied to Deterministic Problems in the Natural Sciences"; Macmillan: New York, 1974.
 Friedlander, S. K. "On the Particle-Size Spectrum of Atmospheric Aero-
- sols," J. Meteorol. 1960, 17, 373-374.

 17. Friedlander, S. K. "Similarity Considerations for the Particle-Size Spectrum of a Coagulating, Sedimenting Aerosol," J. Meteorol. 1960, 17, 479-483

- Oceanic Particle Size Distributions
- Harris, J. E. "Characterization of Suspended Matter in the Gulf of Mexico —II Particle Size Analysis of Suspended Matter from Deep Water," Deep-Sea Res. 1977, 24, 1055–1061.
 Peterson, L. L. Ph.D. Thesis, California Institute of Technology, Pasadena,
 - CA, 1974.
- 20. Faisst, W. K. Chapter 12 in this book.
 21. Carder, K. L.; Beardsley, C. F., Jr.; Pak, H. "Particle Size Distributions in the Eastern Equatorial Pacific," J. Geophys. Res. 1971, 76(21), 5070-
- 22. Jerlov, N. G. "Maxima in the Vertical Distribution of Particles in the Sea,"
- 23. Grant, H. L.; Hughes, B. S.; Vogel, W. M.; Moilliet, A. "Some Observations of the Occurrence of Turbulence in and Above the Thermocline," J. Fluid Mech. 1968, 34, 443-448.

 24. Hunt, J. R., Ph.D. Thesis, California Institute of Technology, Pasadena,

RECEIVED September 25, 1978

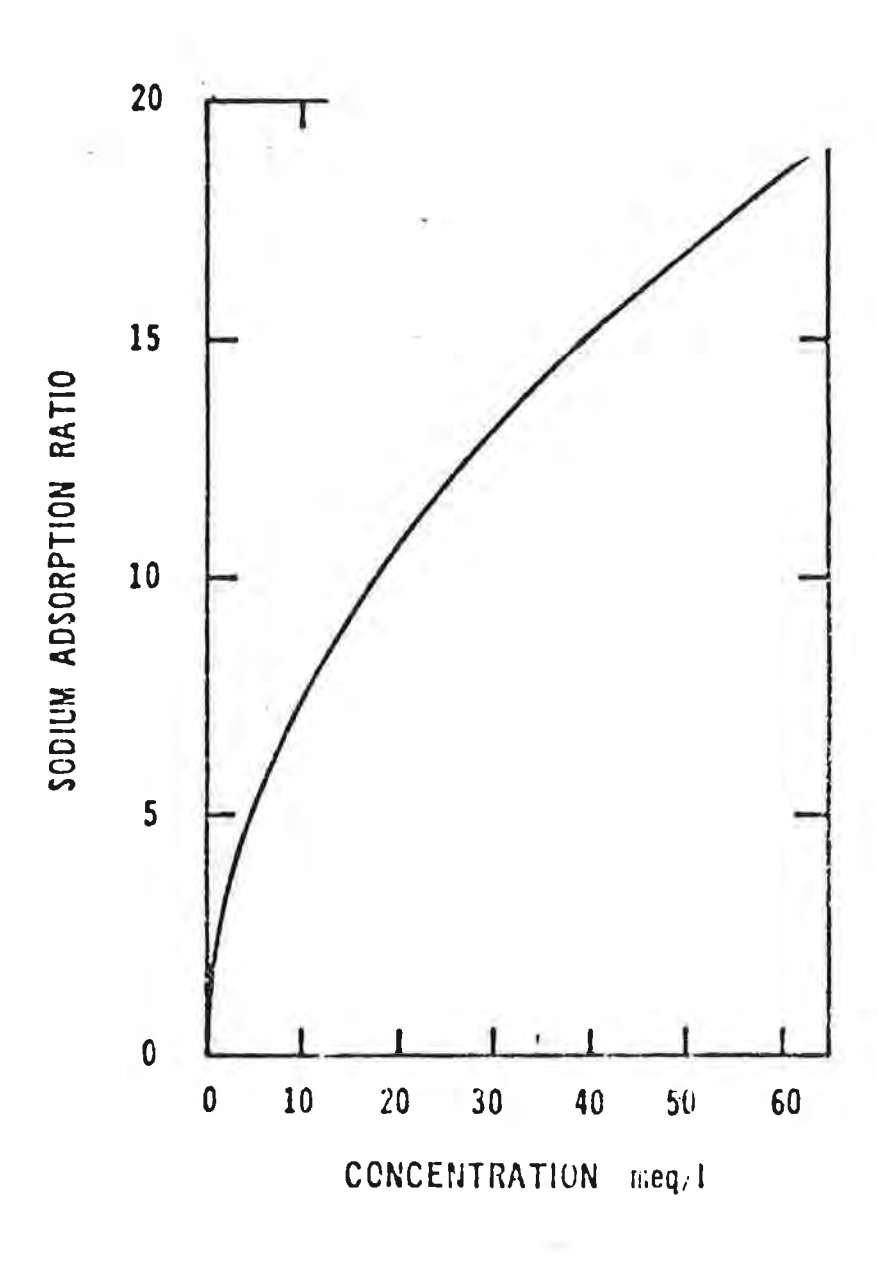


Figure 5. Variation of SAR with Concentration for Sea Water.

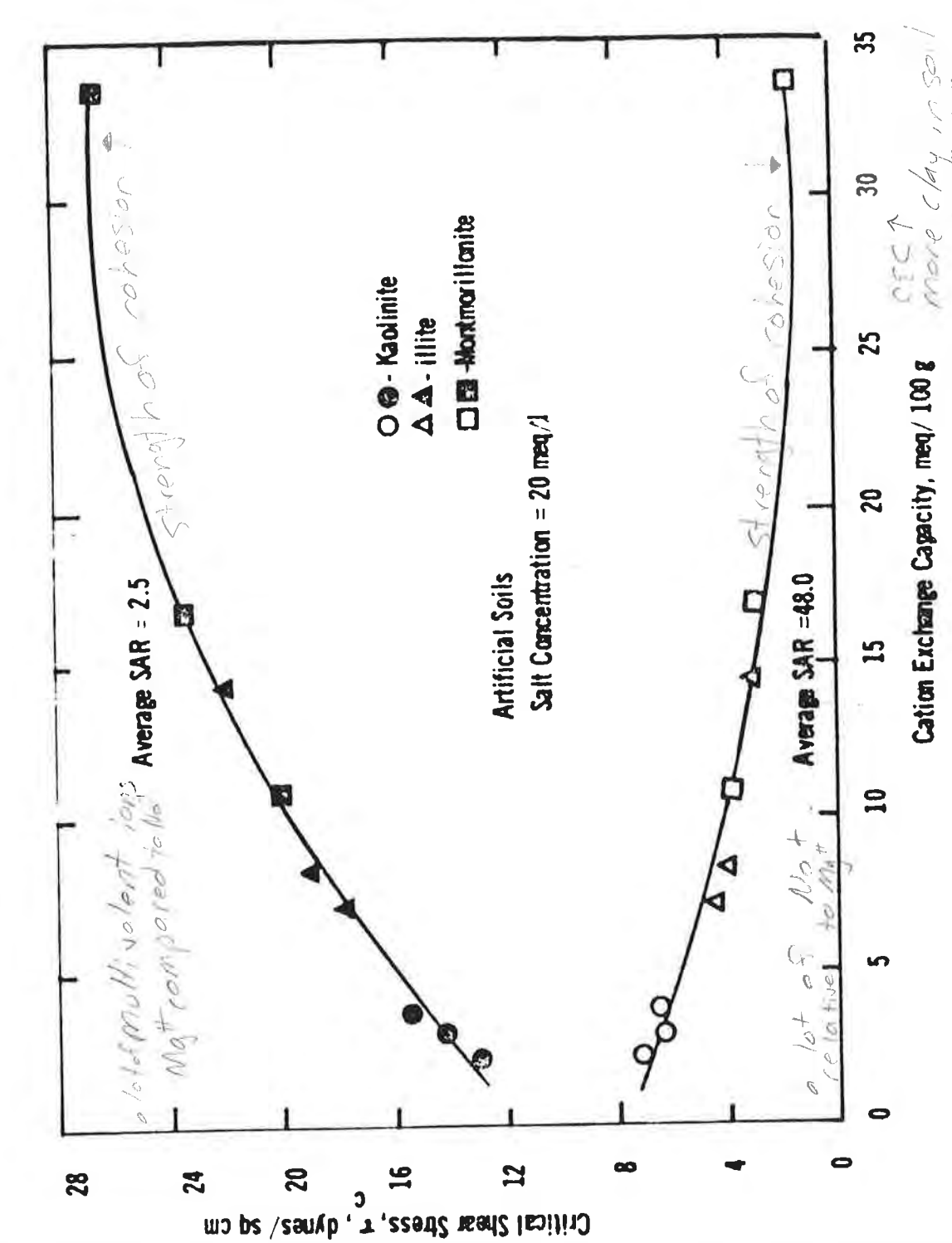


Figure 11. (a). Relationship Between Critical Shear Stress and Cation Exchange Capacity, Plotted According to the Parabolic Relationship.

BOUNDA PLY

0.4 to 0.8 and at $R = 25 \mu$, from 0.2 to 0.9. The maximum values of \ni (at $r^* F \approx 0.7$) in these two cases are 0.25 and 0.90 respectively.

Although the sedimentation of drops of this size corresponds to Re_f va and only 0.10-0.30, calculation of the collection efficiency on Stokes' approxima. can result in grave errors, since it involves the determination of the trajectories of the alops, beginning with a large distance ϱ between them (up to 50 R) at which $\beta = V_s \varrho v > 1$ (see p. 101).

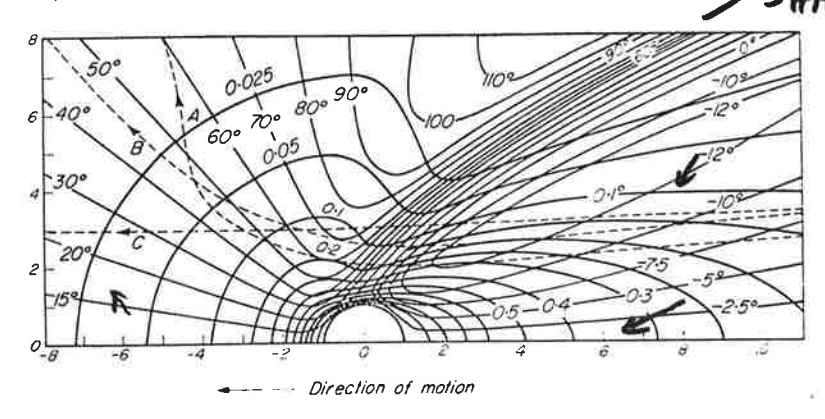


Fig. 74a. Field of flow around a sphere ($Re_f = 4$).

Pearcey and Hill [823] considered this problem using Oseen's approximation; simplified forms of Oseen's equations for the field of flow around a moving sphere, applicable at large ϱ/R only, were used. The error then increases as the surface of the sphere is approached. The authors determined the field of flow produced by the motion of two spherical drops by adding the fields produced by each drop separately, making use of the zero approximation (see (13.1)), which does not satisfy strictly the boundary conditions on the surfaces of the drops. This error, also, grows as the drops approach each other. The view of the authors that the drops ran through the zone in which the errors are large so quickly that there is little effect on the final result is far from convincing.

The field of flow around a falling water drop having $R = 73\mu$ (Re_f = 4) is shown in Fig. 74 a. The solid lines connect points relating to identical flow velocities, expressed in fractions of the velocity of fall of the drop, and points at which the flowlines have a definite slope θ to the axis of motion. $\theta < 0$, if the lines approach the axis. The graph shows that a wake is formed behind the drop in which the flow velocity decreases slowly with an increase in the distance from the drop and the flow lines are directed towards the axis. In front of the drop, and to the side, the flow velocity diminishes much more rapidly and the flow lines are directed sideways at large angles. Consequently, drops moving behind the given drop of radius R will not only overtake it (see p. 102) but will also be drawn into its wake and approach the axis of flow. The trajectories of drops overtaking a given drop of radius R are shown in Fig. 74a by broken lines. The radii of these drops are 0.1 per cent (A), 1.1 per cent (B) and 11 per cent (C) larger than R. Initially, when at a large distance from the given drop, these drops were in the same place. The smaller the difference in the sizes and fall velocities, the more time is available for both drops to approach each other.

Turnys

10-22-91-

COAGULATION RATES OF CLAY MINERALS AND NATURAL SEDIMENTS'

RONALD J. GIBBS

Center for Colloidal Science College of Marine Studies University of Delaware Newark, DE 19711

ABSTRACT: Coagulation experiments conducted using illite, kaolinite, montmorillonite, and four natural sediment samples in blade and Couette reactors with solutions of various salinities yielded collision-efficiency factors significantly higher than those in the previous literature, indicating that coagulation begins at lower salinities (1/2-1%e). The natural sediments do not generally behave as might be predicted for a mixture of the standards of the minerals of which the natural sediment samples were comprised. The half-times for coagulation of the particles indicate that, in nature, the coagulation process would probably be completed in the first few parts-per-thousand salinity.

INTRODUCTION

The majority of suspended material entering the marine environment from rivers is fine-grained particulate material. This material is responsible for filling estuaries and for building deltas and submarine fans over geological time spans. Knowledge of the processes acting on this fine-grained particulate material are important both in dredging activities and in our search for petroleum. In addition, the majority of toxic metals and organic materials produced by man are carried into estuaries on these fine particles. Therefore, it is critical that we understand the processes related to the transport and sedimentation of fine particles in estuaries and deltas.

The major complicating factor in our present understanding of these processes is that when fine particles first encounter a trace of sea water they are attracted to each other to form flocs. The presence of aggregates in the marine environment has been discussed by Berthois (1961), Biddle and Miles (1972), Edzwald (1972), Edzwald and O'Melia (1975), Gibbs (1977), Gibbs et al. (1983), Kranck (1975 and 1980), Krone (1962 and 1978), Schubel and Kana (1972), Sheldon (1968), and Zabawa (1978). The formation of these flocs is predictable from the principles of colloidal chemistry.

That lateral variations exist in the clay min-

erals of bottom sediments extending seaward from rivers has been documented by Van Andel and Postma (1954), Nelson (1960), Porrenga (1966), Powers (1957), Edzwald and O'Melia (1975), and Gibbs (1977). Few, if any, trends have been found by Kunge et al. (1968), Schubel (1968), and O'Brien and Burrell (1970), but these seem to be the exception and, generally, can be explained by special circumstances. Many of these authors attribute the trends to the process of coagulation.

Coagulation of clay minerals in the laboratory was studied extensively by Whitehouse et al. (1960), and later by Krone (1962, 1972, and 1978), Shiozawa (1970), Hahn and Stumm (1970), Edzwald (1972), Edzwald et al. (1974), Eppler (1975), and Hunt (1980).

This paper includes research on the rates of coagulation of pure clay minerals and natural sediments, conducted over a number of years, and reviews relevant research. Some parts of the blade-reactor experiments have been presented in a thesis (Lathrop 1980).

Before coagulation can occur, the particles must be destabilized by compression of the ion double layer around each particle, usually because of increasing of the ionic strength (especially the divalent cations) of sea water mixed with the river water. Once the particles are completely destabilized, a collision between two particles will produce a floc, and the process can continue until equilibrium is attained, with the floc consisting of hundreds of original particles.

There are three processes causing coagula-

¹Manuscript received 8 January 1982; revised 25 January 1983.

JOURNAL OF SEDIMENTARY PETROLOGY, Vol. 53, No. 4, DECEMBER, 1983, P. 1193-1203
Copyright © 1983. The Society of Economic Paleontologists and Mineralogists 0022-4472/83/0053-1193/503-00

tion of destablized particles in nature: 1) thermal agitation, 2) velocity gradient (turbulence), and 3) differential settling.

In thermal agitation, the collision frequency (I_B) of suspended particles is defined by Smoluchowski (1917) as

$$l_B = 4\pi DRn_{...}$$

where D = diffusion coefficient, R = collision radius (particle diameter), and n_o = number of particles per cubic centimeter. Thermal agitation in the environment occurs, for the most part, with particles less than one micrometer in diameter. In the turbulent environment of natural waters, thermal agitation would be overwhelmed by the velocity-gradient mechanism for all but the < 1/2 μ m material.

In the studies undertaken, all of the material was $> 1/2 \mu m$ in diameter; therefore, thermal agitation is not considered as an important process.

The major mechanism causing coagulation in the environment and in these studies is velocity gradient (turbulence). The equation that describes coagulation under turbulent conditions was originally developed by Smoluchowski (1917) and has been improved by a number of researchers (Camp and Stein 1943; Reerink and Overbeek 1954). A simple form of this rate equation is

$$\frac{dn}{dt} = -\frac{4}{\pi} \alpha \Phi nG,$$

where α is the collision efficiency factor, ϕ is the volume of solid material per unit volume of solution, n is the number concentration of particles, and G is the mean velocity gradient.

In our experiments, we measured dn/dt (the change in particle number with time), n, and φ; therefore, α can be calculated. The same procedure has been utilized by other researchers in numerous coagulation studies on a wide variety of materials. The work of Edzwald (1972) and Hahn and Stumm (1970) discussed coagulation of clay minerals in these terms.

PROCEDURES

The fluid shear obtained in laboratory mixers can be in either laminar or turbulent-flow conditions. The Couette reactor produces a laminar flow whereas the blade reactor produces a turbulent flow. Both kinds of reactors have advantages and disadvantages. Several researchers have found comparable results for the two kinds of reactors in coagulation-rate studies using other than natural sedimentary material and very high shear rates (Swift and Friedlander 1964; Birkner and Morgan 1968). The advantage of using the Couette reactor is that the shear rate in the space between the cylinders; with the narrow spacing (< 1 cm) used, shear would be uniform. Its disadvantage is that laminar shear does not simulate turbulent flow in nature.

The advantage of using the blade reactor is that it does produce a turbulent flow; the disadvantage is that it does not produce a uniform turbulence having the energy spectrum found in nature. There is high shear at the edges of the blades and baffles which could disrupt some flocs, thereby producing a slow rate of coagulation (longer time to attain a half-particle number) and lower collision-efficiency factor (a). Measurement of the turbulence in the blade reactor with hot-film anemometry revealed that about 99 percent of the volume of the reactor had turbulence spectra similar to that encountered in an estuarine environment. One can see that there are problems to consider in using either kind of reactor.

The coagulation experiments were conducted in a blade reactor (Lathrop 1980) similar to that used by Edzwald (1972) and in a Couette double-cylinder reactor similar to that used by Hunt (1980). These two reactors are the devices most widely used in coagulation studies. The Couette reactor consists of two cylinders with the 900-ml sample in the 1-cm gap between the cylinders. The laminae shear as the cylinders turn relative to each other. The blade reactor contained 900 ml and had two small flat blades that rotated on a central axis. Shear was determined by measuring torque for the blade reactor and was calculated from reactor geometry and speed for the Couette reactor.

To eliminate background counts, the waters used were filtered through 0.45-µm diameter Millipore filters. Experiments using the Couette reactor were conducted with 150 mg/l particle concentration, and at the critical coagulation salinity (salinity at which coagulation increases rapidly) dilutions of filtered sea water were used, with pH maintained at 7. Experiments using the blade reactor were conducted with 150-160 mg/l particle concentration at

for rate tary and is r is cyl-lin-ed, hat

is isrm nd of ne igile or de iat or n-

ignormalization of the contraction of the contracti

'S 'F 'C 'C 'C 0.5, 1.1, 4.4, and 17.5%, using dilutions of artificial sea water (Kester et al. 1967) with pH maintained at 8.1 ± 0.3 .

Both experiments used API standard clay minerals: illite #35, kaolinite #3, and montmorillonite #27. The API standard clays were ground by hand and size fractionated using a centrifuge. The size fractions for the blade reactor experiments were 1/2 to 1, 1 to 2, 2 to 4 μm, and for the Couette reactor experiments. I to 4 µm. The natural sample used for the experiment using the blade reactor was a mudbottom sample taken in Delaware Bay off Lewes, Delaware. The 2- to 4-µm fraction of this sample was comprised of 62% illite and 38% kaolinite. The natural samples used in the experiment using the Couette reactor were from the Amazon River, having a composition of 27% montmorillonite, 24% illite, and 38% kaolinite: from the Yukon River, having a composition of 20% montmorillonite, 29% illite, and 45% chlorite; and from the continental shelf off Guiana, South America, having a composition of 45% montmorillonite, 18% illite, and 30% kaolinite. The procedures utilized for mineralogy followed the procedures of Gibbs (1965 and 1967). The floc samples were taken from the reactors using a pipet with a 2-mm diameter opening. They were carefully placed on a slide in a 400-um deep well. Typically, more than 200 particles were counted, producing the high accuracy reported. Possible error is less than the size of the symbols on the graphs; where it is larger, it is given as an error bar on the graph.

RESULTS

Illite.—The experiment to determine the coagulation rate using illite in the blade reactor was designed to test the effect of particle size, mineralogy, and salinity on coagulation (Table 1). The decreases in particle number with time

TABLE 1.—Collision efficiency factor obtained in blade reactor using API clay minerals at various salinities

	Salinety			
	0.57	1.1%	4 414	17.5%
Mite				
1-2 µm		192		216
2-4 µm	.063	159	171	172
Kanlinite				•
2-4 µm		.166	.153	164
Montmorillonite				
2-4 µm		089	1.19	182

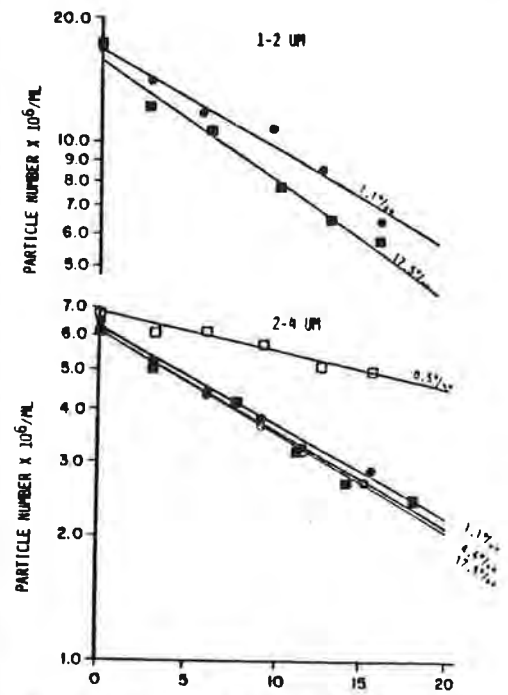


Fig. 1.—Relationship of particle number and time for illite of various size fractions with 0.5 (open squares), 1.1 (dots), 4.4 (circles), and 17.5 (squares) % salinities in the blade reactor.

are shown in Figure 1, and the effect of salinities can be seen in the slopes of the regression lines. The collision-efficiency factor (a) for illite increased rapidly at low salinity, then leveled off at several parts per thousand (Fig. 2). Tests for the effect of size on the coagulation rate of illite at various salinities (Fig. 3) shows that, at all salinities, the 1- to 2-µm fraction coagulates faster than does the 2- to 4-µm fraction. It also appears that the 1- to 2-µm fraction begins to coagulate at a lower salinity than does the 2- to 4-µm fraction. This could be caused by the larger surface area per unit volume for the 1- to 2-µm fraction than for the 2- to 4-µm fraction. This effect of size on the rate of coagulation was predicted by Verwey and Overbeek (1948), but later was not verified by the experimental work of Reerink and Overbeek (1954). However, in the case of clay minerals, the edge-broken bonds cause the size effect not found in the studies on latex coagulation by these researchers.

Results from the experiments using the Couette reactor with illite (Fig. 4) indicate a

Obstinity to coagniation to figure I lower with the total increases very rapidly high salinity of increases very spins figure particle site.

I - 2 um particle begin to coagniate.

In lower salinity uncontration and faither than does the 2 - 4 - um particles.

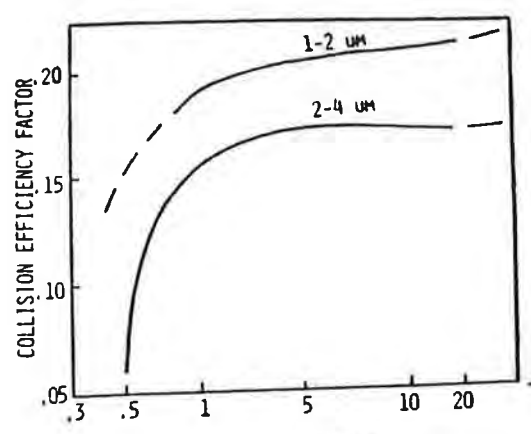


Fig. 2.—Relationship of the collision-efficiency factor and salinity for illite in the blade reactor.

rate of coagulation $(T_{1/2} = 12 \text{ min})$ the same as that measured in the experiments using the blade reactor (T_{1/2} = 12 min). Particle halftime (T_{1/2}) is the time for the particle number to reach one-half the original particle number. However, the a for the experiments using the Couette reactor was 0.76 sec-1 and for the experiment using the blade reactor was 0.16 secbecause the \alpha calculation includes the different shears of the two systems. Because the only significant differences between the experiments using the two reactors with illite are the kind of fluid flow and the level of shear, the different coagulation rates are apparently caused by the different hydrodynamics conditions,

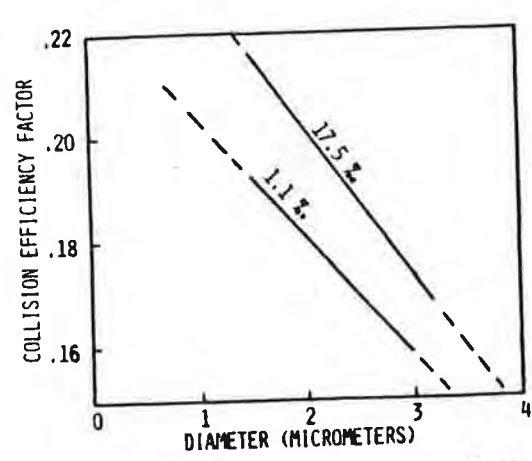


Fig. 3.—Relationship of the collision efficiency factor and particle diameter for illite at 1:1 and 17.5% salinity in the blade reactor.

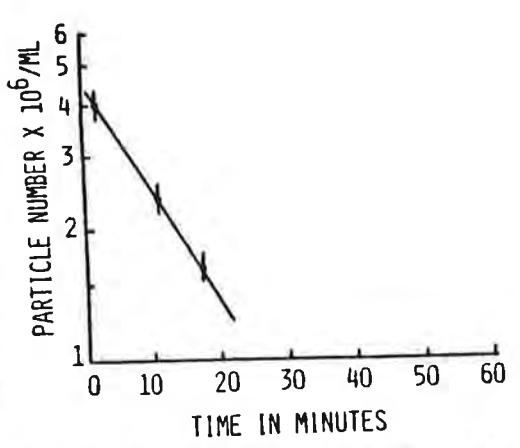


Fig. 4.—Relationship of particle number and time for illite in the Couette reactor with 0.77% salinity.

which will be discussed later.

Kuolinite.-The decrease in particle number with time for kaolinite in the blade reactor (Fig. 5) shows very little variation for 0.5, 1.1, 4.4, and 17.5% salinities. The collision-efficiency factor, α , is respectively 0.140, 0.166, 0.153, and 0.164 sec-1 for these experiments. The collision-efficiency factor (a) for kaolinite (Figure 6) rises rapidly at low salinities and

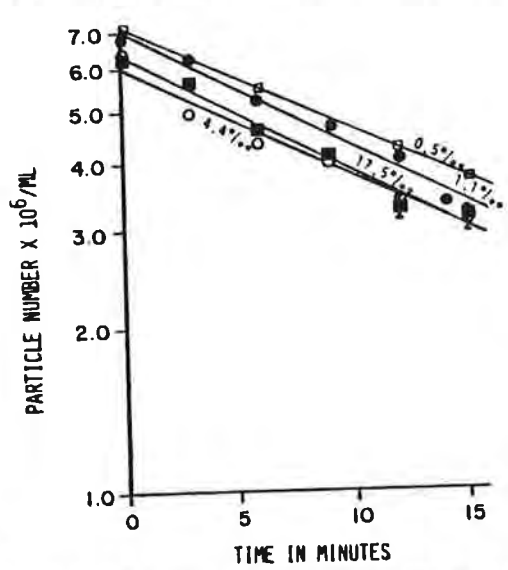


Fig. 5.—Relationship of particle number and time for the 2-4 µm fraction of kaolinite with 0.5 (open squares), 1.1 (dots), 4.4 (circles), and 17.5 (squares) % salinities in the blade reactor.

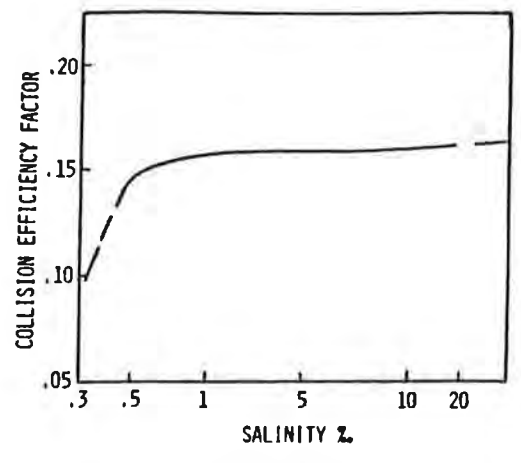


FIG. 6.—Relationship of the collision-efficiency factor (α) and salinity for kaolinite in the blade reactor.

levels off as salinity increases. The coagulation rate for the same kaolinite in the Couette reactor produces a $T_{1/2}$ of 26 min (Fig. 7), whereas the coagulation rate in the blade reactor is 14.5 min for the same salinity. The α for the experiment using the Couette reactor is 0.390 sec⁻¹ compared to about 0.16 sec⁻¹ at 1.1‰ salinity for the experiment using the blade reactor.

Montmorillonite.—Decrease in the particle number over a period of time using the blade reactor for montmorillonite (Fig. 8) shows the progressive increase in slope (dn/dt) with increasing salinity. The relationship between salinity and coagulation rate are shown in Figure 9. The collision efficiency factors (α) for montmorillonite are 0.089 sec⁻¹ for 1.1‰,

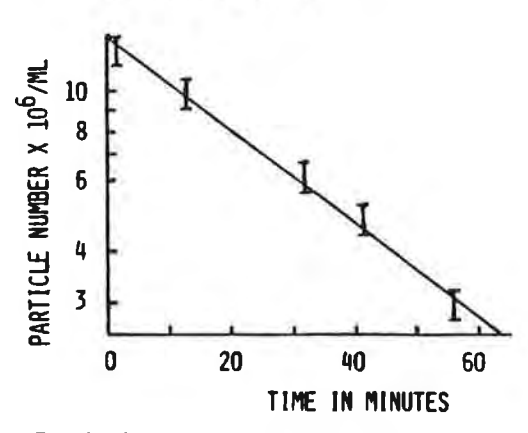


Fig. 7.—Relationship of particle number and time for kaolinite in the Couette reactor in 2% salinity.

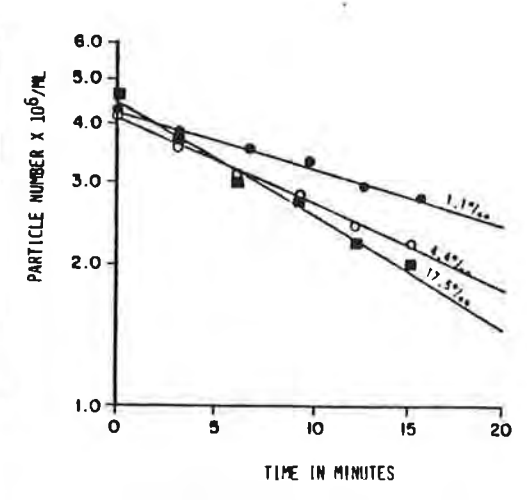


Fig. 8.—Relationship of particle number and time for montmorillonite with 1.1 (dots), 4.4 (circles), and 17.5 (squares) $\Re a$ salinity in the blade reactor.

 0.139 sec^{-1} for 4.4%c, and 0.182 sec^{-1} for 17.5%c.

Natural Samples.—The coagulation-rate experiments for the 1/2 to 1, 1 to 2, and 2 to 4
µm size fractions of Delaware Bay sediments all indicate an increasing rate of coagulation with increasing salinity (Fig. 10). The collision-efficiency factors (a) at various salinities for this natural sample are shown in Figure 11. One can see that the natural sample coagulation rates for the three size fractions are significantly lower than that measured for illite, even though the natural sample contained from 59 to 64 percent illite.

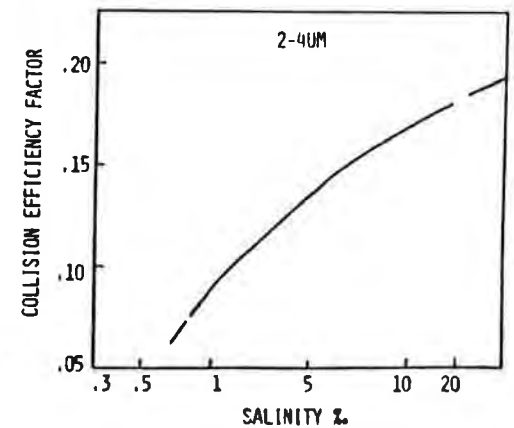


Fig. 9.—Relationship of the collision-efficiency factor and salinity for montmorillonite in the blade reactor.

60

a for

ber ig. .4. ncy 53. he

ınd

!X!

for s),

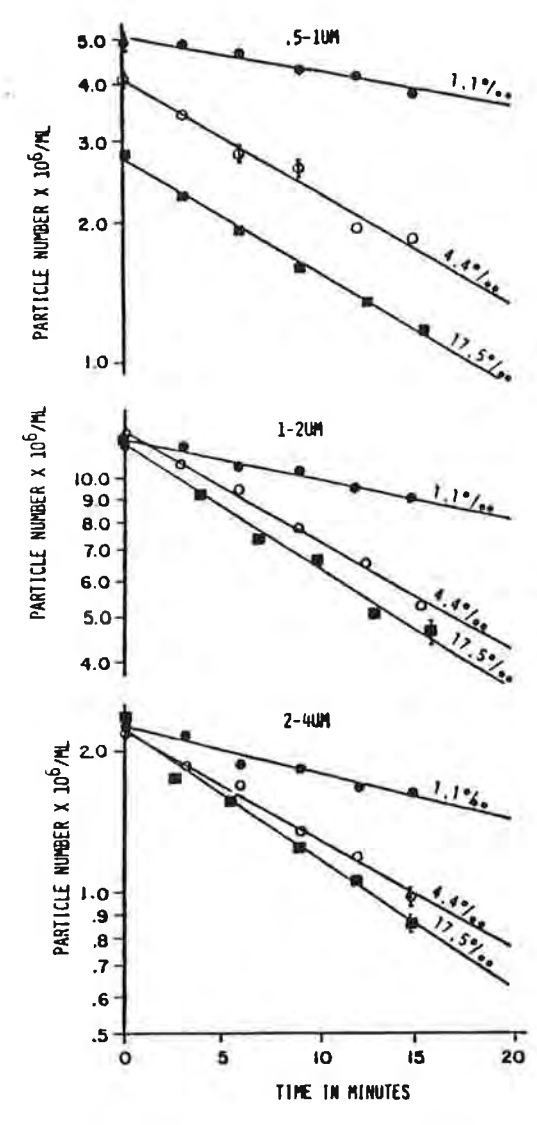


Fig. 10.—Relationship of particle number and time for the $1/2-1~\mu m$, $1-2~\mu m$, and $2-4~\mu m$ size fractions of the Delaware Bay sample with 1.1 (dots), 4.4 (circles), and 17.5 (squares) %c salinity in the blade reactor.

The sample from the Amazon River (38% kaolinite, 27% montmorillonite, and 24% illite), coagulated in the Couette reactor with 2% salinity solution (Fig. 12), had a collision-efficiency factor α of 0.697 sec⁻¹ and a $T_{1/2}$ of 15 min.

The ocean sediment sample taken off Guiana, coagulated in the Couette reactor (45% montmorillonite, 30% kaolinite, and 18% illite) with

0.9% salinity solution (Fig. 12), had a collision-efficiency factor of $0.219~\text{sec}^{-1}$ and a $T_{1/2}$ of 46 min.

The sample from the Yukon River (45% chlorite, 29% illite, and 20% montmorillonite), coagulated in the Couette reactor with 0.6% salinity solution (Fig. 12), had a collision efficiency of 0.198 sec⁻¹ and a T_{1/2} of 52 min.

DISCUSSION

Effect of Size.—The effect of particle size on coagulation in colloidal chemistry was shown by Verwey and Overbeek (1948) to be directly proportional to particle radius. Reerink and Overbeek (1954), on the other hand, found no dependence of a latex suspension stability on the particle size; however, they were not using clay minerals or natural sediments. The experimental data on several size fractions of illite (Fig. 2) show a definite relationship, with the collision efficiency (α) for the 1- to 2-μm fraction 25% higher than for the 2- to 4-μm fraction.

The effect of particle size in the experiments on natural sediment samples showed a trend generally opposite to that of illite (Fig. 13). The greatest change was for the 1.1% salinity experiments in which the 2- to 4-µm fraction had a collision factor (a) that was 26% larger than that of the 1/2 to 1-µm fraction. However, the higher salinity experiments showed only 8.4% smaller for 4.4% and 6.7% larger for 17.5%. For this natural sediment sample,

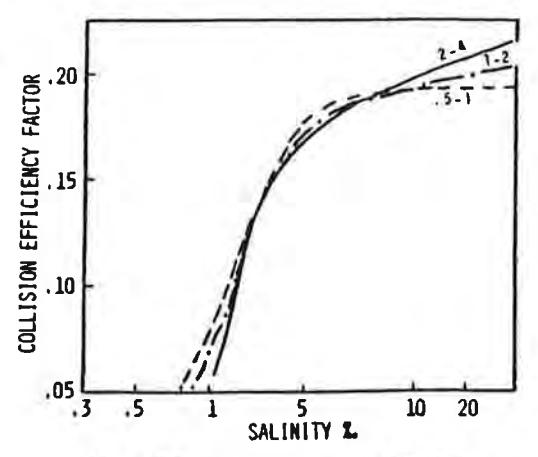


Fig. 11.—Relationship of the collision-efficiency factor (α) and salinity for the Delaware Bay sample in the blade reactor.

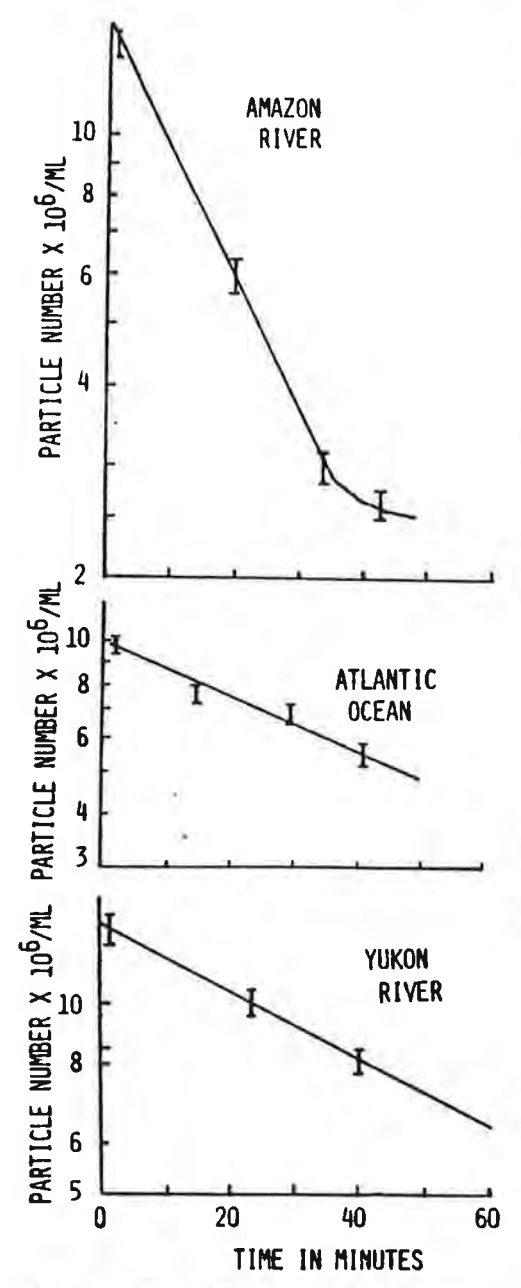


Fig. 12.—Relationship of particle number and time using 2% salinity in the Couette reactor for the Amazon River, Atlantic Ocean, and Yukon River.

the effect of size is most pronounced at lowest salinity. This could be significant in the zone of initial coagulation. If the particle passage time through this salinity zone were sufficient. it would be completely coagulated, possibly producing a segregation by particle size in the flocs. A possible cause for the natural sediments reacting to the effect of particle size in a manner different from that of illite could be due to the organic and metallic coatings on the natural sediments or to interactions among a multi-mineral suspension. Because the size fractions for the natural sediments had from 59 to 64% illite, a meaningful comparison between the experiments can be made. The effect of size on the coagulation rate of clay minerals and natural sediments deserves additional research.

Effect of Salinity. - The major factor affecting coagulation rate is the salinity of the solution. The three clay minerals studied all reacted to salinity in slightly different manners, as shown for the 2- to 4-µm fractions in Figure 14A. Kaolinite was the first to be affected by increasing salinity, followed by illite, and then montmorillonite. The coagulation rates for kaolinite and illite increased rapidly with increasing salinity while the rate for montmorillonite increased gradually. The coagulation rates obtained in the experiments using the blade reactor (discussed earlier in this paper) were obtained using the same API clay mineral standards and under the same conditions as those of Edzwald (1972), and are readily comparable. Edzwald's (1972) data replotted and positioned with the data from the experiment using the blade reactor in the present study (Figure

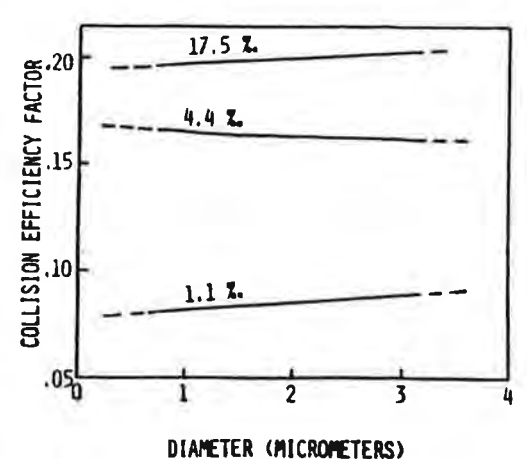


Fig. 13.—Relationship of the collision-efficiency factor and particle diameter for various size fractions of the Delaware Bay sample.

14B) show differences and similarities. In Edzwald's experiments, it is likely that flocs were broken with pipets, giving lower coagulation rates (Gibbs and Konwar 1982). Montmorillonite produces the strongest flocs, there fore, in Edzwald's work, had the least breakage, with results closest to those of this work. Illite showed the greatest difference between Edzwald's work and the present study and probably the greatest breakage, and kaolinite showed intermediate differences between Edzwald's work and the present study. It can be

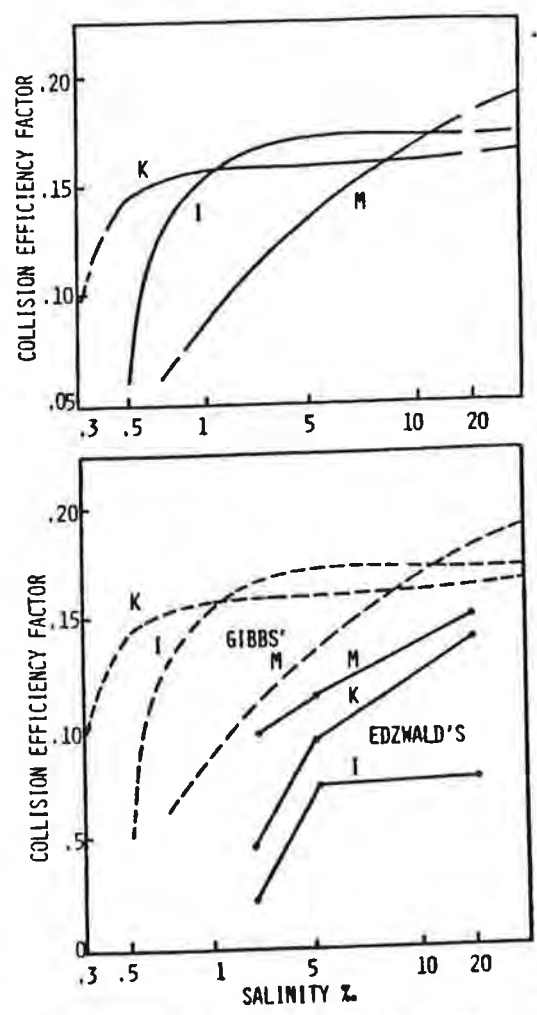


Fig. 14.—Relationship of the collision-efficiency factor (a) and salinity for (A) illite, kaolinite and montmorillonite from this study and (B) for illite, kaolinite and montmorillonite from the data of Edzwald (1972).

TABLE 2.—Comparison of measured and calculated collision efficiency factor for natural sediments

	Measured	Calculated
Blade Reacine		
Delaware Bay, 2-4 µm		
1.1%c	077	162
4.4%	.171	164
17 5%.	.207	169
Couette Reactor		
Amazon River	0 697	0.376
Atlantic Ocean	0.219	0 3273
Yukon River	0.198	0 430

seen that the majority of collision-efficiency factors for the clay minerals are significantly higher at all salinities for this paper compared to Edzwald's (1972) work.

In a similar study, Eppler et al. (1975), using NaCl solutions and a blade reactor, obtained collision-efficiency factors significantly lower than those reported here, perhaps because of a lack of divalent ions in the solution and possible floc breakage. Hunt (1980) conducted coagulation studies using a Couette reactor, but these results are not comparable with experiments using a blade reactor. At higher shear, he found the coagulation rate for kaolinite greater than that for illite, and for illite greater than that for montmorillonite, but varying salinities were not considered. In our studies, the collision-efficiency factors obtained with the Couette reactor were significantly higher than those obtained with the blade reactor. The cause for this difference could be breakage of flocs at the high shear at the blade edges. Additional studies are required to elucidate the effects of the two types of reactors on coagulation rates and to compare them to conditions found in nature. The effect of turbulence is obviously a major factor, deserving serious investigation.

Prediction of Collision-Efficiency Factor.— Comparison of α of the natural sediment sample and the percentage-weighted α based on the mineralogic composition of the natural sediments is given in Table 2. Agreement for the experiments using the blade reactor is poor at low salinities and good at 4.4‰ salinity. For the Couette reactor, the calculated α is reasonable for the Atlantic Ocean and Yukon River samples and is not in agreement for the Amazon River. This lack of ability to calculate the α for particles could be caused by coatings on natural particles, by different clay mineral characteristics between natural sediments and clay mineral standards, or by the fact the α mixture of clay minerals behaves differently than the sum of its components because of interactions between minerals. Obviously, our current state of knowledge does not permit a prediction of coagulation rates of natural sediments. Additional research is needed on the subject.

Environmental Implications. - The coagulation processes in the environment that bring individual particles together to form flocs are especially important when the dispersed material carried by rivers is mixed with seawater and when turbulence in the environment disperses particles, as during storms and in wave action, allowing coagulation of the particles afterwards. In the case of river input, the particles usually encounter a progressively increasing salinity. The amount of time the particles are exposed to each salinity will be shortest when a river discharges directly into the ocean, as does the Mississippi River, with the longest exposure time occurring with discharge into large estuaries, such as the Chesapeake Bay. The question must be raised as to how long an exposure to various salinities is required for the particles to coagulate completely. Would they coagulate entirely in 1 or 2‰ salinity, or would coagulation occur in higher salinity values? The particle half-time for illite, kaolinite and montmorillonite shows that, from 1/2 to 1%, the time drops from 25 to 35 minutes to less than 15 minutes at higher salinities (Fig. 15A). Montmorillonite shows a progressive change with increasing salinity. For comparison, the particle half-times for the Delaware Bay sample show that this natural sample material is not as sensitive to low salinity (Fig. 15B). For the nonspecialist, these particle half-times may be easier to understand than the collision-efficiency factors, but it must be remembered that this time would represent the time when total particle number was one-half the original number. It would obviously take longer for the coagulation process to reach equilibrium. On the basis of the rate studies for natural sediments reported upon here, in which the half-times ranged from 15 to 55 minutes, chances are good that coagulation would be complete within the first few parts per thousand of salinity in all environments. This would predict that the coagulation in the first few parts per thousand salinity would be critical.

One of the major variables yet to be under-

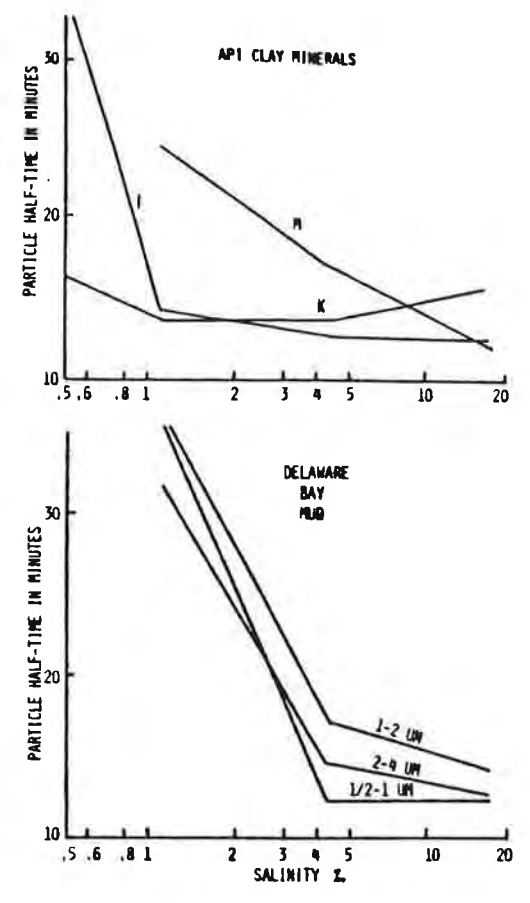


Fig. 15.—Relationship of particle half-time and salinity for (A) illite, kaolinite, and montmorillonite, and (B) for the Delaware Bay Sample.

stood is the effect of turbulence in nature on the coagulation process at these low salinities. Turbulence has two effects on the coagulation process: first, it brings the particles together to form the flocs in the first place; second, it controls the size the flocs can attain by splitting and eroding any larger flocs.

In the case of particles dispersed by high turbulence (storms, tides, etc.), the coagulation processes would occur as the turbulence decreases no matter what salinity prevailed at the site. These sediments could be somewhat more easily coagulated because of previous destabilization in high-salinity waters when compared to river-delivered sediments. The data presented in this report should be used with caution in determining coagulation rates in fullstrength seawater because none of the samples were preconditioned in seawater.

CONCLUSIONS

The collision-efficiency factors for clay minerals presented in this paper are significantly higher than those in the literature and indicate that the coagulation process starts at lower salinities (1/2 to 1%). The effect of size is significant in the case of the illite studies. The effect of different flow regimes (laminar and turbulent) is pronounced as evidenced by the different collision-efficiency factors for blade versus Couette reactors.

Natural polymineralic sediment samples produced collision-efficiency factors similar to those of individual API-reference clay minerals, but, in general, they could not be predicted with certainty at all salinities from the mathematically averaged API clay mineral data.

Many aspects of coagulation of clay minerals need further study, including the effects of size, turbulence, multimineral mixtures, low salinities, and organic and metallic coatings on particles.

ACKNOWLEDGMENTS

The author would like to thank the following students: Joan Lathrop, Michael Leslie, and Jeff Perine, for various parts of the laboratory experiments. This research was funded by the Office of Naval Research and NOAA's Office of Marine Pollution Assessment.

REFERENCES

- BERTHOIS, L., 1961, Observations directe des particules sedimentaries fins dans l'eau; Revue Geogr. Phys. Geol. Dyn. IV, 1, 39-42.
- BIDDLE, P., AND MILES, J. H., 1972, The nature of contemporary silts in British estuaries: Sed. Geology, v. 7, 23-33.
- BIRKNER, F. B., AND MORGAN, J. J., 1968, Polymer flocculation kinetics of dilute colloidal suspensions: Jour. American Water Works Assoc., v. 60, p. 175-191.
- CAMP, T. R., AND STEIN, P. C., 1943, Velocity gradients and internal work in fluid motion: Jour. Boston Society of Civil Engineers, v. 30, p. 219-237
- EDZWALD, J. K., UPCHURCH, J. B., AND O'MELIA, C. R., 1974, Coagulation in estuaries: Environmental Science and Technology, v. 8, p. 58-63.
- EDZWALD, J. K., AND O'MELIA, C. R., 1975, Clay distribution in recent estuarine sediments: Clays Clay
- Minerals, v. 23, p. 39-44. EPPLER, B., NEIS, U., AND HAHN, H. H., 1975, Engineering aspects of the coagulation of colloidal particles in natural water: Progress in Water Technology, v. 7. p. 207-216.

- GIBBS, R., 1965. Error due to segregation in quantitative clay mineral X-ray diffraction mounting techniques: Am. Mineralogist, v. 50, p. 741-751.
- , 1967. Quantitative X-ray diffraction analysis using clay mineral standards extracted from the sample to be analyzed: Clays Clay Minerals, v. 7, p. 79-90.
- Gisss, R. J., 1977, Clay mineral segregation in the marine environment: Jour. Sed. Petrology, v. 47, p. 237-
- GIBBS, R. J., AND KONWAR, L., 1982, Effect of pipetting on mineral flocs: Environmental Science and Technol-
- OBY, V. 16, p. 119-121. GIBBS, R. J., KONWAR, L., AND TERCHUNIAN, A., 1983, Coagulation process in Delaware Bay: Canadian Jour.
- Fisheries Aquatic Sci., in press. HAHN, H. H., AND STUMM, W. W., 1970. The role of coagulation in natural waters, Am. Jour. Sci., v. 268, p. 354-368.
- HUNT, J. R., 1980, Coagulation in continuous particle size distributions; theory and experimental verification [Ph.D. thesis]: Calif. Inst. Tech., 171 p.
- KESTER, D. R., DUEDALL, I. W., CONNORS, D. N., AND PYTKOWITZ, R. M., 1967, Preparation of artificial seawater: Limnology Oceanography, v. 12, p. 176-179. KRANCK, K., 1975, Sediment deposition from flocculated
- suspensions. Sedimentology, v. 22, p. 111-123. 1980, Variability of particulate matter in a small coastal inlet: Canadian Jour. of Fisheries and Aquatic
- Sci., v. 37, p. 1209-1215. KRONE, R. B., 1962, Flume studies of the transport of sediment in estuarial shoaling processes: Final Report
- to San Francisco District, U.S. Army Corps of Engi-1972. A field study of flocculation as a factor in
- estuarial shoaling processes: Technical Bulletin #19 prepared for the Committee on Tidal Hydraulics, ACE,
- , 1978, Aggregation of suspended particles in estuaries, in Kjerfve, B., ed., Estuarine Transport Pro-cesses: Columbia, Univ. South Carolina Press, p. 177-
- KUNZE, G. W., KNOWLES, L. I., AND KITANO, Y., 1968, The distribution and mineralogy of clay minerals in the Taku estuary of southeastern Alaska, Marine Geology, v. 6. p. 439-448.
- LATHROP, J. E., 1980, Coagulation kinetics of natural clay sediments [M.S. thesis]: Univ. Delaware, 101 pp.
- NELSON, B. W., 1960, Clay minerals of the bottom sediments, Rappahannock River, Virginia, Clays and Clay Mineral, 7, 135-147.
- O'BRIEN, N. R., AND BURRELL, D. C., 1970, Mineralogy and distribution of clay size sediment in Glacier Bay. Alaska, Jour. Sed. Petrology, v. 40, 650-655
- PORRENGA, D. H., 1966, Clay minerals in recent sediments of the Niger Delta. Clays and Clay Minerals, v. 14. p. 221-223.
- POWERS. M. C., 1957 Adjustment of land derived clays to the marine environment, Jour. Sed. Petrology, v. 27, 355-372
- REERINK, H., AND OVERBEEK, J. TH. G., 1954, The rate of congulation as a measure of the stability of silver iodide sols, Discussion: Faraday Society, 18, 74-84.
- SCHUBEL, J. R., 1968. The turbidity maximum of the Chesapeake Bay, Science, v. 161, p. 1013-1015. SCHUBEL, J. R., AND KANA, T. W., 1972, Agglomeration
- of fine-grained suspended sediment in northern Ches-

apeake Bay, Powder Technology, v. 6, p. 9-16.
SHELDON, R. W., 1968, Sedimentation in the estuary of

the River Crouch, Essex, England, Limnology Ocean-

ography, v. 13, p. 72-83.
Shiozawa, T., 1970, Experimental study on differential flocculation of clay minerals—an application of its results to recent sediments in Ishikari Bay, Japanese Assoc. Mineralogists, Petrographers, Economic Geologists Jour., v. 63, p. 75-84. SMOLUCHOWSKI, M., 1917, Versuch einer mathematischen

theorie der koagulations-kinetik kolloider losungen. Aeitschrift für physicalische Chemie, v. 92, p. 129-

SWIFT, D. L., AND FRIEDLANDER, S. K., 1964, The coagulation of hydrosols by Brownian motion and lami-

nar shear flow, Jour. Colloid. Sci., v. 19, p. 621-647. VAN ANDEL, T. H., AND POSTMA, H., 1954, Recent sediments of the Gulf of Paria, in Reports of the Orinoco Shelf Expedition, K. Nedri, Akad. Wese sch, Verb.,

v. 20, p. 42-56. VERWEY, E. J. W., AND OVERBEEK, J. TH. G., 1948. Theory of stability of lyophobic colloids, New York.

Elsevier, 210 p.

WHITEHOUSE, U. G., JEFFREY, L. M., AND DEBRECHT, J. D., 1960, Differential settling tendencies of clay minerals in saline waters, Clays Clay Minerals, 7th Na-

tional Conference, p. 1-79.

ZABAWA, C., 1978, Microstructures of agglomerated suspended sediments in northern Chesapeake Bay Estuary. Science, v. 202, p. 49-51.

Effect of Natural Organic Coatings on the Coagulation of Particles

Ronald J. Glbbs

Center for Colloidal Science, College of Marine Studies, University of Delaware, Newark, Delaware 19711

■ Coagulation experiments with four natural samples and the same samples with the organic coatings removed were conducted in Couette- and blade-type reactors. These experiments showed that the natural coated samples coagulated significantly slower than the samples with the coatings removed. Dissolved organic material did not have a significant effect relative to the particle organic coatings.

Introduction

Fine-grained particles make up the majority of the sediments entering the marine environment. These particles carry the majority of toxic metals and organic substances carried by rivers and discharged into estuaries and the ocean. These muds are responsible for filling estuaries and marshes and for depositing deltas and submarine fans over geological time spans. Therefore, it is critical that we understand the coagulation processes related to fine particles in estuaries and deltas.

The major complicating factor in our present understanding of these processes is that when fine particles first encounter a small amount of seawater, they are attracted to each other to form aggregates or flocs. The presence of aggregates in the environment has been discussed by Berthois (1), Biddle and Miles (2), Gibbs et al. (3), Kranck (4, 5), Krone (6), Schubel and Kana (7), Sheldon (8), and Zabawa (9).

Coagulation of clay minerals in the laboratory was studied extensively by Whitehouse et al. (10) and later by Krone (6, 11, 12), Shiozawa (13), Hahn and Stumm (14), Edzwald (15), Edzwald et al. (16), Eppler et al. (17), Hunt (18), and Gibbs (19).

The surface electrical properties of particles undergo a change as they pass from a river environment into the ocean mainly because of the polyvalent ions present in seawater. This change has been discussed by Pravdic (20), Martin et al. (21), and Hunter and Liss (22). Natural organic surfactants have an effect on the properties of surfaces of natural particles in seawater through the formation of films, as proposed by Neihof and Loeb (23–25) and Hunter and Liss (22). These previous studies all measured an electrical property of the particles (electrophoresis, electroosmosis, or streaming potential or current).

Specifically, they studied the effect of absorbed surfaceactive dissolved substances on the electrical properties of the particles.

The present study was designed to measure directly the effect that natural organic coatings have on the coagulation process of natural particles. To provide the best control on isolating this effect, a laboratory study was utilized.

Procedures

The coagulation experiments were conducted in a Coutte-type double cylinder reactor (26) similar to that used by Hunt (18) and in a blade-type reactor (19, 27) similar to that used by Edzwald (15). These two reactors are the devices most widely used in coagulation studies in a variety of disciplines. Shear was determined by measuring torque for the blade-type reactor and was calculated for the Coutte-type reactor. The mixing rate in the blade-type reactor was maintained at a shear of 60g and the rate in the Couette-type reactor was maintained at a shear of 17g.

To eliminate background counts, the water used was filtered through 0.45- μm diameter Millipore filters. Experiments using the Couette-type reactor were conducted at 150 mg/L particle concentration (typical of many turbidity maxima in estuaries) and at the critical coagulation salinity (the salinity at which coagulation increases rapidly) by using dilutions of filtered seawater (34 ‰) with pH maintained at 7 by adding small amounts of HCl. Experiments using the blade-type reactor were conducted with 150-160 mg/L particle concentrations at 1.1, 4.4, and 17.5 ‰ by using dilutions of artificial seawater (28), with pH maintained at 8.1 ± 0.3 by adding small amounts of HCl. The artifical seawater was free of dissolved organic substances because of either high-temperature (500 °C) treatment of the salts or ultraviolet treatment of the water and some salt solutions.

The natural samples used in the experiments using the Couette-type reactor were Amazon River material having a composition of 27% montmorillonite, 24% illite, and 38% kaolinite, Yukon River material having a composition of 20% montmorillonite, 29% illite, and 45% chlorite, and material from the continental shelf off Guiana, South

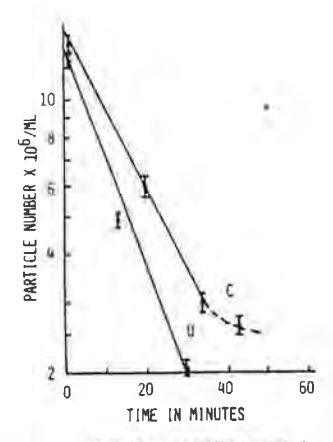


Figure 1. Relationship of particle number and time for the Amazon River sample with and without coating using 2 ‰ salinity in the Couette-type reactor.

America, having a composition of 45% montmorillonite, 18% illite, and 30% kaolinite. The samples were taken from the reactors by using a glass tube having a 2-mm diameter. Each was carefully placed in a 400 μ m deep well on a microscope slide. Typically, more than 200 particles were counted, producing the high accuracy reported. Possible error is less than the size of the symbols on the graphs; when it is larger, it is given as an error bar on the graph. In order to determine the effect of organic coating on the coagulation rates, the experiments were conducted with the particles in their natural condition and after the organic coatings were removed by oxidizing with sodium hypochlorite (29).

Before coagulation can occur, the particles must be destabilized by compression of the double layer around each particle and/or sorption by increasing the ionic strength (especially the divalent cations) with seawater as it mixed with the river water. Once the particles are completely destabilized, a collision between two particles will produce an aggregate of two, and the process can continue until an equilibrium is attained, with the aggregate consisting of hundreds of the original particles.

There are three processes causing coagulation of destabilized particles in nature: (1) thermal agitation; (2) velocity gradient (turbulence); (3) differential settling.

In thermal agitation the collision frequency (I_B) on suspended particles is defined by Smoluchowski (30) as

$$I_{\rm B} = 4\pi DRn_0$$

where D= diffusion coefficient, R= collision radius (particle diameter), and $n_0=$ number of particles per cubic centimeter. Thermal agitation in the environment occurs, for the most part, with particles less than 1 μ m in diameter. In the turbulent environment of natural waters, thermal agitation would be overwhelmed by the velocity gradient mechanism for all but the $<1/2-\mu$ m material.

mechanism for all but the <1/2-\mu material.

In the studies undertaken, all of the material was >1/2-\mu m in diameter. Therefore, thermal agitation is not considered as an important process.

The major mechanism causing coagulation in the environment and in these studies is velocity gradient (turbulence). The equation that described coagulation under turbulent conditions was originally developed by Smoluchowski (30) and has been improved by a number of researchers (31, 32). A simple form of this rate equation is

$$dn/dt = -(4/\pi)\alpha\phi nG$$

where α is the collision efficiency factor, ϕ is the volume of solid material per unit volume of solution, n is the number concentration of particles, and G is the mean

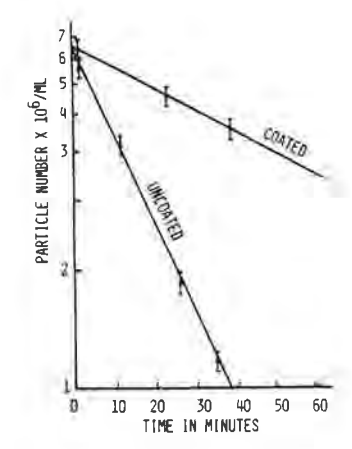


Figure 2. Relationship of particle number and time for the Yukon River sample with and without coating using 0.6~% salinity in the Couette-type reactor.

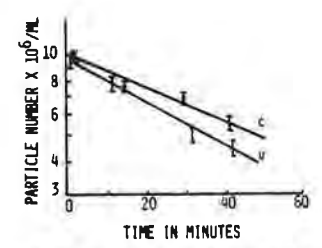


Figure 3. Relationship of particle number and time for a ocean sample with and without coating using 0.9 ‰ salinity in the Couette-type reactor.

velocity gradient. In our experiments we measured $\mathrm{d}n/\mathrm{d}t$ (the change in particle number with time), n, and ϕ ; therefore, α can be calculated. The same procedure has been utilized by other researchers in numerous coagulation studies on a wide variety of materials. The work of Edzwald (15) and Hahn and Stumm (14) discussed coagulation of clay minerals in these terms. The collision efficiency factor, α , is a measure of the particles likelihood to coagulate.

Results

The experiments with the Couette-type reactor on the Amazon River sample material at 2 % salinity (Figure 1) show that the natural sample (coated) coagulated slower (lower slope, α of 0.69) than the sample from which the coating had been removed with α of 0.82. After about 30 min, the coagulation rate of the natural sample material slowed down. The experiments with the Yukon River sample material at 0.6 % using the Couette-type reactor exhibited a striking difference between the slope of the lines (Figure 2). The sample with the coating removed had a coagulation rate 4 times the rate of the natural sample. The natural sample took about 55 min for the particle number to decrease to half the starting number, called half-time $(T_{1/2})$, whereas the uncoated sample took only about 11 min. The natural sample had an α of 0.23 compared to 0.77 for the sample without the coating. The experiment using the ocean sample in the Couette-type reactor at 0.9 ‰ salinity again showed that the natural (coated) sample coagulated more slowly than did the uncoated sample (Figure 3). The natural sample had a α of 0.19 and a $T_{1/2}$ of 46 min, whereas the treated sample without the coating had an α of 0.26 and a $T_{1/2}$ of 33 min. It can be seen that all the experiments conducted in the Couette-type reactor showed that the natural samples with coatings coagulated slower than did the samples with coatings removed.

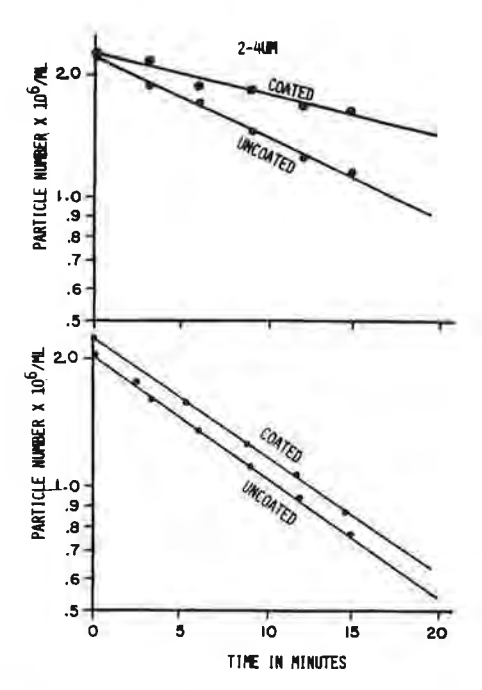


Figure 4. Relationship of particle number and time for Delaware Bay sample with and without coatings using 1.1 % (4a) and 17.5 % (4b) in the blade-type reactor.

The experiments in the blade-type reactor (27) using the 2-4-µm diameter fraction of the Delaware Bay sediments at 1.1 ‰ salinity showed a significant difference in the coagulation rate between the natural (coated) sample and the uncoated sample (Figure 4a). The natural sample had an α of 0.077 and a $T_{1/2}$ of 32 min, whereas the sample with the coating removed had an α of 0.145 and a $T_{1/2}$ of 19 min. Similar experiments at a salinity of 4.4 ‰ indicate that coagulation rates for coated and uncoated material are closer than at 1.1 ‰ salinity. The natural coated sample had an α of 0.207 and a $T_{1/2}$ of 14 min, and the uncoated sample had an α of 0.177 and a $T_{1/2}$ of 12 min. The experiments at 17.5 % salinity (Figure 4b) indicated that coagulation rates for the natural (coated) sample are nearly the same as those for the uncoated sample. The natural coated sample had an α of 0.207 and a $T_{1/2}$ of 12.5 min, and the uncoated sample had an α of 0.216 and a $T_{1/2}$ of

All of the experiments conducted with the blade-type reactor used organic-substance-free artificial seawater. In order to evaluate whether the natural dissolved organic substances had an effect on the coagulation processes, the blade-type reactor experiments were repeated with filtered natural seawater (retaining its natural dissolved organic substances). The results were not significantly different from the experiments using organic-free artificial sea water. From this, we can conclude that the effect of the dissolved organic substance is insignificant relative to removal of natural organic coatings and/or that the natural level of 150 mg/L of particles overwhelms the small amount of dissolved organic substances.

The effect of salinity can be studied in the blade-type reactor experiments. Figure 5 is a plot of the collision efficiency factor, α , and the salinity. It shows the large difference between coated and uncoated samples at low salinities and how the difference decreases at higher salinity. A simpler method of portraying the coagulation rate is plotting the particle half-time, $T_{1/2}$. In Figure 6 the long times and large differences between coated and uncoated material at low salinities is shown, whereas at high salinities the time is shorter and the difference between the coated and uncoated material is smaller. In the environ-

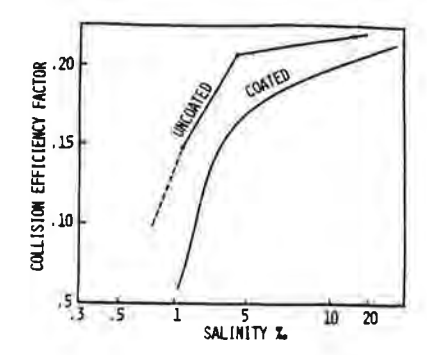


Figure 5. Relationship of collision efficiency factor (α) and salinity for Delaware Bay sample in the blade-type reactor.

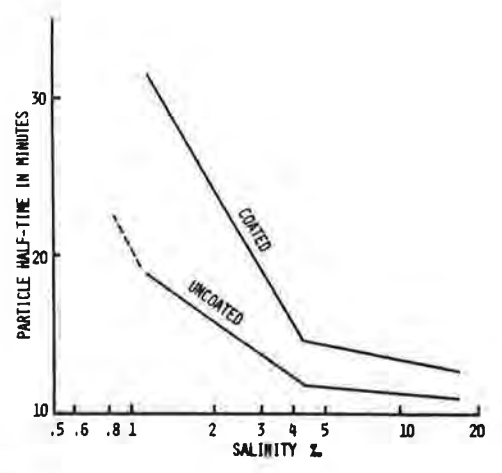


Figure 6. Relationship of particle half-time and salinity for Delaware Bay sample in the blade-type reactor.

ment, this would imply that the region in which this difference in coagulation properties would be most significant is the brackish low-salinity portions and that in any region with salinity higher than about 15 % this difference would be very small.

Conclusion

The effect of the organic coatings on particles has a significant impact on the coagulation rate of natural particles. This effect is largest at low salinities and decreases with increasing salinity.

Literature Cited

- (1) Berthois, L. Rev. Geogr. Phys. Geol. Dyn. 1961, 1, 39-42.
- (2) Biddle, P.; Miles, J. H. Sediment. Geol. 1972, 7, 23-33.
- (3) Gibbs, R. J.; Konwar, L.; Terchunian, A. Can. J. Fish. Aquat. Sci., in press.
- (4) Kranck, K. Sedimentology 1975, 22, 111-123.
- (5) Kranck, K. Nat. Can. (Que.) 1979, 106, 163-173.
- (6) Krone, R. B. Final Report, U.S. Army Corps of Engineers, San Francisco District, 1972.
- (7) Schubel, J. R.; Kana, T. W. Powder Technol. 1972, 6, 9-16.
- (8) Sheldon, R. W. Limnol. Oceanogr. 1968, 13, 72-83.
- (9) Zabawa, C. Science (Washington, D.C.) 1978, 202, 49-51.
- (10) Whitehouse, U. G.; Jeffrey, L. M.; Debrecht, J. D. Clays Clay Miner. 1960, 1-76.
- (11) Krone, R. B. Final Report, U.S. Army Corps of Engineers, San Francisco District, 1962.
- (12) Krone, R. B. "Estuarine Transport Processes"; Kjertve, G., Ed.; University of South Carolina Press: Columbia, SC, 1978; pp 177-190.
- (13) Shiozawa, T. J. Jpn. Assoc. Miner. Petrol. Econ. Geol. 1970, 63, 75–84.
- (14) Hahn, H. H.; Stumm, W. Am. J. Sci. 1970, 268, 354-368.
- (15) Edzwald, J. K. Publication UNC-SG-72-06, Chapel Hill, NC, 1972.
- (16) Edzwald, J. K.; Upchurch, J. B.; O'Melia, C. R. Environ. Sci. Technol. 1974, 8, 58-63.

- (17) Eppler, B.; Neis, U.; Hahn, H. H. Prog. Water Technol. 1975, 7, 207-216.
- (18) Hunt, J. R. Ph.D. Dissertation, California Institute of Technology, 1980.
- (19) Gibbs, R. J. J. Sediment. Petrol., in press.
- (20) Pravdic, V. Limnol. Oceanogr. 1970, 15, 230-233.
- (21) Martin, J. M.; Jednacak, J.; Pravdic, V. Thalassia Jugosl. 1971, 7, 619–636.
- (22) Hunter, K. A.; Liss, P. S. Nature (London) 1979, 282, 823-825.
- (23) Neihof, R. A.; Loeb, G. I. Limnol. Oceanogr. 1972, 17, 7-16.
- (24) Neihof, R. A.; Loeb, G. I. J. Mar. Res. 1974, 32, 5-12.
- (25) Loeb, G. I.; Niehof, R. A. In "Applied Chemistry at Protein Interfaces"; Baier, R. E., Ed.; 1975; pp 319-335.

- (26) Ham, R. K.; Christman, R. F. J. Sanit. Eng. Div. Am. Soc. Civ. Eng. 1969, 95, 481-502.
- (27) Lathrop, J. E. M.S. Thesis, University of Delaware, 1980.
- (28) Kester, D. R.; Duedall, I. W.; Connors, D. N.; Pytkowitz,
 R. M. Limnol. Oceanogr. 1967, 12, 176-179.
- (29) Anderson, J. V. Clays Clay Miner. 1963, Tenth National Conference, 380–388.
- (30) Smoluchowski, M. v. Z. Phys. Chem. 1971, 92, 129-168.
- (31) Camp, T. R.; Stein, P. C. J. Boston Soc. Civ. Eng. 1943, 30, 219-237.
- (32) Reeink, H.; Overbeek, J. T. Faraday Soc. Discuss. 1954, 18, 74-84.

Received for review July 14, 1982. Accepted December 27, 1982.

SEDIMENTATION REVISITED

R. B. Krone

Abstract

Relations describing the rates of deposition of suspended cohesive sediment from flowing water were presented in the early 1960's. One of these relations has been widely incorporated in models, and it is useful to review its origins and limitations with the perspective of more recent experience. This relation includes the flux of settling sediment and the probability that settling sediment will stick to the bed. Aggregation and break up rates become important as the concentration of suspended particles increase, and the aggregates that are partially dispersed in the viscous layer at the bed can have lower settling velocities than those settling to the viscous layer. Dispersed aggregates not depositing mix upward and are reaggregated in the lower velocity gradients above. A near steady state is postulated, depending on the concentration of suspended particles and the bed shear stress. A method is given for calculating the aggregate break up rate. This review brought out the importance of recognizing the transport regime in selecting a deposition relation.

Introduction

Relations describing the deposition of cohesive sediment from flowing suspensions were presented by Krone in 1962. The differentiated form of one of these relations has been used widely in numerical models with varying but heartening success since its first application by Odd and Owen in 1972 to modeling sediment transport in the Thames (Arithurai and Krone, 1974; Onishi and Trent, 1982; Schoellhamer, 1986; Nicholson and O'Connor, 1986). It is appropriate to review the concepts and data that led to these relations for the benefit of future modelers. Such a review would also identify areas that would benefit from further research. These are the objectives of this paper.

<u>Cohesive Sediment Deposition</u>

The deposition rate relation used in models is

$$\frac{dC}{-1} = -\frac{w_sC}{D} - (1 - C_w / C_{cr}) ; \quad \mathcal{T}_w < \mathcal{T}_{cr}$$
 (1)

where C is the uniform concentration of suspended sediment by weight over the water depth D, t is time, w is the near-bed settling velocity of suspended aggregates, \mathcal{T}_{w} is the bed shear stress, and \mathcal{T}_{c} is the critical shear stress above which there is no net deposition. The product w C is the flux of suspended particles to the bed surface, and $(1 - \mathcal{T}_{w} / \mathcal{T}_{cr})$ is the probability that an arriving aggregate would be

retained on the bed.

The concepts that underlie this relation include the existence of a viscous layer on the surface of the sediment bed through which the aggregates settle. At any location on the bed, the thickness of this viscous layer grows until it becomes unstable, then is wiped out by flow instability. Aggregates that settle to the bed can be pulled off by the transient instability, possibly tearing off a part of the deposited aggregate or the aggregate and a portion of the bed to which it is stuck. The shear stress in equation 1 is the average over relevant space and time scales.

Equation 1 appears to be straight forward. The settling velocity of aggregates can be altered by processes that change their sizes and densities, however, and \mathcal{T}_{CR} is determined by the shear strengths of depositing aggregates. Information about densities and shear strengths of suspended aggregates was obtained using rheological measurements (Krone, 1963, 1984), and a brief description of the means of obtaining this information will be useful for illuminating the factors that affect \mathbf{w}_{S} and \mathcal{T}_{CR} in equation 1.

Bingham proposed that the shear stress -- velocity gradient relation in a cohesive suspension could be the result of mechanical and viscous momentum transfer. His relation is given with constant coefficients as:

$$\mathcal{C} = \widetilde{\iota}_{B} + \gamma_{d} du/dz$$
 (2)

where $\tau_{\rm B}$ is the shear due to interparticle contact and disruption and du/dz is the shear due to viscous momentum transfer. $\eta_{\rm d}$ is the differential viscosity, and du/dz is the local velocity gradient. Both of the coefficients depend on the <u>structure</u> of the suspension. If suspended aggregates retain their structure throughout the range of velocity gradients of concern, then the coefficients will be constant. Otherwise the coefficients will vary with processes that affect the structure of the suspension or matrix. The basic concept, that the mechanical and viscous momentum transfer processes can be superposed, continues to be useful, however.

Relations between the coefficients of (2) and particle concentration were established experimentally for a number of estuarial sediments and were extrapolated to a volume concentration of 1.0 to obtain the shear strengths and densities of the suspended aggregates. Different aggregate structures became apparent in this study that could be described as primary particle aggregates, aggregations of primary aggregates, aggregations of these primary aggregate aggregates, and so on. Such aggregations are conveniently described as "zero order" aggregates, "first order" aggregates, and so forth. Separate orders were isolated in the viscometer and each prevailed over a range of velocity gradients. The primary importance of this model results from the observation that the bed surface is an aggregation of the aggregates settling on it, and the bed surface shear strength is that of one order

An early laboratory investigation was designed for study of the deposition process that provided controlled, if not ideal, hydraulic conditions for aggregation and deposition of suspended sediment in free surface flows (Krone, 1962). A 30.5 m (100 ft) long rectangular channel, 0.915 m (3 ft) wide, was equipped with a low head propeller pump at its downstream end and 0.254 and 0.305 m (10- and 12-inch) return lines to the upstream end. These return lines could be opened individually to provide shears that prevented deposition in the lines with minimum disruption of suspended aggregates. Open channel flow conditions prevailed in the channel; the recirculating flume represented continuous channel flow conditions modified by the shears in the recirculation facility and vertical mixing at the upstream end of the channel.

The experimental procedure began with suspension of various concentrations of sediment from parts of the San Francisco Bay system in synthesized sea water. The concentration of salts exceeded that at which cohesion was found to be complete at all times. The initial suspension was achieved by circulating the material at the highest pump setting, approximately 0.9 m/s (3 ft/s) in the channel, and breaking the previous deposit with a hoe. Circulation was continued until all material was suspended. The flow velocity was then reduced to a velocity that promoted deposition, and samples were taken at the mixed discharge of the return lines for gravimetric analyses of suspended solids concentrations and optical density measurements.

Deposition at Low Concentrations Aggregation rates decrease rapidly with decreasing number concentration. It is therefore desirable to begin with description of the deposition at low suspended solids concentrations to minimize this complication. Results of deposition experiments using sediment from the harbor at Redwood City, on South San Francisco Bay, are presented in Figure 1. This figure shows a semilogarithmic decrease in concentration after a short initial period. The rate of deposition increased at slower flows. The fraction of suspended sediment deposited per hour is plotted in Figure 2 against the bed shear stress for each of the curves shown in Figure 1. Figure 2 shows a linear relation between the bed shear stress and the deposition rate, with a critical shear stress of .06 N/m² (0.6 dynes/cm²). The plots in Figures 1 and 2 are described by the integrated form of 1:

$$C(t) = C_0 \exp [-w_s t(1 - \gamma_w / \gamma_{cr}) / D]$$
 (3),

where w_s/D is the ordinate intercept in Figure 2 and C is the concentration at the beginning of the semilogarithmic portion of the curves.

It is evident from these figures that w was constant throughout the semi-log portions of the plotted curves in Figure 1. Aggregation was virtually complete at the beginning of this phase of the deposition

R. B. Krone 10-15-91

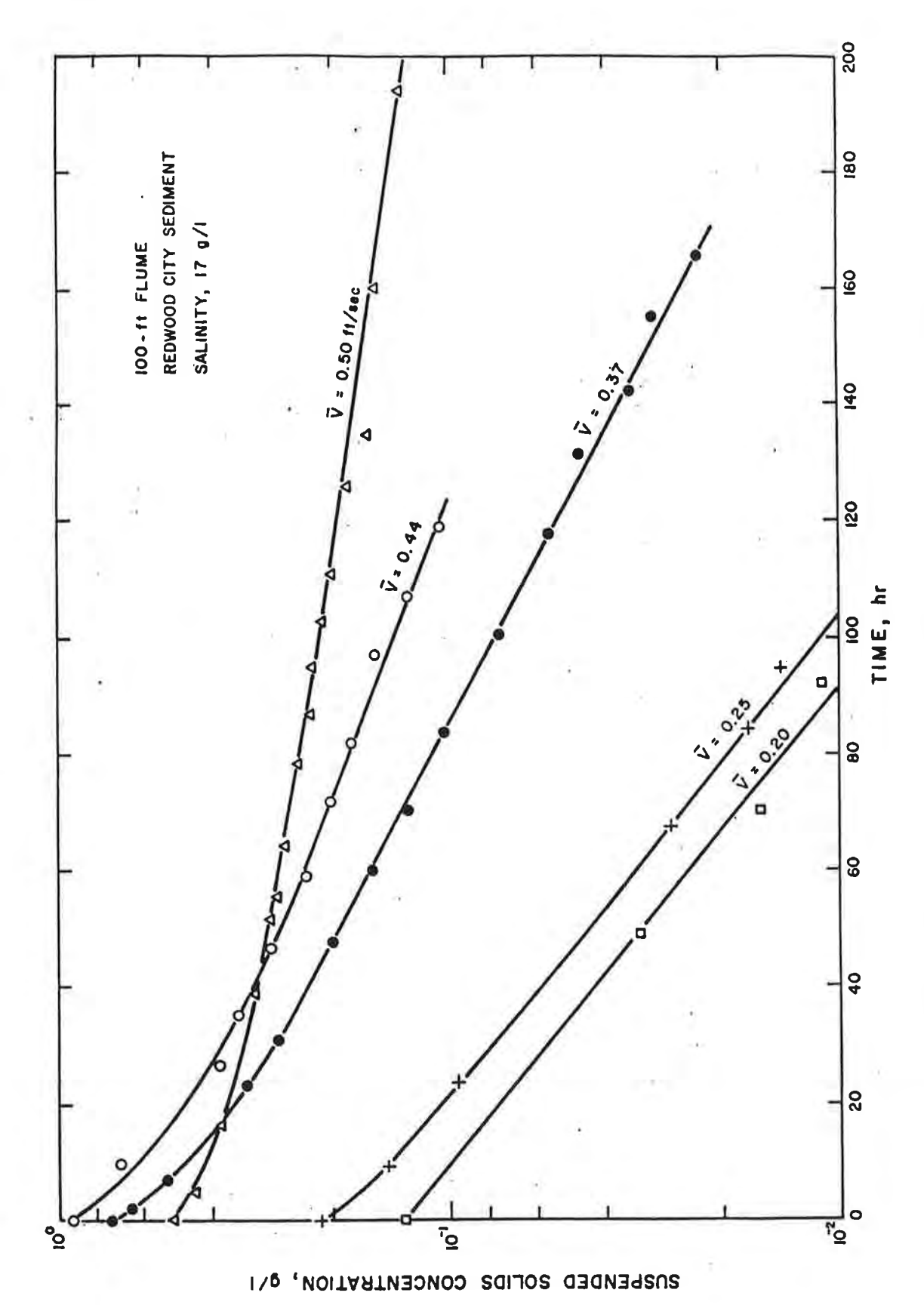


FIGURE 1 DEPOSITION OF SEDIMENT FROM FLOWING WATER

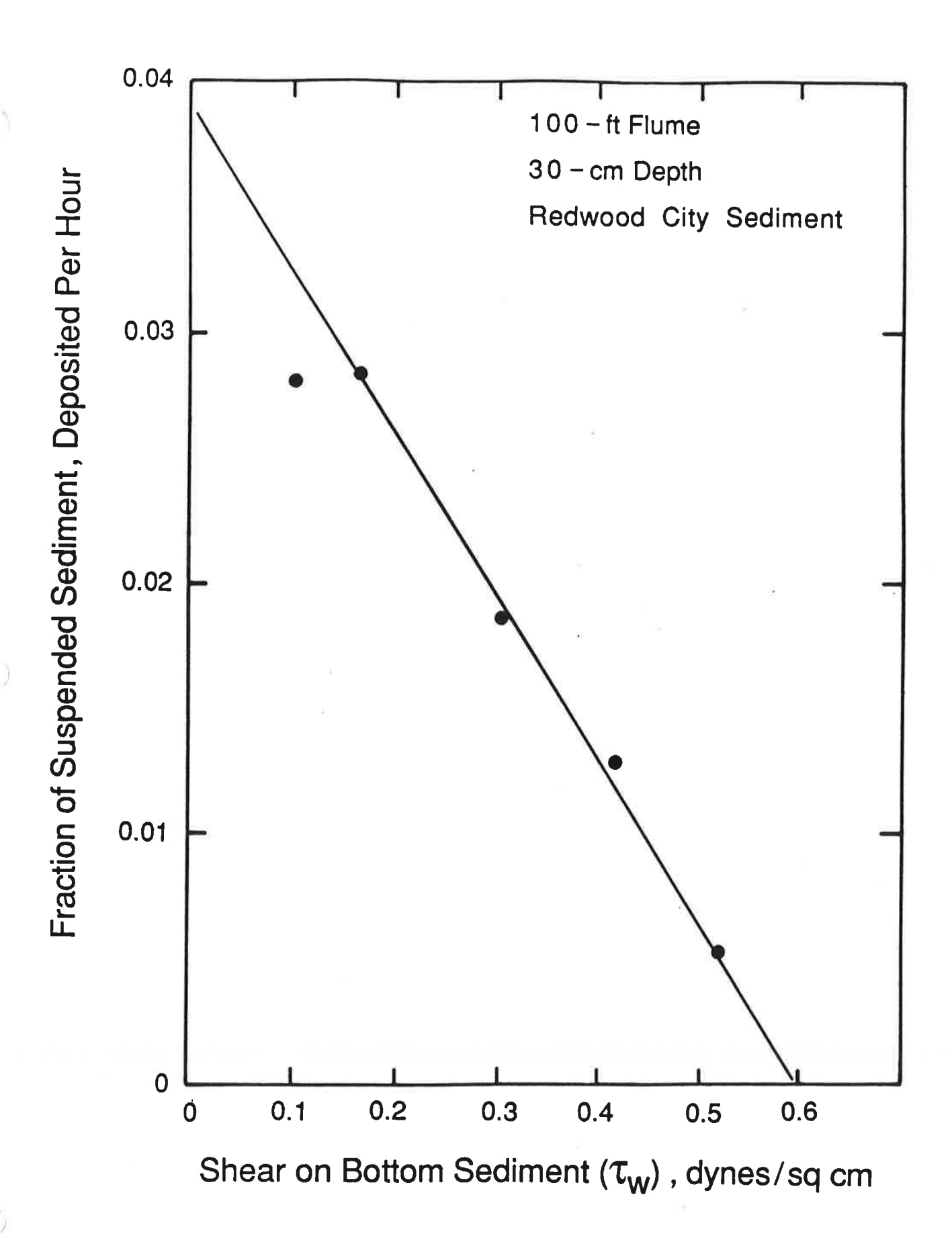


FIG. 2. NET DEPOSITION RATE OF BAY SEDIMENT IN FLOWING WATER.

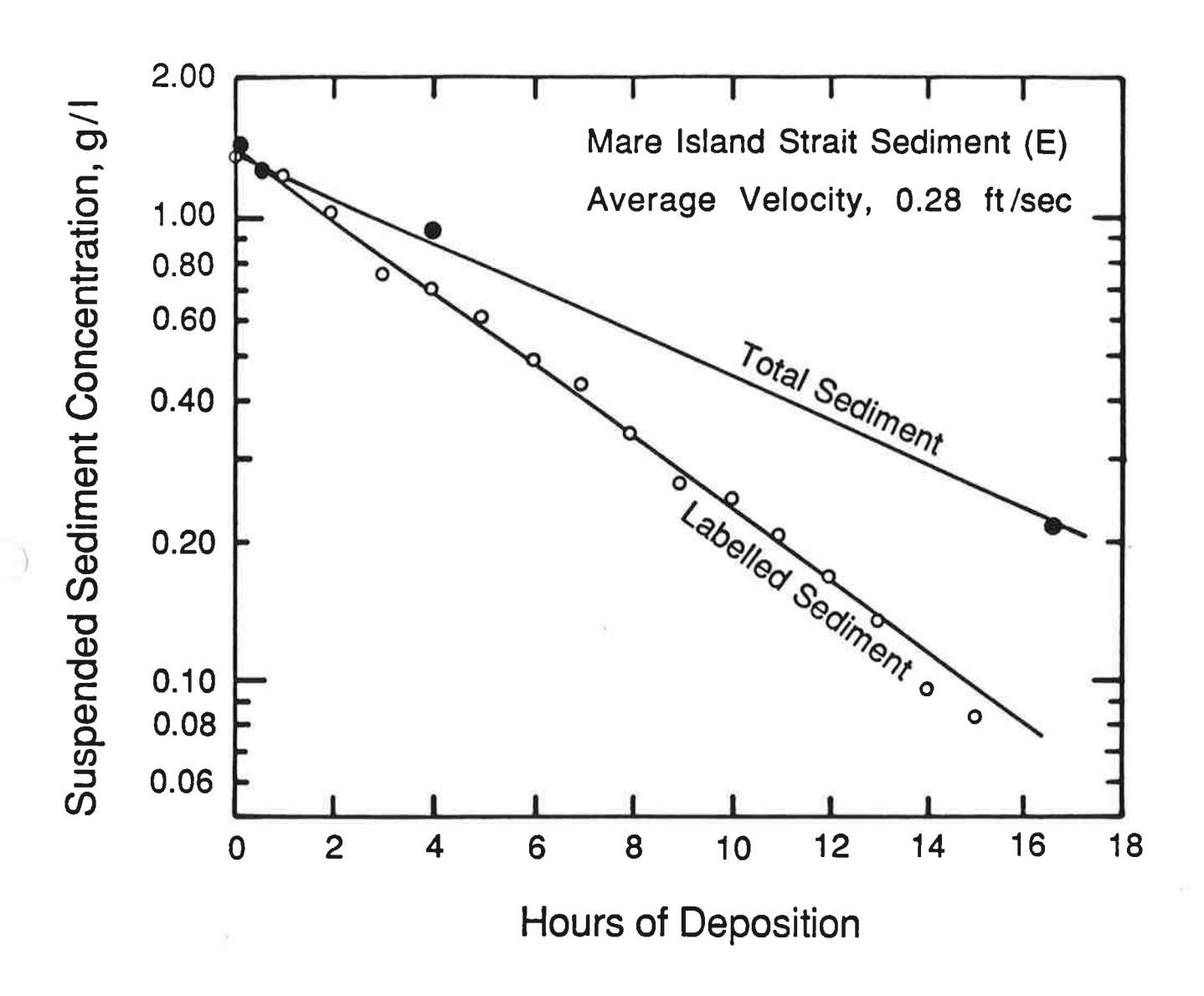
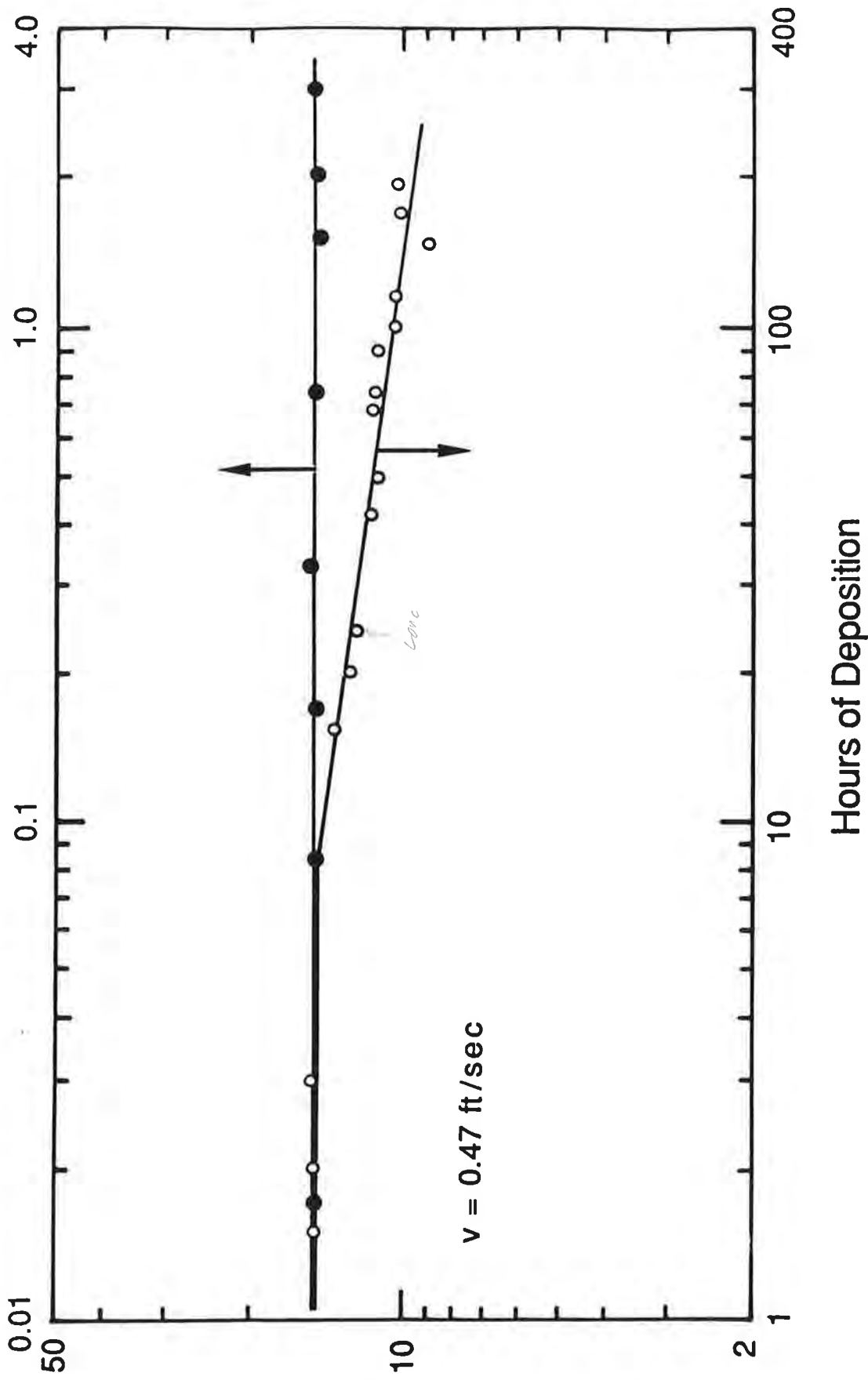


FIG. 3. SUSPENDED TRACE SEDIMENT CONCENTRATION IN FLUME DURING DEPOSITION.



INITIAL DEPOSITION AFTER A VELOCITY REDUCTION. NOTE DIFFERENT SCALES FOR UPPER AND LOWER CURVES. FIG. 4.

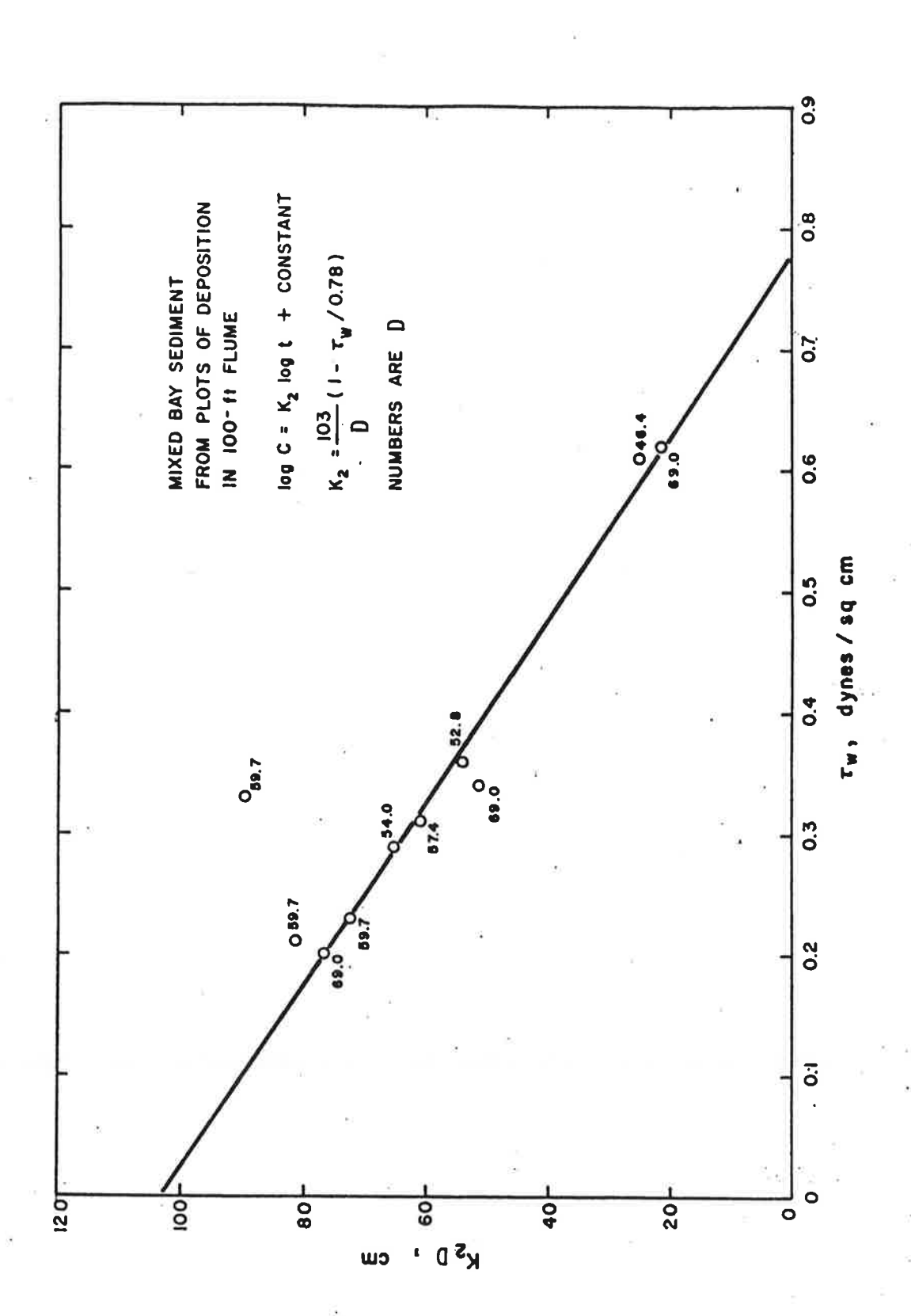
process, and disaggregation and reaggregation rates were negligeable.

The model of the sedimentation process described above postulates interchange of suspended and deposited sediment. A deposition experiment in a flume 0.305 m (1 ft) wide and 18.3 m (60 ft) long using a gold-198 radioactive label was made to examine this process. After the bed material was all suspended and the flow reduced for deposition for a short time, a small amount of labelled mud was added to the flow. Subsequent concentrations of suspended solids and radioactive tracer are shown in Figure 3. This plot shows that the labelled suspended sediment was deposited at a rate that was faster than that of the total. The suspended sediment load was augmented by unlabeled material torn from the bed. (See further discussion of these data by Mehta, 1991.)

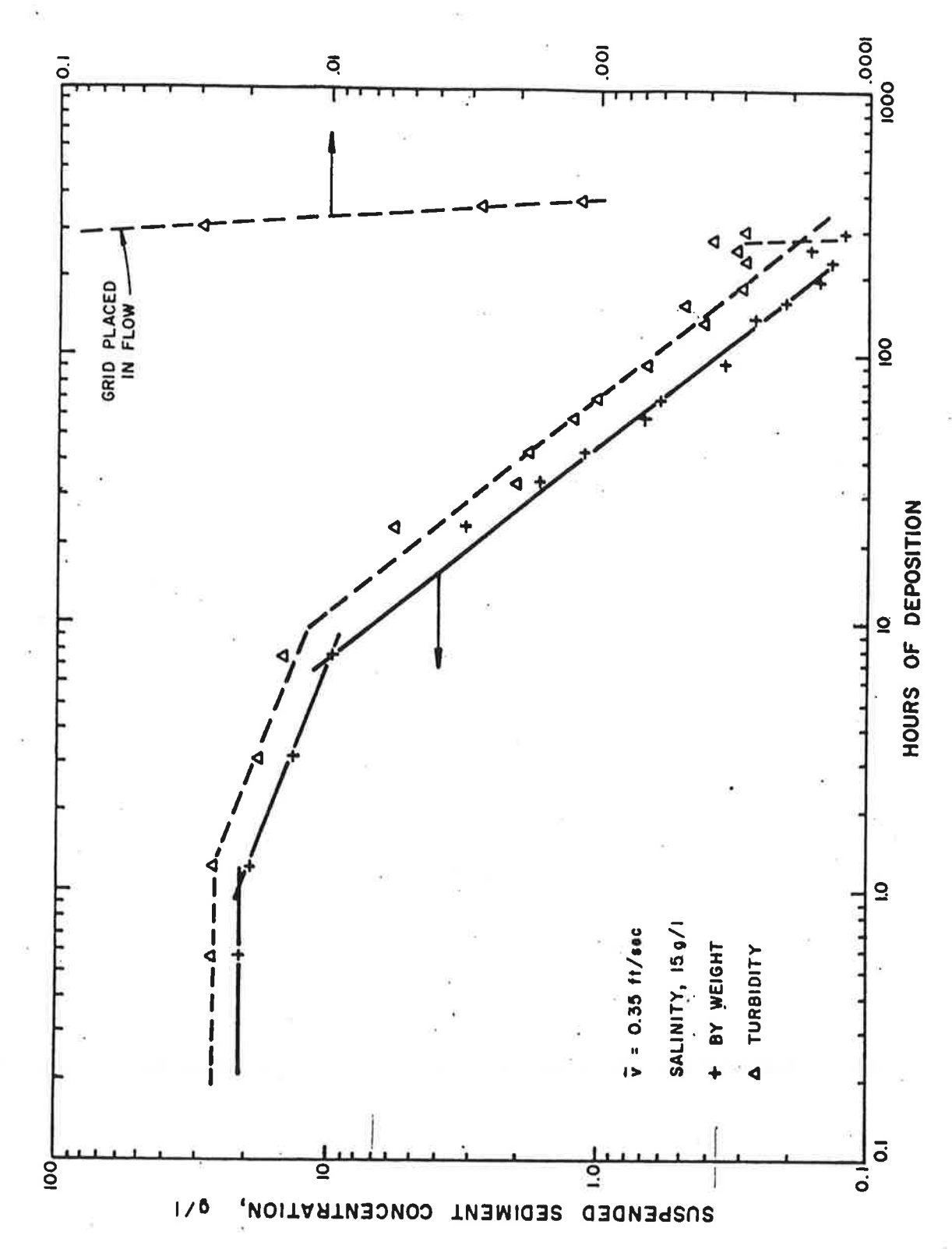
Deposition at Concentrations between 21 and 10 kg/m{3} Cohesive sediments can be transported in suspension at much higher concentrations than those shown in Figure 1, particularly in estuaries where deposition rates lead to expensive waterway maintenance. Experiments using the 0.915 m (3 ft) wide flume were made using sediment from Mare Island Strait at the mouth of the Napa River3 California, at suspended solids concentrations beginning at 21 kg/m³ to investigate the deposition processes at these higher concentrations. The results of two experiments illustrate deposition in the flume over the concentration range below 21 kg/m³.

After suspending the material at a velocity near 0.9 m/s (3 ft/s), the velocity was reduced to 0.18 m/s (0.6 ft/s) for 45 hours. The suspended sediment concentration was 17 kg/m at that time. The velocity was then reduced to 0.14 m/s (0.47 ft/s), and the first sample, about nine minutes after the velocity reduction, had a suspended sediment concentration of 15 kg/m . The concentrations of suspended solids after that time are shown in Figure 4. This figure shows that there was an initial lag period of about six hours before deposition of the remaining suspended material began, then the concentration decreased This lag phenomenon is also observed in the quiescent settling of a mixed mud slurry. There was a lag period before settling begins, then deposition slowed by hindered settling followed. An explanation is that the mixed slurry has initially a nearly homogeneous undifferentiated structure, with particles in contact throughout the slurry. Time is required for thermal motions of the particles, biased by the water seeking upward paths to allow settling of the matrix, to create a less homogeneous structure having locally dense aggregates with pore spaces between them. Initiation of deposition from a flowing suspension is similar, except that low velocity gradients in the slurry cause slow growth of dense aggregates that can withstand the collisions with other aggregates.

Deposition in the flume beginning with a suspension concentration of $21~kg/m^2$ and continuing for a longer time is shown in Figure 5. The plot shows several sedimentation regimes. During the first hour there was no deposition, then apparently hindered deposition began at a slow



DEPOSITION EXPONENT FOR SEDIMENT CONCENTRATIONS LESS THAN 10 g/1 9 FIGURE



DEPOSITION OF FLOCCULATED SEDIMENT IN FLUME FIGURE 5

rate, as shown in more detail in Figure 4. When the suspended solids concentration fell to about 10 kg/m 3 the deposition rate increased markedly.

<u>Deposition below 10 kg/m{3}</u> The portion of the plot in Figure 5 between 10 kg/m and 300 mkg/m can be described by

$$\ln (C/C_0) = -K_2 \ln (t/t_0).$$
 (4)

A plot of K₂ D against bed shear stress for a number of such experiments is shown in Figure 6. This figure shows that \mathcal{C}_{r} for the sediment used in these experiments is .078 N / xm² (0.78 dyne² cm²). Evidently K₂ = K (1 - \mathcal{C}_{r} / \mathcal{C}_{r}) / D. Equation 4 differs from equation 3 in that w² t in equation 4 is now K ln t. This change in the deposition rate relation is attributed to disaggregation in the viscous layers on the bed and in the return lines at these concentrations and to reaggregation in the region above the viscous layer. The rates of both of these processes diminish as the volume concentration of suspended aggregates decreases.

Disaggregation and reaggregation rates were not significant during deposition at the lower concentrations shown in Figure 1, as indicated by the constant settling velocity throughout the semi-log deposition. Suspended aggregates are free to rotate in a velocity gradient, and the shear stresses on their surfaces are very much lower than that on the bed. Erosion of an aggregate surface, or break up of a suspended aggregate, requires contact with another aggregate or with the bed as described above. The rate of disaggregation, therefore, must depend on the volume concentration of suspended aggregates, their shear strength, and on the velocity gradient. Burban, et. al. (1989), using a concentric cylinder Couette flocculator, observed that aggregate sizes decreased with increasing weight concentrations and with increasing velocity gradients.

A description of aggregate break up in the viscous layer can be developed from viscometer data. The dimensions of $\frac{7}{2}$ are N / cm² (dynes / cm²) or J / m³ (ergs / cm³). These latter dimensions can be viewed as the energy required to disaggregate the aggregates to the next lower order.

The rate of energy dissipation per unit volume, E, in the fluid in the viscous sublayer is

$$E = \mathcal{C} du/dz.$$
 (5)

Rearranging equation \not to obtain du/dz and inserting it in 5 leads to

$$E = \frac{\tau^2}{\eta_d} - \frac{\gamma \tau_B}{\eta_d}.$$
 (6)

The first term on the right is the total energy dissipation rate per unit volume, and the second is that due to collisions and disruptions of aggregates, $E_{\rm bu}$. The bed shear stress can be expressed as ρ u_{\star} , where is the suspension density and u_{\star} is the friction velocity, leading to

$$E_{bu} = \frac{\rho u_{\star}^2 \mathcal{T}_{B}}{\rho}$$
 (7)

As shown earlier (Krone, 1984), η_d can be described as

$$\eta_d = \eta_1 \exp \left[\kappa_3 C \right] \tag{8}$$

and $\mathcal{T}_{\mathbf{R}}$ by

$$\widetilde{\iota}_{B} = K_{4} c^{5/2} \tag{9}$$

where the K's are experimental constants to be determined for each sediment at the concentrations of concern. Combining 7, 8, and 9 leads to

$$E_{bu} = \frac{f' u_{*}^{2}}{\eta_{1}} K_{4} C^{5/2} \exp [-K_{3} C]$$
 (10)

kg from rheological measurements (Krone, 1963), K₄ is 2.12₃ J m for kg (66.9 ergs cm / g) and K₃ is 1.0 m / kg (10.0 cm / g) for first order aggregates of the San Francisco Bay sediment. Calculated values of E_{by} at the channel bed for the conditions in Figure 5, where was .023 M / m (0.23 dynes/ cm) and η_1 was near .010 poise, are shown below.

gm/cm ³	ergs/s,ucm ³	Eallsaggs(3)	Fraction of Aggreg. Vol. broken / sec.	Enu/E
.010	.0139	0.156	.089	
.003	.0074	.000736	.016	
.001	.000048	.0000482	.0031	

The third column was calculated using an extension of Einstein's relation for the viscosity of suspensions of spherical particles that was based on the assumption that the apparent viscosity that each aggregate sees is that of the surrounding suspension (Krone, 1963). This extension led to

$$\eta_d = \eta_1 \exp[2.5\phi]$$
,

where ϕ is the volume fraction of the aggregates. Comparing this relation to (8) leads to K₂ C = 2.5 , from which ϕ can be calculated for each value of C. The energy to disperse all aggregates is \mathcal{T}_{B} .

R. B. Krone 10-15-91

The fraction dispersed per second is then E_{bu} / E_{all} aggs.

These calculations show that the rate of energy dissipation due to aggregate breakup falls off very rapidly as the concentration decreases. At the highest concentration, however, nine percent of the aggregates near the channel bed were dispersed to the next lower order per second. The velocity gradients in the viscous layers in the return lines of the flume were higher, so that the break up rates in the flume were greater than those in a continuous channel. Continuing break up in the viscous layer and reaggregation in the lower velocity gradients above it occurs. A near bed equilibrium between these processes must prevail in estuary waters. This concept was also described by Mehta (1991).

The time average thickness of the viscous layer at the end of this experiment was .0024 m (0.24 cm). It was thicker at the beginning of the deposition phase because of the increased viscosity resulting from the high concentration of suspended aggregates.

Deposition at Low Concentration with Increased Velocity Gradient When the suspended sediment concentration had fallen to about 0.13 kg / m³ (130 mg/l) and the conditions described in Figure 1 prevailed, an industrial floor grid was placed across the flow in the flume to enhance the velocity gradients in the flow between the bed and the water surface. The velocity gradients were high at the grid and dissipated downstream, which promoted interparticle contacts in the suspension and enhanced the sizes of the aggregates. The result is shown by the rapid decrease in the optical density in Figure 5, which is plotted against the ordinate scale on the right side of the figure; the water cleared rapidly when the collision frequency was increased by moderate velocity gradients.

Particle size distributions measured during the sequence of deposition regimes shown in Figure 5 showed that the aggregates that settled out first contained a greater silt content than did the later aggregates.

The importance of aggregate break up to deposition rates was shown by Mehta's studies of kaolinite using an annular flume (Mehta, 1973). The annular flume was rotated in one direction while a lid that fit into the top of the flume rotated in the opposite direction to create a flow in the channel. This facility avoided the pump and return lines of the flume described above, and the opposite rotations reduced the secondary circulations that result from centrifugal forces to low levels. There were, however, viscous layers having high velocity gradients both on top of the flow and at the bed, and to a lesser extent at the walls. Kaolinite is only weakly cohesive, and it typically has a wide particle size distribution.

It was found that, after suspending all of the material in the channel and reducing the velocity, a fraction of the material deposited and the remainder continued indefinitely in suspension. The fraction

depended on the bed stress, and all of the suspension deposited at the lowest stress tested. Mehta showed (Mehta, 1986) that the observed deposition rates could be described by the sum of deposition of fractions of the suspended sediment, each of which fit equation 1 with different w_s and $\varepsilon_{\rm cr}$. The kaolinite was dispersed by the velocity gradients and the classes represented a gradation of either particle sizes or cohesion.

Regimes The deposition experiments show the existence of four deposition regimes. Characteristics of these regimes are summarized in Table 1. The first is typified by constant w and occurs at low concentrations and by velocity gradients limited to the near bed region. Under conditions where collisions of suspended aggregates are frequent, Regime 2, break up near the bed and recombination at higher elevations make the settling velocity a function of concentration and near bed gradients. At still higher concentrations of suspended particles, hindered settling occurs, combined with more rapid break up and recombination of suspended aggregates. At yet higher concentrations and velocity gradients, a suspension becomes a homogeneous matrix or slurry. noted in Table 1, the suspension concentration and velocity gradients, which determine the aggregate structures, are important in Regimes II, III, and IV. The material in suspension at 15 kg/m 3 in Figure 4 began in Regime IV after flowing some time at 0.9~m / s (3ft/s), then after the velocity was reduced so that aggregates more dense than the slurry average density could form, hindered settling of Regime III appeared. A surprising aspect of the data is that the transition from one regime to another by changes in the velocity gradients or concentration are so abrupt.

Other Experiments and Discriptions of Deposition Rates

A number of investigators of sediment deposition processes have used annular flumes with flow driven by a rotating lid and with the flume rotated in the direction opposite that of the lid to minimize secondary currents. This device was developed to avoid the possibility of aggregate break up in the pump and return lines of a recirculating flume. The velocity gradients in an annular flume are unlike those in an open channel throughout the volume of the flume, however, with high velocity gradients near the lid and near the bed, as shown by the work of Maa (this volume). Moreover, the large depth to width ratio of the channels typical of these flumes makes velocity gradients near the side walls occupy a large portion of the cross-section. Erosion and deposition processes are sensitive to the distribution of velocity gradients in the flow, making the application of annular flume data to estuarial flows difficult. Breakup of aggregates in a recirculating flume can be minimized by suitable selection of cross-sections of return lines. Flow down the flume channel has velocity gradient distributions similar to those in an estuarial channel, especially when the depth to width ratio of the flow is small.

Mehta originally presented a log-probability description of

deposition that fit his experimental data (Mehta, 1973). The coefficients could be determined from flume tests, although the differences in hydraulic conditions between the flume and an estuary channel make such tests questionable. Alternatively, the coefficients can be adjusted to verify field observations (as can the settling velocity and critical shear stress in equation 1, or the coefficients of any of the other relations.)

Sheng (1983) developed a "deposition velocity" that he multiplied by the difference between the concentration and an equilibrium concentration to obtain a deposition flux. He measured the rate of entrainment of sediment in an annular flume and a steady concentration that he considered to be an equilibrium concentration to obtain the deposition velocity. The resulting velocities were about half of the quiescent settling velocities. This difference can be due to the break up of aggregates in the high velocity gradients at the top and bottom of the channel described above. The observation of a steady concentration may not indicate an equilibrium between the suspended and deposited material, but rather that a depth of the bed had been reached where further erosion did not occur.

Schoellhamer and Curwick (1986) tried three deposition relations in a model of sediment transport in the lower Mississippi River. One was equation 1, a second was $dc/dt = -(\alpha w_s/D)(C - C_{eq})$, where ω is an adjustable parameter and C_{eq} is an equilibrium concentration, and the third was the settling flux minus vertical diffusion from a bed layer. The first and second relations modeled the deposition satisfactorily, but the third did not.

<u>Settling Velocity</u>

The deposition rate is very sensitive to the settling velocity. An effort to determine the settling velocity of aggregates in the body of the flow included dipping a graduated cylinder into the flow with as little disturbance as could be achieved, and determining the median settling velocity by the pipette method. The break up at the bed and reaggregation in the low velocity gradients in the upper part of the flow was also simulated by placing various concentrations of sediment in one liter graduated cylinders, raising and lowering a plunger ten times to produce high velocity gradients, then removing the plunger to let aggregation proceed in the decaying eddies and measuring the settling velocities by the pipette method. The median settling velocities observed (median by weight) for both experiments are shown as a function of concentration in Figure 7.

This figure shows that, <u>under these conditions</u>, the settling velocity is proportional to the concentration to the 4/3 power both in the flume and in the graduated cylinders. As shown above, when the concentration of suspended sediment and the velocity gradient are sufficient to facilitate break up in the viscous layer w_s at the bed will be less than indicated by

$$w_s = K C^{4/3}$$
. (12)

When the concentration of suspended sediment is low enough that the rate of break up is negligible, the settling velocity will remain that at the beginning of deposition. Use of equation 12 will lead to conservative (on the high side) deposition rates because it does not include the effect of aggregate break up near the bed.

Combining equations 1 and 12 yields a settling relation that describes deposition rates as functions of C and \mathcal{C}_w for Regime II conditions:

$$-\frac{dC}{dt} = -\frac{K}{D} \frac{C^{7/3} \mathcal{F}}{D} (1 - \gamma_{W} / \gamma_{C}); \quad \gamma_{W} < \gamma_{C}$$
 (13)

This relation is useful for estimating a representative suspended sediment concentration from existing deposition rate data. Successive hydrographic surveys of enclosed harbors, or surveys of local marshes at different times, dating core samples of marshes, all provide an integral of the varied suspended sediment concentrations over time. Including these areas in a model and adjusting C to reproduce the observed deposition provides a quick way to find a concentration that is representative of the actual varying concentrations over the long term. Such determinations from a marsh and an enclosed harbor in the San Francisco Bay system yielded concentrations well within the range of those observed (Krone, 1987).

P. Shrestha (1991) presented the relation:

$$-\frac{dC}{dt} = -\frac{K(G)}{D} \frac{C}{D} \frac{n(G)}{(1 - z_{W} / z_{C})}; \quad z_{W} < z_{C}$$

where G is the depth average velocity gradient and K and n are constant or linear functions of G. He found from from the data in Figure 1 that K and n were nearly constant and that n was near 1. Using data from Hunt and Pandaya (1984), however, which appears to be in Regime II, he found that n was nearly constant at 2+ and that K linearly increased with G. He incorporated this relation in the Resources Management Associates model STUDH.

Deposition in an estuary where appreciable reversing flows occur may be important only during times near slack water, with possibly erosion of sediment during the strength of flow. Aggregates suspended in the body of flow above the region of the viscous layer may then settle to the bed without being dispersed. Aggregates suspended in waters flowing into an enclosure or side arm may also settle without being dispersed.

In view of the present lack of better means for determining \mathbf{w}_{S} , the

R. B. Krone 10-15-91

measurement of settling velocities in the estuary using an Owen tube (Owen, 1971), or other means of direct measurement, appears to be the best approach. The Owen tube should sample as near the bed as is feasible at times before slack water in channels when the bed stress approaches that allowing deposition. Sampling at entrances to side arms and enclosures near the bed will give the most useful data for calculating deposition rates in these areas. Sampling should be repeated to provide w at different concentrations, and the concentration should be measured. It would also be desirable to make such measurements after different anticedent tidal currents. These w can then be used in equation 1 with appropriate adjustments for suspended sediment concentration and anticedent currents.

Conclusions

The material presented here demonstrates that deposition rates in estuarial flows are determined by the settling velocity, shear strength, and concentration of depositing aggregates as they encounter the higher velocity gradients near the bed. Low concentrations and moderate velocity gradients, with infrequent aggregate collisions, let aggregates survive. Increasing frequency of collision of suspended aggregates, resulting from increased concentration or increased velocity gradients, either promote aggregation or break up, depending on the velocity gradient. Where the near bed concentration and velocity gradient causes break up, upwardly diffusing aggregate remanents reaggregate in the lower velocity gradients at higher elevations above the bed. When the velocity, and bed stress, of the flow is diminished, such as at times near slack water or when flows enter a region of quieter water, aggregates suspended at elevations above the near-bed region deposit.

Further increasing the concentration can lead to reduced downward flux due to hindered settling, and still further increase to downward movement limited by consolidation.

Revisiting the data from the early deposition experiments brought forth the importance of aggregate concentration in the near-bed region to aggregate break up and provided an opportunity to reemphasize the importance of identifying the transport regime when selecting a deposition relation. It also illustrates needs for field and laboratory studies to relate settling velocities to velocity gradients and suspended solids concentrations. Eventually we should be able to describe the distributions of aggregate settling velocities throughout the flow profile.

REFERENCES

- Ariathurai, C. R., and Krone, R. B., Finite element model for cohesive sediment transport, <u>J. Hydr. Div</u>, ASCE, v103, no. HY3, 323-338, 1976.
- Burban, P-Y, W. Lick, and J. Lick, The flocculation of fine-grained sediments in estuarine waters, <u>J. Geophysical Research</u> v. 94, no. C6, 8323-8330, 1989.
- Hunt, J. R., and Pandya, J. D., Sewage sludge coagulation in seawater, Env. Sci. and Techn. v18, 119-121, 1984.
- Krone, R. B., Flume studies of the transport of sediment in estuarial shoaling processes, Hydr. Engr. Lab. and Sanitary Engr. Res. Lab., U. of California, Berkeley. Prepared for the San Francisco Dist., Corps of Engrs. 1962.
- ______, The significance of aggregate properties to transport processes, in <u>Estuarine Cohesive Sediment Dynamics</u>, A. J. Mehta, Ed., Lecture Notes on Coastal and Estuaring Studies, Springer-Verlag, 66-84, 1984.
- , A method for simulating historic marsh elevations, <u>Proceedings</u> of <u>Coastal Sediments</u> 87, New Orleans, LA, May 12-14, 1987.
- Mehta, A. J., Depositional behavior of cohesive sediments, <u>Ph.D.</u> <u>Dissertation</u>, University of Florida, Gainesville, Florida 1973.
- Mehta, A. J., Deposition and erosion of cohesive sediment from a laboratory perspective, <u>Proc. Int. Symp. on Physical Processes in Estuaries</u>, Delft, The Netherlands, 1986.
- Mehta, A. J., Review notes on cohesive sediment erosion, <u>Procedings of a Specialty Conference on Quantitative Approaches to Coastal Sediment Processes</u>, Seattle, WA, June 25-27, 1991.
- Nicholson, J., and B. A. O'Connor, Cohesive sediment transport model, <u>J. Hydraulic Engineering</u>, v.112, no. 7, 621-639, 1986.
- Odd, N. V. M., and M. W. Owen, A two-layer model of mud transport in the Thames Estuary, Proc. Instn. Civ. Engineers, Suppl. 9, 175-205, 1972.
- Onishi, Y., and D. S. Trent, Mathematical Simulation of Sediment and

Direct Measurement of the Relation between Interlayer Force and Interlayer Distance in the Swelling of Montmorillonite¹

BRIAN E. VIANI, PHILIP F. LOW, AND CHARLES B. ROTH²

Department of Agronomy, Purdue University, West Lafayette, Indiana 47907

Received February 10, 1983; accepted April 7, 1983

Oriented gels of eight Na-montmorillonites having values of the surface charge density, σ , ranging from ~28,000 to 56,000 esu/cm² were confined in a closed chamber between a N₂-gas piston and a porous ceramic plate in contact with a solution of 10^{-4} N NaCl. Successively higher pressures up to 6.9 bars were applied by the N₂-gas piston while the NaCl solution was maintained at atmospheric pressure. After equilibration at each applied pressure, the c axis spacing of the silicate layers was measured by X-ray diffraction. Subsequently, the thickness of a silicate layer was subtracted from this spacing to obtain the corresponding interlayer separation, λ . Since, at equilibrium, the swelling pressure, Π , is equal to the applied pressure, it was thus possible to determine Π as a function of λ for each montmorillonite. We found that Π is an exponential function of $1/\lambda$. Also, at any value of Π , the value of λ is independent of the value of σ . Neither of these findings is consistent with the double-layer (i.e., osmotic) theory of swelling. Therefore, an additional force, which is the dominant force at the observed values of λ , must be responsible for swelling. In view of an empirical relation that exists between Π and any property of the water in the swollen system, we postulate that this additional force results from the in-depth perturbation of the water by the surfaces of the montmorillonite layers.

INTRODUCTION

Clay minerals normally occur as crystals of colloidal size in which parallel silicate layers about 10 Å thick are stacked one above the other like the leaves of a book. These layers are negatively charged because of ionic substitutions at various sites within their structures and, as a result, exchangeable cations are adsorbed on their surfaces. Also, they are either fully expandable (separable by water to a distance that varies with the applied pressure), partially expandable (separable by water to a fixed distance of 5-10 Å that is essentially independent of the applied pressure), or nonexpandable, depending on the surface charge density and the size and valence of the exchangeable cations.

Fully expandable, partially expandable, and nonexpandable layers can coexist in the same crystal. When a mass of clay crystals is placed in contact with water or an aqueous solution, water is absorbed between the fully expanding layers and, to a limited extent, between the partially expanding layers of the cyrstals. It is also absorbed between the crystals. Hence, intracrystalline and intercrystalline swelling occur. If, however, the mass of crystals is confined, a swelling pressure develops.

The swelling of clay minerals, particularly the montmorillonites, is of great importance in nature. For example, it affects the drainage and erosion of soils, the stability of highways and buildings, and the production of oil wells. The most widely held concept of swelling is that it is due to an excess osmotic pressure that develops between the superimposed silicate layers because of the overlap of their ionic atmospheres and that it is describable by conventional double-layer theory (1-6).

¹ Journal paper 9346, Purdue University Agricultural Experiment Station, West Lafayette, Ind. 47907.

² Department of Agronomy, Purdue University, West Lafayette, Ind. 47907.

However, recent evidence suggests that hydration of the surfaces of the silicate layers (7-14) or of the ions adsorbed on them (15, 16) plays an important role. It is impossible to assess the quantitative adequacy of either the double-layer theory or the theory of surface hydration by the usual procedure of observing the gross volume, or water content, of the system as a function of swelling pressure. It is necessary to have a direct and accurate determination of the relation between the interlayer repulsive force and the interlayer distance under conditions that allow both the surface charge density and the salt concentration in the external solution to be assessed. Such a determination has been attempted for a montmorillonite and a vermiculite (17) as well as a mica (10, 15, 16). However, in none of these studies was the surface charge density measured directly. Moreover, the interlayer distances reported for the montmorillonite were of questionable accuracy since the X-ray diffraction peaks used to determine them were very broad and of low intensity. For these reasons, and because of our interest in the swelling of montmorillonite, we decided to accurately determine the relationship between interlayer repulsive force and interlayer separation for a series of montmorillonites with a wide range of measured surface charge densities.

METHOD

Samples of the <2- μ m fractions of eight montmorillonites, prepared for a previous study (13), were used in the present experiments. These samples, listed in Table I, had been saturated with sodium, dialyzed free of excess salts and freeze dried. They were suspended in sufficient 10^{-4} N NaCl to make a 1% suspension and allowed to equilibrate for 12-24 hr. Then a gel (5.5 cm long, 1.6 cm wide, and having \cong 17 mg clay/cm²) was prepared by slowly filtering the suspension through a membrane filter (pore diameter = 0.025 μ m) under a pressure of 1/3 bar. This method of preparation assures a rela-

TABLE I
Properties of Montmorillonites Used in This Study

Sample	Specific Surface area (m²/g)	Cation exchange capacity (mEq/g)	Surface charge density (esu/cm² × 10 ⁻⁴)
Yellow Western	777	0.745	2.77
California Red			2
Тор	605	0.620	2.96
Upton	800	0.900	3.25
Polkville	729	0.900	3.57
Rio Escondido	664	0.915	3.99
Mexican	617	0.965	4.52
Otay	634	1.120	5.11
Cameron	351	0.680	5.60

tively high degree of orientation of the basal planes of the montmorillonite layers. Several drops of another suspension containing about 1 mg of mica (2-44 μ m in equivalent spherical diameter) were subsequently placed on the center of the gel and pressure was reapplied until the mica was deposited on its surface. The mica served as an internal alignment standard in determining the modal interlayer separation between adjacent montmorillonite layers in the gel. This separation was measured at various applied pressures by X-ray diffraction using a modification of a procedure presented by Rhoades *et al.* (18).

X-Ray diffraction of the gel samples equilibrated at selected pressures was accomplished using the enclosed sample support shown schematically in Fig. 1. The oriented gel, g, on the membrane filter, h, was placed on a porous ceramic plate, i, set into a stainless-steel holder containing grooves, j, that were connected to the outside atmosphere by tube k. Plate i (air entry pressure = 15 bar) had been previously saturated with a solution of 10⁻⁴ N NaCl that also filled grooves, j, and tube k. This assembly, B, was mounted inside a pressure chamber A, on the axis of a Siemens X-ray goniometer. The beryllium window, a, on the chamber cover was transparent to the CuK_a X-rays used, yet was strong enough to support pressure ≤10 bars. The chamber was pressurized using H2O-saturated nitrogen gas that was maintained at

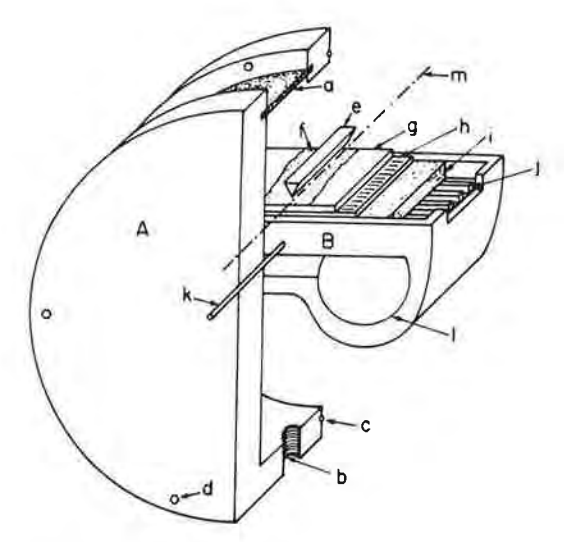


FIG. 1. Schematic drawing of the enclosed sample support.

selected pressures (±0.014 bar) by means of a Cartesian manostat. Thus, the nitrogen acted as a gas piston that expressed water from the gel, via i, j, and k, until equilibrium was achieved at the given pressure. It should be noted that this pressure acted equally on both the clay matrix and the interstitial water.

Samples were initially equilibrated at 0.5 bar and then at successively greater pressures up to 6.9 bar. X-Ray diffraction data were collected only after a sample had reached equilibrium at a given pressure. Preliminary measurements showed no detectable changes in the X-ray diffraction patterns after 8-12 hr equilibration but at least 18-24 hr were allowed at each pressure before data were collected.

X-Ray diffraction data were collected in the following manner. Diffracted beam intensities were recorded at $0.01-0.02^{\circ}$ intervals over the (001) peak of the montmorillonite, and at 0.04° intervals thereafter out to 7° 2θ . The thin mica deposit, f, served as an internal standard by which the elevation of the sample chamber could be adjusted so as to maintain the surface of the sample tangent to the diffractometer focusing circle (18), an adjustment which was necessary since the

thickness of the gel decreased with each increase in pressure. A separate step scan over the mica (001) peak at 0.01° intervals allowed the displacement of this peak from its known position to be determined and, thereby, the correction (generally on the order of 0.01°) that had to be applied to the observed montmorillonite peak for any residual displacement error. Counting times were adjusted so that 10,000 to 15,000 counts were collected at each step over the main part of the montmorillonite (001) peak. A narrow divergence slit $(1/8^{\circ})$ and an edge aperture. e, centered on the goniometer axis, m, effectively decreased the background intensity at very small angles and allowed observation of diffraction peaks down to $0.7^{\circ} 2\theta \ (\simeq 125 \text{ Å})$.

In order to compute the c axis spacing, the raw data were transformed as follows. The digitalized data from the X-ray diffractometer were collected on magnetic tape and transmitted to a computer where they were corrected for the residual displacement error, corrected point-by-point to agree with the best-fitting cubic polynomial describing the smooth curve through the nearby data points and corrected for the Lorentz-polarization (Lp) factor. The single-crystal version of this factor was used because of the high degree of particle orientation in the sample and the low angles of diffraction involved. The position of the resulting (001) diffraction peak was estimated (to 0.01°) from the maximum of a parabola fitted to the peak apex (19). Variation of the layer structure factor across the (001) peak is relatively small and was found to have a negligible effect on the position of the peak maximum. Finally, the c axis spacing of the montmorillonite was computed from the position of the peak maximum by using Bragg's law. Statistical analysis of the measured c axis spacings of duplicate samples showed that the mean variance of random error associated with the method was less than 1 Å.

The X-ray goniometer was calibrated in the low-angle region (corresponding to c axis spacings between 10 and 65 Å) using a mix-

ture of mica, silicon metal, and a long-chain alcohol by the method of Brindley and Wan (20). At c axis spacings near 10 and 65 Å the measured values underestimated the true values of 0.05 and 2.7 Å, respectively. However, because no calibration standards were available for c axis spacings > 65 Å, which occurred at applied pressures below 1.5 bar, none of the measured values was corrected.

The c axis spacing of the layers in a swollen montmorillonite gel, as computed above, may be regarded as the mode of the distribution curve of the probability of finding comparable atomic planes in adjacent montmorillonite layers a given distance apart. Hence, λ , the modal separation between the surfaces of the layers, was obtained by subtracting the thickness, t, of the layers from the modal c axis spacing. For all montmorillonites but the Cameron, t was assigned a value of 9.3 Å, which is the thickness of the unit or elementary layer (21). However, for the Cameron montmorillonite, t was assigned a value of 19.4 Å, which is the thickness of a pair of elementary layers plus the distance (0.8 Å) between them in their collapsed state. The reason for assuming that the layers of Cameron montmorillonite consisted of pairs of elementary layers is that the c axis spacings of this montmorillonite were consistently 8-10 Å larger than those for the other montmorillonites at the same applied pressures. Moreover, the Cameron clay is classified as an interstratified montmorillonite/illite (22) in which collapsed illitic layers having a fixed c axis spacing of ~ 10 Å are interleaved with expanding layers having a c axis spacing governed by the applied pressure.

RESULTS AND DISCUSSION

Consider a clay gel confined between a compressed gas and a porous plate in contact with an aqueous solution at P_a , the pressure of the atmosphere. If P is the absolute pressure that must be exerted by the gas to make G_g , the partial molar free energy of the water

in the gel, equal to G_s , the partial molar free energy of the water in the solution (and, thereby, establish equilibrium) we can write

$$\vec{G}_{s} = \vec{G}_{g} + \int_{P_{a}}^{P} (\partial \vec{G}_{g}/\partial P) dP$$

$$= \vec{G}_{g} + \vec{v}_{g}(P - P_{a}) \quad [1]$$

where \bar{v}_g is the partial molar volume of the water in the gel, which, in view of the extremely small compressibility of water, is assumed to be independent of the pressure. On rearrangement, Eq. [1] becomes

$$\bar{G}_{\rm g} - \bar{G}_{\rm s} = -\bar{v}_{\rm g}(P - P_{\rm a}). \tag{2}$$

However, at equilibrium, $P-P_a$ is equal to Π , the swelling pressure, i.e., the net repulsive force between the particles. We see, therefore, that the free energy of the water in the system is related to the swelling pressure of the system and that whatever affects the former will affect the latter. Also, if the swelling pressure is not significantly affected by forces arising from interparticle contact or bridging, that is, if Π reflects solely the net repulsive forces acting between particles at a distance, then the experimentally determined curves of Π vs λ can be directly compared with those predicted by double-layer theory.

It has been suggested that edge-to-face association between montmorillonite tactoids (i.e., swollen crystals) is responsible for the observed difference between curves of II vs water content for the initial and subsequent compressions of unoriented montmorillonite gels (6, 8, 23). This suggestion is based on the reasonable assumption that the initial compression tends to irreversibly rearrange the tactoids from a random to a parallel arrangement and, thereby, alters the relation between II and water content. In addition, it has been suggested that the edge-to-face association of montmorillonite layers is responsible for the fact that the experimental curves of Π vs λ are below those predicted by double-layer theory (17). However, we believe that our method of preparing highly oriented gels precludes an appreciable degree

of this kind of association; and we believe that the failure of double-layer theory to predict the experimental results is the fault of the theory as applied to clays. Our beliefs are supported by the reproducibility of the data for replicate samples (Figs. 4a and b), the reproducibility of the data for successive compressions of the same sample (Fig. 5), and the coincidence of the data for samples of different montmorillonites (Fig. 10). Attention is called to the fact that edge-to-face association would likely occur randomly throughout an assemblage of tactoids or layers and hence, any arrangement resulting therefrom would not be reproducible from sample to sample, especially if the samples were composed of different montmorillonites having different axial ratios and different densities and distributions of surface charge.

C-Axis Spacings versus Applied Pressure

Figures 2 and 3 show examples of the diffraction patterns (smoothed and corrected for displacement errors but uncorrected for Lp effects) which were obtained. Those in Fig. 2 are representative of the Yellow Western, California Red Top, Upton, Polkville,

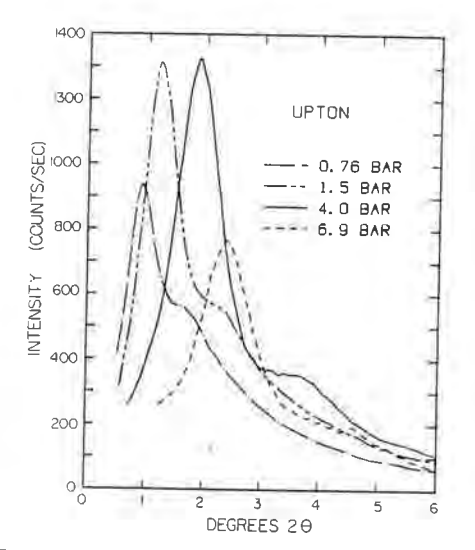


FIG. 2. X-Ray diffraction patterns of Upton montmorillonite in equilibrium with 10^{-4} N NaCl at four applied pressures.

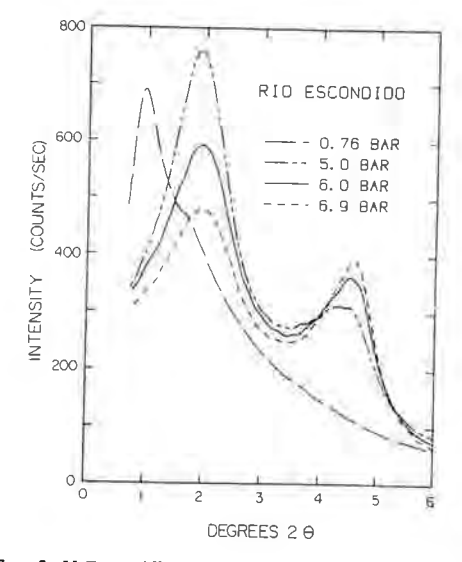


FIG. 3. X-Ray diffraction patterns of Rio Escondido montmorillonite in equilibrium with 10⁻⁴ N NaCl at four applied pressures.

and Cameron montmorillonites; whereas, those in Fig. 3 are representative of the Rio Escondido, Mexican, and Otay montmorillonites. In Fig. 2, the lower angle peak of each pattern represents the first-order reflection of a fully expanded phase and the higher angle peak (or shoulder) represents the second-order reflection of the same phase. Note that both peaks shift progressively to higher angles with increasing Π , i.e., the c axis spacing decreases with increasing pressure.

In Fig. 3, the lower angle peak of each diffraction pattern also represents the firstorder reflection of the fully expanded phase. It, like that in Fig. 2, shifts to higher angles as II increases but the shift is less obvious, partly because more of the diffraction patterns in this figure correspond to relatively high values of II where the rate of decrease of the c axis spacing is small. These diffraction patterns were chosen to illustrate a change in phase when II exceeds 5.0 bars. Note the increase in intensity of the higher angle peak at the expense of the lower angle peak. Also, note that the higher angle peak becomes narrower and the lower angle peak becomes broader. According to diffraction

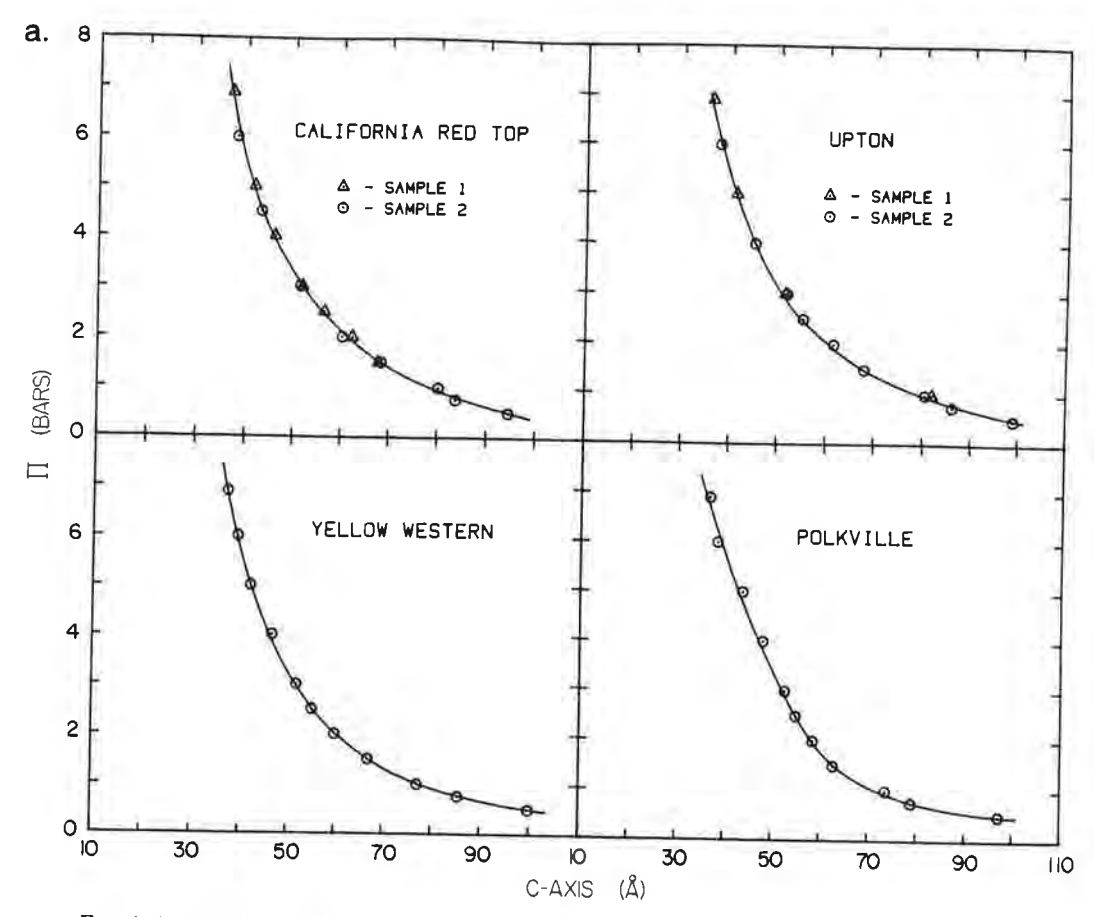


FIG. 4. (a) Relation between Π and the c axis spacing for the California Red Top, Upton, Yellow Western, and Polkville montmorillonites in equilibrium with 10^{-4} N NaCl. (b) Relation between Π and the c axis spacing for the Mexican, Otay, Rio Escondido, and Cameron montmorillonites in equilibrium with 10^{-4} N NaCl.

theory and observation (e.g., Fig. 2), a peak identified with a second-order reflection should decrease in intensity and broaden with decreasing c axis spacing, i.e., with increasing Π . Therefore, in Fig. 3, the higher angle peak of each pattern at $\Pi \geq 5.0$ bars, unlike that at $\Pi = 0.76$ bars, cannot be ascribed entirely to the second-order reflection of the fully expanded phase. It likely includes the first-order reflection of a 19-Å (i.e., partially expanded) phase. Such a phase frequently coexists with a fully expanded phase in montmorillonite gels (3, 18, 24). Evidently, the fully expanded phase with variable c axis spacing converts progressively to

the 19-Å phase as II increases above 5.0 bars. In the present paper, we will focus our attention exclusively on the fully expanded phase. Note that it is the phase in which the interlayer distance is large enough for the diffuse part of a double layer to form. From the diffraction patterns presented in Figs. 2 and 3, it is obvious that precise c axis spacings of this phase are measurable.

The variation of the modal c axis spacing with Π , for the first compression, is shown for all the montmorillonites in Figs. 4a and 4b. The curves for the Upton, California Red Top, Mexican and Otay include data for measurements made on two separate sam-

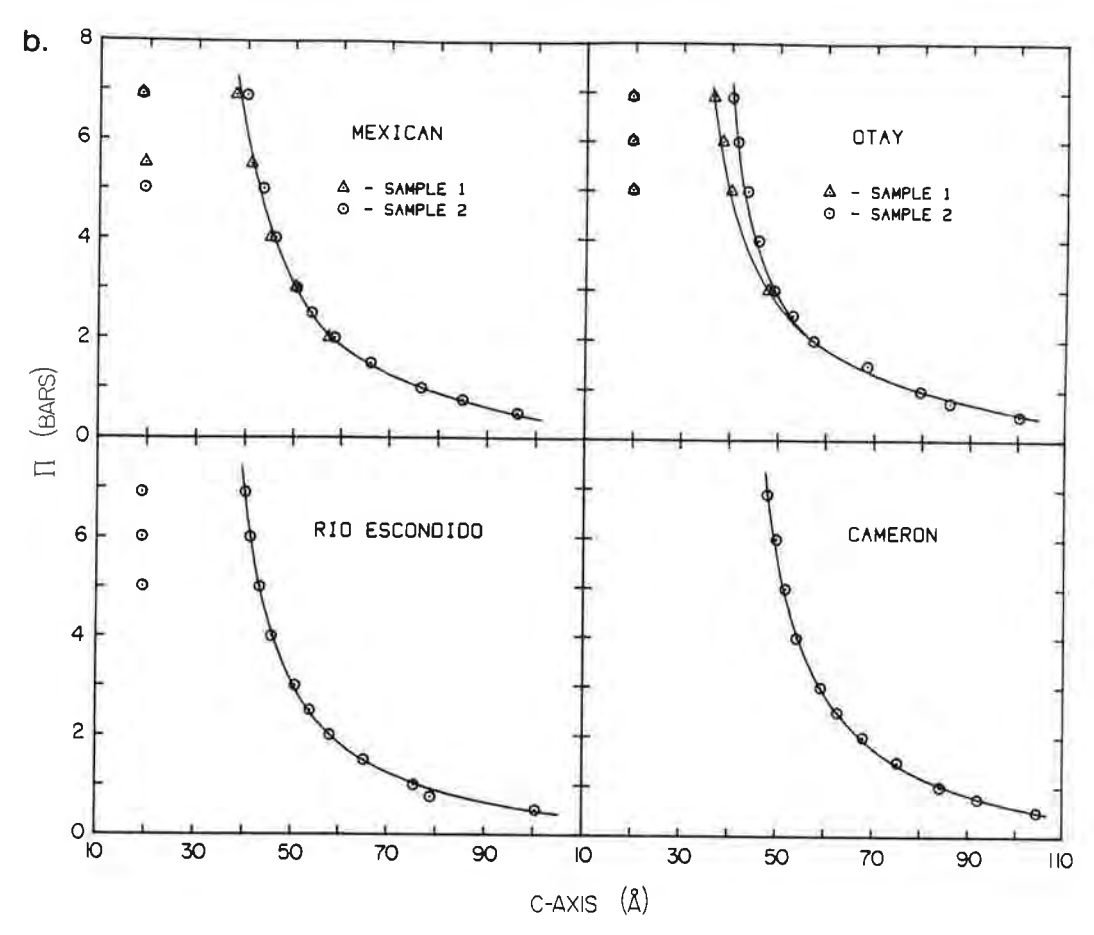


FIG. 4—Continued.

ples and illustrate that, for three of these montmorillonites, the reproducibility was excellent. As noted earlier, the random error was <1 Å. For the fourth, i.e., the Otay montmorillonite, the data for the two samples are significantly different and the difference is greater than experimental error. It is possible that this difference is due to the water in one of the samples being in a metastable state, or to a difference of unknown origin in the surface properties of these samples.

Figure 5 shows the results for the first and second compressions of the same sample of Upton montmorillonite. Although fully expanded layers were converted to partially expanded layers during the second compression only, the relation between Π and c axis

spacing for the expanded layers was nearly the same for both and, hence, is essentially reversible. It should be noted that, between the first and second compressions, the sample was allowed to reswell for 11 days under a pressure of 0.015 bar. This period of time was allowed for reswelling because of the low permeability of the montmorillonite. Consequently, any difference between the two compressions could be due to a change in the character of the montmorillonite arising from the slow release of Al3+ or Mg2+ from its structure (26, 27). Or it could be due to an irreversible reorganization of the water during the first compression. For the reasons mentioned earlier, it was not likely the result of any reorientation of the tactoids or layers

Journal of Colloid and Interface Science, Vol. 96, No. 1, November 1983

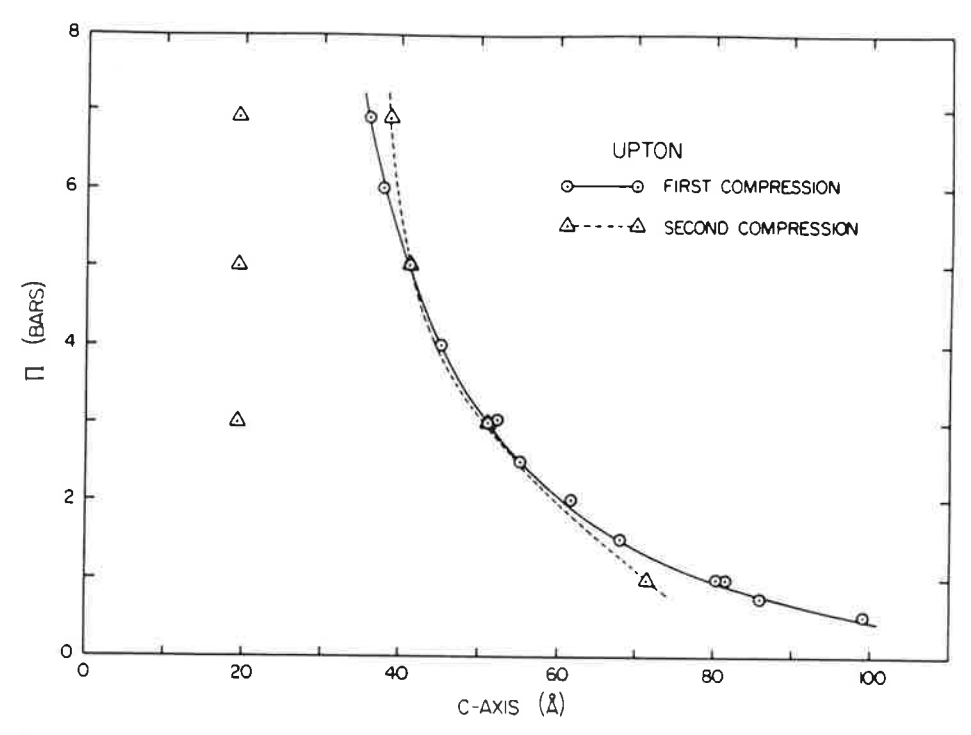


Fig. 5. Relation between Π and the c axis spacing for the first and second compressions of Upton montmorillonite in equilibrium with 10^{-4} N NaCl.

induced by the first compression. In this regard, attention is called to the observation of Israelachvili and Adams (10) that the forcedistance relation for a single pair of mica sheets was different for the first and second compressions even though these sheets could not reorient with respect to each other.

The Relation between Applied Pressure and Interlayer Separation

In a previous report (13), the relation between Π and $m_{\rm m}/m_{\rm w}$, the mass ratio of montmorillonite to water, was measured for 35 different montmorillonites confined, as described here, between a gas piston and a porous plate in contact with water. The swelling pressure was shown to be described by a logarithmic equation.

$$\ln (\Pi + 1) = \alpha (m_{\rm m}/m_{\rm w}) + \ln B$$
 [3]

where α and B are constants that are characteristic of the montmorillonite. Since λ is

linearly related to $m_{\rm w}/m_{\rm m}$ (3, 24, 25, 28), Eq. [3] suggests that $\ln (\Pi + 1)$ should be linearly related to $1/\lambda$. Figures 6a and b show that this is the case, i.e.,

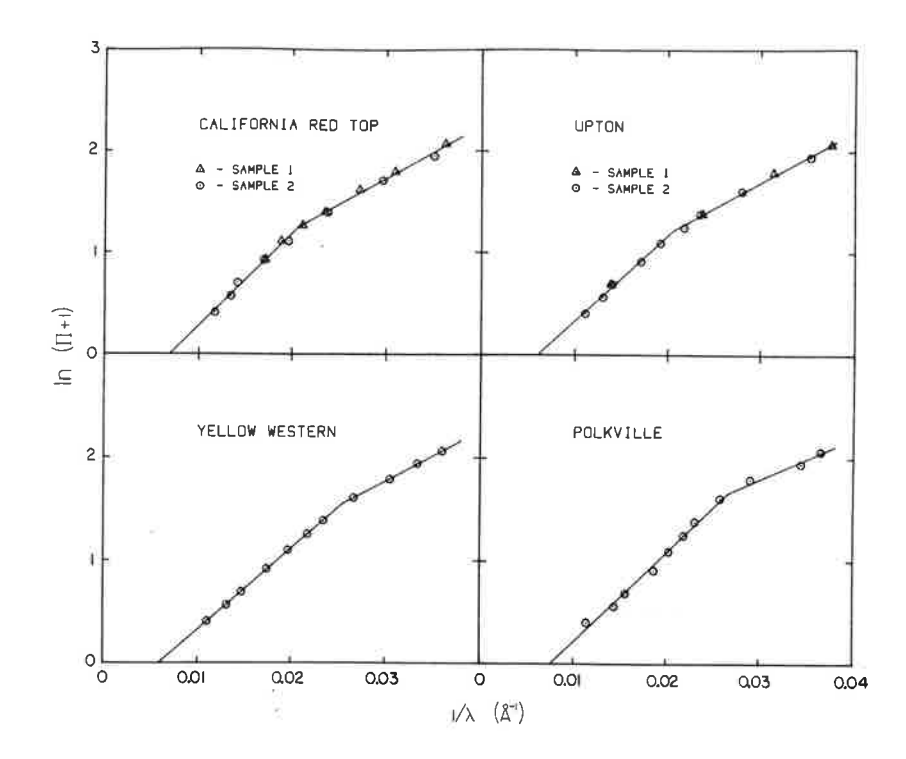
$$\ln (\Pi + 1) = k(1/\lambda) + \ln b$$
 [4]

OΓ

$$(\Pi + 1) = \exp k[(1/\lambda) - (1/\lambda_0)]$$
 [5]

where k is a constant, $b = \exp(-k/\lambda_0)$, and λ_0 is the modal separation between the surfaces of the layers when $\Pi = 0$. However, note that, for half of the samples, the logarithmic plots exhibit a sudden change in slope at values of Π between 2.4 and 4.3 bars. This change in slope necessarily means that there is a corresponding discontinuity in $d\Pi/d\lambda$ which was not apparent from Figs. 4a and b. Independent experimental observations of the effect of pressure on the properties of clay-water systems support the concept that a phase change in the water in the system is responsible for the abrupt change in $d\Pi/d\lambda$





b.

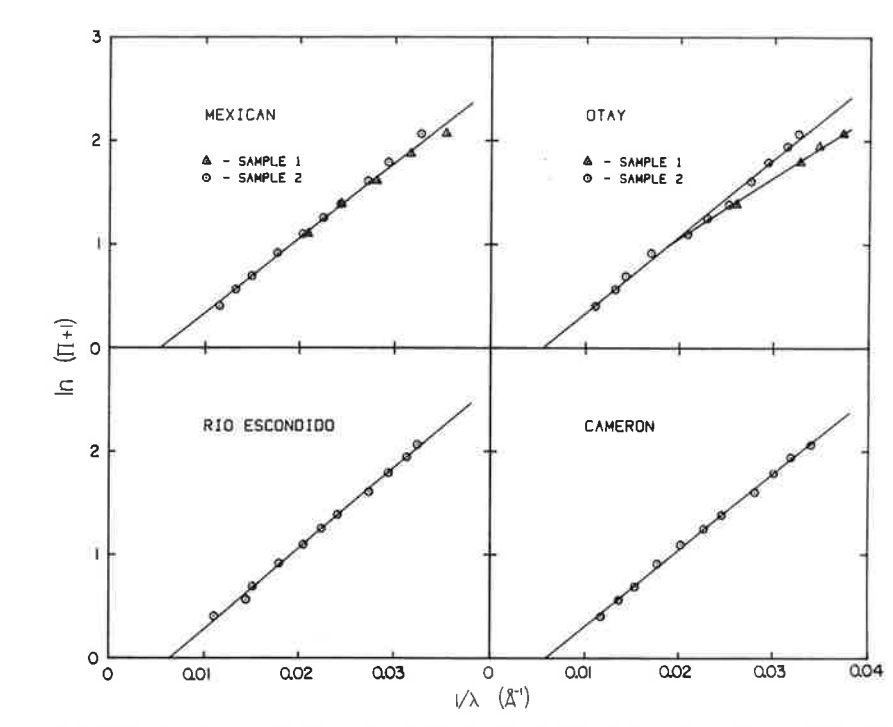


FIG. 6. (a) Relation between $\ln (\Pi + 1)$ and $1/\lambda$ for the California Red Top, Upton, Yellow Western, and Polkville montmorillonites in equilibrium with 10^{-4} N NaCl. (b) The relation between $\ln (\Pi + 1)$ and $1/\lambda$ for the Mexican, Otay, Rio Escondido, and Cameron montmorillonites in equilibrium with 10^{-4} N NaCl.

in the Upton, California Red Top, Yellow : 67.5 and 93.5 Å. In other words, the depth Western, and Polkville samples. For example, it has been observed that, during the isothermal compression of certain gas-free montmorillonite gels in a closed system, abrupt changes occur in the heat of compression, activity of the sodium ion and electrical conductance at pressures between 1.5 and 2.5 bar (29). Logic dictates that only a pressureinduced restructuring of the water can account for these changes.

Presented in Table II are values for the constants in Eq. [4] that apply to the different montmorillonites. These constants were obtained statistically by the method of least squares. The initial values apply below the intersections of the straight lines in Figs. 6a and b, whereas, the final values apply above these intersections. When the values of k_i and $\ln b_i$ are used to obtain the respective values of λ_0 , it is found that the latter range from 135 to 187 Å. Although these values of λ_0 depend on the extrapolation of Eq. [4] to $\Pi = 0$, this extrapolation is reasonable in view of the fact that the analog of Eq. [4], i.e., Eq. [3], has been shown to be valid down to $\Pi = 0.025$ bars (13). Consequently, it appears that G_g becomes equal to G_s when the thickness of the water film $(\lambda_0/2)$ on the surface of each montmorillonite layer is between

TABLE II The Initial Values, Designated by the Subscript i, and the Final Values, Designated by the Subscript f, for k and In b in Eq. [4]

Sample	k _i	In b _i	k _f	In be
Yellow Western	79.4	-0.472	50.0ª	0.2734
California Red Top	90.4	-0.630	52.3	0.157
Upton	84.5	-0.513	50.3	0.188
Polkville	86.2	-0.638	40.3	0.588
Rio Escondido	78.1	-0.496	10.5	0.500
Mexican	72.3	-0.386		
Otay	74.4	-0.408	58.8	~0.117
Cameron	71.0	-0.397	50.0	0.117

^a When values of k_f and $\ln b_f$ are not reported for a sample, the reported values of k_i and k_i apply to the entire pressure range studied.

of influence of the layer on the surrounding water is within these limits.

Comparison of Experimental Observations with the Predictions of Double-Layer Theory

The equations of double-layer theory have been derived elsewhere (e.g., 5, 30). As applied to the swelling of parallel clay layers of constant surface charge density in a 1:1 electrolyte solution they are

$$p = 2nkT(\cosh u - 1)$$
 [6]

$$\sigma = (\epsilon nkT/2\pi)^{1/2}(2\cosh z - 2\cosh u)^{1/2}$$
[7]

$$\int_{z}^{u} (2 \cosh y - 2 \cosh u)^{-1/2} dy = -\kappa d [8]$$

$$\kappa^2 = 8\pi n e^2 v^2 / \epsilon k T$$
 [9]

and, in addition, the van der Waals attraction is given by

$$f = (A/6\pi)[(1/\lambda)^3 - 2/(\lambda + t)^3 + 1/(\lambda + 2t)^3]$$
 [10]

where $y = \nu e \Psi/kT$, $z = \nu e \Psi_0/kT$, $u = \nu e \Psi_0/kT$ kT, p is the repulsive pressure, n is the number of ions per cm3 in the external solution, k is the Boltzmann constant, T is the absolute temperature, σ is the surface charge density, ε is the dielectric constant, κ is the Debye-Hückel constant, d is the half-distance between the surfaces of adjacent layers, e is the electronic charge, ν is the ionic valence, f is the van der Waals' attractive force per unit area, A is the Hamaker constant, λ is the interlayer distance ($\lambda = 2d$), t is the thickness of the clay layers, Ψ is the electrostatic potential in a plane at a distance x from the surface of the layer, Ψ_0 is the electrostatic potential at x = 0, and Ψ_d is the electrostatic potential at x = d. Equation [8] cannot be integrated analytically. However, it can be transformed to an expression involving elliptic integrals of the first kind for which numerical solutions are available from mathematical tables. To determine the theoretical

relation between Π and λ at each of several values of σ when n is equivalent to 10^{-4} mole/liter and T = 298°K, we assigned different values to u and calculated the corresponding values of p and z by means of Eqs. [6] and [7], respectively. The resulting combinations of u and z were then used to obtain appropriate limits for the aforementioned elliptic integrals and, thereby, values of kd from which values of λ were determined by dividing through by κ , calculated by means of Eq. [9], and multiplying by 2. These values of λ were substituted into Eq. [10] to calculate the related values of f. In this calculation, A was assigned a value of 2.2×10^{-20} J in keeping with the results of Israelachvili and Adams (10) and t was assigned the value mentioned earlier, namely, 9.3×10^{-8} cm. Since $\Pi = p - f$, values of Π were calculated by subtracting values of f from the corresponding values of p. Thus, we were able to obtain the theoretical curves in Fig. 7.

Note from Fig. 7 that the only theoretical curves that are qualitatively similar to the observed curve for the Rio Escondido montmorillonite, which is a typical curve, are those for which the values of σ are comparable to the respective values listed in Table I. The latter were determined in an earlier

study (14) from the measured cation exchange capacities and specific surface areas and, hence, represent the values of σ at the solid-solution interface as governed by ionic substitutions in the crystal structure. This similarity might be construed to mean that double-layer theory describes the swelling of montmorillonite. However, we do not believe that such is the case for reasons which we will now discuss.

Although the theoretical curves of Π vs λ for relatively high values of σ are somewhat similar to the observed curve, the similarity is only superficial. Note, for instance, that the observed curve intersects several theoretical curves representing a range of values of σ . Moreover, as can be seen from Fig. 8, the observed relation between $\ln (\Pi + 1)$ and $1/\lambda$ is linear, in keeping with Eq. [4]; whereas, the theoretical relations for different values of σ are curvilinear. It follows, therefore, that the observed and theoretical curves are described by equations of different form.

Observe from Fig. 7 that, theoretically, we would expect λ to be a function of σ at any value of Π , or Π to be a function of σ at any value of λ . However, as shown in Figs. 9 and 10, this expectation is not realized experimentally. In Fig. 9, the values of λ at each

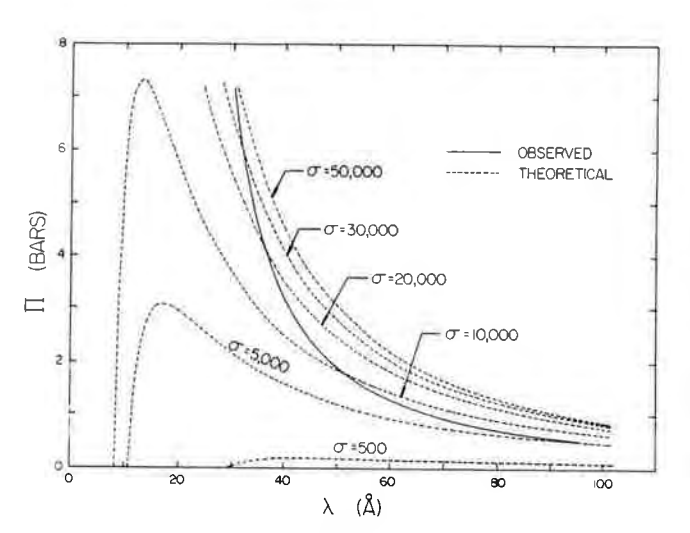


FIG. 7. Comparison of the observed curve of Π versus λ for a typical montmorillonite (Rio Escondido) with the theoretical curves for different values of σ .

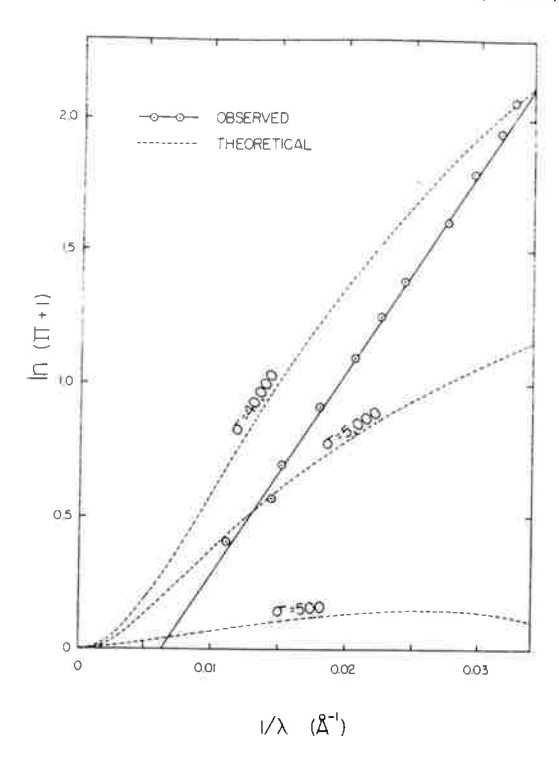


FIG. 8. Comparison of the observed relation of $\ln (\Pi + 1)$ and $1/\lambda$ for a typical montmorillonite (Rio Escondido) with the theoretical relations for different values of σ .

value of Π were obtained from the data in Figs. 4a and b and the corresponding values of σ were taken from Table I. In Fig. 10, the lines defining the upper and lower limits of the stippled area coincide with the extreme portions of the collected curves of Π versus λ for the montmorillonites that we studied. Hence, all of these curves fall within the stippled area. Note that this area is very narrow despite the wide variation in σ for the montmorillonites included therein.

We have found that neither the relation between Π and λ nor the relation between Π (or λ) and σ is consistent with electrical double-layer theory. We are obliged to conclude, therefore, that either the theory is wrong or the electric double layers of montmorillonites are so poorly developed that they contribute little to swelling. The latter alternative is preferable because, in earlier work (14), the effective surface charge density, i.e., the surface charge density in the plane where the diffuse part of the double layer begins, was found from the measured zeta potentials of 35 montmorillonites to be only ~ 500 esu cm⁻². Reference to Fig. 7

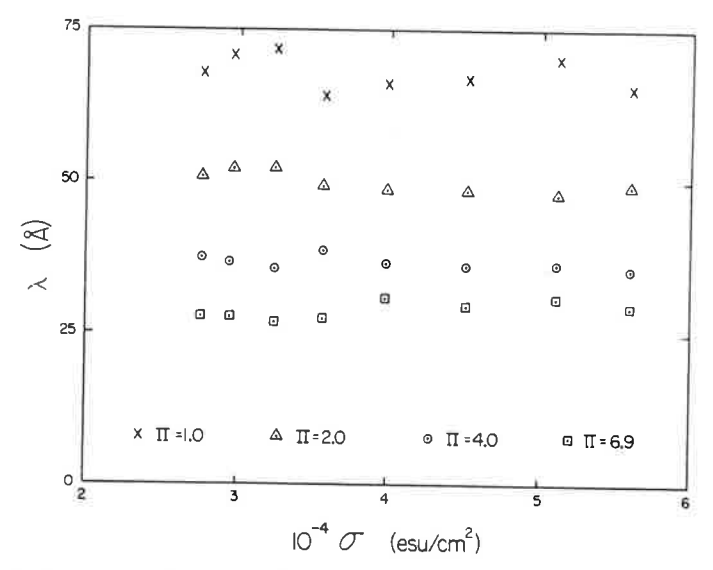


FIG. 9. The relation between λ and σ at four values of Π as indicated by the data for eight different montmorillonites (to identify the value of σ plotted here with the respective montmorillonite, see Table I).

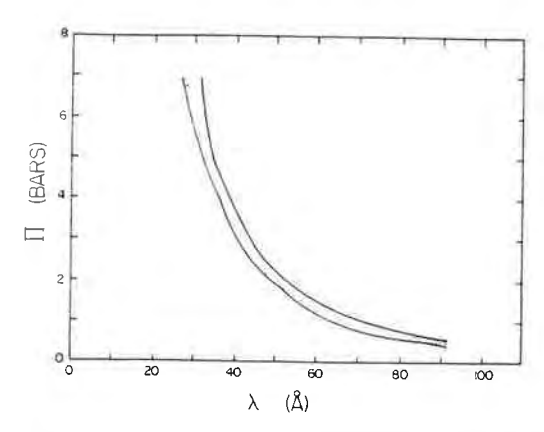


Fig. 10. The limits (solid lines) that encompass all of the curves of II versus λ for the different montmorillonites.

shows that the value of Π corresponding to this value of σ is negligible. Moreover, it is highly unlikely that the relation between $\ln (\Pi + 1)$ and $1/\lambda$ could be linearized, in keeping with Figs. 6 and 8, by the addition of another repulsive force to the double-layer repulsive force. It is more reasonable to believe that the added repulsive force is dominant and obeys the aforementioned relation.

In the preceding discussion, we have established the fact that σ has an insignificant effect on the swelling of the fully expandable layers. However, this fact should not be construed to mean that the swelling of a clay crystal is entirely unaffected by σ . Nor should it be construed to mean that the swelling of the crystal is unaffected by the nature of the exchangeable cations that neutralize σ . We believe that both σ and the nature of the exchangeable cations affect the depth of the energy well occupied by the layers in the partially expanded state and, thereby, the fraction of the layers in this state. Obviously, intracrystalline swelling will be affected by the relative fractions of fully expandable and partially expandable layers. Our ideas on the effect of exchangeable cations on the expansion of the clay layers and on the properties of the interlayer water are presented in greater detail elsewhere (14, 45).

Comparison of the Force-Distance Relations for Montmorillonite Layers and Mica Sheets

A curve of F/R vs D, where F is the force between crossed mica cylinders of radius R and D is the distance between them, was published for Na-mica in $5 \times 10^{-4} N$ NaCl solution by Pashley (16). His curve was transformed to the corresponding curve of Π vs λ by (1) obtaining the coordinates of the data points with a digitizer (Hewlett-Packard Graphics Plotter 9872 B), (2) converting the resulting values of F/R to equivalent values of energy/area by means of the Derjaguin approximation (31), (3) plotting a curve of energy/area vs D, which now equals λ , (4) digitizing this curve, and (5) determining values of Π at specific values of λ from the slopes of the curve, obtained by numerical differentiation, at these values of λ . The results of this transformation are shown, along with our results for the Upton and Rio Escondido montmorillonites, in Fig. 11.

Observe from Fig. 11 that the curve for the mica is nearly parallel to the curves for the montmorillonites and is displaced from them by only 6-10 Å at values of $\Pi \ge 1.0$ bar. It is likely that the true displacement is even

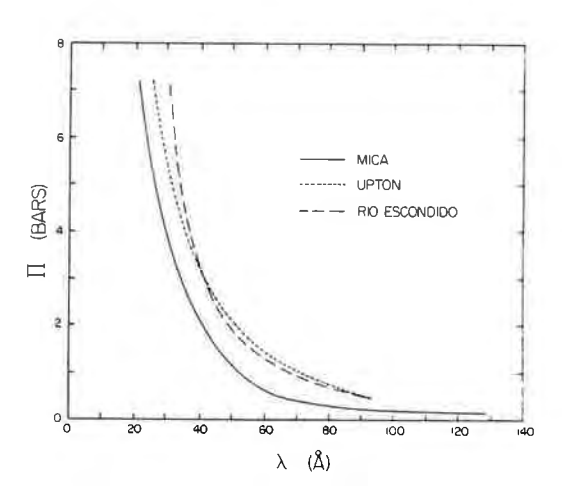


FIG. 11. Comparison of the curves of Π versus λ for two montmorillonites and a mica (the curve for the mica was derived from the data of Pashley (16)).

smaller because the absolute values of λ for the mica were underestimated. In the relevant experiments, λ was assigned a value of zero when the mica sheets were in "contact," i.e., when they could not be pressed closer together or, in some cases, when they had passed over an energy barrier and were in the primary energy minimum. However, the actual distance between mica sheets in "contact" is not zero. Although it was reported that this distance was ±4 Å relative to uncleaved mica (10), we believe that it must have been closer to +6 Å, which is the thickness of two molecular layers of adsorbed water. Our belief is based on the fact that the last two molecular layers of water between the surfaces of layer silicates are difficult to remove. It has been shown that two molecular layers of water remain between the surfaces of sodium montmorillonites in equilibrium with air at a relative humidity, p/p_0 , of ≈0.7 (32, 33) and when the freezing point depression, θ , is greater than 40°K (34, 35). By means of the thermodynamic equations relating the relative partial molar free energy to Π , p/p_0 , and θ , we find the corresponding values of Π to be ~500 and \geq 500 bar, respectively. Since the compressive force did not reach this magnitude when the mica sheets were separated by a solution, there is no reason to believe that the last two molecular layers of water were expelled. Nor is there any reason to believe that they were expelled when the mica sheets were in a primary energy minimum. In fact, Pashley and Quirk (36) have reported that the depth of the primary minimum for mica sheets immersed in electrolyte solution is very much less than that for sheets of uncleaved mica, and have attributed the difference to residual water layers on the mica surfaces at the point of "contact," i.e., the point at which they let $\lambda = 0$. Also, Fig. 4b shows that the distance between layers of montmorillonite in the primary energy minimum is 10 Å (c axis spacing = 19 Å), and evidence which we will publish later will show that the corresponding dis-

tance for layers of vermiculite is 6 Å (c axis spacing = 15 Å). Both of these minerals are structurally similar to mica. Consequently, the curve for the mica in Fig. 11 should be translated to the right, by as much as 6–10 Å, where it will become nearly coincident with the other curves in this figure and will fall within the limits indicated in Fig. 10. It appears, therefore, that the results for mica agree with those for montmorillonite despite the fact that the former has a relatively high value of σ .

Relation between the Properties of Interlayer Water and Swelling Pressure

Early in his career, one of us postulated that the interaction of water with clay surfaces produces a hydrostatic repulsive force that contributes to clay swelling (37, 38). This postulate was difficult to test but it was felt that, if surface-water interaction altered the structure-sensitive properties of the water, it would also affect \bar{G}_{g} and, thereby, Π in keeping with Eq. [2]. Consequently, experiments were conducted over many years on the structure-sensitive properties of water in montmorillonite-water systems (e.g., 39-42). When sufficient data had been accumulated for a systematic analysis (43), it was discovered that all of these properties obey an empirical equation, namely,

$$J_i = J_i^0 \exp(\beta_i m_{\rm m}/m_{\rm w})$$
 [11]

where J and J^0 are the values of the property, i, in the montmorillonite-water system and in pure bulk water, respectively, and β is a constant that is characteristic of the property. Subsequently, this equation was found to hold for the isothermal compressibility, molar absorptivity and rotational correlation time of the interlayer water (44, 45). Combination of Eqs. [3] and [11] yields

$$(\Pi + 1) = B(J_i/J_i^0)^{\alpha/\beta_i}$$
 [12]

and so we see that Π is related to the properties of the water in the system. This rela-

tion, and the evidence against the existence of double-layer repulsion, leads to the conclusion that the interaction of water with the surfaces of montmorillonite causes swelling. In other words, this interaction reduces $G_{\rm g}$ and, as a result, Π develops. Thus, the postulate mentioned above has been substantiated but, contrary to this postulate, surfacewater interaction not only contributes to clay swelling but is almost entirely responsible for it.

As mentioned earlier, evidence in support of a hydrostatic repulsive force or hydration force has been presented by several investigators. However, opinions differ with respect to its origin. Derjaguin and Churaev (9) favor the concept that it originates because of the hydration of the surface; whereas, Pashley (15, 16) favors the concept that it originates because of the hydration of the adsorbed counter ions. We have consistently favored the former concept (7, 14, 28, 38, 46) and still do. If counterion hydration causes swelling, there should be some relation between swelling and σ , which governs the number of counter ions. We have found no such relation even though the surface density of Na in our samples varies by almost a factor of two, i.e., from 0.57 to $1.1 \times 10^{14} \text{ ions/cm}^2$. Moreover, the mere presence of the surface itself may perturb the water to appreciable distances. This concept is supported by the results of a recent computer simulation of the dynamics of water molecules near a rigid, uncharged surface composed of oxygen atoms (47). It is also supported by the observation, which will be reported in a forthcoming paper, that pyrophyllite (which has no counterions) undergoes appreciable intercrystalline swelling.

In summary, the net repulsive force developed between adjacent montmorillonite layers in sodium-saturated montmorillonite gels has been shown to be related to $1/\lambda$, the inverse of the interlayer separation, by a simple exponential equation. Over the range of λ 's studied, double layer forces are too weak

to account for the observed swelling pressures. An additional force, which dominates the interaction between montmorillonite layers, is present. Presumably, it arises because of the in-depth perturbation of the water by the surfaces of these layers.

ACKNOWLEDGMENTS

The authors gratefully acknowledge funding provided by the National Science Foundation (Grant CME78-24431) and the U. S. Army Research Office (Grant DAAG29-80-C-004, subcontract 79-104).

They also acknowledge the generosity of Drs. R. M. Pashley and J. P. Quirk for making their manuscript available prior to publication.

REFERENCES

- 1. Langmuir, I., J. Chem. Phys. 6, 873 (1938).
- Schofield, R. K., Faraday Soc. Trans. 42B, 219 (1946).
- 3. Norrish, K., Faraday Soc. Disc. 18, 120 (1954).
- Bolt, G. H., and Miller, R. D., Soil Sci. Soc. Amer. Proc. 19, 285 (1955).
- van Olphen, H., "An Introduction to Clay Colloid Chemistry." Interscience, London, 1963.
- Callaghan, I. C., and Ottewill, R. H., J. Chem. Soc. Faraday Disc. 57, 110 (1974).
- Davidtz, J. C., and Low, P. F., Clays Clay Miner. 18, 325 (1970).
- Barclay, L. M., and Ottewill, R. H., Faraday Soc. Spec. Disc. 1, 138 (1970).
- Derjaguin, B. V., and Churaev, N. V., J. Colloid Interface Sci. 49, 249 (1974).
- Israelachvili, J. N., and Adams, G. E., J. Chem. Soc. Faraday Trans. 1 74, 975 (1978).
- Derjaguin, B. V., Rabinovich, Y. I., and Churaev, N. V., *Nature (London)* 272, 313 (1978).
- Low, P. F., and Margheim, J. F., Soil Sci. Soc. Amer. J. 43, 473 (1979).
- 13. Low, P. F., Soil Sci. Soc. Amer. J. 44, 667 (1980).
- 14. Low, P. F., Soil Sci. Soc. Amer. J. 45, 1074 (1981).
- 15. Pashley, R. M., J. Colloid Interface Sci. 80, 153 (1981).
- Pashley, R. M., J. Colloid Interface Sci. 83, 531 (1981).
- Norrish, K., and Rausell-Colom, J. A., Clays Clay Miner. 10, 123 (1963).
- Rhoades, J. D., Ingvalson, R. D., and Stumpf, H. T., Soil Sci. Soc. Amer. Proc. 33, 473 (1969).
- 19. Wilson, A. J. C., Brit. J. Appl. Phys. 16, 665 (1965).
- Brindley, G. W., and Wan, Hsieu-Ming, Clays Clay Miner. 22, 313 (1974).
- 21. Bailey, S. W., in "Crystal Structures of Clay Min-

- erals and Their X-Ray Identification" (G. W. Brindley and G. Brown, Eds.), p. 2. Mineralogical Society, London, 1980.
- 22. Schultz, L. G., Clays Clay Miner. 17, 115 (1969).
- Warkentin, B. P., Bolt, G. H., and Miller, R. D., Soil Sci. Soc. Amer. Proc. 21, 495 (1957).
- Foster, W. R., Savins, J. G., and Waite, J. M., Clays Clay Miner. 3, 296 (1955).
- Fink, D. H., and Nakayama, F. S., Soil. Sci. 114, 355 (1972).
- 26. Barshad, I., Science 131, 988 (1960).
- Shainberg, I., Low, P. F., and Kafkafi, U., Soil Sci. Amer. Proc. 38, 751 (1974).
- Ravina, I., and Low, P. F., Clays Clay Miner. 25, 109 (1972).
- Kay, B. D., and Low, P. F., J. Colloid Interface Sci. 40, 337 (1972).
- Verwey, E. J. W., and Overbeek, J. Th. G., "Theory of the Stability of Lyophobic Colloids." Elsevier, Amsterdam, 1948.
- 31. Derjaguin, B. V., Kolloid-Z. 69, 155 (1934).
- Mooney, R. W., Keenan, A. G., and Wood, L. A., J. Amer. Chem. Soc. 74, 1371 (1952).
- Margheim, J. F., Ph.D. Thesis, Purdue University, West Lafayette, IN, Univ. Microfilms, Ann Arbor, MI, Diss. Abstr. 38, 2985B (1977).

- 34. Ahlrichs, J. L., and White, J. L., *Science* **136**, 1116 (1962).
- Anderson, D. M., Hoekstra, P., Soil Sci. Soc. Amer. Proc. 29, 498 (1965).
- Pashley, R. M., and Quirk, J. P., Colloids Surf. (in review).
- 37. Low, P. F., and Deming, J. M., Soil Sci. 75, 178 (1953).
- Hemwall, J. B., and Low, P. F., Soil Sci. 82, 135 (1956).
- Anderson, D. M., and Low, P. F., Soil Sci. Soc. Amer. Proc. 22, 99 (1958).
- Oster, J. D., and Low, P. F., Soil Sci. Soc. Amer. Proc. 28, 605 (1964).
- 41. Kay, B. D., and Low, P. F., Clays Clay Miner. 23, 266 (1975).
- 42. Low, P. F., Soil Sci. Soc. Amer. J. 40, 500 (1976).
- 43. Low, P. F., Soil Sci. Soc. Amer. J. 43, 651 (1979).
- Oliphant, J. L., and Low, P. F., J. Colloid Interface Sci. 95, 45 (1983).
- Mulla, D. J., and Low, P. F., J. Colloid Interface Sci. 95, 51 (1983).
- 46. Low, P. F., Adv. Agron. 13, 269 (1961).
- Mulla, D. J., Low, P. F., Cushman, J. H., and Diestler,
 D. J., J. Phys. Chem. (in review).

COASTAL SEDIMENTS

Proceedings of a Specialty Conference on Coastal Sediment Processes Quantitative Approaches to

Seattle, Washington June 25-27, 1991 Sponsored by the Committee on Coastal Engineering of the Waterway, Port, Coastal and Ocean Division of the American Society of Civil Engineers

Canadian Society for Civil Engineering Headquarters, Chief of Engineers Waterways Experiment Station American Geophysical Union Cosponsored by the Corps of Engineers Seattle District

National Oceanic and Atmospheric Administration Committee on Coastal Engineering Japan Society of Civil Engineers Geological Society of America

Pacific Marine Environmental Laboratory Society for Sedimentary Geology (SEPM) National Sea Grant College Program Jniversity of Washington U.S. Geological Survey

Hosted by: ASCE Seattle Section

Edited by Nicholas C. Kraus, Kathryn J. Gingerich, David L. Kriebel



American Society of Civil Engineers New York, New York 10017-2398 345 East 47th Street Published by the

REVIEW NOTES ON COHESIVE SEDIMENT EROSION

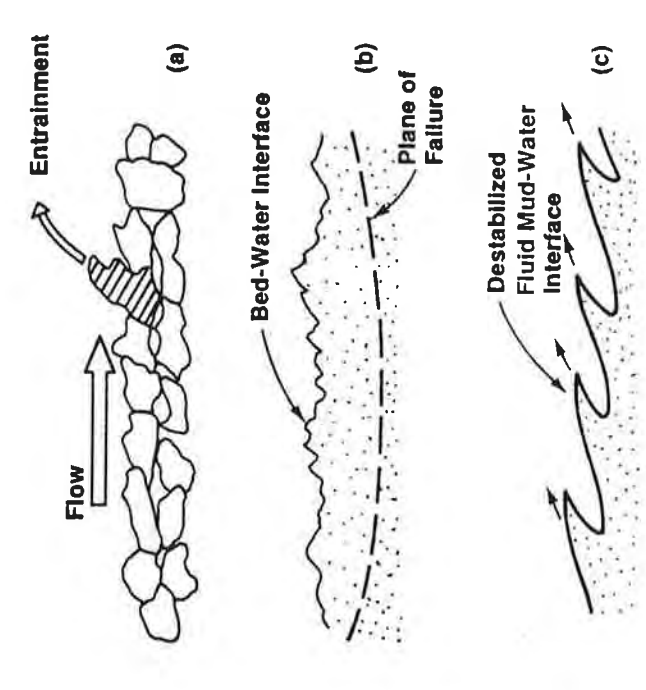
Ashish J. Mehta¹, Member, ASCE

measuring devices are unsuitable for measuring the bed is argued that erosion can be viewed either as a process evidence is presented to show that mass erosion can occur Finally, it is suggested that the entrainment of fluid sediment beds, and the entrainment of fluid mud. The rate process theory is recapped to highlight the dependence of introducing the concept of a "stirred" near-bed layer it exchange process involving ABSTRACT: Comments are made on issues related to surface and mass erosion phenomena associated with cohesive surface crosion rate on the excess bed shear stress and the absolute temperature. A qualitative argument is standard soil strength erosion shear strength which, in freshly deposited beds, is influenced both by consolidation and gelling. By simultaneous entrainment and settling. Some experimental at comparatively low applied stresses over weak beds. mud can not be modeled in the same way as bed erosion. involving solely upward entrainment of broken presented to emphasize that as an or

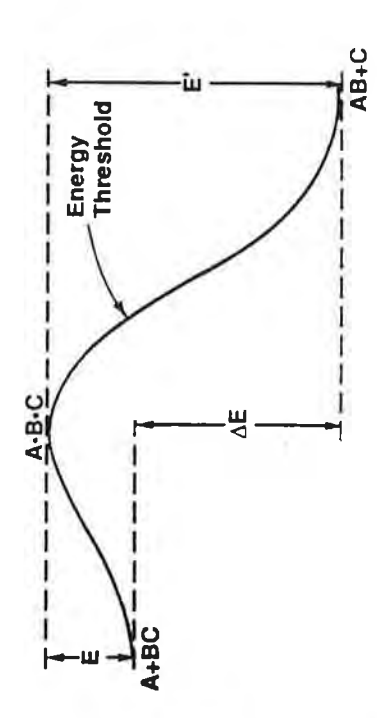
INTRODUCTION

Erosion of cohesive particulate aggregates, dependent as it is on the composition and the structure of the bottom material that characterizes bottom resistance and the character of the eroding force, can occur in several modes which are not wholly distinct and independent of each other, but may be conveniently treated as such. As an illustration consider the three modes depicted in Fig. 1a,b and can the first is flow-by-flow surface crosion in which the floes or aggregates at the bed-water surface, initially attached to their

¹Prof., Coast. and Ocean. Dept., Univ. of Florida, Gainesville, FL 32611.



II. 1. Three modes of cohesive sediment erosion: a) surface erosion of bed aggregates; b) mass erosion of the bed; c) entrainment of fluid mud.



Relationship between reactants A and BC, and products AB and C, through the intermediate activated complex according to the rate process theory.

neighbors by inter-particle electrochemical bonds, break up and are entrained as a result of hydrodynamic lift and drag. The second mode is referred to as mass erosion, wherein the bed fails at a deeply embedded plane such that all the material above this plane is almost instantly brought into suspension, in the third mode the bed is first fluidized, and flow-induced destabilization of the fluid mud-water interface thus formed causes interfacial entrainment and mixing.

Surface erosion under current- and wave-induced bottom stresses has been treated previously (Parchure and Mehta, 1985; Maa and Mehta, 1987), while mass erosion has been mentioned only briefly (Mehta, 1988). Those citations constitute the background material for this note, in which some of the issues related to surface erosion are further explored, and preliminary evidence presented for the mass erosion phenomenon. Some evidence for bed fluidization and associated implications for erosion have been given more recently (Ross and Mehta, 1990). The issue of subsequent destabilization of the interface and its entraliment have been briefly examined by Srinivas and Mehta (1989). Reference is made in this note to the entraliment behavior.

A THEORETICAL BASIS FOR SURFACE EROSION

The time rate of increase of suspended sediment mass per unit bed area, m, is given in the functional form by

$$\frac{\mathrm{d}n}{\mathrm{d}t} = \mathrm{f}(\tau_{\mathrm{b}} - \tau_{\mathrm{a}}, \nu_{\mathrm{1}}, \nu_{\mathrm{2}} \dots \nu_{\mathrm{n}}) \tag{1}$$

where τ_b : τ_s is the bed shear stress, τ_b , in excess of the bed shear strength with respect to exosion, τ_s , and $\upsilon_1...\upsilon_n$ are erosion resistance defining parameters. In its most common form Eq. 1 is stated as

where $t_{\rm H}$ is a rate coefficient, which is equal to the value of ϵ when $r_{\rm a} = 2r_{\rm b}$. The magnitudes of $t_{\rm H}$ and $r_{\rm s}$ can vary widely depending upon the properties of the sediment-fluid mixture and the bed structure. For example, the range of $t_{\rm H}$ can be from 10^{-4} to 10^{-2} g cm²min⁻¹, while $r_{\rm s}$ can vary from nil for organic floc layers to as much as 10 Pa for very hard soils (Lavelle and Mofjeld, 1985; Sargunam et al., 1973). If the bed properties are uniform, $r_{\rm s}$ remains constant; hence for a fixed $r_{\rm h}$, the rate of erosion is constant. More generally, bed properties exhibit stratification with depth, and $r_{\rm s}$ typically increases with depth so that as bed scour proceeds ϵ decreases with

Surface erosion essentially involves micro-level interactions between hydrodynamic and physico-chemical forces. Hence the development of any useful theoretical basis to explain the erosion phenomenon amounts to relating the micro-theory to observations via integration of the micro-level processes over rather significant

COHESIVE SEDIMENT EROSION

temporal and spatial scales. A heuristic interpretation of the chemical reaction rate process theory (Eyring, 1936) is one approach which, although limited by the nature of the interpretation itself, provides a qualitative basis for the form of Eq. 1, and the effect of temperature on the erosion rate. The reaction rate process can be briefly described as follows.

Two molecules A and BC will react to form products AB and C through a weakly bonded and unstable activated complex, A.B.C, according to

$$A + BC = A.B.C \Rightarrow AB + C$$

likewise can react with C to produce A and BC. However, as depicted in Fig. 2, conditions for the forward reaction are more favorable than the backward one, inasmuch as the total energy of AB + C is less than Activation, E, represents the energy which must be exceeded for the forward reaction to occur. Likewise E' is the energy of activation for required for the reaction to proceed, and it can be shown that the L/RI) for the forward reaction, where R is the molar gas constant and rate of the backward reaction; hence the net reaction rate of the The arrows imply that the reaction process is reversible such that AB that for A + BC by an amount AE. The total energy of the activated complex is the highest of the three states such that the energy of the backward reaction. "Successful" intermolecular collisions are fraction of molecules having energy in excess of E is equal to exp[-I is the absolute temperature. This exponential factor controls the Into of the forward reaction. Likewise, exp[-E'/RT] determines the molecular flow units is proportional to the difference, exp[-E/RT]. This is the basic premise of the rate process theory. Mitchell et al. (1968) applied the rate process theory to soil creep and obtained an expression for the strain rate, ϵ_s , associated with creep:

$$\mathbf{q_b} = \mathbf{K}(kT/h_p) \cdot \exp[-E''/RT]$$
 (4)

Where K is a time and structure dependent dimensionless coefficient, K is the Boltzmann constant, h_p is the Planck's constant, and E'' is called the experimental activation energy, which is proportional to ℓ , the shear stress on the particulate flow units in the creeping coil. Interpreting Eq. 4 for surface erosion would mean that ℓ_s would represent the erosion rate ℓ , and ℓ would be replaced by the excess there stress, $\ell_b - \ell_s$. In summary we therefore note the following.

1. Surface erosion can be thought of as a rate process in which particle entrainment occurs when there is a "successful" application of flow-induced shear causing the inter-particle cohesive bonds to brak. This probabilistic behavior highlights the essentially stochastic nature of the erosion phenomenon.

2. By virtue of Eq. 4, the log of ϵ/T must be proportional to 1/T in malogy with the Arrhenius relationship for chemical reaction rates

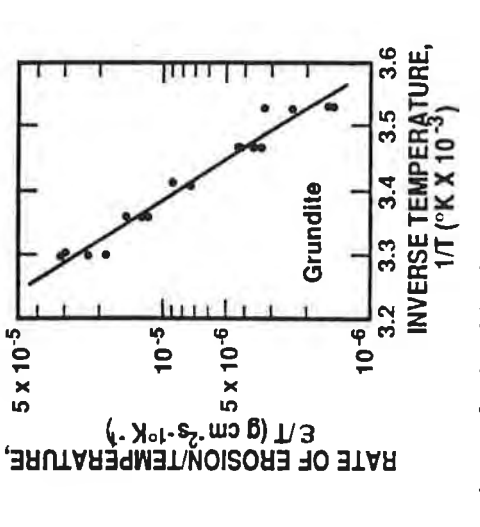
COHESIVE SEDIMENT EROSION

temperature could be carefully controlled and altered. The erosion rate data in Fig. 3 obtained at a constant applied fluid stress and confirm the Arrhenius trend, and demonstrate the sensitivity of the erosion rate coefficient, $\boldsymbol{\varepsilon}_{H},$ to The second point is essentially a test of the applicability of the rate process theory to surface erosion. Kelly and Gularte (1981) conducted erosion tests using a remolded Grundite (with 50 % water the water in a recirculating water tunnel in which different temperatures indeed water temperature.

STIRRED LAYER

Viewing the bed (initially at z = 0) in conjunction with the variation small rate of further increase due to the fact that the instantaneous (represented by $r_{\rm b}$), and likewise the bed shear strength at any horizontal plane can exhibit a variability about the mean value, $r_{\rm s}$. of C, the erosion flux (arrow upward from the bed) will eventually suspension concentration, it is worth examining the time-variation of the water column depth-averaged concentration, C, resulting from erosion. In Fig. 4, typically observed variation of C with time is sketched together with what is believed to occur at and near a stratified bed. Considering the situation in which the applied bed shear stress, τ_b , is initially greater than the bed shear strength τ_s , stress, r_b - r_s , decreases with increasing scour, the rate of rise of C will decrease. Eventually rb will equal rs at some final depth of scour at which C will attain a practically constant value, with a very bed shear stress can be different from the turbulence-mean value Since bed scour is represented by the corresponding variation of the C will increase relatively rapidly at first but, as the excess shear becomes practically zero as well.

Mehta, 1985), or as one involving simultaneous exchange due to upward entrainment and settling at $z=\delta$ (Lick, 1982). While in both cases near-bed "stirred" layer whose upper and lower boundaries straddle the entrainment by turbulent diffusion. Once however there is sediment in suspension, settling will occur and a convective circulation cell set up, with sediment moving upward as well as downward across the z = δ level. Finally, as bed erosion stops, the upward and downward fluxes (arrows) will become equal in magnitude, implying an equilibrium condition. Thus the mechanism of erosion can be explored either as one Eq. 2 can represent the upward mass flux, in the second case, i.e. at $z=\delta$, a rate expression for settling must be included as well (Ross The mass fluxes can also be viewed from another, compatible perspective. This perspective is based on what occurs at $z=\delta$, a small height above the bed. We may conceive of a comparatively thin z - δ level. This layer can be construed to serve as a storage volume for the eroding bed sediment. Initially there would be no sediment in this layer, so that the mean concentration in the layer, $G_{\rm b}$, would be zero. With the commencement of erosion however, G_{b} will rise and, per unit time, more sediment will go into the layer from the bottom by erosion than will leave through the upper level due to upward bed scour at z = 0 involving upward mass flux only (Parchure and and Mehta, 1989).



rate of erosion and absolute temperature (after Kelly and Gularte, 1981). Fig. 3. Arrehenius relationship between the

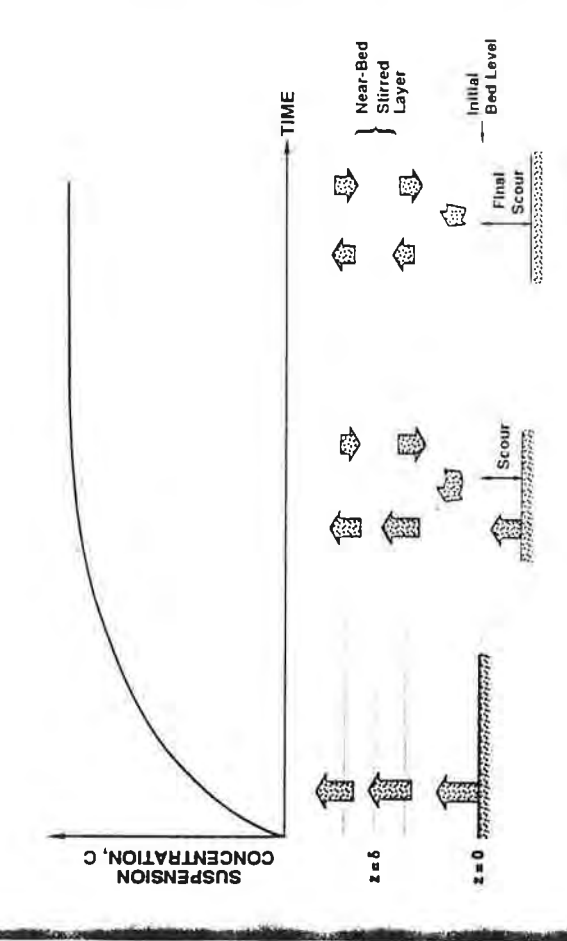


Fig. 4. Entrainment and settling during erosion of a stratified bed at a constant applied stress.

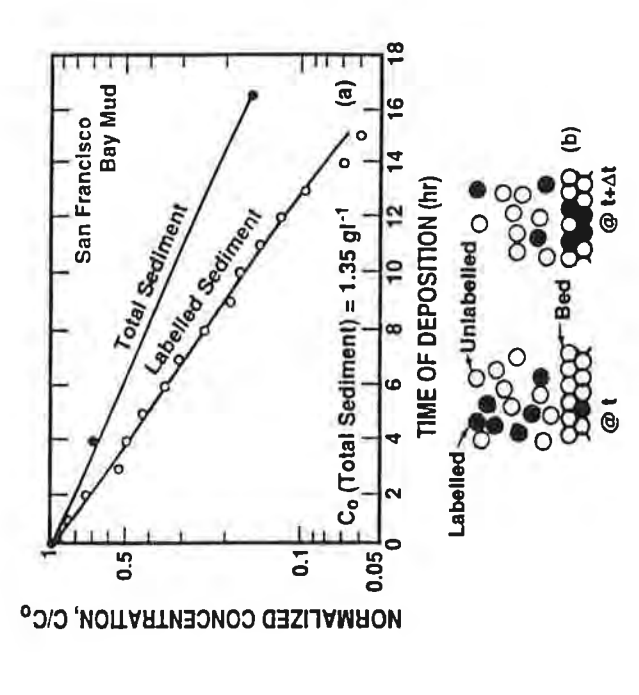
COHESIVE SEDIMENT EROSION

is three times that of the unlabelled ones. This difference arises because, due to the presence of a much larger number of unlabelled initially fully suspended in saline water by mixing at a high flow suspension due to settling was determined by measuring the suspension initially suspended sediment (having a very small Co value) was was compared with that of the labelled one. Both sediments exhibited a first order rate of dilution, i.e. dC/dt was the labelled material deposited at a faster rate than the total; the respective α values being 0.175 s⁻¹ and 0.109 s⁻¹ (Fig. 5a). the settling property of the sediment it can be inferred that as the sediment was settling, some of it was re-entrained from the formed stirred layer as well. Thus the effective rate with which the total sediment deposited was lower than the actual rate at which it settled; the Consider the simple case depicted is Fig.5b, in which at time t the so that effectively the rate of deposition of the labelled particles particles in the bed than labelled ones, more of the former are re-Evidence of exchange of sediment between that in a dilute suspension such a layer, was demonstrated by Krone (1962) in a flow recirculating flume using sediment from the San Francisco Bay. The sediment was velocity was then lowered to 8.5 cm s-1 and the rate of dilution of the concentration, C, at different times t. A very small fraction of the latter being given by the rate of deposition of the labelled sediment. number of unlabelled and labelled particles in suspension is 9 and 6, respectively. At time t + Δt the corresponding numbers are 8 and 3, and in the stirred layer, and hence by inference the occurrence of found to be equal to $-\alpha C(t)$, where α is the deposition rate constant. labelled with gold-198 radioisotope, and the dilution rate of velocity such that the suspension concentration, C_0 , was 1.35 gl⁻¹. entrained from the bed than the latter during the interval Δt . Assuming that labelling did not materially change total sediment as well. However,

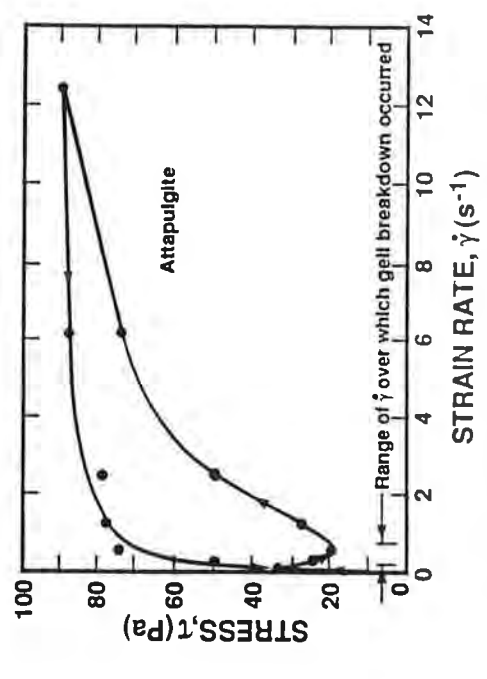
EFFECTS OF STRESS HISTORY

hydrogen bonding. This arrangement causes a slight expansion of the Shearing this matrix will break up the structure and release the water (Day and Ripple, 1966). This breakup for instance is manifested as a strength against erosion, 74, would increase quite rapidly in the Gelling involves the development of a structural arrangement of the water molecules in the pore water close to the clay particles via If the flow were stopped, the fluid-like stirred layer would rapidly form a particle-supported matrix, or a cohesive bed, and the bed shear matrix, hence some additional water is taken up by the matrix. first day or two due to dewatering, and also due to gelling in clays. drop of the applied torque in a viscometer.

type Brookfield viscometer is shown for a Florida attapulgite. The g cm⁻³ bulk density is observed to 0.2 to 4 s⁻¹, while at higher rates (up γ , in the approximate range of 0.2 to 4 s⁻¹, while at higher rates (up to $12~{\rm s}^{-1}$) the behavior seems to approach Newtonian. Differences in the rising and the falling parts of the hysteresis loop (arrows indicate the path followed by first increasing and then decreasing $\dot{\gamma}$ in the In Fig. 6 the stress-strain rate relationship obtained in a vane rheological behavior of this thixotropic pseudoplastic material at 1.1 cm-3 bulk density is observed to be non-Newtonian at strain rates,



a) Time-concentration relationship during the deposition of total and labelled suspended sediments in a flume (after Krone, 1962); b) schematization of the settling and exchange behaviors of unlabelled and labelled sediments F1g. 5.



Stress-strain rate relationship for a Florida attapulgite in tap water at a bulk density of $1.1~{\rm g~cm^{-3}}.$ Fig. 6.

49

viscometer) suggest differences in the formation and breakup of aggregate structures with changing $\dot{\gamma}$. Note particularly the drop in stress, r, in the range of $\dot{\gamma}$ from 0.2 to 0.7 s⁻¹, which is believed to be due to the breakdown of the initially formed gell structure.

range of 0.02 to 0.5 Pa (Krone, 1963). Measurement of such low layer by layer erosion of the bed (Parchure and Mehta, 1985). On the other hand the vane shear strength $\tau_{\rm v}$, for example, which can be three decades greater in magnitude than $\tau_{\rm s}$, is a decidedly unsuitable measure of surface erosion (Parthentades, 1965). This point can be stressed with the help of a somewhat crude but plausible argument The erosion shear strength being related to the inter-particle bond strength, especially for soft deposits, tends to be of the same order of magnitude as the strength of the aggregates themselves, e.g. in the strengths can for example be carried out in laboratory flumes through involving length scales.

We have $\nu=10^{-6}~{\rm m}^2~{\rm s}^{-1}$ for water, and $\epsilon_{\rm n}=10^{-2}~{\rm m}^2~{\rm s}^{-3}$ as a reasonable Thus $L_{\rm t}$ = 10^{-4} m, which yields $L_{\rm r}/L_{\rm t}$ = 1. This result is of course shear length scale and L_t - near-bed turbulent eddy length scale. We select L_r = 0.1 mm = 10 4 m as a typical value, and L_v = 1 cm = 10 2 m (vane dimension). We note that the ratio $L_{\rm r}/L_{\rm v}=10^2$, which we heuristically interpret to imply that the scale of the device that disrupts the aggregates in the vane shear test is incompatible with the aggregate scale; the vane actually measures bulk resistance which the ratio τ_s/τ_v <<1. Next we will assume $L_t=(\nu^3/\epsilon_n)^{1/4},$ the Kolmogoroff turbulent eddy length scale, where ν is the kinematic value of the dissipation rate corresponding to typical rms velocity Consider a resistance defining length scale, $L_{\rm r}$ - characteristic aggregate size, and two disruption defining length scales; I_{ν} - vane This difference can in turn be considered to be the explanation for viscosity of water and en is the rate of kinetic energy dissipation. expected since eddy induced stresses are responsible for aggregate is the integral of the resistance of a large number of aggregates. fluctuations on the order of $10^{-2}~\mathrm{m~s^{-1}}$ near the bed (Hinze, 1959). Next we will assume $L_t = (\nu^3/\epsilon_n)^{1/4}$,

turbulence, is assumed to be the agent necessary for surface aggregate the aggregate is viscous dominated. Consider for example 0.2 Pa as a typical value of the bed shear stress at incipient erosion (Parchure and Mehta, 1985). The corresponding friction velocity, $u_*=0.014~\rm m~s^{-1}$. Then, given a typical bed roughness $k=4.6 {\rm kl} 0^{-4}~\rm m$ for cohesive sediment beds in Inhoratory (lumes (Mehta, 1973), the roughness Reynolds number $R_w=u_ak/\nu=6.4.$ At this very low value of R_w , the surface aggregate will be surrounded by a viscous sublayer. Thus bond itself will be due to the transfer of momentum across the boundary A final note on surface erosion concerns the observation that while in the above argument the Kolmogoroff length scale, and hence occur under conditions in which the ambient fluid in the vicinity of breakup will occur by the torque due to the viscous stress which breakup, flume observations reveal that incipient entrainment can between the sublayer and the ambient turbulent flow field.

context at least, studying the growth and breakup of cohesive sediment aggregates in viscous flow fields (e.g. Krone, 1963) seems justified.

COHESIVE SEDIMENT EROSION

erosion of this type has been observed to occur at applied shear erosion occurs (Ariathurai et al., 1977). Furthermore, when the soil soil is often observed. The erosion rate coefficient, ϵ_{M} , is also Equation 2, although derived from surface erosion studies, has also been used for simulating mass erosion in an approximate way. Commonly, stresses that are considerably higher than those at which surface is hard, pitting of the bed due to dislodgement of large pleces of the measurably larger than that for surface erosion of the same bed. The stresses at which mass erosion occurs strongly depend on the bed fibrous organic matter of peaty origin. During the flume erosion tests It was found that for a bed of given density, while surface erosion structure. Figs. 7a,b show variations of $r_{\rm s}$ and $\epsilon_{\rm H}$ with bed bulk density for a lake mud with a very high (40 % by weight) fraction of occurred at low stresses, the entire bed failed and was entrained at a well defined higher stress. However, as noted from Fig. 7a, the stresses at which mass erosion occurred were actually not very high, being less than 2 Pa for a bed with a density of $1.2~\mathrm{g~cm}^{-3}$.

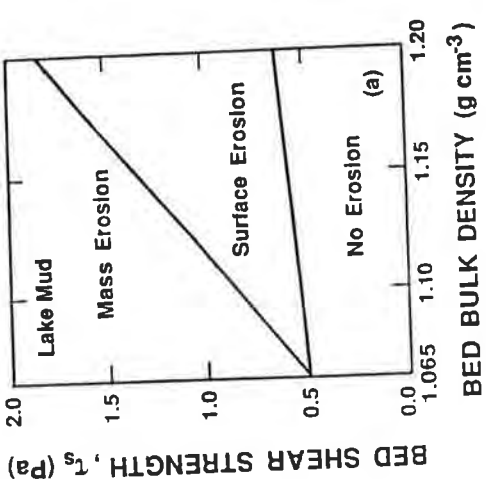
strength of the bed, which was quite uniform over the depth by virtue of the role of the fibrous organic matter in determining the bed By testing beds of different densities it was feasible to construct the plots of Figs. 7a,b, which simultaneously characterize two different erosion modes. It should be noted that at densities less than 1.065 g cm⁻³ the mud occurred as a fluid-supported slurry, which did not possess a structured matrix (Hwang, 1989); hence at this density surface erosion and mass erosion practically represented the The stress at which failure occurred was essentially the "bulk" same entrainment process. matrix.

ENTRAINMENT OF FLUID MUD

a bentonite (Srinivas and Mehta, 1989). Here the Richardson number Riu shear flow can be treated as a stratified flow problem. Thus the entrainment flux is dependent on the Richardson number, as shown in Fig. 8, which is based on prefiminary studies carried out in a "race - hab/U2, h being the depth of the upper mixed layer, U the mean Once the bed is fluidized, e.g. by wave action over a settled bed (Ross and Mehta, 1990), the entrainment of fluid mud by the ovelying track" flume using fluid muds composed of a commercial kaolinite and buoyancy being defined as b = $g(\rho_{\rm f}-\rho_{\rm w})$, with g = acceleration due to gravity, $ho_{\rm f}$ - fluid density and $ho_{\rm w}$ - water density. The non-dimensional entrainment rate, $E = (g/\rho_w^{\Lambda b}U).dm/dt$. For values of Ri_u less than about 10, at comparatively high entrainment rates, the curve trend and is analogous to what occurs in salt-stratified flows (Narimousa velocity of this layer and ab is the interfacial buoyancy step; indicates dm/dt to be proportional to U^3 , which is equivalent to $r.\mathrm{U}$,

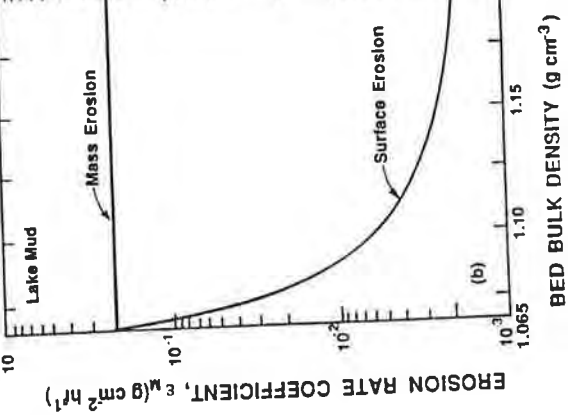
COHESIVE SEDIMENT EROSION





BED BULK DENSITY (g cm⁻³)

Mass Erosion Lake Mud 9



domains of surface erosion and mass erosion of a mud high in organic content; b) Variation (lines) of the corresponding a) Variation of bed shear strength with bed bulk density; erosion rate coefficients,

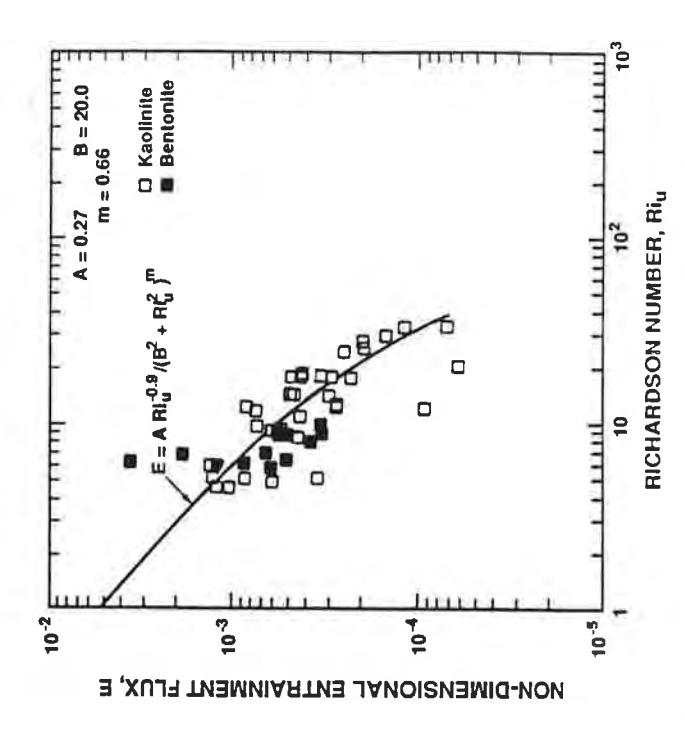
1 Fig.

and Fernando, 1987). Thus entrainment in this situation depends on fluid power rather than stress, hence Eq. 1 (or Eq. 2) is not sediment entrainment is damped in comparison with salt, which is at applicable to this phenomenon. At Rl_{u} values greater than about 10, least partly due to the settling tendency of the sediment suspension.

In addition, turbulence is drastically damped across the sedimentwater interface (Wolanski et al., 1989).

CONCLUDING COMMENTS

deformation of the bed matrix and the occurrence of a "stirred" layer whose behavior, not well understood at present, is critical in controlling near-bed aggregate dynamics (Newman, 1990). Like strong since it is ubiquitious, understanding the underlying physics in Cohesive sediment bed erosion requires an understanding of the in turn characterize erosion resistance. Surface erosion is complicated by the latter being the case when the bed bulk strength is exceeded. Since beds, weak ones can as well undergo surface or mass erosion; the fluid mud entrainment is distinctly different from bed erosion, and tandem with bed erosion poses challenging issues for future research. the bed material which physico-chemical properties of



Non-dimensional fluid mud entrainment flux versus Richardson number (after Srinivas and Mehta, 1989). Fig. 8.

ACKNOWLEDGEMENT

Thanks are due to Prof. Ray B. Krone for his comments on the gelling Support by the U.S. Army Engineer Waterways Experiment Station, cksburg, MS, through contract DAGW39-90-K-0010 is acknowledged. Vicksburg,

REFERENCES

Ariathurai, R., MacArthur, R.C. and Krone, R.B., 1977. Mathematical model of estuarial sediment transport. Tech. Rept. D-77-12, U.S. Army Eng. Waterways Expt. Sta., Vicksburg, MS, 158 pp.

and Ripple, C.D. 1966. Effect of shear on suction in saturated clays. Soil Sci. Soc. Amer. Proc., 30: 675-679 Eyring, H., 1936. Viscosity, plasticity and diffusion as examples of absolute reaction rates. J. Chem. Phys., 4: 283-291.

Hinze, J.O., 1959. Turbulence, McGraw-Hill, New York, 595 pp.

Hwang, K.-N., 1989. Erodibility of fine sediment in wave-dominated environment. M.S. Thesis, Univ. of Fla., Gainesville, FL, 159 pp. Kelly, W.E. and Gularte, R.C., 1981. Erosion resistance of cohesive soils, J. Hydr. Div., ASCE, 107(HY10): 1211-1224. Krone, R.B., 1962. Flume studies of the transport of sediment in estuarial shoaling processes. Final Rept., Hydr. Engrg. Lab. and San. Engrg. Res. Lab., Univ. of Calif., Berkeley, CA, 118 pp.

Krone, R.B., 1963. A study of rheological properties of estuarial sediments. Tech. Bull. No. 7, Committee on Tidal Hydraulics, U.S. Army Eng. Waterways Expt. Sta., Vicksburg, MS, 105 pp.

inciplent motion and erosion really exist?. J. Hydr. Engrg., 113(3): Lavelle, W.J. and Mofjeld, H.O., 1985. Do critical stresses for

Lick, W., 1982. Entrainment, deposition and transport of fine-grained sediment in lakes. Hydrobiologia, 91: 31-40.

Mehta, A.J., 1973. Depositional behavior of cohesive sediments. Ph.D. study. Cont. Shelf Res., 7(11/12): 1269-1284.

Dissertation, Univ. of Fia., Gainesville, FL, 297 pp.

Maa, P.-Y. and Mehta, A.J., 1987. Mud erosion by waves: A laboratory

Mehta, A.J., 1988. Laboratory studies on cohesive sediment erosion and deposition. In: Physical Processes in Estuaries, J. Dronkers and W. van Leussen eds., Springer-Verlag, New York, pp. 427-445.

COHESIVE SEDIMENT EROSION

ø rate process. J. Soil Mech. and Found. Div., ASCE, 94(SM1): 231-253. Mitchell, J., Campanella R.G. and Singh, A., 1968. Soil creep as

Narimousa, S. and Fernando, H.J.S., 1987. On the sheared interface of an entraining stratified fluid. J. Fluid Mech., 174: 1-22.

sediments. Ph.D. Dissertation, Mass. Inst. Technol., Cambridge, MA, Newman, K.A., 1990. Cycling of fine particles between water

sediment deposits. J. Hydr. Engrg., 111(10): 1308-1326. and Mehta, A.J., 1985. Erosion of Parchure, T.M.

Parthenlades, E., (1965). Erosion and deposition of cohesive soils, J. Hydr. Div., ASCE, 91(1): 105-139.

Ross, M.A. and Mehta, A.J., 1989. On the mechanics of lutoclines and fluid mud. J. Goast. Res., S15: 51-61.

Ross, M.A. and Mehta, A.J., 1990. Fluidization of soft estuarine mud by waves. In: The Microstructure of Fine-grained Sediments: From to Shale, R.H. Bennett ed., Ch. 19, Springer-Verlag, New York, 185-191.

Sargunam, A., Riley, P., Arulanandan, K. and Krone, R.B., 1973. Physico-chemical factors in erosion of cohesive soils. J. Hydr. Div., ASCE, 99(HY3): 555-558. Srinivas, R. and Mehta, A.J., 1989. Observations on estuarine fluid mud entrainment. Int. J. Sed. Res., 5(1): 15-22.

Wolanski, E., Asaeda, T. and Imberger, J., 1989. Mixing across lutocline, Limnol. Oceanogr., 34(5): 931-938

SOFT MUD RESPONSE TO WATER WAVES

By Jerome P.-Y. Maa, Associate Member, ASCE, and Ashish J. Mehta,2 Member, ASCE

viscoelastic material characterized by constant density, viscosity, and shear modulus of elasticity, for approximately simulating depth-varying bed properties as degree of bed consolidation and sediment composition. In the absence of adequate data on bed shear stress over mobile, partially consolidated mud beds, this method offers an approximate procedure useful for bed shear stress estimation required for ABSTRACT: Motion within soft mud beds, wave-induced bed shear stress, and alytic approach to gain insight into the mechanism by which coastal mud responds to water waves. The cohesive mud bed is discretized into layers of simple linear well as energy dissipation. Model results on wave orbital velocities, dynamic pressure, and wave attenuation are compared with limited data from wave flume tests on partially consolidated beds under relatively low deformations and show acceptable agreement. Wave attenuation coefficients exhibit dual dependence on the wave attenuation under small amplitude waves are briefly examined using an anresuspension-rate calculations in small laboratory flumes

INTRODUCTION

soft, movable mud beds (Tubman and Suhayda 1976; Schuckman and Yamamoto 1982; Wells 1983; Suhayda 1986). Studies on wave-mud interaction worthy phenomena that result from an interaction between water waves and change of characteristics of surface water waves caused by dissipation of wave energy in the bottom mud. Additional complexities arise from the in-Iluences of the physico-chemical properties of cohesive sediments (Mehta 1983), as well as the effects of depth- and time-varying bed structures under High turbidity levels and wave attenuation at muddy coasts are two notenave been limited partly because of the difficulty in quantifying the complex wave loading (Parchure 1984; Schuckman and Yamamoto 1982).

the soft bed to be rigid. Considering the mobility of soft mud, however, a As far as erosion of the mud bed is concerned, most early studies (Alishahi better approach to estimate the shear stress at the water-mud interface, and and Krone 1964; Anderson 1972; Jackson 1973; Thimakorn 1984) assumed thus the erosion rate, is highly desirable, and was a key motivating factor in the present study.

As a first step, it must be recognized that in a large number cases in the laboratory and even in the field, the water-mud interface remains relatively intact even when turbidity generation by waves is seemingly high (van Rijn 1985). Therefore, as a first-order approximation, water may be considered sediment free. Prior to any mathematical consideration of the wave-mud interaction problem, however, a constitutive model characterizing mud dynamics and dissipative properties must be selected. Defining the properties

²Prof., Coast. and Oceanographic Engrg. Dept., Univ. of Florida, Gainesville, FL and Mary, Gloucester Point, VA 23062.

'Asst. Prof., Virginia Inst. of Marine Sci./Sch. of Marine Sci., Coll. of William

22, 1989. This paper is part of the *Journal of Waterway*, *Port*, *Coastal*, and *Ocean Engineering*, Vol. 116, No. 5, September/October, 1990. @ASCE, ISSN 0733-950X/90/0005-0634/\$1.00 + \$.15 per page. Paper No. 25070. Note. Discussion open until February 1, 1991. To extend the closing date one month, a written request must be filed with the ASCE Manager of Journals. The manuscript for this paper was submitted for review and possible publication on March

(Krone 1963; Migniot 1968; Gularte 1978; Englund and Zhaohui 1984) was selected recently by Mei and Liu (1987) in an analytical approach to solve the motion of a vertical one-dimensional water-mud system. Most muds, this model yields quite large velocities in the mud layer unless an unrealistically large mud viscosity is selected (Maa 1986). An elastic model was used by Mailard and Dalrymple (1977) and Dawson (1978). The evident drawback of this model for present purposes is that it does not account for energy dissipation. The poro-elastic model chosen by Yamamoto (1983) and Yamamoto and Takahashi (1985) does not enable typically low permeability cohesive sediment beds to conform to this model. The Bingham fluid model however, exhibit a pseudoplastic behavior at low rates of strain, and thereever, these models are evidently not globally applicable to the type of wavesoft mud interaction problem considered here. For example, a viscous fluid model was used by Gade (1958) and Dalrymple and Liu (1978); however, applicable models are available, and these have been used by researchers with various degrees of success in their respective areas of interest. Howof soft mud beds is in itself an interesting subject, since sever fore only approximate Bingham plastic behavior.

in these two studies, the results indicated that the Voigt model is capable of onstrating that the Voigt model is indeed a more suitable choice than, for While the Voigt description is by no means the ideal or even final choice considering the complexity of mud rheological behavior, this description was used in the present study to develop a relatively simple predictive model for selected by MacPherson (1980) and Hsiao and Shemdin (1980) to simulate simulating significant wave damping associated with relatively small bottom example, another simple viscoelastic description, namely the Maxwell model. A simple viscoelastic constitutive description, the Voigt model, has been the attenuation of water waves. Although some simplifications were made motions. Maa and Mehta (1988) also gave simple rheometric evidence demwave-mud system response.

sented. The approach is based on a linearized set of equations, which are thus applicable to small deformations only. Laboratory experiments (Maa 1986) and even some field evidence, e.g., that of Tubman and Suhayda (1976), suggest that the small deformation assumption is not always overly restrictive. Hence, the results should find application under conditions wherein It is also noteworthy that previous studies with some exceptions, e.g., Yamamoto's numerical model (1983) and the more recent work of Nakano et al. (1987), have assumed only one mud layer with constant properties. Such has been the case even though the concept of bed layering, and particularly its simulation in cohesive sediment transport modeling, is not new (Ariathurai and Krone 1976). Fluid shear in the water column has also been typically neglected, except, for example, in Dalrymple and Liu's (1978) approach. In this paper, an analytical approach that treats mud as a continuum and accounts for the rheology of soft, mobile mud beds, the depth-varying bed properties, and the effects of shear in the water column, is briefly prelarge bed deformations are not involved, as is often the case in small laboratory flumes.

CONSTITUTIVE MODEL FOR MUD BED

The mud beds considered here are limited to those with sediment concentrations in excess of 150 gL⁻¹, and in general those that are partially

conso_ted. In other words, fluidized mud with lower concentrations is excluded from this analysis. The Voigt constitutive model is based on the mechanical analogy of a spring-dashpot system. The constitutive equation is

$$\mathbf{T}' = 2G\mathbf{E}' + 2\mu\dot{\mathbf{E}}'. \tag{}$$

where T and E = the stress and strain tensors, respectively; prime indicates the deviator part of these two tensors; the dot indicates derivative with respect to time; and G and μ = the shear modulus of elasticity and viscosity, respectively, which are treated as constants in the described approach.

Macpherson (1980) considered the simple harmonic motion of mud beds representing the shear modulus as the imaginary part of an apparent viscosity v_{\star} (see Eq. 2), keeping the kinematic viscosity as the real part:

$$v_{e} = v + j \frac{G}{\rho \sigma} \tag{2}$$

where $j = (-1)^{1/2}$, $\rho = \text{mud}$ bulk density; $\sigma = 2\pi/T$; and T = the wave period. This approach greatly simplifies the equations of motion of a simple viscoelastic material under oscillatory loading and is conveniently incorporated into the formulation described next.

MODEL FORMULATION

Momentum and Continuity

Fig. 1 is a definition sketch of the water-mud system in which water waves propagate in the x-direction, with free surface displacement η . The water layer has a thickness d_1 and the underlying mud bed is considered to be composed of several layers of the Voigt material with thicknesses d_i ($i = 2, 3, \ldots, N$, where N is the total number of layers). The displacement at each interface is ξ_1 , ξ_1 being the mud-water interfacial displacement. The displacements η and ξ_i can be expressed simply as

$$\eta = a_0 \exp \left[j(kx - \sigma t) \right]. \tag{3a}$$

$$\xi_i = b_{0i} \exp \left[j(kx - \sigma t) \right] \dots (3b)$$

where a_0 = the given water wave amplitude at x = 0; b_{0i} = unknown com-

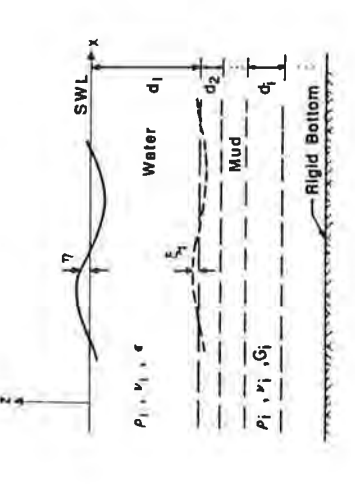


FIG. 1. Schematic Drawing of Multilayered Water-Mud System

plex variables for the interfacial wave amplitudes and phases = 0; t = time; and k = a complex wave number. The real part of k, i.e., k, = $2\pi/L$, is related to the wavelength, L. The imaginary part, k_m , represents the wave attenuation coefficient defined as

$$a(x) = a_0 \exp(-k_{im}x)$$
 (4)

This expression has been shown to be acceptable in representing wave decay in flumes (Schuckman and Yamamoto 1982; Nagai et al. 1982).

The linearized equations of motion for the incompressible upper fluid (water) and incompressible viscoelastic mud layers under oscillatory loading are

$$\frac{\partial u_i}{\partial t} = -\frac{1}{\rho_i} \frac{\partial p_i'}{\partial x} + \nu_{ei} \left(\frac{\partial^2 u_i}{\partial x^2} + \frac{\partial^2 u_i}{\partial z^2} \right) \tag{5a}$$

$$\frac{\partial w_i}{\partial t} = -\frac{1}{\rho_i} \frac{\partial p_i'}{\partial z} + \nu_{ei} \left(\frac{\partial^2 w_i}{\partial x^2} + \frac{\partial^2 w_i}{\partial z^2} \right) \tag{5b}$$

where u and w = velocities in the x- and z-directions, respectively. For the water layer the apparent viscosity v_{c1} contains the kinematic viscosity v_{c1} and a constant eddy viscosity ϵ . The purpose of including ϵ in the model is for bed shear stress calculation, rather than for simulation of wave motion in the water column, inasmuch as over most of the water column, except near the bed, the pressure and inertial forces are usually dominant. Ama and Mehta (1989) have presented one method to estimate ϵ in such system. In this method, the model is used to solve for the bed shear stress for the rigid bed condition, which is simulated by using a high value of G e.g., on the order of G Nm⁻². The bed shear stress is then calibrated against commonly available data for such a system by adjusting ϵ .

For each mud layer, v_n contains a kinematic viscosity v_l and a shear modulus G_l as mentioned earlier. The term p' is the total pressure defined as

$$a_i^{\dagger} = p_i - p_i g_z - p_i^0$$
 (6a)

pue

$$a_i^0 = 0$$
, for $i = 1$

$$p_i^0 = \sum_{m=1}^{i-1} \left\{ (p_{m+1} - p_m) g\left(\sum_{r=1}^{i-1} d_r\right) \right\}, \quad \text{for } i > 1 \dots (6b)$$

where m and r = dummy indices.

The continuity equation is

$$\frac{\partial u_i}{\partial x} + \frac{\partial w_i}{\partial z} = 0 \tag{7}$$

Following Dalrymple and Liu (1978), solutions for velocities and pressure are assumed separable according to

$$u_i(x,z,t) = \hat{u}_i(z) \exp \left[j(kx - \sigma t)\right] \dots$$
 (8a)

$$w_i(x,z,t) = \hat{w}_i(z) \exp \left[j(kx - \sigma t)\right] \dots (8b)$$

$$p_i(x,z,t) = \hat{p}_i(z) \exp \left[j(kx - \sigma t)\right] \dots (8c)$$

Substitute, if Eqs. 8a and b into the continuity equation, one obtains

$$a_i = \frac{j}{k} \hat{w}_i' \tag{6}$$

where the prime in this case indicates differentiation with respect to z. Introducing Eqs. 8 and 9 into Eq. 5a yields

$$\hat{\boldsymbol{\rho}}_i = \left(\frac{\boldsymbol{\mu}_{ci}}{k^2}\right) (\hat{\boldsymbol{w}}_i'' - \hat{\boldsymbol{w}}_i' \lambda_i^2) \tag{10}$$

in which $\lambda_i^2 = k^2 - j\sigma v_{ei}^{-1}$. Substituting \hat{p}_i into Eq. 5b yields the equation $\hat{w}_i''' - (k^2 + \lambda_i^2)\hat{w}_i'' + k^2\lambda_i^2\hat{w}_i = 0$. (11)

The solutions for the water layer and the underlying mud layers are of the form

$$\hat{\mathbf{w}}_1(z) = A_1 \sinh Z_1 + B_1 \cosh Z_1 + C_1 \exp (\lambda_1 z)$$

$$+ D_1 \exp [-\lambda_1(z + d_1)]$$
....(12a)

$$\hat{w}_i(z) = A_i \sinh Z_i + B_i \cosh Z_i + C_i \sinh N_i + D_i \cosh N_i \dots (12b)$$

in which $Z_i = k(d_1 + d_2 + ... + d_i + z)$; and $N_i = \lambda_i(d_1 + d_2 + ... + d_i + z)$. Finally, the shear stress τ can be obtained from

$$\tau = \frac{J}{k} \mu_e(\hat{w}'' + k^2 \hat{w}) \exp \left[j(kx - \sigma t) \right] \dots (13)$$

To solve Eqs. 12a and 12b, 5N boundary conditions are required. For only one mud layer, there are eight unknown complex coefficients in Eq. $12 (A_1, ..., D_2)$ and two unknown complex variables $(k \text{ and } b_{01})$. Therefore, 2N = 10 boundary conditions are required. These 10 boundary conditions, presented by Dalrymple and Liu (1978) in their viscous fluid model, have also been selected in this study because of their completeness. A simple method was developed to solve for Eq. 12, enabling N to be assigned any positive integral value to account appropriately for the depth variation of bottom-mud properties. To illustrate this approach, the 10 boundary conditions for just two layers are noted in what follows; details have been given elsewhere (Dalrymple and Liu 1978; Maa 1986).

Boundary Conditions

At the free surface, there is no external driving force (e.g., wind). Therefore, the normal stress and the shear stress are zero. The third boundary condition is the linearized kinematic boundary condition at the mean water surface. These three surface boundary conditions give three equations that are reduced to two by eliminating the known wave amplitude a_0 to obtain a homogeneous matrix equation for solution purposes. At the mean water-mud interface the horizontal velocity, vertical velocity, normal stress, and shear stress for the water and mud layers are matched. The linearized kinematic boundary condition at the mean water-mud interface serves as the eighth boundary condition. At the rigid bottom $(z = -d_1 - d_2)$, the no-slip condition (u = w = 0) must be satisfied. These nine equations, derived from the 10 boundary conditions, can be written in the form of $\mathbf{X} = 0$, where

c is a 9×9 homogeneous matrix, and X is a column matrix tt. Jontains the coefficients A_1 , B_1 , ..., and b_{01} . The unknown complex wave number k is involved in the matrix c. This represents an eigenvalue problem, since the system has solutions only for special k values for which the matrix c is singular, i.e., the determinant of c is zero (Wylie 1966).

Selecting two layers instead of one for the mud would mean five more unknowns; four coefficients from Eq. 12b and b_{20} for the mud-mud interfacial wave amplitude. Five corresponding additional boundary conditions must also be specified; matching the horizontal velocities, the vertical velocities, the shear stresses, and the normal stresses at the mud-mud interface, and the linearized kinematic boundary condition at this interface. The size of matrix c in this case expands to 14×14 , and five more coefficients $(A_3 - D_3)$, and b_{02}) are appended to the column matrix X. The matrix equation, however, remains in the same form, and the same technique can be used to solve it. The generation of matrix c can be performed iteratively, and a computer program can handle any number of layers easily.

The secant method (Grove 1966) was used to find the complex wave number k by rendering the coefficient matrix \mathbf{c} singular. In this approach, the first guess of k, denoted k, is selected as though the mud layers were rigid. Thus k_1 is a real number, and the subsequent modifications to the k value represent the influence of nonrigid mud layers. The absolute difference between two consecutive complex wave numbers, $|k^{r+1} - k^r| < 10^{-14}$, was used as the convergence criterion instead of setting $|\mathbf{c}| = 0$. This criterion requires only a reasonable number of iterations (e.g., less than 40) to obtain the final result.

Other eigenvalues for this system of equations are possible; however, they are not physically meaningful because the occurrence of soft mud layers only modifies to some extent the characteristics of the water waves. In other words, the meaningful eigenvalue should be around k_1 . Thus, the eigenvalue obtained by this procedure yields the desired wave number.

The elements of the column matrix X, obtained by solving the matrix equation, do not represent the true answers, but are proportional to the true values of the variables sought. One of the water surface boundary conditions is then invoked to obtain the proportionality constant, and from it the true A, B, ... and b, ... Pressure, velocity, and shear stress amplitudes are then determined from Eqs. 9, 10, and 13.

RESULTS

Application

The model was applied to 13 test cases derived from a series of experimental runs carried out in a 20-m-long and 45-cm-wide wave flume. Experimental details can be found elsewhere (Maa 1986; Maa and Mehta 1987). The mud beds were placed in the center 8-m test section of the flume. Progressive, nonbreaking waves were generated by a plunging-type wave-maker upstream of the test section. The total mud thickness in these experiments was varied from 11 cm to 15 cm. Bed sediment composition, period of bed consolidation, wave amplitude a₀, and period T for each case are given in

In Table 2, water and mud layer thicknesses as well as the coefficients defining water and mud layer shear modulus and viscosity for each mud

TABLE 1. Bed and Wave Conditions and Calculated Interfacial Shear Stress

		Consolidation	Wave	Wave	Shear
굞		period	amplitude, a,	period, /	Stress, Tho
number	Sediment	(day)	(cm)	(s)	(EN)
Ξ	(2)	(3)	(4)	(2)	(9)
=	Kaolinite	7	3.3	1.9	0.25 (0.19)
1-2	Kaolinite	7	5.4	1.3	0.39 (0.30)
2-1	Kaolinite	4	2.7	1.9	0.17 (0.16)
2-2	Kaolinite	14	4.4	1.2	0.29 (0.29)
3-1	Kaolinite	2	2.7	1.8	0.21 (0.18)
3-2	Kaolinite	2	3.8	1.2	0.29 (0.26)
4-1	C. K. mud.	7	3.7	9.1	0.20 (0.19)
4-2	C. K. mud"	7	6.2	1:1	0.30 (0.29)
5-1	C. K. mud	2	4.4	1.7	(72.0) 72.0
5-2	C. K. mud*	2	8.9	1.2	0.42 (0.43)
1-9	C. K. mud*	4	3.8	8.	0.23 (0.20)
6-2	C. K. mud"	14	5.6	1.4	0.35 (0.31)
6-3	C. K. mud	14	7.3	1.0	0.43 (0.38)

[&]quot;A mixture of kaolinite and natural mud from Cedar Key, Florida.

layer are given. These, together with water and mud densities, constitute the input data for the model. Separate rheometric experiments to measure the viscoelastic parameters were conducted (Maa and Mehta 1988). The shear modulus G (Nm⁻²) and μ (Nsm⁻⁷) were empirically correlated with mud dry density (concentration), ρ_0 (kg m⁻³), as follows:

TABLE 2. Water and Mud Layer Thicknesses and Viscoelastic Coefficients

	2	lud Lay	Mud Layer Thicknesses	knesse	S	Shear Coeff	Shear Modulus Coefficients	Viscosity Coefficien	Viscosity Coefficients
Run number	(cm)	d_2 (cm)	d, (cm) (4)	d ₄ (cm) (5)	<i>d</i> , (cm) (6)	(Nm ⁻²)	m (m³kg ⁻¹) (8)	(Nsm ⁻²)	" (m³kg ⁻¹) (10)
3	21.7	2.5	2.5	4.0	5.0	3.0	10.63	270	-3.38
1-2	24.2	1.5	3.0	3.0	4.0	3.0	10.63	270	-3.38
2-1	19.2	1.5	3.0	3.0	4.0	83.0	0.56	305	-0.89
2-2	19.7	1.0	3.0	3.0	4.0	83.0	0.56	305	-0.89
3-1	16.2	2.5	3.0	4.0	5.0	0.74	12.14	1,150	-5.98
3-2	18.2	1.5	2.0	4.0	5.0	0.74	12.14	1,150	-5.98
4-1	26.4	1.3	2.0	3.0	3.0	0.78	18.23	330	-4.12
4-2	28.7	1.0	1.0	2.0	3.0	0.78	18.23	330	-4.12
5-1	19.7	2.0	3.0	5.0	0.9	7.4	8.43	56	11.11
5-2	21.1	1.6	2.0	5.0	0.9	7.4	8.43	56	11.11
6-1	24.7	1.0	2.0	3.0	5.0	3.0	18.65	250	-4.34
6-2	25.2	0.5	2.0	3.0	5.0	3.0	18.65	250	-4.34
6-3	25.2	0.5	2.0	3.0	5.0	3.0	18.65	250	-4.34

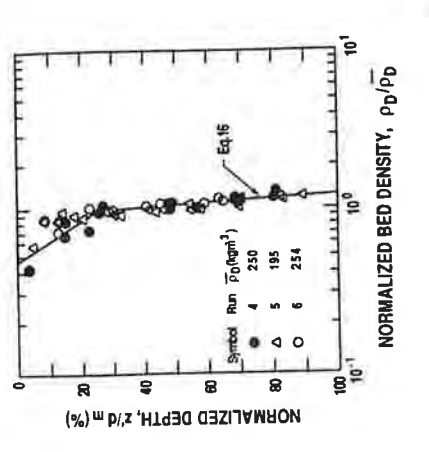


FIG. 2. Dimensionless Mud Dry Density (Concentration) Profiles for Beds of Cedar Key Mud

where G_0 , μ_0 , m, and n= constant coefficients (Table 2). These operational correlations are based on a purely empirical approach; a better approach is pending further investigation. However, such expressions are likely to find continued application in practice, since the density is an easily measured parameter in the laboratory and particularly in the field.

Fig. 2 illustrates plots (runs 4, 5, and 6) of the measured dry density p_D normalized by the depth-averaged dry density \bar{p}_D versus the normalized mud elevation z'/d_m , where the coordinate z' increases downwards from the watermud interface and d_m is the total bed thickness. These density profiles are typical of beds that are not fully consolidated, exhibiting a marked density variation in this case over the top 25% of the bed thickness. The following relationships were used (similar relationships were obtained for runs 1, 2, and 3)

$$\frac{p_D}{\tilde{p}_D} = 0.46 \exp\left(2.831 \frac{z'}{d_m}\right), \quad \text{for } \frac{z'}{d_m} \le 0.25$$

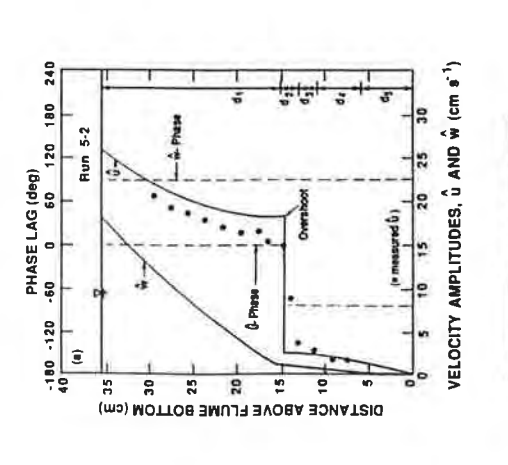
$$\frac{p_D}{\hat{p}_D} = 0.84 \exp\left(0.410 \frac{z'}{d_m}\right), \quad \text{for } \frac{z'}{d_m} > 0.25$$
 (16)

The bulk density ρ required to run the multilayered model was obtained from ρ_D , given the grain density $\rho_s = 2.60 \text{ gcm}^{-3}$ and water density $\rho_w = 1 \text{ gcm}^{-3}$. Selection of the number of mud layers and thicknesses was guided by the

Selection of the number of mud layers and thicknesses was guided by the need to simulate adequately the variation of measured density profile. For the water layer the following values were selected: $p_w = 1,000 \text{ kgm}^{-3}$, $\nu_1 = 1 \times 10^{-6} \text{ m}^3\text{s}^{-1}$, and $\epsilon = 0$ (because of the relatively small wave Reynolds numbers in the experiments, $R_w < 10^4$; see for example Jonsson 1966). Model results in terms of velocities, pressure, and shear stress, as well as the corresponding wave attenuation coefficient, are illustrated by examples given herein.

Velocities

As might be expected, the horizontal wave velocity amplitude, \hat{u} , was reduced significantly in the mud layers. Also, the phase shifted between 90°



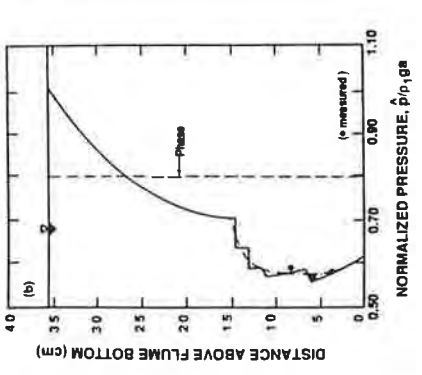


FIG. 3. Comparison between Model Simulated and Measured Quantities for Run 5-2: (a) Velocities; and (b) Pressure

to 120° in the mud layers relative to the water layer. In Fig. 3(a), this shift is approximately 90°. Fig. 3(b) shows the corresponding pressure profile, which is discussed later. The wave boundary layer thickness for the mud layers, $(v_{el}/2\sigma)^{1/2} \approx 10$ cm, was greater than the thickness of each layer in Fig. 3(a), and resulted in the buildup of a horizontal velocity overshoot above the water-mud interface. Measured horizontal velocities in water (obtained by an electromagnetic current meter) and in mud layers (obtained by visual observation of the motion of particles) are also shown (Maa 1986). The limited data show reasonable agreement with laboratory flume data presented by Migniot (1968). Also, representative shear strains within the mud were less than about 0.09 rad (Maa 1986). At this upper strain limit, soft mud can be assumed to be approximately linear-viscoelastic, although Stevenson (1973), among others, observed some nonlinear effects at strains exceeding 0.04 rad.

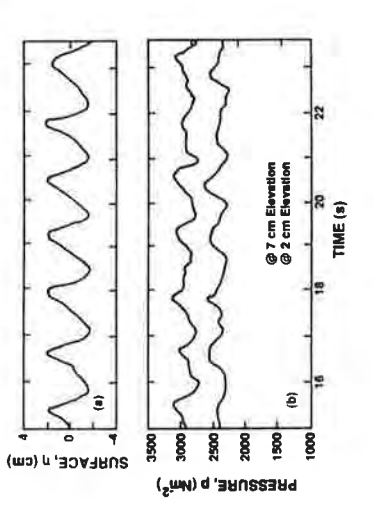


FIG. 4. Measurements of (a) Water Surface Elevation Fluctuation; and (b) Dynamic Pressures in Mud Layer

ressure

By virtue of the governing equations selected, the dynamic pressure within the mud is always in phase with that in the water layer. Fig. 4, which shows pressure measurements both in the water and mud layers, generally supports this phase equality.

The solid line in Fig. 3(b) shows an example of the calculated profile of the pressure amplitude β normalized by $\rho_i ga$. Measured pressure amplitudes within mud are also displayed. The calculated amplitude decreases downwards in the water column, drops at each interface, and increases within a mud layer. This type of behavior can be explained easily by the following:

$$p = -\sigma_{\eta} + 2\mu \frac{\partial w}{\partial z}.$$
 (17)

$$\frac{\partial \hat{p}}{\partial z} = p[j\sigma\hat{w} - (k^2\hat{w} - \hat{w}'')\nu_e].....(18)$$

Inasmuch as the boundary condition requires that the normal stresses at an interface be equal, a significant change in $\mu \partial w/\partial z$ will cause a corresponding drop in the dynamic pressure (Eq. 17). At the interface between two consecutive mud layers there is a measurable increase in μ , even though there may be only a small change in $\partial w/\partial z$; this leads to a large drop in pressure across the interface. Eq. 18 can be used to explain why the pressure increases in a mud layer. For low-viscosity fluid (e.g., water), the first term on the right-hand side of Eq. 18 dominates, and therefore yields a positive pressure gradient. With the coordinate origin located at the water surface, $\partial p/\partial z$ is negative downwards, and therefore p decreases with depth in the water layer. In a mud layer where ν_i is large, the second term is also important and may result in a negative pressure gradient, and thus the pressure may increase, as shown in Fig. 3(b). Since the model uses layers of mud that have constant properties to simulate continuously varying bed properties, the true pressure profile may be represented by a smooth curve, e.g., the broken line in Fig. 3(b).

Shear Stress

The shear stress is negligible in the water column except near the water-

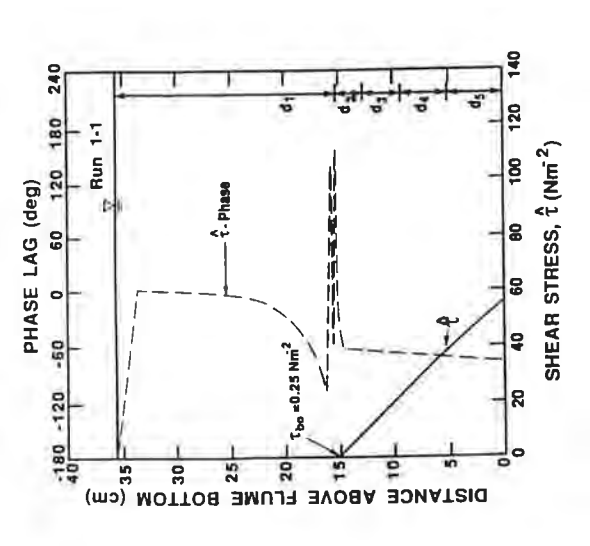


FIG. 5. Simulated Shear Stress Profile for Run 1-1

mud interface (see Fig. 5). In the bed, the shear stress amplitude increases practically linearly with depth. This linearity is possibly due to the small total mud thickness, which is less than 20% of the wavelength. For a relatively large mud thickness, the shear stress would eventually reach a maximum and then decrease (Mallard and Dalrymple 1977). The phase of the shear stress in the mud layers exhibits a nearly 90° shift, which implies that the shear stress in the mud is induced by the longitudinal variation of wave pressure at the mud surface.

The comparatively high shear stress in the mud causes the mud layers to oscillate with the water wave. At the water-mud interface the calculated shear stress τ_{10} was 0.25 Nm^{-2} in run 1-1. However, during the experiments the bed structure was not materially destroyed, and mass or bulk erosion (Mehta 1986) of mud layers did not occur. In fact, erosion occurred only at the water-mud interface by floc entrainment resulting from the application of shear stress (Maa and Mehta 1987).

Model-calculated shear stress amplitudes at the water-mud interface τ_{10} for the 13 test cases are listed in Table 1. Corresponding calculated shear stress amplitudes based on the rigid bed assumption using the formulation proposed by Jonsson (1980) and the friction factor proposed by Kamphuis (1975) are listed in parentheses for comparison. The model predicts generally larger τ_{10} (up to 30%) than those over a corresponding rigid bed. This difference is the result of the opposite (100°–120° phase lag) motion between water and mud (Maa 1986).

Water Wave Decay

A comparison between predicted and measured wave attenuation coefficients k_{im} is given in Fig. 6. The viscous damping mechanism within mud implies that the greater the mud velocity, the higher the rate of energy dis-

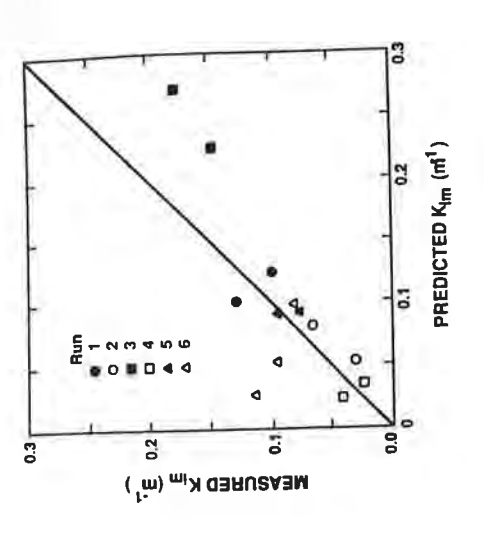


FIG. 6. Comparison between Measured and Predicted Wave Attenuation Coefficients

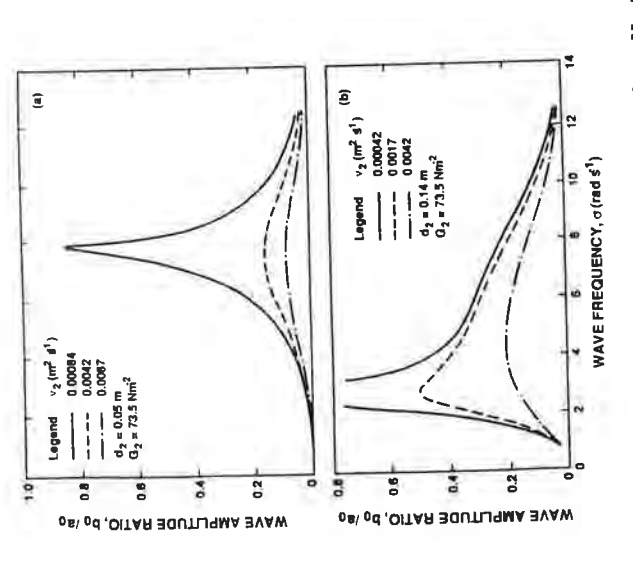
sipation (Maa and Mehta 1988). Therefore, k_{im} varies strongly with the degree of bed consolidation, e.g., kaolinite bed of the 2-day consolidation period in run 3 damped the water wave much more than the bed of the 14-reported by, among others, Schuckman and Yamamoto (1982). Bed sediment composition likewise influences surface wave damping. For two-day and seven-day consolidation periods, damping was greater with kaolinite than Cedar Key mud. This trend was reversed, however, at 14 days. In general, model predictions are consistent with measurements with regard to the effects of consolidation and sediment composition on wave damping.

Resonance Characteristics

The selection of the Voigt model for mud bed rheology can lead to resonance when the frequency of oscillatory loading approaches the natural frequency of the system. This behavior is due to the characteristics of the spring in the Voigt element. For a two-layered system, Fig. 7 demonstrates resonance by the large ratio of mud surface amplitude b_0 to water wave amplitude a_0 . Fig. 7(a) shows calculated amplitude ratios for a system with a 30-cm-deep water layer and a 5-cm-thick mud layer. Fig. 7(b) shows the response of a similar system that has a 21-cm water layer and a 14-cm mud layer. Notice the different peak resonance frequencies caused by the different mud layer thickness, with resonance occurring at lower frequencies in a thicker

The significance of the resonance behavior of the water-mud system is that this feature might be useful in identifying the viscoelastic constants G and µ. A similar technique, the resonant column method, was developed to measure Young's modulus and shear modulus for clays with typically low water contents (Prakash 1981). Although this issue is beyond the scope of the present study, it is an interesting topic for further investigation. In the 13 laboratory tests, however, no noticeable resonance was observed. This may have been due to the frequency of wave loading's being far from the

ō



Calculated Resonance Response In Two-Layered Water-Mud System: (a) with $d_2 = 5$ cm; and (b) with $d_2 = 14$ cm

thermore, the depth-varying mud properties and the inherently nonlinear reresonance frequency, as well as due to comparatively high values of μ . Fursponse of mud may be complicating factors.

Model Limitation

mud interface, requires consideration of the nonlinear effects, which must tially, the Taylor expansion technique is used, and only the basic harmonic term is considered. Thus, this approach implies that the system is applicable only to small-amplitude waves. To study an important feature of the waterbe included in future studies. Furthermore, inclusion of nonlinear response of the mud beds, e.g., as in the bilinear model of Thiers and Seed (1968), mud-mud interfaces are unknown a priori, the boundary conditions specified at those levels have been applied at the corresponding mean levels. Essenmud system, namely horizontal mass transport of sediment near the watershould materially improve model performance at large deformations and res-Because the actual free water surface, the water-mud interface, and the

vation of sediment mass, thus enabling the model to simulate the wave-The model assumes no net vertical transport of sediment. This limitation induced sediment erosion process as the next step in understanding the turcan essentially be removed, if desired, by adding the equation of conserbidity-generation problem.

original shear strength under cyclic wave loading. The lost shear strength is recovered gradually after this loading is removed. However, the mechanisms In laboratory experiments, Nagai et al. (1982), Schuckman and Yamamoto (1982), and Figueroa et al. (1985) found that the mud loses a part of its

absequent erties could not be included in the present model. However, since the model the time dependence of mud properties, if known, can be incorporated in recovery are not well understood. Thus the time-dependence of mud propis capable of simulating system response whenever mud properties are known, leading to bed strength degradation under wave loading or it the model easily.

Inasmuch as the mud is treated as a continuum, seepage motion of pore water is not accounted for in the model. For cohesive sediments having typically low permeability, this would be a reasonable assumption, but not necessarily for fine-grained and mostly noncohesive sediments with higher permeabilities.

1978). Thus, relationships similar to Eqs. 14 and 15 can be obtained. This shallow water environments. Furthermore, the required density profile can measurements could conceivably be modified for in situ measurements in be obtained by using, for example, a nuclear densitometer (Nichols et al. cially available instrumentation to obtain such information. It is noteworthy, however, that procedures described by Maa and Mehta (1988) for laboratory properties are required. At present, there are no easy methods or commen-To apply this model to field cases, vertical profiles of mud viscoelastic can be an objective for future studies.

CONCLUDING REMARKS

position on wave damping. Predicted velocities in water and mud showed reasonable agreement with limited data. The case was the same with dyfacial bed shear stresses were, in general, larger than the bed shear stresses tween water and mud. In the absence of direct measurements of water-mud interfacial stress, this model provides a useful method for evaluating this stress in laboratory flumes, which is essential for calculating the rate of eronamic pressure variation within the mud. The calculated water-mud intercalculated by assuming the mud to be rigid, due to out-of-phase motion be-A linearized multilayered model was used to simulate approximately the dynamics of wave-mud interaction. A simple viscoelastic model, the Voigt model, was selected for modeling mud rheology and energy dissipative characteristics under small deformations. The model showed the predicted wave attenuation coefficients to be generally in agreement with flume measurements, highlighting the influences of bed consolidation and sediment comsion of cohesive sediments by waves.

ACKNOWLEDGMENT

iment Station, Vicksburg, Miss., for financial support under Contract DACW39-84-C-0013. This paper is a contribution of the Virginia Institute Acknowledgement is due to the U.S. Army Engineer Waterways Experof Marine Science, No. 1601.

APPENDIX 1. REFERENCES

Alishahi, M. R., and Krone, R. B. (1964). "Suspension of cohesive sediment by wind-generated waves." *Tech. Rept. HEL-2-9*, Hydr. Engrg. Lab., Univ. of California, Berkeley, Calif.

647

1972). "Resuspension of estuarine sediments by small amplitude waves." J. Sed. Fet., 42(3), 602-607.

Ariathurai, R., and Krone, R. B. (1976). "Finite element model for cohesive sediment transport." J. Hydr. Div., ASCE, 102(3), 323-338.

Dalrymple, R. A., and Liu, P. L.-F. (1978). "Waves over soft muds: A two-layer fluid model." J. Phys. Ocean., 8, Nov., 1121-1131.

Dawson, T. H. (1978). "Wave propagation over a deformable sea floor." Ocean

Engelund, F., and Zhaohui, W. (1984). "Instability of hyperconcentrated flow." J. Engrg., 5(4), 227-234.

Gade, H. G. (1958). "Effects of a nonrigid impermeable bottom on plane surface Hydr. Engrg., ASCE, 110(3), 219-232.

waves in shallow water." J. Mar. Res., 16(2), 61-82. Grove, W. E. (1966). Brief numerical methods. Prentice-Hall, Englewood Cliffs,

sented to the University of Rhode Island, at Kingston, R.I., in partial fulfillment Gularte, R. G. (1978). "Erosion of cohesive sediment as a rate process," thesis preof the requirements for the degree of Doctor of Philosophy.

Hsiao, S. V., and Shemdin, O. H. (1980). "Interaction of ocean waves with a soft bottom." J. Phys. Ocean., 10(4), 605-610.

fackson, J. R. (1973). "A model study of the effects of small amplitude waves on the resuspension of fine-grain cohesive sediments," thesis presented to the University of New Hampshire, at Durham, N.H., in partial fulfillment of the requirements for the degree of Master of Science.

onsson, I. G. (1966). "Wave boundary layer and friction factors." Proc., 10th Coast.

Engrg. Conf., ASCE, 1, 127-148. Ionsson, I. G. (1980). "A new approach to oscillatory rough turbulent boundary

layers." Ocean Engrg., 7(1), 109-152.

Kamphuis, J. W. (1975). "Friction factor under oscillatory saves." J. Wirwy., Port, Coast. Engrg. Div., ASCE, 101(2), 135-144.

Krone, R. B. (1963). "A study of rheologic properties of estuarial sediments." Tech.

Bull. No. 7, Committee on Tidal Hydr., U.S. Army Corps of Engrs., Wtrwys. Experiment Sta., Vicksburg, Miss.

Maa, P.-Y. (1986). "Erosion of soft muds by waves," thesis presented to the University of Florida, at Gainesville, Fla., in partial fulfillment of the requirements

for the degree of Doctor of Philosophy.

Maa, P.-Y., and Mehta, A. J. (1987). "Mud erosion by waves: A laboratory study." Cont. Shelf Res., 7(11/12), 1269–1284.
Maa, J. P.-Y., and Mehta, A. J. (1988). "Soft mud properties: The Voigt model." J. Wirwy., Port, Coast., and Ocean Engrg., ASCE, 114(6), 765–769.

Maa, J. P.-Y., and Mehta, A. J. (1989). "Considerations on bed response in wave resuspension of muds." Estuarine circulation, B. J. Neilson, A. Kuo, and J. Brubaker, eds., Humana Press, Clifton, N.J., 309-336.

Mathews, J. H. (1987). Numerical methods. Prentice Hall, Englewood Cliffs, N.J. Macpherson, H. (1980). "The attenuation of water waves over a non-rigid bed." J.

Fluid Mech., 97(4), 721-742.

Mallard, W. W., and Dalrymple, R. A. (1977). "Water waves propagating over a deformable bottom." Proc., 9th Offshore Tech. Conf., 3, Houston, Tex., 141-

Mehta, A. J. (1983). "Characterization tests for cohesive sediments." Proc., Fron-

iters of Hydr. Engrg. Conf., ASCE, Cambridge, Mass., 79-84.
Mei, C.-C., and Liu, K.-F. (1987). "A Bingham-plastic model for a muddy scabed under long waves." J. Geophys. Res., 92(13), 14581-14594.

Migniot, C. (1968). "A study of the physical properties of various forms of very fine sediment and their behavior under hydrodynamic action." La Houille Blanche, 7, 591-620 (in French, with English abstract).

Nagai, T., Figueroa, J. L., and Yamamoto, T. (1982). "Nonlinear mechanics of seabed interactions, part III--Wave tank experiments on soil mass transport in clay beds associated with wave damping." Rept., Rosenstiel Sch. of Marine and Atmospheric Sci., Univ. of Miami, Miami, Fla.

ing of mud layer due to an interaction of waves with a mud bottom." Report of Port and Harb. Res. Inst., 26(2), 172-212 (in Japanese with English abstract). Nakano, S., Tsuruya, H., and Takahama, J. (1987). "On wave attenuati

Nichols, M. M., Thompson, G. S., and Faas, R. W. (1978). "A field study of fluid mud dredged material: Its physical nature and dispersal." Tech. Rept. D-78-40,

U.S. Army Engr. Wtrwys. Experiment Station, Vicksburg, Miss.

Parchure, T. M. (1984). "Erosion behavior of deposited cohesive sediments," thesis presented to the University of Florida, at Gainesville, Fla., in partial fulfillment of the requirements for the degree of Doctor of Philosophy.

Prakash, S. (1981). Soil dynamics. McGraw-Hill, New York, N.Y.

clay beds." Tech. Rept. TR 82-1, Rosenstiel Sch. of Marine and Atmospheric Sci., Schuckman, B., and Yamamoto, T. (1982). "Nonlinear mechanics of sea-bed interactions, part II—Wave tank experiments on water wave damping by motion of Univ. of Miami, Miami, Fla.

Stevenson, H. S. (1973). "Vane shear determination of the viscoelastic shear modulus of submarine sediments," thesis presented to Texas A & M University, at College Station, Tex., in partial fulfillment of the requirements for the degree of Master of Science.

Thimakom, P. (1984). "Resuspension of clays under waves." Seabed Mech., B.

Denness, ed., Graham & Trotman, London, United Kingdom, 191-196. Tubman, M. W., and Suhayda, J. N. (1976). "Wave action and bottom movements in fine sediments." Proc, 15th Coast. Engrg. Conf., ASCE, 2, 1168-1183.

van Rijn, L. C. (1985). "The effect of waves on kaolinite/sand beds." Rept. M2060, Delft Hydraulics, Delft, The Netherlands.

Wells, J. T. (1983). "Dynamics of coastal fluid muds in low-, moderate-, and hightide-range environments." Can. J. Fish. and Aquat. Sci., 40(1), 130-142. Wylie, C. R. (1966). Advanced engineering mathematics. 3rd Ed., McGraw-Hill,

New York, N.Y.

waves." J. Soil Dyn. and Earthquake Engrg., 2(2), 92-100. Yamamoto, T., and Takahashi, S. (1985). "Wave damping by soil motion." J. Wtrvy., Yamamoto, T. (1983). "Numerical integration method for seabed response to water

Port, Coast., and Ocean Engrg., ASCE, 111(1), 62-77.

APPENDIX II. NOTATION

The following symbols are used in this paper:

surface wave;

surface wave amplitude at x = 0;

ith interfacial mud wave amplitude at x = 0, a complex num-

complex coefficient matrix c(i,j);

Ш

thickness of ith layer; d

total mud layer thickness; 11

11

small strain tensor, $E_{ij} = 0.5[\partial \xi_i/\partial x_j + \partial \xi_j/\partial x_i)$; deviator part of the small strain tensor, $E_{ij}' = E_{ij} - E_{rr}/3$; 11

rate of shear strain; П $\vec{E}\cdot\vec{E} \stackrel{a}{E} \vec{J}$

shear modulus of elasticity; 11

shear modulus related coefficient; 11 ပ်

gravitational constant, 9.8 m/s^2 ; 11

free indices; ĮĮ. g.

shear modulus related coefficient or free indices; Ш

free index or $(-1)^{1/2}$;

complex wave number, $k = k_r + jk_{im}$;

```
imaginary part of the complex wave number, also the wave
                                               attenuation coefficient;
```

real part of the complex wave number;

wavelength;

number of layers in the hydrodynamic model;

viscosity related coefficient;

dynamic pressure;

correction term for the static pressure resulting from density

difference;

total pressure;

dynamic pressure amplitude;

wave Reynolds number;

wave period or stress tensor;

deviator part of the stress tensor, $T'_{ij} = T_{ij} - T_{rr}/3$;

horizontal and vertical velocities, respectively, in the x- and zu. W.

directions for the ith layer;

horizontal and vertical velocity amplitudes; a_i, \hat{w}_i

first and second derivatives of $\hat{w_i}$ with respect to z;

ongitudinal direction;

column matrix containing $A_1, B_1, \ldots, C_N, D_N$, and $b_{0,N-1}$;

vertical coordinate, zero at the water surface, positive upwards; vertical coordinate, zero at the mud surface, positive down-

wards;

wave frequency;

normal stress;

material bulk density;

mud dry density (concentration);

grain density;

sed shear stress amplitude at x = 0; 5 g 7 z L m, ~

water surface displacement;

ith mud wave displacement;

small strain;

viscosity in the viscoelastic model; eddy viscosity coefficient;

viscosity related coefficient;

apparent dynamic viscosity, $\mu_{e} = \rho \nu_{e}$;

kinematic viscosity; and

apparent kinematic viscosity.

t al. [12] which ential well with nimum lifetime e scale for mass earance thresh-

ind an absolute e order of 10-20

as provided by

earch, High En-

Schwarz, Intern. J.

ire/reactivity and

ind S. Lias (Reidel,

la, T. Drewell and

nd Y. malinovich,

. van Hemert and

and J.H. Beynon,

J. Chem. Phys. 88

. Boyer and C.K. ...

on, eds. T.D. Märk

) pp. 137-197, and

n. Phys. 35 (1961) =

1warz, Chimia 39

ind L. Radom, J.

. Chem. Phys. 83

and J.T. Herron, T

, eds. T.D. Märk

ock, J.T. Herron, 💆

tials, appearance &

o. 58.

) 305.

987

THE STRUCTURE OF INTERLAYER WATER IN A HYDRATED 2:1 CLAY

N.T. SKIPPER, A.K. SOPER 1, J.D.C. McCONNELL and K. REFSON Department of Earth Sciences, Oxford University, Parks Road, Oxford OX1 3PR, UK

Received 16 November 1989; in final form 5 December 1989

Neutron diffraction in conjunction with substitution of deuterium (D) for hydrogen (H) has been used to study the structure of water in a hydrated crystal of Ni-vermiculite. The intensities of the (00l) Bragg reflections were measured as a function of the H/D content, up to l=30. Difference analysis was then used to obtain separate density profiles, $\rho(z)$, for the hydrogen and the oxygen plus the clay sheets. We have confirmed the existence of interlayer Ni2+ (H2O)6 complexes, in which the water molecules are strongly hydrogen bonded to the surface. More importantly, we have found that within the limits of the experiments all the additional water is located near the hexagonal rings of SiO4 and AlO4 tetrahedra, which comprise the surface.

1. Introduction

Smectites and vermiculites together form the group of 2:1 clay minerals which expand in the presence of water [1]. They comprise negatively charged micalike sheets which are held together by charge balancing cations [2]. These interlayer cations often have a strong tendency to hydrate, thereby forcing the layers apart. The remaining space between the sheets may then be occupied by additional water. The layer spacing and the total amount of water absorbed depend on the type of interlayer cation, the relative humidity and the position and density of the layer charge.

The hydration properties of the 2:1 clay minerals, in particular the smectites, are important in many natural and industrial processes [3]. However, the positions of the interlayer water molecules in these systems have not previously been established. The aim of the work presented in this paper is therefore to determine the microscopic structure of all the fractions of water in a hydrated 2:1 clay.

We chose to study a vermiculite because they occur naturally as macroscopic crystals, in contrast to the smectites which are found only in the form of microplatelets. The particular sample we used was a crystal of Ni-vermiculite from Llano, Texas, with the quoted structural formula [1];

 $(Mg_{2.95}Al_{0.10})(Si_{2.78}Al_{1.22})O_{10}(OH)_2:Ni_{0.45}nH_2O.$

The sample had approximate dimensions $10 \times 10 \times 4$ mm, and we therefore avoided the problems associated with obtaining high resolution diffraction data from colloidal suspensions of smectites [4].

Under the experimental conditions (room temperature and 85% relative humidity) vermiculite is hydrated: $n \approx 4.5$ [5] and the layer spacing is 14.4 Å (the dry value is 10.0 Å [6]). Being primarily interested in the water structure, we used neutron diffraction in conjunction with H/D substitution. The neutron scattering lengths, b, for H and D are both large, but of opposite sign ($b_H = -3.74$ fm, $b_D = 6.67$ fm). Difference analysis of diffraction data from H and D enriched samples can therefore be used to isolate all interatomic distances involving H [4].

2. Experimental

Experiments were conducted using the LAD diffractometer on the ISIS pulsed neutron source at the Rutherford Appleton Laboratory [7]. The sample was held between two thin vanadium sheets and oriented so that the c^* -axis was parallel to the scattering

Chilton, Didcot, Oxon OX11 0QX, UK.

ous positive ions

Neutron Science Division, Rutherford Appleton Laboratory,

Two complete sets of data were obtained. The first were recorded using the hydrogenated crystal, while the second were collected after the same sample had been deuterated by repeated dessication and soaking in NMR standard D_2O at 50° , over a period of four days.

3. Results and discussion

The raw diffraction patterns were corrected for absorption; the data obtained from the deuterated sample are presented in fig. 1. The integrated (00/) Bragg intensities, I(Q), derived from these patterns are shown in fig. 2. They are related to the neutron scattering density along the c^* -axis, $\rho(z)$, via structure factor, F(Q),

$$I(Q) = |F(Q)|^2 \tag{1}$$

and

$$F(Q) = \int_{-c/2}^{c/2} \rho(z) e^{iQz} dz, \qquad (2)$$

where c is the lattice spacing. Density profiles, $\rho(z)$, were obtained by Monte Carlo simulation of the integrated intensities [9]. The simulations were started from a uniform background density with clay peaks placed in the positions measured by X-ray diffraction [10]. The entire structure, including the clay layers, was then refined. Because of the H/D substitution we were able to separate the hydrogen distribution from the oxygen plus clay distribution (fig. 3). The fits to the intensity data had an R-factor of 2.8%. Since the composition of the internal oxygen layer has been determined by chemical analysis [1], the area of the peak at 1.09 Å was used to normalise the density profiles. The data can then be interpreted as follows.

Considering the layer region first, the sharp peaks in the oxygen plus clay profile at 0.0, 1.09, 2.74 and 3.35 Å can be assigned to the clay structure (table 1). These positions are entirely consistent with those obtained from X-ray crystallography [10]. In ad-

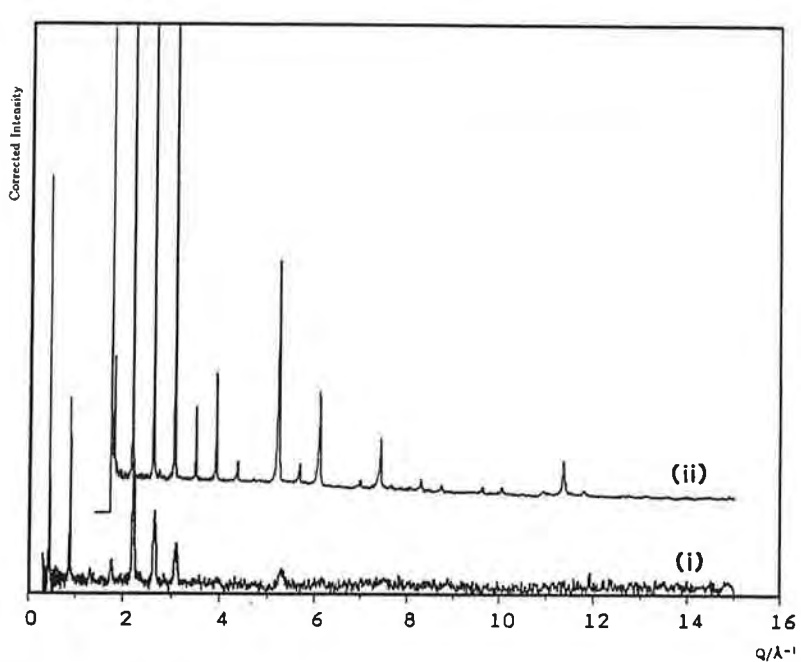


Fig. 1. Corrected diffraction patterns, in arbitrary units, for deuterated Ni-vermiculite, using scattering angles of (i) 20° and (ii) 150°,

Fig. 2. The deuterate experime respective

Fig. 3.

this dia

oxygen

propose

Volume Ir

1990

e inirted
eaks
fracclay
subdis(fig.)
r of
/gen
[1],
alise

eted

aks and

ab'

lOSt

ad-

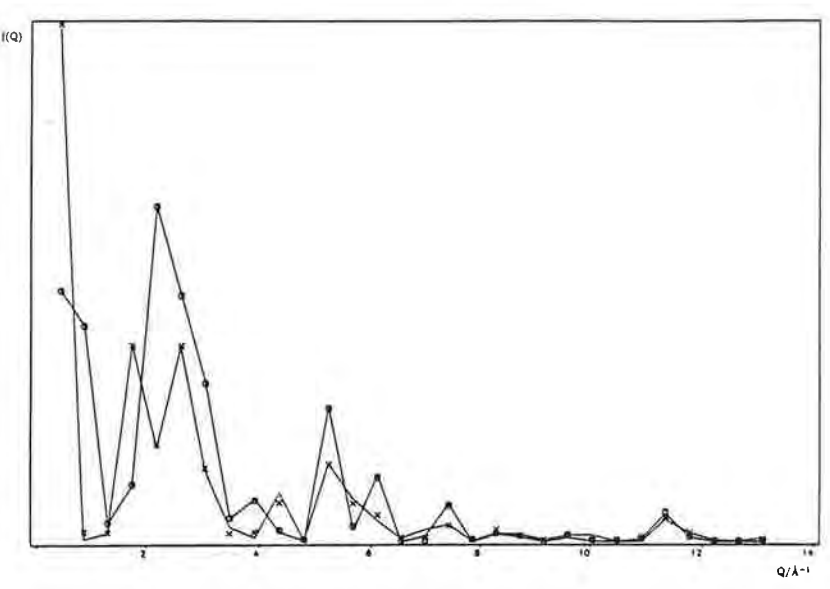


Fig. 2. The integrated (001) intensities, I(Q), for (i) the hydrogenated sample (points joined by the solid line) and (ii) the same sample, deuterated by repeated dessication and soaking in D_2O at $50^{\circ}C$ over a period of four days (points joined by the broken line). The experimental values are compared with the results obtained from the simulated density profiles presented in fig. 3 (circles and crosses respectively).

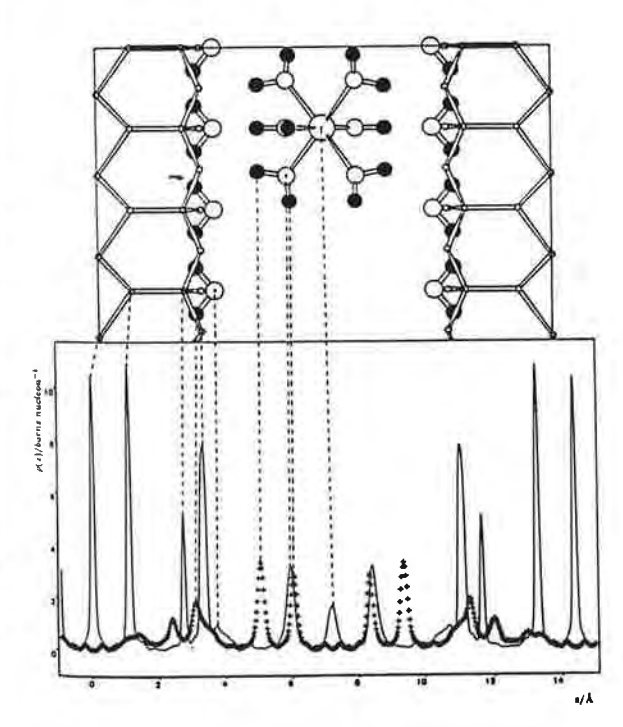


Fig. 3. Neutron scattering density profiles, $\rho(z)$, for oxygen plus layer (solid line) and hydrogen (crosses). For the purposes of this diagram hydrogen has assigned the same scattering length as oxygen. The insert above shows the assignment of peaks in the proposed structural model (the hydrogen atoms are shaded in).

dition to the clay peaks, there is a broader feature at around 3.7 Å. We attribute this to the oxygen atoms of absorbed water molecules. After subtracting the areas due to the tetrahedral cations (at 2.74 Å) and surface oxygen atoms (at 3.35 Å), there is an area equivalent to 0.91 oxygen atoms between 2.3 and 4.4 Å.

The most striking feature of the hydrogen density within the layer is the absence of a peak at 2.0 Å. This would be due to the structural hydroxyl groups of the clay, and has been reported in previous experiments conducted at lower humidities. Instead, we find a broad density which contains 2.58 hydrogen atoms and has peaks at 2.4 and 3.08 Å. We therefore propose that up to one water molecule can be sited near each hexagonal ring of six SiO₄ and AlO₄ tetrahedra. The hydrogen atoms of these water molecules point towards the clay sheet, being attracted to the negative charges arising from substitution of Al3+ for Si4+ in the tetrahedral layer. The hydrogen atoms of the structural hydroxyl group are then either flattened towards the plane of the layer, accounting for the intensity around 1.4 Å, or possibly form H₃O⁺ ions with the absorbed water.

Interpretation of the density profiles in the interlayer region is straightforward. The central peak at

Table 1 Analysis of peaks in the simulated density profiles of Ni-vermiculite (fig. 3) 4)

r b)	Assignment	A °)	Chemical equivalent		
0.0	octahedral cations	1.52	0.96 (Mg _{2.81} Al _{0.08}))	
1.09	oxygen	1.74 ^{d)}	3.0 O	alau lavas	
2.74	tetrahedral cations	0.79	Si _{2.89} Al _{1.11}	clay layer	
3.35	oxygen	1.76	3.03 O	J	
3.70	oxygen	0.53	0.91 O)	
1.40	hydrogen	0.46	0.79 H	absorbed water	
2.40	hydrogen	0.49	0.84 H	absorbed water	
3.08	hydrogen	1.01	1.74 H	J	
7.2	interlayer cations	0.60	0.58 Ni ²⁺)	
5.92	oxygen	1.01	1.74 O		
5.01	hydrogen	0.95	1.63 H	interlayer complexes	
6.04	hydrogen	0.83	1.42 H	J	

a) Only peaks between -0.5 and 7.5 Å are considered. b) r is the peak position (Å). c) A is the measured area (b nucleon 1).

7.2 Å in the clay plus oxygen profile may be assigned to the interlayer cations, and is equivalent to 0.58 Ni²⁺ per structural unit (table 1). If this assignment is correct the peak at 5.92 Å would correspond to the oxygen atoms of the cation hydration spheres. This peak has an area equivalent to 3.01 oxygens per Ni²⁺, confirming the existence of Ni²⁺(H₂O)₆ complexes, within the limits of our experiments. If these Ni²⁺(H₂O)₆ complexes were perfectly octahedral the projected Ni2+-O distance of 1.28 Å in the z-direction would give an Ni²⁺-O bond length of 2.22 Å: this compares with 2.07 Å in aqueous solutions [11]. More probably the octahedra are slightly distorted, so that O-O distance of the interlayer complexes more closely matches that of the surface. Hydrogen peaks due to the interlayer Ni²⁺(H₂O)₆ complexes are located at 5.01 and 6.04 Å. Since the O-H bond length in water is 0.96 Å [12] the hydrogen atoms at 5.01 Å lie directly above the surface AlO₄ or SiO₄ tetrahedra, forming hydrogen bonds to the oxygen atoms (the location of the interlayer cations has been established in previous experiments [10]). The O-H distance of these hydrogen bonds is 1.66 Å, compared with 1.76 Å in ice and 1.85 Å in liquid water [12].

4. Conclusion

The results presented confirm the existence of Ni²⁺(H₂O)₆ complexes between the layers in Nivermiculite. These complexes act as pillars holding the clay sheets apart, but are also strongly bonded to the surfaces. More importantly, we have produced the first evidence that a layer of water molecules lies within 0.4 Å of the clay surface, and the molecules are sited within the hexagonal rings of SiO4 or AlO₄ tetrahedra. At the experimental humidity these two regions account for all the water in the system.

Acknowledgement

We gratefully acknowledge the assistance of the technical staff at ISIS and of Derek Preston in the Department of Earth Sciences, Oxford University.

References

- [1] A.C.D. Newman, Chemistry of clays and clay minerals (Mineralogical Society Longman, London, 1987).
- [2] G.W. Brindley and G. Brown, Crystal structures of clay minerals and their X-ray identification (Mineralogical Society, London, 1980).
- [3] R.E. Grim, Applied clay mineralogy (McGraw-Hill, New York, 1962).

[4] R.K. Hawkins a

Volume 166, number 2

- (1980) 19.
- [5] W.F. Bradley an (1980) 260. [6] J.A. Rausel-Colo
- Alcover and L. G [7] W.S. Howells, R
- Report, RL-80-0
- [8] J.M. Adams and 444.

d) To normalise the data this area was compared with a chemical analysis of the clay sheets [1].

Volume 166, number 2

- [4] R.K. Hawkins and P.A. Egelstaff, Clays Clay Miner. 28
- [5] W.F. Bradley and J.M. Serratosa, Clays Clay Miner. 28 (1980) 260.
- [6] J.A. Rausel-Colom, M. Fernandez, J.M. Serratosa, J.F. Alcover and L. Gatineau, Clay Miner. 15 (1980) 37.
- [7] W.S. Howells, Rutherford Appleton Laboratory Internal Report, RL-80-017 (1980).
- [8] J.M. Adams and C. Reikel, Clays Clay Miner. 28 (1980)
- [9] S.V. Semenovskaya, K.A. Khachaturyan and A.G. Khachaturyan, Acta Cryst. A 41 (1985) 268.
- [10] A.McL. Mathieson and G.F. Walker, Am. Miner. 39 (1954) 231.
- [11] G.W. Neilson and J.E. Enderby, Proc. Roy. Soc. A 390 (1983) 353.
- [12] A.K. Soper and M.G. Phillips, Chem. Phys. 107 (1986) 47.

complexes

vater

(b nucleon -1).

1 the existence of the layers in Nit as pillars holding strongly bonded to we have produced ater molecules lies and the molecules rings of SiO₄ or [5] ental humidity these 🖫 vater in the system.

assistance of the ek Preston in the ford University.

s and clay minerals idon, 1987). al structures of clay tion (Mineralogical

aw-Hill, New

ρλ

T. M. Parchure¹ and A. J. Mehta²

ABSTRACT

The top thin layer of an estuarial muddy bed is typically a partially consolidated cohesive sediment deposit. The erosive resistance of this layer of the order of 1 cm thickness is characterized by the cohesive shear strength. Laboratory resuspension tests were conducted in a flume in order to determine the shear strength of thin beds of kaolinite and a lake mud deposited in waters of different salinities. Overburden and associated physico-chemical changes within the bed structure cause the shear strength to increase with depth. The depth-averaged shear strength, $\tau_{\rm S}$, was found to vary with the sediment-fluid composition as well as with the period of bed consolidation prior to resuspension. Values of $\tau_{\rm S}$ were found to range from 0.15 to 0.39 Nm-2.

INTRODUCTION

The erosive behavior of muddy deposits in estuaries and in the tidal flow dominated regions of the estuarial shelf is of engineering interest because of the need to predict the rates of transport of fine suspended sediments in navigable waters. The thickness of the cohesive sediment deposit that is influenced by the flow can typically range, in order of magnitude, from a centimeter to as much as a meter. The upper portion of the deposit is generally overturned each tidal cycle, while the lower layers may be resuspended only during spring tides. The bed is therefore found in a state of partial consolidation, since almost complete consolidation may take several weeks or months. The top layer of the order of 1 cm thickness tends to exhibit a marked depth-variation in the bed properties, while the lower layers are more uniform due to consolidation. An important property characterizing the resistance to bed erosion is the cohesive bed shear strength. A series of laboratory experiments were conducted in a flume in order to determine the depth-variation of the shear strength of comparatively thin top layers of partially consolidated cohesive sediment deposits. Results of these experiments are summarized below. Details are found elsewhere (11).

RESUSPENSION UNDER TIDAL WATERS

The phenomena of deposition, consolidation, erosion and transport of suspended muddy sediments in estuarial waters under tide-dominated flows are schematically represented in Fig. 1 (9). Deposition of the suspension in horizontal transport occurs when the flow velocity (and therefore the bed shear) is low or when slack water occurs. This in turn results in the

¹Graduate Assistant, Coastal and Oceanographic Engineering Department, University of Florida, Gainesville, Florida, U.S.A.

²Associate Professor, Coastal and Oceanographic Engineering Department, University of Florida, Gainesville, Florida, U.S.A.

formation of a comparatively dense stationary or static suspension in the near-bed zone. Such a suspension does not move horizontally, by definition (12), but there can be a net downward movement of the sediment. At the bottom a bed with small but measurable shear strength begins to develop as the suspended material continues to settle. The deposit is partially consolidated, and, after a period of the order of weeks or months, depending upon the bed properties, a settled bed is formed, provided it is not resuspended in the mean time. The erosion of a stationary suspension has been termed redispersion (12), while the erosion of a partially consolidated deposit or a settled bed may be referred to as resuspension. Redispersion is not a well-understood phenomenon and is a subject matter for future research, whereas numerous studies on the resuspension of the settled bed have been reported (7,9). The more general case of a partially consolidated bed was not investigated until recently, and is the subject of present interest.

COHESIVE SHEAR STRENGTH

Soft muddy deposits of the type studied in the present investigation tend to have a very high water content which can exceed 100% and, consequently, possess a low bulk density. The cohesive shear strength of such deposits is usually small and cannot be measured accurately by devices such as a vane shear apparatus or a penetrometer. A special laboratory procedure was therefore developed to determine the shear strength layer by layer in a flume. This procedure is described subsequently.

Earlier preliminary results (from tests conducted at the University of Florida) which were verified and extended under the present study indicated that the shear strength, $\tau_{\rm S}$, varies with depth z below the fluid-bed interface as shown qualitatively in Fig. 2 (1,8,10,13). Beginning with a small value, $\tau_{\rm C}$, close to the bed surface, $\tau_{\rm S}$ increases relatively rapidly at first. Below a certain depth, $z_{\rm Ch}$, corresponding to a shear strength, $\tau_{\rm Ch}$, which is a characteristic of the bed, the variation of $\tau_{\rm S}$ with z is less significant and, in fact, $\tau_{\rm S}$ approaches a maximum value, $\tau_{\rm SM}$. Given such a distribution of $\tau_{\rm S}(z)$, under a time-mean value of the bed shear stress $\tau_{\rm b} = \tau_{\rm bA}$, the bed will erode to a depth $z_{\rm A}$ at which point $\tau_{\rm bA} = \tau_{\rm sA}$. Since the rate of bed erosion depends on the excess shear stress, $\tau_{\rm b} - \tau_{\rm S}$ (9), the equality condition, $\tau_{\rm bA} = \tau_{\rm SA}$, implies that erosion is arrested at this point in time, and depth, $z_{\rm A}$. Similarly, if $\tau_{\rm b}$ is equal to $\tau_{\rm bB}$ or $\tau_{\rm bC}$, the corresponding depths of erosion will be $z_{\rm B}$ or $z_{\rm C}$, respectively. Finally, for $\tau_{\rm bD} > \tau_{\rm sM}$, the bed will continue to erode indefinitely, at least in principle, since the condition $\tau_{\rm bD} = \tau_{\rm sD}$ cannot be attained.

The time-variation of the depth-averaged suspended sediment concentration, C, during resuspension is related to the dry density, ρ_D , of the bed according to

$$\overline{C}(t) = \frac{1}{h} \int_{0}^{z(t)} \rho_{D}(z) dz$$
 (1)

where t = time and h = depth of flow assumed to be constant. The density, ρ_D , typically increases with depth z (9). With reference to Fig. 2, after a relatively short time period of initial rise, C will approach a constant value C_A under a bed shear stress τ_{bA} , as τ_{bA} approaches τ_{sA} . Similarly under τ_{bB} and τ_{bC} , the corresponding final concentrations will

be $\overline{C_B}$ and $\overline{C_C}$, respectively. Under τ_{bD} , \overline{C} will continue to increase with time indefinitely. In a test conducted by Krone (4) using a silty-clay from San Francisco Bay, \overline{C} continued to increase even after 500 hours.

The significance of the shear strength, τ_{ch} , is that when $\tau_b < \tau_{ch}$, \overline{C} increases slowly with time. This is because the excess shear stress, $\tau_b - \tau_s$, approaches zero relatively rapdily inasmuch as τ_s increases rapidly with depth z (Fig. 2). When $\tau_b > \tau_{ch}$, \overline{C} increases more rapidly because $\tau_b - \tau_s$ decreases more slowly inasmuch as τ_s increases slowly with z.

EXPERIMENTAL APPARATUS AND MATERIAL

The experiments were conducted in an annular rotating flume which has been described in detail elsewhere (6). The two main components of this flume were: an annular fiberglass channel (0.21 m wide, 0.46 m deep and 1.5 m in mean diameter) containing the fluid-sediment mixture, and an annular ring of slightly smaller width positioned within the channel and in contact with the fluid surface. A simultaneous rotation of the two components in opposite directions generated a turbulent flow field free from sediment floc-disrupting elements such as pumps and diffusers in which excessively high rates of flow shearing usually prevail. By a proper adjustment of the speeds of the two components, the rotation-induced secondary currents near the bed were eliminated, and the distribution of the bed shear stress across the channel width was found to be uniform. A special arrangement was made for replacing the suspension slowly by sediment-free water, when necessary, without stopping the flume. A Hewlett Packard HP-85 mini-computer together with two digitalto-analog converter units were provided to exercise a precise control over the speeds and the accelerations of the channel and the ring.

Bed density and its variation with depth were measured at various consolidation periods with the help of a specially designed 2.5 cm metal tube in which core samples were frozen in situ, using a mixture of alcohol and dry ice (10).

Sediments used included a commercially available kablinite (median size = 1 μm ; cation exchange capacity = 6 milliequivalents per hundred grams) and a natural lake mud (median size = 1 μm ; cation exchange capacity = 94 milliequivalents per hundred grams). Minerals in the lake mud were: smectite, illite, kablinite and quartz. The fluids were: tap water (total salts concentration = 0.28 ppt; pH = 8.1) and saline water (salinites of 0.5, 1, 2, 5, 10 and 35 ppt; pH = 7.5).

EXPERIMENTS AND RESULTS

Sediment Exchange

In general, the suspended sediment concentration, \overline{C} , during resuspension can attain a constant value under a constant time-mean bed shear stress, τ_b , when either 1) τ_b becomes equal to τ_s at some depth z and erosion is arrested, or 2) the rate of erosion equals the rate of deposition under an equilibrium condition resulting from an exchange of sediment between the bed and the fluid above. The occurrence of the second phenomenon in preference to the first would lead to a different interpretation of the bed structure (2) than the one noted here.

In order to evaluate the degree of sediment exchange between the bed and the fluid, an experiment was conducted in the annular flume using a deposited bed of kaolinite in tap water. The depth h was $0.25 \,\mathrm{m}$ and $\tau_{\mathrm{b}} = 0.20 \,\mathrm{km}^{-2}$. After a relatively short period of initial rise, C attained a constant value of 3.85 gl $^{-1}$ within a few hours. The test was continued for a period of 122 hours. At the end of this period the suspension was gradually flushed out over a period of 4 hours, by replacing it simultaneously with sediment_free water, without distrubing the bed or stopping the flow. As a result, C dropped to $0.03~{\rm gl}^{-1}$. The flushing process was then stopped and the test was continued (with $\tau_b=0.20~\text{Nm}^{-2}$) for another 24 hours. At the end_of this period C rose to 0.1 gl⁻¹. It can be inferred that at 122 hours, C had become nearly constant as $\tau_b \rightarrow \tau_s$ at the exposed bed surface. At this point, no significant sediment exchange occurred as suggested by the subsequent flushing process which indicated that there was almost no erosion of the bed. The very small increase in concentration during the last 24 hour period may be attributed to floc entrainment which can occur even when τ_b = τ_s , inasmuch as the instantaneous value of the bed shear stress can exceed the mean as a result of the statistical nature of near-bed turbulence as well as the shear strength.

Resuspension Experiments

Three experimental series were conducted with different combinations of the sediment and the fluid. These were: kaolinite in tap water (series KT), kaolinite in salt water (series KS) and lake mud in salt water of different salinities (series LM). In each test, the general procedure was as follows: 1) a given amount of sediment (of concentration C_0) was completely suspended in the flow at a high bed shear stress, $\tau_{\rm m}$, for a duration $T_{\rm m}$, 2) the sediment was then allowed to deposit under a comparatively low shear stress, $\tau_{\rm d}$, for a period $t_{\rm d}$, 3) the flow was stopped and the bed was allowed to consolidate for a period $t_{\rm d}$ and 4) the bed was resuspended under a series of bed shear stresses, $t_{\rm d}$, of increasing magnitudes, each held constant over a time-step of duration T.

As an example, Fig. 3 shows a test under the KS series with $C_0=41.1~{\rm gl}^{-1}$, $\tau_m=0.9~{\rm Nm}^{-2}$, $\tau_d=0~{\rm Nm}^{-2}$, $t_d{\approx}0~{\rm hr}$, $T_{\rm dc}=5.6~{\rm days}$ and bed shear stresses, τ_b , during resuspension as indicated in the figure, with each value held constant over a duration $T=1.0~{\rm hr}$. The nature of the time-variation of C suggests that up to $\tau_b=0.30~{\rm Nm}^{-2}$, C approached a constant value at the end of each time-step. With reference to Fig. 2, erosion under bed shear stresses τ_{bA} , τ_{bB} or τ_{bC} would represent this condition. During the last two steps when τ_b was $0.36~{\rm and}~0.43~{\rm Nm}^{-2}$, respectively, C continued to increase at the end of each time-step. This occurred either because the duration T was insufficient to erode the bed to a depth where the condition $\tau_b=\tau_S$ would have been attained, or because τ_b was greater than τ_{Sm} .

In Fig. 4, \overline{C} at the end of each time-step is plotted against the corresponding τ_b . The observed relationship is typical of what is found for most tests. The trend of the data corresponding to the first seven time-steps during which \overline{C} attained a constant value can be approximated by a straight line. The remaining two data points give a line of a steeper slope. The two lines intersect at $\tau_b = \tau_{Ch}$ (= 0.34 Nm⁻²), the characteristic shear strength. As noted previously with reference to Fig. 2, the steeper slope of the upper line results from a comparatively higher time-rate of change of \overline{C} when $\tau_h > \tau_{Ch}$.

The value of z_{ch} can be found from

$$\overline{C}(T)_{ch} = \frac{1}{h} \int_{0}^{z_{ch}} \rho_{D}(z) dz$$
 (2)

where $\overline{C}(T)_{ch}$ (= 2.0 gl⁻¹ in Fig. 4) is the value of $\overline{C}(T)$ corresponding to τ_b = τ_{ch} . The measured $\rho_D(z)$ profile is shown in Fig. 5. Equation 2 yields (by trial and error) z_{ch} = 0.26 cm. Another feature of Fig. 4 is that the lower straight line, when extrapolated to intersect the $\overline{C}(T)$ = 0 axis, yields the surface shear strength τ_C = 0.04 Nm⁻².

Assuming that the condition $\tau_b = \tau_S$ is attained at the end of each of the first seven time-steps, τ_S can be plotted against the corresponding depth of erosion, z, since the latter quantity can be calculated from Eq. 1, knowing $\rho_D(z)$ (Fig. 5) and C(T) at the end of each time-step (Fig. 4). This procedure was used to plot $\tau_S(z)$ profiles for all tests in the KS series in Fig. 6. Several features of this plot are noteworthy. 1) By virtue of the definition of z_{ch} , the $\tau_S(z)$ plots extend up to a depth which is slightly less than or equal to z_{ch} . 2) The surface value, $\tau_C(=0.04 \text{ Nm}^{-2})$, does not change measurably with the consolidation time, T_{dc} , because there is no overburden at the surface. 3) τ_S below the surface increases with T_{dc} as the excess pore pressure decreases with time and the inter-particle bonds rearrange themselves. Finally, 4) the influence of T_{dc} on τ_S increases with depth.

In Table 1, results from all tests in the three series are summarized. The depth z_{ch} is relatively small (ranging from 0.03 to 0.40 cm) and it can be considered to represent the thickness of the top layer of the deposit. Accordingly, a corresponding representative mean shear strength, $\tau_{\rm S}$, of this top layer may be obtained from

$$\frac{-}{\tau_{S}} = \frac{1}{z_{ch}} \int_{0}^{z_{ch}} \tau_{S}(z) dz$$
 (3)

As noted earlier, the $\tau_s(z)$ profiles in Fig. 6 extend to a depth $z \approx z_{ch}$, and therefore can be used to estimate τ_s using Eq. 3. Results are given in Table 1. Values of τ_s range from 0.15 to 0.39 Nm⁻². Such low values are difficult to measure using standard soil testing apparatuses.

It is interesting_to note the variation of τ_S with T_{dC} and with salinity. In Fig._7, τ_S is plotted against T_{dC} for series KT and KS. It is observed that: 1) τ_S increases initially with T_{dC} and, at least in the case of KS, approaches a constant value as T_{dC} approaches 10 days, and 2) KT values are generally higher than KS, for a given T_{dC} . The latter observation is consistent with the_flocculation characteristics of kaolinite as also noted later. In Fig. 8, τ_S is plotted against salinity for series LM (T_{dC} = 1.7 days in all tests). The magnitude of τ_S increases with increasing salinity, but the rate of increase decreases as the salinity approaches 10 ppt. Previous observations on the influence of salinity on the properties of muds indicate that cohesion increases up to about 10 ppt above which the effect of salinity is relatively small (3,5). It might therefore be expected that τ_S at sea water_salinity (35 ppt) would not be significantly different from the value of τ_S at 10 ppt.

With reference to the dependence of the characteristic shear strength τ_{Ch} on T_{dc} and on salinity, the trends from Table 1 can be shown to be similar to those for τ_{S} , as would be expected. It should, however, be noted that τ_{Ch} is the shear strength at depth z_{Ch} only, and does not necessarily represent the mean shear strength of the entire bed. This is because τ_{Ch} gives no indication of the shear strength variation of the bed at depths below z_{Ch} .

Further inferences regarding the structure of the top layer can be made by examining the influences of T_{dc} and salinity on z_{ch} . In Fig. 9, z_{ch} is plotted against T_{dc} for series KI and KS. Two relevant observations are: 1) z_{ch} appears to exhibit a decreasing trend with increasing T_{dc} , and 2) z_{ch} for KS is greater than that for KT for a given T_{dc} . The magnitude of z_{ch} decreases with increasing T_{dc} because the bed properties, including τ_{s} , become more uniform with increasing T_{dc} , starting from the bottom and progressing upwards as the material consolidates under overburden. The thickness z_{ch} (of the layer of non-uniform variation of τ_{s}) is greater in the case of KS in comparison with KT because the flocculation characteristics of kaolinite are such that this sediment in salt water has a more open structure than in tap water (11).

In Fig. 10, z_{ch} has been plotted against salinity for series LM. It is observed that, after exhibiting a trend of decreasing magnitude with increasing salinity up to 2 ppt, z_{ch} increases with increasing salinity. Further experiments are required to establish the significance of the observed behavior of z_{ch} up to 2 ppt salinity. The trend of increasing z_{ch} with salinities greater than 2 ppt is consistent with the known trend of increasing inter-particle cohesion of muddy sediments with increasing salinity. With increasing cohesion, the structure acquires greater stability against overburden, and is able to retain its non-uniform character more easily (11).

A complete characterization of the $\tau_s(z)$ profile requires specification of τ_{ch} , z_{ch} , τ_s , τ_c , τ_{sm} , and the depth at which τ_{sm} might be encountered. The τ_c values are reported in Table 1. As noted earlier, τ_c does not vary with τ_c . However, it does vary with the type of the sediment and the fluid. The observed trends in Table 1 are consistent with those for τ_s . In typical laboratory tests with beds of the order of 5-10 cm thickness, $\tau_s(z)$ often tends to increase down to the flume bottom so that when $\tau_b > \tau_{ch}$, the entire bed would erode. In the reported tests, τ_s could be determined down to z_{ch} which is at least an order of magnitude smaller than the depth at which τ_s could be expected to become uniform (and attain the value τ_{sm}). Further analysis of the test data in terms of the dependence of the rate of erosion on τ_{b} - τ_{s} is required to estimate τ_{sm} . Using such an analysis presented elsewhere, τ_{sm} was found to be 2.0, 0.6 and 0.7 Nm⁻² for series KT, KS and LM, respectively (11). The value of τ_{sm} does not depend on τ_{ch} but the depth at which it is first encountered reduces with increasing τ_{ch} as the bed becomes increasingly uniform. For LM, the reported value of 0.7 Nm⁻² should be considered as the average for all five tests at different salinities, since the change in τ_{sm} as a result of the change in salinity was not measurable in this series.

CONCLUSIONS

1) The erosive resistance of the top thin layer of a partially consolidated cohesive sediment deposit depends on the shear strength, τ_{S} , which

- increases rapidly with depth, beginning with a value, $\tau_{\text{C}},$ near the surface.
- 2) The top layer is_defined by a thickness z_{ch} and a representative mean shear strength, τ_s . Laboratory experiments involving layer by layer erosion of the deposit are required to determine z_{ch} and τ_s .
- 3) The following ranges of values were obtained. Kaolinite in tap water (series KT): $z_{ch} = 0.03-0.16$ cm, $\tau_{s} = 0.23-0.26$ Nm⁻²; kaolinite_in salt water of 35 ppt concentration (series KS): $z_{ch} = 0.26-0.40$ cm, $\tau_{s} = 0.15-0.33$ Nm⁻²; lake mud in water of salinities varying from 0.5 to 10 ppt (series LM): $z_{ch} = 0.09-0.17$ cm, $\tau_{s} = 0.16-0.39$ Nm⁻².
- 4) The parameters z_{ch} and $\overline{\tau}_s$ are influenced by the period of bed consolidation as well as by salinity.
- 5) Additional parameters which, together with z_{ch} and $\overline{\tau}_s$, define the depth-variation of τ_s in the top thin layer are τ_c (the value of τ_s near the surface) and τ_{ch} (the value of τ_s at depth z_{ch}).
- 6) For depth z below z_{ch} , τ_s varies less significantly with z than for z less than z_{ch} , and reaches a maximum value, τ_{sm} , at some depth which typically is much greater than z_{ch} .

ACKNOWLEDGEMENT

Support provided by the U.S. Environmental Protection Agency (Grant No. R806684010) and the Special Appropriation to the Coastal and Oceanographic Engineering Department, University of Florida, by the Florida State Legislature, is sincerely acknowledged.

REFERENCES

- Dixit, J. G., "Resuspension Potential of Deposited Kaolinite Beds," M.S. Thesis, University of Florida, Gainesville, FL, 1982.
- 2. Fukuda, M. K., and Lick, W., "The Entrainment of Cohesive Sediments in Fresh Water," <u>Journal of Geophysical Research</u>, Vol. 85, No. C5, May, 1980, pp. 2813-2824.
- 3. Hayter, E. J., and Mehta, A. J., "Modeling of Estuarial Fine Sediment Transport for Tracking Pollutant Movement," Report UFL/COEL-82/009, Coastal and Oceanographic Engineering Department, University of Florida, Dec., 1982.
- 4. Krone, R. B., "Flume Studies of the Transport of Sediment in Estuarial Processes," Final Report, Hydraulic Engineering Laboratory and Sanitary Engineering Research Laboratory, University of California, Berkeley, CA, June, 1962.
- 5. Krone, R. B., "Aggregation of Suspended Particles in Estuaries," in Estuarine Transport Processes, edited by P. Kjerfve, the Belle W. Baruch Library in Marine Science, No. 7, University of South Carolina Press, Columbia, 1978, pp. 177-190.

- 6. Mehta, A. J., "Depositional Behavior of Cohesive Sediments," Ph.D. Thesis, University of Florida, Gainesville, FL, 1973.
- 7. Mehta, A. J., "Review of Erosion Function for Cohesive Sediment Beds,"
 Proceedings of the First Indian Conference on Ocean Engineering, Vol. I,
 Indian Institute of Technology, Madras, India, Feb., 1981, pp. 122-130.
- 8. Mehta, A. J., and Partheniades, E., "Kaolinite Resuspension Properties," Journal of the Hydraulics Division, ASCE, Vol. 105, No. HY4, April, 1979, pp. 409-416.
- 9. Mehta, A. J., Parchure, T. M., Dixit, J. G. and Ariathurai, R., "Resuspension Potential of Deposited Cohesive Sediment Beds," In: Estuarine Comparisons, edited by V. S. Kennedy, Academic Press, New York, 1982, pp. 591-609.
- 10. Parchure, T. M., "Effect of Bed Shear Stress on the Erosional Characteristics of Kaolinite," M.S. Thesis, University of Florida, Gainesville, FL, 1980.
- 11. Parchure, T. M., "Erosional Behavior of Deposited Cohesive Sediments," Ph.D. Dissertation, University of Florida, Gainesville, FL, 1983.
- Parker, W. R., and Kirby, R., "Fine Sediment Studies Relevant to Dredging Practice and Control," Proceedings of the Second International Symposium on Dredging Technology, BHRA, Paper B2, Texas A & M University, College Station, TX, Nov., 1977.
- 13. Yeh, H. Y., "Resuspension Properties of Flow Deposited Cohesive Sediment Beds," M.S. Thesis, University of Florida, Gainesville, FL, 1979.

NOTATION

The following symbols are used in this paper:

 \overline{C} = depth-averaged suspended sediment concentration;

 $\overline{C}_A, \overline{C}_B, \overline{C}_C$ = three values of \overline{C} ;

 $\overline{C}(T)$ = value of \overline{C} at the end of time-step of duration T;

 $\overline{C}(T)_{ch}$ = value of $\overline{C}(T)$ corresponding to the depth z_{ch} ;

 C_0 = initial suspension concentration;

h = depth of flow;

T = duration of time-step during resuspension;

 $T_m = mixing time;$

 T_{dc} = period of bed consolidation;

t = time;

 t_d = time during which the sediment deposits;

z = depth coordinate below bed surface;

 z_A, z_B, z_C = three values of z;

 z_{ch} = thickness of the top layer of the deposit;

 ρ_{N} = dry density of the bed;

 τ_b = time-mean bed shear stress;

 $\tau_{bA}, \tau_{bB}, \tau_{bC}, \tau_{bD} = \text{four values of } \tau_{b};$

 τ_{c} = value of τ_{s} near bed surface;

 τ_{ch} = characteristic bed shear strength;

 τ_d = bed shear stress during deposition;

 τ_m = bed shear stress during mixing;

 τ_S = cohesive bed shear strength;

 τ_{S} = representative mean shear strength of the top layer of deposit; and

 τ_{SM} = maximum value of τ_{S} .

Table 1

Properties of Surficial Layer

Series	Salinity (ppt)	T _{dc} (days)	[⊤] ch (Nm ⁻²)	^z ch (cm)	τ _S	τ _C (Nm ⁻²)
KT	≃0	1.0	0.30	0.16	0.23	0.10
KT	≃0	2.0	0.30	0.11	0.23	0.10
KT	≃0	3.0	0.35	0.03	0.26	0.10
KS	35	1.0	0.21	0.40	0.15	0.04
KS	35	1.7	0.29	0.30	0.22	0.04
KS	35	3.0	0.33	0.32	0.23	0.04
KS	35	5.6	0.34	0.26	0.33	0.04
KS	35	10.0	0.40	0.40	0.37	0.04
LM	0.5	1.7	0.21	0.09	0.16	0.08
LM	1.0	1.7	0.27	0.07	0.24	0.12
LM	2.0	1.7	0.33	0.05	0.28	0.17
LM	5.0	1.7	0.40	0.12	0.34	0.17
LM	10.0	1.7	0.62	0.17	0.39	0.17

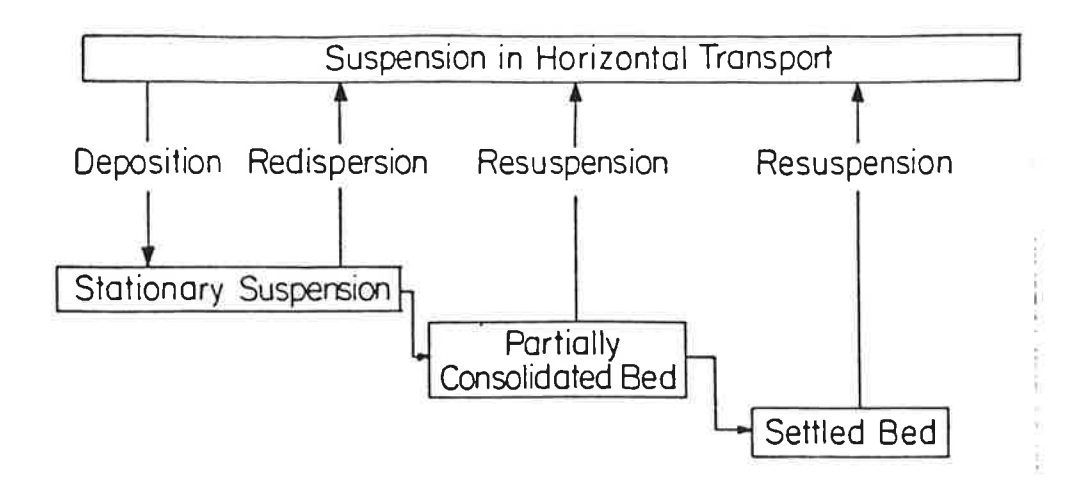


Fig. 1. A Representation of the Physical States of Fine, Cohesive Sediment under Tide-Dominated Flows.

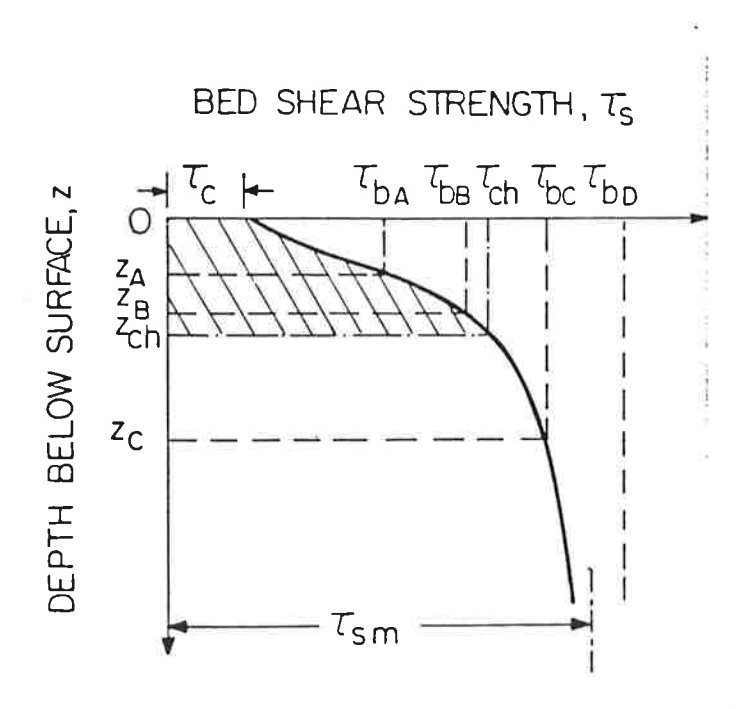


Fig. 2. A Representation of the Depth-Variation of the Bed Shear Strength.

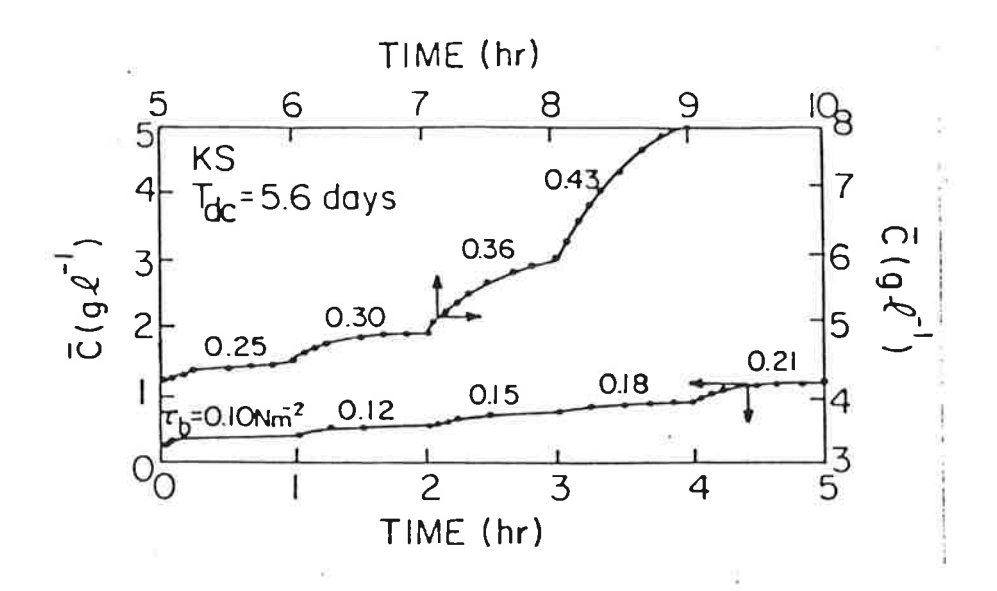


Fig. 3. An Example of Experimentally Observed Time-Variation of Suspended Sediment Concentration, Series KS, T_{dc} = 5.6 Days.

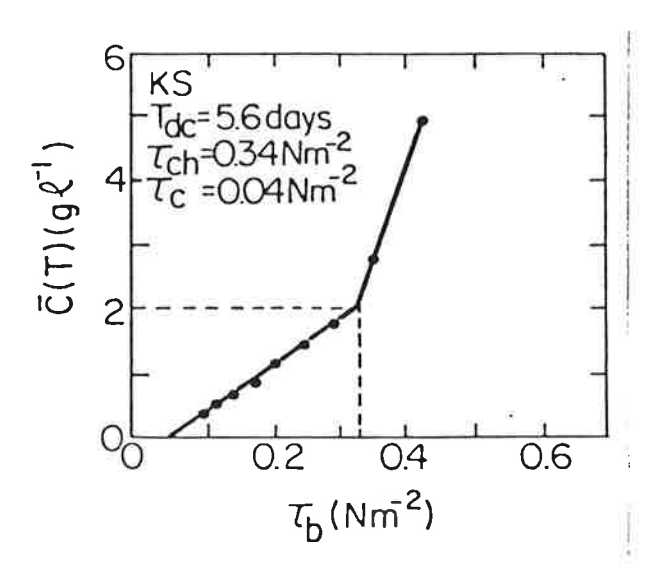


Fig. 4. Concentration, $\overline{C}(T)$, at the End of a Time-Step against Corresponding Bed Shear Stress, τ_b , Series KS, T_{dc} = 5.6 Days.

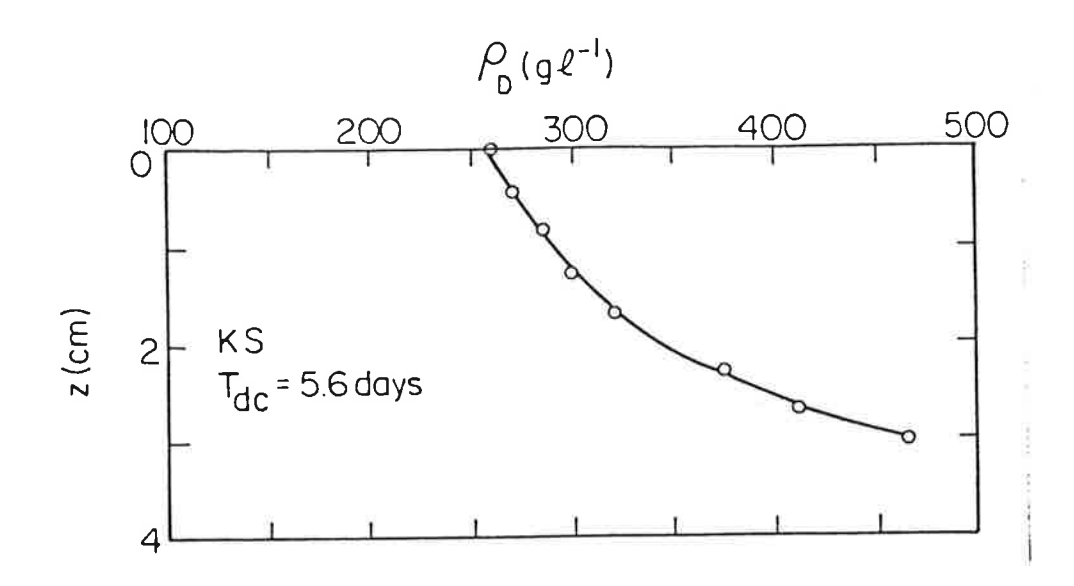


Fig. 5. Depth-Variation of Bed Dry Density, Series KS, T_{dc} = 5.6 Days.

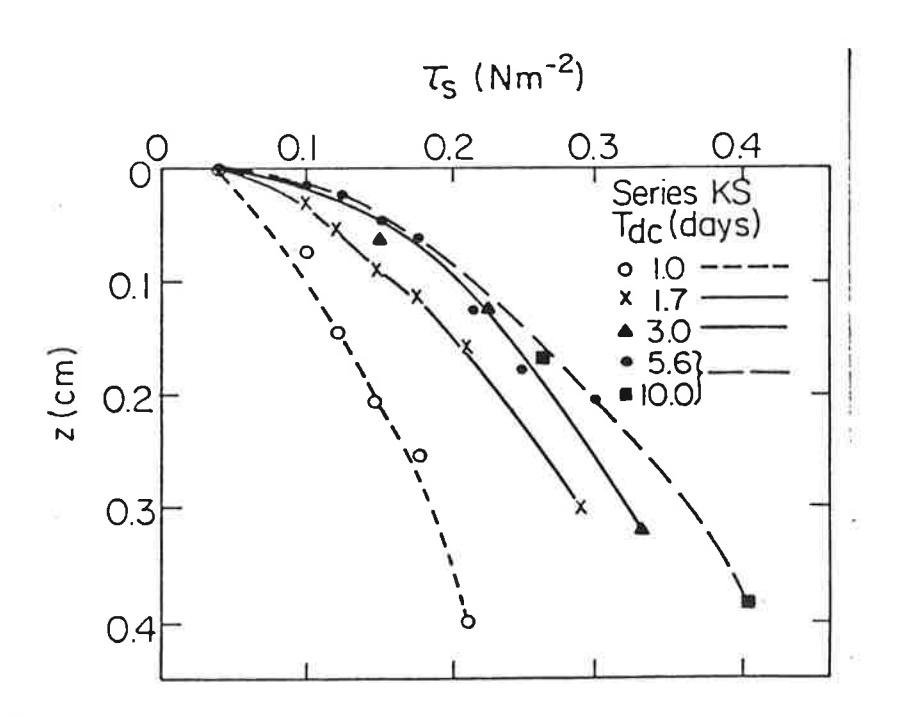


Fig. 6. Bed Shear Strength $\tau_{\rm S}(z)$ Profiles, Series KS.

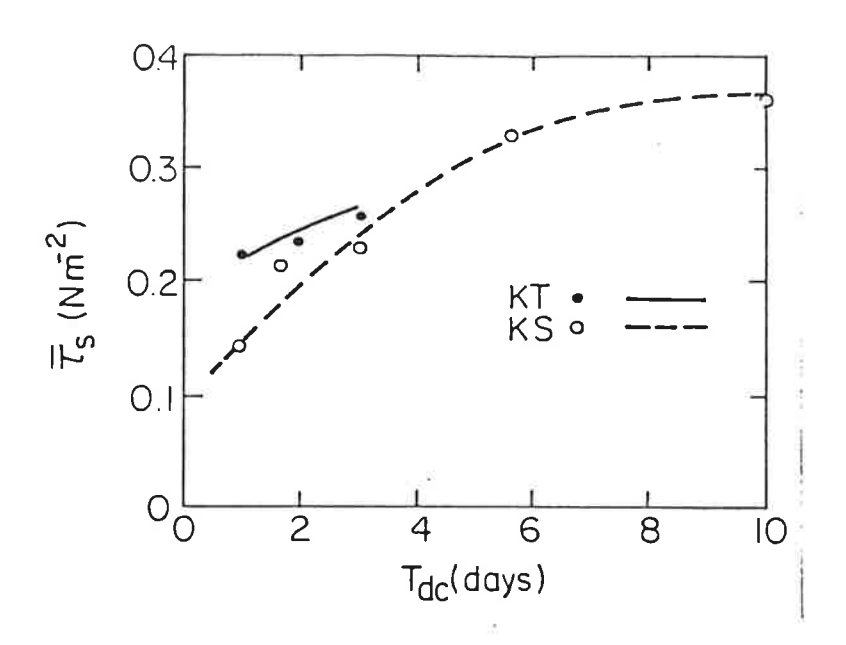


Fig. 7. $\overline{\tau}_{\text{S}}$ against T_{dc} , Series KT and KS.

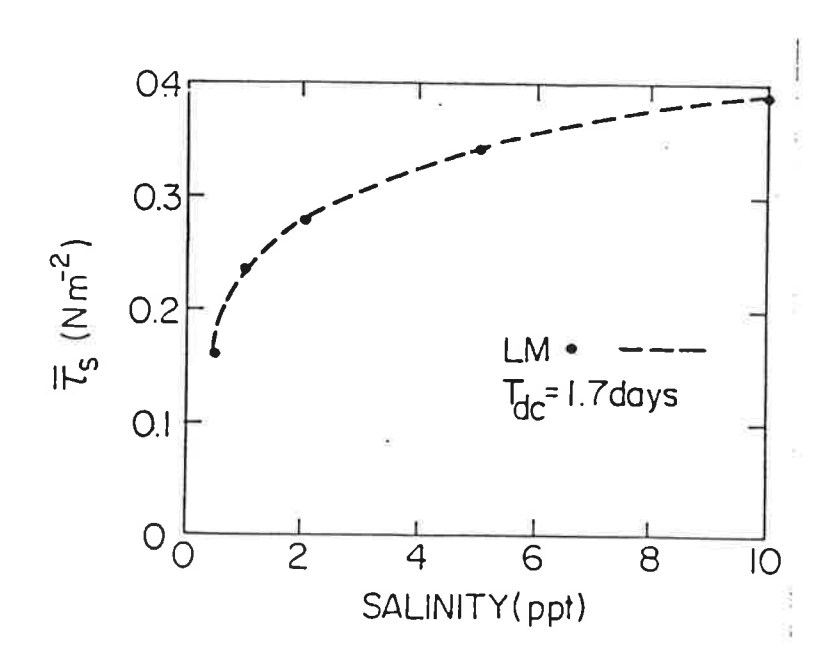


Fig. 8. $\overline{\tau}_{\text{S}}$ against Salinity, Series LM.

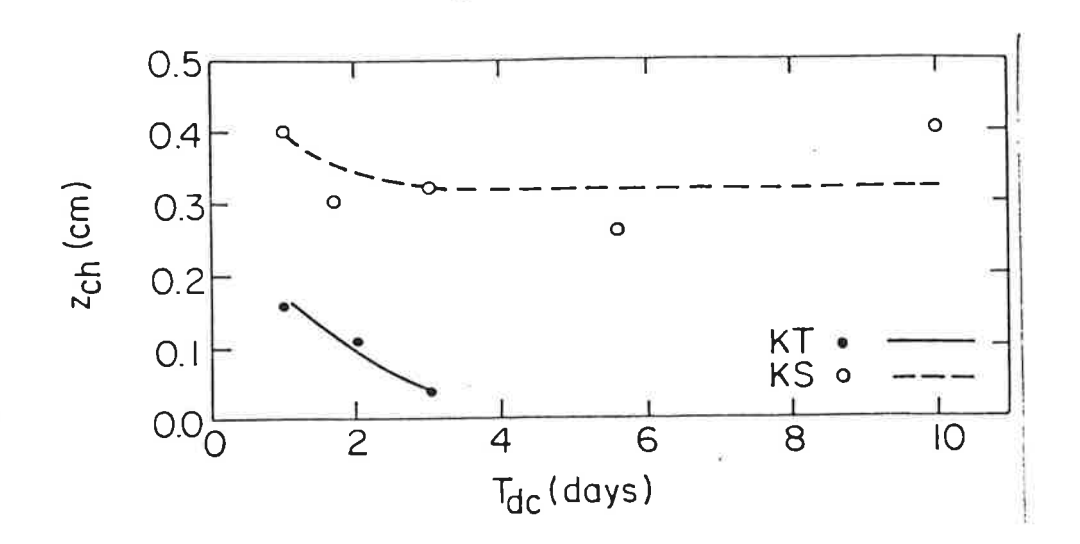


Fig. 9. z_{ch} against T_{dc} , Series KT and KS.

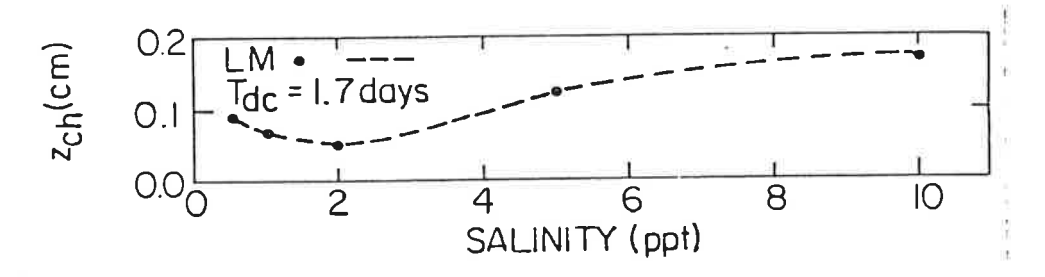


Fig. 10. z_{ch} against Salinity, Series LM.

Rough walls

Sucooth Walls

$$\int_{u_{\star}}^{\rho i \rho e} \frac{\overline{u}}{u_{\star}} = 5.75 \log 13.5 \frac{R}{\varepsilon}$$

$$\frac{ii}{u_{\star}} = 5.75 \log 4.05 \frac{Ru_{\star}}{v}$$

$$\frac{1}{\sqrt{1+c_1}} \frac{\overline{u}}{u_{\star}} = 5.75 \log 11.1 \frac{Z}{\varepsilon}$$

$$\frac{c\overline{c}}{u_x} = 5.75 \log 3.67 \frac{Rac}{D}$$

For average \mathcal{C} around boundary, steady uniform flow, $\mathcal{C} = pgRS = SRS$

FROM U.S. GEOLOGICAL SURVEY WATER SUPPLY PAPERS

SACRAMENTO RIVER BASIN

11447500 SACRAMENTO RIVER AT SACRAMENTO, CA--Continuel

		96	7.736	. 50. 31	2 127404	· 4 * 5 * * * *	- 1557-64	Emza rd	3EPTE 4-14	379		
2		147		195130 78	3.5	ore talls						
					****	*44	120	W 1 T	304	HYL	3116	SEP
A *	116.7	44.	35.0	714		3.00						
			222	500		40.00					23.0	5.53
£6						***					24.5	2
2		1.5.0		5.				25.0				23.5
16	51.0	A + + -	5.5.5			1	(5.0)		66.5			25.0
	****		2. 5.							***		24.)
*		1										
			85.00		***		***	14.5		51.0	23.0	
5			~ · ^		0.450	13.5				***	5.5-5	24.5
7	14.5				1							
+		14.00	11.5	4.3		***	15.0	15.0	20.0			
4		*				11.3		15.0			55.0	7.7
10	1		4.5			40.70		18/52				
							**-		22.5			
1.1			7.7			14.2	16.0			22.5		24.5
12	18.5			10.					21.0	22.5		22.5
1.3		4.5	79.	11.5	3.5				1000	55.5	222	
1 4			2.0			12.00				23.0	22.5	555
15		C . 7		4.	1	D (2000)						
				0.750 124					20.0			25.0
16	17.4		T-5-5	10.			15.5	19.0	20.0	25.0	21.0	
1.7		1.1.0		10.0		12.5	100					22.5
1.4		9.2		11		(2.5	14.5		23.0		27.5	
14	17.5		9.4	2.4.0		17.5	0.00			23.5	23.5	23.0
20			0.00									
					3092	13.0			20.5			
21				4.5	5	14.3			22.	24.0		
25				11.0	17.5	14.5	14.5	41.5				
23			2.0		4.0			224	22.5	25.0		
24	14.5	11.		***			15.5		, eeee	22.5		
25		10.3		3.0	1 - , 5		17.7					
						12.2	15.0	40.0	21.0			(5.55)
2 5	The said	1000				* <u>505</u>		19.5	A-4-2		24.0	
27				S-3.7.2	• • •					22.5		21.5
2 14	56.0			4.5				19.0	23.5	22.0	22.5	22.0
24		2.25				12.3	12.5	14.5				
30	10.0	10.0	. 1	1775		14.3	12.5				22.0	
31		400	7.47	1.0			222					
	0/5350					445				***		
27. 40.					***							

SUSPENDED-SEDIMENT DISCHARGE (TONS/DAY). WATER YEAR OCTOBER 1978 TO SEPTEMBER 1979

	-	• •							
		OCTOBER			NOVEMBER			DECEMBER	
		001000						MEAN	
		MEAN			MEAN	SEDIMENT	MEAN	CONCEN-	SEDIMENT
	MEAN	CONCEN-	SEDIMENT	MEAN	CONCEN-	DISCHARGE	DISCHAPGE	TRATION	DISCHARGE
	DISCHARGE	TRATION	DISCHARGE	DISCHARGE	TRATION	(TONS/DAY)	(CFS)	(MG/L1	(TONS/DAY)
DAY	(CFS)	(MG/L)	(YAC\ZNCT)	(CFS)	(MG/L)	(TUNS/UNT)	(6,3)	17.10.2.	
				11100	27	809	13400	23	832
1	15700	28	1190	10990	26	765	13400	23	832
2	15500	32	1340		22	647	13630	5.5	808
3	15300	29	1160	10900	23	658	13500	22	802
	14500	27	1060	10600	25	715	13000	25	877
5	14700	28	1070	10630	2 3	713			
				10900	24	706	12800	30	1047
6	14200	30	1150	11300	25	763	12900	26	905
7	14200	32	1230	11300	24	732	13000	18	632
8	14000	30	1130	11200	24	726	12900	17	592
9	14300	28	1080		23	689	12800	16	553
10	13600	2 4	881	11100	23	• • • • • • • • • • • • • • • • • • • •			
			919	11100	23	687	12730	15	514
11	12500	27		11300	22	671	12700	20	695
12	12500	38	1280 1410	11500	17	528	12300	1 7	5.53
13	12400	42		11700	16	505	12900	21	725
14	15100	39	1270	11900	16	514	12900	18	627
15	12100	42	1370	11400					
			1290	11900	21	675	12900	18	521
16	11900	* 0	1280	12000	23	745	13270	17	606
1.7	11670	4.1	1280	15000	22	713	13560	19	693
18	1130)	42	1280	12200	25	823	13360	16	596
19	11300	42		13100	29	1030	13900	5.3	1093
50	11300	39	1190	12102	•				
		39	1190	14100	34	1290	13500	2.5	943
51	11300		1080	15000	4.2	1770	13500	1.8	650
22	11100	36	839	16100	48	2090	13500	1.5	437
23	11100	28	756	15700	53	2250	13500	13	474
2 4	11200	25	726	14890	4.1	1640	13300	13	467
25	11200	2 4	125	14047					
		25	800	14200	33	12'0	13300	13	467
56	11400		824	13800	33	1239	13200	13	463
27	11300	27	742	13512	32	1170	13200	13	≜ 53
24	11000	25	772	13400	33	1190	13200	13	463
29	11000	25		13500	27	984	13200	13	463
30	10400	25	736	13390	W - H		13400	15	5▲3
31	11000	24	713	2.3.3					100
			33038	373300		28987	409300	***	20471
TOTAL	387100		91016	3.3377					

127

SE TOURSES PINER BASIN

11447500 SALRAMUNTA RIVER AT SACRAMENTO, CA--Continued

SUSPENDED-SEDIMENT DISCHAPGE (TONS/DAY), WATER YEAR OCTOBER 1978 TO SEPTEMBER 1979

		JANUARY			FEBPUARY			⊭ APCH	
DAY	MEAN DISCHARGE (CFS)	MEAN CONCEN- TRATION (MS/L)	SEDIMENT DISCHARGE (TOWS/DAY)	MEAN DISCHARGE (CFS)	MEAN CONSEN+ TRATION (MG/L)	TEDIMENT DISCHARGE (TONS/DAY)	MEAN DISCHARGE (CFS)	REAN CONCEN- TRATION WWGZE)	SEDIMENT DISCHARGE (TOMSMOAY)
1	13300	18	646	15000	30	1220	43500	7.6	
2	13200	13	463	14700			42200	75	€550
3	13100	15	531	14700	31 29	1230	50600	75	1 0 5 0 0
	13300	14	503				52400	70	9500
5		_		13200	23	320	47500	65	6340
5	13300	15	539	12900	5.3	801	4 2 2 9 0	€ 5	7410
6	13300	14	503	12700	22	754	3 8 0 0 0	75	7690
7	13300	1.4	503	12500	23	776	34500	90	5390
8	13600	15	551	12200	21	592	31500	98	8330
9	14500	28	1100	11900	19	610	2 - 5 0 0	105	6120
10	16100	35	1520	11000	20	6 2 6	00005	101	7640
11	19100	4.8	2480	11400	23	158	1150 0	95	6230
12	30500	130	10700	11400	20	616	25000	84	5670
13	35500	130	12500	12400	23	770	23500	71	4500
14	34800	140	13200	16700	35	1580	21500	60	3480
15	38200	150	16500	31800	270	13200	20400	50	2750
16	43600	220	25900	37600	390	39400	20500	50	2770
17	46100	360	47300	39100	360	35000	22800	60	3690
18	~ 3700	280	33000	41100	260	28900	26800	65	4700
19	38300	160	16500	41600	165	16600	23600	60	4530
20	33400	105	9470	46500	180	22600	28900	55	4290
21	29500	95	7590	51400	ã 2 O	30500	2720 0	50	3670
22	25800	70	4680	57000	180	27700	23900	56	3610
23	23300	50	3150	65600	190	34200	21600	60	3500
24	21400	55	3180	71300	160	30800	20300	60	3290
25	19800	65	3470	70790	115	22000	19100	60	3090
26	18300	48	2370	66400	110	19700	18400	60	2980
27	17400	40	1880	57100	115	17700	18700	56	2830
28	16400	38	1680	47400	95	12200	21600	80	4670
29	15800	34	1450				29800	210	16900
30	15500	32	1340				32200	360	31300
31	15300	31	1280	222			36400	365	30000
TOTAL	718900		226679	908400	***	378003	904100		233680

SUSPENDED-SEDIMENT DISCHARGE (TONS/DAY), WATER YEAR OCTOBER 1978 TO SEPTEMBER 1979

			APRIL			HAY			JUNE	
		MEAN	MEAN CONCEN-	SEDIMENT	MEAN	HEAN CONCEN-	SEDIBENT	HEAN	FEAN CONCEN-	SEDIMENT
		DISCHARGE	TRATION	DISCHARGE	D15CHARGE	TRATION	DISCHARGE	DISCHARGE	TRATION	DISCHARGE
	CAY	(CFS)	(MG/L)	(TONS/DAY)	(CFS)	(HG/L)	(TENS/DAY)	(CFS)	(MG/L)	(TONS/DAY)
				1.0.3,041,			1.013.0417		(, 0, 2,	(
	1	28200	220	16800	14300	34	1310	15500	26	1090
,	2	26100	120	8460	14400	34	1320	13800	23	857
	3	2 4 8 0 0	85	5690	14600	36	1440	13200	22	784
	4	23800	82	5270	14100	32	1220	13100	19	672
	5	22400	78	4720	12900	27	940	12200	22	725
	6	20400	68	3750	12900	27	940	11500	20	621
	7	18800	60	3050	12900	28	1250	11300	24	732
	8	18500	58	2900	17200	36	1670	11800	27	860
	9	18000	56	2720	19600	40	2120	11400	27	631
	10	17000	56	2570	20100	46	2500	11000	24	713
	10	17000	36	2370	50100	-0	2300	11000	24	(13
	11	16100	56	2430	19000	4.3	2210	11000	22	653
	12	15900	54	2320	16800	38	1720	11100	22	659
	13	14700	52	2060	15800	36	15+0	11600	21	658
	14	13400	46	1660	16200	30	1660	11600	2 2	689
	15	12600	40	1360	17200	4.4	2040	11800	5.5	701
	16	12500	39	1320	18000	56	2720	11600	22	689
	17	12800	40	1380	18190	62	3030	11300	24	732
	18	13100	30	1060	18500	61	3050	11300	24	732
	19	13100	25	884	19300	59	3070	11600	27	846
	20	12700		892	20300	55	3010		27	868
	20	12700	26	692	20300	22	3010	11800	21	000
	21	11200	25	756	20400	54	2970	11900	2 6	835
	2.2	10100	25	682	20600	48	2670	12100	32	1050
	23	11000	29	861	21800	43	2530	11900	27	868
	24	13200	36	1280	22100	40	2390	12200	27	889
	25	14900	43	1730	55600	41	2500	12700	27	926
	26	16300	49	2160	22300	38	2290	12700	26	892
	27	16300	45	1980	20700	36	2010	12500	24	810
	28	16200	40	1750	19700	32	1700	13100	30	1060
	29	16600	38	1700	18890	S 32	1620	13500	33	1200
	30	15700	37	1570	18000	30	1460	14100	34	1290
	31	15/00	37	1210	17100	29	1340	W	34	1290
	31				11100	29	1340			
1	IATO!	496400		85765	557500		62040	366200		24924

SACRAMENTO RIVER BASIN 11447500 SACRAMENTO RIVER AT SACRAMENTO, CA--Continued

SUSPENDED-SEDIMENT DISCHARGE (TONS/DAY), WATER YEAR OCTOBER 1978 TO SEPTEMBER 1979

		JULY			AUGUST			SEPTE #8ER	
DAY	MEAN DISCHARGE (CFS)	MEAN CONCEN- TRATION (MG/L)	SEDIMENT DISCHARGE (TONS/DAY)	MEAN DISCHARGE (CFS)	MEAN CONCEN- TRATION (MG/L)	SEDIMENT DISCHARGE (TONS/DAY)	MEAN DISCHARGE (CFS)	MEAN CONCEN- TRATION (MG/L)	SECIMENT DISCHAPSE (TONS/CAY)
1		34	1370	17200	30	1390	13800	48	1790
2		35	1460	17100	28	1290	14300	46	1780
3	16200	35	1530	17100	29	1340	14500		
	16600	35	1570	17000	30	1380	14400	46	1800
5	16500	34	1510	16990	30	1370	14700	46 45	1790 1790
6	16400	33	1460	17100	30	1390	14800		
7	16300	32	1410	17300	31	1450	15100	44	1760
а	16300	32	1410	17500	32	1510		43	1750
9	16600	33	1480	17630	27	1280	15300 15700	. 42	1740
10	16800	32	1450	17400	25			42	1780
					25	1170	15900	41	1760
11	16900	33	1510	17000	24	1100	15500	41	1720
12	16430	32	1420	17000	27	1240	15500	40	1670
13	16000	32	1380	17000	28	1290	15400	40	1660
14	15600	33	1390	16690	28	1250	15100	39	
15	15600	32	1350	16400	26	1150	14900	39	1590 1570
16	15300	29	1200	15900	26	1120	15100		
17	15200	27	1110	15900	26		15100	38	1550
18	15000	26	1050	15820	29	1120	15100	37	1510
19	15100	28	1140	15600	30	1240	14900	36	1450
20	15800	29	1240			1260	14600	34	1340
20	13000	27	1240	15500	27	1130	14500	35	1250
21	17000	33	1510	15300	27	1120	14400	34	
22	17600	34	1620	14700	28	1110	14500		1320
23	17800	34	1630	14400	28	1990	14300	34	1330
24	17800	30	1440	14300	35	1240	14300	33	1270
25	17500	28	1320	13800	33	1230	14000	32 31	1240 1170
26	17500	28	1320	13700	•			_	
27	17200	28	1300	13300	34	1260	13200	28	998
28	16800	27	1220		37	1330	13100	26	920
29	16700	28		12900	39	1360	13200	25	891
30	16900		1260	12800	37	1280	13200	24	855
		28	1280	12800	34	1180	13700	23	851
31	17003	31	1420	13100	46	1630			
TOTAL	508800	-	42760	486000		39300	437000		43895
YEAR	6553000		1219542						

SUMMARY OF WATER AND SEDIMENT DISCHARGE, WATER YEAR OCTOBER 1978 TO SEPTEMBER 1979

HONTH	WATER DISCHARGE	SUSPENDED SEDIMENT DISCHARGE	BEDLOAD Discharge	TOTAL SEDIMENT DISCHARGE
	CFS-DAYS	TONS	TONS	TONS
OCT08ER 1978	387100.00	33038.00	417	33500
NOVEMBER	373300.00	28987.00	406	29400
DECEMBER	409300.00	20471.00	473	20900
JAMUARY 1979	718900.00	226879.00	23600	250000
FEBRUARY	909400.00	378003.00	87700	466000
MARCH	904100.00	233680.00	37400	271000
APRIL	495400.00	85765.00	3550	89300
MAY	557500.00	620*0.00	3730	65800
JUYE	366200.00	24924.00	302	25200
JUL7	503300.00	42760.00	1890	44600
AUGUST	485000.00	39300.00	1530	40900
SEPTEMBER	437000.00	43675.00	900	44830
TOTAL	6553000.00	1219542.00	161948	1381400

PERIODIC DETERMINATIONS OF SUSPENDED-SEPTEMENT CONCENTRATION AND TURBIDITY, WATER YEAR OUT SEE 1978 to SEPTEMBER 1878.

SATE_	TIME	STREAM- FLCW+ INSTAN- TANEOUS (CFS)	TEMPER- ATURE: WATER (DEG C)	SED:- MENT. SUS- PENCED (MG/L)	SEDI- MENT DIS- CHARGE: CUS- PENDED (TYDAY)	TUR- 810- 1TY (NTU)
OCT 03 07 10 12 12 12 18 19 24 26 30 NOV	2030 2045 2015 1205 1245 1345 2015 1910 1630 1930 1710 1630	13900 12200 13800 13690 13200 12200 12900 2400 10900 11700 11460 8220 8980	21.5 18.5 18.5 18.5 18.5 17.0 17.5 18.5 18.5 18.5 18.5	22 30 26 34 40 42 41 39 20 28 24 19	826 968 969 1250 1380 1380 1310 937 589 635 739 422 461	7.0 10 5.6 8.0 10 7.0 8.0 6.0 8.0 7.0 6.0
02 63 65 68 13 17 18 24 25 26 30	1610 1740 1620 1445 1930 1645 1645 1230 1615 1645 0920 2130	8590 8100 11400 10300 12000 9300 10600 14100 14200 14900 14500	13.5 14.5 14.0 8.5 8.5 11.0 10.5 11.0 10.5	22 16 42 22 16 13 20 20 53 35 30 28 24	510 350 1290 612 518 326 572 626 2020 1340 1130 1060 940	7.0 6.0 7.0 6.0 7.0 6.0 7.0 6.0 7.0 12 10 8.0
DEC 04 06 08 10 11 11 11 14 18 19 20 23 28 30 31	1745 1615 2030 2015 1300 1545 1415 1620 1315 1415 1530 1530 1815	13100 13000 14000 13900 11800 11200 13130 13100 13600 13700 13600 9810 10100	10.0 8.0 11.5 7.5 7.0 5.8 9.5 8.0 7.5 7.5 6.5	19 33 20 17 13 11 13 19 19 16 33 12 11	672 1160 756 638 414 333 397 621 698 592 1210 428 291 245 484	5.0 6.0 4.0 5.0 4.0 5.0 6.0 5.0 6.0 5.0 4.0
JAN 01 02 03 08 19 12 13 16 16 18 18 18 22 24 25 28 31	1405 2030 1450 1545 2115 1040 1625 2200 0945 1615 1645 1340 1720 1715 1720 1745 1720 1745	13900 10900 13800 13200 31600 35600 34800 34900 43200 43400 43400 43400 25100 25100 21900 13500 13600	6.5 6.0 7.0 14.0 9.5 10.0 10.5 9.0 10.0 10.0 10.0 10.0 10.0 10.0 10.0	24 11 16 13 36 141 125 145 145 145 145 231 257 228 257 220 130 66 58 37 31	901 324 596 463 1600 12000 13600 26900 23500 25700 30300 25700 13100 4820 3930 3930 3930 3930 3930 3930 3930 39	6.0 5.0 6.0 17 45 65 90 160 90 95 85 50 40 28 28 28 18
FEB 03 07 08 09 11 15 16 21 21 21	0730 1445 1745 1940 1845 1715 1645 1740 0835 0940 1845	14200 9940 13000 12200 12400 35200 38000 42100 50800 51300 58600	7.0 9.5 9.5 10.0 10.5 12.0 9.5 9.5 9.5	33 19 26 22 19 25 365 400 244 237 195 183	1270 510 913 790 626 837 34700 41000 27700 32500 26700 25300 25900	14 10 13 10 10 9.0 70 160 90 70 75 70

SACRAMENTO RIVER BASIN

11447500 SACRAMENTO RIVER AT SACRAMENTO, CA--Continued

PERIODIC DÉTERMINATIONS OF SUSPENDED-SEDIMENT CONCENTRATION AND TURBIDITY, WATER YEAR OCTOBER 1978 to SEPTEMBER 1979

OATE	TIME	STREAM- FLOM: INSTAN- TANEOUS (CFS)	TEMPER- ATURE, WATER (DEG C)	SEDI- MENT. SUS- PENOED (MG/L)	SEDI- MENT DIS- CHARGE: SUS- PENDED (T/OAY)	TUR- 8[D- ITY (NTU)
FEB 23 25 27	0930 1345 2140 1840	66600 70800 53700 43500	9.0 10.5 9.5 9.5	204 112 114 83	36700 21400 16500 9750	120 40 50 45
MAR 04 17 18 18 19 21 22 26	1530 1910 1840 1615 1610 1715 1615 1340 1745 1845 2120	46600 34500 28000 25000 20500 28200 29100 26700 23900 18200 31200	11.5 12.5 13.0 14.5 12.5 12.5 13.0 14.0 12.5	63 93 100 82 49 64 58 49 62 60	7930 8660 7560 5540 2710 4870 4560 3530 4000 2950 34600	21 24 25 24 16 17 13 15 17 23 160
APR 02 04 09 12 17 17 19 23 25	1830 1745 1615 1720 0740 0915 1035 1645 2115 1645 1845	26300 23900 16900 14500 9840 11000 12770 14000 13400 14200 15400	13.5 15.0 15.0 16.0 15.5 15.5 14.5 14.5 15.5 15.5	99 81 51 60 33 30 37 25 35 43 49	7030 5230 2330 2350 877 891 1270 945 1270 1650 2040	25 20 16 17 17 13 13 12 13 14 14
30 MAY 03 06 10 17 23 26 27 29 30	1830 1615 1230 1430 1430 1730 2045 2020 1545 1300	15700 12900 20500 21100 18700 21400 20700 20100 19600 18430	15.0 14.5 15.0 16.0 19.0 21.5 20.0 19.5 19.5 19.5	38 25 41 50 65 39 36 32 29 32	1610 871 2270 2850 3280 2250 2010 1740 1540 1590	13 11 13 17 14 12 10 10 10
JUN 04 09 11 13 16 17 19 21 24 26 26 26 26	1545 2020 1630 1610 1845 1945 1415 1945 1430 2015 1000 1025 1045 1710	12900 10300 12400 13300 12900 12900 11200 11200 12800 13400 13500 13500	22.5 20.0 22.5 21.0 20.0 23.0 23.5 22.5 22.5 20.5 20.5 20.5 20.5 20.5	19 26 24 22 23 24 26 24 27 27 26 38 35	662 723 804 790 801 797 786 771 1290 726 933 977 927 1390	7.0 9.0 10 8.0 9.0 9.0 12 9.0 12 12 11
JUL 96 12 13 15 17 29 24 25 24 29	2020 1710 2015 2010 2045 1515 1545 2015 1430 1310 1215	16500 17209 16100 15900 15900 14700 15700 17200 18810 16201 17000 17600	21.0 22.5 22.5 22.5 23.0 25.0 25.0 26.0 22.5 22.5	33 34 32 33 30 25 27 34 32 29 26 28	1470 1580 1390 1420 1290 992 1150 1580 1620 1430 1190	9.0 8.0 10 10 8.0 9.0 11 9.0 9.0 9.0
AUG 01 02 10 17 17 17	2015 1530 1715 1530 1530 0810 3919 0925 1010	17100 16700 16800 18400 16000 17200 17300 17300 17400	23.0 24.5 23.0 22.0 22.5 22.0 21.0 21.0	38 28 23 25 26 27 29	1750 1260 1270 1149 1089 1210 1260 1360	8.0 9.0 6.0 9.0 10 11 10 9.0

BACRAMENTO RIVER BASIN

11447500 SACRAMENTO RIVER AT SACRAMENTO, DA--Continued

PARTICLE-SIZE DISTRIBUTION OF SURFACE BED MATERIAL. MATER YEAR OCTOBER 1978 TO SEPTEMBER 1979

											. , , ,	
DATE OCT	TIME	STREAM- FLOW: INSTAN- TANEOUS (CFS)	FEMPER- ATURE: WATER (DEG C)	NUMBER OF SAM- PLING POINTS	BEB MAT. SIEVE DIAM. & FINER THAN .U62 MM	BED MAT. SIEVE DIAM. & FINER THAN .125 MM	BED MAT. SIEVE DIAM. & FINER THAN .250 MM	GED MAT. SIEVE DIAM. % FINER THAN .500 MM	BED MAT. SIEVE DIAM. % FINER THAN 1.00 MM	BED MAT. SIE/E DIAM. FINER THAN 2.00 MM	BED MAT. SIEVE DIAM. & FINER THAN 4.30 MM	SED TAM. SIEVE DIAM. FINES THAN 8.00 MM
12	1230	12000	18.5	5								
12	1231				0	2	6	68	96	100		
12	1232				0	1	4	68	98			9.9
12	1213				0	1	11	87	98	100		5.5
12	1234			-5.5		0	14	7.7	94	98		(2/2)
DEC					0	3	54	97	99	100	100	90.00
11	1305	11800	7.0	5	0					100		***
11			4		1	3	64	98	99	99	100	
11	1307			-		2	23	96	100		100	92
11	1308				0	1	12	84	99	100		***
11 JAN	1309				6	17	3	61	97	100		
10	1.000				J		24	66	93	99	100	3630
19	1400	43600	10.0	5	5	15	24					
18	5041				0	1	7	67	94	100		(22)
18	1403			-	0	ī	27	66 89	97	100	-	**
18	1404					0	22	87	99 96	100		58363
FEd					0	2	60	100	76	99	100	* *
21	0835	50800	9.5	5	_			100				
21	0836				0	1	14	63	97	100		
21	0837	**				0	11	66	97	100		(7.7
21	0838					9	10	77	98	100		
21	0839				0	0	27	94	98	99	100	***
MAR 21					U	3	67	100			100	3.3
21	1300	26400	14.0	5		2	19					3.5
51	1301					ō	3	71	98	100		***
21	1302 1303					ě	5	80	98	100		2.5
21	1304				0	ĭ	23	82	97	99	100	221
APR	1304				0	ī	58	94 99	99	100	-	
17	0915	11000	15.5	_			30	99	100			7.5
17	0916	11000	12.5	7	7.7	76	86	93	97	• •		
17	0917				2	2	10	50	94	99	100	16.60
17	0918				8	12	20	88	98	100		18.80
17	0919				0	l	11	90	98	100	100	
17	0920				10	1	22	97	99	100	45	34047
17	0951	~-			27	18	68	97	99	99	100	7550
MAY					2.7	69	94	99	100		7.00	
30	1530	13500	18.5	5	42	0	37					9.4
30.,.	1531 1532				0	1	17	96	100			200
30	1533		44		0	2	15	92	98	100		5272
30	1534		***			ō	6	94	100			
JUN	1234		75.S		1	2	12	87 64	99	100		
26	1014	13300	20.5				• • •	0.7	94	99	100	
26	1015	13300	~U.S	5	9	14	26	63	92			
26	1016				1	3	9	90	99	100		
26	1017				2	3	7	78	96	100 98		
26	1018				l O	2	12	81	97	100	100	
JUL					V	1	36	96	99	100		
25,	1235	18200	24.0	5	6							
25	1236				ō	13 1	31	74	95	100		
25	1237 1238				ì	ž	7	77	97	100		
25	1238				0	2	32	90	100			
AUG	1234				1	3	51	93 98	97	98	99	100
17	0930	17300	31 -			_	٠.	70	100			
17	0931	17300	51.0	5	0	3	16	61	0.2			
17	0932					0	š	72	93 96	100		
17	0933				0	l	8	82	96	100		
17	0934				0	1	13	94	99	100		
SEP					1	4	45	97	99	100		••
13	1330	12700	22.5	5	1					100		
13	1331			##:	0	4	21	69	96	100		
13	1332		~ -		0	2	9	92	99	100		
13	1333				0	2	11	91	98	100		
	1334				õ	2	19	90	95	96	98	100
						_	42	99	100		70	100

SACRASENTO RIVER BASIN

11447500 SACRAMENTO RIVER AT SACRAMENTO, CA

LOCATION. -- Lat 35°35'12", long 121°50'16", Sacramento Jounty, Hylrologic [hit 1302010], on left mank 1,170 ft 300 m) upstream from 2 Street Bridge, in city of Sacramento, and 0.5 hi = 0.3 km) downstream from American

DRAINAGE AREA. ... 3,502 ml2 (50,370 km2).

REVISED RECORDS. -- WOR IA- 16-4: Orainage areasy

WATER-DISCHARGE RECORDS

PERIJO OF RECORD. -- January 1904 to July 1905 (gage heights only), June to November 1921, October 1948 to current year. Sage heights collected in this vicinity November 1879 to May 1888, December 1890 to September 1965 are contained in reports of U.S. Weather Bureau.

GE.--water-stage recorder. Datum of gage is National Deodetic Vertical Datum of 1929. Prior to Oct. 15, 1912, nonrecording gage in vicinity of I Street Bridge. Oct. 15, 1912, to Nov. 16, 1956, water-stage recorder at various sites in vicinity of I Street Bridge. Prior to Nov. 16, 1956, datum of gages at low-water mark of Oct. 25, 1856, 0.12 ft (0.037 m) NGVD. Auxiliary water-stage recorder on right bank 10.8 mi (17.4 km) downstream near Freeport. GAGE. -- water-stage recorder.

REMARKS.--Records good above 8,000 ft³/s (22⁻ m³/s) and fair below. Natural flow of stream affected by storage reservoirs, power development, diversions for irrigation, and return flow from irrigated areas. Flood flows bypass station through Yolo Bypass (stations 11426000), 11455000).

AVERAGE DISCHARGE.--31 years (water years 1949-79), 23,590 ft³/s (668 m³/s), 17,091,000 acre-ft/yr (21.1 km³/yr);

EXTREMES FOR PERIOD OF RECORD (since 1943)..-Maximum discharge, 104,000 ft³/s (2,950 m³/s) Nov. 21, 1950, elevation, 30.14 ft (9.187 m) site and datum then in use; minimum daily, 3,970 ft³/s (112 m³/s) Oct. 15, 1977.

EXTREMES OUTSIDE PERIOD OF RECORD. -- Maximum discharge known prior to Nov. 21, 1950, 103,000 ft³/s (2,920 m³/s) Jan. 17, 1909, elevation, 29.6 ft (9.02 m) present datum, from reports of California Department of Water

EXTREMES FOR CURRENT YEAR. -- Maximum Taily discharge, 71,300 ft³/s (2,020 m³/s) Feb. 24; minimum daily, 10,100 ft³/s (286 m³/s) Apr. 22.

DISCHARGE: IN CUBIC FEET PER SECOND: MATER YEAR OCTOBER 1978 TO SEPTEMBER 1979 MEAN VALUES

YAG	ост	NOV	DEC	PAL	FER	MAR	APR	MAY	NUL	JUL	≜UG	SEP
1	15700	11100	13400	13300	15000	42200	28200	14300	15500	14900	17200	13800
	15500	10900	13400	13200	14700		26100	14400	13801	15500	17100	14300
2			13600	13100	14000		24800	14820	13200	16200	17100	14500
\3	15300	10900		13300	13200		23800	14100	13100	16500	17000	14400
)4	14500	10600	13500		12900		22400	12910	12200	16500	16900	14700
5	[4500	10600	13000	13300	12900	42230	22-00	12970	12200			
6	14200	10900	12800	13300	12700	38000	20400	12900	11500	16:00	17100	14800
7	14200	11300	12900	13300	12500	34500	18900	13900	11300	16330	17300	15100
8	14000	11300	13000	13600	12200		18500	17200	11800	16300	17500	15300
		11200	12400	14600	11900		19000	19610	11400	16510	17600	15700
9	14300	11100	12800	16100	11600		17000	20100	11000	16313	17430	15900
10	13600	11100	12000	10100	11000	20,50						
11	12600	11100	12700	19100	11400	26500	16100	19000	11000	16900	17000	15500
15	12530	11300	12700	30500	11400	25000	15900	16890	11100	16400	17000	15500
13	12400	11500	12900	35500	12400	23500	14700	15800	11600	16000	17000	15400
14	12100	11700	12900	34300	15700		13400	16210	11500	15600	1,6600	15100
			12900	OCSAE	31800		12600	17290	11800	15600	16400	14900
15	12100	11900	12900	34510	31500	20400	12.700	,.				
16	11900	11900	12900	43600	37600	20500	12500	18000	11600	15300	15900	15100
17	11600	12000	13200	45172	39100	00ESS	12800	18190	11303	15200	15900	15100
18	11300	12000	13500	43700	41100		13103	18500	11300	15000	15800	14900
19	11300	12200	13800	38300	41800		13100	19300	11600	15100	15600	14500
		13100	13900	33433	45500		12700	20300	11800	15800	15500	14500
2 0	11300	13100	13410	33477	13300	23.70						
21	11300	14100	13500	29500	51400	27200	11200	20400	11900	17000	15300	14400
55	11100	15600	13500	25300	5700)		10100	20600	12100	17600	14700	14500
53	11100	16100	13500	23 100	55000		11000	21900	11900	17800	14477	14300
24	11200	15700	13500	21400	71300		13200	22100	12200	17800	14333	14300
		148)0	13300	19830	70700		14900	22500	12700	17500	13800	14000
25	11200	14570	13300	190)9	, , , , ,	27170						
26	11430	14210	13300	18310	66400	18-00	16300	22300	12700	17500	13700	13500
27	11300	138)0	13200	17400	57100		16300	20700	12500	17233	13330	13100
28	11000	13500	13200	16-00	47400		16215	19700	13100	16800	12900	13200
		13400	13200	15300			15630	13800	1350)	16750	12900	13200
29	11000			15500	200		15700	18000	14100	16911	12901	13700
30	10900	13500	13200		-			17100		1700)	13150	
31	11000		13+00	15301		30411		11103				
TOTAL	387100	373300	497300	714933	900 = 10	904100	495431	557500	366210	508300	+85500	437000
MEAN	12497	12440	13200	23190	32447	29:50	16350	17920	15510	16410	15431	14579
MAK	15710	16100	13900	46100	71300		28211	22510	15500	17810	17611	15700
4[4	10950	10600	12700	13102	11-33		10100	12990	11000	14900	12800	13100
		743450	911400	1425000	[805000		984600	1106000	725430	1009300	+5→900	866830
4C-FT	767800	149470	011300	140000	1071711	1.75079		, .				
CAL YO	1973 70	TA1 435	7900 ME	AN 255+1	X A M	79301 414	10500	ACHF T	18561010			
#IR YR				AN 17950		71300 415	10100	AC-FT	13000000			
4 · A · A	1777 10		3.00									

TIDE TABLES 1978

HIGH AND LOW WATER PREDICTIONS

WEST COAST OF NORTH AND SOUTH AMERICA

Including the Hawaiian Islands

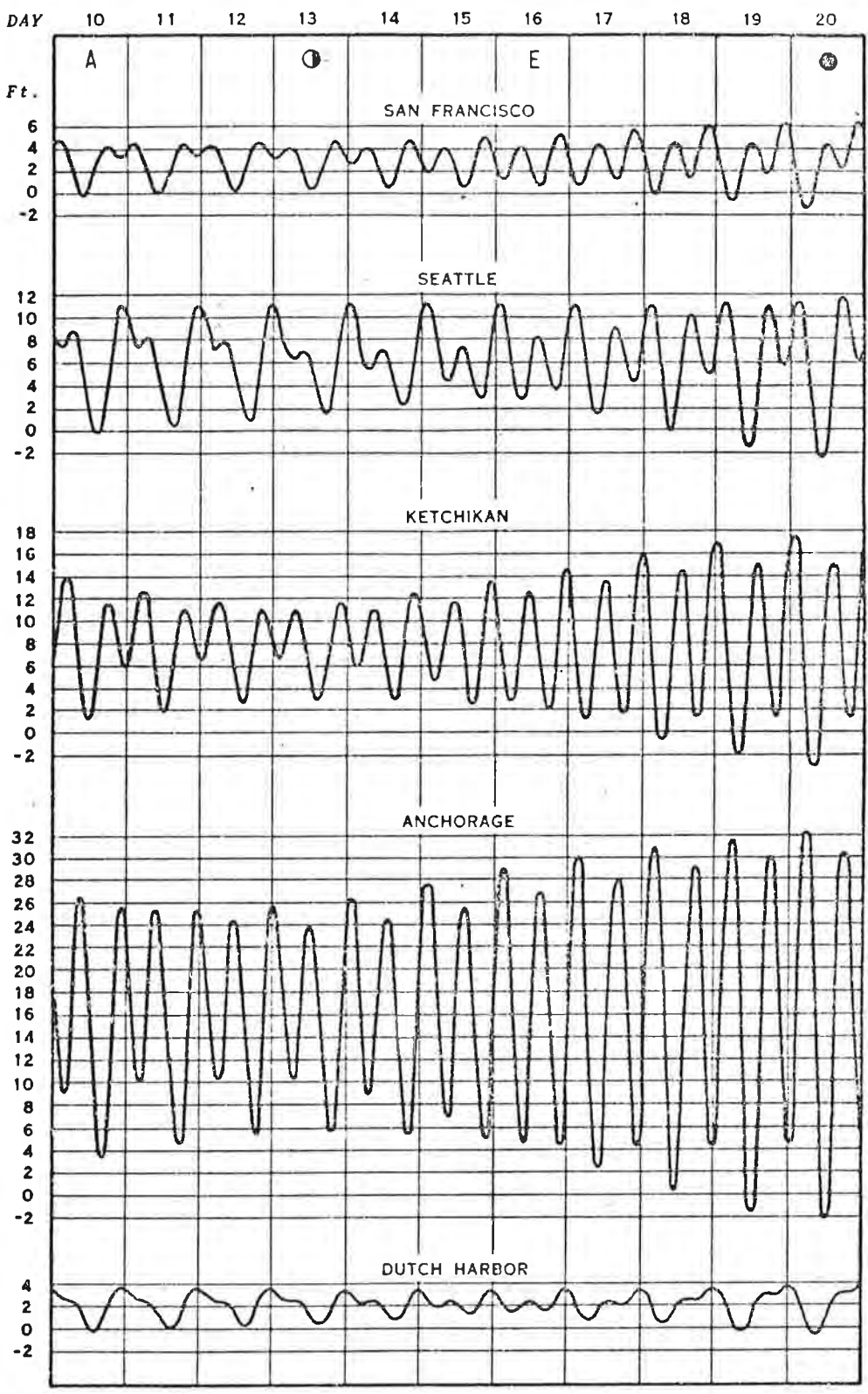
Issued 1977



DEPARTMENT OF COMMERCE Atmospheric Administration SURVEY Elliot L. Richardson, Secretary

National Oceanic and Robert M. White, Administrator

NATIONAL OCEAN Allen L. Powell, Director



A discussion of these curves is given on the preceding page.

A - Moon in apogee Lunar data:

O - last quarter E - Moon on Equator

new Moon

Range.—The mean range is the difference in height between mean high water and mean low water. The spring range is the average semidiurnal range occurring semimonthly as the result of the Moon being new or full. It is larger than the mean range where the type of tide is either semidiurnal or mixed, and is of no practical significance where the type of tide is diurnal. The diurnal range is the difference in height between mean higher high water and mean lower low water.

Caution.-For stations where the tide is chiefly diurnal the time differences and the height differences and ratios are intended primarily for predicting the higher high and lower low waters. When the lower high water and the higher low water at the reference station are nearly the same height, the corresponding tides often cannot be obtained satis-

factorily by means of the tidal differences.

Datum.—The datum of the predictions obtained through the height differences or ratios is also the datum of the largest scale chart for the locality. To obtain the depth at the time of high or low water, the predicted height should be added to the depth on the chart unless such height is negative (-), when it should be subtracted. To find the height at times between high and low water see table 3. On some foreign charts the depths are given in meters and in such cases the heights of the tide can be reduced to meters by multiplying by 0.3 before being applied to the charted depths. Chart datums for the portion of the world covered by these tables are approximately as follows: Mean lower low water for the Pacine coast of the United States, Alaska and the Hawaiian Islands; mean low water springs for Central America and Mexico. For the rest of the area covered by these tables the datums generally used are approximately mean low water springs, Indian spring low water, or the lowest possible low water.

Mean Tide Level (Half Tide Level) is a plane midway between mean low water and

mean high water. Tabular values are reckoned from chart datum.

Note. - Dashes are entered in the place of data which are unreliable, unknown, or given in another part of this book.

	14	PC	OSITI	ОИ				DIFFER	RENG	CES		RAN	GES	
No.	PLACE		T				Tim	e	1	Heig	ht	1		Mean Tide
No.	rosec	Lat.		Long	3.	Hig		Low		High water	Low water	Mean	Di- urnal	Level
	17		,			h.	m.	h. m		feet	feet	feet	feet	feet
	CALIFORNIA—Continued San Francisco Bay—Continued	N.	1	w.		on	SAN	FRAN	ICI:	SCO, p	.72			
671	Time meridian, 120°%. Bay Farm Island Bridge	37 4	5 5	22	14	+0	41	+0 5	2	+0.8	0.0	4.8	6.5	3.5
531	Oakland Airport	37 4	1.	22	12	C+	40	+0 4	0	+0.8	0.0	4.8	6.5	3.5
535	Potrero Point	37 4	16	122	23	+0	29	+0 4		+0.6	0.0	4.6	6.3	100
537	Point Avisadero, Hunters Point	37 4		122		+0		+0 4		+0.9	0.0	4.9	6.6	
539	Roberts Landing, 1.3 miles west of	37 4	10	122	12	+0	48	+1 2	22	+1.5	+0.1	5.4	7.2	3,9
541	Point San Bruno	37 3	39	122	23	+0	34	+1 0	4	+1.2	+0.1	5.1	6.9	3.7
543	Counts Point	37	36	122	19	+0	37	+1 (+1.5	0.0			
545	San Mateo Bridge	37	35	122	15	+0	39	+1 1	4	+1.9	+0.1	1		
547	Covote HIII Slough entrance	37		122			54	+1 2		;+2.1	+0.1	6.0	4	
549	Redwood Creek entrance (Inside)	37	31	122	12	+1	02	+1 3	52	+2.2	+0.1	6.1	7.9	4.2
551	Smith Slough	37	30	122	14	+1	11	+1 5	4	+2.2	0.0	6.2		
553	Dumbarton Highway Bridge	37	1	122			48	+1 2		+2.7	+0.1	6.6	100	
555	Palo Alto Yacht Harbor	37		122	- 1		52	+1 4	- 1	+2.9	+0.1	1 .		
557	Calaveras Point, west of	37	- 1	122			01	+1 4		+2.9	+0.1	6.8	100	100
559	Mud Slough Railroad bridge	37		121			20	+2 (+3.5	+0.1			/K
561	Alviso (bridge), Alviso Slough	37	46	121	39	ŦI	20	TE .		10.0	10,1	'.~	1	1.0
563	Guadalupe Slough			122			05	+2		+3.5	+0.1			
565	Sauca to	37		122			09	+0		-0.1	0.0		10.	1
567	Angel Island (west side)			122			22	+0	- 1	0.0	0.0			
569	Angel Island (east slde)			122			24	+0		0.0	0.0			7 3.
571 573	Berkeley	37	52	122	18	+0	17	+0	32	+0.2	0.0	4.2	2 5.9	3.2
575	Point Isabel	37	54	122	19	+0	19	+0	27	+0.2	0.0			
577	Dishmond			122			21	+0	- 1	+0.1	0.0			
579	Point Richmond			122			36	+0	- 1	+0.2	0.0			
581	Polat Orlentaresesses			122			47	+0	- 1	+0.1	0.0		1000	
583	Point San Quentin	37	2.1	122	29	TU	46	175	20	0.0	0.0	-	-	-
	San Pablo Bay													1
585	McNear	37		122			L 05		200	+0.1	0.0	1.7		
587	Pinole Point	38		122		1	l 19 l 26		100	+0.4				
589	Hercules	38			30		1 15		-	+0.5				
591	Lakeville, Petaluma River	. 38		122			1 47	1	- 1	+0.8	-0.	1 4.	9 6.	4 3.
593 595	Upper drawbridge, Pataluma River	- 38			37	+3	1 54	+2	43	+1.0	-0.	1 5.	1 6.	
597	Sonoma Creek entrance	- 38	09	122	24	+	1 30) +2	21	+0.4	-0.	2 4.	6 6.	0 3.
	Carquinez Strait											1		
599	Selby	- 38	03	12.	2 15	+	1 25	5 +1	58					
601	Mare Island Strait entrance	- 38	04	12	2 15		1 4		03	1				2
603	Vallaia Mare Island Strait	- 1 38			2 16		1 4	- 1	04			2011		
605	Nana Nana River	- 38			2 17		2 1	3	46	+	24			3 3
607		- 1 30			2 13 2 08		1 5 1 5		23	1				
609	Benicla, Army Point	36			2 07		2 0		34	1				8 3.
611	Suisun Point	- 00	, 02	1	~ • 1		- 0	-						
	Suisun Bay			1									1	
613	3 Port Chicago	_ 38	04	12	2 0		12 3		14					.4 2
615	New York Slough	- 30			1 53		-3 2		13		. 1	- 10		4 2
617	/ Dolot Ruck or	- 1 00			2 01	6	2 3		18			1	-	5 2.
619	Suicup Slough entrance	- 0	-		2 0		+2 4		27	4		- 1		.3 2
623		- 1 30			2 02		+3 2 +3 2		13					6 2
	Meins Landing, Montezuma Slough	- 1 - 37	Uč	11 LC	T 34	10 T		-e-1 T4	-	- U.	V U	1 *		

JANUARY FEBRUARY MARCH

												FEBI	KUAR	Y						Μ.	ARCH			
	Time	He	ight		Tin	ie H	eight			Time	Н е	eight		Time	. He	eight		Tim	e He	eight		Time	Не	ight
Day	h m	ft		C	ay				Da.	у			D	a y			D	a y			D	ау		3,70
	0559	5.6	m 1.7	,	h n	_				h m	ft	m		h m	ft	m		h m	ft	m		hм	ft	m
Su	1306 2000 2354	1.3 3.5 2.9	0.4		6 061 M 132 205	9 0.	1 0.	0		0016 0640 1406 2158	6.0 0.2	1.8		6 0152 h 0757 1506 2223	6.2	1.9		1 045 W 122 204 235	4 0.6	0.2		5 0046 1 0635 1346 2106	5.5 0.1	1.7
M :	0637 1355 2119	5.8 0.7 3.8	0.2		7 004 u 071 142 215	4 6.		0 1	2 Th	0127 0734 1451 2231	6.2	1.9	1	7 0249 F 0852 1548 2259	6.2	0.9 1.9 -0.1 1.5		2 060 h 1326 211	0.1	0.0		7 0151 0744 1437 2145	2.8 5.5 0.0	0.9 1.7 0.0
Tu (0054 0722 1438 2215	3.2 6.1 0.2 4.2	1.9		8 014 W 081 152 224	1 6. 0 -0.	7 2.	0 2		0223 0825 1534 2303	6.5	2.0		3 0339 3 0940 1624 2331	2.6 6.1	0.8 1.9		3 0109 F 0707 1419 2148	5.8	1.0 1.8 -0.1 1.4		0242 0839 1515 2217	2.3 5.4 0.0	1.5 0.7 1.6 0.0 1.5
W 0	0152 0804 1517 2257	3.5 6.3 -0.3 4.5	1.9		9 024 h 090 160 232	0 6.7 5 -0.8	2.0	2		0312 0920 1615 2335	-1.1	2.0		0421 1022 1656 2359	5.9	1.8		4 0209 a 0809 1502 2219	3.0 6.0	0.9 1.8	19 Su	0327 0929 1551 2245	1.9	0.6 1.6 0.0 1.5
Th 0	559 335	-0.7	1.1 2.0 -0.2 1.4	21	0 034 F 094 164		2.0)	Su	0358 1006 1654				0500 11101 1724	5.6	0.6 1.7 -0.1		5 0258 3 0904 1544 2248	6.2	0.7 1.9 -0.3 1.5		0404 1014 1619 2309	1.5	0.5
F 0		6.7	1.1 2.0 -0.3		000 043 103 172		1.6 0.9 2.0))	М	0004 0445 1055 1733	2.3 6.6	1.6 0.7 2.0 -0.4		0025 0536 1140 1753	5.0 1.8 5.3 0.2			0345 1 1000 1623 2318	6.2			0439 1056 1648 2329	1.1 4.9 0.6 5.0	0.3 1.5 0.2 1.5
	413 017	4.8 3.4 6.8 -1.3	1.0		004: 051: 111: 175:	3 2.9	1.6 0.9 1.9		Tu	0037 0533 1146 1809	1.9	1.6 0.6 1.9 -0.3		0047 0611 1218 1821	5.0 1.6 5.0 0.6	1.5 0.5 1.5 0.2		0434 1052 1702 2350	6.1			0514 1138 1716 2350	0.8 4.7 0.9 5.1	0.2 1.4 0.3 1.6
	455 103	3.2	2.1	23 M	0555 1148		0.8		W	0624 1239	5.5 1.4 5.9 -0.3	0.4	Th	0108 0647 1257 1844	5.1 1.4 4.6 1.1	1.6 0.4 1.4 0.3		0521 1148 1738		0.2		0546 1217 1741	0.6 4.5 1.4	0.2 1.4 0.4
	545 150	5.1 3.0 6.6 -1.2	0.9		0142 0637 1227 1859	2.6 5.4			Th	0145 0720 1336 1929	5.8 1.1 5.3 0.4	1.8 0.3 1.6 0.1		0132 0726 1342 1914	5.2 1.3 4.2 1.7	1.6 0.4 1.3 0.5		0023 0610 1243 1818		0.0		0011 0618 1300 1806		1.6 0.1 1.3 0.6
	537 240	5.2 2.7 6.2 -0.9	0.8	W	0210 0720 1306 1928	2.4 5.0	1.5 0.7 1.5 0.2		F	0221 0820 1443 2009		1.8 0.2 1.4 0.4		0155 0811 1433 1939	5.3 1.2 3.9 2.2	1.6 0.4 1.2 0.7	1 0 F	0057 0703 1345 1857	-0.2	1.5		0033 0657 1349 1835		1.6 0.1 1.2 0.7
	736 336	2.4	1.6 0.7 1.7 -0.1		0233 0805 1349 1957		1.5 0.7 1.4 0.3		Sa (0301 0929 1604 2100	6.2 0.6 4.1 2.1	1.9 0.2 1.2 0.6		0226 0903 1545 2011				0136 0758 1454 1943	6.2 -0.3 4.5	1.9		0102 0736 1445 1903	5.4	1.6 0.1 1.2 0.9
12 03 Th 08 14 20	38	5.6 2.0 4.9 0.4	0.6		0302 0857 1442 2028	2.1	1.6 0.6 1.2 0.5	5	Su 1	0350 1041 1745 2159	6.2 0.5 3.9 2.8	1.2	М	0304 1002 1736 2053	1.1 3.5		1 2 S u	0217 0900 1616	6.2	1.9 -0.1 1.3	М	0134 0824 1554 1940	5.4 0.4 3.8	1.6 0.1 1.2
13 03 F 09 15 21	54 54	5.9 1.6 4.3 1.2	0.5 1.3	Sa	1000	5.3 1.9 3.6 2.3	0.6	1	M 1	0444 201 930 319	6.3 0.3 4.1 3.2	0.1 1.2	Tu	0354 1112 1943 2212	0.9 3.7	0.3	M	0312 1013 1749 2154	6.1 0.0 4.1	1.9 0.0 1.2	28 Tu	0216 0920 1731	5.3 0.4	1.6 0.1 1.2
14 04 Sa 11 17 22	11 32	6.1 1.1 3.9 2.0	0.3	Su	0407 1105 1740 2142	5.4 1.6 3.4 2.9	1.0	T	u 1		6.2 0.1 4.4	0.0					Tu	0413 1129 1919 2323	5.9 0.2 4.3	1.8 0.1 1.3	29 W		5.3 0.4 3.9	1.6 0.1 1.2
15 05 Su 12 19 23	23 19	6.4 0.6 3.9 2.7	0.2	М	0449 1211 1957 2248	5.6 1.2 3.5 3.4	0.4		₩ 0 1	653 416 -	3.4 6.2 0.1 4.7	1.9					W	0523 1242 2020	5.7	1.7	30 Th	0415 1135	5.2 0.2 4.1	1.6 0.1 1.2
				Tu	0544 1310 2117	5.7 0.8 3.9	0.2														31 F	0528 1241 2023	5.2	1.6

⁾ Time meridian 120° W. 0000 is midnight. 1200 is noon. Heights are referred to mean lower low water which is the chart datum of soundings.

Times and Heights of High and Low Waters

API	RIL	M.	AY	JUN	E
Time Height Day	Time Height Day	Time Height Day	Time Height Day	Time Height Day	Time Height Day
hm ft m	hm ft m	hm ft m	hm ft m	hm ft m	hm ft m
1 0058 2.9 0.9 Sa 0644 5.2 1.6 1335 -0.3 -0.1 2055 4.6 1.4	16 0227 1.7 0.5 Su 0821 4.5 1.4 1429 0.5 0.2 2124 5.0 1.5	1 0142 1.3 0.4 M 0741 4.5 1.4 1335 0.2 0.1 2031 5.4 1.6	16 0244 0.7 0.2 Tu 0908 3.8 1.2 1412 1.6 0.5 2047 5.3 1.6	1 0307 -1.0 -0.3 Th 1014 4.3 1.3 1436 2.2 0.7 2106 6.7 2.0	16 0332 -0.3 -0.1 F 1103 4.1 1.2 1452 3.1 0.9 2103 6.0 1.8
2 0154 2.2 0.7 Su 0753 5.3 1.6 1421 -0.4 -0.1 2125 4.9 1.5	17 0308 1.1 0.3 M 0916 4.4 1.3 1505 0.8 0.2 2150 5.0 1.5	2 0231 0.4 0.1 Tu 0852 4.6 1.4 1422 0.6 0.2 2106 5.8 1.8	17 0323 0.2 0.1 W 1007 3.9 1.2 1451 2.0 0.6 2115 5.5 1.7	2 0356 -1.5 -0.5 F 1113 4.6 1.4 1529 2.6 0.8 2150 6.8 2.1	17 0408 -0.6 -0.2 Sa 1145 4.3 1.3 1533 3.3 1.0 2141 6.1 1.9
3 0245 1.4 0.4 M 0856 5.4 1.6 1505 -0.3 -0.1 2156 5.3 1.6	18 0345 0.7 0.2 Tu 1007 4.3 1.3 1537 1.1 0.3 2211 5.1 1.6	3 0319 +0.4 -0.1 W 0959 4.7 1.4 1511 1.1 0.3 2142 6.2 1.9	18 0355 -0.2 -0.1 Th 1059 4.0 1.2 1526 2.4 0.7 2143 5.6 1.7	3 0444 -1.7 -0.5 Sa 1212 4.7 1.4 1621 2.8 0.9 2235 6.8 2.1	18 0443 -0.9 -0.3 Su 1227 4.4 1.3 1615 3.4 1.0 2220 6.2 1.9
4 0331 0.5 0.2 Tu 0956 5.4 1.6 1545 0.0 0.0 2228 5.7 1.7	19 0419 0.3 0.1 W 1054 4.3 1.3 1608 1.4 0.4 2233 5.3 1.6	4 0407 -1.1 -0.3 Th 1104 4.7 1.4 1553 1.6 0.5 2220 6.5 2.0	19 0430 -0.5 -0.2 F 1146 4.1 1.2 1603 2.7 0.8 2213 5.7 1.7	4 0530 -1.7 -0.5 Su 1304 4.8 1.5 1712 3.0 0.9 2321 6.6 2.0	19 0521 -1.1 -0.3 M 1302 4.5 1.4 1655 3.4 1.0 2300 6.2 1.9
5 0420 -0.2 -0.1 W 1054 5.3 1.6 1625 0.4 0.1 2302 6.0 1.8	20 0451 0.0 0.0 Th 1139 4.3 1.3 1637 1.9 0.6 2254 5.4 1.6	5 0454 -1.6 -0.5 F 1203 4.8 1.5 1639 2.1 0.6 2300 6.6 2.0	20 0502 -0.7 -0.2 Sa 1231 4.2 1.3 1637 3.0 0.9 2245 5.8 1.8	5 0617 -1.6 -0.5 M 1353 4.8 1.5 1807 3.1 0.9	20 0559 -1.2 -0.4 Tu 1341 4.6 1.4 1738 3.4 1.0 2341 6.1 1.9
6 0506 -0.8 -0.2 Th 1154 5.2 1.6 1707 1.0 0.3 2338 6.3 1.9	21 0523 -0.3 -0.1 F 1224 4.2 1.3 1706 2.3 0.7 2321 5.5 1.7	6 0542 -1.7 -0.5 Sa 1302 4.8 1.5 1727 2.5 0.8 2343 6.5 2.0	21 0537 -0.8 -0.2 Su 1317 4.3 1.3 1712 3.2 1.0 2317 5.8 1.8	6 0009 6.3 1.9 Tu 0703 -1.3 -0.4 1445 4.8 1.5 1903 3.1 0.9	21 0638 -1.2 -0.4 W 1419 4.7 1.4 1826 3.2 1.0
7 0555 -1.1 -0.3 F 1254 4.9 1.5 1749 1.6 0.5	22 0556 -0.4 -0.1 Sa 1310 4.2 1.3 1737 2.7 0.8 2348 5.5 1.7	7 0631 -1.6 -0.5 Su 1401 4.7 1.4 1819 2.9 0.9	22 0615 -0.9 -0.3 M 1403 4.3 1.3 1751 3.4 1.0 2356 5.8 1.8	7 0055 5.9 1.8 W 0749 -0.9 -0.3 1533 4.8 1.5 2008 3.1 0.9	22 0026 5.9 1.8 Th 0719 -1.1 -0.3 1455 4.8 1.5 1924 3.1 0.9
8 0014 6.4 2.0 Sa 0646 -1.2 -0.4 1355 4.7 1.4 1835 2.2 0.7	23 0631 -0.4 -0.1 Su 1401 4.1 1.2 1809 3.0 0.9	8 0028 6.3 1.9 M 0723 -1.3 -0.4 1502 4.7 1.4 1916 3.1 0.9	23 0655 -0.9 -0.3 Tu 1448 4.4 1.3 1836 3.5 1.1	8 0147 5.3 1.6 Th 0837 -0.5 -0.2 1616 4.8 1.5 2117 2.9 0.9	23 0115 5.6 1.7 F 0802 -0.8 -0.2 1533 5.0 1.5 2030 2.8 0.9
9 0057 6.3 1.9 Su 0739 -1.0 -0.3 1504 4.5 1.4 1927 2.8 0.9	24 0020 5.5 1.7 M 0713 -0.4 -0.1 1454 4.1 1.2 1845 3.3 1.0	9 0118 6.0 1.8 Tu 0816 -0.9 -0.3 1603 4.6 1.4 2024 3.2 1.0	24 0038 5.7 1.7 W 0740 -0.9 -0.3 1536 4.4 1.3 1930 3.5 1.1	9 0239 4.8 1.5 F 0923 0.0 0.0 1658 4.8 1.5 2229 2.6 0.8	24 0211 5.1 1.6 Sa 0846 -0.4 -0.1 1612 5.2 1.6 2140 2.3 0.7
10 0145 6.1 1.9 M 0838 -0.7 -0.2 1618 4.4 1.3 2033 3.1 0.9	25 0100 5.5 1.7 Tu 0759 -0.3 -0.1 1559 4.0 1.2 1933 3.5 1.1	10 0209 5.5 1.7 W 0912 -0.5 -0.2 1704 4.6 1.4 2144 3.2 1.0	25 0123 5.5 1.7 Th 0827 -0.7 -0.2 1621 4.5 1.4 2038 3.3 1.0	10 0338 4.2 1.3 Sa 1009 0.5 0.2 1739 4.9 1.5 2339 2.2 0.7	25 0319 4.5 1.4 Su 0932 0.2 0.1 1653 5.5 1.7 2253 1.7 0.5
11 0239 5.8 1.8 Tu 0944 -0.3 -0.1 1736 4.4 1.3 2154 3.3 1.0	26 0142 5.3 1.6 W 0851 -0.3 -0.1 1702 4.1 1.2 2040 3.6 1.1	11 0312 5.0 1.5 Th 1012 -0.1 0.0 1757 4.7 1.4 2305 2.9 0.9	26 0219 5.1 1.6 F 0919 -0.5 -0.2 1705 4.7 1.4 2201 3.0 0.9	11 0447 3.7 1.1 Su 1056 1.0 0.3 1813 5.1 1.6	26 0439 4.0 1.2 M 1024 0.9 0.3 1735 5.9 1.8
12 0344 5.4 1.6 W 1053 0.0 0.0 1845 4.5 1.4 2321 3.1 0.9	27 0241 5.2 1.6 Th 0950 -0.2 -0.1 1801 4.2 1.3 2212 3.4 1.0	12 0417 4.5 1.4 F 1108 0.2 0.1 1843 4.8 1.5	27 0328 4.7 1.4 Sa 1011 -0.2 -0.1 1747 4.9 1.5 2318 2.4 0.7	12 0037 1.7 0.5 M 0617 3.4 1.0 1145 1.5 0.5 1846 5.2 1.6	27 0005 1.0 0.3 Tu 0617 3.7 1.1 1119 1.6 0.5 1817 6.2 1.9
13 0453 5.0 1.5 Th 1200 0.2 0.1 1939 4.6 1.4	28 0347 4.9 1.5 F 1053 -0.2 -0.1 1843 4.4 1.3 2334 3.0 0.9	13 0018 2.4 0.7 Sa 0533 4.1 1.2 1202 0.6 0.2 1923 4.9 1.5	28 0444 4.3 1.3 Su 1106 0.2 0.1 1826 5.3 1.6	13 0130 1.1 0.3 Tu 0746 3.4 1.0 1231 2.0 0.6 1918 5.4 1.6	28 0107 0.2 0.1 W 0756 3.8 1.2 1218 2.2 0.7 1904 6.5 2.0
14 0039 2.7 0.8 F 0612 4.8 1.5 1258 0.3 0.1 2021 4.8 1.5	29 0503 4.7 1.4 Sa 1153 -0.1 0.0 1924 4.7 1.4	14 0115 1.8 0.5 Su 0650 3.9 1.2 1248 0.9 0.3 1956 5.0 1.5	29 0024 1.5 0.5 M 0613 4.0 1.2 1159 0.7 0.2 1904 5.6 1.7	14 0212 0.6 0.2 W 0908 3.6 1.1 1319 2.5 0.8 1951 5.6 1.7	29 0206 -0.4 -0.1 Th 0916 4.1 1.2 1321 2.7 0.8 1954 6.7 2.0
15 0139 2.2 0.7 Sa 0719 4.6 1.4 1349 0.4 0.1 2055 4.9 1.5	30 0043 2.2 0.7 Su 0622 4.6 1.4 1246 0.0 0.0 1957 5.0 1.5	15 0202 1.2 0.4 M 0805 3.8 1.2 1333 1.2 0.4 2024 5.2 1.6	30 0122 0.6 0.2 Tu 0741 3.9 1.2 1254 1.2 0.4 1943 6.0 1.8	15 0254 0.1 0.0 Th 1010 3.8 1.2 1408 2.8 0.9 2024 5.8 1.8	30 0259 -0.9 -0.3 F 1022 4.4 1.3 1420 3.0 0.9 2042 6.9 2.1
			31 0218 -0.2 -0.1 W 0903 4.1 1.2 1346 1.7 0.5 2024 6.4 2.0		

Time meridian 120° W. 0000 is midnight. 1200 is noon. Heights are referred to mean lower low water which is the chart datum of soundings.

SAN FRANCISCO (Golden Gate), CALIFORNIA, 1989 Times and Heights of High and Low Waters

JULY AUGUST SEPTEMBER T1me Height Time Height T1me Height Time Height T1me Helaht. Time Day Height Day Day Day Day Day h m ft h m ft m h m ft m h m ft m h m ft m h m 1 0350 -1.3 -0.4 16 0345 -0.5 -0.2 0503 -0.8 -0.2 16 0431 -0.9 -0.3 1 0536 Sa 1118 1.4 4.5 0.4 4.7 Su 1126 0.1 16 0510 0.3 0.1 1.4 Tu 1218 5.0 W 1144 5.0 2.3 3.1 1.5 5.2 1225 1.6 1513 Sa 1151 6.0 1.8 1653 2.6 0.8 0.7 2134 6.9 2.1 1755 1743 2119 6.4 2.0 0.1 0.0 6.3 1.9 2235 2.0 2 0435 -1.4 -0.4 17 0422 -0.8 -0.2 2 0539 -0.7 17 0509 5.0 0.9 5.2 Su 1205 4.9 1.5 -0.9 -0.3 2 0010 1.5 M 1157 4.6 1.4 1251 17 0020 5.5 5.0 5.2 1.5 1212 1.6 Sa 0604 3.1 0.3 Su 0549 1736 0.3 1710 0.5 1248 2202 2339 1.6 1227 6.2 1.9 1833 1836 -0.2 -0.1 18 0501 Tu 1230 0520 -1.4 -0.4 3 0611 -0.4 -0.1 18 0545 4.9 -0.2 1248 -0.6 3 0052 1.5 4.7 3.1 1.4 18 0121 M 0631 5.1 1.7 6.4 5.0 1.5 1244 5.5 1703 1.4 Su 0632 0.4 0631 0.5 1821 1310 6.6 1303 1.6 1928 -0.3 -0.1 4 0602 -1.2 5.0 -0.4 19 0538 19 0016 5.8 Sa 0621 -0.1 1316 5.7 -1.2 -0.4 4 0021 F 0643 1.6 Tu 1330 4 0136 1.5 W 1301 4.9 4.3 1.3 19 0230 1.5 0.0 0.0 M 0658 3.0 0.0 2.0 0.6 1727 2.8 0.9 1348 Tu 0716 2.4 5.0 1.5 2332 2354 1.7 1337 5.3 1346 6.3 0.6 6.5 2.0 1853 1955 0.4 0641 20 0615 Th 1333 -1.1 5.0 5 0103 1.5 4.9 5.0 20 0114 1.5 5 0232 Tu 0729 1409 4.1 20 0347 1.5 0715 0.5 4.5 Su 0659 0.6 0.2 0.8 0809 3.0 0.9 1417 1351 6.0 1.8 1405 1.6 1439 6.4 1952 2.0 0.6 0.2 2044 0.4 2136 21 0017 6.0 1.0 F 0655 -0.8 -0.2 1409 5.2 1.6 0.0 0.0 6 0036 6 0145 Th 0720 -0.6 -0.2 4.5 21 0217 6 0343 W 0758 4.8 1.5 21 0516 4.4 3.4 6.2 Su 0747 1.1 0.3 М 0742 1431 0.4 1.3 3.1 5.4 0.9 1.0 0.8 6.2 1.6 1540 0.5 2040 2252 0.1 0.0 1 - 6 22 0110 5.5 0239 22 0333 0757 4.3 2.1 -0.1 0.0 1.3 7 0529 Sa 0732 -0.4 1443 5.5 3.8 1.2 M 0815 22 0642 -0.1 1.8 0.5 Tu 0827 1520 4.9 0.6 Th 0847 3.5 1.1 F 1053 3.5 5.9 1.1 1511 5.3 1.6 1517 1,9 2038 2.6 0.8 1534 5.4 1.6 2009 1652 1.8 0.5 2139 2201 0.4 0.1 2251 0.3 8 0207 4.6 23 0209 4.9 0.3 1.5 8 0346 3.7 Sa 0833 1.1 23 0507 0.1 4.0 8 0729 0814 23 0008 0.2 Tu 0851 2.4 0.7 0.1 5.0 0926 2.8 0.9 1016 1.2 Sa 0747 1219 1518 5.8 1.8 4.8 1.5 5.4 1546 1610 6.4 2139 2.0 2117 3.3 5.8 0.4 1.5 0.1 0.5 2317 1808 1.8 24 0322 M 0859 9 0259 4.3 0531 3.5 3.0 24 0651 Su 0911 1.0 9 0003 Sa 0822 0.3 1.3 24 0114 1.1 0.2 0.3 W 0936 0.9 0.1 Th 1042 1714 3.3 1.0 4.2 1.3 1.6 1602 6.0 1.8 Su 0836 5.0 1.5 1629 5.5 2242 2227 0.3 1326 2.9 0.9 0.4 1744 1.7 10 0409 3.6 1.1 25 0450 3.9 10 0741 25 0033 0953 0.5 0.1 0.0 10 0104 0.5 0.2 Tu 0948 1.9 25 0207 0.6 0.2 0.1 Th 1042 3.4 1.0 0810 4.5 1658 5.3 1.6 1.4 Su 0857 1.3 1648 M 0914 1.9 5.6 5.2 1.6 1208 3.4 1.0 1.6 0.5 2340 1303 3.5 1.1 0.2 2.4 0.7 1823 1847 5.7 2016 11 0547 3.3 26 0635 3.8 1.2 11 0053 Tu 1039 0.9 0.3 26 0139 0.0 0.1 0.7 1051 11 0156 0.0 26 0249 0.2 0.1 F 0857 4.0 0906 4.8 1.5 M 0927 1740 1.4 Tu 0950 5.3 1.6 1208 3.7 1.1 1.0 1356 3.1 0.9 1508 1.9 0.6 5.8 1.8 1927 1949 2113 12 0044 W 0743 1.2 3.4 2.8 27 0051 0.1 0.0 12 0146 0.5 27 0236 -0.2 0.2 -0.1 27 0327 W 1019 4.0 1.0 0812 12 0238 -0.2 1.2 0.1 0943 1317 Sa 4.3 1.3 Su 0951 1424 5.0 3.0 4.8 Τu 0953 1203 1.5 5.3 3.6 1.1 1814 0.9 1442 0.8 1837 1547 0.4 6.0 1.8 2028 2045 1.6 13 0135 0.2 28 0154 -0.1 13 0234 0.0 4.5 3.5 0.0 Th 0908 3.7 -0.3 -0.1 13 0317 W 1019 0924 -0.4 -0.1 28 0359 4.4 1.3 1015 0.6 0.2 1.4 M 1030 5.1 1.6 5.1 1.8 1237 3.2 1.0 1.6 Th 1044 5.3 1410 1.6 0.8 1515 2.6 1527 1.8 1938 0.5 1623 2011 1.9 2137 14 0221 F 1010 2243 0.1 0.3-0.6 4.7 14 0316 M 1043 1457 -0.2 -0.1 29 0400 0.3 5.1 2.2 1010 4.0 14 0359 Sa 1017 1.4 -0.4 -0.129 0429 F 1108 0.9 5.4 0.8 4.6 1.4 1105 1.6 1336 3.4 Th 1051 3.2 1.0 1.6 1601 1.2 1611 0.4 2100 2.0 2206 6.0 1.8 2328 15 0304 -0.1 Sa 1047 4.3 1428 3.5 0.0 30 0340 -0.8 -0.2 1.5 15 0356 -0.7 -0.2 30 0435 -0.2 -0.1 15 0435 1.3 Su 1102 1517 4.9 -0.1 0.0 30 0456 Sa 1128 Tu 1112 1542 4.8 1134 5.2 1.9 1.6 1120 1657 5.7 1.7 5.4 3.1 0.9 1.6 0.9 1641 2032 6.2 0.6 0.2 2251 2323 5.8 31 0422 -0.9 -0.3 31 0507 0.0 0.0 5.0 1.5 Th 1202 5.2 1.6 1607 2.9 0.9 1719

1.6

0.5

Time meridian 120° W. 0000 is midnight. 1200 is noon. Heights are referred to mean lower low water which is the chart datum of soundings.

2212

6.5

SAN FRANCISCO (Golden Gate), CALIFORNIA, 1989 Times and Heights of High and Low Waters

OCTOBER NOVEMBER DECEMBER

			0010	DEK							HOTE								0202				
Day	Time	Hei	ght	Day		Hel	ght	Da	Time	Hei	ght	Day		Не1	ght	Day		Hei	ght	Da y		Heig)ht
-	h m	ft	m	Ī	h m	ft	m		h m	ft	m		h m	ft	m		h m	ft	m		h m	ft	m
Su	0011 0525 1151 1805	4.7 1.8 5.5 0.4	1.4 0.5 1.7 0.1		0030 0520 1143 1817	6.8	0.6		0152 0553 1159 1854	3.4 5.8	1.3 1.0 1.8 0.0			5.0 3.4 6.6 -1.0	1.0		0232 0619 1215 1917	3.7	1.4 1.1 1.8 -0.2		0302 0736 1324 2014	3.2 5.9	1.6 1.0 1.8 -0.1
M	0055 0553 1212 1837	4.5 2.3 5.5 0.4	1.4 0.7 1.7 0.1			6.8	0.8 2.1		0246 0628 1235 1936		1.3 1.1 1.7 0.0			5.0 3.5 6.1 -0.5	1.1 1.9						0346 0843 1416 2100		
Tu	0143 0618 1238 1916	4.3 2.8 5.6 0.5	1.3 0.9 1.7 0.2		0657 1315	4.9 3.1 6.6 -0.7	0.9		0343 0710 1316 2027	5.6	1.3 1.2 1.7 0.0		0432 0909 1445 2141	3.4 5.5	1.5 1.0 1.7 0.0			4.7 3.6 5.3 -0.2	1.6			2.8	1.6 0.9 1.4 0.2
W	0239 0650 1310 2005	3.3	1.3 1.0 1.7 0.2		0351 0800 1409 2112	3.4	1.9		0442 0817 1411 2122		1.3 1.2 1.6 0.1		0526 1034 1554 2241	3.2	1.6 1.0 1.5 0.1		0435 0924 1451 2137	3.4	1.5 1.0 1.5 0.0		0512 1112 1628 2230	2.4	1.6 0.7 1.2 0.4
	0351 0726 1355 2057	4.1 3.6 5.5 0.7	1.2 1.1 1.7 0.2		0504 0923 1514 2222	3.6	1.5 1.1 1.8 0.0		0537 0948 1517 2222	3.8	1.4 1.2 1.6 0.1		0613 1151 1710 2337	5.2 2.7 4.4 0.8	1.6 0.8 1.3 0.2		0517 1048 1607 2230	4.4	0.9		0549 1217 1802 2319	1.9	1.6 0.6 1.1 0.6
F	0518 0821 1447 2202	4.1 3.9 5.3 0.7	1.2 1.2 1.6 0.2		0613 1053 1624 2330	3.4	1.5 1.0 1.6 0.1		0619 1115 1629 2319	4.7 3.4 4.8 0.3	1.4 1.0 1.5 0.1		0655 1257 1833		1.6 0.6 1.2	W	0555 1154 1734 2325	2.1 4.1	1.7 0.6 1.2 0.3		0626 1313 1943	5.6 1.4 3.6	1.7 0.4 1.1
	0637 1005 1553 2311	3.9	1.3 1.2 1.6 0.2		0709 1215 1742		1.5 0.9 1.6		0655 1226 1752		1.5 0.8 1.4		0025 0733 1348 1951	5.5	1.7		0633 1258 1910	1.2	1.8 0.4 1.2		0014 0702 1403 2104	2.4 5.7 0.9 3.8	0.7 1.7 0.3 1.2
	0726 1139 1705	3.7	1.3 1.1 1.6	M	0029 0751 1319 1858	0.5 5.2 2.4 4.9	0.2 1.6 0.7 1.5		0015 0730 1319 1911	5.3 1.8	0.2 1.6 0.5 1.4		0110 0805 1431 2100	5.6	0.5 1.7 0.3 1.2	F	0017 0712 1351 2036	6.3	1.9		0106 0735 1448 2207	2.9 5.9 0.4 4.1	0.9 1.8 0.1 1.2
	0014 0758 1245 1819	4.7	0.1 1.4 1.0 1.6		0122 0829 1411 2004	0.6 5.3 1.8 4.7	0.2 1.6 0.5 1.4		0104 0802 1411 2027		0.2 1.7 0.3 1.4		0152 0832 1513 2201	2.0 5.8 0.4 4.2	0.6 1.8 0.1 1.3		0113 0754 1444 2150	6.7 -0.5	2.0		0158 0814 1523 2253	6.1	1.0 1.9 0.0 1.3
	0107 0829 1339 1927	0.2 4.9 2.5 5.3	0.1 1.5 0.8 1.6		0203 0858 1453 2103	0.9 5.5 1.3 4.6	0.3 1.7 0.4 1.4		0152 0836 1456 2137	6.2	0.3 1.9 0.0 1.5		0234 0859 1545 2251	2.4 5.9 0.0 4.4	0.7 1.8 0.0 1.3		0209 0837 1533 2251	7.0	2.1		0247 0853 1558 2335	3.4 6.2 -0.3 4.6	1.9
	0153 0857 1425 2029	0.1 5.2 1.7 5.3	0.0 1.6 0.5 1.6		0241 0926 1532 2157	1.2 5.5 0.8 4.6	0.4 1.7 0.2 1.4		0241 0913 1542 2241	6.6			0313 0927 1617 2340	6.0 -0.2	1.8		0923	-1.5	2.2		0329 0931 1636	3.5 6.3 -0.5	
Th	0235 0929 1511 2132	0.2 5.6 0.8 5.4		F	0317 0951 1606 2246			Sı	0326 0950 1630 2340	6.9	2.1 -0.4	M	0348 0956 1652	6.1	1.9	Τt	1009	7.3	0.9 2.2 -0.5		0014 0408 1007 1709		1.1
	0317 0958 1557 2231	5.9 0.0	0.2 1.8 0.0 1.6		0349 1014 1638 2332	5.7 0.1	1.7 0.0		3 0412 4 1031 1716		2.2		0427 1029		1.9		10446	3.2	1.6 1.0 2.2 -0.5			3.5 6.4	
			-0.2		0421 1036 1710		1.8				0.9 2.2				1.1 1.9		0539 1146	3.3	1.6 1.0 2.1 3-0.4		0121 0527 1127 1820	3.5 6.3	1.5 1.1 1.9 -0.3
	0437 1106 1728		2.0		0021 0452 1101 1742	2.7	0.8 1.8				2.1	Th		3.7 6.1		1	1236	6.5	1.6 1.0 2.0 -0.3	Sa	1859	3.3 6.1 -0.8	1.0 1.9 -0.2
							0.9 1.8															3.2 5.7	

Time meridian 120° W. 0000 is midnight. 1200 is noon. Heights are referred to mean lower low water which is the chart datum of soundings.

NO.	PLACE		TION			Ţ	D: tme	IFFE	RENCES Heig	ht		GES	Mean
NO.	PLACE	Lat.	Lon	ıg.	Hig wat			ow ter	High water	Low water	Mean D	iurnal	Tide Level
	CALIFORNIA San Pedro Channel Time meridian, 120°W	N	H		h.			m. ANG	ft ELES, p.6	ft 8	ft	ft	ft
439 441 443	Los Angeles Harbor, Mormon Island El Segundo, Santa Monica Bay Santa Monica, Municipal Pier	33 45 33 55 34 00	118 118 118	26	+0 +0 +0	13	+0	02 13 06	-0.1 *0.96 -0.1	0.0 *0.96 0.0	3.8 3.7 3.7	5.4 5.3 5.4	2.8 2.7 2.8
	Santa Barbara Channel												
445 447 449 451 453 455	Mugu Lagoon (ocean pier) Port Hueneme Ventura Rincon Island, Mussel Shoals Santa Barbara Gaviota	34 06 34 09 34 16 34 21 34 25 34 28	119 119 119 119 119 120	12 17 27 41	+0 +0 +0 +0 +0 +0	10 09 21 26		13 16 22 26	*0.96 -0.1 -0.1 *0.99 *0.97 *0.96	*0.96 0.0 0.0 *1.04 *0.97 *0.96	3.7 3.7 3.7 3.7 3.6 3.6	5.3 5.4 5.5 5.4 5.3	2.7 2.8 2.8 2.8 2.8 2.8
	Santa Barbara Islands												
457 459 461 463 465 467 469 471	Wilson Cove, San Clemente Island	33 00 33 26 33 21 33 29 33 16 34 01 34 00 34 03	118 118 119 119 119 120 120	30 19 02 30 41	-0 +0 -0 +0 +0 +0 +0	11 06 02 10 25 37	+0 +0 +0 +0 +0	04	*0.94 *0.94 *0.96 *0.92 *0.88 *0.90 *0.96 *0.94	*0.94 *0.96 *0.92 *0.88 *0.90 *0.96 *0.94	3.6 3.7 3.5 3.3 3.4 3.6 3.5	5.2 5.3 5.1 4.9 5.3 5.2	2.7 2.7 2.7 2.6 2.5 2.6 2.8 2.7
	Outer Coast												
473 475 477 479 481	Point Arguello Port San Luis Wharf Morro Beach, Estero Bay San Simeon	34 35 35 10 35 24 35 38 36 31	120 120 120 121 121	45 52 11	+0 +0 +0 +0 +1	48 56 56	+0 +0	43 51 56 58 13	*0.94 *0.98 *0.94 *0.97 *0.96	*0.94 *0.98 *0.94 *0.97 *0.96	3.5 3.6 3.5 3.6 3.5	5.2 5.4 5.2 5.3 5.2	2.7 2.9 2.8 2.8 2.8
						οņ	SAN	FRA	NCISCO, p	.72			
483 484 485 487 489 491	Monterey, Monterey Bay. General Fish Company Pier Moss Landing, Ocean Pier. Elkhorn Yacht Club Elkhorn Slough, Highway 1 Bridge Pacific Mariculture Dock.	36 36 36 48 36 48 36 49 36 49 36 49	121 121 121 121 121 121	47 47 47 47	-1 -1 -1 -1 -1	08 10 09 06	-0	46	-0.5 -0.6 -0.7 -0.6 -0.7 -0.5	0.0 -0.1 -0.1 -0.1 -0.1	3.6 3.5 3.5 3.5 3.5	5.4 5.3 5.2 5.2 5.4	2.9 2.8 2.8 2.8 2.8
493 495 497 499 501 503 505 507	Elkhorn, Elkhorn Slough Kirby Park, Elkhorn Slough. Elkhorn Slough railroad bridge Santa Cruz, Monterey Bay Ano Nuevo Island Princeton, Halfmoon Bay Southeast Farallon Island San Francisco Bar Ocean Beach, outer coast.	36 49 36 50 36 51 36 58 37 06 37 30 37 42 37 46 37 46	121 121 121 122 122 122 123 122	45 45 01 20 29 00 38	-0 -0 -1 -1 -1 -0 -0	43 36 15 24 06 39 35	-0 -0 -0 -1 -0 -0 -0	39 39 58 04 50 19	-0.6 -0.4 -0.4 -0.6 -0.7 -0.3 -0.3 -0.2	0.0 -0.1 -0.1 0.0 -0.1 0.0 0.0 0.0	3.5 3.7 3.7 3.5 3.5 3.8 3.8 4.2	3555325660 555555556	2.8 2.9 2.9 2.8 2.7 3.0 3.0 3.0
	San Francisco Bay												
5113 5513 5513 5513 5513 5513 5513 5513	Point Bonita, Bonita Cove SAN FRANCISCO (Golden Gate) Alcatraz Island	37 49 37 48 37 49 37 49 37 48 37 48 37 48 37 46 37 46 37 46 37 46 37 40 37 39 37 36 37 36 37 36 37 36	122 122 122 122 122 122 122 122 122 122	28 225 222 220 220 118 117 114 112 221 112 223 223 223 223 229 200 8	-0 +0 +0 +0 +0 +0 +0 +0 +0 +0 +0 +0 +0 +0	14 13 23 22 33 37 23 33 33 33 49 47 32 55 48 44 42 42 40 40 40 40 40 40 40 40 40 40 40 40 40		18 11 25 40 36 48 41 41 42 44 45 59 22 85 67 71 70 70 70 70 70 70 70 70 70 70 70 70 70	+0.3 redictions 0.0 +0.4 +0.3 +0.2 +0.5 +0.6 +0.6 +0.8 +0.5 +1.4 +1.2 +1.1 +1.4 +1.5 +1.8 +0.3 +0.9 +1.8	0.0 0.0 0.0 0.0 0.0 0.0 0.0 0.0	4.3 4.1 4.3 4.6 4.4 4.3 4.7 4.5 7 4.9 4.6 5.5 5.3 5.3 5.3 5.3 5.3 5.3 5.3 5.3 5.3	6.0 5.8 5.8 6.3 6.1 6.6 6.4 6.6 6.4 6.6 6.6 77.2 77.6 77.6 77.6 77.7	3.3 3.2 3.1 3.3 3.4 3.3 3.2 3.4 3.3 3.6 4.6 3.6 8.8 9.8 3.7 7 3.9 4.1 1 2.9 3.1

Endnotes can be found at the end of table 2.

NO	PLACE	PO Lat	NOTTE		Time D	FFERENCE:	S Height		RANGES	
_		200	• Long	Hi	gh Lo	w Higi	Lo	W	n Diurna	I Tid Lev
	San Francisco Bay-Continued Time meridian, 120°W	N	H	h.			f	-	ft ft	f
5691557555555555555555555555555555555555	Redwood Creek Marker #8. Redwood Creek entrance (Inside) South Bay Wreck Corkscrew Slough Redwood City, Wharf 5	37 32 37 31 37 33 37 30 37 30 37 30 37 31 37 30 37 30 37 30 37 30 37 30 37 30 37 30	2 122 1 122 1 122 1 122 1 122 1 122 1 122 1 122 1	2 +0 22 +1 1	53 +1 06 +1 103 +1 158 +1 11 +1 11 +1 100 +1	28 +2.338 +2.337 +2.542 +2.336	1 +0.1 +0.2 +0.2 +0.2 +0.2 +0.2 +0.2 +0.2 +0.2	1	6 8.4 - 0 - 3 8.3 - 8 8.5 - 6 6 7 8 8.5 - 7 8 8 8.5 - 7 8 8 8 8 8 8 8 8 8 8 8 8 8 8 8 8 8 8	4.33.4.4.4.4.4.4.4.4.4.4.4.4.4.4.4.4.4.
39 41 43 45 47 49 51 63 65	Point San Pedro Pinole Point Hercules. Petaluma River entrance. Lakeville, Petaluma River Upper drawbridge, Petaluma River Gallinas Creek. Hog Island, San Antonio Creek. Sonoma Creek. Wingo, Sonoma Creek. Carquinez Strait	38 01 38 01 38 07 38 12 38 14 38 01 38 09 38 09	122 27 122 22 122 18 122 30 122 34 122 37 122 33 122 24 122 26	+0 59 +1 13 +1 25 +1 22 +1 59 +2 10 +1 11 +1 47 +1 31 +2 12	+1 25 +1 49 +2 11 +2 50	+0.1 +0.1 -0.1 +0.5 +0.7 +0.1 +0.3 -0.2 +0.1	0.0 -0.1 -0.2 -0.1 -0.2 -0.2 -0.1 -0.2 -0.3	4.3 4.3 4.2 4.4 4.8 5.0 4.7 4.2 4.5	5.9 5.7 5.7 5.9 6.2 6.4 5.9 6.1 5.6 5.6	3.2 3.2 3.0 3.2 3.3 3.4 3.1 3.2 3.0 3.1
	Mare Island Mare Island Strait Edgerley Island, Napa River Brazos Drawbridge, Napa River Napa, Napa River Selby Crockett Benicia Suisun Point Suisun Bay	38 06 1 38 12 1 38 12 1 38 18 1 38 03 1 38 04 1 38 03 1	122 15 122 16 122 19 122 18 122 17 122 15 22 15 22 13 22 08 22 07	+1 36 +1 47 +2 02 +2 02 +2 16 +1 29 +1 39 +2 11 +2 08	+2 00 +2 14 +2 29 +2 29 +2 52 +2 04 +2 03 +2 34 +2 36	-0.3 -0.1 +0.3 +0.7 +1.4 +0.6 -0.2 -0.6	-0.2 -0.3 -0.2 0.0 0.0 -0.2 -0.3 -0.3	4.0 4.2 4.7 5.0 5.5 4.7 4.0 3.8 3.7	5.5 5.7 6.1 6.5 7.1 6.3 5.5 5.1	2.9 3.0 3.2 2.5 3.8 3.4 3.0 2.7 2.6
A P M	Suisun Slough entrance. Pierce Harbor, Goodyear Slough. Joice Island, Suisun Slough. Suisun City, Suisun Slough. Haval Weapon Station, Suisun Bay. Hontezuma Slough Bridge. Fradmoor Island, Nurse Slough. Heins Landing, Montezuma Slough. Hontezuma Slough.	38 08 1 38 11 1 38 14 1 38 03 1 38 11 1 38 11 1 38 11 1 38 08 12 38 08 12 38 06 12 38 03 12	22 04 22 06 22 03 22 02 22 02 21 59 21 55 21 54 21 53 22 01 21 55	+2 45 +3 04 +3 00 +3 12 +2 31 +3 09 +3 30 +3 29 +3 47 +2 40 +3 26 +3 30	+3 32 +3 46 +3 49 +4 08 +3 52 +4 12 +4 16 +4 33 +3 24 +4 03 +4 13	-1.1 -1.1 -0.8 -0.7 -0.9 -0.6 -1.0 -1.5 -0.3 -1.7	-0.4 -0.4 -0.4 -0.4 -0.4 -0.4 -0.4 -0.5 -0.3	3.4 3.7 3.8 3.6 3.6 3.9 3.1 4.1 2.9	4.5 4.8 5.0 4.9 4.8 5.2 4.7 4.2 5.5 4.0	2.4 2.5 2.6 2.5 2.5 2.5 2.5 2.5 2.5 2.5
1	ntioch		1 49 1 41	+4 05 +4 54	+4 45 +5 54		*0.52 *0.45	2.7		. 9

Endnotes can be found at the end of table 2.

NO.	PLACE	POSI	TION			1	D Time	FFE	RENCES Heig	ht	RAN		Mean
110.	PLACE	Lat.	LOI	ng.	H1	gh ter	L i	w	High water	Low water	Mean D	1urna)	Tide Leve
	San Joaquin River-Continued Time meridian, 120°W	N N	•	H ,	h.	m. on	h. SAN		ft NCISCO, p	ft .72	ft	ft	ft
705 707 709 711	Prisoners Point	38 04 38 03 38 00 37 58	121 121 121 121	30 25	+6 +6	53 16 32 37	+6	45 57 21 39	*0.60 *0.58 *0.62 *0.68	*0.45 *0.36 *0.36 *0.43	2.6 2.5 2.7 3.1	3.5 3.4 3.6 4.0	1.8 1.7 1.8 2.0
713 715 717 719 721 723 725 727 728 729	Georgiana Slough entrance Terminous, South Fork New Hope Bridge <4> Bishop Cut, Disappointment Slough False River Irish Landing, Sand Mound Slough Orwood, Old River Holt, Whiskey Slough Borden Highway Bridge, Old River Borden Highway Bridge, Middle River Grant Line Canal (drawbridge)	38 08 38 07 38 14 38 03 38 03 38 02 37 56 37 56 37 55 37 54 37 49	121 121 121 121 121 121 121 121 121 121	30 29 25 39 35 34 26 34 29	+6 +6 +5 +5 +6 +7 +7	05 25 49 43 16 56 59 45 11 22 41	+6 +7 +7 +7 +5 +6 +7 +7 +7 +7 +9	17 58 18 51 36 35 41 41 59	*0.54 *0.58 *0.62 *0.66 *0.55 *0.62 *0.63 *0.67 *0.53	*0.38 *0.36 *0.45 *0.43 *0.42 *0.45 *0.45 *0.45 *0.45	2.4 2.5 2.7 2.9 2.4 2.7 2.8 3.0 2.3 2.4 2.8	3.2 3.4 3.6 3.9 3.3 3.7 3.2 3.2	1.6 1.7 1.8 2.0 1.7 1.8 1.9 2.0
	Sacramento River												
733 735 737 739 741 743	Collinsville	38 04 37 06 38 09 38 12 38 16 38 25 38 35	121 121 121 121 121 121 121	42 42 37 29 31	+4 +4 +7 +6	43 20 05 55 31 25 34	+4 +5 +5 +5 +8 +8 +9	04 13 54 42 04	*0.65 *0.69 *0.81 *0.67 *0.40 *0.50	*0.55 *0.55 *0.55 *0.42 *0.27 *0.27	2.8 3.0 3.6 3.0 1.8 2.3 2.3	3.8 4.0 4.7 4.0 2.5 2.9	2.0 2.1 2.4 2.0 1.2
	Outer Coast												
747 749 751 755 755 757 761 763 7767 777 777 777 7781	Bolinas Bay Bolinas Lagoon Point Reyes Tomales Bay entrance Blakes Landing, Tomales Bay Inverness, Tomales Bay Inverness, Tomales Bay Bodega Harbor entrance Fort Ross Arena Cove Point Arena Albion Little River Harbor Mendocino, Mendocino Bay. Fort Bragg Landing Noyo River Westport Shelter Cove Cape Mendocino	37 54 37 55 38 00 38 14 38 10 38 06 38 18 38 55 38 57 39 16 39 18 39 27 39 28 40 02 40 26	122 122 122 122 122 123 123 123 123 123	41 58 59 55 54 03 15 44 46 47 48 48 47 04	-0 -0 +0 +0 +0 -0 -0 -0 -0 -0 -0 -0 -0	25 11 50 12 32 38 40 38 51 40 42 31 33 31 31 39 28	-0 +0 +1 +1 -0 -0 -0 -0 -0 -0 -0 -0 -0 +0	37 26 20 15 16 30 17 21 19 20 12 20 12 21 20	-0.1 -1.6 -0.1 *0.87 -0.7 -0.6 -0.2 -0.2 -0.0 -0.1 -0.1 -0.1 -0.1 -0.1 +0.1 -0.1	0.0 -0.4 0.0 0.91 -0.2 -0.1 -0.2 +0.1 0.0 0.0 0.0 0.0 0.0 0.0 0.0 0.0 0.0	4.0 3.0 4.0 3.5 3.6 3.7 3.8 3.9 4.0 4.0 4.0 4.1 4.1 4.1 4.0	5.7 4.3 5.2 2.2 4.3 5.5 5.5 5.5 5.5 5.5 5.5 5.5 5.5 5.5 5	3.1 2.2 2.7 2.6 2.6 3.1 3.1 3.1 3.1 3.1 3.1
785	Eel River entrance	40.30	124	,,					DT BAY, p			<i>e</i> 2	١.,
785 787 789 791 793 794 795 796 797 799 801 803	Humboldt Bay Entrance HUMBOLDT BAY (North Spit) Fields Landing Hookton Slough Elk River Railroad Bridge (18) Bucksport Eureka Eureka Slough Bridge Samoa Arcata Wharf Trinidad Harbor. Crescent City	40 38 40 46 40 43 40 41 40 45 40 48 40 48 40 50 40 51 41 03 41 45	124 124 124 124 124 124 124 124 124 124	15 13 13 13 12 12 10 08 11 07	-0 +0 +0 +0 +0 +0 +0 +0 +0	31 09 10 15 10 05 17 23 19 48 25 26	+0	y p 02 25 26 02 07 06 07 54	-0.6 -0.7 rediction -0.1 -0.2 -1.8 +0.1 +0.4 +0.5 +0.4 -0.2 +0.1 -0.2	0.0 0.0 0.0 0.0 0.0 0.0 0.0 0.0 0.0 0.0	4.4 4.3 5.0 4.9 4.8 4.0 5.0 5.3 5.5 5.4 5.0 4.9	6.3 6.2 6.8 6.6 5.1 7.0 7.3 7.4 7.0 7.0 7.0	3.4 3.3 3.7 3.7 3.6 2.4 3.8 3.9 4.0 3.8 3.6 3.8
	OREGON												
807 809 811 813	Brookings, Chetco Cove	42 03 42 26 42 44 43 07	124 124 124 124	25 30	- 0 - 0	25 17 19 03	-0 +0 -0 +0	02 05	+0.1 -0.2 +0.4 +0.1	0.0 -0.1 +0.1 -0.1	5.1 4.9 5.3 5.2	6.9 6.7 7.3 7.0	3.7 3.6 3.9 3.7
815 817 819	Charleston Empire Coos Bay Umpqua River	43 21 43 24 43 23	124 124 124	17 13	+0+1	04 46 35	+0 +1 +1	06	+0.7 -0.2 +0.5	0.0 -0.1 -0.1	5.7 4.9 5.6	7.5 6.7 7.3	4.1 3.5 3.9
821 823 825	Entrance	43 41 43 44 43 42	124 124 124	07	+1	14 05 20	+0 +1 +1	25	+0.1 -0.1 -0.1	0.0 -0.2 -0.2	5.1 5.1 5.1	6.9 6.7 6.7	3.7 3.5 3.6

Endnotes can be found at the end of table 2.

PART III: PROTOTYPE DATA ANALYSIS

9. A harmonic analysis was performed on both water surface elevation and current data. The analysis techniques are presented in detail by Outlaw (1983). We outline briefly the techniques and results of the analysis for water surface elevations and currents in turn below.

Water Surface Elevations

- 10. The harmonic analysis for surface elevation tidal constituents was conducted for 22 NOAA tidal elevation stations and three Raytheon pressure cells employing hourly data. Station numbers and locations are as shown in Table II-1. The NOAA stations are representative of tidal elevations in the nearshore region and along the Mississippi Sound barrier islands. The pressure cell data are representative of the tide in the Gulf approximately 27 miles* south of the barrier islands.
 - 11. The harmonic analysis included:
 - <u>a</u>. Editing to remove data spikes, insertion of missing data, and subtraction of the mean from the data record.
 - ${f \underline{b}}$. Filtering to remove high and low frequency trends from the data.
 - c. Harmonic analysis for tidal constituents.

The NOAA surface elevation data had been edited by NOAA and was continuous over the record length. During the analysis, pressure cell data were converted to surface elevation and corrected for barometric pressure changes prior to removing the mean.

- 12. A digital band-pass filter was applied to eliminate frequencies in the data outside the semidiurnal to diurnal tidal frequency range.
- 13. In the harmonic analysis, the tidal elevation at a given station is represented as follows:

$$h(t) = H_o + \sum_{i=1}^{n} f_i H_i \cos \left(\frac{2\pi t}{T_i} + (V_o + u)_i - \kappa_i \right)$$

^{*} A table of factors for converting non-SI units of measurement to SI (metric) units is presented on page 12.

where

h(t) = tidal elevation as a function of time t = time $H_o = \text{mean of the filtered data record}$ $f_i = \text{node factor for constituent } i$ $(V_o + u)_i = \text{equilibrium argument for constituent } i$ $T_i = \text{period for constituent } i$ n = number of constituents considered $H_i = \text{mean amplitude for constituent } i$ $\kappa_i = \text{local epoch for constituent } i$

The constituents included in the analysis and their periods are:

Harmonic Constituent	Symbol	Period, hr
Principal lunar diurnal	01	25.82
Lunisolar diurnal	K1	23.94
Principal solar diurnal	P1	24.07
Smaller lunar elliptic	M1	24.84
Small lunar elliptic	J1	23.10
Larger lunar elliptic	01	26.87
Principal lunar	M2	12.42
Principal solar	S2	12.00
Larger lunar elliptic	N2	12.66

- 14. The mean amplitude, H_i , and local epoch, κ_i are determined by minimizing the variance between the filtered record and the predicted record given in the equation above.
- 15. Mean elevations of the NOAA Data Record relative to mean lower low water are given in Table III-1. The constituent amplitude and phases are presented in Tables III-2 and III-3, respectively. The length of the data record and the root mean square (RMS) error are given in Table III-4. The principal tidal constituents are the diurnal constituents 01, K1, P1, and the semi-diurnal constituents M2 and S2.

Currents

16. The harmonic analysis for currents was conducted for all observed data separately for the east-west and north-south components. In this manner analyzed current components correspond in orientation to the numerical model current components thereby facilitating comparisons.

Table III-1

Mean Elevation of Observed NOAA Data Record

Relative to Mean Lower Low Water

Station*	Elevation, ft
873-1269	0.71
873-1952	0.69
873-5184	ā.5
873-5523	0.73
873-5587	0.96
873-7048	0.85
874-0199	0.85
874-0405	0.88
874-1196	0.88
874-2221	0.90
874-3081	1.07
874-3495	
874-3735	1.01
874-4586	1.04
874-4671	==
874-4756	0.90
874-6819	0.99
874-7437	0.87
874-9704	
876-0412	0.56
876-0595	0.71
876-0742	0.92

^{*} Refer to Table II-1 for T designations used in Figure II-3.

* Refer to Table II-1 for T designations used in Figure II-3.

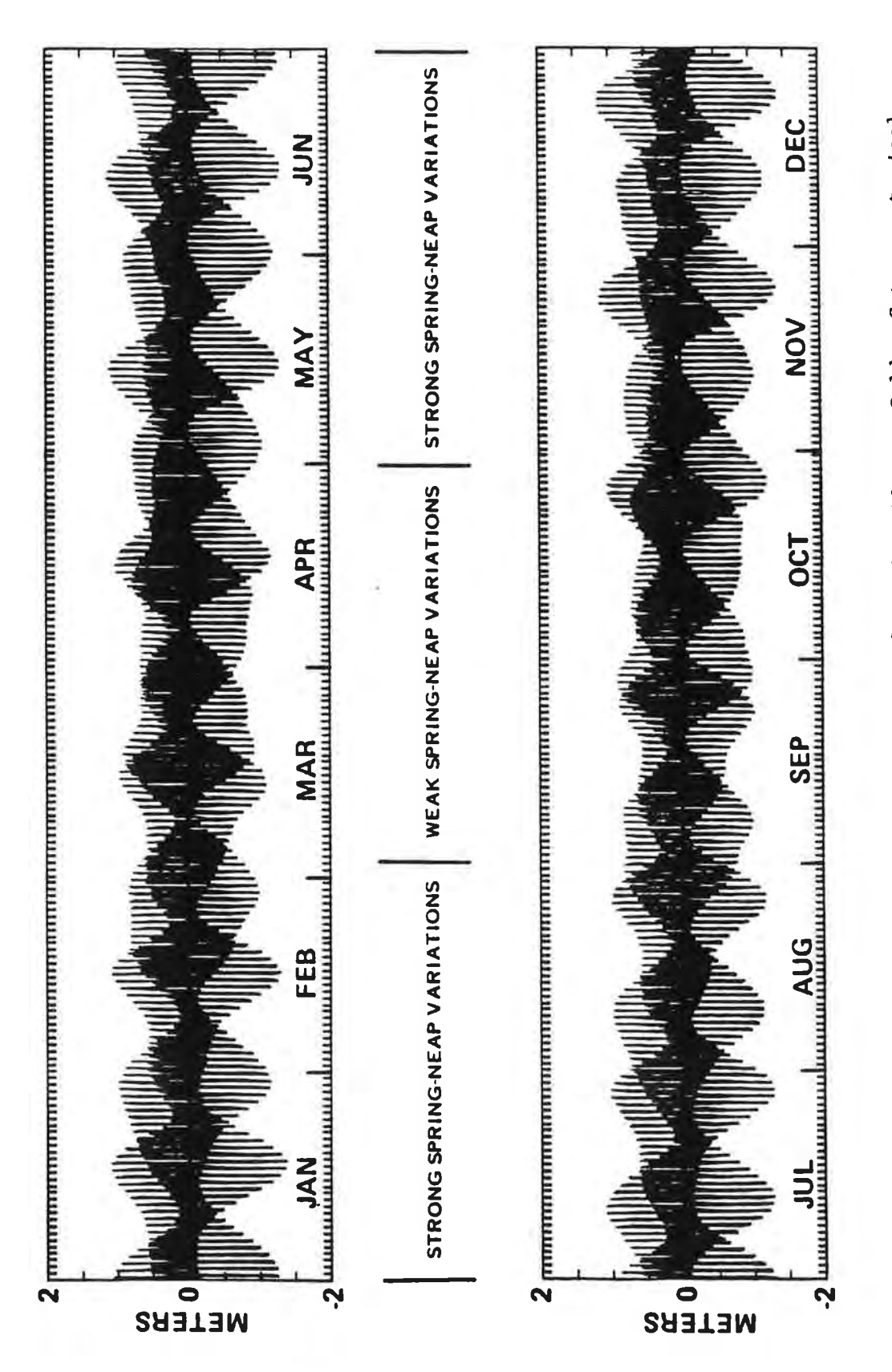
Table III-2 Surface Elevation Mean Amplitude (ft)

					Constituent	nt			
Station	01	K1	l l	MI	17	01	M2	S2	N2
P22	0.46	6.47	0.15	0.01	0.02	0.11	0.00	0.05	0.02
P23	U. 40	্ ক. ত	0.15	0.01	0.02	0.10	0.0	0.02	0.05
P24	0.4√	0.43	0.14	9.0 00.0	0.05	0.12	0.09	0.08	e. e
3-126	0,40 0,40	0.46	0.16	0.01	0.05	0.12	0.10	0.05	0.00 0.00
0-1-0	٠	0 0 0 0	0.13	0.01	0,05	0.11	0.02	0.01	0.01
0-010	0 t 0	0.41	0.13	0.01	0.03	0.11	0,04	0.05	0.01
0.000-0	ঝ	0 4.0	u. 16	0.03	0.01	0.11	0,08	0.05	0.09
000010 00100	u")	0.51	0.15	0.05	0,03	0.12	0.10	寸○ ° ○	0.03
0-704	च •	0.47	0.16	0,01	0,02	0.12	0.08	0.00	0.05
4-010	া	⊕ 1 =	0.13	0.00	0.03		σ° 0° 0	0.02	0.05
ロサローサ	্ব	ুক ক	0.14	0.01	0.0		0.00	0.04	0.08
10 T T T T	. च	्र च -	चि । ।	0.00	0.00		0.00	0.00	0.05
· (0,000) • (0,100) • 村	u".	0.01	10 T T	0.09	0	0.12	30°0	0.00	0.08
1000 T M		(M)	41.0	0.00	0.03		0.11	0.08	0.0%
() () () () () () () () () () () () () (d)	(M)	0.14	0. 0.	0.00		0.12	50°0	† O * O
0.00	ر آل -	40.0	U. 10	0.05	0.05	0.13	0.11	0.00	0,00
) (0)) (1)) (1)) (1)	(i)	000°5	0.14	0.03	0.03	0.14	0.11	0.00	0.0
の	0.00 0.00	0.03	0.13	0.09	0,03	0.13	0.13	0.10	φ', Θ', Θ
(i) (i) (i) (ii) (ii) (ii) (ii) (ii) (i	40	0.91	0.15	0.03	0.09	0.14	0.11	۵. د.	
4-604	цЭ,		0.15	0.0g	O. 09	0.13	0.11	0.0	
4 - 7 d 3	W)	©. ©	0.13	0.05	0.01	0.10	0.10	= 000 =	0 0 0
0 N J - 1	-00	00 00 0	0.13	⊕. 000	0,03	0.10	0.00	च □ □	0.00
7 - 7 - 7 - 10 - 10	(2)	0.00 0.00	0.14	0.00	0.08	0.07	0.04	0 0	0.01
r Oracles Tracket Oracles	T)	44.0	0.13	0,01	0,01	(A)	0°0	0.08	6.01
1 1 1 1 1 1 1 1 1 1 1 1 1 1 1 1 1 1 1	4	0.82	0.15	0.05	0,01	0.12	(A)	ē. 0 <u>ē</u>	0.00°
5									

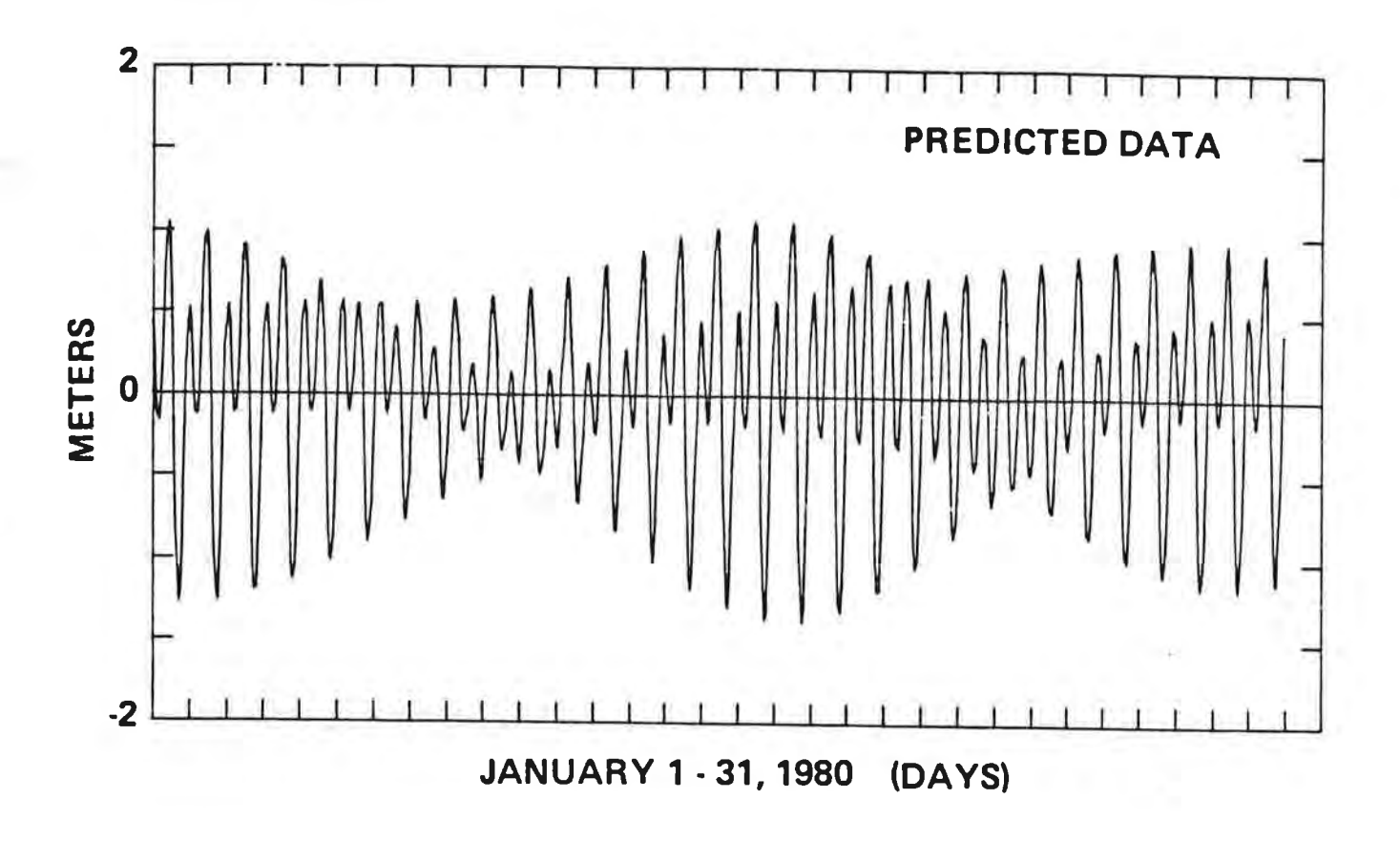
Table III-3
Surface Elevation Local Epoch (deg)

					Constituent	int			
Station	01	K1	P1	MI	11	10	M2	\$2	N2
α	(T) (T)	6	9	51.	8	Ψ (0)	0.0	00 (0.	1
\sim	ր_ ՄՆ	ġ	#	N . の寸の	Ţ,	(1) (2) (0)	0.) —) hø
	4. 00.00	0.00	300.0	30	320.5	281.1	0111.0) in 1 (0) 2 (0)) d) d) ()
73-126	ტ დ	(?) (%)	00	0.00 0.00	Q Q	1	O Fs	Ü	
70-195	<u>.</u>	01	60	ر ن	. (0)) (<u>(</u>	90	Ū₫ M
73-518	ë.	របិ 01	w ou	οij	. 66	0	j -	.))	Ďφ
000-07 000-07	က်	寸 (0)	[- -	ou ou		(<u>-</u>	- 13 - 10		តែប្រ បញ្ជ
00 90 10 10 10 10	ÛÜ.	8	00	νĎ	(T)	(T	- 60	Din	j r
402-07	(0)		0.0	r-	6- 01	ijŢ,	U .	l N	- 1
0.1⊕±6.	ru Oh	6	O	Ţ.	7	ر ان	(0) (0)	<u>-</u>	1 - J
コサローサム	in Th	ġ	雪.	(i) (ii)	6	Ó		(1) (),	१ च
74-119	u i	9	⊡	ტ ს	्रा क		100	. T	Ē
74-000	T.	ф С	<u>.</u>	ம் மி	00 00	00	THE STATE OF	। ज	i gr
74-308	Š.	oi ai	00 01		о Ф	Fig.			N.
のかのしかん	0	oi Si	7.	5 10	ή- Ο	(0) (T)			ıτ
94-070	00	<u>-</u>	ा च ००	51.	9	00	רט רט		
94-460	<u>.</u>	#	<u>o</u> .	•	(i)	10	ı Liğe		• 1 • 1
r.	u)	on out		च ८	4.878	0.00 0.00	(1) (1)) () () () (
924-42	(Th		φ Φ		(1)	[् च	11	
74-681	=	• []	· 寸	-	ij	(Th	<u>1</u>	o	। (*) र च
24-740	O	10 (10)	· 寸	-	<u>.</u>	<u>.</u>	ir.	ı T	
24-970	00 00	ú	(9) (3)	įά	00	<u>-</u>	i ijīn	00	. ф (()
76-041	Û	ስ ሰ-	gy Gy	-	Ġ	0		· · ·	=
96-059	ું. ભું	oj.	Ď	Ϊ.	ġ.	ហ្វ	-	, । ज	
26-074	÷	(1) (2)	()		u?		() () ()	() () ()) (f)) (f)
								1	1

* Refer to Table II-l for T designations used in Figure II-3.



mixed semidiurnal and diurnal; variations of spring and neap tides are clearly The tides at Golden Gate are typical Predicted tides at Golden Gate for 1980. depicted. Figure 1.12



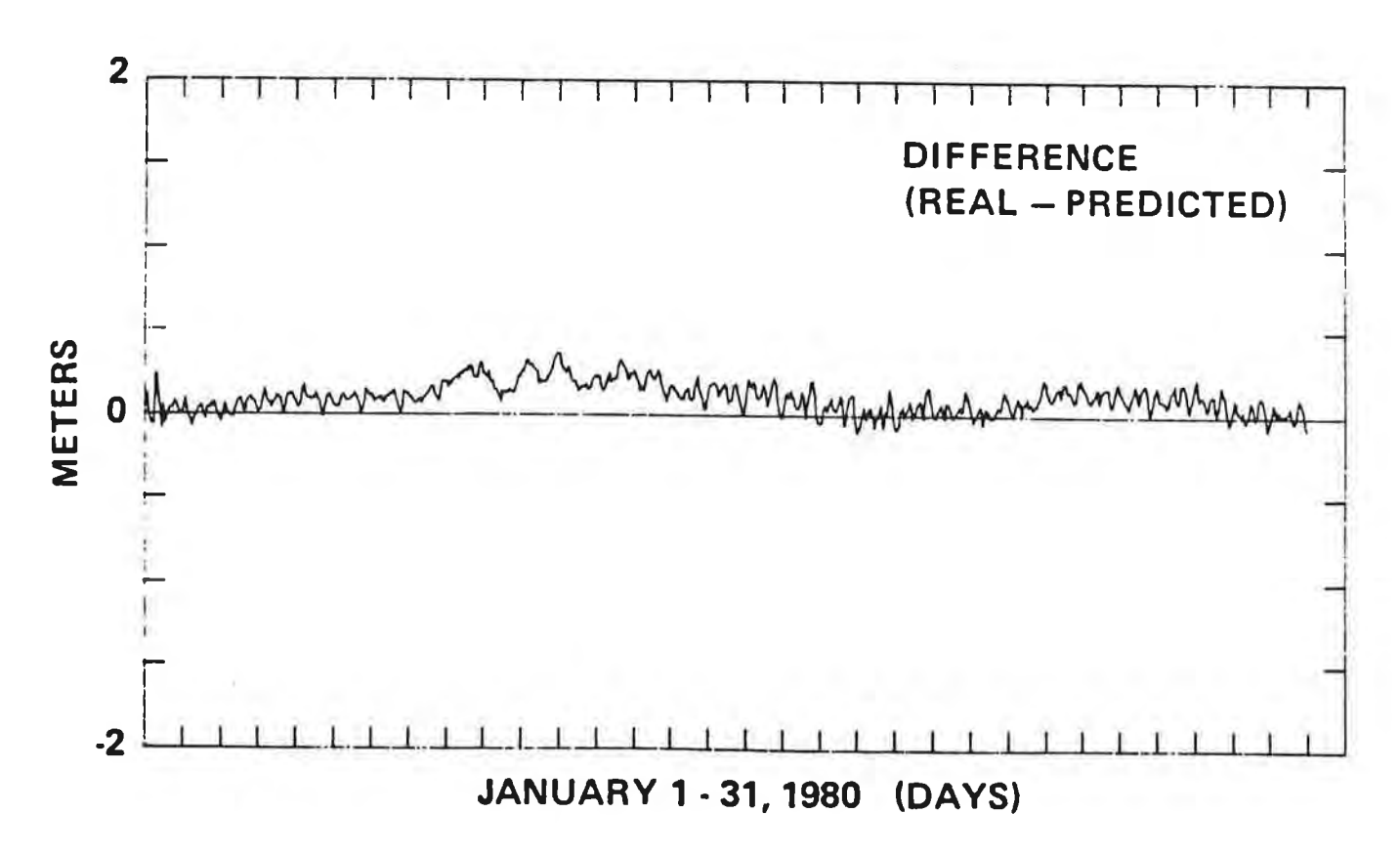


Figure I.llb. One month of predicted tides at Golden Gate generated from partial tidal constituents. The bottom graph shows the difference between the field and predicted data.

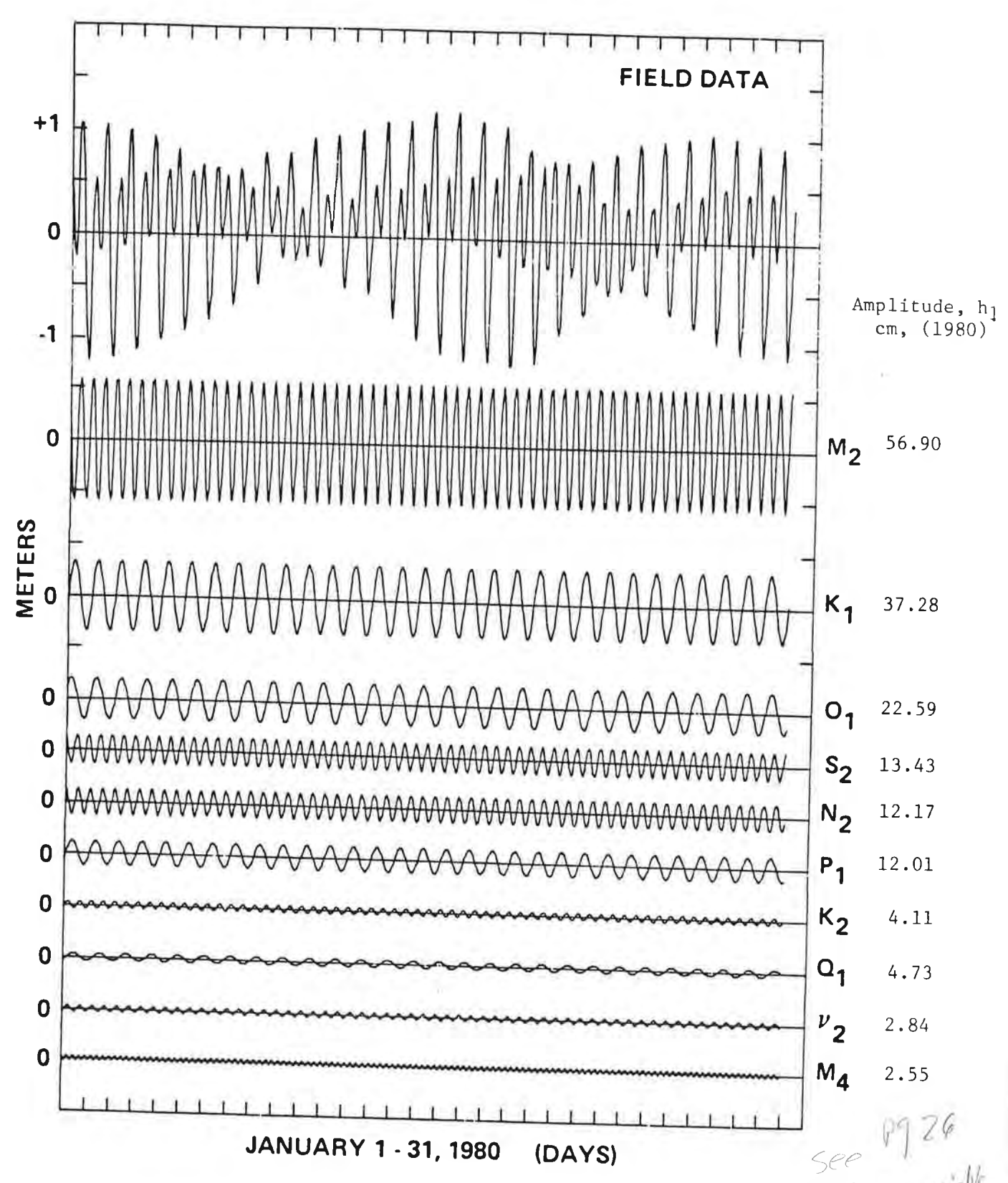
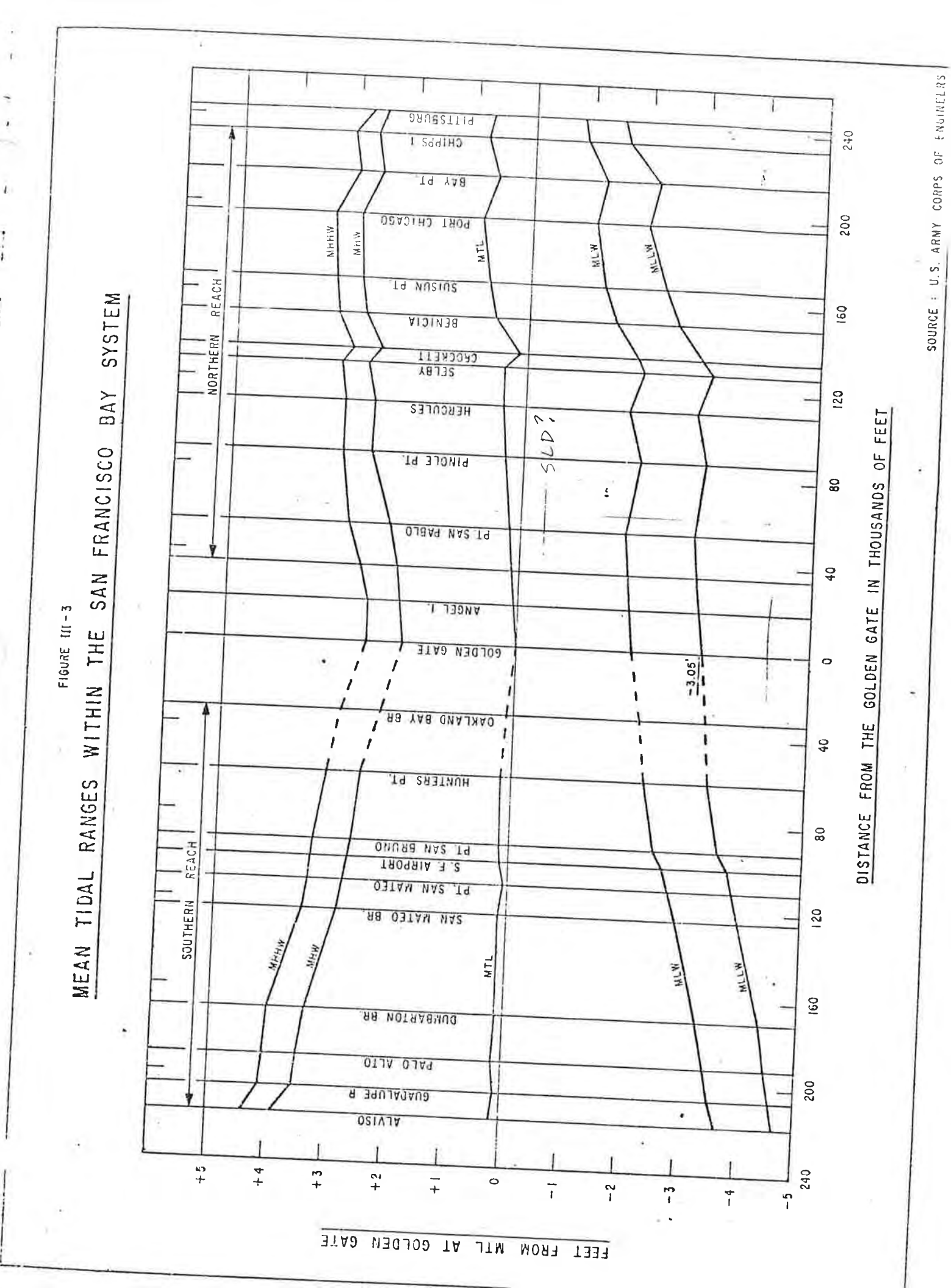


Figure I.lla. One month of field observations of tides at Golden Gate decomposed into tidal harmonics.

for variable



11-14-91

A New Evaluation of the Wind Stress Coefficient Over Water Surfaces

J. AMOROCHO AND J. J. DEVRIES

Departments of Civil Engineering and Land, Air and Water Resources University of California, Davis, California 95616

An analysis of data from numerous investigators, as well as information obtained directly by the authors, indicates that a large portion of the difficulties encountered in the past in establishing a relationship between the wind stress coefficient C_{10} and the wind velocity U_{10} can be attributed to computationally induced scatter of the data points. However, plots of the shear velocity u_{\bullet} against U_{10} reveal clear trends which show that three regions exist in the development of the wind shear stress: (1) a lower region in which the wind waves have not begun to break, and for which C_{10} is approximately constant; (2) a transitional region, after the onset of breakers, for which C_{10} varies nonlinearly with U_{10} ; and (3) a limiting region for which C_{10} tends again toward a constant value, and corresponds to a condition of breaker saturation. A single general equation to express C_{10} as a function of U_{10} is proposed, which agrees with the above findings. It is shown that in contrast with the perception of previous investigators, Charnock's coefficient $\alpha = z_0 g/u_*^2$, where z_0 is the roughness length and g is the acceleration due to gravity, is not constant anywhere in the range of wind velocities $0 < U_{10} < 40$ m/s. Finally, the data indicate that the wind flow boundary in each one of the three regions described above can be classified as having 'low roughness,' 'transitional,' and 'high roughness,' respectively.

INTRODUCTION

For the past 100 years or so, numerous investigators have carried out measurements of wind shear over water surfaces, both in the laboratory and at sea. A large volume of data has been collected, but no concensus has been reached yet on its interpretation. In particular, a variety of opinions has arisen with respect to the 'wind stress,' 'wind shear,' or 'surface drag' coefficient C_z as it has been variously termed. Some recent workers [e.g., SethuRaman and Raynor, 1975; Kitaygorodskiy, 1973; Pond et al., 1971; Ruggles, 1970] maintain that C_z does not vary with wind speed; others [e.g., Sheppard et al., 1972; Davidson, 1974; Wu, 1969, 1972; Garratt, 1977; Melville, 1977] have presented data supporting the notion that it does. The values of C_z have been disputed, as well as the appropriate expressions needed to represent it.

To set the stage for a reexamination of this problem, a few basic notions are recalled here.

Let it be assumed that for wind blowing over water, under conditions of neutral thermal stability, the logarithmic law of air velocity change with height is accepted, as given by the expression

$$U_z = \frac{u*}{\kappa} \ln \left(z/z_0 \right) \tag{1}$$

Here

- Uz mean wind velocity measured at elevation z above the water surface;
- κ von Karman constant (normally taken as 0.4);
- u* shear velocity, equal to $(\tau_w/\rho)^{1/2}$;
- z_0 vertical intercept of a semilogarithmic plot of z versus U_z ;
- τ_w wind shear stress at the water surface;
- ρ air density.

An established practice has been to measure wind velocity profiles over water, to determine the shear velocity via (1), and to compute τ_w therefrom.

Copyright © 1980 by the American Geophysical Union.

Because it is not always practical to perform velocity profile measurements in field situations, it has become customary to express the relationship between the wind shear stress and the velocity measured at a single location z above the mean water level by the expression

$$C_z = \frac{\tau_w}{\rho U_z^2} \tag{2}$$

where C, is the 'wind stress coefficient.'

One of the most complete summaries of published values of C_z was assembled by Wu [1969] and comprises data from 42 different investigations. This summary shows that the points originated from laboratory studies are widely scattered, and although the 'field' data show a general trend, their dispersion makes the selection of wind stress coefficients uncertain.

In an attempt to fit a single curve to the dispersed data on C_z , Charnock [1955] proposed an expression based on a parameter α which has become known as Charnock's coefficient, as follows:

$$C_z = \left[\frac{\kappa}{\ln \left(C_z^{-1} U_z^{-2} z g / \alpha \right)} \right]^2 \tag{3}$$

Here, α is given by the ratio

$$\alpha = \frac{gz_0}{u_*^2} \tag{4}$$

where g is acceleration due to gravity.

Charnock's coefficient has been generally assumed to be a constant when U_2 exceeds certain values. From the limited amount of data available to Charnock for short fetches in the field, as well as from laboratory data obtained by Wu [1968], Hidy and Plate [1966], and others, it appeared that at wind speeds approaching 10 m/s, α had a value of about 0.011. However, Kraus [1972] reports that when field data for long fetches are used, the required α to match (3) varies from about 0.008 to much higher values. Similar difficulties have been noted by many others.

From the above remarks, it is clear that many questions re-

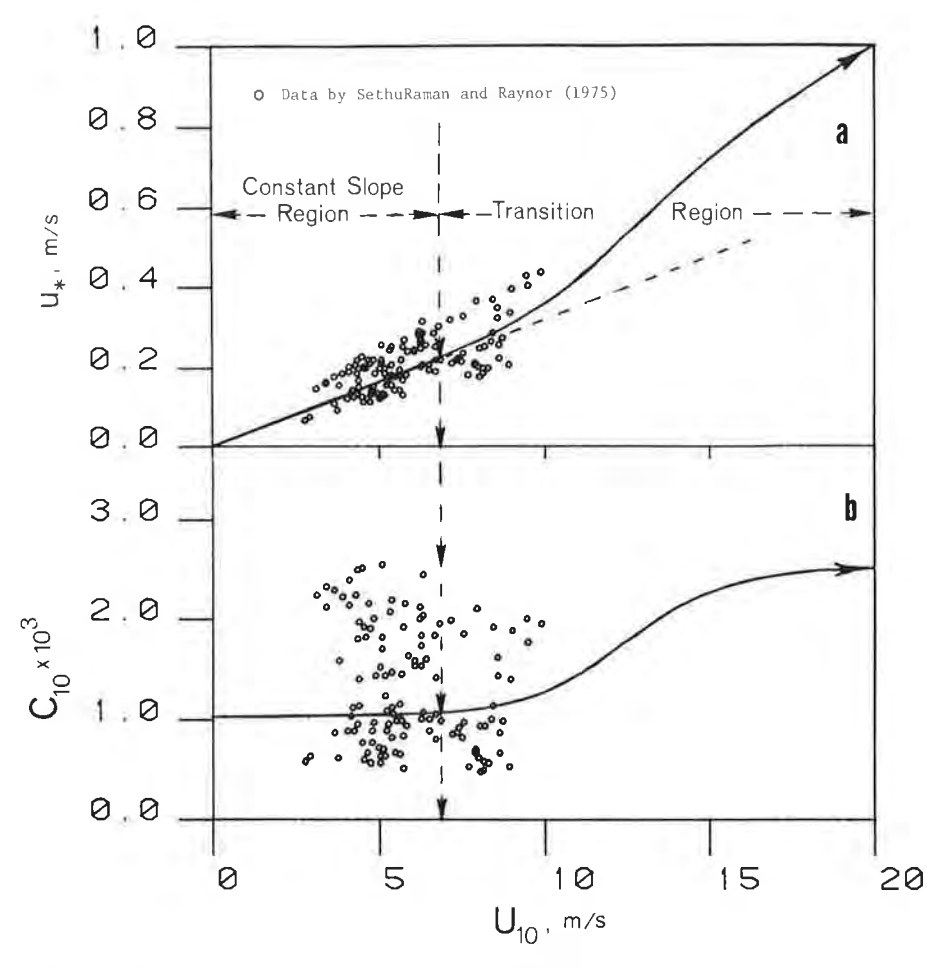


Fig. 2. Plots of u* and C₁₀ versus wind velocity U₁₀ from data by SethuRaman and Raynor [1975].

classes of U_{10} at intervals of 1 m/s. This information was not included in Wu's summary. Other data originating from surface stress computations by the geostrophic departure method during hurricanes were also cited by Garratt. For the present paper, the C_{10} values found in the original sources [Miller, 1964; Palmén and Riehl, 1957; Hawkins and Rubsam, 1968] were used, and also converted to u_* .

Finally, data cited by SethuRaman and Raynor [1975] for C_6 and u* versus U_6 were also considered. These values, scaled from the original paper and converted to z=10 via (1), were plotted separately in Figures 2a and 2b in order to avoid excessive clutter and overlap with Wu's data.

The contrast in the scatter between the C_{10} and u* plots is evident. The trend of the points, which is ill defined in the case of C_{10} , is fairly well defined for u*. Note that the dispersion of all the data sets is about the same for the lower wind velocities. The hurricane data points at $U_{10} > 15$ ms are more dispersed. This may be due to the greater imprecision associated with the inference of shear stresses from tropical cyclone information. *Kraus* [1972] suggests that this imprecision may cause on occasion overestimates or underestimates of the stress by a factor of 2. In fact, some C_{10} values from the sources cited are as high as 0.003-0.004 at wind speeds U_{10} between 35 and 50 m/s. These values seem doubtful to the authors and were not included in the present analysis. Future measurements made from instrumented platforms at sea may yield more reliable information.

The scatter of the u* points is certainly not surprising, since they originate from many different sources, and reflect the true experimental errors, as well as the lack of homogeneity of the conditions of measurement. Clearly, since the fetch of the water surfaces varied widely in the different studies involved, one would expect nonuniformity in the development of wave heights and hence in the overall water surface roughness for equal wind velocities. The variability of the wind in time can also be expected to have caused some of the dispersion. Finally, it is uncertain whether appropriate corrections were introduced in all the data for the effects of the state of thermal stability of the water-atmosphere system, particularly in the earlier investigations. Nevertheless, the u* points appear reasonably organized along a smooth curve as shown, and some important conclusions can be reached.

It is noted in Figure 1a that two well-defined regions with relatively low scatter are apparent. The first corresponds to points for which $0 < U_{10} < \sim 7$ m/s and the second to points for which $U_{10} > \sim 20$ m/s. The points fit straight lines passing through the origin with high coefficients of correlation (0.83 for $0 < U_{10} < \sim 7$ m/s and 0.94 for $U_{10} > \sim 20$ m/s). From these lines, the following expressions result, approximated to the fourth decimal place:

$$u* = 0.0323 U_{10}$$
 $0 < U_{10} < ~7 \text{ m/s}$ (6)

$$u* = 0.0504 U_{10}$$
 $U_{10} > \sim 20 \text{ m/s}$ (7)

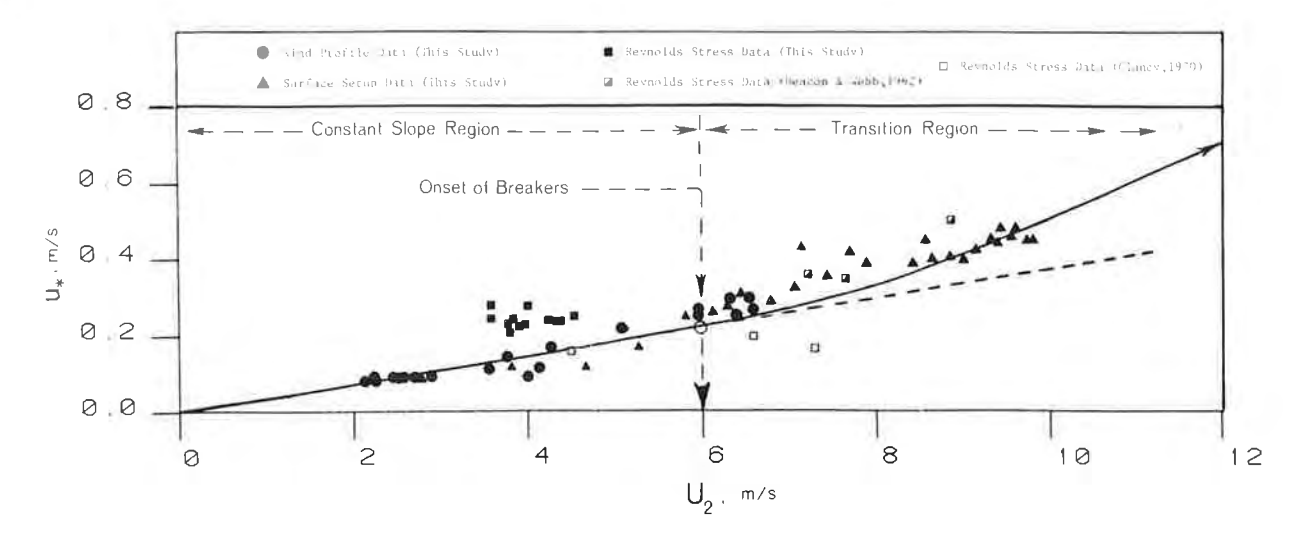


Fig. 4. Plot of u* versus wind velocity U2 from California Aqueduct data.

flow velocity, S_i is the channel boundary friction slope, Z_0 is the elevation of the channel bottom, and y is the water depth.

In the laboratory, τ_w was evaluated by discretizing (10) between the end points of a selected channel reach and by measurement of the right-hand side terms of (10) for various wind velocities $U_{c,1}$ averaged over a period of time. The corresponding u_{\cdot} was computed from τ_w . These measurements gave rise to a set of data points that exhibited a smaller dispersion than the wind profiles. This result could be expected, because the mean wind slopes evaluated over a reach are less sensitive to the local wind field perturbations produced by the waves, and tend to attenuate their overall effect.

In these experiments the waves began to break when $U_{c,1}$ reached a value of about 9 m/s. In Figure 3 a straight line was fitted by least squares to the points for the interval $0 \le U_{c,1} \le 9$ m/s. The equation of this line, averaged for all the data, is

$$u* = 0.0663 U_{c.1} \tag{11}$$

For $U_{c\perp} > 9$ m/s, the data suggest an upturn of the trend. With the equipment available it was not possible to attain higher wind velocities than about 12 m/s, so the behavior of u for a wider range of $U_{c\perp}$ could not be observed. The indication that a change of regime occurs after the waves start breaking is, however, clear. Similar results have been obtained by other investigators, including Wu [1969], who reports an abrupt change in $C_{0\perp}$ at about 8 m/s. The velocity $U_{0\perp}$ at which the breakers occur depends to a variable degree on factors such as fetch and water depth, and thus may vary between different laboratory flumes.

It is noted that the velocity $U_{10} = 7$ m/s at which the breakers begin to form over the sea corresponds to $U_{c+1} = 4.37$ m/s if the logarithmic velocity distribution law is assumed. At this point, for which $u_* = 0.23$ m/s, the waves do not break in the laboratory. Conversely, the velocity $U_{c+1} = 9$ m/s at which the first breakers occur in the laboratory corresponds to $U_{10} = 22$ m/s and $u_* = 1.11$ m/s, for which sea surfaces are already saturated with breakers. This can simply be attributed to the fact that the laboratory fetches are too short for the waves to grow in height sufficiently to break at wind velocities which are ample to produce breakers at sea. The key result here is that in the lower range of wind velocities u_* is a linear function of U_c , and hence C_c is constant, only as long as breakers do not form.

The authors also obtained measurements of wind shear velocities in the California Aqueduct, a large canal running north to south along the western flank of the San Joaquin Valley in California. This canal experiences strong axial wind action during certain seasons of the year. The canal has a width of some 50 m. The length of the reach observed, which has a nearly straight alignment, is approximately 10 km. Details on these studies are reported by DeVries [1978] elsewhere. Of interest here, among the results of that investigation, are data showing the relationship between U_2 (wind velocity 2 m above the water) and u_* .

The shear velocities were obtained for various wind conditions from profile measurements, from measurements of the Reynolds stresses (eddy correlation method) taken with hotfilm anemometers, and from the wind slopes, as evaluated by determination of the wind 'set-up.' These data are plotted in Figure 4, together with other information for open water cited by Deacon and Webb [1962] and Clancy [1970]. The points corresponding to the Reynolds stress measurements depart from the general trend of the wind profile and the wind set-up data probably due to instrumental difficulties, as discussed by one of the authors elsewhere [De Vries, 1978]. In this canal, the waves started breaking at $U_2 = 6$ m/s approximately (equivalent to $U_{10} = 7$ m/s). A straight line fits the points in the interval $0 < U_2 < 6$ m/s. For $U_2 > 6$ the points trend upward, in a manner similar to that observed in the laboratory experiments after the onset of breakers, as well as that indicated by the data given in Figure 1. The solid line drawn through the points corresponds to the equation proposed by the authors as described in the following section.

The above information tends to confirm the hypothesis that in the transition region the values of u* and U_{10} are related to the development of breaking waves. The following theory is based on this premise.

A THEORY ON THE VARIATION OF C_{10}

The coefficient C_{10} can be considered to be composed of two elements: (1) an element C_r due to roughness drag associated with nonbreaking waves and ripples, and equal to a lower limiting value $C_{10\text{min}} = 0.00104$; (2) an element due to form drag C_f , associated with flow separation behind the breakers. It is postulated here that this second element is proportional to a function depending on the area covered by

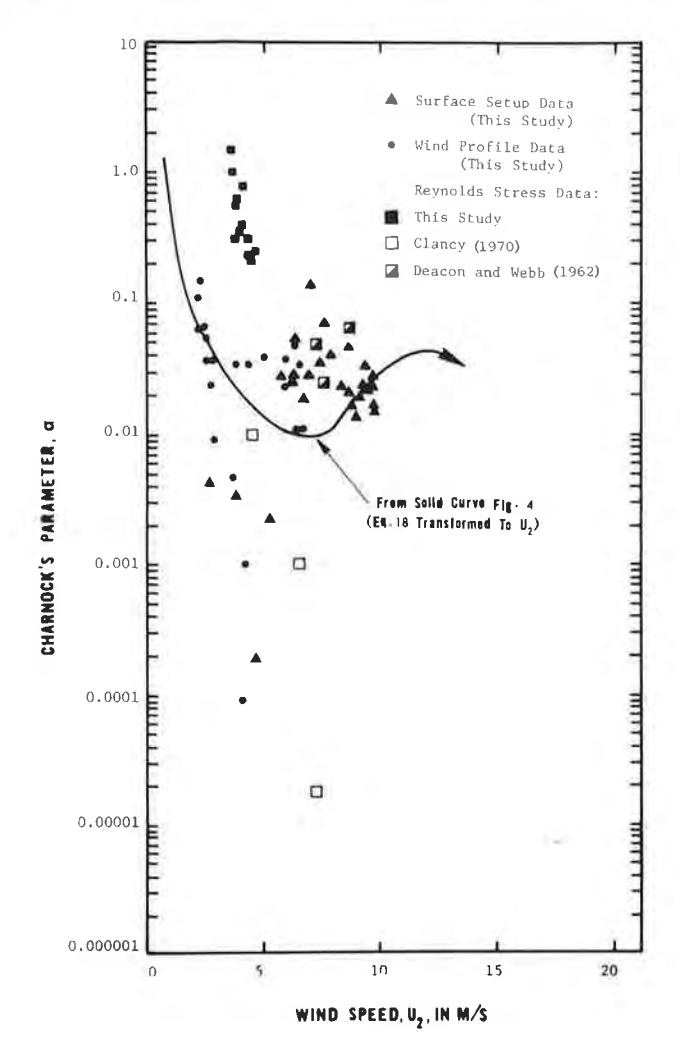


Fig. 6. Plot of Charnock's α versus wind speed U_2 from California Aqueduct data and other sources.

The relationship between U_{10} and U_z can be evaluated by expressing U_{10} and U_z through (1) and subtracting one from the other. After some manipulation, the following results are obtained:

$$U_z = U_{10} - \frac{u*}{\kappa} \ln (10/z) = U_{10} [1 - (C_{10})^{1/2} \kappa^{-1} \ln (10/z)]$$
 (21)

Combining this with (20), we get

$$C_z = C_{10} \left[1 - (C_{10})^{1/2} \kappa^{-1} \ln (10/z) \right]^{-2}$$
 (22)

With these equations, a curve expressing the relationship C_z versus U_z can be constructed for any z, given C_{10} values computed from (19). It is remarked here that (19) describes a curve that only reaches the maximum and minimum values $C_{10\text{max}} = 0.00254$ and $C_{10\text{min}} = 0.00104$ asymptotically. However, the convergence on both sides of the central region is very rapid and the curve ordinates are indistinguishable from these limiting values within an approximation of 10^{-5} in the close vicinity of $U_{10} = 7$ m/s and $U_{10} = 20$ m/s. Therefore the essential constancy of C_{10} at the high and low wind velocity ranges is practically preserved.

Equation (18) was also used to plot the curve shown on Figure 4, with proper scaling for U_2 by means of (21). The agreement between this curve and the plotted points indicates that

the shear stress relationship proposed applies equally well to large canals and to open water surfaces such as lakes and the sea, as long as the canal fetches are sufficient to permit the formation of breaking waves.

CHARNOCK'S COEFFICIENT a

The validity of the assumption that Charnock's α is constant was tested from the experimental data obtained by the authors, as well as from (18).

Combining (1) and (4), one gets

$$\alpha = gz[\exp(\kappa U_z/u_*)]^{-1}u_*^{-2}$$
 (23)

Figure 5 is a plot of α versus U_{c+} based on the u* values found in the laboratory. The points were computed from individual u* values, and the curve corresponds to the solid curve shown in Figure 3. Figure 6 shows a similar plot based on the measurements made at the California Aqueduct, and Figure 7 represents the behavior of α based on (18). It is clear from these three plots that α cannot be considered to be constant anywhere in the range of wind velocities shown. While Charnock's idea of a nondimensional parameter relating the 'roughness length' to the shear velocity may be valid, the roughness length, is a derived quantity and its determination is very imprecise. The plots illustrate the large uncertainty involved in evaluating α from individual measurements of u_* . The fact that this uncertainty was not recognized for the many years elapsed since its use was first proposed is quite surprising. Charnock suggested that the parameter was constant for $U_{10} > 10$ m/s on the basis of the results of extrapolations of logarithmic plots of velocity profiles. Such extrapolations are extremely imprecise, but the illusion of the constancy of α has persisted nevertheless. One can only attribute this persistence to the circumstance that the illusion could not be dispelled due to the equally enduring reliance on strongly scattered diagrams for the definition of C_{10} . Another difficulty has arisen from the circumstance that in the past, complete data sets covering a wide range of wind velocities from zero to, say, 35 m/s, could not be obtained directly by individual investigators from their own measurements. In some cases the workers drew far reaching conclusions from a limited range of results. For example, the data of SethuRaman and Raynor are contained mostly within the lower region of U_{10} values for which C_{10} is constant. This constancy certainly should not be assumed to extend beyond the range of the data. The conclusion that Charnock's α is constant and equal to 0.016 '... for moderately rough sea conditions and 0.072 for fully rough conditions . . .' appears somewhat contrived and is not supported either by the data of SethuRaman and Raynor themselves or by the additional information presented here.

Other authors have chosen to ignore large masses of available information. The exclusive use of data not included in Wu's summaries, for example, may have led Garratt to overlook the existence of the transition region of the shear stress, and to propose that a value of $\alpha = 0.0144$ describes adequately the variation of C_{10} in the region $4 < U_{10} < 21$ m/s.

It is certainly possible to obtain an expression for Charnock's α by combining (18) and (23). However, quite aside from the complicated form of such an expression, it would seem that to use it for finding a nonconstant α as a vehicle for computing C_z , and thence, eventually, τ_w , is a rather pointless exercise. Therefore it seems to the authors that since Charnock's α has lost its virtue as a constant parameter, its future use can hardly be justified. The value proposed by Garratt

- ture and budgets of the hurricane on October 1, 1964, Mon. Weather Rev., 96, 617, 1968.
- Hidy, G. M., and E. J. Plate, Wind action on water standing in a laboratory channel, J. Fluid Mech., 26, 651, 1966.
- Kitaygorodskiy, S. A., The Physics of Air-Sea Interaction, vol. 15, translated from Russian by A. Baruch, p. 86, Israel Program for Scientific Translations, Jerusalem, 1973.
- Kotsch, W. J., Weather for the Mariner, U.S. Naval Institute, Annapolis, Md., 1970.
- Kraus, E. B., Atmosphere-Ocean Interaction, Oxford University Press, New York, 1972.
- Malkus, J. A., Large scale interactions, chap. 4, in *The Sea, Physical Oceanography*, edited by M. N. Hill, John Wiley, New York, 1962.
- Melville, W. K., Wind stress and roughness length over breaking waves, J. Phys. Oceanogr., 7, 702, 1977.
- Miller, B. I., A study of the filling of Hurricane Donna (1960) over land, Mon. Weather Rev., 92, 389, 1964.
- Miyake, M., M. Donelan, A. McBean, C. Paulson, F. Badgley, and E. Leavitt, Comparison of turbulent fluxes over water determined by profile and eddy correlation techniques, *Quart. J. Roy. Meteorol. Soc.*, 96, 132, 1970.
- Palmen, E., and H. Riehl, Budget of angular momentum and energy of tropical cyclones, J. Meteorol., 14, 150, 1957.
- Pond, S., and G. L. Pickard, *Introductory Dynamic Oceanography*, Pergamon, Oxford, England, 1978.
- Pond, S., T. Phelps, J. E. Paguin, G. McBeau, and R. W. Stewart, Measurement of the turbulent fluxes of momentum, moisture and sensible heat over the ocean, J. Atmos. Sci., 28, 901, 1971.

- Reid, L. J., and J. Berkson, Application of the logistic function to experimental data, J. Phys. Chem., 33, 760, 1929.
- Ruggles, K. W., The vertical wind profile over the ocean for light to moderate winds, J. Appl. Meteorol., 9, 389, 1970.
- SethuRaman, S., and G. S. Raynor. Surface drag coefficient dependence on the aerodynamic roughness of the sea, J. Geophys. Res., 80, 4983, 1975.
- Sheppard, P. A., D. T. Tribble, and J. R. Garratt, Studies of turbulence in the surface layer over water (Lough Neagh), Quart. J. Roy. Meteorol. Soc., 98, 627, 1972.
- Smith, S. D., and E. G. Banke, Variation of the sea surface drag coefficient with wind speed, Quart. J. Roy. Meteorol. Soc., 101, 665, 1975.
- Veenhuizen, S. D., Turbulent air flow over wind excited laboratory waves, Ph.D. dissertation, 110 pp., Colo. State Univ., Fort Collins, 1973.
- Wu, J., Laboratory studies in wind-wave interactions, J. Fluid Mech., 34, 91, 1968.
- Wu, J., Wind stress and surface roughness at air-sea interface, J. Geophys. Res., 74, 444, 1969.
- Wu, J., Physical and dynamical scales for generation of wind waves, J. Waterways Harbors Coastal Eng. Div. Amer. Soc. Civil Eng., 98 (WW2), 163, 1972.

(Received April 12, 1979; revised July 10, 1979; accepted August 6, 1979.)

A Comparison of Methods for Estimating u_z From Given u_z and Air-Sea Temperature Differences

PAUL C. LIU AND DAVID J. SCHWAB

Great Lakes Environmental Research Laboratory, National Oceanic and Atmospheric Administration, Ann Arbor, Michigan

This paper presents an objective assessment of four methods for estimating sea surface friction velocity u_* from wind speed at height z, u_z , and air-sea temperature difference. The methods are compared by using the computed friction velocity as the normalization factor in parametric correlations of wind-wave parameters with the wind and wave measurements made by NOMAD buoys in the Great Lakes. The results show that (1) wind profile parameters obtained from the four methods are generally comparable, (2) parametric correlations with parameters normalized by u_* lead to significantly decreased percentage deviations over correlations normalized by u_z , and (3) correlations based on u_* derived from the four methods show nearly identical percentage deviations. The conclusions are that (1) u_* normalization acts to eliminate the effect of atmospheric stability and (2) any of the four methods can be used effectively in practical applications.

1. Introduction

One of the basic tools for studying wind waves, surface currents, mixing, and sea-air interactions in the upper ocean is to nondimensionalize the relevant parameters in order to find universal correlations for use with theoretical models. Wind speed at 10 m above sea surface, u_{10} , has frequently been used in the nondimensionalization. While it is convenient to use u_{10} , many routinely available wind speeds are measured at other levels, that is, 19.5 m from a ship or 5 m from a buoy. To reconcile these different wind measurements as well as to eliminate the effects of surface roughness and atmospheric stability, the friction velocity u, is used for nondimensionalization. As u, is not a readily measured parameter, a number of empirical methods have been developed to obtain u, from measurements of u_z and air-sea temperature differences. In this paper we examine four of these methods and apply them to the wind, wave, and temperature data recorded from NOMAD buoys deployed in the Great Lakes. Since in this case there is no measured u for direct verification of the results, we simply apply the estimated u_* to correlations of windwave parameters. We expect that an effectively estimated u will be free from atmospheric stability effects, and hence its application in the parametric wind-wave correlations will act to reduce the scatter.

2. Methods

The four empirical methods we examine in this paper are (1) the Great Lakes Environmental Research Laboratory (GLERL) method [Schwab, 1978] based on the works of Long and Shaffer [1975], Businger et al. [1971], and Smith and Banke [1975], (2) the Kondo method based on Kondo [1975], (3) the Large and Pond method based on Large and Pond [1981, 1982] and Keller et al. [1985], and (4) the Smith method based on Smith [1981] and Dyer [1975]. All four methods start with the similarity theory of Monin and Obukhov [1954] that expresses wind shear and temperature gradi-

This paper is not subject to U.S. copyright. Published in 1987 by the American Geophysical Union.

Paper number 7C0228.

ent in the form

$$\partial u/\partial z = (u_{\bullet}/kz)\phi_{m}(\zeta) \tag{1}$$

$$\partial \theta / \partial z = (\theta_{-}/kz)\phi_{h}(\zeta) \tag{2}$$

respectively, where u_{\bullet} is the friction wind velocity, θ_{\bullet} is the scaling temperature, k=0.4 is the von Karman constant, $\zeta=z/L$ is the dimensionless stability height, and $L=\theta u_{\bullet}^{2}/(gk\theta_{\bullet})$ is the Monin-Obukhov stability length.

One difference in the methods tested here is in the definition of functions $\phi_m(\zeta)$ and $\phi_h(\zeta)$ by the authors listed in Table 1. The functions are shown graphically in Figure 1. While the differences are almost nonexistent for unstable cases with $\zeta < 0$, the functions tend to diverge, in some cases significantly, for the stable case with large ζ . Following *Paulson* [1970] we can integrate (1) and (2) to give the wind and temperature profiles as:

$$u = (u_*/k)[\ln(z/z_0) - \psi_m]$$
 (3)

$$\theta = \theta_0 + (\theta_*/k) [\ln(z/z_0) - \psi_h] \tag{4}$$

where z_0 is the surface roughness length, θ_0 is the extrapolated temperature at z=0, and the expressions of $\psi_m(\zeta)$ and $\psi_h(\zeta)$ corresponding to ϕ_m and ϕ_h are those listed in Table 2. Note in Table 2 that Long and Shaffer [1975] further divide the stable condition into two parts: the upper part for mildly stable cases (that is, $0 < \zeta < 1$) and the lower part for strongly stable cases ($\zeta \geq 1$). These solutions are functions of three unknown parameters: u_* , z_0 , and L. Different authors have devised their own methods for estimating L. In addition, u, can be linked with wind speed u_z or z_0 through various theoretical or empirical relations. The Charnock [1955] relation, for example, states that gz_0/u_*^2 is a universal constant, where g is the gravitational acceleration; hence zo, characterizing the aerodynamic roughness at the surface, is proportional to u_{\bullet}^{2} . Smith [1981] further postulated that roughness length for a smooth surface should be added to achieve gradual transitions from smooth to rough surface conditions. Thus

$$z_0 = au_{\bullet}^2/g + (v/u_{\bullet}) \exp(-5.5k)$$
 (5)

where a is the Charnock constant, and v is the dynamic viscosity of air ($\approx 14 \times 10^{-6} \text{ m}^2 \text{ s}^{-1}$).

	ϕ_m	(ζ)	4	$b_n(\zeta)$
	Stable	Unstable	Stable	Unstable
Businger et al. [1971] (GLERL)	1. + 4.7ζ	$(115.\zeta)^{-1/4}$	$0.74 + 4.7\zeta$	$0.74(19.\zeta)^{-1/2}$
Kondo [1975])	$1. + 6.\zeta/(1. + \zeta)$	$(116.\zeta)^{-1/4}$	$1. + 6.\zeta/(1. + \zeta)$	$(116.\zeta)^{-1/2}$
Large and Pond [1981]	$1. + 7.\zeta$	$(116.\zeta)^{-1/4}$	$1. + 7.\zeta$	$(116.\zeta)^{-1/2}$
Dyer [1975], Smith [1981]	$1 + 5.\zeta$	$(116.\zeta)^{-1/4}$	$1. + 5.\zeta$	$(116.\zeta)^{-1/2}$

In general, all four methods follow a two-stage approach: first, obtain the neutral bulk coefficient and then use air-sea temperature differences to estimate the diabatic conditions. In Smith's method the neutral bulk coefficient is given by

$$C_{zz} = k/\ln (z/z_0)^2$$
 (6)

which can be estimated iteratively along with (5). Kondo's method, on the other hand, obtains C_{zn} from the neutral 10-m-level-bulk coefficient by

$$C_{zn} = k^2 [kC_{10n}^{-1/2} + \ln(z/10)]^{-2}$$
 (7)

In the work by Kondo [1975], C_{10} , is empirically related to the wind speed by:

$$10^{3}C_{10_{n}} = 1.08u_{10}^{-0.15} \qquad 0 < u_{10} \le 2.2 \text{ ms}^{-1}$$

$$10^{3}C_{10_{n}} = 0.771 + 0.0858u_{10} \qquad 2.2 < u_{10} \le 5 \text{ ms}^{-1}$$

$$10^{3}C_{10_{n}} = 0.867 + 0.0667u_{10} \qquad 5 < u_{10} \le 8 \text{ ms}^{-1} \qquad (8)$$

$$10^{3}C_{10_{n}} = 1.2 + 0.025u_{10} \qquad 8 < u_{10} \le 25 \text{ ms}^{-1}$$

$$10^{3}C_{10_{n}} = 0.773 \qquad 25 < u_{10} < 50 \text{ ms}^{-1}$$

Note here that u_{10} is the neutral 10-m-level wind speed. To proceed with a nonneutral u_z , Kondo [1975] gave a simple iteration procedure that can be used to obtain an estimate of neutral u_{10} . Large and Pond's [1981] first-stage approach is similar to Kondo's method except that they used a simpler empirical formulation for C_{10} :

$$10^{3}C_{10_{n}} = 1.14 \qquad 0 < u_{10} \le 10 \text{ ms}^{-1}$$

$$10^{3}C_{10_{n}} = 0.49 + 0.065u_{10} \qquad 10 < u_{10} < 50 \text{ ms}^{-1}$$
(9)

The GLERL approach uses the Charnock relation to obtain z_0 with the Charnock constant determined from setting $u_{10} = 15 \text{ ms}^{-1}$ in the C_{10} , versus u_{10} relation given by Smith and Banke [1975] as:

$$10^3 C_{10} = 0.63 + 0.066 u_{10} \tag{10}$$

In the second stage the GLERL method uses the iteration scheme of Long and Shaffer [1975] to obtain L and hence the values of ψ . Large and Pond [1981] developed semitheoretical formulas for directly calculating ζ from given wind speed u_z , air temperature T_a , and sea temperature T_s , in which the u_s calculation is given by Keller et al. [1985] as:

$$u_{\star} = u_{\star}(C_{\star n})^{1/2} / [1 - (C_{\star n})^{1/2} \psi_{m} / k]$$
 (11)

The Smith [1981] approach requires iterations in which u_* , θ_* , and ψ functions are adjusted to yield the desired C_{zn} . Kondo [1975] perhaps provided the most simplified approach by developing approximate formulas for calculating C_z from a neutral C_{zn} .

Figure 2 presents plots of C_{10} versus u_{10} for different air-sea temperature differences with the four methods. The neutral stratification case is shown by the heavy line. The thin lines correspond to air-sea temperature differences ranging from -20° C (curves above the neutral curve) to $+20^{\circ}$ C (curves below the neutral curve) at 1° C increments. The main differences are at wind speeds less than 2.5 ms⁻¹; the Kondo, Large-Pond, and Smith methods show the unstable drag coefficient increasing as wind speed decreases to zero, while the GLERL method shows it continuously decreasing. This is clearly a result of the different formulations of the methods.

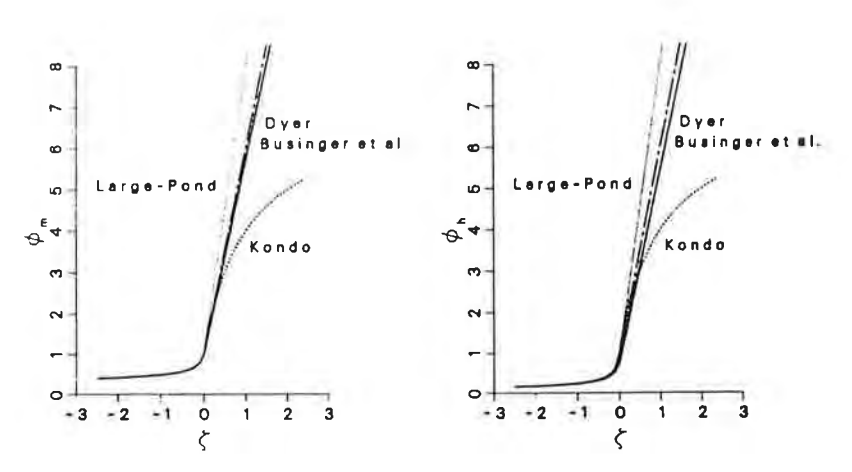


Fig. 1. Comparison of different wind shear and temperature gradient formulas.

TABLE 2. Diabatic Wind and Temperature Profiles as Given by Different Authors

		$\psi_{m}(\zeta)$	
	Stable	Unstable*	
Long and Shaffer	$0.74 \ln (\zeta/\zeta_0) + 4.7(\zeta - \zeta_0)$	$\ln \left[(x-1)(1+x_0)/(1+x)(x_0-1) \right]$	
[1975] (GLERL)	$-\ln \zeta_0 + 4.7/\zeta_0 + 5.7 \ln \zeta$	$+ 2[\tan^{-1} x - \tan^{-1} x_0]$	
Kondo [1975]	$\ln \left(\zeta/\zeta_0 \right) + 6 \ln \left[(1+\zeta)/(1+\zeta_0) \right]$	$\ln \left[(x_0^{\frac{1}{2}} + 1)(x_0 + 1)^2/(x^2 + 1)(x + 1)^2 \right] + \ln \left(\zeta/\zeta_0 \right) + 2\left[\tan^{-1} x - \tan^{-1} x_0 \right]$	
Large and Pond [1981]	−7.ζ	$2 \ln \left[\frac{(1+x)}{2} \right] + \ln \left[\frac{(1+x^2)}{2} \right] \\ - 2 \tan^{-1} x + \frac{\pi}{2}$	
Smith [1981]	– 5.ζ	2 $\ln [(1 + x)/2] + \ln [(1 + x^2)/2]$ - 2 $\tan^{-1} x + \pi/2$	
		$\psi_h(\zeta)$	
	Stable	Unstable*	
Long and Shaffer [1975] (GLERL)	$\ln (\zeta/\zeta_0) + 4.7(\zeta - \zeta_0) -0.74 \ln \zeta_0 + 4.7/\zeta_0 + 5.44 \ln \zeta$	0.74 ln $[(x^2 - 1)(x_0^2 + 1)/(x^2 + 1)(x_0^2 - 1)]$	
Kondo [1975]	$\ln \left(\frac{\zeta}{\zeta_0} \right) + 6 \ln \left[\frac{(1+\zeta)}{(1+\zeta_0)} \right]$	$\ln \left[(x+1)(x_0+1)/(x_0-1)(x+1) \right]$	
Large and Pond [1981]	$-7.\zeta$	$\ln \left[(1+x^2)/2 \right]$	
Smith [1981]	$-5.\zeta$	$2 \ln \left[(1 + x^2)/2 \right]$	

^{*}Where $x = (1 - a\zeta)^{1/4}$, $x_0 = (1 - a\zeta_0)^{1/4}$, and a = 15. or 16.

While the methods have different emphases which possibly tend to accentuate each author's own data, the differences are generally no greater than the data point scatter from which they were derived. All four methods can be readily used to estimate a wind profile and hence u_{\bullet} from a given wind speed and air-sea temperature difference. In the following we shall compare the results as they are applied to actual wind and wave measurements.

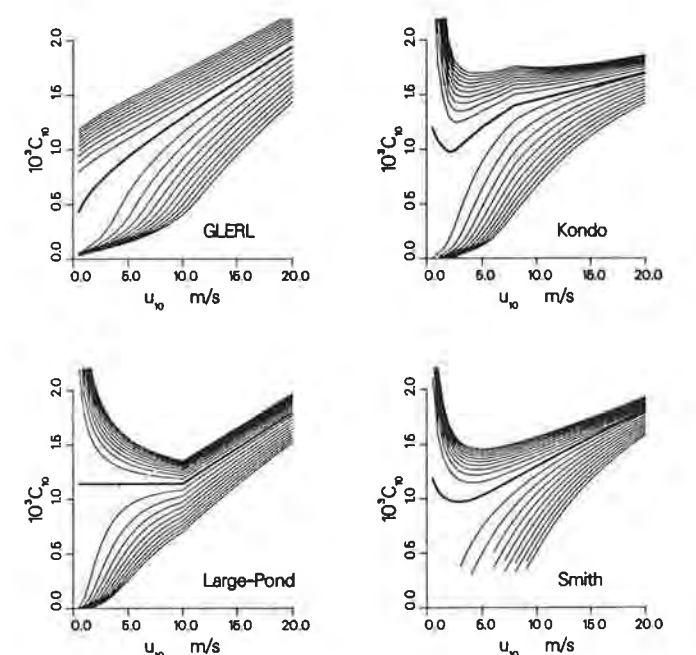


Fig. 2. Comparison of different bulk transfer coefficient formulas as a function of 10-m wind speed for air-sea temperature differences from -20°C to $+20^{\circ}\text{C}$ at 1°C increment. The heavy line is the neutral case.

3. Data

There have been eight NOMAD buoys moored in the Great Lakes since 1981 in water depths ranging from 15 to 250 m (Figure 3). These buoys are boat shaped, 6 m in length, with an electronic payload for measuring wind speed, wind direction, barometric pressure, air temperature, sea surface temperature, and surface wave spectral data. Most of the meteorological sensors are located 5 m above the water surface. Data are reported hourly. The wind speed and direction, as well as air and surface water temperatures, are 8.5-min averages of samples obtained at 1-s intervals. The waves are measured with an accelerometer using an on-board Wave Data Analyzer system [Steele and Johnson, 1977] that transmits acceleration spectral data via the UHF GOES satellite to a shore collecting station, where wave frequency spectra with 48 degrees of freedom are calculated from 20 min of measurements. In this study we examined all the data recorded during 1981-1984, an average of over 4000 hourly measurements from each buoy every year. The results from different buoys and from



Fig. 3. Great Lakes map showing the locations of the eight National Data Buoy Center NOMAD buoys.

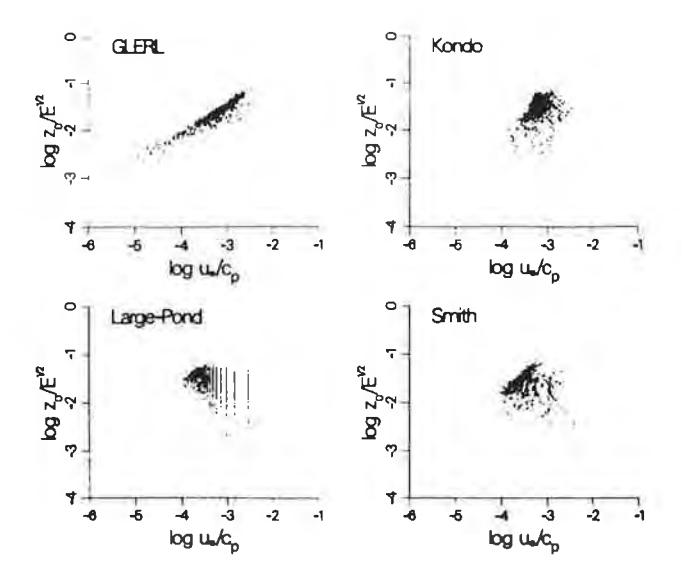


Fig. 4. Comparison of $z_0/E^{1/2}$ versus u_{\bullet}/c_p correlations.

different years are very similar, however. Therefore the detailed analyses presented here use data from the 1984 northern Lake Michigan buoy number 45002 as representative of all the buoys. Buoy 45002 recorded 4212 simultaneous measurements of wind speed, air-sea temperature difference, significant wave height, and peak energy wave period in 1984 with a maximum wind speed of 15 ms⁻¹ and a maximum significant wave height of 4.5 m. In the following analyses, calculations were based on all of the 4212 data points, while the graphs show only 1056 points (about every fourth point) in order to reduce crowding.

4. RESULTS AND DISCUSSION

4.1. Roughness Length

The purpose of the empirical methods discussed above is to estimate values for the roughness length z_0 and for friction velocity u_* when these cannot be measured directly. The roughness length z_0 is conceptually an important parameter in the study of wind waves. However, it is difficult to measure or

even define physically. Of the four methods we considered here, only the GLERL and Smith methods use z_0 explicitly; the Kondo and Large-Pond (as interpreted by Keller et al. [1985]) methods do not, although a value for z_0 can be estimated from these methods. To examine these z_0 estimations in connection with sea state studies, we follow Huang et al. [1986] and plot z_0 normalized by rms wave height $E^{1/2}$ versus u_{\bullet} normalized by peak energy wave speed c_{p} . The results are shown in Figure 4. The GLERL method is the only one that shows a consistent correlation between normalized values of z_0 and u_{\bullet} ; this merely reflects the use of the Charnock relation in that method. The Smith method uses a nonlinear function for z_0 that approaches the Charnock relation at large u_* . The Kondo and Large-Pond methods do not use z_0 explicitly. None of these methods show any clear correlation between the normalized z_0 and u_* . Since all four methods are primarily formulated to estimate the drag coefficient C_z and the friction velocity u_* under diabatic conditions, z_0 did not receive a detailed treatment. The results of the correlations reflect this effect. The exact form of the relation between z_0 and u_* is still an active area of research; Greenaert et al. [1986], for example, discuss six different models for the relation.

4.2. u. Normalizations

To examine the results for u_* , we apply the estimated u_* to the normalization of wind wave parameters. For a given wind and wave field with wave spectral energy density S(f), total wave energy $E = \int S(f) df$, peak energy wave frequency f_m , and fetch distance F, the following parameters have been frequently used in the literature [e.g., Hasselmann et al., 1973; Mitsuyasu et al., 1980]: $\varepsilon_* = gE/u_*^2$, the nondimensional energy; $v_* = f_m u_*/g$, the nondimensional peak energy frequency; and $\xi_* = gF/u_*^2$, the nondimensional fetch. We affix a subscript z to the parameters which are normalized directly with measured wind speed u_z .

Correlating these various parameters has led to a number of universal power law relations that played important roles in developing numerical wave prediction models. Hasselmann et al. [1973, 1976], Mitsuyasu et al. [1980], and Toba [1978] have all deduced similar empirical equations characterizing the correlations among the parameters based on their own

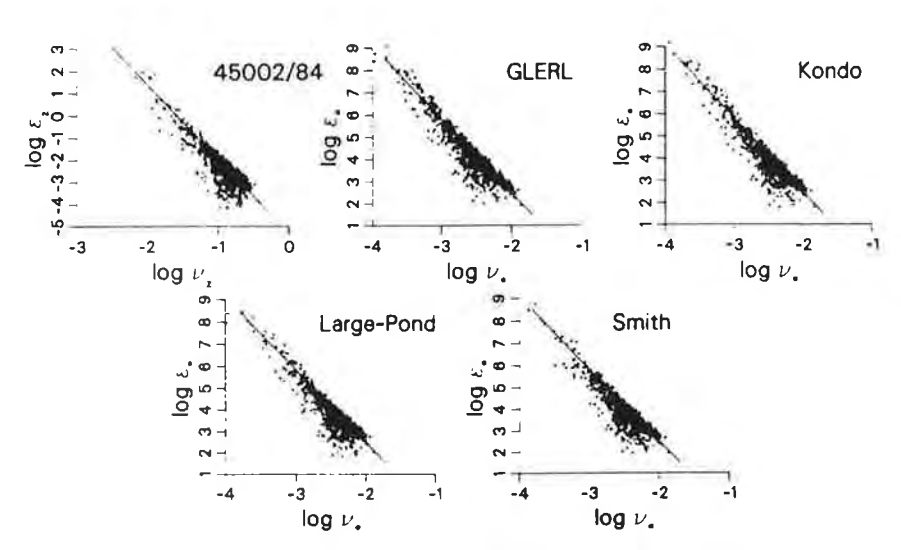


Fig. 5. Comparison of ε_{\star} versus ν_{\star} correlations. The straight lines are given by JONSWAP relations $\varepsilon = 5.3 \times 10^{-6} \nu^{-10/3}$ and $\varepsilon_{\star} = 5.3 \times 10^{-5} \nu_{\star}^{-10/3}$.

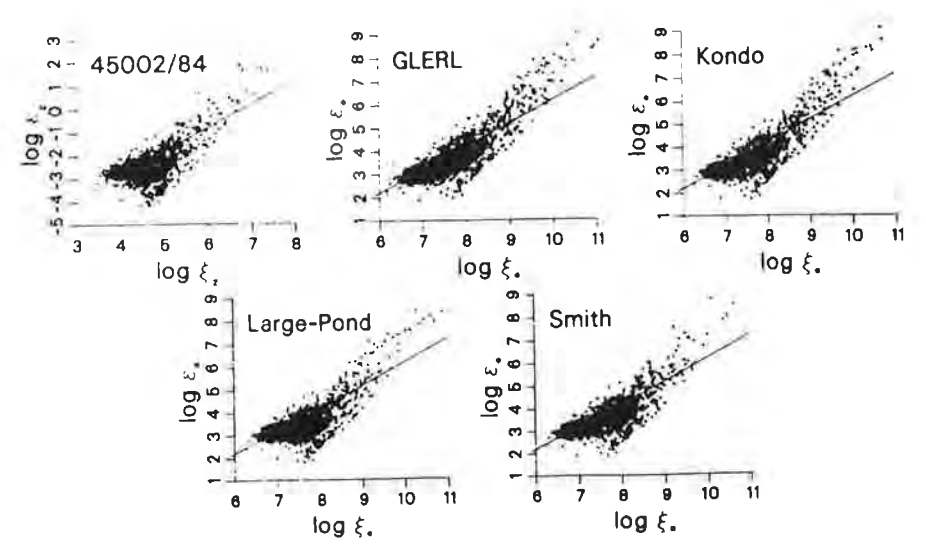


Fig. 6. Comparison of ε versus ξ correlations. The straight lines are given by JONSWAP relations $\varepsilon = 1.6 \times 10^{-7} \xi$ and $\varepsilon_{\bullet} = 1.6 \times 10^{-4} \xi_{\bullet}$.

measurements. An examination of these universal correlations was given by Liu [1984, 1985].

Figures 5-7 present the three intercorrelations ν versus ξ , ε versus ξ , and ε versus ν , respectively. In each figure we present the u, normalization graph along with four u, normalization graphs corresponding to the four methods. The empirical JONSWAP relations [Hasselmann et al., 1973, 1976] for the respective parameters are plotted as the straight line in each graph for reference. As discussed by Liu [1985], the data points appear to be clustered around galaxylike regions rather than universal lines. The straight lines provide only a crude approximation of the data that can be accurate at times and erroneous at other times. This may be due to failure of the simple power law relations in unsteady conditions or to other processes. The power laws were developed mainly from growing sea states, whereas the data in Figures 5-7 represent both growing and dissipating waves. As shown by Liu [1985], however, even using carefully selected growth episodes does not lead to less scatter in the correlations. Clearly, none of the

four methods of u_{\bullet} estimation show any particular advantage in reducing the scatter. The scatter shown in the u_{\bullet} normalization graphs is somewhat less than the u_z normalization graphs.

4.3. Assessments

In order to examine the correlations shown in Figures 5-7 on a quantitative basis we calculated and compared several statistical entities relevant to the correlations. Specifically, we sought the general relation $y = cx^b$ from our data and analyze the results statistically. Since all the correlations are plotted on the log-log scale, we simply let $X = \log(x)$, $Y = \log(y)$, and $a = \log(c)$, and by fitting a straight line of the form Y = a + bX through the data points by least squares method we can calculate the following:

standard error =
$$[\Sigma(Y - a - bX)^2/(n-2)]^{1/2}$$
 (12)

percentage deviation =
$$\Sigma |(Y - a - bX)/Y|(100/n)$$
 (13)

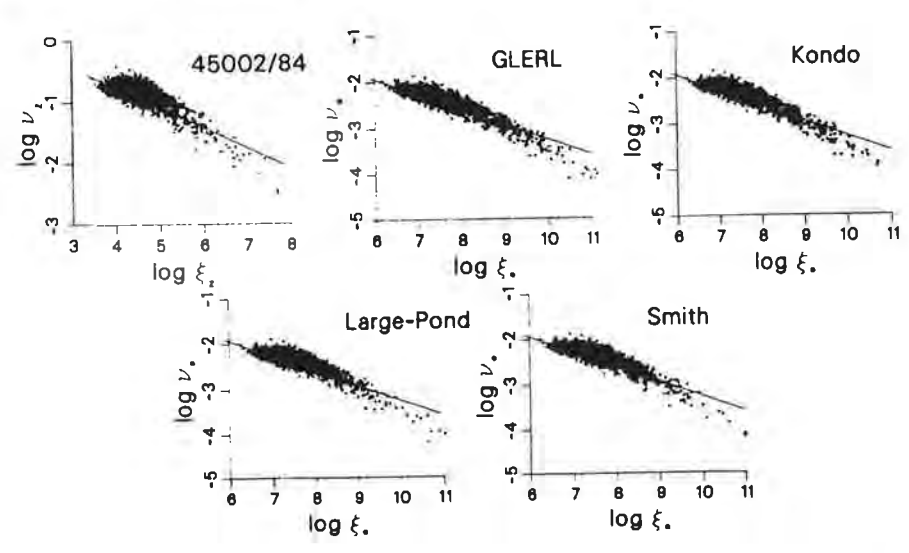


Fig. 7. Comparison of ν versus ξ correlations. The straight lines are given by JONSWAP relations $\nu = 3.5 \xi^{-0.33}$ and $\nu_* = 1.08 \xi_*^{-0.33}$.

TABLE 3.	Summary of Calculated Standard Errors and Percentage Deviations for the Various
	Correlations

		Standard Erro	г	Percentage Deviation			
Nomalization	ε versus ν	ε versus ζ	ν versus ζ	ε versus ν	ε versus ξ	ν versus ζ	
и,	0.384	0.578	0.133	17.24	30.27	11.98	
GLERL u	0.373	0.581	0_135	6.78	11.83	4.49	
Kondo u	0.393	0.629	0.140	7.81	13.53	4.71	
Large-Pond u	0.408	0.655	0.141	8.44	14.08	4.73	
Smith u	0.364	0.540	0.130	7.17	11.52	4.38	

where n is the total number of data points (4212 for our 1984 North Lake Michigan buoy data set). Table 3 lists the calculated standard errors and percentage deviations for each of the 15 correlations shown in Figures 5–7. A well-fitted correlation should provide lower standard error and lower percentage deviation.

An examination of Table 3 shows that based on the calculated standard errors alone we are still unable to make any distinction among the various normalizations. For each of the three correlations, ε versus ν , ε versus ξ , and ν versus ξ , the standard errors are virtually the same. Since it is applied to $\log(x)$ and $\log(\nu)$, an average standard error of 0.4, as in the case of ε versus ν , indicates that the actual estimates can vary by a factor of 2.5 from the regression line. Similarly, the average standard errors of 0.6 (ε versus ξ) and 0.135 (ν versus ξ) lead to variation factors of 4.0 and 1.4, respectively.

When we examine the calculated percentage deviations, we find that there are significantly lower percentage deviations for the u_{\bullet} normalizations. Among the four methods, although there are slight variations in the percentage deviations, none shows any particular advantage in improving the fit significantly. In general, either the GLERL, Kondo, Large-Pond, or Smith method can be used to provide u_{\bullet} as well as u_{10} estimations for practical applications.

In the above analysis we predetermined the functional form of $y = ax^b$ and chose the dependent and independent variables y and x, respectively, according to the familiar JONSWAP formulations (that is, ε in terms of v, ε in terms of ξ , and v in terms of ξ). We also tried correlating them inversely by interchanging y with x as dependent variables as well as estimating the slope coefficient in the linear relationship by the maximum likelihood method [e.g., Kendall and Stuart, 1973]. While both of these analyses resulted in different sets of numbers, the implications are precisely identical to our previous discussions. Hence alternate analysis will not alter the results presented here.

In this analysis we have used all the data available without discriminating between cases representative of swell or wind waves. This is mainly because there is so little swell activity in Great Lakes waves that separation of swell cases from wind wave cases would not improve the results significantly.

In Figure 2 the GLERL method is considerably different from the other three methods at low wind speeds for unstable cases. Approximately 10% of the data we used in the analysis were of unstable cases with wind speed less than 5 ms⁻¹. However, we find there is no discernible difference due to this effect in the results. Apparently, this divergence does not have a significant effect on the parametric correlations.

5. CONCLUDING REMARKS

From detailed examination of the four methods used to estimate u_{\cdot} from a given u_{z} and air-sea temperature difference and application of these estimates to wind-wave parametric correlations we expected to distinguish a method which effectively reduced the scatter. We find instead that the four methods examined are virtually indistinguishable. Because all methods follow the same basic approach, with different but comparable empirical formulations, this result is by no means surprising. In practice, any of the four methods will provide similar estimates of u_{\cdot} . Until further detailed wind stress and wind profile measurements can be conducted to ascertain or validate the empirical formulations these methods will remain useful tools in providing wind stress, bulk transfer coefficients, and wind profile estimations where only minimal input data are available.

Acknowledgment. We would like to thank W. H. Brutsaert of Cornell University for initially suggesting this study. Great Lakes Environmental Research Laboratory contribution 509.

REFERENCES

Businger, J. A., J. C. Wyngaard, Y. Izumi, and E. F. Bradley, Flux-profile relationships in the atmospheric surface layer, J. Atmos. Sci., 28, 181-189, 1971.

Charnock, K. H., Wind stress on a water surface, Q. J. R. Meteorol. Soc., 81, 639-640, 1955.

Dyer, A. J., A review of flux-profile relationships, Boundary Layer Meteorol., 17, 363-372, 1975.

Geernaert, G. L., K. B. Katsaros, and K. Richter, Variation of the drag coefficient and its dependence on sea state. J. Geophys. Res., 91(C6), 7667-7679, 1986.

Hasselmann, K., T. P. Barnett, E. Bouws, H. Carlson, D. E. Cartwright, K. Enke, J. A. Ewing, H. Gienapp, D. E. Hasselmann, P. Kruseman, A. Merrburg, P. Muller, D. J. Richter, W. Sell, and H. Walden, Measurements of wind-wave growth and swell decay during the Joint North Sea Wave Project (JONSWAP), Dische. Hydrogr. Z., A12, 95 pp., 1973.

Hasselmann, K., D. B. Ross, P. Muller, and W. Sell, A parametric wave prediction model, J. Phys. Oceanogr., 6, 200-228, 1976.

Huang, N. E., L. F. Bliven, S. R. Long, and P. S. DeLeonibus, A study of the relationship among wind speed, sea state, and the drag coefficient for a developing wave field, J. Geophys. Res., 91(C6), 7733– 7742, 1986.

Keller, W. C., W. J. Plant, and D. E. Weissman, The dependence of X band microwave sea return on atmospheric stability and sea state, J. Geophys. Res., 90(C1), 1019-1029, 1985.

Kendall, M. G., and A. Stuart, The Advanced Theory of Statistics, vol. 2, chapter 29, Hafner Press, New York, 1973.

Kondo, J., Air-sea bulk transfer coefficients in diabatic conditions, Boundary Layer Meteorol., 9, 91-112, 1975.

Large, W. G., and S. Pond, Open ocean momentum flux measure-

- ments in moderate to strong winds, J. Phys. Oceanogr., 11, 324-336, 1981.
- Large, W. G., and S. Pond, Sensible and latent heat flux measurements over the ocean, J. Phys. Oceanogr., 12, 464-482, 1982.
- Liu, P. C., In search of universal parametric correlations for wind waves, in *The Ocean Surfaces.*, edited by Y. Toba and H. Mitsuyasu, pp. 171-178, D. Reidel, Hingham, Mass., 1984.
- Liu, P. C., Testing parametric correlations for wind waves in the Great Lakes, J. Great Lakes Res., 11, 478-491, 1985.
- Long, P. E., Jr., and W. A. Shaffer, Some physical and numerical aspects of boundary layer modeling, NOAA Tech. Memo. NWS TDL-56 (COM75-10980), 37 pp., 1975.
- Mitsuyasu, H., F. Tasai, T. Suhara, S. Mizuno, M. Ohkusu, T. Honda, and K. Rikiishi, Observation of the power spectrum of ocean waves using a cloverleaf buoy, J. Phys. Oceanogr., 10, 286–296, 1980.
- Monin, A. S., and A. M. Obukhov, Basic laws of turbulent mixing in the atmosphere near the ground, Tr. Akad. Nauk SSSR Geofiz. Inst., 24, 163-187, 1954.
- Paulson, C. A., The mathematical representation of wind speed and temperature profiles in the unstable atmospheric surface layer, J. Appl. Meteorol., 9, 857-861, 1970.

- Schwab, D. J., Simulation and forecasting of Lake Erie storm surges, Mon. Weather Rev., 106, 1476-1487, 1978.
- Smith, S. D., Coefficients for sea-surface wind stress and heat exchange, Report BI-R-81-19, 31 pp., Bedford Inst. of Oceanogr., Bedford, Nova Scotia, Can., 1981.
- Smith, S. D., and E. G. Banke, Variation of the sea surface drag coefficient with wind speed, Q. J. R. Meteorol. Soc., 101, 665-673, 1975.
- Steele, K., and A. Johnson, Jr., Data buoy wave measurements, in *Ocean Wave Climate*, edited by M. D. Earle and A. Malahoff, pp. 301-316, Plenum, New York, 1977.
- Toba, Y., Stochastic form of the growth of wind waves in a single-parameter representation with physical implications, J. Phys. Oceanogr., 8, 494-507, 1978.
- P. C. Liu and D. J. Schwab, Great Lakes Environmental Research Laboratory, NOAA, 2205 Commonwealth Boulevard, Ann Arbor, MI 48105.

(Received September 5, 1986; accepted February 5, 1987.)

ye 76. Vol. 4 in to Oregon State

Amer. Soc. Civil

del of a tidal estuesources. Pentech

ento and San Joa-

SEDIMENTATION IN THE SAN FRANCISCO BAY SYSTEM

RAY B. KRONE

Department of Civil Engineering, University of California, Davis, Davis CA 95616

Sediment inflows to the San Francisco Bay system have been significantly affected by man since the 1860's. Mining and agriculture caused large increases in sediment inflows during the late 1800's, and rapidly increasing fresh water diversions for irrigation are now causing depleted sediment inflows. In addition, maintenance dredging within the system alters sediment transport.

Sediments entering the system with land drainage consist largely of silts and clay minerals. These materials enter with high winter river flows and settle initially in the upper bays. Daily spring and summer onshore winds generate waves that suspend fine materials and hold them in suspension while tidal- and wind-driven currents circulate the suspended material throughout the system and to the ocean.

The effectiveness of waves in suspending deposited material increases rapidly with decreasing water depth. As the upper bays fill with sediment to depths where wave action resuspends the annual load at the same rate as the supply, the water depths tend to remain constant there, and further accumulation of sediment in the system occurs seaward. Evaluation of historical bathymetric surveys, including the effects of rising sea level, shows progressive sedimentation in the system that is now approaching Central Bay. Future fresh water diversions will materially slow this trend and will cause reduced turbidity from sediment particles.

The processes of aggregation, deposition, suspension, erosion, and circulation of sediment materials in the San Francisco Bay system have been described by Einstein and Krone (1961), Peterson et al. (1975), Krone (1976), Conomos and Peterson (1977), and the U. S. Army Corps of Engineers (1977). These descriptions have time scales on the order of a year or less, and while they are largely qualitative, the descriptions illuminate the sediment movements in the system. Longer term descriptions of sedimentation were made by Gilbert (1917), who described the excessive accumulations in the Bay system that resulted from hydraulic mining activities during the period 1850 to 1884, and by Smith (1965) who extended Gilbert's calculations of changes in Bay water volumes using more recent bathymetric survey data.

Both the short and long term sediment studies and studies of hydrodynamics by McCulloch et al. (1970) and Imberger et al. (1977) show that the Bay system is dominated by effects of changing sediment and water discharges through the Sacramento-San Joaquin River system (Fig. 1) from Great Central Valley drainage. There has been for decades a continuing trend of increasing consumptive use of water in the Central Valley and of export of water — and sediments — that would otherwise flow through the San Francisco Bay system. The diversion of fresh water has accelerated during recent years, and during the past two years of drought the fresh water flow to the Bay system has been the lowest in history. In view of the decreases in fresh water flows that the system is experiencing and the possibility of further decreases, it is appropriate that the existing information on sedimentation be re-examined to identify areas that may concern those responsible for management of sediments and Bay system water quality. This chapter presents an overall description of sediment movements and identifies areas of concern.

SAN FRANCISCO BAY

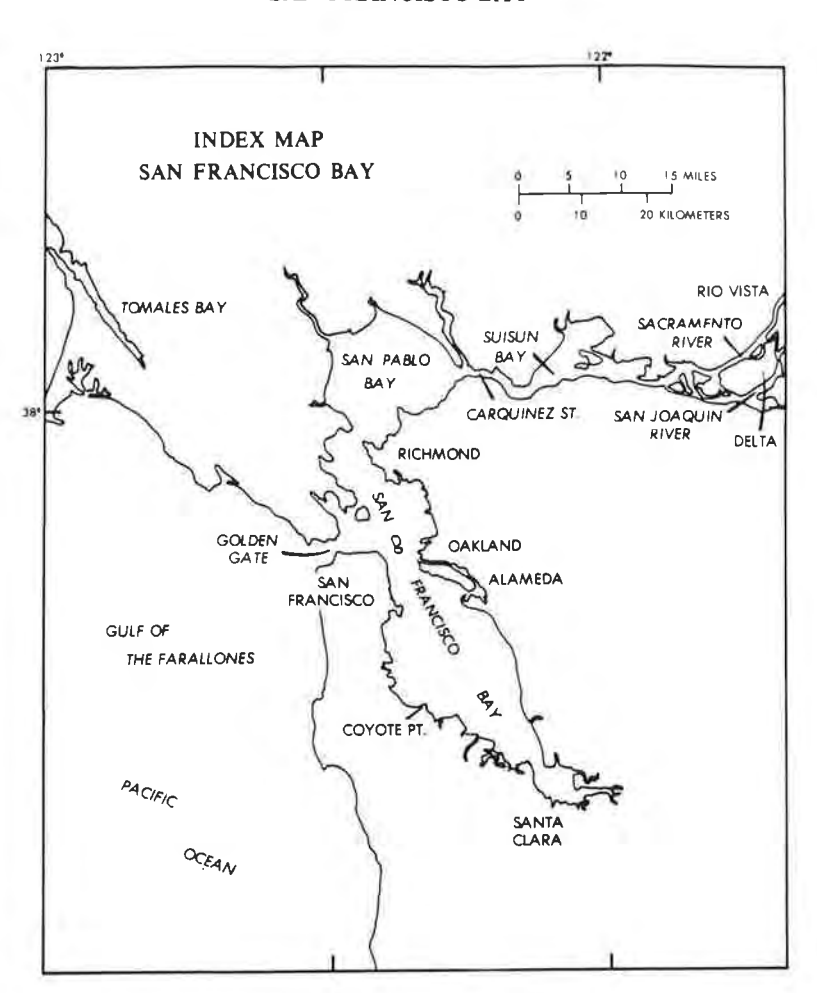


Fig. 1. San Francisco Bay system and environs,

SEDIMENT SUPPLY

Roughly 80 to 90% of the sediment entering the system is the product of soil erosion in the 163,000-km² inland drainage basin. The remainder comes from erosion of lands adjacent to the Bay system. The rate of sand transport by river flows of the Central Valley is diminished in the lower reaches of the rivers, so that the material entering San Pablo Bay is the remnant of the eroded soil and consists of clay and silt minerals carried in suspension as wash load, with only a small amount of fine sand. Most of the sediment enters with the higher winter and spring flows that result from rainfall and snowmelt.

Very large amounts of clay and silt were carried by Central Valley streams during the hydraulic-mining era in the Sierra Nevada, and this material remained in suspension in stream waters until the water velocity slowed in the broad shallow expanses of Suisun and San Pablo bays. Deposition in these upper bays was enhanced further by the increased salinities of these bays, which made suspended particles cohesive, and by the waves and gentle turbulence that caused suspended particles to collide repeatedly and form aggregates. Such aggregates have very greatly enhanced

KRONE: SEDIMENTATION

settling velocities. These "schlickens" created huge deposits in the upper bays and all but obliterated Vallejo Bay (now Carquinez Strait) at Martinez. Gilbert (1917) estimated the clay and silt deposit in the upper bays from mining debris by calculating the change in water volume. He believed that mining debris was still entering the Bay system at the time of his study, and he calculated that during the period 1849 to 1914 a total of 1.146x109 yd3 was deposited. Undoubtedly additional amounts were lost to the ocean.

Hydraulic mining was stopped in 1884. Fresh water diversions for irrigation gradually increased until the early 1940's when the Central Valley Project and the federal dams in the San Joaquin Valley streams were built (see, for example, Gill et al. 1971). Very rapid decline in fresh water and sediment outflows occurred thereafter. A program for measuring suspended sediment outflows was initiated by the U.S. Geological Survey in 1957 (Porterfield et al. 1961), and estimates of sediment production are limited to calculations using subsequent suspended solids data and historic water outflows.

Estimates of sediment inflow to the Bay system were made by establishing a relation between annual water flow and annual sediment production during later years (Krone 1966). Annual production is useful because the long dry summers return the drainage system to virtually the same condition by 1 October, the start of the "water year," and each year's runoff can be considered independent of preceding years (Fig. 2). The data (Fig. 2) include those both for the San Joaquin

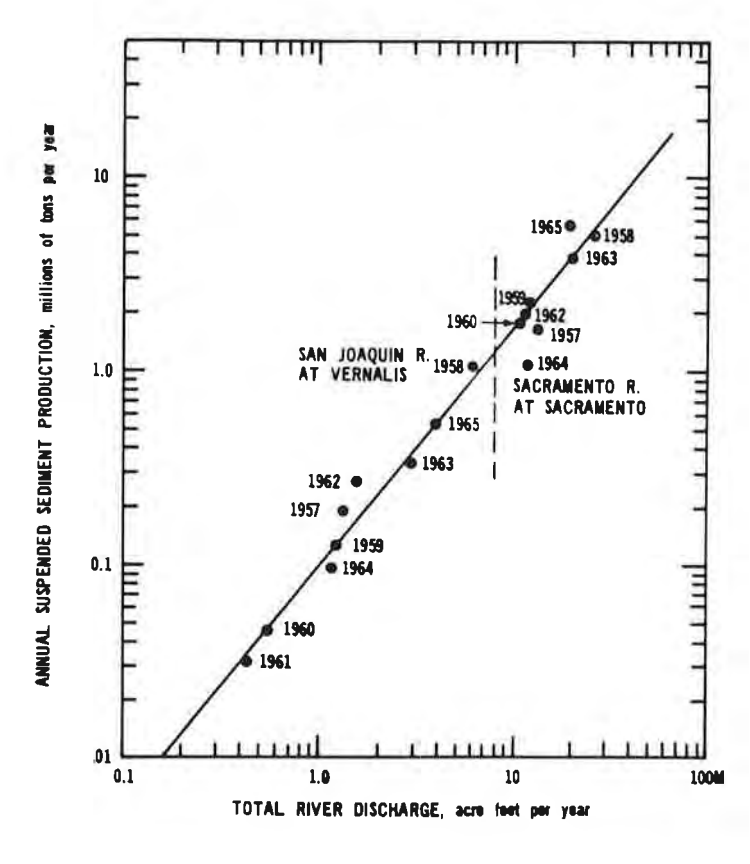


Fig. 2. Relation of annual suspended sediment production to river discharge. Reproduced from Krone (1966).

soil erosion in the ls adjacent to the diminished in the mant of the erodwith only a small ring flows that re-

ms during the hyn in stream waters Pablo bays. Depothese bays, which caused suspended greatly enhanced

SAN FRANCISCO BAY

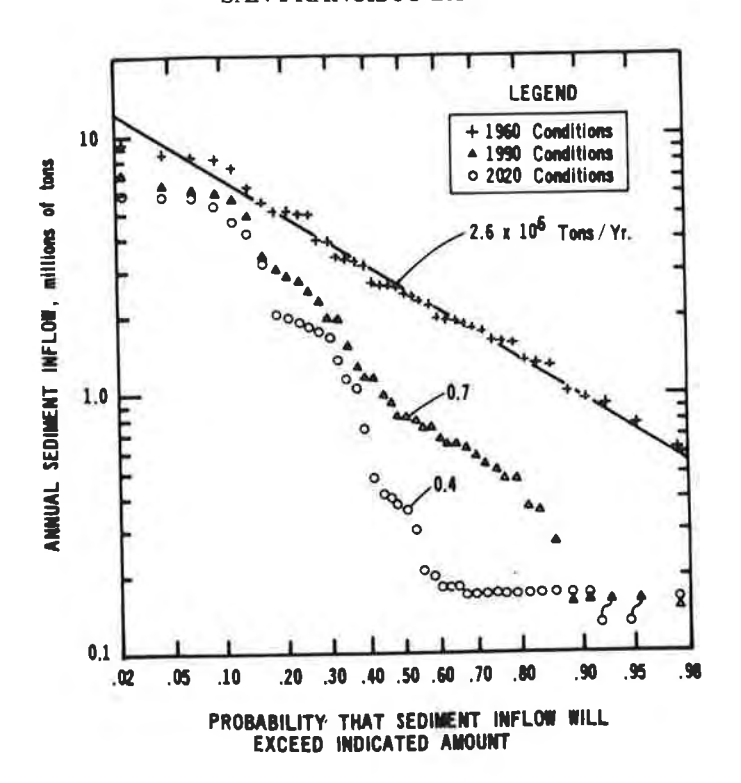


Fig. 3. Annual suspended sediment inflow from the Delta to the Bay system. Reproduced from Krone (1966).

and Sacramento rivers; the plots show that the relation indicated by the line represents both rivers reasonably well.

This relation was applied to the historic fresh water flows, modified by the U.S. Bureau of Reclamation (USBR) to the fresh water flows to the Bay system that would have occurred if the facilities and demands of 1960 existed throughout the period of record. The resulting sediment production for the wide range of flows that occurred between 1921 and 1971 is plotted on logarithmic-probability ordinates (Fig. 3). This plot, shown by the crosses, shows a 20-fold range, with a median annual production of 2.6 million t. The USBR projected water development and water demands for the years 1990 and 2020 and appropriate water management operations are applied to the same historic data, leading to the other two plots. These plots show that if such plans are realized the Bay system will experience "droughts" of sediment inflow a larger and larger fraction of the time.

The estimated annual average sediment inflows are presented in Table 1. If the bed load is taken to be 0.065 of the total and the dry unit weight of the sediment deposit is 33 lbs·ft⁻³ (Schultz 1965), the average annual volume of sediment "deposit" under 1960 conditions would be 10.5 million yd³ which is close to Schultz' (1965) estimated of 11.1 million yd³.

Decisions on future water diversions are lacking, and the projections shown for 1990 and 2020 are subject to decisions between competing political pressures for fresh water diversion and Bay system water quality. Figure 3 does show, however, the drastic reductions in sediment inflow to the Bay system that would result from future diversions planned by USBR in 1966.

KRONE: SEDIMENTATION

TABLE 1. ESTIMATED ANNUAL AVERAGE SUSPENDED SEDIMENT PRODUCTIONS $(10^6 \, t \cdot yr^{-1})^a$

Sediment Source	Stream Conditions			
	1960	1990	2020	
Sediment supplied to the Delta	3.75	3.42	3.34	
Sediment from the Delta to San Francisco Bay system	3,35	1.79	1.22	
Sediment from local streams to: b				
Suisun Bay	0.23	0.23	0.23	
San Pablo Bay	0.29	0.29	0.29	
San Francisco Bay	0.51	0.51	0.51	
Total sediment to Bay system	4.38	2.82	2.25	

^a 1.0t (common short ton) = 0.907t (metric tonnes)

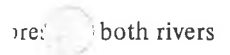
SEDIMENT CIRCULATIONS

The fine cohesive particles that comprise most of the material are transported in suspension. Their transport throughout the system is determined by the water movements, and by the local hydraulic conditions that facilitate deposition, erosion, and aggregation. The water movements in the Bay system are exceedingly complex and are very strongly affected by fresh water flows, the distribution of salinity, and wind stresses. A description of the general character of water movements will serve to explain sediment movements, however.

The Bay system consists of a number of broad shallow bays interconnected by narrow openings (Fig. 1). The western part of North San Francisco Bay and the narrow opening to the Pacific Ocean (Golden Gate) are quite deep, however, and water depths are maintained by the strong tidal currents. The large surface areas of the bays, combined with the restricted connections, cause progressive delays in the tides with distance from the ocean and relatively deeper channels at the narrow openings. The system is resonant to the tides, with the result that the mean range of the tide at the southern tip of South Bay is 2.2 m, 1.0 m greater than the mean ocean tide range of 1.2 m at the Golden Gate (U. S. Army Corps of Engineers 1961). This resonance causes north-south tidal currents in the central portion of the Bay system that is out of phase with flows through the Golden Gate, with the result that there is circulation between San Pablo Bay and South San Francisco Bay.

Fresh water outflows from Central Valley drainage superimpose another circulation system on the oscillatory tidal flows. More dense ocean waters tend to move upstream under the seaward flowing fresh waters (see also Conomos 1979). The oscillatory flows that result from tidal motion, combined with irregularities of the bed, cause vertical mixing with the result that there is an oscillatory but net landward movement of saline water near the bed, and this water dilutes fresh seaward flowing water above. The location and length of this mixing zone depend strongly on the fresh water flow and the flow history (McCulloch et al. 1970; Peterson et al. 1975; Imberger et al. 1977; Conomos 1979). During extremely large discharges the mixing zone extends out into the

stem, Reproduced



the U.S. Bureau of ave occurred if the resulting sediment 971 is plotted on ws a 20-fold range, development and ent operations are show that if such a larger and larger

If the bed load is posit is 33 lbs·ft⁻³ anditions would be

own for 1990 and vater diversion and in sediment inflow 1966.

^b From Smith (1965, Table 5). 1957 to 1959 values, measured and estimated, are data of Porterfield et al. (1961).

SAN FRANCISCO BAY

Pacific Ocean. More commonly during winter flows the mixing zone extends from the Golden Gate to Carquinez Strait. As winter fresh water flows decrease the mixing zone moves landward, and during typical summer flows during the period 1943 to 1970, the mixing zone extended from mid San Pablo Bay to Antioch.

South San Francisco Bay is also strongly affected by high fresh water flows, with fresh water "lenses" developing during high flows (McCulloch et al. 1970; Imberger et al. 1977; Conomos 1979).

Winds affect water circulations, particularly in the broad bays where the fetch is appreciable. The winds of greatest importance appear to be the daily onshore breezes that blow from the ocean to the hot Central Valley during spring and summer. These winds also generate waves in the shallow bays every day during these months (see also Conomos 1979).

There is strong evidence that large amounts of sediment are deposited in Suisun and San Pablo bays during winter runoff (U. S. Army Corps of Engineers 1977). Waves that appear daily on the bays suspend this material and hold it in suspension while slow tidal currents transport the material to channels (Einstein and Krone 1961). During flood tides this material moves upstream through Carquinez Strait, and because the particles aggregate rapidly at the high suspended sediment concentrations that prevail, the aggregates tend to settle and there is a higher concentration near the bed (Arthur and Ball 1979). These particles move upstream with the net upstream flow near the bed, mixing vertically upward with the more saline waters. Aggregates whose settling velocities approximate or exceed the upward velocity of the more saline waters accumulate in the mixing zone and cause the well-known "turbidity maximum" there (Conomos and Peterson 1977).

Little deposition occurs in this mixing zone now because the large tidal prisms of Suisun, Grizzly, and San Pablo bays, combined with the narrow channels, cause high velocity currents that keep the channels scoured to their self-maintained depths. An attempt to cut an 11-m deep approach basin for a wharf at Benicia, however, resulted in the formation of a 5-m deep deposit in three months. Large amounts of sediment are in motion there.

Material suspended by waves in San Pablo Bay continually feeds this net upstream flow. The vertical density gradient in the mixing zone causes the velocity profile there to have exceptional velocity gradients. These gradients promote the collision of suspended particles and thereby promotes their aggregation (Krone 1972). Particles and aggregates from San Pablo Bay mix upward with riverborne dispersed particles and "scavenge" them. Algae are also scavenged this way. Aggregates carried seaward in the upper portions of the flow settle as the tidal current slows in San Pablo Bay, to either be carried back upstream for another cycle or to circulate further in San Pablo Bay.

Suspension of deposited material by waves is a process that has several important aspects. For a given wave, the maximum bed shear stress is very sensitive to water depth and is proportional to the square of the maximum near-bed orbital velocity, u_{max}^2 ,

$$u_{\text{max}}^2 = [\pi H/(T \cdot \sin h \cdot 2\pi h/L)]^2$$
, approximately

where H is the wave height, T is the wave period, L is the wave length, and h is the water depth (Komar and Miller 1973). Since $1/(\sin h \cdot 2\pi h/L)$ falls off very rapidly with depth, and its square falls even faster, it is evident that the applied stress is sensitive to depth. The suspending force is periodic, and upward diffusion is weak. The result is that fine particles are winnowed from coarser particles, so that over a period of time when suspended material is transported away by tidal currents, the remaining material is coarser than the original deposit. The applied shear stress must exceed the shear strength of the deposit before there is any suspension (Alishahi and Krone 1964).

KRONE: SEDIMENTATION

Winnowing of sediments in San Pablo Bay is shown by the data of Storrs et al. (1963) (Fig. 4). The surface of the bed was coarser during the summer and fall than it was after the high fresh water flows. An armor having a high content of fine sand and silt is found in wind-swept shallow parts of San Pablo Bay. Below this armor, which can support a person, reside large depths of the mud from hydraulic mining.

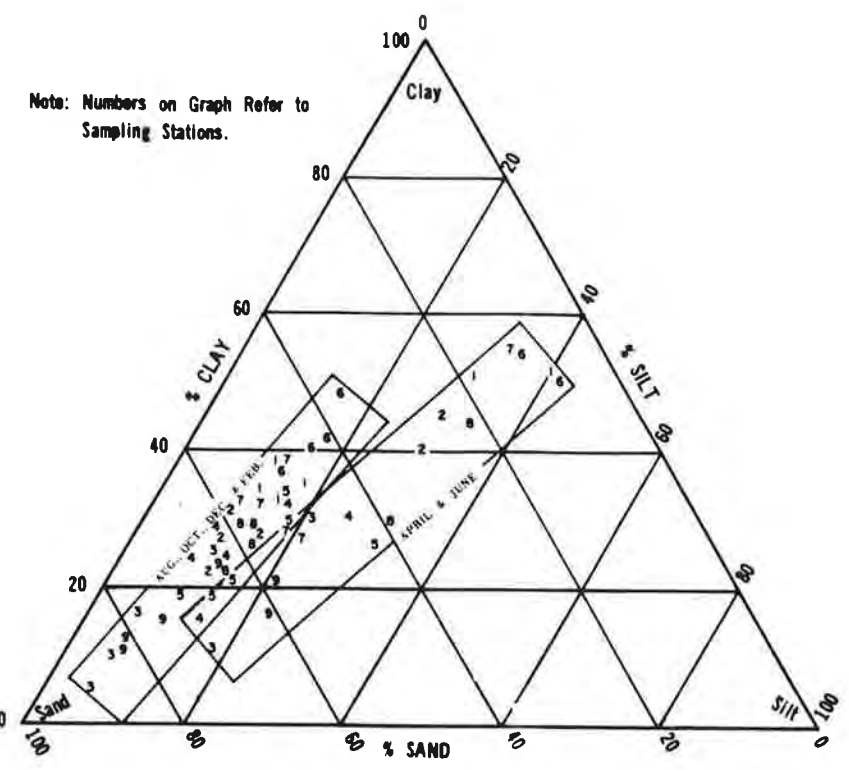


Fig. 4: Surface sediment particle-size distribution, San Pablo Bay, August 1961-June 1962. Data from Storrs et al. 1963. Numbers refer to Sanitary Engineering Research Laboratory (SERL) sampling stations.

Material suspended in San Pablo Bay and carried southward with tidal currents contains less fine sand and is easily carried with tidal currents as they circulate throughout the system. Suspended material settles wherever the water is quiet, such as in shallow areas at night when the wind dies, or in navigation facilities. Where subsequent wave action or tidal currents are insufficient to resuspend deposited material, it accumulates. Material from San Pablo Bay may deposit and be resuspended many times as it circulates and finds its way to a resting place or is carried to sea, progressively becoming finer-grained and more easily transported. Marsh areas now diked off once accumulated this fine material and probably reduced the loss to the ocean.

The scenario is repeated in miniature for each of the streams tributary to the bays, and areas of sandy material can be found near their mouths and near eroding banks. Bay waters are muddy during periods of high runoff and progressively become clearer during each year as the quantity remaining in suspension diminishes.

from the Golden e m s landward, one ended from

's, with fresh water il. 1977; Conomos

etch is appreciable. ow from the ocean e waves in the shal-

in Suisun and San s that appear daily currents transport his material moves ily at the high susid there is a higher tream with the net waters. Aggregates more saline waters in there (Conomos

l prisms of Suisun, locity currents that an 11-m deep api-m deep deposit in

ip:)n flow. The o have exceptional ticles and thereby lo Bay mix upward avenged this way. lal current slows in that further in San

important aspects. and is proportion-

is the water depth opth, and its square suspending force is nowed from coarser rted away by tidal and shear stress must i and Krone 1964).

SAN FRANCISCO BAY

LONGER-TERM SEDIMENT DEPOSITION

The surface of the oceans is rising at an approximate rate of 0.2 m·century-1 (Fig. 5). If there were no deposition of sediment, the bays would continually deepen. Alternately, if deposition is so rapid that the water depths become shallow, wave action erodes the new deposit down

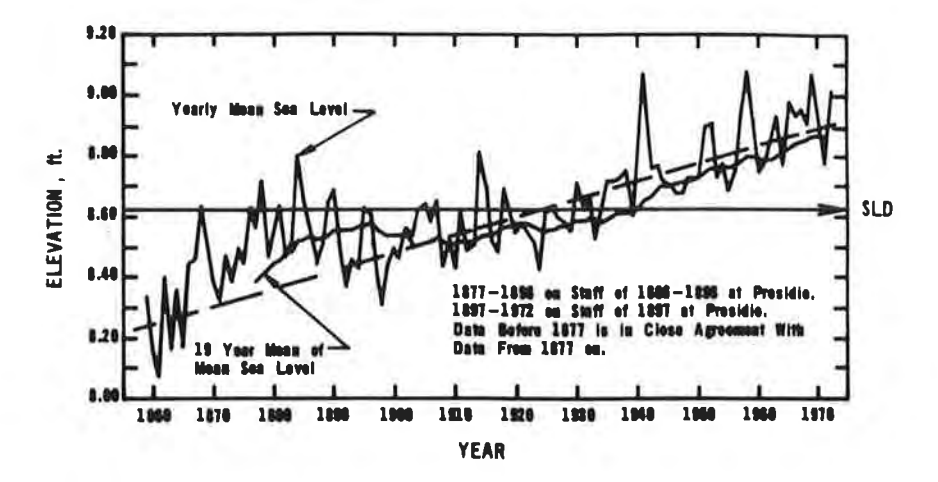


Fig. 5. Yearly mean sea level changes at San Francisco, California, 1860-1970. Data from National Ocean Survey.

to a depth where wave erosion compensates deposition, assuming no armoring by coarse material. When the supply of sediment inflow is adequate, therefore, water depths would tend to remain constant, and the rate of deposition would follow sea level rise. When the sediment supply is inadequate, the water depths would increase.

Smith (1965) reported calculations made by the U. S. Army Corps of Engineers that used averages of water depths over 1/8-min quadrangles. Averages for successive bathymetric surveys were compared to obtain changes in water depths with no allowance made for sea level rise. Tables 2 and 3 were constructed from Smith's data using linear interpolation where necessary to determine the changes over comparable time periods. The tables are arranged with areas in their geographical sequence from the Delta southwestward through the system. A pattern of deposition becomes apparent from the data in Table 2 when the accumulation or loss during successive periods is compared for successive bays. Suisun and Grizzly bays filled during the first periods and lost relatively small amounts during the second and third periods. San Pablo Bay accumulated a large amount during the first period when hydraulic mining provided a supply and successively smaller amounts during the next two periods. North San Francisco Bay showed negligible accumulation during the first period and markedly increasing amounts during the later periods. South San Francisco Bay showed deepening water during all three periods.

The rise in sea level was evidently sufficiently rapid prior to 1870 so that the sediment accumulation rate in most of the system was not sufficient to compensate the increase in water volume due to sea level rise. The very large amount of finer-grained material produced by hydraulic mining and by poor agricultural practices caused very rapid deposition in Grizzly, Suisun, and San Pablo bays. The erosion in Suisun and Grizzly bays shown to occur during the subsequent two periods indicates that the rate of supply during the first period exceeded the transport capacity of waves and currents. In fact, erosion during the second and third periods indicates that some of the

KRONE: SEDIMENTATION

TABLE 2. APPARENT SEDIMENT ACCUMULATION (106 yds3)a,b

Area	1870-1896 (27 years)	1897-1922 (26 years)	1923-1950 (28 years)
Suisun & Grizzly Bays & Carquinez Strait	64.3	-17.2	-4 .7
San Pablo Bay	181.3	60.2	17.4
North San Francisco Bay	0.66	67.4	106.4
South San Francisco Bay	-36.1	-51.1	-55.0

^a Data from Smith (1965)

 $b \frac{3.0 \text{ J}}{1.0 \text{ y}} d^3 = 0.76 \text{ m}^3$

itury⁻¹ (Fig. 5). If ernately, if deposinew deposit down



)-1970. Data from

by coarse material.

Ild to remain

ent supply is inade-

ngineers that used athymetric surveys ha level rise. Tables necessary to determeas in their geotern of deposition during successive hirst periods and ay accumulated a and successively negligible accumuperiods. South San

at the sediment accrease in water volduced by hydraulic ly, Suisun, and San subsequent two peansport capacity of es that some of the material deposited during the first period was transported toward San Pablo Bay in addition to the river-borne material that entered during these later periods. As this material eroded under wave action, the finer-grained fraction was washed out, and the bed became progressively more resistant to erosion. The water depths in Grizzly and Suisun bays probably now are approaching values that can be expected to remain constant unless the supply of sediment is stopped.

San Pablo Bay continued to accumulate sediment during the second and third periods, but at decreasing rates.

North San Francisco Bay did not receive much material during the period of hydraulic mining discharge, which suggests that the upper bays trapped most of the sediment that remained in the system. The losses of water volumes during the second and third periods show that the capacities of the upper bays to store material were decreasing, and the material worked its way through the upper bays until it found a permanent resting place in North San Francisco Bay. This interpretation is strengthened by the presentation of average annual apparent deposition rates presented in Table 3.

The average annual loss in water volume (the apparent sediment accumulation rate) for the total of Suisun, Grizzly, San Pablo, and North San Francisco bays is 4.2 million yd³-yr⁻¹ for both second and third periods.

The figures for South San Francisco Bay in Tables 2 and 3 are strikingly different: the water volume increased during all three periods. The average annual rate of sea level rise was used to calculate the annual change in water volume. As shown in Table 3, the observed increase in water volume exceeded that due to sea level rise during all three periods. Considering the uncertainties in the determination of sea level in the earliest bathymetric surveys it can be concluded that there were comparable rates of slow erosion in South San Francisco Bay during all three periods. Hydraulic mining debris did not cause accumulations in the open water areas of South San Francisco Bay, nor did material from Central Valley appear to be accumulating there even in 1950.

The data in Tables 2 and 3 are temporal and spatial averages. While they are valuable for the analysis given above, they are not suitable for descriptions of local areas. Sediment can move around within each of the areas used in Tables 2 and 3 without affecting the average. Smith's report shows the local changes in 1/8 min quadrangles between bathymetric surveys. Further, the data do not preclude the movement of fine material into and back out of South San Francisco Bay each year. All present evidence indicates that annual supplies of Central Valley sediments do in fact enter South San Francisco Bay under present conditions. Only the finest material, clay and silt, remains in the suspended load, however, and deposits are stable only in areas protected from

SAN FRANCISCO BAY

TABLE 3. AVERAGE ANNUAL SEDIMENT ACCUMULATION RATES (10⁶ yds³·yr⁻¹)^a

Area	1897-1922 (26 years)	1923-1950 (28 years)
Suisun & Grizzly Bays & Carquinez Straits	-0.66	-0.17
San Pablo Bay	2.31	0.62
North San Francisco Bay	2.59	3.80
Loss of Water Volume	4.24	4.25
Volume of Sealevel Rise	1.29	1.29
TOTAL	5.5	5.5
South San Francisco Bay		
Loss of Water Volume	-1.96	-1.96
Volume of Sealevel Rise	1.07	1.07
TOTAL	-0.91	-0.91

^a Calculated from data in Table 2.

waves and currents. I believe that a much smaller portion of the fine-grained sediments were transported into South San Francisco Bay during the hydraulic-mining era because the trap efficiency of the upper bays was much greater then.

If the 1960 condition data (Fig. 3) can be compared with the data for 1923 to 1950 in Table 3, it is possible to calculate a sediment balance that shows the average budget (Fig. 6). The 5.5 million yd³ deposited in the upper bays is assumed to have come entirely from inflow. The increase in water depths in South San Francisco Bay, which would result largely from erosion of very fine-grained material that would be carried to the ocean or to marsh areas, is assumed not to have contributed to deposition in the northern bays.

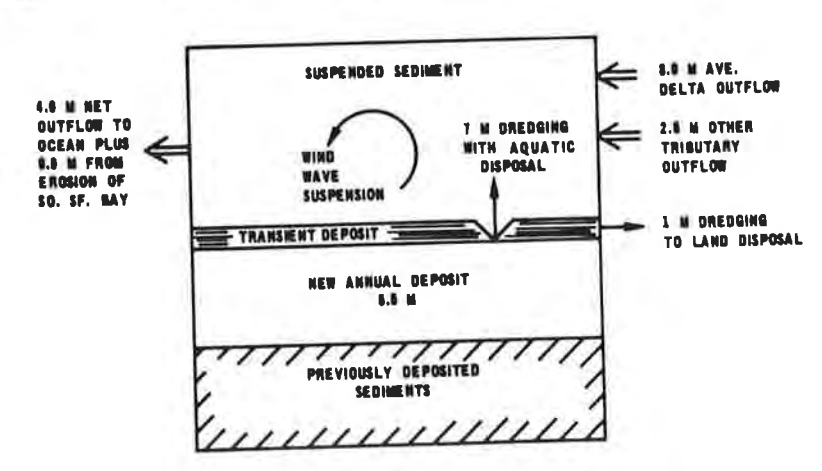


Fig. 6. Average annual San Francisco Bay sediment deposition budget. Values in millions of cubic yards of deposit.

KRONE: SEDIMENTATION

FUTURE CHANGES

Projected fresh water diversions indicate that future supplies of suspended sediment to the Bay system will be less than historic supplies and will vary over a much wider range. At present, the Bay system steadily removes fine suspended material during each year following the winter and spring runoffs. If less sediment is supplied as the result of increased water diversion, Bay system waters will clear. Several successive years of very low flows will surely result in greatly reduced suspended sediment concentrations in Bay waters and reduced turbidity. The ample nutrient levels in Bay waters, particularly with low fresh water flows, will promote growth of algae to objectionable levels.

The clay minerals sorb toxic materials from waste discharges and thereby remove such materials from the water column. The sorbed materials are removed from the water column when the sediments are removed from suspension and thereby provide an assimilative capacity for such undesirable substances. If significant reductions of sediment inflows are to be made, either waste discharges into the Bay system will have to be greatly modified or water quality will deteriorate.

We have not acquired the necessary field data nor made quantitative calculations that show the effects of changing fresh water and sediment flows to the Bay system on the quality of Bay waters. Decisions on water diversions are being made without such information. Detailed descriptions of the water and sediment transport are needed in order to predict the effects of various fresh water and sediment outflows on the Bay system.

New bathymetric surveys will be made in a few years. These data, combined with continuing measurements of suspended sediments, should enable more precise descriptions of trends in sediment accumulation in the Bay system.

LITERATURE CITED

- Alishahi, M. R., and R. B. Krone. 1964. Suspension of cohesive sediment by wind-generated waves. University of California, Berkeley, Calif. IER Tech. Rep. HEL-2-9, 23 pp.
- Arthur, J. F., and M. D. Ball. 1979. Factors influencing the entrapment of suspended material in the San Francisco Bay-Delta estuary. Pages 143-174 in T. J. Conomos, ed. San Francisco Bay: The Urbanized Estuary. Pacific Division, Amer. Assoc. Advance. Sci., San Francisco, Calif.
- Conomos, T. J. 1979. Properties and circulation of San Francisco Bay waters. Pages 47-84 in T. J. Conomos, ed. San Francisco Bay: The Urbanized Estuary. Pacific Division, Amer. Assoc. Advance. Sci., San Francisco, Calif.
- Conomos, T. J., and D. H. Peterson. 1977. Suspended-particle transport and circulation in San Francisco Bay: An overview. Pages 82-97 in L. E. Cronin, ed. Estuarine Processes. Vol. 2. Academic Press, New York.
- Einstein, H. A., and R. B. Krone. 1961. Estuarial sediment transport patterns. J. Amer. Soc. Civil Eng. H12:51-59.
- Gilbert, G. K. 1917. Hydraulic mining debris in the Sierra Nevada. U. S. Geol. Surv. Prof. Paper 105. 148 pp.
- Gill, G. S., E. C. Gray, and D. Seckler. 1971. The California water plan and its critics: A brief review. Pages 3-27 in D. Seckler, ed. California Water; A Study in Resource Management. University of California Press, Berkeley, Calif.
- Imberger, J., W. B. Kirkland Jr., and H. B. Fischer. 1977. The effect of delta outflow on the density stratification in San Francisco Bay. ABAG (Assoc. San Francisco Bay Area Govern.) Rep. HBF-77/02. 109 pp.
- Komar, P. D., and M. C. Miller. 1973. The threshold in sediment movement under oscillatory water waves. J. Sed. Petrol. 43(4):1101-1110.

-0.17

0.62

3.80

4.25

1.29

5.5

-1.96

1.07 -0.91

nents were transne trap efficiency

to 1950 in Table (Fig. 6). The 5.5 a inflow. The infrorerosion of is at led not to

SAL

lues in millions of

SAN FRANCISCO BAY

- Krone, R. B. 1966. Predicted suspended sediment inflows to the San Francisco Bay system. Report to Central Pacific River Basins Comprehensive Water Pollution Control Proj., Federal Water Pollution Control Proj., Federal Water Pollution Control Admin. (Southwest Region). 33 pp.
- Krone, R. B. 1972. A field study of flocculation as a factor in estuarial shoaling processes. U. S. Army Eng. Comm. on Tidal Hydraulics. Tech. Bull. 19. Waterways Expt. Sta., Vicksburg, Miss. 61 pp.
- Krone, R. B. 1976. Ultimate fate of suspended sediment in estuaries. Pages 180-201 in Proc. Specialty Conf. on Dredging and its Environmental Effects. Amer. Soc. Civil Eng., Mobile, Ala.
- McCulloch, D. S., D. H. Peterson, P. R. Carlson, and T. J. Conomos. 1970. A preliminary study of the effects of water circulation in the San Francisco Bay estuary. U. S. Geol. Surv. Circ. 637(A, B). 34 pp.
- Peterson, D. H., T. J. Conomos, W. W. Broenkow, and P. C. Doherty. 1975. Location of the non-tidal current null zone in northern San Francisco Bay. Estuarine Coastal Marine Sci. 3(1):1-11.
- Porterfield, G., N. L. Hawley, and C. A. Dunnam. 1961. Fluvial sediments transported by streams tributary to the San Francisco Bay area. Open-file rep. U. S. Geol. Surv. 70 pp.
- Schultz, E. A. 1965. San Francisco Bay dredge spoil disposal. Prepared for presentation to the Comm. on Tidal Hydraulics, 53rd meeting, San Francisco, May 1965. 48 pp.
- Smith, B. J. 1965. Sedimentation in the San Francisco Bay system. Pages 675-708 in Proc. Federal Interagency Sedimentation Conf. 1963. U. S. Dep. Agr. Misc. Pub. 970.
- Storrs, P. N., R. E. Selleck, and E. A. Pearson. 1963. A comprehensive study of San Francisco Bay 1961-62. Sanitary Eng. Res. Lab. and School Publ. Health, University of California, Berkeley, Calif. 220 pp.
- U. S. Army Corps of Engineers. 1963. San Francisco Bay and tributaries, California. Appendix H. Hydraulic Model Studies. Tech. Rep. San Francisco Bay Barriers, vol. 1. U. S. Army Eng. District, San Francisco, Calif. 280 pp.
- U. S. Army Corps of Engineers. 1977. Dredge disposal study, San Francisco Bay and estuary. Appendix E. Material Release. U. S. Army Eng. District, San Francisco, Calif. 623 pp.

Density, Volume Fraction, Particulate Concentration Pelations for Aggregates of Solid Cohesive Particles

In the following relations it is assumed that the densities of the suspended particles and of the fluid medium do not change with particle association. These assumptions are not always true, but the importance of these assumptions can be judged by the surface properties of the solids. The assumptions consider that the boundary between the solid and the fluid is sharply defined at the particle surface.

Symbols

m mass,

V volume,

ρ density

volume fraction,

c weight concentration
 of solid particles,

f porosity = $(1 - \phi_p)$

$$\epsilon$$
 void ratio = $\frac{1 - \phi_p}{\phi_p}$

c.g.s. Units

grams

cubic centimeters

grams/cubic centimeter

volume of particles or aggregates/
volume of suspension

grams particles/cubic centimeters of suspension

Subscripts

- 1 fluid (liquid)
- s suspension
- p primary solid particle
- a aggregate

The subscripts will occasionally be used in combinations such as m_{al} for mass of "aggregate liquid," or mass of liquid included in

between aggregated particles.

Note that these quantities are interrelated as follows:

$$m_{i} = \rho_{i}V_{i} \quad (a) \qquad \phi_{p} = V_{p}/V_{s}$$

$$m_{p} = cV_{s} \quad (b) \qquad \phi_{a} = V_{a}/V_{s}$$

$$\phi_{p} = c/\rho_{p} \quad (c)$$

$$f = (1 - \phi_{p}) \qquad \epsilon = \frac{(1 - \phi_{p})}{\phi_{p}}$$

$$(1)$$

Suspensions of Aggregated or Dispersed Particles

From the basic assumptions,

$$\sqrt{m_s} = m_p + m_1$$

$$\sqrt{s} = \sqrt{p} + \sqrt{1}$$
(2)

Substituting the appropriate m/ρ for each term in Equation 3 and eliminating m_1 between Equations 2 and 3 leads to

$$\rho_{s} - \rho_{1} = \phi_{p} (\rho_{p} - \rho_{1}) \cdot \phi_{HO} = 1 - \phi_{p}$$
 (4)

Equation 4 is useful for finding ϕ_{D} .

Substituting Equation 1c in 4 gives

$$\rho_{S} = \frac{C}{\rho_{D}} (\rho_{D} - \rho_{1}) + \rho_{1}$$
 (5)

which is useful for finding ρ_s from c .

Suspensions of Aggregates

From Equation la and the basic assumptions,

$$\rho_{a} = \frac{m_{p} + m_{a1}}{\phi_{a} V_{s}} \tag{6}$$

Also, as in Equation 3,

$$\frac{m_{a1}}{\rho_1} + \frac{m_p}{\rho_p} = \phi_a V_s. \tag{7}$$

Eliminating m_{al} from Equations 6 and 7 and substituting cV_s for m_{d} leads to

$$\rho_{a} = \frac{1}{\phi_{a}} \frac{c}{\rho_{p}} (\rho_{p} - \rho_{1}) + \rho_{1} \qquad (8)$$

or

$$\rho_{a} = \frac{\phi_{p}}{\phi_{a}} (\rho_{p} - \rho_{1}) + \rho_{1}$$
 (8a)

Equation 8 parallels Equation 5. Substituting Equation 5 into 8 gives

$$\rho_{a} = \frac{1}{\phi_{a}} \left(\rho_{s} - \rho_{1} \right) + \rho_{1} \tag{9}$$

It is occasionally desirable to calculate the fraction of solids f, by weight. Combining Equation 1a, 2, and 3 leads to

$$\frac{1}{\rho_{S}} = \frac{f}{\rho_{p}} + \frac{1 - f}{\rho_{1}} \tag{10}$$

Robert Mac Arthur

LANDSLIDES AND DEBRIS FLOWS

Landslides occur in virtually every country in the world, and they have a variety of causes: heavy rains, melting snow or ice, earthquakes, volcanoes, and human activities. Landslides often extend beyond the bounds of a single state or country, burying homes and other structures and disrupting transport and the delivery of emergency services.

Notable landslides of the recent past include the Reventador, Ecuador, landslides of March 1987. A magnitude 6.9 earthquake following a month of heavy rains precipitated landslides scouring the slopes of Mount Reventador. Early estimates show 1,000 dead and 4,000 missing. In addition, the event ruptured the trans-Ecuador oil pipeline--the nation's prime economic asset--causing an approximate \$1.5 billion loss. In 1962 and 1970, disastrous slides plunged from the slopes of Mount Huascaran in Peru. In the 1970 event, caused by a 7.8 magnitude earthquake, nearly 20,000 died as mudflows buried the nearby towns of Yungay and Ranrahirca. In the United States, the April 1983 thaw of a heavy snow pack precipitated a landslide near Thistle, Utah, which caused more than \$200 million in direct losses, cutting two major highways and a transcontinental rail link and damming the Spanish Fork River.

Landsliding in the United States causes at least \$1-2 billion in economic losses and the 25-50 deaths each year. Despite a growing understanding of the geology of landslides and a rapidly developing engineering capability for landslide control, losses continue to increase. This rise is largely a consequence of residential and commercial development that continues to expand onto the steeply sloping or unstable terrain that is most prone to landslides.

There are methods for mitigating landslide losses. Land use management, building and grading codes, the use of well-designed engineering techniques for landslide control and stabilization, the timely issuance of emergency warnings, and the availability of landslide insurance can significantly reduce the catastrophic effects of landslides. Though some techniques for predicting landslides have been developed, research in this are is insufficient. For example, recurrence interval techniques and other temporal descriptions of risk are essentially unexplored. Some research has been carried out on the use of early warning systems to alert the public to individual local landslides, and there have been a few successful demonstrations. But there has never been extensive implementation of an early warning system in any country.

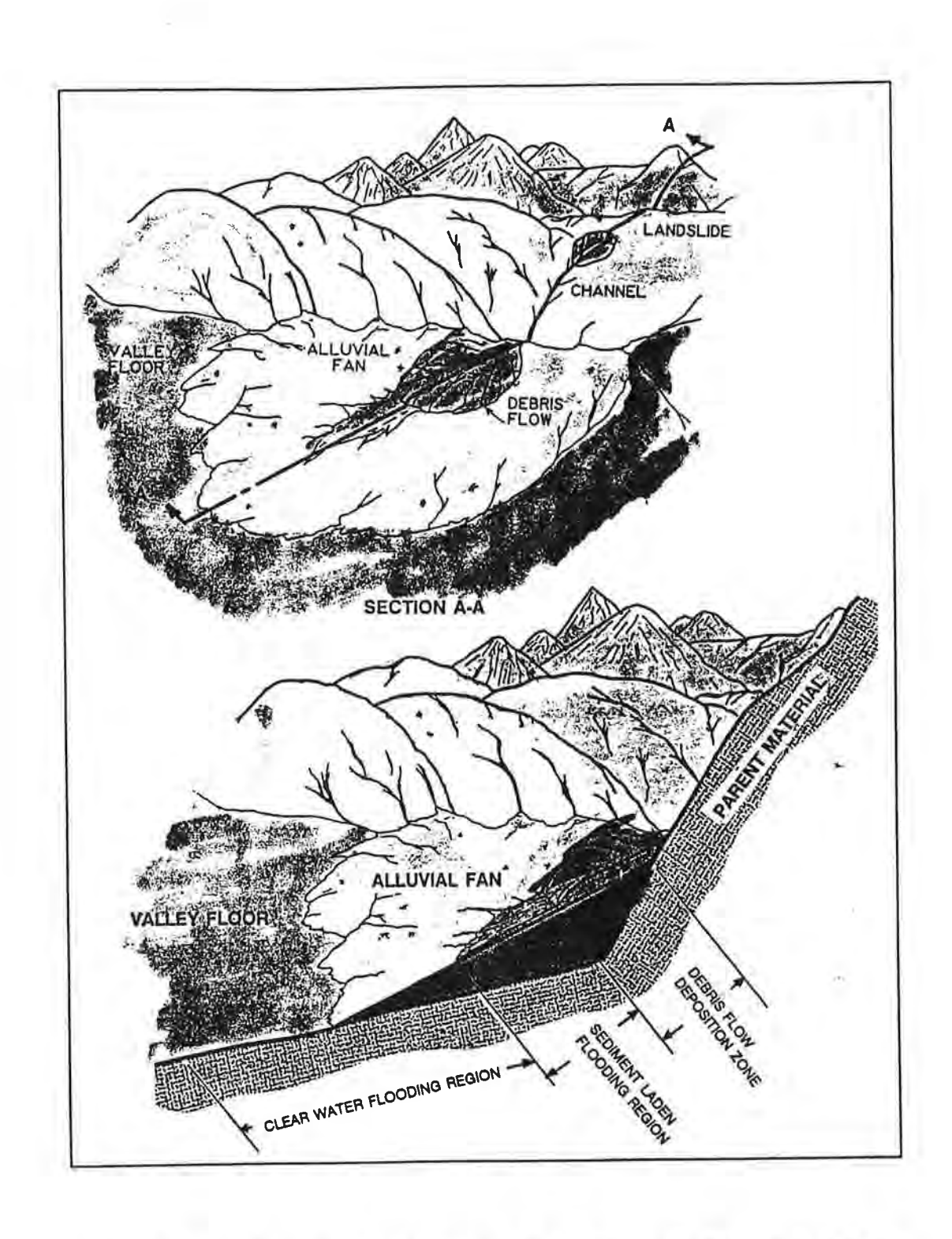
Successful and cost-effective landslide mitigation programs can be implemented, and such programs do exist (Japan, for example). Though there have been some impressive local demonstrations of landslide control in other countries, information about them has not been widely disseminated.

Selected* Natural Disasters of This Century

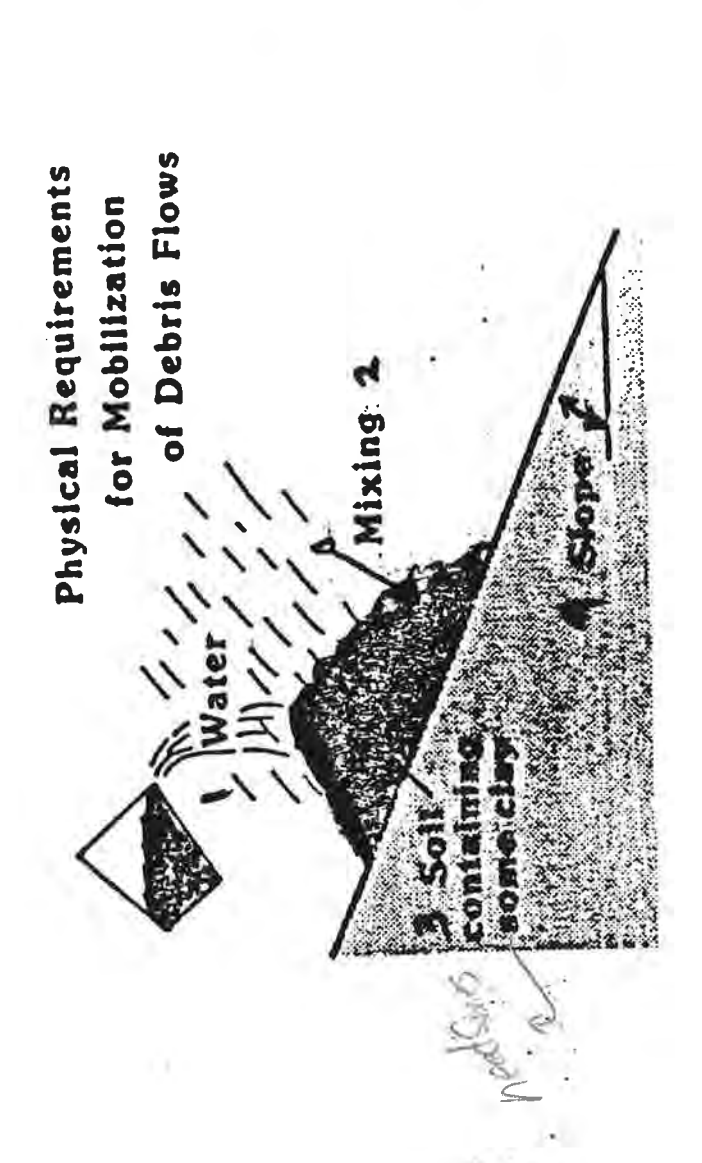
Year	Event	Location	Approximate Death Toll
1900	Hurricane	USA	6,000
1902	Volcanic Eruption	Martinique	29,000
902	Volcanic Eruption	Guatemala	6,000
906	Typhoon	Hong Kong	10,000
906	Earthquake	Taiwan	6,000
	Earthquake/Fire	USA	1,500
906	Earthquake	Italy	75,000
908		Philippines	1,30
911	Volcanic Eruption	Italy	30,00
915	Earthquake	Italy, Austria	10,00
916	Landslide	Indonesia	5,20
919	Volcanic Eruption	China	200,00
920	Earthquake/Landslide	_	143,00
1923	Earthquake/Fire	Japan USA	2,00
1928	Hurricane/Flood		1,40
1930	Volcanic Eruption	Indonesia	70,00
1932	Earthquake	China	3,00
1933	Tsunami	Japan	60,00
1935	Earthquake	India	60
1938	Hurricane	USA	30,00
1939	Earthquake/Tsunami	Chile	1,20
1945	Floods/Landslides	Japan	1,40
1946	Tsunami	Japan	100,00
1948	Earthquake	USSR	57,00
1949	Floods	China	12,000-20,00
1949	Earthquake/Landslide	USSR	2,90
1951	Volcanic Eruption	Papua New Guinea	1,80
1953	Floods	North Sea coast (Europe)	20
1954	Landslide	Austria	40,00
1954	Floods	China	4,60
1959	Typhoon	Japan	12,00
1960	Earthquake	Morocco	12,00
1961	Typhoon	Hong Kong	
1962	Landslide	Peru	4,000-5,00
1962	Earthquake	Iran 🖟	12,00
1963	Tropical Cyclone	Bangladesh	22,00
1963	Volcanic Eruption	Indonesia	1,20
1963	Landslide	Italy	2,00
1965	Tropical Cyclone	Bangladesh	17,00
1965	Tropical Cyclone	Bangladesh	30,0
1965	Tropical Cyclone	Bangladesh	10,0
1968	Earthquake	Iran	12,0
1970	Earthquake/Landslide	Peru	70,0
1970	Tropical Cyclone	Bangladesh	300,000-500,0
1971	Tropical Cyclone	India	10,000-25,0
1976	Earthquake	China	250,0
1976	Earthquake	Guatemala	24,0
1976	Earthquake	Italy	9
1977	Tropical Cyclone	India	20,0
1978	Earthquake	Iran	25,0
	Volcanic Eruption	Mexico	1,7
1982	Tropical Cyclone	Bangladesh	10,0
1985	Earthquake	Mexico	10,0
1985 1985	Volcanic Eruption	Colombia	· 22,0
170)	ADICALLIC TERBOLOU	China	2

^{*}Disasters selected to represent global vulnerability to rapid-onset natural disasters.

SOURCES: Compiled from (a) Office of U.S. Foreign Disaster Assistance (1987); (b) National



TYPICAL SEDIMENTATION SCENARIO



9.12E) gates into a debris flow (see chap. 6). Transformation of Once a saturated, noncohesive or slightly cohesive, granular soil mass fails by sliding, it commonly digre-

surges may occur. Decrease in slope gradient at the base of the hill initiates deposition of the 'bris (fig.

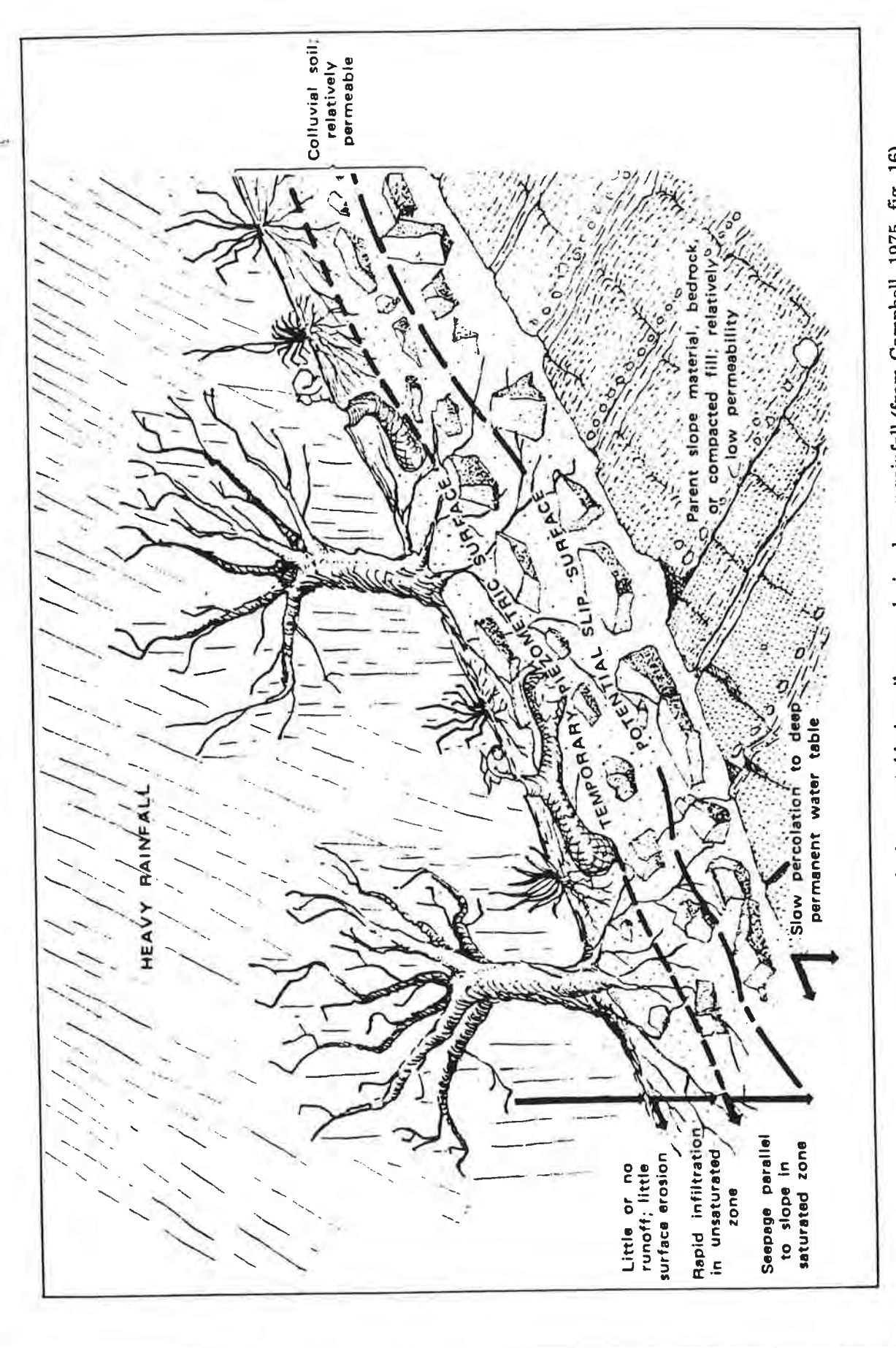


FIGURE 9.11.—Buildup of a perched water table in soil cover during heavy rainfall (from Campbell, 1975, fig. 16).

ine sites

suffivi and

ssary

easing

y also

ante-

flows ed that se that

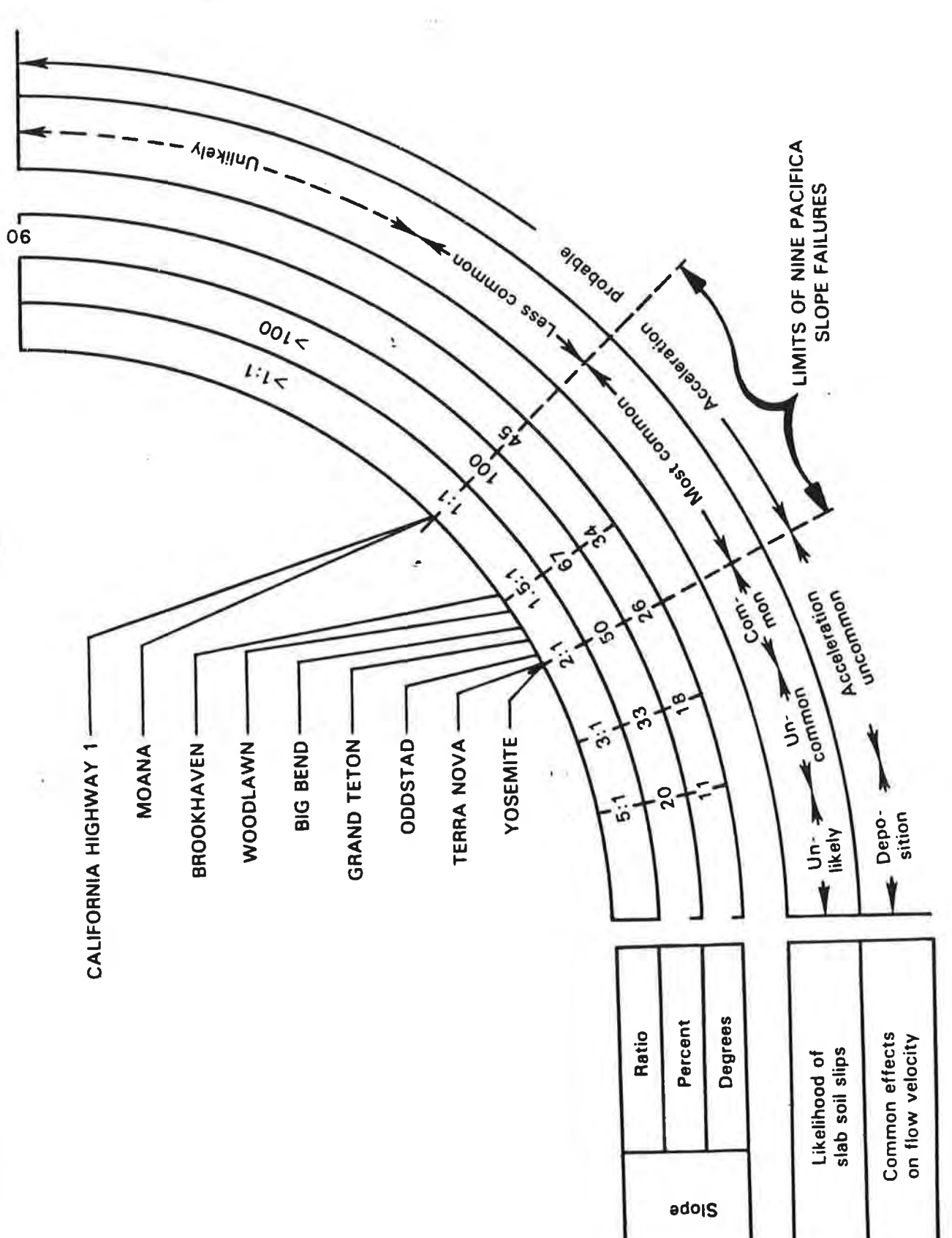


FIGURE 9.9.-Slopes at sources of nine landslides in Pacifica compared with the range of natural slopes, the likelihood of shallow slides, and the effects of slope on the velocity of debris flows (modified from Campbell, 1975, fig. 8).

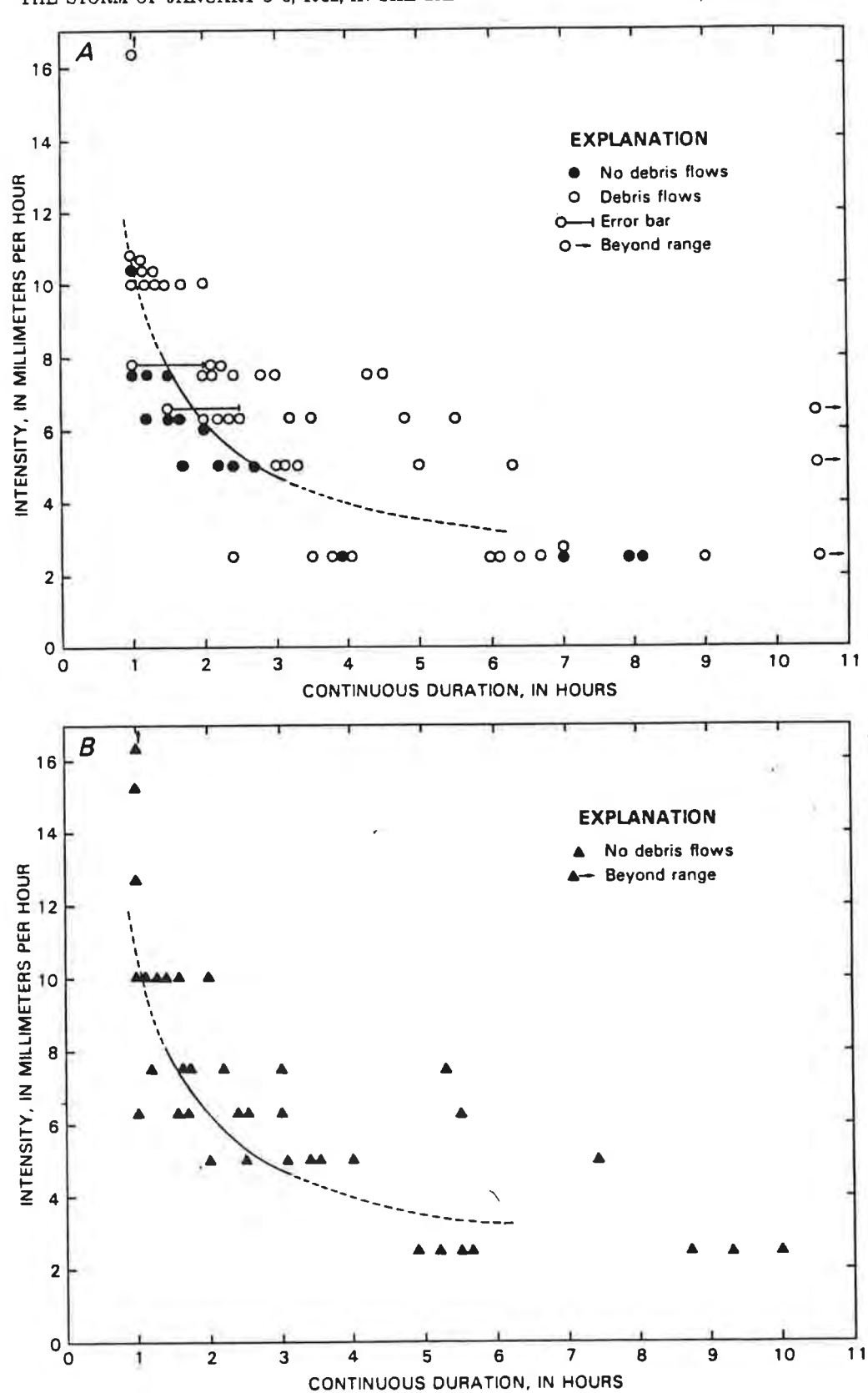


FIGURE 5.11.—Relations among rainfall intensity-duration from records of 22 storms in the study area from data listed in table 5.3. A, Values from storms that occurred after a prestorm seasonal threshold of 280 mm (11 in.). Solid line represents intensity-duration threshold that delineates storm-rainfall conditions which resulted in debris flows; line is dashed where threshold is less certain. B, Values from storms that occurred before a prestorm rainfall of 280 mm (11 in.) had been reached. Threshold line from figure 5.11.4 is shown for comparison.

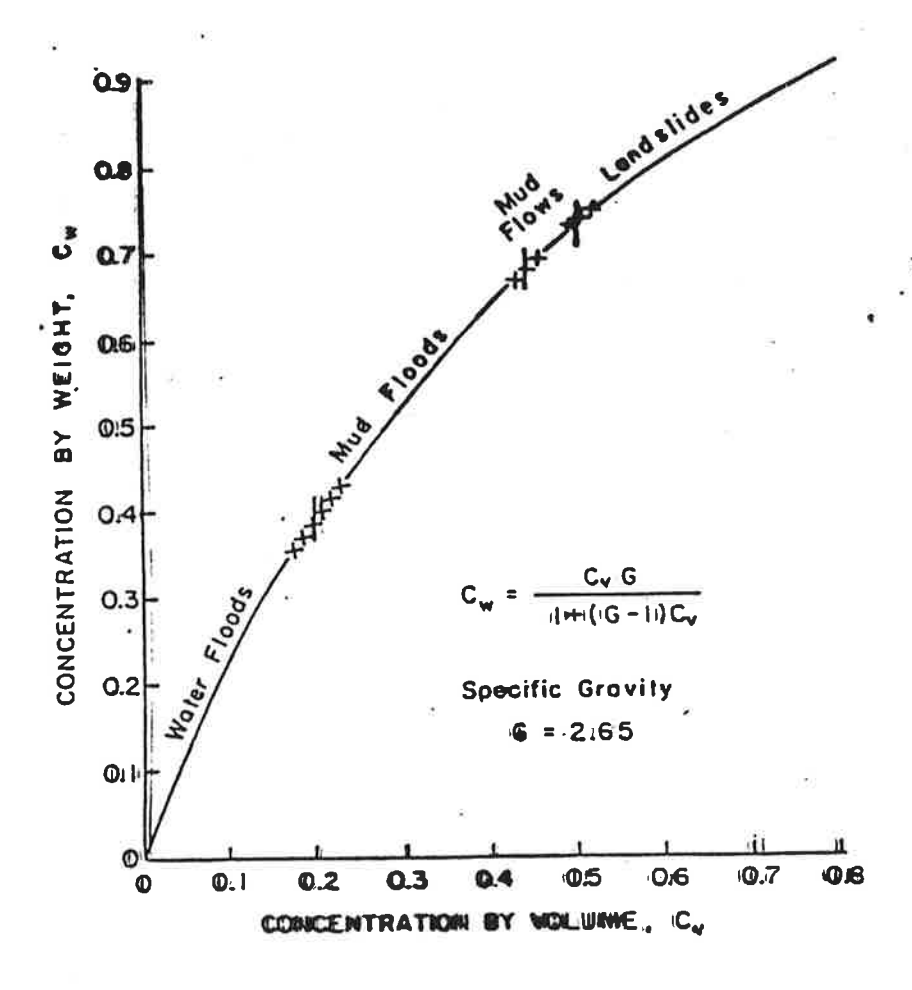


FIGURE 2.1 HMPERCONCENTRATED SEDIMENT FLOWS CLASSIFICATION

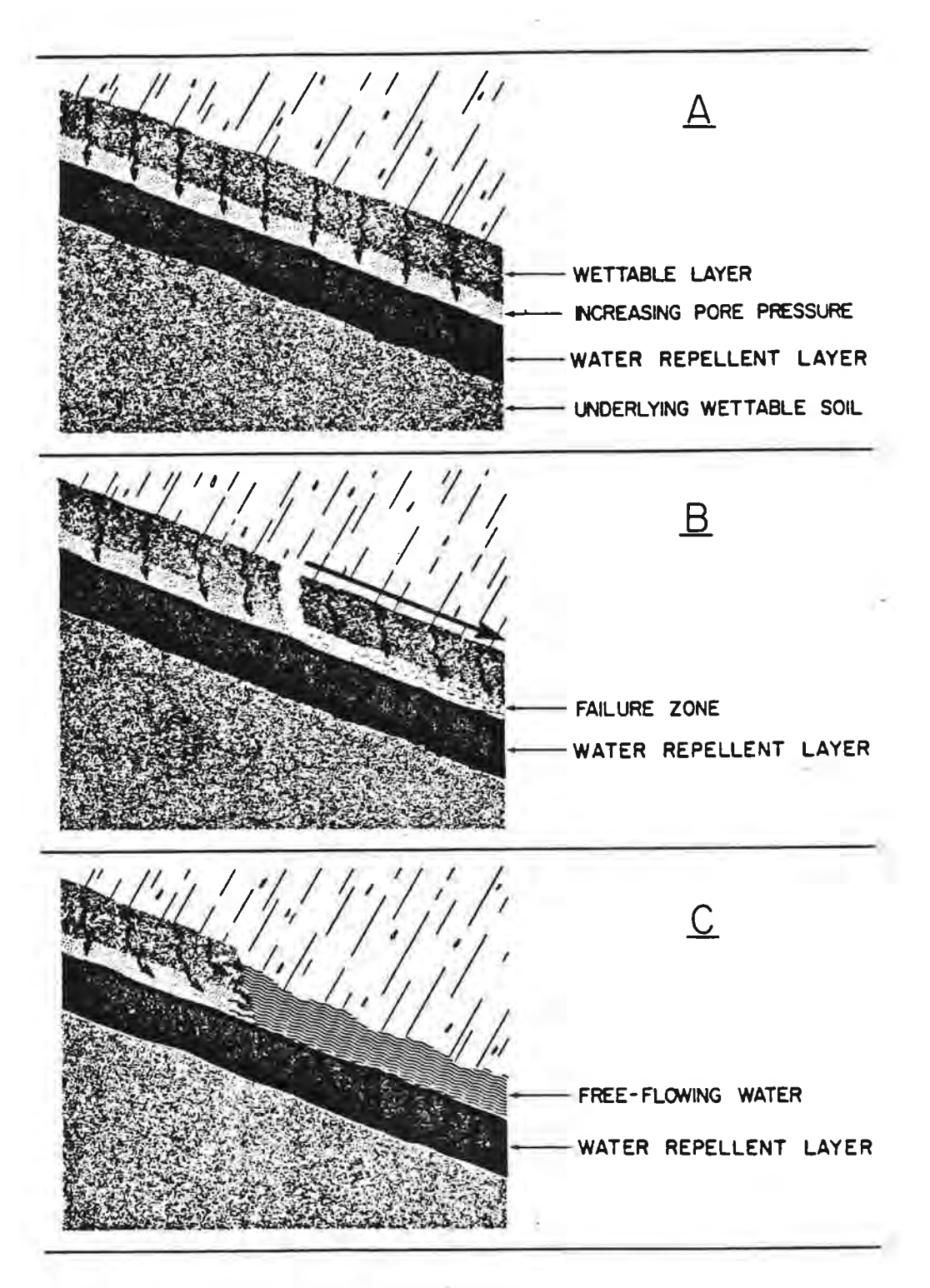


Figure 5. Process of rill formation over water-repellent soil layer. A, Water enters soil and encounters water-repellent layer; pores fill and pore pressures build up. B, Soil liquifies above water-repellent layer, causing small onslope failure that slides downslope, creating small onslope debris flow. C, Rill formed by small debris flow fills with water that then moves rapidly downslope.

TABLE 1

Annual Rainfall, Runoff, and Sediment Delivery from a 0.008 Hectare Plot on the San Dimas Experimental Forest (Data from Wells, 1981)

			Fern Canyon Plots			
Year Rainfall (mm)		Rainfall		Runoff		
	(mm)	(% rainfall)	(m ³ /km ² /yr			
		635	8	1.4	7	
1935-36		1120	10	1.0	4	
1936-37		1331	8	0.6	9	
1937-38		133.	ern Canyon plots	burned on Nov	vember 18, 1938	
	1	559	36	6.4	1907	
1938-39	ž	820	15	1.9	231	
1939-40	•	1468	15	1.0	69	
1940-41		495	1	0.2	1	
1941-42		1359	5	0.5	1	
1942-43		1029	25	1.0	1	
1943-44		902	5	0.2	¥ 1	
1944-45 1945-46		762	10	0.4	1	

 $[\]mathbf{1}_{\mathrm{Water}}$ year. Begins October 1 and runs to September 30.

TABLE 2

Measured Effects of Fire Heating on Grain Size
Distributions for Two Typical Soils
(After Wells, 1981)

	Pine	Canyon	Soil	Johnst	one Peal	k Soil
Temperature	Sand	Silt	Clay	Sand	Silt	Clay
	(% by weight)					
Unheated	61.4	26.6	12.0	38.0	43.4	18.6
400°C	68.4	30.3	1.3	43.7	51.0	5.3
600°C	72.7	26.8	0.5	40.7	51.6	7.7
800°C	77.0	23.0	0.0	44.5	50.8	4.7

A METHOD FOR SIMULATING HISTORIC MARSH ELEVATIONS

R. B. Krone*

Abstract

A method for simulating the historical marsh elevations is presented that utilizes historical mean tides, a dated core sample, and recently measured marsh surface elevations. Simulation of a marsh on the edge of South San Francisco Bay is presented to illustrate the method. This simulation showed that changes in the rate of sea level rise affects the elevation of a marsh relative to the mean high water datum.

Introduction

Historical elevations of tidal marshes are useful for the determination of land boundaries of reclaimed marsh lands, for evaluating marsh soil profiles, and for estimating the loss of suspended sediment from estuaries to adjacent marsh-lands. Waterward land boundaries are commonly determined at the "ordinary high water mark" that existed at some time prior to diking or other physical alteration or that might exist if the marsh had not been diked. This boundary is located where the elevation of the land intersected the ordinary high water datum, which is usually interpreted as the elevation of mean high water (MHW). Both the elevation of mean high water and that of a tidal marsh change with rising sea level. Pertinent questions are, "Is there a consistent relation between the elevation of a marsh and the mean high water datum?" "If so, is the marsh above or below this datum?" Simulation of historic marsh elevations can answer these questions and can provide valuable support for the interpretation of marsh soil profiles. Marshes in South San Francisco Bay are used in this paper to illustrate a method of simulating historical marsh elevations.

Sea level has been rising for thousands of years (1). Tidal marshes have developed along the margins of estuaries as the result of sea level rise, sedimentation, and the growth of marsh plants. A brief description of the process of marsh growth now is useful for presenting its simulation later.

The elevations of annual mean sea levels at the Golden Gate in San Francisco Bayas presented in Figure 1. This figure shows the fluctuations in sea level that occur from year to year, as well as different rates of rise that have occurred during the period of record. Variations in rates of sea level rise have been observed on both the east and west coasts of the United States (4). These



^{*}Department of Civil Engineering, University of California, Davis, CA 95616

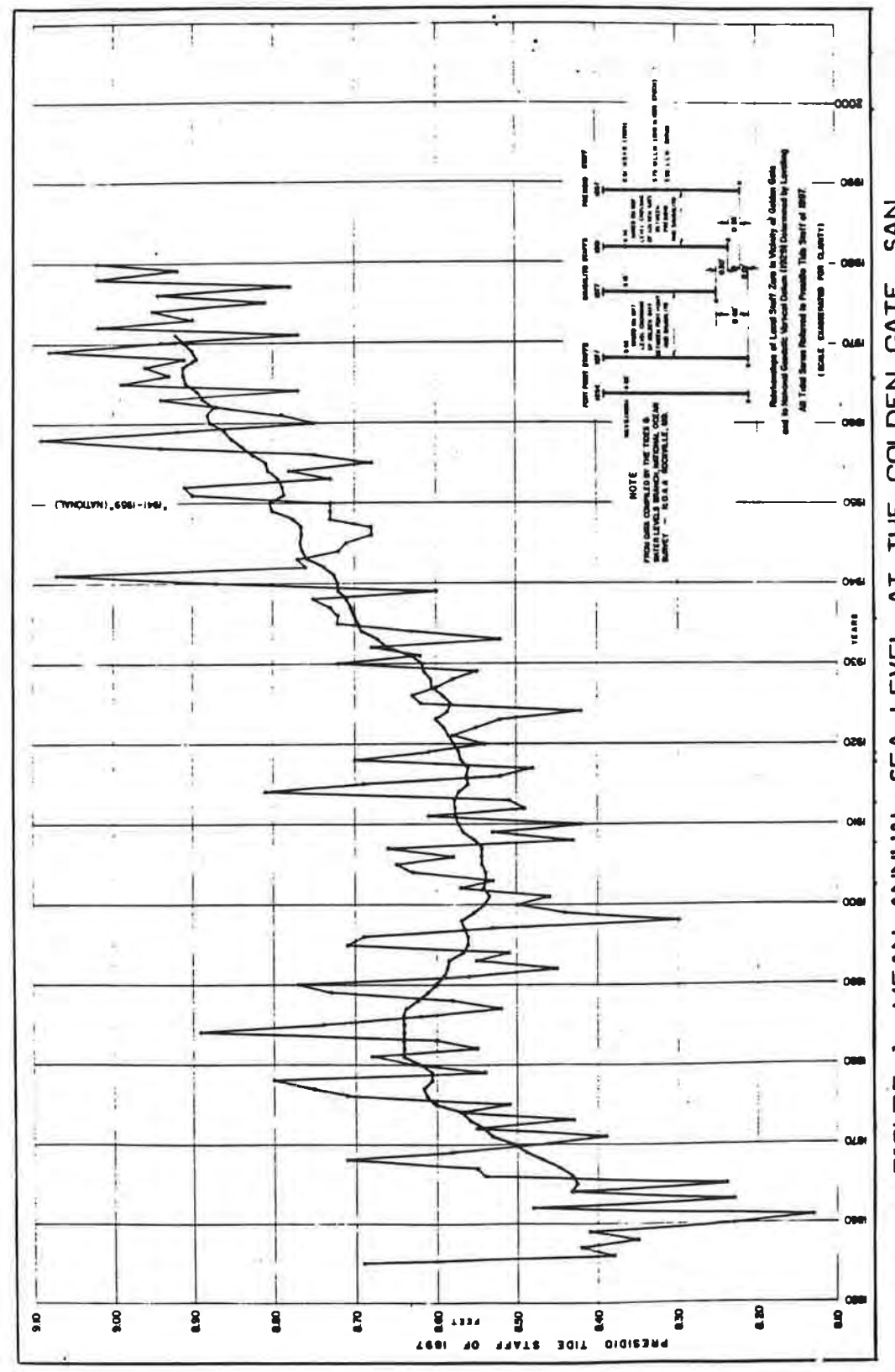


FIGURE 1. MEAN ANNUAL SEA LEVEL AT THE GOLDEN GATE, SAN FRANCISCO BAY, CALIFORNIA

variations are due to melting of polar ice fields, warming of the oceans, rise and fall of the land as lithospheric plates grind against each other, and possibly to changing weight of the melting ice caps (3). Rising sea level has filled coastal valleys, and sediments carried by land drainage have deposited in these valleys to various extent as determined by local transport conditions. Deposition near shore is often favored by protection from wind and partial stabilization of deposits by dessication while they are exposed during low tides. The annual fluctuations shown in Figure 1 provide times when these mud flats are more exposed than otherwise, and inundation tolerant plants, such as <u>Spartina</u>, can become established. These plants greatly enhance the rate of deposition of the clay and silt particles that comprise marsh soils and protect deposited particles from subsequent erosion by wind generated waves.

Two outstanding aspects of tidal marshes are the sinuous dendritic patterns of drainage channels and the very small variation in marsh surface elevation. Drainage channels in a protomarsh are typically perpendicular to the shore (6). As the marsh surface elevation rises and the marsh invades the land, however, these channels erode headward toward the lowest elevation, where drainage is concentrated. Elevations of the marsh immediately adjacent to the channel edges tend to accumulate sediment at a slightly higher rate because the most rapid deposition occurs as sediment-laden water overflows the channel banks during rising tides (7). Extension of the channels headward toward lowest elevations brings the channels into areas that previously had lower sedimentation rates. The result of these processes is a marsh surface that is uniformly irrigated and drained and that has a remarkably uniform elevation. Thompson (8) found that, except for channels, the elevation of Bird Island in South San Francisco Bay and a marsh island in South Bay had geometric standard deviations of 1.079 and 1.151, including their margins. (1.000 is uniform.)

This description of marsh evolution is supported by the plant material found at depth in cores (2), by the vertical walls of marsh channels, and by the very uniform elevation of marsh surfaces.

The elevation of the marsh rises after plants become established at rates that depend on the availability of suspended sediment and the depth and periods of inundation by high tides. As the elevation of the marsh rises relative to sea level, however, the frequency and duration of inundation diminishes and the rate of sediment accumulation falls. On the other hand, rising sea level tends to increase the frequency and periods of inundation, increasing the rate of marsh rise. Because of these compensating processes, a steady rate of sea level rise and unchanging average suspended sediment concentrations would lead to a constant marsh elevation relative to a sea level datum. Under these conditions the historical relative elevation could be determined by measuring present elevations. Figure 1 shows, however, that the rate of sea level rise has changed over the period of record, and estimation of the elevation of the marsh at various historical times requires a quantitative simulation.

The method of simulation described here includes calculation of the amount

of material that deposits during each period of inundation by a high tide and summing the amount of deposit over the period of record. The uniformity of marsh surface elevation indicates that a calculation of the mean elevation would be useful, so the computation is limited to the vertical dimension. A mass balance of suspended sediment over a unit area of marsh during flooding leads to:

$$(Y_w - Y_m) dC/dt = -w_s C + (C_* - C) dY_w/dt$$
 (1)

 $C_* = C_0$ during rising tide, $dY_w/dt > 0$

 $C_* = C$ otherwise, $dY_w/dt \le 0$

where Y_{w} and Y_{m} are the elevations of the water and marsh surfaces, C is the suspended sediment concentration, t is time, w_{s} is the median settling velocity of suspended particles, and C_{o} is the concentration of suspended sediment in flooding waters. The first term is the change in mass of suspended particles per unit area of marsh, the second is the flux of particles to the marsh surface, and the third is the change in concentration of suspended particles due to the addition of sediment-laden water during rising tide. Equation (1) assumes that all of the material that settles to the bed remains there. Hydraulic resistance to flow by the plants and the flat terrane both lead to the conclusion that there is very little shear stress on the marsh surface.

Krone (5) found that for suspensions of cohesive estuarial sediment particles in waters having low velocity gradients, and after aggregation of the suspended particles had progressed to the point where further aggregation is slow, the median settling velocity by weight can be closely described by

$$w_{a} = A C^{4/3}$$
 (2)

where A is 110 for $\mathbf{w}_{\mathbf{S}}$ in centimeters per second and C in grams per cubic centimeter.

The deposition during a period of flooding by a high tide is

$$\Delta Y_{m} = \int_{\pi} w_{s} C dt / C_{s}$$
 (3)

where C_8 is the grams of solids per cubic centimeter of marsh, the "dry density of the inorganic material." In this example, the rise of the marsh surface is calculated from the deposition of suspended solids with the assumption that the organic matter content is constant with depth. Pestrong (6) found an average dry density of Salicornia marsh in the region to be 0.671 g/cu cm with an organic matter content of 16.4 percent. The dry density of inorganic solids is therefore 0.561 g/cu cm.

The solution of equation (1) over the time of interest requires the elevations of high tides over that period. In this example, the amplitudes of high tides

relative to mean tide level at the San Mateo Bridge in South San Francisco Bay for the year 1981 were used, and the elevations of annual mean tides shown in Figure 1, adjusted for the difference in elevation between the staff and mean tide level at San Mateo, were used to obtain historic mean tide levels at San Mateo. The tides were represented as sine curves for the short periods of inundation. A period of 12.41 hours was used.

This location was selected because average marsh elevations of 3.58 and 3.60 ft NGVD were determined at nearby Bird Island in 1973 and 1976, respectively, and the date of a core segment at 4.0 ft below the surface, taken in 1974, was found to be year 1454 plus or minus 90 years (2). While these are sparse data, they serve to illustrate the usefulness of such measurements for simulating marsh elevations.

Integration of equation (1) was calculated by first calculating C at a half step forward in time to obtain a trial value of C for computation of w_s by equation (2), followed a full step forward from the starting time using that value of w_s . The initial value of C and the value of C at the end of this full step were then averaged to obtain a final value of w_s via equation (2), and the initial full step was repeated to obtain a trial value of C for the next step. Thereafter alternating full steps from previously determined values of C were used to obtain successively trial and average values of C for calculation of w_s . Equation (3) was integrated over each inundating tide by summing the raise in elevation for each $\Delta t/2$. This explicit method is very stable, and no significant benefit was observed for time steps less than 600 seconds.

The two unknowns needed for integration of equation (1) are the initial marsh elevation and the suspended sediment concentration in the flooding water. These were obtained by the following arguments. The rate of sea level rise during the period 1920 to 1982 appears to be linear. A least squares fit of these data showed a slope of 7.4164 E-3 ft/yr and a root mean square deviation (RMSD) of 0.101 ft: a straight line fits these data well. The difference between the elevation of the mean tide level at San Mateo calculated from this curve and the elevation of the marsh in 1976 was 3.00 ft. The elevation of the marsh in 1930 was calculated to be the same distance above mean tide level at that time, and the marsh rise was simulated using observed annual mean tides and trial values of C_0 until the observed elevations in 1973 and 1976 were reproduced. That suspended sediment concentration was 1.20 E-4 g/cu cm. This "effective continuous concentration" is well within observed concentrations at the months of sleague.

Extrapolation of this best fit line to 1454, assuming that the marsh elevation was the same distance above mean tide level, showed that the marsh surface would be 7.4164 E-3 * 520, or 3.84 ft below the present surface -- well within the errors of the dating. Evidently, the steady rate of sea level rise since 1920 is the norm, and the deviations between 1855 and 1920 were transient disturbances.

The period 1855 to 1880 fit a straight line with a RMSD value of .003 ft. Extrapolation of this line to intersect with the 1920 to 1982 line showed that it

would intersect in 1803. The initial marsh elevation was then set at the same elevation above mean tide level in 1803 as now occurs, and the elevation of the marsh was simulated from that time on using linear rise to 1855, then observed mean sea levels from 1855 to 1976. The 52 year period before 1855 is long enough that the assumed initial elevation has little effect. Computation of the suspended sediment concentration that would give the observed marsh elevations in 1973 and 1976 yielded 1.12 E-4 g/cu cm. This concentration is not greatly different from the 1.20 E-4 g/cu cm calculated for the rise from 1930 to 1976, and leads to the conclusion that the average suspended sediment concentration did not vary significantly during that period.

The calculated marsh elevations during the period 1855 to 1980 are plotted in Figure 2. An extrapolation of a least square fit of the marsh elevations from 1930 to 1980 is also shown in Figure 2 for comparison. This figure shows that the marsh rose at a higher rate from 1855 to about 1885, while sea level was rising steeply, that the marsh was higher than the extrapolated line from about 1895 to 1920 when sea level fell slightly and began to resume its normal rise, then established a steady rate of rise after the rate of sea level rise became stable. The differences between the elevations of the marsh and that of mean high water are plotted at the bottom of Figure 2. This plot shows that the marsh surface tended to be below MHW during the steep rise in sea level, rose above it during the 1885 to 1920 hiatus, then tended to remain slightly above MHW from then on.

Refinements to this simulation can include measurements of marsh density and organic matter content profiles from cores, obtaining actual high tide elevations over the period of concern, and dating of additional cores. The inclusion of these data in the simulation is straight forward. The exercise shown here illustrates the method and shows the effects of the rate of sea level rise on elevations of a marsh surface relative to mean high water. It also points out the problems associated with determining initial marsh elevations and effective suspended sediment concentrations. Profiles of marsh densities and ages would reduce these problems.

Conclusions

The method of simulating marsh rise presented here is a straight forward computation of sediment accumulation. The major difficulties are the acquisition of the needed data on tides and marsh soil properties. Simulation of rising marsh levels under the conditions in South San Francisco Bay showed that the elevation of a marsh surface relative to mean high water depends on the rate of sea level rise, and only attains a steady relative elevation after the the rate of sea level rise becomes constant.



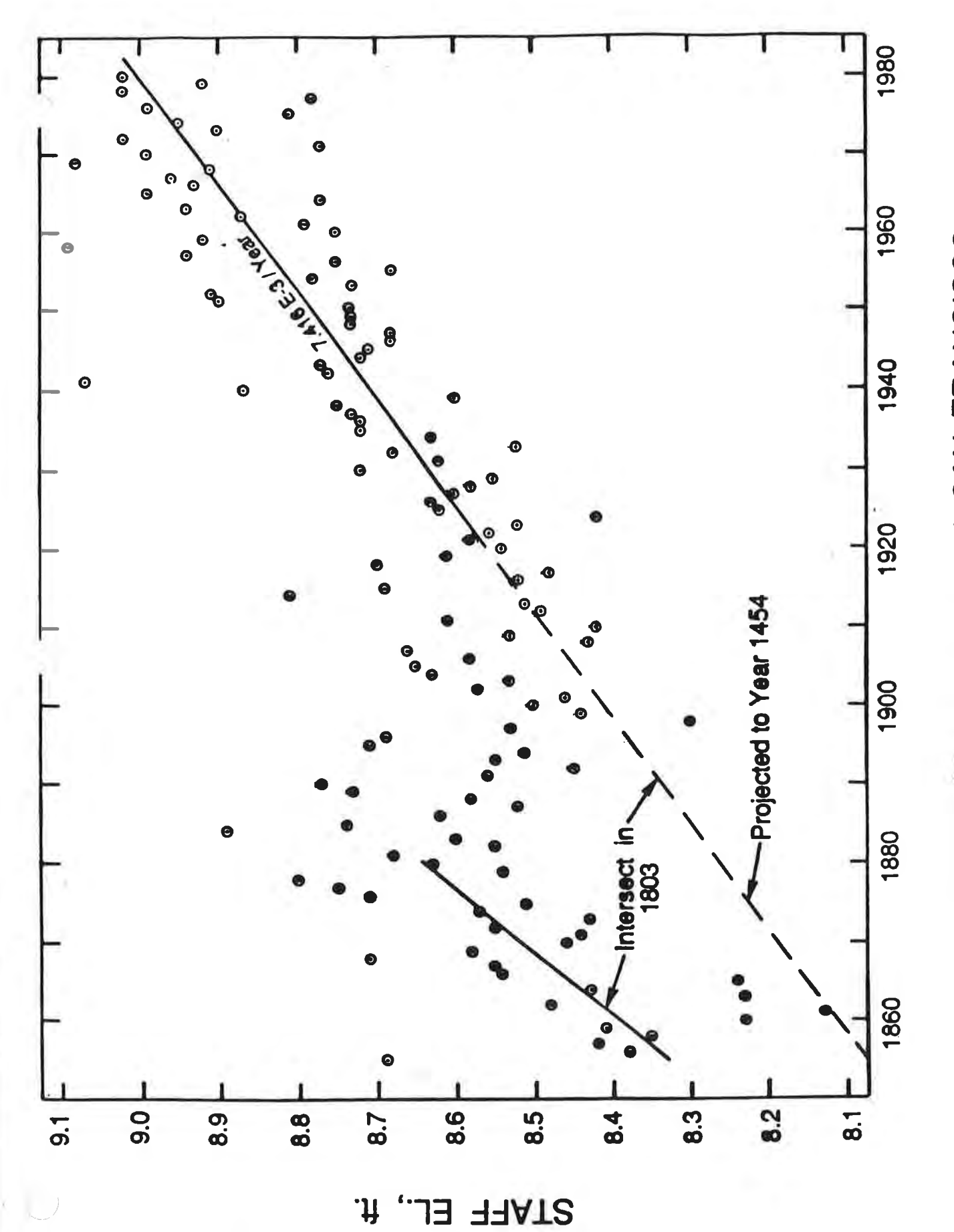
FIG 1. ANNUAL AVERAGE SEA LEVEL AT THE GOLDEN GATE

FIGURE ? CINAL JLATED ELEVATIONS OF MARSH

References

- 1. Atwater, B. F., Hedel, C. W., "Distribution of Seed Plants with Respect to Tide Levels and Water Salinity in the Natural Tidal Marshes of Northern San Francisco Bay Estuary, California," U.S.G.S. Open File Report 76-389, 1976.
- 2. Atwater, B. F., "Paleocology of Some Estuarine Sediments from a Core under Greco Island, San Francisco Bay," Rept to Calif. Div. Mines and Geol., Aug.7, 1974.
- 3.Clark, J. A., Farrell, W. E., and Peltier, W. R., "Global Changes in Post-glacial Sea Level: a Numerical Calculation," Quaternary Res., 9, 265 287, 1978.
- 4. Hicks, S. D., and Crosby, J. E., "Trends and Variability of Yearly Mean Sea Level," NOAA/NOS Tech. Mem. NOS 13, March, 1974.
- 5. Krone, R. B., "Flume Studies of the Transport of Sediment in Estuarial Shoaling Processes," Hydr. Engr. Res. Lab. and San. Engr. Res. Lab., U. Calif., Berkeley, 1962.
- 6. Pestrong, R. "The Development of Drainage Patterns on Tidal Marshes," Stanford U. Publications, Geol. Sci. \underline{X} , No. 2, Stanford, CA, 1965.
- 7. Pestrong, R., "San Francisco Bay Tidelands," Calif. Geol. 25, No. 2, Feb., 1972.
- 8. Thompson, W. C., Personal Communication.





ANNUAL MEAN TIDES AT SAN FRANCISCO





12-4-91

A New Evaluation of the Wind Stress Coefficient Over Water Surfaces

J. AMOROCHO AND J. J. DEVRIES

Departments of Civil Engineering and Land, Air and Water Resources University of California, Davis, California 95616

An analysis of data from numerous investigators, as well as information obtained directly by the authors, indicates that a large portion of the difficulties encountered in the past in establishing a relationship between the wind stress coefficient C_{10} and the wind velocity U_{10} we also attributed to computationally induced scatter of the data points. However, plots of the shear velocity u_{\bullet} against U_{10} reveal clear trends which show that three regions exist in the development of the wind shear stress: (1) a lower region in which the wind waves have not begun to break, and for which C_{10} is approximately constant; (2) a transitional region, after the onset of breakers, for which C_{10} varies nonlinearly with U_{10} ; and (3) a limiting region for which C_{10} tends again toward a constant value, and corresponds to a condition of breaker saturation. A single general equation to express C_{10} as a function of U_{10} is proposed, which agrees with the above findings. It is shown that in contrast with the perception of previous investigators, Charnock's coefficient $\alpha = z_{0g}/u_{*}^{2}$, where z_{0} is the roughness length and g is the acceleration due to gravity, is not constant anywhere in the range of wind velocities $0 < U_{10} < 40$ m/s. Finally, the data indicate that the wind flow boundary in each one of the three regions described above can be classified as having 'low roughness,' 'transitional,' and 'high roughness,' respectively.

Introduction

For the past 100 years or so, numerous investigators have carried out measurements of wind shear over water surfaces, both in the laboratory and at sea. A large volume of data has been collected, but no concensus has been reached yet on its interpretation. In particular, a variety of opinions has arisen with respect to the 'wind stress,' 'wind shear,' or 'surface drag' coefficient C_z as it has been variously termed. Some recent workers [e.g., SethuRaman and Raynor, 1975; Kitaygorodskiy, 1973; Pond et al., 1971; Ruggles, 1970] maintain that C_z does not vary with wind speed; others [e.g., Sheppard et al., 1972; Davidson, 1974; Wu, 1969, 1972; Garratt, 1977; Melville, 1977] have presented data supporting the notion that it does. The values of C_z have been disputed, as well as the appropriate expressions needed to represent it.

To set the stage for a reexamination of this problem, a few basic notions are recalled here.

Let it be assumed that for wind blowing over water, under conditions of neutral thermal stability, the logarithmic law of air velocity change with height is accepted, as given by the expression

$$U_z = \frac{u*}{\kappa} \ln \left(z/z_0 \right) \tag{1}$$

Неге

- U_z mean wind velocity measured at elevation z above the water surface;
- κ von Karman constant (normally taken as 0.4);
- u* shear velocity, equal to $(\tau_w/\rho)^{1/2}$;
- z_0 vertical intercept of a semilogarithmic plot of z versus U_z ;
- τ_w wind shear stress at the water surface;
- ρ air density.

An established practice has been to measure wind velocity profiles over water, to determine the shear velocity via (1), and to compute τ_w therefrom.

Copyright © 1980 by the American Geophysical Union.

Because it is not always practical to perform velocity profile measurements in field situations, it has become customary to express the relationship between the wind shear stress and the velocity measured at a single location z above the mean water level by the expression

$$C_z = \frac{\tau_w}{\rho U_z^2} \tag{2}$$

where C_z is the wind stress coefficient.

One of the nost complete summaries of published values of C_z was assembled by Wu [1969] and comprises data from 42 different investigations. This summary shows that the points originated from laboratory studies are widely scattered, and although the 'field' data show a general trend, their dispersion makes the selection of wind stress coefficients uncertain.

In an attempt to fit a single curve to the dispersed data on C_n , Charnock [1955] proposed an expression based on a parameter α which has become known as Charnock's coefficient, as follows:

$$C_{z} = \left[\frac{\kappa}{\ln \left(C_{z}^{-1} U_{z}^{-2} z g / \alpha \right)} \right]^{2} \tag{3}$$

Here, α is given by the ratio

$$\alpha = \frac{gz_0}{u^*} \tag{4}$$

where g is acceleration due to gravity.

Charnock's coefficient has been generally assumed to be a constant when U_z exceeds certain values. From the limited amount of data available to Charnock for short fetches in the field, as well as from laboratory data obtained by Wu [1968], Hidy and Plate [1966], and others, it appeared that at wind speeds approaching 10 m/s, α had a value of about 0.011. However, Kraus [1972] reports that when field data for long fetches are used, the required α to match (3) varies from about 0.008 to much higher values. Similar difficulties have been noted by many others.

From the above remarks, it is clear that many questions re-

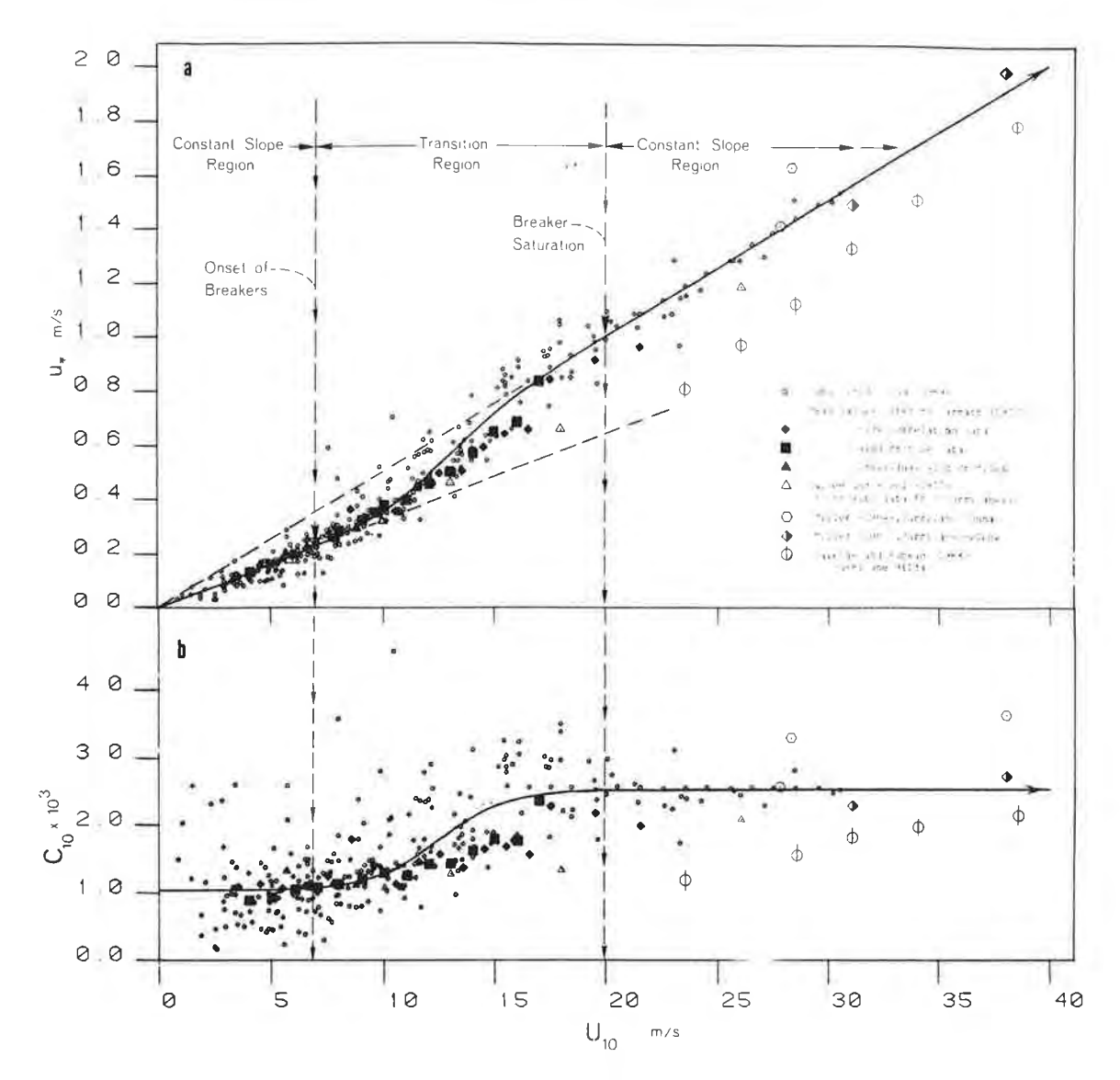


Fig. 1. Plots of u_* and C_{10} versus wind velocity U_{10} from data by u_{10} [1969] and others.

main unanswered regarding the dispersion of the values of C_n , the relationship between laboratory and field data, the appropriateness of the assumption of constancy of the Charnock parameter, and, in fact, the best manner of evaluating the wind shear. In an attempt to elucidate these questions it was decided to reexamine the wind shear problem from some theoretical aspects as well as from the results of new measurements.

THE EVALUATION OF C_z

Dispersion of C, Plots

The authors suspected, upon the beginning of the present studies, that a major cause for the scatter encountered by many investigators in plots of C_z versus U_z was due to errors inherent in the customary method of computation of individual wind stress coefficient values. Given single velocity profiles plotted on semilogarithmic paper, u_* is found directly as κ times the slope of each line. U_z is either measured explicitly or read off from the profiles. Therefore if u_* is graphed versus U_z , whatever scatter of points may result stems only from the experimental errors contained in the values of u_* and U_z .

Consider now values of C_z computed from each pair of values of u* and U_z . I som (1) and (2) and the expression for u*, it follows that

$$C_z = \left[\frac{u*}{U_z}\right]^2 \tag{5}$$

This relationship shows that the computation of C_z involves the squaring of the two variables u* and U_z , and hence that its error is a function of the squared errors of the variables.

A formal analysis of the expected relative dispersions of plots of u* and $(u*/U_z)^2$ as found from individual velocity profile measurements was performed. This analysis [DeVries, 1978] shows that the ratio of the dispersion of C_z (as measured by its coefficient of variation) to the dispersion of u* can be expected to be very high for low values of U_z . It decreases to about 2 for the range $2 < U_{10} < 20$ and further thereafter.

Plots of the C_{10} data cited by Wu, and the corresponding shear velocities are presented in Figures 1a and 1b. Also plotted are data given by Garratt [1977] on C_{10} values from various sources, computed from Reynolds stress (eddy correlation) and wind profile measurements and averaged for

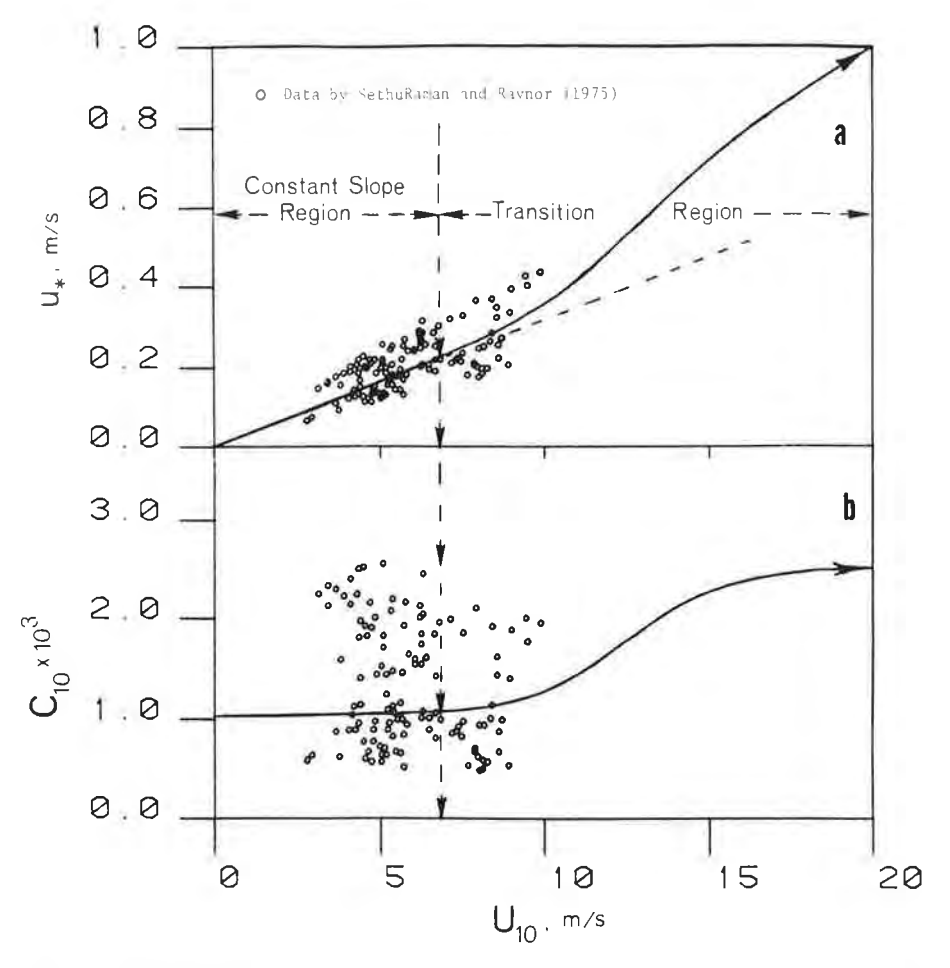


Fig. 2. Plots of u* and C₁₀ versus wind velocity U₁₀ from data by .ethuRaman and Raynor [1975].

classes of U_{10} at intervals of 1 m/s. This information was not included in Wu's summary. Other data originating from surface stress computations by the geostrophic departure method during hurricanes were also cited by Garratt. For the present paper, the C_{10} values found in the original sources [Miller, 1964; Palmén and Riehl, 1957; Hawkins and Rubsam, 1968] were used, and also converted to u*.

Finally, data cited by SethuRaman and Raynor [1975] for C_6 and $u \cdot versus$ U_6 were also considered. These values, scaled from the original paper and converted to z = 10 via (1), were plotted separately in Figures 2a and 2b in order to avoid excessive clutter and overlap with Wu's data.

The contrast in the scatter between the C_{10} and u* plots is evident. The trend of the points, which is ill defined in the case of C_{10} , is fairly well defined for u*. Note that the dispersion of all the data sets is about the same for the lower wind velocities. The hurricane data points at $U_{10} > 15$ ms are more dispersed. This may be due to the greater imprecision associated with the inference of shear stresses from tropical cyclone information. Kraus [1972] suggests that this imprecision may cause on occasion overestimates or underestimates of the stress by a factor of 2. In fact, some C_{10} values from the sources cited are as high as 0.003-0.004 at wind speeds U_{10} between 35 and 50 m/s. These values seem doubtful to the authors and were not included in the present analysis. Future measurements made from instrumented platforms at sea may yield more reliable information.

The scatter of the u* points is certainly not surprising, since they originate from many different sources, and reflect the true experimental errors, as well as the lack of homogeneity of the conditions of measurement. Clearly, since the fetch of the water surfaces varied widely in the different studies involved, one would expect nonuniformity in the development of wave heights and hence in the overall water surface roughness for equal wind velocities. The variability of the wind in time can also be expected to have caused some of the dispersion. Finally, it is uncertain whether appropriate corrections were introduced in all the data for the effects of the state of thermal stability of the water-atmosphere system, particularly in the earlier investigations. Nevertheless, the u* points appear reasonably organized along a smooth curve as shown, and some important conclusions can be reached.

It is noted in Figure 1a that two well-defined regions with relatively low scatter are apparent. The first corresponds to points for which $0 < U_{10} < 7$ m/s and the second to points for which $U_{10} > 20$ m/s. The points fit straight lines passing through the origin with high coefficients of correlation (0.83 for $0 < U_{10} < 7$ m/s and 0.94 for $U_{10} > 20$ m/s). From these lines, the following expressions result, approximated to the fourth decimal place:

$$u* = 0.0323 U_{10}$$
 $0 < U_{10} < \sim 7 \text{ m/s}$ (6)

$$u* = 0.0504 U_{10}$$
 $U_{10} > \sim 20 \text{ m/s}$ (7)

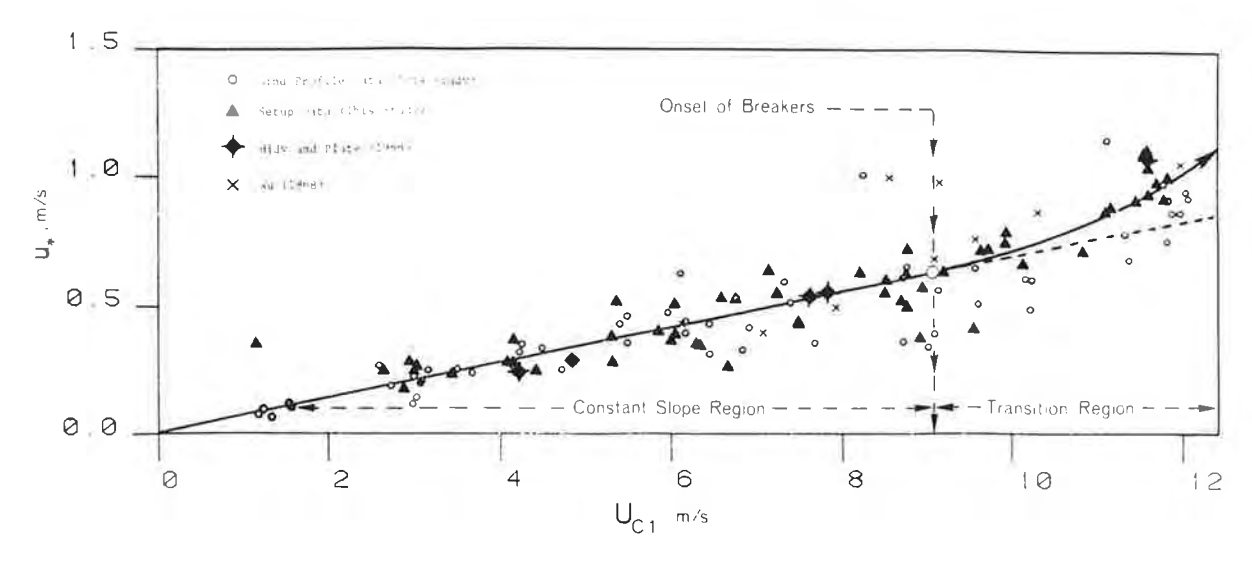


Fig. 3. Plot of u_{\bullet} versus wind velocity $C_{c,1}$ from laboratory data.

The corresponding values for C_{10} are

$$C_{10 \text{ min}} = 0.00104 \qquad 0 < U_{10} < -7 \text{ m/s}$$
 (8)

$$C_{10 \text{ max}} = 0.00254$$
 $U_{10} > \sim 20 \text{ m/s}$ (9)

Since the above C_{10} values were derived from explicit expressions for u*, the question of dispersion of data points does not arise here. It is apparent therefore that, so far as the data reveal, the wind stress coefficient tends to be constant at low and at high velocities. Between these two end regions a third, transitional, region occurs. The line drawn in Figure 1a represents this trend, which agrees with the concept suggested in the past by various workers [e.g., Malkus, 1962; Wu, 1969; Pond and Pickard, 1978] who have speculated that the drag coefficient may behave in this manner.

Effect of Breaking Waves

The wind velocity U_{10} for which the u* data start departing consistently from the straight line relationship given by (6) corresponds to the approximate value at which breakers begin to appear in open waters [Kotsch, 1970; Harding and Kotsch, 1965]. From the U.S. Navy aerial photographs presented by Kotsch it is seen that the number of breaking waves increases gradually with the wind velocity until a state of saturation is reached in the neighborhood of 20 m/s. This suggests that the rate of development of breakers is associated with a form drag due to flow separation, which determines the values of u and C_{10} in the transition region noted above. This hypothesis has been also supported by physically based arguments presented by Melville [1977], who has shown that strong changes of the value of the shear velocity, and consequently of C_{10} are to be expected after the onset of breaking waves, when u* = 0.23m/s approximately. While it is recognized that the photographic material mentioned above does not provide more than a qualitative indication of the existence of a state of breaker saturation in the neighborhood of $U_{10} = 20$ m/s, the data of Figure 1 certainly provide a strong support for the assumption of a region of constant slope above this velocity. The curve proposed by Garratt [1977] provides neither the double inflexion required to fit the data, nor, as will be seen later, corresponds to the character of Charnock's α .

To obtain further evidence on the mode of change of u*

upon the appearance of breakers, measurements were made by the authors in a wind-wave flume at the University of California, Davis, and on a large open channel [De Vries, 1978].

The equipment used in the laboratory experiments consisted of a 1×2 ft (0.31 \times 0.61 m) rectangular channel approximately 19 m long, covered over its top, and associated devices that permitted the simultaneous flow of water and air. Mean air velocities could be varied between 0 and 12 m/s. Details of the installation are given elsewhere [De Vries, 1978]. The wind sheal was determined by wind velocity profiles measured with a sot-film anemometer, and by the wind slope. The latter was computed from longitudinal energy profiles determined from a tailed measurements of pressure and mean water surface en ations. The results are shown in Figure 3. The points originated from the wind velocity profiles have the greater scatter. They represent data obtained by the authors as well as results of experiments by Wu [1968] and Hidy and Plate [1966]. The wind velocities, designated here with the symbol U_{c1} have the value $U_{c1} = U_{01} - V_{\kappa s}$, where U_{01} is the velocity taken at a stationary point 0.1 m above the mean water level, and V_{n-1} , the mean velocity of the water at its surface, as determined by timing the travel of small floating particles. This surface velocity represents the net boundary motion due to wind drift and forward channel flow.

Most of the depersion of the points at the higher wind speeds is due to save-induced fluctuations. This study confirmed the findings of *Veenhuizen* [1973], which show that air velocity profiles measured at fixed locations near the water in enclosed flumes are affected by the wave motion to an elevation of about four wave heights above the mean liquid surface. An emometer readings sampled at random intervals showed that the variations between sample points relative to the average of all the measurements of an experimental run were relatively large, and indeed increased with the mean wind speed. The wind slope S_w in a steady state is given by the expression

$$S_{n} = \frac{\tau_{n}}{\gamma D} = \frac{d}{dx} (h + V^{2}/2g) + S_{n}$$
 (10)

where D is the hydraulic depth, γ is the specific weight of water, h is the piezometric head (given by $h = Z_0 + y + p_a/\gamma$), p_a is the air pressure on the water surface, V is the mean water

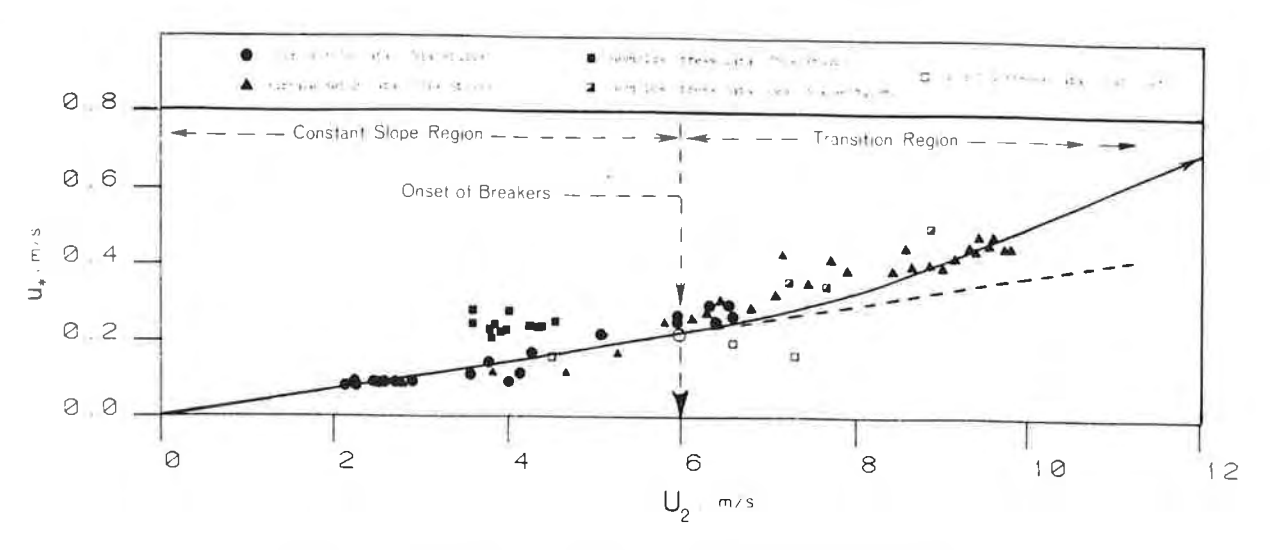


Fig. 4. Plot of u_* versus wind velocity U_2 from California Aqueduct data.

flow velocity, S_i is the channel boundary friction slope, Z_0 is the elevation of the channel bottom, and y is the water depth.

In the laboratory, τ_{∞} was evaluated by discretizing (10) between the end points of a selected channel reach and by measurement of the right-hand side terms of (10) for various wind velocities U_{c+} averaged over a period of time. The corresponding u_{-} was computed from τ_{∞} . These measurements gave rise to a set of data points that exhibited a smaller dispersion than the wind profiles. This result could be expected, because the mean wind slopes evaluated over a reach are less sensitive to the local wind field perturbations produced by the waves, and tend to attenuate their overall effect.

In these experiments the waves began to break when $U_{c,1}$ reached a value of about 9 m/s. In Figure 3 a straight line was fitted by least squares to the points for the interval $0 \le U_{c,1} \le 9$ m/s. The equation of this line, averaged for all the data, is

$$u* = 0.0663 U_{c+} \tag{11}$$

For $U_{c\perp} > 9$ m/s, the data suggest an upturn of the trend. With the equipment available it was not possible to attain higher wind velocities than about 12 m/s, so the behavior of u- for a wider range of $U_{c\perp}$ could not be observed. The indication that a change of regime occurs after the waves start breaking is, however, clear. Similar results have been obtained by other investigators, including Wu [1969], who reports an abrupt change in $C_{0\perp}$ at about 8 m/s. The velocity $U_{0\perp}$ at which the breakers occur depends to a variable degree on factors such as fetch and water depth, and thus may vary between different laboratory flumes.

It is noted that the velocity $U_{10} = 7$ m/s at which the breakers begin to form over the sea corresponds to $U_{c,1} = 4.37$ m/s if the logarithmic velocity distribution law is assumed. At this point, for which $u_* = 0.23$ m/s, the waves do not break in the laboratory. Conversely, the velocity $U_{c,1} = 9$ m/s at which the first breakers occur in the laboratory corresponds to $U_{10} = 22$ m/s and $u_* = 1.11$ m/s, for which sea surfaces are already saturated with breakers. This can simply be attributed to the fact that the laboratory fetches are too short for the waves to grow in height sufficiently to break at wind velocities which are ample to produce breakers at sea. The key result here is that in the lower range of wind velocities u_* is a linear function of U_* , and hence C_* is constant, only as long as breakers do not form

The authors also obtained measurements of wind shear velocities in the California Aqueduct, a large canal running north to south along the western flank of the San Joaquin Valley in California. This canal experiences strong axial wind action during certain seasons of the year. The canal has a width of some 50 m. The length of the reach observed, which has a nearly straight alignment, is approximately 10 km. Details on these studies are reported by DeVries [1978] elsewhere. Of interest here, among the results of that investigation, are data showing the relationship between U_2 (wind velocity 2 m as we the water) and u_* .

The shear venetities were obtained for various wind conditions from pre e measurements, from measurements of the Reynolds stress (eddy correlation method) taken with hotfilm anemomet s, and from the wind slopes, as evaluated by determination of the wind 'set-up.' These data are plotted in Figure 4, together with other information for open water cited by Deacon and Webb [1962] and Clancy [1970]. The points corresponding to the Reynolds stress measurements depart from the general trend of the wind profile and the wind set-up data probably due to instrumental difficulties, as discussed by one of the authors elsewhere [De Vries, 1978]. In this canal, the waves started breaking at $U_2 = 6$ m/s approximately (equivalent to $U_{10} = 7 \text{ m}$ s). A straight line fits the points in the interval $0 < U_2 < 6 \text{ m}$ s. For $U_2 > 6$ the points trend upward, in a manner similar to that observed in the laboratory experiments after the onset at breakers, as well as that indicated by the data given in figure 1. The solid line drawn through the points corresponds to the equation proposed by the authors as described in the following section.

The above information tends to confirm the hypothesis that in the transition region the values of u* and U_{10} are related to the development of breaking waves. The following theory is based on this premise.

A THEORY ON THE VARIATION OF C_{10}

The coefficient C_{10} can be considered to be composed of two elements: (1) an element C_r , due to roughness drag associated with nonbreaking waves and ripples, and equal to a lower limiting value $C_{10\text{min}} = 0.00104$; (2) an element due to form drag C_r , associated with flow separation behind the breakers. It is postulated here that this second element is proportional to a function depending on the area covered by

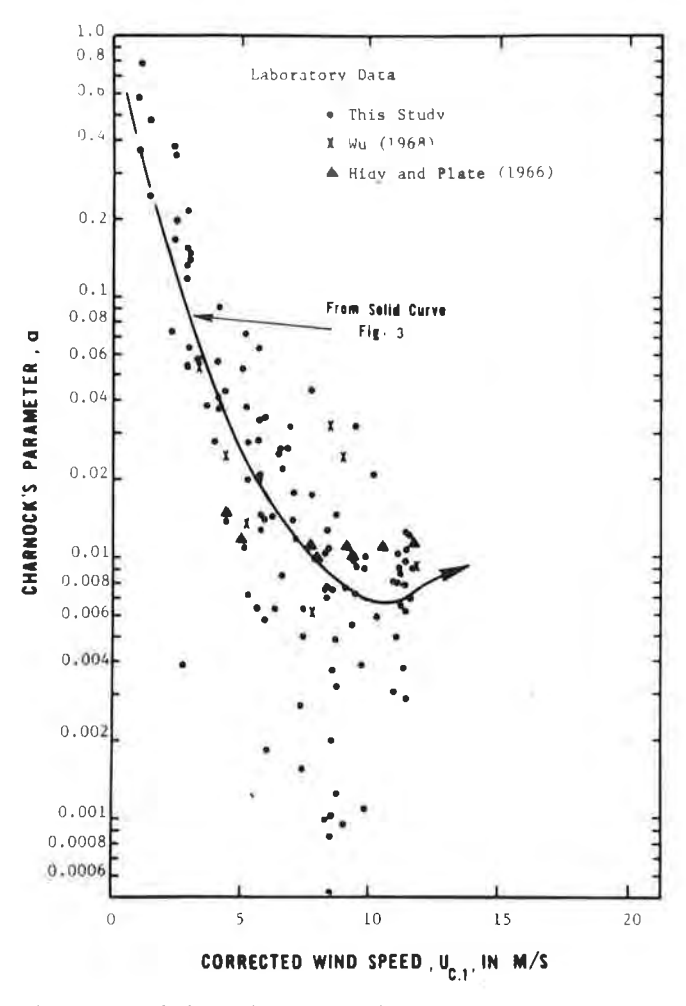


Fig. 5. Plot of Charnock's α versus wind speed $U_{c,1}$ from laboratory data.

breakers of various heights per unit area of water surface. This function shall be called here breaker density. Its value depends on the wind velocity and is denoted by the symbol $F(U_{10})$.

The data discussed in the previous sections suggest that the number of breakers per unit area, and hence the breaker density obeys a law similar to that of growth processes limited by a state of saturation. The growth of certain populations under nutritional or space constraints, or the rates of chemical reactions, are examples of such processes [Reid and Berkson, 1929], which can be described by the equation

$$\frac{dF(U_{10})}{dU} = \frac{1}{s} \left[F(U_{10}) - A \right] \left[B - F(U_{10}) \right]$$

$$A \le F(U_{10}) \le B \qquad B - A = 1$$
(12)

where s is a positive constant, and A and B are the lower and upper limits of $F(U_{10})$. In words, (12) can be said to represent a process wherein the rate of growth of $F(U_{10})$ is proportional to the excess of $F(U_{10})$ over its lower limiting value A, multiplied by its deficiency with respect to the final saturation value B. This description is consistent with the photographic evidence, which suggests a rapid initial rate of increase of the number of breakers after U_{10} exceeds 7 m/s, followed by a more gradual, and finally a zero rate of increase, near $U_{10} = 20$ m/s.

Integration of (12) leads to

$$F(U_{10}) = \frac{B \exp[(U-m)/s] + A}{\exp[(U-m)/s] + 1} = \frac{(B-A)}{1 + \exp[-(U-m)/s]} + A$$
(13)

where m, s are constants to be determined.

Since no breakers exist at $U_{10} < 7$ m/s, we can write $F(U_{10} < 7) = A = 0$. Hence (13) becomes

$$F(U_{10}) = B \left\{ 1 + \exp - \left[(U - m)/s \right] \right\}^{-1}$$
 (14)

The expression in braces can be recognized as the logistic distribution with mean m and standard deviation s. By the assumptions stated earlier regarding the drag coefficient C_{10} we can write

$$C_{10}(U_{10}) = C_c + C_f = C_{10\text{min}} + KF(U_{10})$$

where K is a constant or, from (14),

$$C_{10}(U_{10}) = KB \{1 + \exp{-[(U - m)/s]}\}^{-1} + C_{10min}$$
 (15)

 C_{10min} is the minimum value of 0.00104.

For large values of U_{10} , (15) tends to

$$C_{10}(U_{10}) = C_{10\text{max}} = KB + C_{10\text{min}}$$

Here, $C_{10\text{max}}$ is the maximum value of 0.00254. It follows that

$$KB = C_{10max} - C_{10min} = 0.0015$$

The general equation for C_{10} becomes therefore

$$C_{10} = 0.0015 \left[1 + \exp\left(-\frac{U_{10} - m}{s}\right) \right]^{-1} + 0.00104$$
 (16)

The value of u_* : llows from (5):

$$u* = C_{10}^{1/2} U_{10}$$

$$= \left\{ 0.0015 \left[1 + \exp\left(-\frac{U_{10} - m}{s}\right) \right]^{-1} + 0.00104 \right\}^{1/2} U_{10}$$
 (17)

To obtain the values of the constants m and s, an optimization program was prepared to fit this expression to the data of Figures 1a and 2a by least squares. The results were m = 12.5 m/s, s = 1.56 m/s, so that the final expressions for u* and C_{10} are

$$u* = \left\{0.0015 \left[1 - \exp\left(-\frac{U_{10} - 12.5}{1.56}\right)\right]^{-1} + 0.00104\right\}^{1/2} U_{10}$$
(18)

and

$$C_{10} = 0.0015 \left[1 + \exp\left(-\frac{U_{10} - 12.5}{1.56}\right) \right]^{-1} + 0.00104$$
 (19)

The curves plotted in Figures 1 and 2 follow (18) and (19).

The shear velocities and drag coefficients corresponding to wind velocities taken at other elevations z above the mean water level can be obtained quite simply from (18) and (19) by noting that for the same u_* ,

$$u* = U_{10}(C_{10})^{1/2} = U_z(C_z)^{1/2}$$

and hence,

$$C_z = C_{10} \left(\frac{U_{10}}{U_z} \right)^2 \tag{20}$$

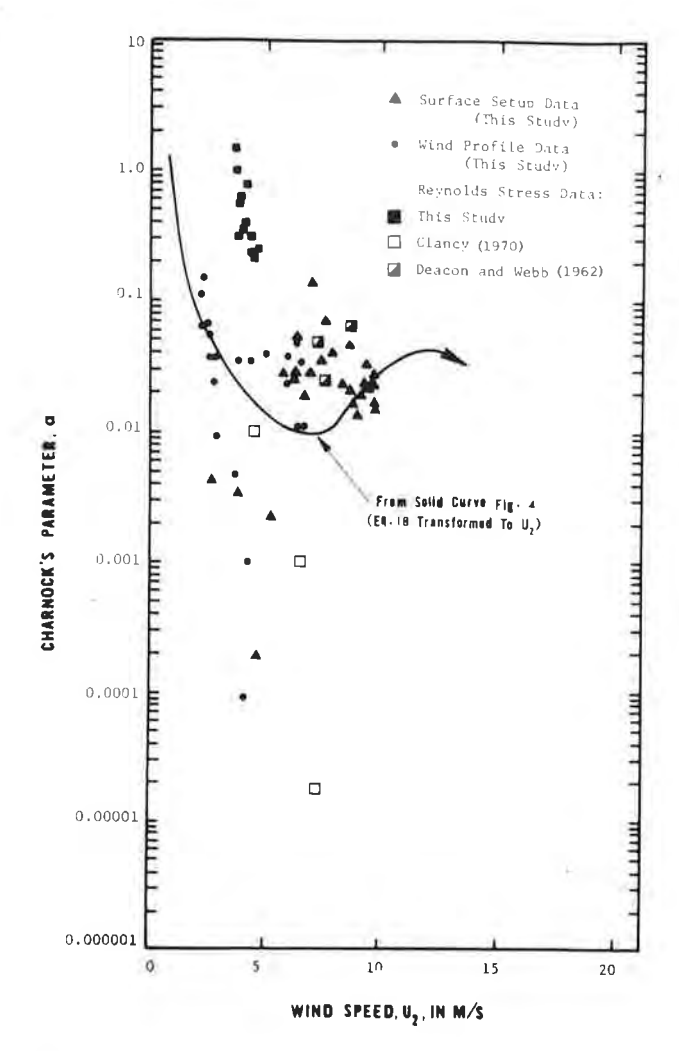


Fig. 6. Plot of Charnock's α versus wind speed U_2 from California Aqueduct data and other sources.

The relationship between U_{10} and U_z can be evaluated by expressing U_{10} and U_z through (1) and subtracting one from the other. After some manipulation, the following results are obtained:

$$U_z = U_{10} - \frac{u*}{\kappa} \ln(10/z) = U_{10} [1 - (C_{10})^{1/2} \kappa^{-1} \ln(10/z)]$$
 (21)

Combining this with (20), we get

$$C_z = C_{10} \left[1 - (C_{10})^{1/2} \kappa^{-1} \ln \left(\frac{10}{z} \right) \right]^{-2}$$
 (22)

With these equations, a curve expressing the relationship C_z versus U_z can be constructed for any z, given C_{10} values computed from (19). It is remarked here that (19) describes a curve that only reaches the maximum and minimum values $C_{10\text{max}} = 0.00254$ and $C_{10\text{min}} = 0.00104$ asymptotically. However, the convergence on both sides of the central region is very rapid and the curve ordinates are indistinguishable from these limiting values within an approximation of 10^{-5} in the close vicinity of $U_{10} = 7$ m/s and $U_{10} = 20$ m/s. Therefore the essential constancy of C_{10} at the high and low wind velocity ranges is practically preserved.

Equation (18) was also used to plot the curve shown on Figure 4, with proper scaling for U_2 by means of (21). The agreement between this curve and the plotted points indicates that

the shear stress relationship proposed applies equally well to large canals and to open water surfaces such as lakes and the sea, as long as the canal fetches are sufficient to permit the formation of breaking waves.

CHARNOCK'S COEFFICIENT a

The validity of the assumption that Charnock's α is constant was tested from the experimental data obtained by the authors, as well as from (18).

Combining (1) and (4), one gets

$$\alpha = gz[\exp(\kappa U_z/u_*)]^{-1}u_*^{-2}$$
 (23)

Figure 5 is a plot of α versus U_{c+} based on the u* values found in the laboratory. The points were computed from individual u* values, and the curve corresponds to the solid curve shown in Figure 3. Figure 6 shows a similar plot based on the measurements made at the California Aqueduct, and Figure 7 represents the behavior of α based on (18). It is clear from these three plots that α cannot be considered to be constant anywhere in the range of wind velocities shown. While Charnock's idea of a nondimensional parameter relating the 'roughness length' to the shear velocity may be valid, the roughness length, is a derived quantity and its determination is very imprecise. The plots illustrate the large uncertainty involved in evaluating α from individual measurements of u*. The fact that this uncertainty was not recognized for the many years elapsed since its use was first proposed is quite surprising. Charnock suggested that the parameter was constant for $U_{10} > 10$ m/s on the basis of the results of extrapolations of logarithmic ploof velocity profiles. Such extrapolations are extremely improvise, but the illusion of the constancy of α has persisted never reless. One can only attribute this persistence to the circums: nee that the illusion could not be dispelled due to the equa venduring reliance on strongly scattered diagrams for the difficulty of C_{10} . Another difficulty has arisen from the circumstance that in the past, complete data sets covering a wide range of wind velocities from zero to, say, 35 m/s, could not be obtained directly by individual investigators from their own measurements. In some cases the workers drew far reaching conclusions from a limited range of results. For example, the Jata of SethuRaman and Raynor are contained mostly within the lower region of U_{10} values for which C_{10} is constant. his constancy certainly should not be assumed to extend i eyond the range of the data. The conclusion that Charnock's is constant and equal to 0.016 '... for moderately rough sea conditions and 0.072 for fully rough conditions...' appears somewhat contrived and is not supported either by the data of SethuRaman and Raynor themselves or by the additional information presented here.

Other authors have chosen to ignore large masses of available information. The exclusive use of data not included in Wu's summaries, for example, may have led Garratt to overlook the existence of the transition region of the shear stress, and to propose that a value of $\alpha = 0.0144$ describes adequately the variation of C_{10} in the region $4 < U_{10} < 21$ m/s.

It is certainly possible to obtain an expression for Charnock's α by combining (18) and (23). However, quite aside from the complicated form of such an expression, it would seem that to use it for finding a nonconstant α as a vehicle for computing C_2 , and thence, eventually, τ_w , is a rather pointless exercise. Therefore it seems to the authors that since Charnock's α has lost its virtue as a constant parameter, its future use can hardly be justified. The value proposed by Garratt

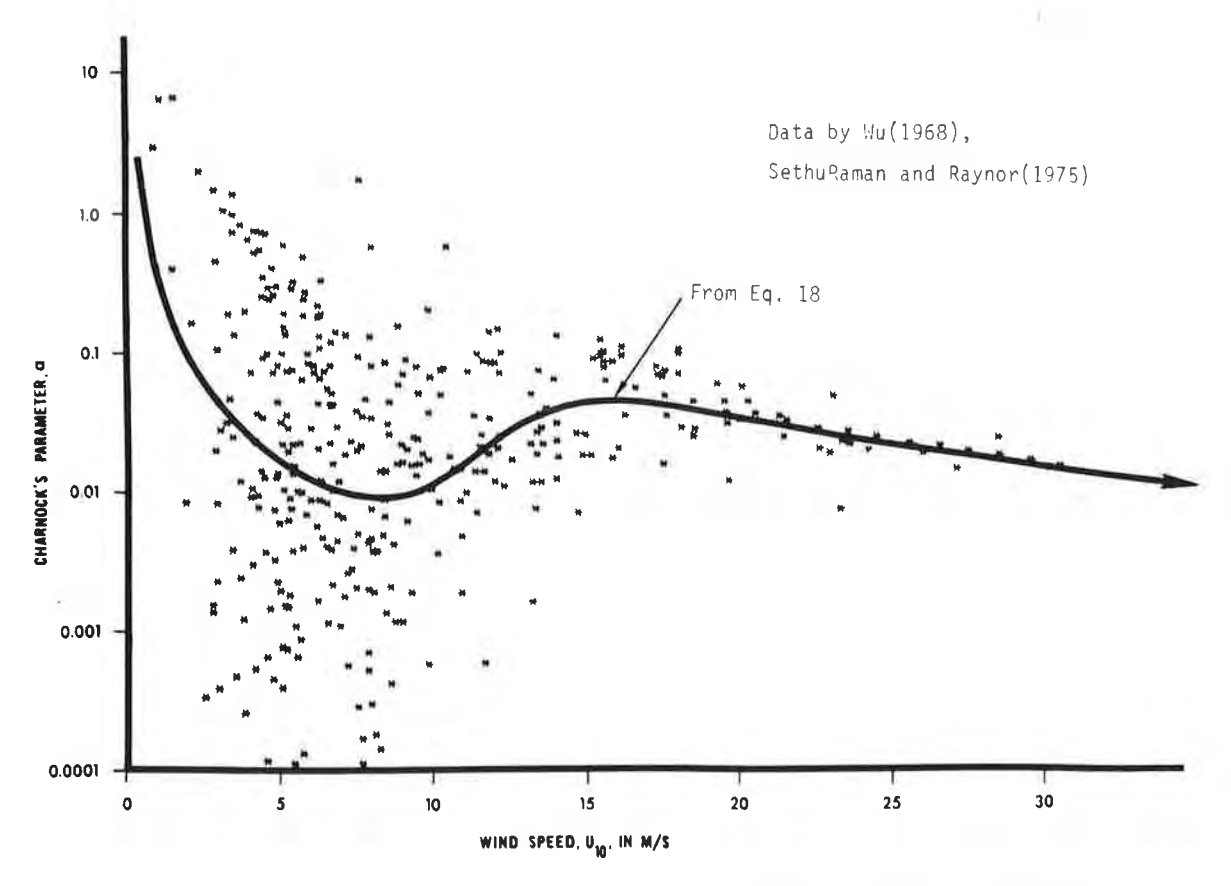


Fig. 7. The form of Charnock's α as a function of wind speed U_{10} from the expression for u_* (18).

leads only to a very rough approximation of the trend of C_{10} which masks the upper and lower levels of constancy and the effect of the breaking waves in the transition region.

CLASSIFICATION OF SURFACE ROUGHNESS

Plots of the variation of the shear velocity u* and of C_z with the roughness Reynolds number $R* = u*z_0/\nu$ have been presented by SethuRaman and Raynor [1975] and Melville [1977]. The former authors concluded from plots of their results that for R* values comprised between the ranges R* < 0.15, 0.15 <R* < 4 and R* > 4 the flow regime could be characterized as 'smooth,' 'moderately rough,' and 'fully rough,' respectively. This division was based on the apparent slopes of lines fitted to plots of C_6 versus R_* . This classification of roughness was also applied by SethuRaman and Raynor to their plot of C_{10} versus U_6 (see Figure 2b) with the interpretation that fully rough conditions correspond to the higher points of their scatter diagram, moderately rough to the intermediate points, and smooth to the lower points. It is difficult to understand how the three states of roughness could occur within the same range of wind velocities in a steady state.

A different classification is proposed here. Values of C_{10} computed from (19) were plotted against R* computed from (1) and (18). This plot is shown in Figure 8. Also shown here are the data presented by *Melville* [1977]. Three regions can be distinguished here, which match those shown in Figures 1 and 2. For R* < 0.76 the flow boundary can be said to have low roughness and corresponds to a water surface devoid of breaking waves. In the range 0.76 < R* < 245 the boundary is transitionally rough and occurs between the onset of breakers

and the neighborh old of breaker saturation. Finally, for R* > 245 the surface has high roughness.

The points takes from Melville's paper agree with the curve obtained here, except in the extreme ranges of R*. It is believed that these discrepancies are due to the experimental and computational scatter of individual C_{10} data as discussed before. It is noted, for example, that the data of SethuRaman and Raynor [1975] in the region 0.001 < R* < 1.0 corresponds to the position of a line passing through the mean of the points for which $C < 1.0 \times 10^{-3}$ in Figure 2. This, of course, tends to underesting the C_{10} in this region. In the upper region the points by Ruggies and Wu [Melville, 1977] are scattered but their centroid lies in the vicinity of the maximum value of C_{10} as given by (18)

Conclusions

The conclusions of this study can be summarized as follows. 1. The difficulties encountered in the past in establishing a relationship between the wind velocity U_{10} and the wind stress coefficient C_{10} can be attributed primarily to computationally produced scatter of the plots of C_{10} versus U_{10} . On the other hand, clear trends emerge in plots of u* against U_{10} , which indicate that three regions can be recognized in the development of the wind shear stress. (1) A lower region for which u* varies linearly with U_{10} , and C_{10} is constant and equal to 0.00104. In this region the wind waves do not break. (2) An intermediate region for which C_{10} varies nonlinearly with U_{10} . This region occurs between the onset of breakers and the condition of full breaker saturation. (3) A limiting region for which u* again varies linearly with U_{10} , and C_{10} is constant

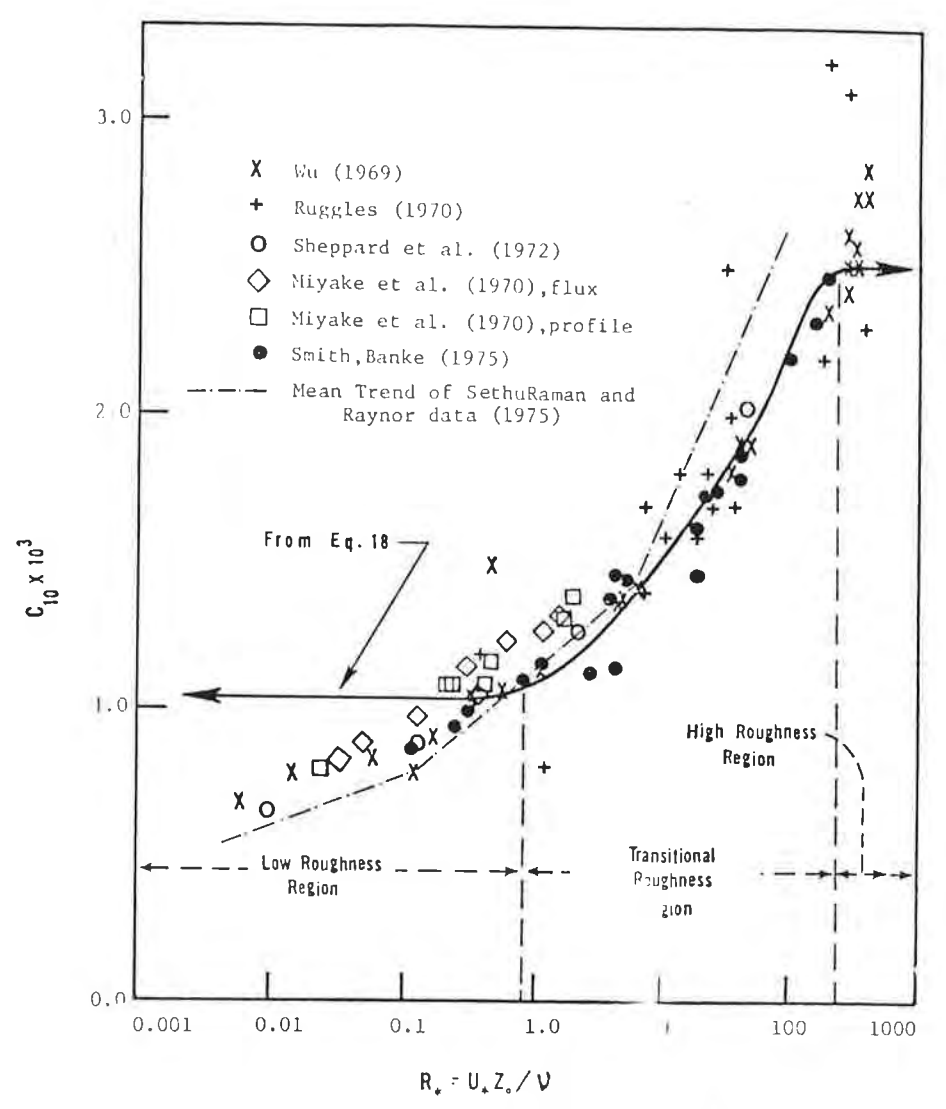


Fig. 8. Plot of C_{10} versus roughness Reynolds number.

and equal to 0.00254. In this region, full breaker saturation prevails. The data obtained by the authors show that within the range of wind velocities recorded in their work ($0 < U_2 < 12$ m/s, or $0 < U_{10} < 15$ m/s), the behavior of large open channels is consistent with that of seaways in the above respects.

- 2. Equations (18) and (19) are proposed to describe the shear velocity and the shear stress coefficient in the range $0 < U_{10} < 40$ m/s. These functions are continuous and consistent with the conditions described under point 1 above.
- 3. The roughness condition of the flow boundary can be classified as follows: (1) low roughness for $R_* \le 0.76$, or $u_* \le 0.23$ m/s, (2) transitional roughness for $0.76 < R_* < 245$, or $0.23 < u_* < 0.98$ m/s, and (3) high roughness for $R_* > 245$, or $u_* > 0.98$ m/s.
- 4. Experimental evidence indicates that Charnock's coefficient α is a nonlinear function of U_{10} over the entire range of values $0 < U_{10} < 40$ m/s and should not be assumed to be a constant for the estimation of C_{10} .

Acknowledgments. This study was made possible through funds partially provided by the Department of Water Resources, State of

California. The or sating personnel of the California Aqueduct are to be thanked for factuating the installation of measuring devices in the canal. The theore: all advice and collaboration of Emlyn Lloyd of the University of Lancuster were particularly valuable in the analysis of the dispersion of the shear stress coefficient data.

REFERENCES

Charnock, H., Whad stress on a water surface, Quart. J. Roy. Meteorol. Soc., 81, 639, 1955.

Clancy, M. T., Sea surface wind stress: Theoretical calculations compared with direct measurements, *Rep. TR-70-6*, Geophys. Sci. Lab., New York Univ. New York, 1970.

Davidson, K. L.. Observational results on the influence of stability and wind-wave coupling on momentum transfer and turbulent fluctuations over ocean waves, *Boundary Layer Meteorol.*, 6, 305, 1974.

Deacon, E. L., and E. K. Webb, Small-scale interactions, chap. 3, in *The Sea, Physical Oceanography*, edited by M. N. Hill, John Wiley, New York, 1962.

DeVries, J. J., Effects of wind on open channels, Ph.D. dissertation, 202 pp., Univ. of Calif., Davis, 1978.

Garratt, J. R., Review of drag coefficients over oceans and continents, Mon. Weather Rev., 109, 915, 1977.

Harding, E. T., and W. J. Kotsch, Heavy Weather Guide, U.S. Naval Institute, Annapolis, Md., 1965

Hawkins, H. F., and D. T. Rubsam, Hurricane Hilda, 1964, II, Struc-

- ture and budgets of the hurricane on October 1, 1964, Mon. Weather Rev., 96, 617, 1968.
- Hidy, G. M., and E. J. Plate, Wind action on water standing in a laboratory channel, J. Fluid Mech., 26, 651, 1966.
- Kitaygorodskiy, S. A., The Physics of Air-Sea Interaction, vol. 15, translated from Russian by A. Baruch, p. 86, Israel Program for Scientific Translations, Jerusalem, 1973.
- Kotsch, W. J., Weather for the Mariner, U.S. Naval Institute, Annapolis, Md., 1970.
- Kraus, E. B., Atmosphere-Ocean Interaction, Oxford University Press, New York, 1972.
- Malkus, J. A., Large scale interactions, chap. 4. in The Sea. Physical Oceanography, edited by M. N. Hill, John Wiley, New York, 1962.
- Melville, W. K., Wind stress and roughness length over breaking waves, J. Phys. Oceanogr., 7, 702, 1977.
- Miller, B. I., A study of the filling of Hurricane Donna (1960) over land, Mon. Weather Rev., 92, 389, 1964.
- Miyake, M., M. Donelan, A. McBean, C. Paulson, F. Badgley, and E. Leavitt, Comparison of turbulent fluxes over water determined by profile and eddy correlation techniques, Quart. J. Roy. Meteorol. Soc., 96, 132, 1970.
- Palmen, E., and H. Riehl, Budget of angular momentum and energy of tropical cyclones. J. Meteorol., 14, 150, 1957.
- Pond, S., and G. L. Pickard, Introductory Dynamic Oceanography, Pergamon, Oxford, England, 1978.
- Pond, S., T. Phelps, J. E. Paguin, G. McBeau, and R. W. Stewart, Measurement of the turbulent fluxes of momentum, moisture and sensible heat over the ocean, J. Atmos. Sci., 28, 901, 1971.

- Reid, L. J., and J. Berkson. Application of the logistic function to experimental data. J. Phys. Chem., 33, 760, 1929.
- Ruggles, K. W., The vertical wind profile over the ocean for light to moderate winds. J. Appl. Meteorol., 9, 389, 1970.
- SethuRaman, S., and G. S. Raynor, Surface drag coefficient dependence on the aerodynamic roughness of the sea. J. Geophys. Res., 80, 4983, 1975.
- Sheppard, P. A., D. T. Tribble, and J. R. Garratt, Studies of turbulence in the surface layer over water (Lough Neagh), Quart. J. Roy. Meteorol. Soc., 98, 627, 1972.
- Smith, S. D., and E. G. Banke, Variation of the sea surface drag coefficient with wind speed. Quart. J. Roy. Meteorol. Soc., 101, 665, 1975.
- Veenhuizen, S. D., Turbulent air flow over wind excited laboratory waves, Ph.D. dissertation, 110 pp., Colo. State Univ., Fort Collins, 1973.
- Wu, J., Laboratory studies in wind-wave interactions, J. Fluid Mech., 34, 91, 1968.
- Wu, J., Wind stress and surface roughness at air-sea interface, J. Geophys. Res., 74, 444, 1969.
- Wu, J., Physical and dynamical scales for generation of wind waves, J. Waterways Harbors Coastal Eng. Div. Amer. Soc. Civil Eng., 98 (WW2), 163, 1972.

(Received April 12, 1979; revised July 10, 1979; accepted August 6, 1979.)